Scientific Publications in 2016

(Xinglong 2.16 m Telescope)

兴隆观测基地 2.16 米望远镜
科学产出论文集

（2016 年）

Contents

The Astrophysical Journal, 832:139 (16pp), 2016 December 1 doi:10.3847/0004-637X/832/2/139

OPTICAL AND ULTRAVIOLET OBSERVATIONS OF THE VERY YOUNG TYPE IIP SN 2014cx IN NGC 337

Fang Huang[1], Xiaofeng Wang[1], Luca Zampieri[2], Maria Letizia Pumo[3], Iair Arcavi[4,5], Peter J. Brown[6], Melissa L. Graham[7], Alexei V. Filippenko[7], WeiKang Zheng[7], Griffin Hosseinzadeh[4], D. Andrew Howell[4,8], Curtis McCully[4], Liming Rui[1], Stefano Valenti[9], Tianmeng Zhang[10], Jujia Zhang[11,12], Kaicheng Zhang[1], and Lifan Wang[6]

[1] Physics Department and Tsinghua Center for Astrophysics, Tsinghua University, Beijing, 100084, China; huangfang@mail.tsinghua.edu.cn, wang_xf@mail.tsinghua.edu.cn
[2] INAF-Osservatorio Astronomico di Padova, Vicolo dell'Osservatorio 5, I-35122 Padova, Italy
[3] INAF-Osservatorio Astronomico di Palermo "Giuseppe S. Vaiana," Piazza del Parlamento 1, I-90134 Palermo, Italy
[4] Las Cumbres Observatory Global Telescope Network, 6740 Cortona Drive, Suite 102, Goleta, CA 93117, USA
[5] Kavli Institute for Theoretical Physics, Kohn Hall, University of California, Santa Barbara, CA 93106-4030, USA
[6] George P. and Cynthia Woods Mitchell Institute for Fundamental Physics & Astronomy, Texas A&M University, Department of Physics and Astronomy, 4242 TAMU, College Station, TX 77843, USA
[7] Department of Astronomy, University of California, Berkeley, CA 94720-3411, USA
[8] Department of Physics, University of California, Santa Barbara, Broida Hall, Mail Code 9530, Santa Barbara, CA 93106-9530, USA
[9] Department of Physics, University of California, Davis, CA 95616, USA
[10] Key Laboratory of Optical Astronomy, National Astronomical Observatories, Chinese Academy of Sciences, Beijing 100012, China
[11] Yunnan Observatories, Chinese Academy of Sciences, Kunming 650011, China
[12] Key Laboratory for the Structure and Evolution of Celestial Objects, Chinese Academy of Sciences, Kunming 650216, China

Received 2016 July 7; revised 2016 September 1; accepted 2016 September 3; published 2016 November 23

ABSTRACT

Extensive photometric and spectroscopic observations are presented for SN 2014cx, a Type IIP supernova (SN) exploding in the nearby galaxy NGC 337. The observations are performed in optical and ultraviolet bands, covering from −20 to +400 days from the peak light. The stringent detection limit from prediscovery images suggests that this supernova was actually detected within about one day after explosion. Evolution of the very early time light curve of SN 2014cx is similar to that predicted from a shock breakout and post-shock cooling decline before reaching the optical peak. Our photometric observations show that SN 2014cx has a plateau duration of ~100 days, an absolute V-band magnitude of ~ -16.5 mag at $t \approx 50$ days, and a nickel mass of $0.056 \pm 0.008\ M_{\odot}$. The spectral evolution of SN 2014cx resembles that of normal SNe IIP like SN 1999em and SN 2004et, except that it has a slightly higher expansion velocity (~4200 km s^{-1} at 50 days). From the cooling curve of photospheric temperature, we derive that the progenitor has a pre-explosion radius of ~640 $R_{\odot}$, consistent with those obtained from SuperNova Explosion Code modeling (~620 $R_{\odot}$) and hydrodynamical modeling of the observables (~570 $R_{\odot}$). Moreover, the hydrodynamical simulations yield a total explosion energy of $\sim 0.4 \times 10^{51}$ erg, and an ejected mass of ~8 $M_{\odot}$. These results indicate that the immediate progenitor of SN 2014cx is likely a red supergiant star with a mass of ~10 $M_{\odot}$.

Key words: galaxies: individual (NGC 337) – supernovae: general – supernovae: individual (SN 2014cx)

1. INTRODUCTION

Type IIP supernovae (SNe IIP) represent the most common subtype of stellar explosions, constituting about one-third of all SNe (Li et al. 2011). This subtype of SNe is thought to arise from core-collapse (CC) explosions of massive red supergiants (RSGs) with an initial mass of 8–25 $M_{\odot}$ according to theoretical models of stellar evolution (Heger et al. 2003). On the other hand, direct analyses of supernova position on pre-explosion images give a much narrower range for the progenitor mass, e.g., 8.5–16.5 $M_{\odot}$ (Li et al. 2007; Smartt 2009). Compared to other CC SNe, SNe IIP are characterized by prominent hydrogen features in their optical spectra (e.g., Filippenko 1997) and an extended plateau phase in their light curves. During the plateau phase, their luminosity remains almost constant as a result of the energy balance between the hydrogen recombination and expansion cooling. The plateau feature distinguishes SNe IIP from the Type IIL subclass, for which the light curve exhibits a linear decline (in mag day^{-1}) after the peak (Barbon et al. 1979). Recent statistical analyses show that the light-curve properties of SNe II may have a continuous distribution (e.g., Anderson et al. 2014; Sanders et al. 2015; Valenti et al. 2016), although there are also studies suggesting a distinct division between Type IIP and IIL SNe (Arcavi et al. 2012; Faran et al. 2014a, 2014b).

Over the years, numerous SNe IIP have been well studied, such as SN 1999em (Leonard et al. 2002), SN 2004et (Sahu et al. 2006), SN 2005cs (Pastorello et al. 2009), and SN 2013ej (Huang et al. 2015). These studies reveal a large spread in luminosities, plateau durations, expansion velocities, and nickel masses for SNe IIP (e.g., Hamuy 2003), which can be well understood with current explosion models (e.g., Kasen & Woosley 2009; Dessart et al. 2010; Pumo & Zampieri 2011, 2013). Nevertheless, early time observations are still sparse for SNe IIP, which are vital to constrain the explosion time and hence determine the properties of their progenitor stars (Nadyozhin 2003; Smartt et al. 2009). In particular, very early light curves of SNe IIP may be affected by a short, sharp blast of light as a result of shock breakout of the stellar surface, as predicted in massive-star core-collapse explosions (Falk & Arnett 1977; Klein & Chevalier 1978). SN 2014cx represents such a CC SN that is captured within about one day after the explosion.

SN 2014cx was independently discovered on UT 2014 September 2 by Nakano et al. (2014) and Holoien et al. (2014) in the nearby SBd galaxy NGC 337. Based on the astrometry

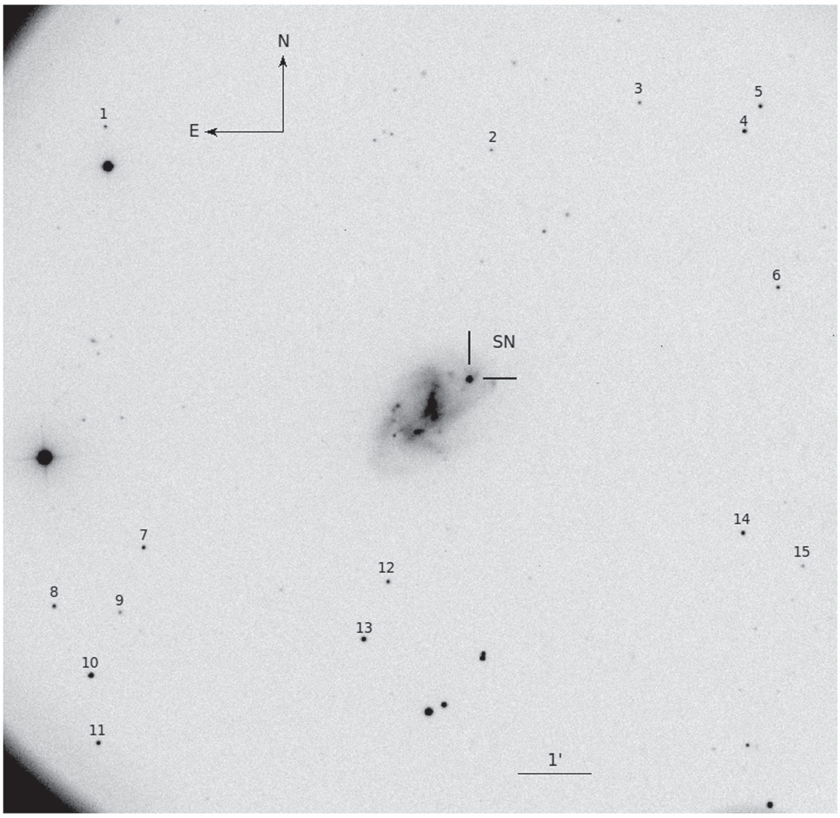

Figure 1. SN 2014cx in NGC 337. This *R*-band image was taken on 2014 October 25 with the 80 cm Tsinghua-NAOC Telescope. SN 2014cx and the 15 local sequence stars are marked.

from the USNO-A2.0 Catalog (Monet 1998), the J2000 coordinates of the SN are derived as $\alpha = 00^{h}59^{m}47\overset{s}{.}83$ and $\delta = -07^{\circ}34'19\overset{''}{.}3$, approximately $21\overset{''}{.}7$ N and $33\overset{''}{.}7$ W from the center of NGC 337 (Holoien et al. 2014). SN 2014cx was reported as a young SN II based on both optical (Elias-Rosa et al. 2014) and near-infrared (NIR; Morrell et al. 2014) spectra taken at about one day after the discovery. It was further classified as a Type IIP event according to the photometric observations by Andrews et al. (2015). We note that another SN IIP, SN 2011dq, also exploded in NGC 337. The distance to NGC 337 is estimated to be 18.0 ± 3.6 Mpc (distance modulus $\mu = 31.27 \pm 0.43$ mag) by the Tully–Fisher method (Sorce et al. 2014); here we adopt this value for SN 2014cx.

In this work, we present the results of our optical and UV observations of the Type IIP supernova SN 2014cx that was discovered at a very young age. The observations and data reduction are addressed in Section 2, the photometric evolution and spectroscopic evolution are described in Sections 3 and 4, respectively, and analysis of the progenitor properties of SN 2014cx via the photospheric temperature cooling curve and hydrodynamical modeling is given in Section 5. The main results are summarized in Section 6.

2. OBSERVATIONS AND DATA REDUCTION

2.1. Photometry

2.1.1. Optical Observations

We started the *UBVRI* follow-up campaign with the 0.8 m Tsinghua University-NAOC Telescope (hereafter TNT) at Xinglong Observatory in China (Wang et al. 2008; Huang et al. 2012). The TNT monitoring of SN 2014cx started on 2014 September 15 and continued until 2015 January 31. High-cadence Johnson *BV* and Sloan *gri* monitoring was conducted using the 1.0 m telescopes in the Las Cumbres Observatory Global Telescope network (hereafter LCOGT; Brown et al. 2013). The LCOGT data cover 2014 September 3 through 2015 September 17. In addition, 55 epochs of unfiltered data were collected with the 0.76 m Katzman Automatic Imaging Telescope (KAIT; Filippenko et al. 2001), extending to 2015 January 5.

All of the images were reduced with standard IRAF[13] routines. Point-spread-function (PSF) photometry was performed on TNT and LCOGT data using the SNOoPY package.[14] KAIT data were reduced using a PSF-based image-reduction pipeline (Ganeshalingam et al. 2010). The SN instrumental magnitudes were calibrated using 15 field stars (marked in Figure 1) from the Sloan Digital Sky Survey Data Release 9 catalog (Ahn et al. 2012) and transformed to the Johnson system. The magnitudes of the reference stars are listed in Table 1. The final flux-calibrated optical magnitudes of SN 2014cx are shown in Tables 2–4.

2.1.2. Swift Ultraviolet Observations

In addition to the ground-based observations, SN 2014cx was also monitored with the Ultraviolet/Optical Telescope

---

[13] IRAF is distributed by the National Optical Astronomy Observatories, which are operated by the Association of Universities for Research in Astronomy, Inc., under cooperative agreement with the National Science Foundation (NSF).

[14] http://sngroup.oapd.inaf.it/snoopy.html

Table 1
Photometric Standard Stars in the Field of SN 2014cx (1σ Uncertainties)

Star ID	α_{J2000} (h m s)	δ_{J2000} (° ′ ″)	U (mag)	B (mag)	V (mag)	R (mag)	I (mag)
1	1:00:07.08	−7:30:33.54	20.07(09)	19.35(06)	18.31(04)	17.69(05)	17.06(09)
2	0:59:45.87	−7:31:12.11	20.17(11)	19.71(06)	18.66(04)	18.04(04)	17.43(08)
3	0:59:37.53	−7:30:40.79	21.32(25)	20.43(08)	18.79(05)	17.69(11)	16.26(22)
4	0:59:31.84	−7:31:09.63	20.16(10)	19.10(08)	17.56(05)	16.62(07)	15.61(15)
5	0:59:30.89	−7:30:49.81	19.23(06)	18.56(05)	17.58(04)	17.00(04)	16.44(08)
6	0:59:30.53	−7:33:19.29	16.08(03)	17.22(04)	17.29(03)	17.37(04)	17.50(08)
7	1:00:06.41	−7:36:20.14	20.47(15)	19.52(08)	17.96(04)	17.01(07)	16.03(15)
8	1:00:11.55	−7:37:03.82	18.61(04)	18.39(05)	17.56(03)	17.08(04)	16.59(07)
9	1:00:07.93	−7:37:12.15	19.69(08)	19.38(05)	18.45(03)	17.89(04)	17.31(08)
10	1:00:09.75	−7:38:02.37	17.27(03)	17.11(05)	16.28(03)	15.77(04)	15.24(08)
11	1:00:09.58	−7:38:58.23	18.38(04)	18.07(05)	17.19(03)	16.66(04)	16.12(08)
12	0:59:53.05	−7:37:00.70	18.26(04)	18.24(04)	17.52(03)	17.08(03)	16.65(06)
13	0:59:54.59	−7:37:46.63	18.04(04)	17.44(05)	16.47(03)	15.89(04)	15.34(08)
14	0:59:33.31	−7:36:38.75	18.08(09)	17.86(04)	17.12(03)	16.69(03)	16.28(06)
15	0:59:30.12	−7:37:08.94	18.66(10)	18.56(03)	18.20(02)	17.98(03)	17.77(05)

Table 2
Optical Photometry of SN 2014cx from TNT (1σ Uncertainties)

UT Date (yy/mm/dd)	MJD	Phase[a] (day)	U (mag)	B (mag)	V (mag)	R (mag)	I (mag)
2014 Sep 15	56915.75	13.86	14.30(04)	15.23(03)	14.89(04)	14.70(10)	14.60(05)
2014 Sep 17	56917.75	15.86	⋯	15.14(03)	14.89(07)	14.70(07)	14.56(03)
2014 Oct 12	56942.75	40.86	16.26(08	15.75(01)	⋯	⋯	⋯
2014 Oct 13	56943.75	41.86	16.37(12)	15.87(04)	15.08(04)	14.75(06)	14.46(04)
2014 Oct 21	56951.50	49.61	16.49(06)	15.87(04)	15.01(03)	14.67(04)	14.40(04)
2014 Oct 24	56954.50	52.61	16.57(11)	15.95(03)	15.05(02)	14.78(04)	14.39(04)
2014 Oct 25	56955.50	53.61	16.67(06)	15.98(04)	15.11(02)	14.75(07)	⋯
2014 Oct 26	56956.50	54.61	16.79(05)	16.07(02)	15.11(03)	14.73(05)	⋯
2014 Nov 08	56969.50	67.61	16.87(09)	16.27(03)	15.11(03)	14.77(03)	14.38(04)
2014 Nov 10	56971.50	69.61	17.07(08)	16.27(05)	15.03(03)	14.75(04)	14.44(05)
2014 Nov 11	56972.50	70.61	17.07(05)	16.23(03)	15.06(04)	14.74(04)	14.38(04)
2014 Nov 12	56973.50	71.61	⋯	⋯	15.07(03)	14.78(02)	⋯
2014 Nov 18	56979.50	77.61	17.28(16)	⋯	15.18(05)	14.89(07)	14.40(06)
2014 Nov 19	56980.50	78.61	17.30(15)	16.36(03)	15.15(04)	14.84(05)	14.41(05)
2014 Nov 22	56983.50	81.61	17.46(06)	16.42(05)	15.19(05)	14.82(06)	14.50(04)
2014 Nov 23	56984.50	82.61	17.47(11)	16.34(02)	15.20(04)	14.84(05)	14.51(03)
2014 Nov 24	56985.50	83.61	⋯	⋯	15.22(02)	14.91(03)	14.48(03)
2014 Dec 03	56994.50	92.61	⋯	16.62(04)	15.37(02)	15.03(05)	14.64(02)
2014 Dec 04	56995.50	93.61	⋯	⋯	15.41(02)	15.06(03)	14.59(02)
2014 Dec 05	56996.50	94.61	17.79(25)	16.73(04)	15.45(02)	15.12(03)	14.65(06)
2014 Dec 07	56998.50	96.61	⋯	16.82(05)	15.66(02)	15.18(02)	14.61(04)
2014 Dec 08	56999.50	97.61	17.88(11)	16.94(04)	15.67(06)	15.28(07)	14.74(06)
2014 Dec 16	57007.50	105.61	⋯	17.22(05)	15.82(03)	99.50(05)	14.90(03)
2014 Dec 17	57008.50	106.61	18.03(09)	17.52(06)	16.13(04)	15.46(06)	15.04(04)
2014 Dec 19	57010.50	108.61	⋯	17.27(05)	16.21(04)	15.64(05)	15.23(05)
2014 Dec 20	57011.50	109.61	⋯	17.57(07)	16.10(06)	15.51(05)	15.22(07)
2014 Dec 21	57012.50	110.61	⋯	17.58(05)	16.28(03)	15.68(04)	⋯
2015 Jan 01	57023.50	121.61	⋯	18.04(09)	17.01(06)	16.30(03)	15.92(04)
2015 Jan 03	57025.50	123.61	⋯	18.20(06)	17.02(07)	16.31(05)	15.86(03)
2015 Jan 06	57028.50	126.61	⋯	⋯	⋯	16.31(05)	15.91(05)
2015 Jan 07	57029.50	127.61	⋯	⋯	17.01(04)	16.39(07)	15.89(06)
2015 Jan 08	57030.50	128.61	⋯	18.09(05)	17.21(05)	16.37(05)	15.91(05)
2015 Jan 12	57034.50	132.61	⋯	⋯	⋯	16.34(02)	15.93(04)
2015 Jan 13	57035.50	133.61	⋯	18.23(05)	17.13(04)	16.36(04)	15.95(04)
2015 Jan 18	57040.50	138.61	⋯	⋯	⋯	16.42(03)	16.00(02)
2015 Jan 19	57041.50	139.61	⋯	⋯	17.18(04)	16.41(05)	16.01(05)
2015 Jan 31	57053.50	151.61	⋯	⋯	⋯	16.67(06)	16.20(04)

Note.
[a] Relative to the explosion date, MJD = 56,901.89.

Table 3
Optical Photometry of SN 2014cx from LCOGT (1σ Uncertainties)

UT Date (yy/mm/dd)	MJD	Phase[a] (day)	B (mag)	V (mag)	g (mag)	r (mag)	i (mag)
2014 Sep 03	56903.130	1.240	15.32(03)	15.32(01)	15.23(03)	15.45(02)	15.54(02)
2014 Sep 03	56903.390	1.500	15.34(03)	15.28(03)	15.16(04)	15.36(03)	15.51(02)
2014 Sep 07	56907.770	5.880	15.12(03)	15.01(03)	14.93(03)	14.84(02)	14.92(03)
2014 Sep 12	56912.685	10.795	15.10(03)	14.93(02)	14.96(01)	14.98(03)	14.98(02)
2014 Sep 14	56914.755	12.865	15.20(03)	14.92(03)	15.07(03)	14.95(03)	14.92(04)
2014 Sep 16	56916.690	14.800	…	…	15.00(02)	14.82(02)	14.93(03)
2014 Sep 18	56918.685	16.795	15.25(04)	14.94(05)	15.03(03)	14.81(02)	14.92(07)
2014 Sep 20	56920.545	18.655	15.30(02)	14.91(02)	…	14.79(03)	14.88(07)
2014 Sep 23	56923.540	21.650	15.29(02)	14.88(03)	15.04(04)	14.76(03)	14.94(05)
2014 Sep 27	56927.545	25.655	15.45(03)	14.92(02)	15.12(03)	14.76(03)	14.82(04)
2014 Sep 29	56929.395	27.505	15.48(03)	14.94(03)	…	…	…
2014 Oct 02	56932.520	30.630	15.58(03)	14.94(02)	15.20(01)	14.76(01)	14.81(05)
2014 Oct 03	56933.715	31.825	15.56(03)	14.97(03)	15.29(04)	14.78(02)	14.79(03)
2014 Oct 09	56939.690	37.800	15.73(04)	15.01(03)	15.34(05)	14.87(03)	14.80(02)
2014 Oct 13	56943.830	41.940	15.80(02)	15.03(02)	15.39(03)	14.80(02)	14.85(02)
2014 Oct 17	56947.475	45.585	15.86(03)	15.06(02)	15.40(01)	14.80(02)	14.79(02)
2014 Oct 21	56951.565	49.675	…	…	15.42(02)	14.87(02)	14.74(02)
2014 Oct 25	56955.405	53.515	15.94(04)	15.12(04)	15.47(03)	14.76(04)	14.80(03)
2014 Nov 01	56962.565	60.675	16.06(03)	15.07(03)	15.55(03)	14.83(03)	14.77(03)
2014 Nov 06	56967.980	66.090	16.13(02)	15.10(03)	15.54(03)	14.82(03)	14.79(03)
2014 Nov 13	56974.630	72.740	16.26(03)	15.16(03)	15.63(04)	14.94(04)	14.85(05)
2014 Nov 18	56979.900	78.010	16.30(03)	15.16(02)	15.68(03)	14.89(02)	14.88(03)
2014 Nov 25	56986.060	84.170	16.43(03)	15.26(02)	15.80(04)	14.99(03)	14.89(03)
2014 Nov 27	56988.890	87.000	16.41(03)	15.25(03)	…	…	…
2014 Nov 28	56989.780	87.890	16.49(04)	15.32(03)	15.83(02)	14.99(02)	14.97(03)
2014 Dec 04	56995.820	93.930	16.65(04)	15.44(02)	15.96(04)	15.08(03)	15.00(02)
2014 Dec 04	56995.850	93.960	16.71(04)	15.47(03)	…	…	…
2014 Dec 09	57000.120	98.230	17.04(05)	15.57(02)	16.15(04)	15.33(03)	15.11(04)
2014 Dec 12	57003.830	101.940	16.95(04)	15.67(02)	16.24(03)	15.33(02)	15.24(05)
2014 Dec 16	57007.545	105.655	17.26(05)	15.92(03)	16.56(04)	15.51(03)	15.46(02)
2014 Dec 20	57011.480	109.590	17.63(04)	16.25(02)	16.84(03)	15.74(02)	15.67(05)
2014 Dec 24	57015.425	113.535	17.84(06)	16.60(03)	17.18(04)	16.03(01)	15.92(03)
2014 Dec 30	57021.430	119.540	18.09(07)	17.04(04)	17.53(05)	16.44(03)	16.44(09)
2015 Jan 02	57024.485	122.595	…	…	17.55(06)	16.48(05)	16.47(06)
2015 Jan 03	57025.795	123.905	18.16(05)	17.04(03)	17.59(04)	16.48(03)	16.43(05)
2015 Jan 05	57027.830	125.940	18.22(05)	17.14(03)	17.66(05)	16.51(02)	16.54(03)
2015 Jan 08	57030.445	128.555	18.36(05)	17.21(04)	17.76(04)	16.59(03)	16.58(03)
2015 Jan 09	57031.815	129.925	18.33(05)	17.19(03)	…	…	…
2015 Jan 10	57032.060	130.170	18.31(05)	17.15(03)	…	…	…
2015 Jan 11	57033.795	131.905	18.37(05)	17.28(02)	17.66(03)	16.64(02)	16.58(02)
2015 Jan 14	57036.070	134.180	18.35(05)	17.23(03)	17.69(04)	16.63(03)	16.61(04)
2015 Jan 15	57037.445	135.555	…	…	17.81(04)	16.58(03)	16.62(03)
2015 Jan 16	57038.790	136.900	18.40(07)	17.23(04)	17.74(04)	16.62(03)	16.64(03)
2015 Jan 22	57044.790	142.900	…	17.24(03)	17.76(04)	16.71(05)	16.65(05)
2015 Jan 28	57050.085	148.195	18.44(07)	17.32(04)	17.86(05)	16.69(03)	16.76(05)
2015 Jan 29	57051.080	149.190	18.41(08)	17.33(04)	17.93(06)	16.72(03)	16.82(05)
2015 Feb 11	57064.775	162.885	18.49(08)	17.52(04)	17.91(04)	16.79(03)	16.85(04)
2015 Feb 20	57073.075	171.185	18.45(08)	17.57(04)	…	…	…
2015 Jun 04	57177.420	275.530	…	…	…	17.81(04)	18.06(10)
2015 Jun 22	57195.790	293.900	…	…	…	18.03(09)	18.02(06)
2015 Jun 30	57203.395	301.505	18.92(05)	18.44(05)	18.65(04)	17.85(04)	18.206(04)
2015 Jul 17	57220.260	318.370	18.93(05)	18.52(04)	18.69(07)	18.11(06)	18.200(06)
2015 Aug 13	57247.330	345.440	…	…	18.70(05)	18.36(05)	18.259(04)
2015 Aug 29	57263.255	361.365	…	…	19.02(21)	18.27(23)	…
2015 Sep 17	57282.390	380.500	…	…	19.03(05)	18.50(05)	18.198(05)

Note.
[a] Relative to the explosion date, MJD = 56,901.89.

(UVOT; Roming et al. 2005) on board the *Swift* spacecraft through the *uvw*2, *uvm*2, *uvw*1, *u*, *b*, and *v* filters. The UV observations began on 2014 September 3 and ended on 2014 October 24. The data were obtained from the *Swift* Optical/Ultraviolet Supernova Archive (Brown et al. 2014). The reduction method for UVOT photometry is

Table 4
Unfiltered Photometry of SN 2014cx (1σ Uncertainties)

MJD	Phase[a]	Mag	Error	Telescope	MJD	Phase[a]	Mag	Error	Telescope
56871.49	−30.40	>18.76	⋯	KAIT	56949.38	47.49	14.87	0.08	KAIT
56876.49	−25.40	>19.16	⋯	KAIT	56950.31	48.42	14.73	0.12	KAIT
56877.48	−24.41	>19.06	⋯	KAIT	56952.31	50.42	14.78	0.06	KAIT
56879.41	−22.48	>18.50	⋯	KAIT	56954.33	52.44	14.79	0.05	KAIT
56880.41	−21.48	>18.67	⋯	KAIT	56957.31	55.42	14.86	0.05	KAIT
56881.39	−20.50	>18.38	⋯	KAIT	56958.33	56.44	14.84	0.05	KAIT
56886.46	−15.43	>19.48	⋯	KAIT	56959.28	57.39	14.80	0.07	KAIT
56887.47	−14.42	>19.05	⋯	KAIT	56960.26	58.37	14.88	0.06	KAIT
56888.45	−13.44	>19.22	⋯	KAIT	56964.29	62.40	14.90	0.07	KAIT
56889.45	−12.44	>19.14	⋯	KAIT	56970.32	68.43	14.80	0.09	KAIT
56890.45	−11.44	>19.13	⋯	KAIT	56971.26	69.37	14.86	0.07	KAIT
56891.44	−10.45	>19.14	⋯	KAIT	56972.26	70.37	14.80	0.06	KAIT
56892.47	−9.42	>19.26	⋯	KAIT	56976.32	74.43	14.90	0.07	KAIT
56893.41	−8.48	>19.15	⋯	KAIT	56977.25	75.36	14.85	0.06	KAIT
56894.48	−7.41	>18.88	⋯	KAIT	56978.25	76.36	14.85	0.12	KAIT
56895.42	−6.47	>19.17	⋯	KAIT	56985.23	83.34	14.89	0.08	KAIT
56896.41	−5.48	>19.22	⋯	KAIT	56986.24	84.35	14.96	0.06	KAIT
56897.49	−4.40	>19.14	⋯	KAIT	56987.23	85.34	15.09	0.05	KAIT
56898.40	−3.49	>19.13	⋯	KAIT	56988.26	86.37	15.11	0.08	KAIT
56900.40	−1.49	>19.19	⋯	KAIT	56989.19	87.30	14.99	0.06	KAIT
56901.39	−0.50	>19.11	⋯	KAIT	56990.18	88.29	15.07	0.05	KAIT
56902.40	0.51	15.69	0.05	KAIT	56999.24	97.35	15.27	0.07	KAIT
56903.36	1.47	15.17	0.07	KAIT	57001.22	99.33	15.28	0.08	KAIT
56920.41	18.52	14.85	0.06	KAIT	57006.14	104.25	15.47	0.09	KAIT
56922.33	20.44	14.65	0.06	KAIT	57015.12	113.23	16.05	0.07	KAIT
56923.30	21.41	14.67	0.08	KAIT	57027.08	125.19	16.54	0.15	KAIT
56924.30	22.41	14.65	0.05	KAIT	56902.57	0.68	15.6	⋯	Koichi Itagaki
56944.36	42.47	14.70	0.07	KAIT	56903.04	1.15	15.2	⋯	T. Yusa
56946.35	44.46	14.83	0.11	KAIT	56906.93	5.04	14.8	⋯	Paolo Campaner

Note.
[a] Relative to the explosion date, MJD = 56,901.89.

Table 5
UV and Optical Photometry of SN 2014cx from *Swift* (1σ Uncertainties)

UT Date (yy/mm/dd)	MJD	Phase[a] (day)	*uvw*2 (mag)	*uvm*2 (mag)	*uvw*1 (mag)	*U* (mag)	*B* (mag)	*V* (mag)
2014 Sep 3	56903.03	1.14	13.62(05)	13.70(05)	13.80(05)	13.95(04)	15.34(06)	15.42(07)
2014 Sep 4	56904.62	2.73	13.70(05)	13.67(05)	13.66(05)	13.74(04)	14.97(05)	15.09(06)
2014 Sep 5	56905.26	3.37	13.86(05)	13.71(05)	13.77(05)	13.78(04)	14.95(05)	15.09(06)
2014 Sep 6	56906.09	4.20	14.06(05)	13.85(05)	13.80(05)	13.78(04)	14.96(05)	15.01(06)
2014 Sep 7	56907.25	5.36	14.32(06)	14.03(06)	13.92(05)	13.78(04)	14.92(05)	15.00(06)
2014 Sep 8	56908.31	6.42	14.54(07)	⋯	14.00(05)	13.80(04)	14.88(05)	⋯
2014 Sep 9	56909.09	7.20	14.80(07)	14.40(06)	14.11(05)	13.83(04)	14.92(05)	14.97(06)
2014 Sep 12	56912.91	11.02	15.48(09)	15.19(08)	14.60(06)	13.99(04)	14.90(05)	14.97(06)
2014 Sep 16	56916.28	14.39	16.22(11)	16.25(10)	15.30(08)	14.24(05)	15.02(05)	14.99(06)
2014 Sep 20	56920.78	18.89	17.67(24)	17.80(24)	16.32(11)	14.62(05)	15.25(06)	14.96(06)
2014 Sep 24	56924.71	22.82	18.21(36)	18.37(42)	16.82(15)	15.28(07)	15.35(06)	14.94(06)
2014 Sep 28	56928.60	26.71	18.55(46)	⋯	17.51(21)	15.62(07)	15.45(06)	14.96(06)
2014 Oct 4	56934.23	32.34	⋯	⋯	18.08(30)	15.85(07)	15.62(06)	14.95(07)
2014 Oct 11	56941.27	39.38	⋯	⋯	⋯	16.22(07)	15.80(06)	15.08(06)
2014 Oct 19	56949.91	48.02	⋯	⋯	18.62(47)	16.46(07)	16.00(06)	15.12(06)
2014 Oct 22	56952.70	50.81	⋯	⋯	⋯	16.39(14)	15.96(09)	15.06(09)
2014 Oct 24	56954.60	52.71	⋯	⋯	⋯	16.56(07)	16.01(06)	15.09(06)

Note.
[a] Relative to the explosion date, MJD = 56,901.89.

based on that of Brown et al. (2009), which includes aperture photometry after subtracting off the underlying galaxy count rates, and adopting the updated zeropoints and time-dependent sensitivity from Breeveld et al. (2011). The final UVOT photometry of SN 2014cx is presented in Table 5.

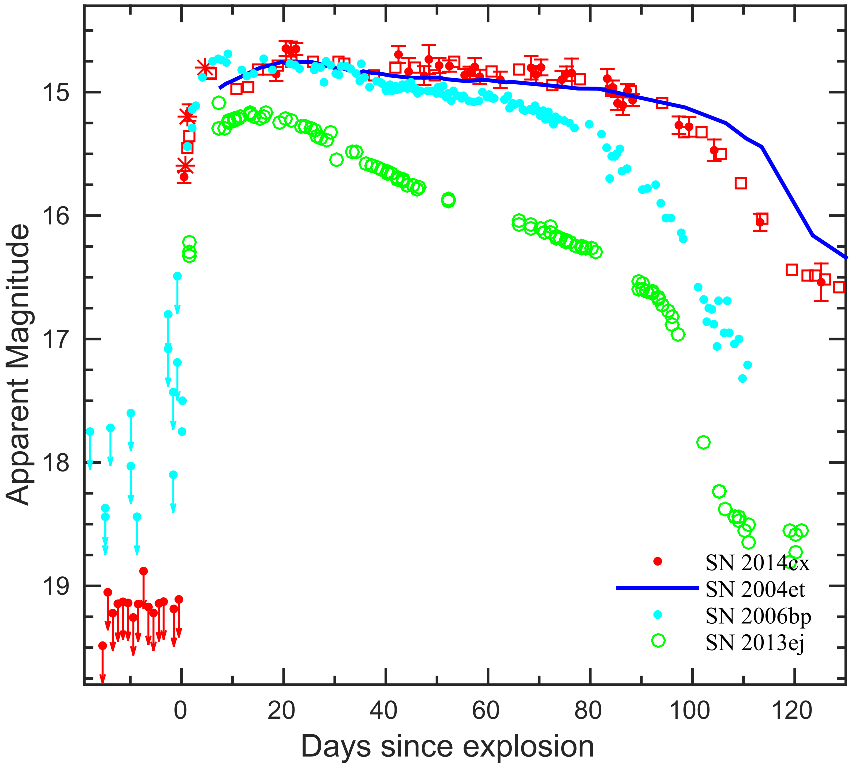

Figure 2. KAIT unfiltered (red circle) and LCOGT *r*-band (red square) light curve of SN 2014cx unfiltered detections from the *Bright Supernovae* website (http://www.rochesterastronomy.org/snimages/; red star), SN 2004et in the *R* band (blue line), SN 2006bp (cyan), and SN 2013ej (green). For KAIT data, detections are plotted with filled circles, and arrows represent 4σ upper limits.

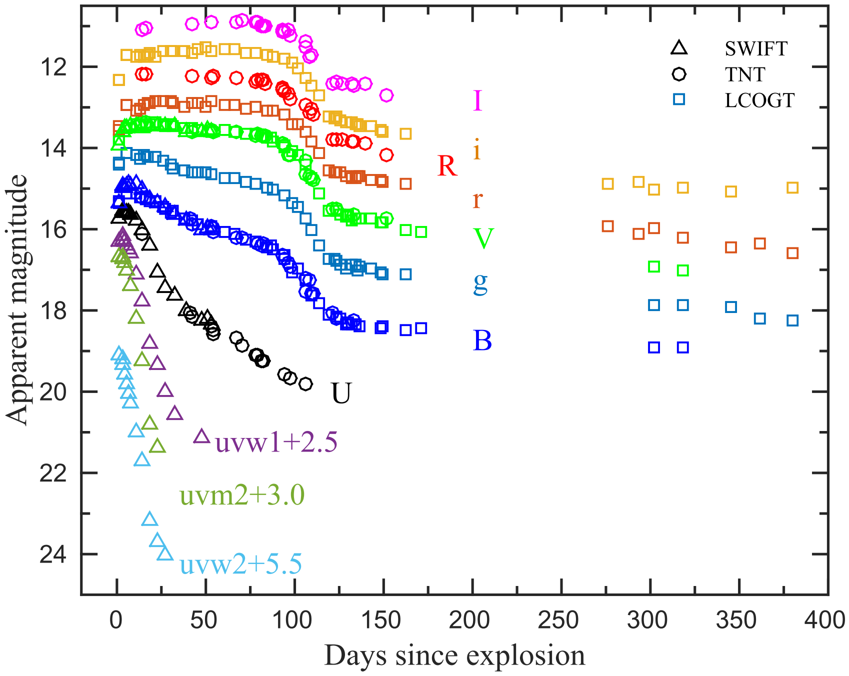

Figure 3. Photometric evolution of SN 2014cx in UV and optical bands. The phase is given relative to the estimated explosion date, MJD = 56,901.89.

2.2. Spectroscopy

The spectroscopic monitoring campaign of SN 2014cx started on 2014 September 7 and continued for ~400 days. Fourteen low-resolution optical spectra were obtained using the LCOGT 2 m Faulkes Telescope South (FTS; with FLOYDS), the Xinglong 2.16 m telescope (with BFOSC), the Lijiang 2.4 m telescope (with YFOSC), the LCOGT 2 m Faulkes Telescope North (FTN; with FLOYDS), the GEMINI-North

Telescope (GNT; with GMOS), and the Keck I 10 m telescope (with LRIS); see Table 7 for the detailed information on the spectroscopic observations.

The spectra were all reduced in a standard manner using various tasks within IRAF. After the preliminary reduction (including bias/overscan correction, flat fielding, and cosmic-ray removal), the one-dimensional spectra were extracted using the optimal extraction method (Horne 1986). Wavelengths of the SN spectra were calibrated using the Fe/Ar and Fe/Ne lamp spectra. For the FLOYDS spectra, a Hg/Ar lamp is used for wavelength calibration. The spectra were then flux calibrated using the instrumental sensitivity curves of spectrophotometric standard stars observed on the same (or nearby) night and with the same instrumental setup.

3. PHOTOMETRIC ANALYSIS

3.1. The Early Time Evolution

With modern high-cadence surveys, we are able to detect young SNe and trigger follow-up observations immediately. Such early time detections help constrain the explosion properties and (with luck) even reveal shock breakout, which often happens hours after explosion (Quimby et al. 2007; Schawinski et al. 2008; Tominaga et al. 2009; Gezari et al. 2015; Dhungana et al. 2016; Garnavich et al. 2016).

The field of SN 2014cx was monitored daily by KAIT in the clear band (i.e., unfiltered) before the explosion, leading to the earliest detection of this object after the explosion. Figure 2 shows the KAIT unfiltered light curve, spanning from a few weeks before the explosion to ~120 days after. A few early time observations obtained by amateurs in unfiltered mode are also overplotted. As can be seen, SN 2014cx was not detected on 2014 September 1 (MJD = 56,901.39) with a limit of >19.1 mag, but it was detected one day later (MJD = 56,902.40) at 15.69 mag. We therefore adopt this epoch (MJD = 56901.89 ± 0.5) as the reference date for the shock breakout for SN 2014cx, and this determination sets one of the tightest constraints on the shock breakout time for a SN IIP based on the observations of ground-based telescopes.

Table 6
Photometric Parameters of SN 2014cx

	U	B	V	R	I
Peak magnitude	13.75	15.08	14.91	⋯	⋯
Phase of maximum[a]	3.29	8.24	10.83	⋯	⋯
Plateau magnitude	⋯	⋯	15.10	14.75	14.38
Decay rate (mag/100 day)	⋯	0.42	0.95	1.09	1.13

Note.
[a] Relative to the explosion date, MJD = 56,901.89.

The unfiltered light curve of SN 2014cx at early time (0–20 days) is very similar to those of SN 2006bp and SN 2013ej. It seems to experience three stages. First, the SN brightened by more than 4 mag over the first 1.5–2.0 days, and it then dimmed and rebrightened toward the primary peak at $t \approx 20$ days. This trend is actually more prominent in the early time evolution of the LCOGT r-band light curve (see Figure 2), with a noticeable dip occurring at $t \approx 10$ days after explosion. Such a behavior is also seen in the comparison object SN 2006bp (and possibly SN 2013ej), which is likely related to the shock breakout of the supernova surface and its cooling phase (Quimby et al. 2007).

3.2. Overall Evolution of the Light Curves

Figure 3 shows the multicolor photometric evolution of SN 2014cx during the period from $t = +1$ to $t = +380$ days after the explosion. At the earliest phases, the light curves exhibit a rapid rise in the UV and optical bands, but with a slower pace at longer wavelengths (see Table 6). By fitting a low-order polynomial to the data around maximum light, we determine the magnitudes and corresponding dates at peak brightness. These results are also presented in Table 6. We note that the rise time in the B band is ~8 days, which agrees well with the statistical result from a large sample of SNe II (González-Gaitán et al. 2015).

One can see from Figure 3 that the UV light curves show rapid post-peak declines, with slopes of 0.16, 0.23, and 0.25 mag day^{-1} in the $uvw1$, $uvw2$, and $uvm2$ bands, respectively. The optical light curves, in contrast, drop slowly and settle to the plateau phase. A decline rate of $\beta_{100}^{B} = 2.5$ mag is

Table 7
Observing Log for Optical Spectra of SN 2014cx

UT Date	MJD	Phase[a] (days)	Range (Å)	Exposure (s)	Telescope + Instrument
2014 Sep 7	56907.74	5.8	3400–8500	2700	LCOGT 2.0 m Telescope South + FLOYDS
2014 Sep 12	56912.69	10.8	3400–8500	1800	LCOGT 2.0 m Telescope South + FLOYDS
2014 Sep 18	56918.66	16.8	3480–8850	2100	Xinglong 2.16 m + BFOSC
2014 Sep 22	56922.46	20.6	3400–9000	1800	LCOGT 2.0 m Telescope South + FLOYDS
2014 Sep 26	56926.71	24.8	3400–10,000	1800	LCOGT 2.0 m Telescope South + FLOYDS
2014 Sep 29	56929.65	27.8	3400–10,000	1800	LCOGT 2.0 m Telescope South + FLOYDS
2014 Oct 3	56933.70	31.8	3400–10,000	2700	LCOGT 2.0 m Telescope South + FLOYDS
2014 Oct 12	56942.46	40.6	3400–10,000	2700	LCOGT 2.0 m Telescope South + FLOYDS
2014 Oct 16	56946.60	44.6	3500–9000	2100	Lijiang 2.4 m + YFOSC
2014 Oct 21	56951.65	49.8	3400–10,000	2700	LCOGT 2.0 m Telescope South + FLOYDS
2014 Dec 7	56998.36	96.5	3400–10,000	2700	LCOGT 2.0 m Telescope North + FLOYDS
2015 Jan 8	57030.43	128.6	3900–8800	2400	Xinglong 2.16 m + BFOSC
2015 Jul 27	57230.62	328.7	3900–9700	900	Gemini-North 8.1 m + GMOS
2015 Oct 10	57305.38	403.5	3800–10,000	1200	Keck I 10 m + LRIS

Note.
[a] Relative to the explosion date, MJD = 56,901.89.

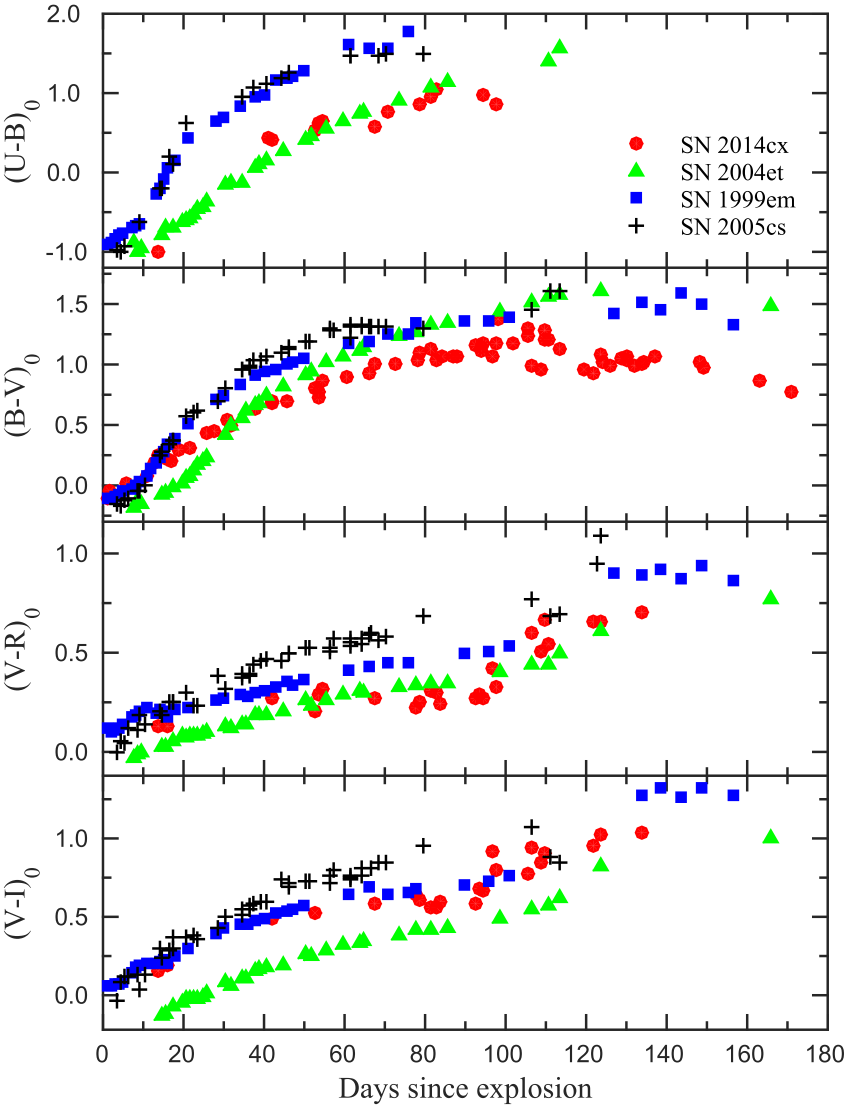

Figure 4. Dereddening optical color evolution of SN 2014cx compared with those of other SNe IIP : SNe 1999em, 2004et, and 2005cs.

measured for the *B*-band light curve over the first 100 days after maximum light, consistent with the typical value obtained for normal SNe IIP (i.e., $\beta^{B}_{100} < 3.5$ mag; Patat et al. 1994). The *V*-band brightness declines by ~0.2 mag in the first 50 days after the peak, which also falls into the SN IIP group according to the criterion of Faran et al. (2014b). For SN 2014cx, the plateau phase lasts for ~100 days, and its brightness stays roughly constant, especially in the *VrRiI* bands.

After the plateau, the SN 2014cx experiences a sudden drop in brightness in all optical bands, with magnitude declines of 1.5–2.0 mag in ~20 days. To derive the parameters about the transitional phase, we fit the *V*-band light curve using Equation (4) from Olivares et al. (2010). The middle date of the transition phase, t_{PT}, is found to be ~109 days, and the width of the transition phase is ~7 days. During the tail phase (i.e., $t \approx 130$–170 days), the decline rates in *B*, *V*, *R*, and *I* are measured to be 0.42, 0.95, 1.09, and 1.13 mag $(100\ \mathrm{day})^{-1}$, respectively. These values are similar to those of normal SNe IIP such as SN 1999em (Elmhamdi et al. 2003). In the *V* and *R* bands, the decline rates are found to be comparable to the values expected for the radioactive decay, 0.98 mag $(100\ \mathrm{day})^{-1}$ (Patat et al. 1994). This indicates that the gamma-ray photons were effectively trapped in the ejecta at this phase. After $t \approx 170$ days, the light curves tend to show slower decline rates relative to the earlier nebular phase. For example, the decline rate of *B*- and *V*-band light curve is measured to be 0.32 and 0.65 mag $(100\ \mathrm{day})^{-1}$ during the period from 170 days $< t <$ 320 days. And this decay rate is found to be 0.46, 0.85, and 0.81 mag $(100\ \mathrm{day})^{-1}$ in *gri* bands at similar phase. This slower evolution can be due to interaction of SN ejecta with the circumstellar materials (CSM) surrounding the SN or a scattered-light echo (see discussions in Section 4.1).

3.3. Color Curves

The Galactic reddening in the direction of NGC 337 is $E(B-V)_{\mathrm{MW}} = 0.10$ mag (Schlafly & Finkbeiner 2011). We did not detect any significant features of Na I D absorption produced by the host galaxy in our 14 low-resolution spectra, suggesting that host-galaxy reddening might be negligible for SN 2014cx. As an alternative, we also use the color method proposed by Olivares et al. (2010) to estimate the reddening

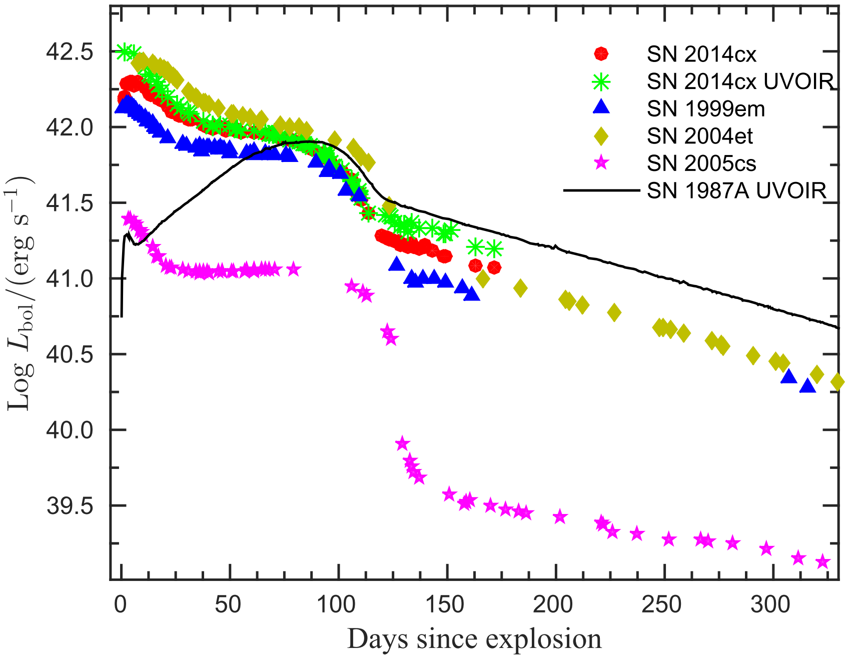

Figure 5. Comparison of the bolometric luminosity evolution of SN 2014cx and other well-studied SNe IIP.

due to the host galaxy. This method assumes that the intrinsic $V - I$ color of SNe IIP is constant (i.e., $(V - I)_0 = 0.656$ mag) toward the end of the plateau. After correcting for the Galactic reddening, the $V - I$ color of SN 2014cx is found to be 0.596 mag at $t = 79$ days, which gives a negative host-galaxy extinction for this object. Thus, we adopt $E(B - V)_{\rm tot} = 0.10$ mag in the following analysis, which corresponds to a total line-of-sight extinction of $A_V = 0.31$ mag assuming the ratio of total to selective extinction $R_V = 3.1$ (Cardelli et al. 1989).

The reddening-corrected $(U - B)_0$, $(B - V)_0$, $(V - R)_0$, and $(V - I)_0$ color curves of SN 2014cx are shown in Figure 4. For comparison, we overplot the dereddened color curves of three well-studied Type IIP SNe 1999em, 2004et, and 2005cs. The color evolution of SN 2014cx follows the general trend seen in SNe IIP: a rapid decrease from blue (high temperature) to red (low temperature) during the photospheric phase. The $(U - B)_0$ and $(B - V)_0$ colors become redder by ~1–2 mag in the first 100 days, while the $(V - R)_0$ and $(V - I)_0$ colors evolve slowly and become red by only ~0.5 mag. The $(B - V)_0$ color turns blue after t ~120 days, when the nebular phase begins. The overall colors of SN 2014cx are bluer than those of SN 1999em at all phases, except in $V - I$ where these two objects have similar colors. This suggests that SN 2014cx has a higher photospheric temperature than SN 1999em.

3.4. Bolometric Light Curve

To derive the bolometric luminosity of SN 2014cx, we first convert the extinction-corrected magnitudes in different bands to flux values at the effective wavelength, and then integrate the combined flux over wavelength. The luminosity can then be calculated using the integrated flux and a distance of 18 Mpc (see Section 2). During the first 50 days, when *Swift* UV photometry was available, we integrated the UV flux and extrapolated it to the optical flux. As the UV flux decreases quickly, we assume that the UV contribution to the bolometric flux is marginal in the late plateau phase and negligible ($\lesssim$1%) during the nebular phase (e.g., Dall'Ora et al. 2014). Owing to the lack of NIR data, we estimate the tail luminosity using Equation (3) in Maguire et al. (2010), where a bolometric correction of 0.33 ± 0.06 mag is adopted.

Figure 5 shows the UV–optical–NIR ("UVOIR") bolometric luminosity curve of SN 2014cx. One can see that it reached a peak of log $[L_{\rm bol}^{\rm peak}/({\rm erg\ s^{-1}})] = 42.47$ at ~3 days after explosion. In Figure 5 we also compare the *UBVRI* quasi-bolometric luminosity of SN 2014cx with that of some well-studied SNe IIP. It is readily seen that the luminosity evolution of SN 2014cx is similar to that of SN 2004et and SN 1999em but lies between these two objects in the early and plateau phases. In the nebular phase, we note that the tail luminosity of SN 2014cx is apparently higher than SN 1999em and even slightly higher than SN 2004et, suggesting that a relatively larger amount of nickel may be synthesized in its explosion (see discussion below).

3.5. ^{56}Ni Mass

For SNe IIP, the light curve in the nebular phase is powered mainly by the radioactive decay chain $^{56}{\rm Ni} \rightarrow {}^{56}{\rm Co} \rightarrow {}^{56}{\rm Fe}$. And the tail luminosity is directly proportional to the mass of synthesized ^{56}Ni supposing that the gamma-ray deposition fraction is similar. For the well-studied Type II-pec SN 1987A, the mass of ^{56}Ni has been determined to be $0.075 \pm 0.005\ M_\odot$ (Arnett 1996). For SN 2014cx we estimate the UVOIR bolometric luminosity at $t \approx 150$ days to be $1.93 \pm 0.14 \times 10^{41}$ erg s^{-1} by making a linear fit to the evolution between $t \approx 120$ days and $t \approx 200$ days. The luminosity of SN 1987A at the same phase is estimated to be $2.47 \pm 0.02 \times 10^{41}$ erg s^{-1}. The ratio of SN 2014cx to SN 1987A is 0.78 ± 0.06, which yields a value of $M_{\rm Ni} = 0.058 \pm 0.006\ M_\odot$ for SN 2014cx.

Based on the assumption that all γ-rays from $^{56}{\rm Co} \rightarrow {}^{56}{\rm Fe}$ are entirely thermalized, Hamuy (2003) found an independent

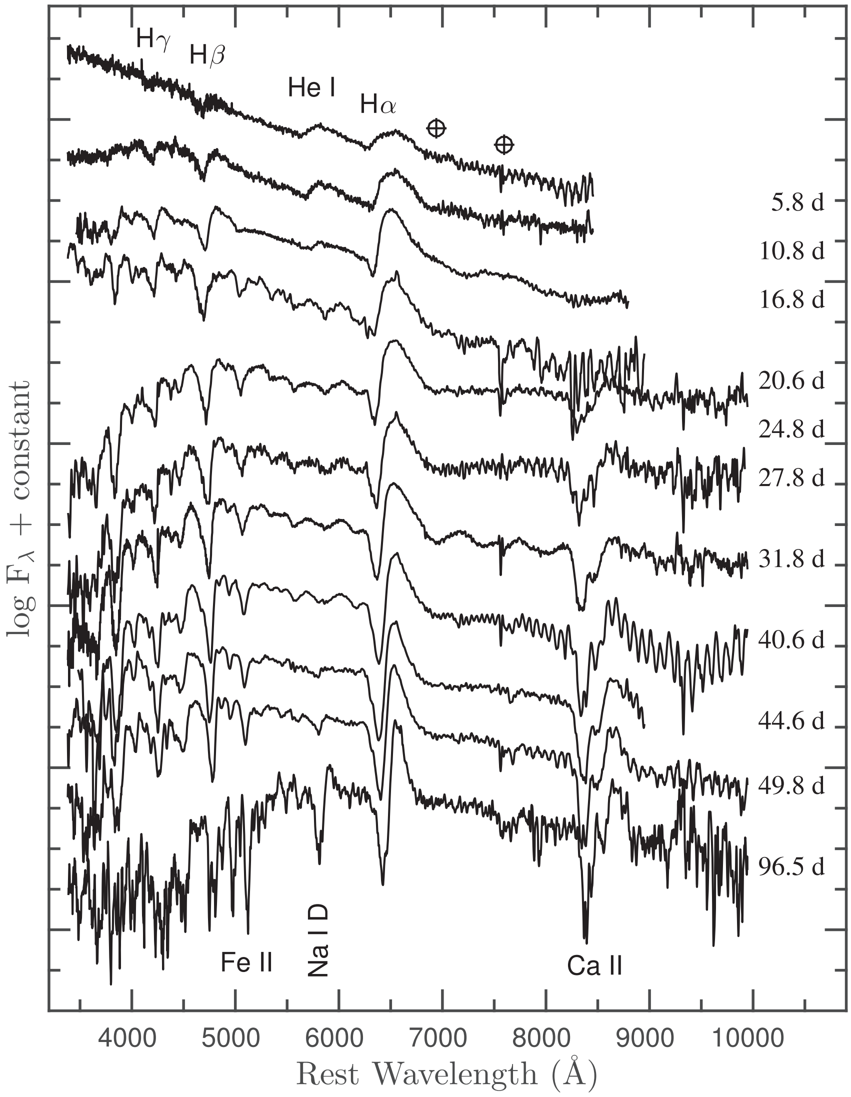

Figure 6. Spectroscopic evolution of SN 2014cx during the photospheric phase. The spectra have been corrected for the redshift of the host galaxy NGC 337 ($z = 0.00549$, via NED). Some key features are labeled, as are residuals from telluric absorption lines. The oscillations in some of the near-infrared spectra (most notably, at 40.6 day) are caused by incomplete removal of CCD fringing.

relationship to estimate the value of ^{56}Ni mass using the tail luminosity (L_t). We calculated L_t of SN 2014cx at 17 epochs from $t \approx 120$ days to ≈ 170 days using the late time V-band magnitude. The mean value of $M_{\rm Ni}$ resulting from Equation (2) of Hamuy (2003) is 0.055 ± 0.011 $M_\odot$, consistent with the result from direct comparison with SN 1987A.

Following the procedures of Elmhamdi et al. (2003), we also estimated the ^{56}Ni mass using the steepness parameter S, which is defined as the steepest value in the V-band light curve at the transitional phase from plateau to nebular tail. For SN 2014cx, we obtain $S = 0.071$ mag day^{-1} and $M_{\rm Ni} = 0.056 \pm 0.007$ $M_\odot$, in good agreement with the values derived from the observed luminosity in the radioactive tail. The weighted mean value of $M_{\rm Ni}$ derived from above three results is 0.056 ± 0.008 $M_\odot$.

4. SPECTROSCOPIC ANALYSIS

4.1. Optical Spectra

The overall spectroscopic evolution of SN 2014cx is displayed in Figures 6 and 7, covering early time ($\sim + 6$ day) up to the nebular phase ($\sim + 404$ day). All of the spectra have been corrected for the recession velocity of the host galaxy (1646 km s^{-1}) but not for the reddening. The main spectral features are labeled according to the lines previously identified for SNe IIP (Leonard et al. 2002).

At $t \approx 6$ days, the spectrum is very blue with a blackbody temperature exceeding 10^4 K. The prominent features at such early phases are Balmer lines and He I λ5876 with broad P-Cygni profiles. At $t \approx 17$ days, the Fe II λ5169 absorption feature is visible, and it becomes stronger by $t \approx 21$ days along with Fe II λ5018. The Na I and He I lines are also detectable at $t \approx 21$ days, and both features grow stronger thereafter. The continuum becomes notably redder from $t \approx 21$ days to $t \approx 25$ days, suggesting a rapid decrease of the photospheric temperature during this period. Consequently, more metal lines (such as Sc II, Ba II, O I, and the Ca II NIR triplet) are formed, and they gradually become the dominant features in the spectra.

At $t \approx 128$ days, SN 2014cx starts to enter the nebular phase. The spectrum shows deep absorption of Na I and prominent emission lines of [O I] λλ6300, 6364, [Fe II] λλ7155, and [Ca II]

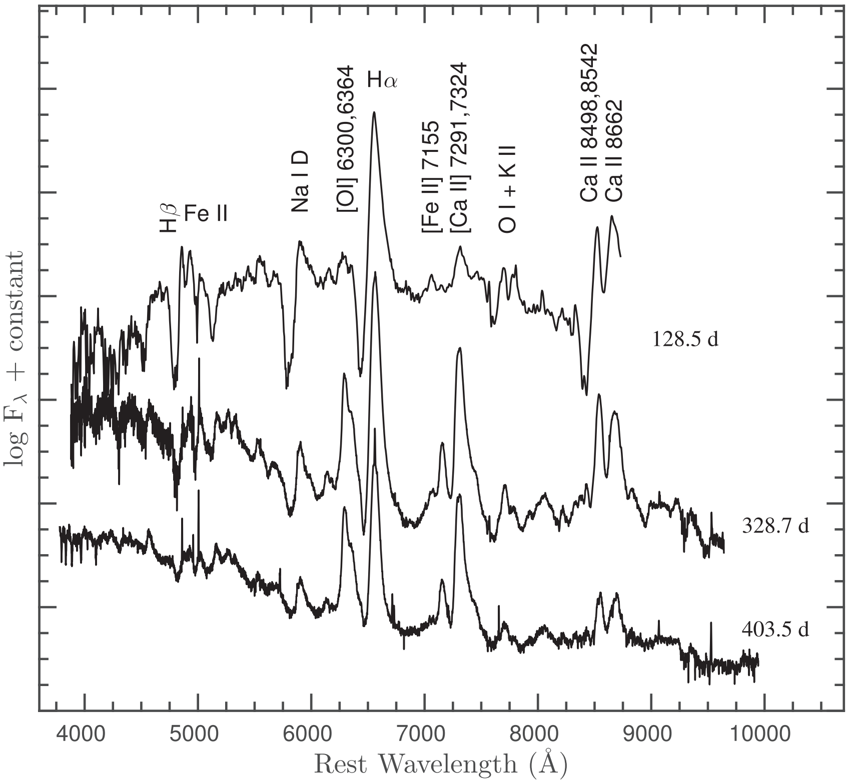

Figure 7. Spectroscopic evolution of SN 2014cx during the nebular phase, when emission lines are dominant features.

$\lambda\lambda$7291, 7324. At $t \approx 329$ days and $t \approx 404$ days, the spectra exhibit emission lines of Hα, [O I], [Fe II], and [Ca II], as well as P-Cygni profiles of Na I, O I, Fe II, and the Ca II NIR triplet. The multiple emission peaks at 5000–5500 Å are likely contributed by [Fe I] and [Fe II] multiplets. We note that the continuum at 3800–5000 Å is relatively bluer than that taken at 128 days perhaps because of either a scattered-light echo off the surrounding CSM (Andrews et al. 2016) or late time CSM interaction (Inserra et al. 2011). For the light-echo scenario, the echoed light should come from earlier phases when the spectra were blue, and the scattering is more efficient at shorter wavelengths. However, the negligible extinction estimated for SN 2014cx in Section 3.3 implies that the CSM potentially causing the light echoes is in the opposite direction of SN 2014cx. In the case of the CSM interaction, we can also see a hint of narrow Hα emission in the spectrum at $t \approx 404$ days.

In Figure 8, we compare the spectra of SN 2014cx at about one week, 50 days, and one year after explosion with those of SN 1999em, SN 2005cs, and SN 2004et at similar phases. It can be seen that SN 2014cx has relatively shallower line profiles than the comparison SNe at early phases. During the plateau phase, $t \approx 50$ days after the explosion, the hydrogen lines of SN 2014cx are similar to those of the comparison SNe IIP, but stronger than those of the subluminous SN 2005cs. In the nebular phase ($t \approx 300$ days), however, SN 2014cx appears to have weaker spectral features than SN 1999em and SN 2004et, but stronger than SN 2005cs, consistent with a flux contribution to the continuum.

4.2. *Expansion Velocities*

We measured the relativistic Doppler velocities of the Hα, Hβ, Fe II λ5169, and Sc II λ6245 lines during the photospheric phase by fitting a Gaussian function to their absorption minima. The velocity evolution of these ions is shown in Figure 9. One can see that the velocities of hydrogen lines are higher than those of metal lines; the hydrogen lines have a lower optical depth and thus are formed at larger radii in the ejecta. The velocities seem to decline with an exponential trend.

To examine the differences of photospheric velocity between SN 2014cx and other SNe IIP, we compared the velocity as measured from the Fe II λ5169 line. As shown in Figure 10, SN 2014cx and SN 2014et have similar velocities at comparable phases, and their expansion velocities are higher than those of SN 1999em (by $\sim$1000 km s^{-1}) and SN 2005cs (by $\sim$3000 km s^{-1}).

5. PROGENITOR ESTIMATES

5.1. *Radius of Progenitor*

For CC SNe, following the shock breakout, the heated stellar envelope expands and then cools down. The different timescales of photospheric temperature evolution depend mainly upon the initial radius of the progenitor and the opacity. A simple analytic function has been proposed by Rabinak & Waxman (2011) to estimate the radius of the progenitor of CC SNe using the early time temperature evolution. Theoretically, the duration that the photosphere can stay at a higher temperature depends on the radius of progenitor star, with longer time for a progenitor with a larger radius (and vice versa).

We constructed the spectral energy distribution (SED) and computed the blackbody temperatures using the *Swift* UV and optical data obtained during the first week after explosion. The luminosity and temperature can then be used to constrain the

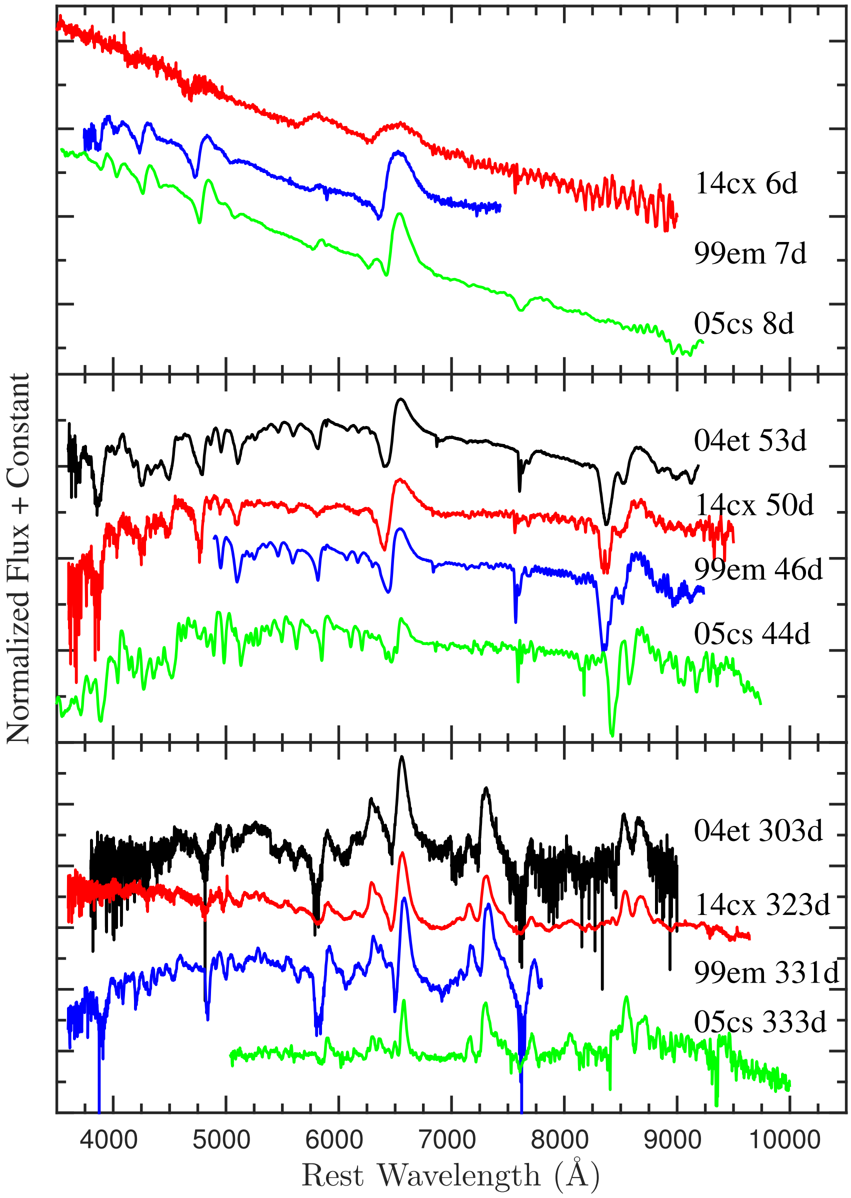

Figure 8. Comparison of the reddening- and Doppler-corrected spectra of SNe 2014cx, 2004et, 1999em, and 2005cs at similar phases. Top panel, one week after explosion; middle panel, about 50 days after explosion; bottom panel, about one year after explosion.

radius of the progenitor star by using Equation (13) of Rabinak & Waxman (2011; e.g., Valenti et al. 2014; Bose et al. 2015; Rubin et al. 2016). Note that the equation is only valid for the first week after explosion, when the light curve is dominated by shock cooling at very early phase, and the photosphere is located at the outer shell of the expanding ejecta (Rubin et al. 2016). Adopting an optical opacity of 0.34 $cm^2\ g^{-1}$ and a typical RSG density profile $f_\rho = 0.13$, we obtained an initial radius of $643 \pm 60\ R_\odot$ for the progenitor of SN 2014cx (see Figure 11), consistent with the typical size of an RSG.

Based on the SuperNova Explosion Code (SNEC; Morozova et al. 2015), Morozova et al. (2016) suggest that the early time evolution of the light curves of SNe IIP relies sensitively on the radius of the exploding star, as explained with an analytical correlation between the g-band rise time and the progenitor radius (i.e., $\log R\,[R_\odot] = 1.225 \log t_{\rm rise}\ [\rm day] + 1.692$). Thus, we fit the early time g-band light curve of SN 2014cx and obtain the rise time as $t_{\rm rise} = 7.90 \pm 0.10$ days. Inserting this value into the rise time–radius relation, we estimate the radius of the progenitor to be $619 \pm 10\ R_\odot$.

5.2. Hydrodynamical Modeling

In this subsection, we further determine the main physical parameters of SN 2014cx and its progenitor (i.e., the explosion energy, the radius of progenitor star, and the ejected mass) using a method of hydrodynamical modeling. This method uses the SN observables (i.e., the bolometric light curve, the velocity evolution, and the temperature of the continuum obtained during the photospheric phase) as input parameters to constrain the physical properties of expanding ejecta and the evolution of SN observables (from the shock breakout up to the nebular phase) using the general-relativistic, radiation-hydrodynamics code. This technique has been successfully applied to the

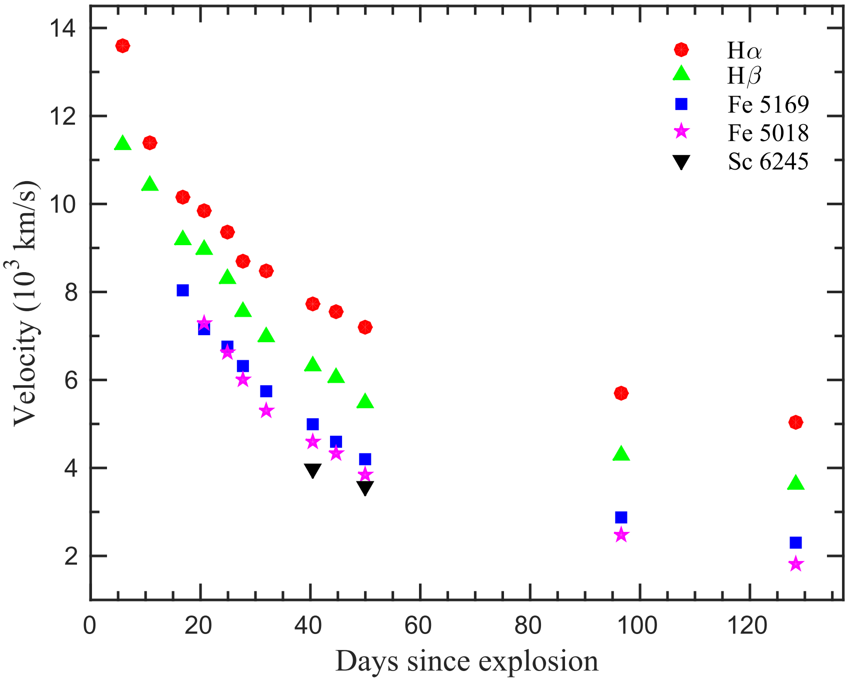

Figure 9. Velocity evolution of Hα, Hβ, and Fe II. The velocities are estimated using the Doppler shift of the absorption minima.

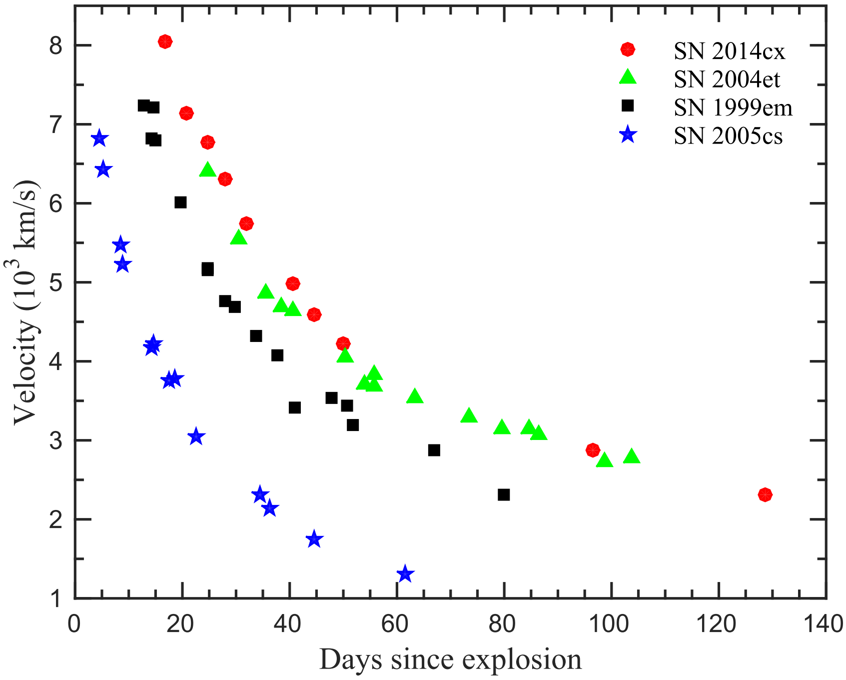

Figure 10. Comparison of the expansion velocities of SN 2014cx measured from Fe II λ5169 to those of the luminous Type IIP SN 2004et, the normal SN 1999em, and the subluminous SN 2005cs.

studies of numerous SNe IIP, including SNe 2007od, 2009bw, 2009E, 2012A, 2013ab, and 2013ej (Inserra et al. 2011, 2012; Pastorello et al. 2012; Tomasella et al. 2013; Bose et al. 2015; Huang et al. 2015). Details about this hydrodynamical model are well described in Zampieri et al. (2003), Pumo et al. (2010), and Pumo & Zampieri (2011).

Based on the estimates of the explosion epoch (MJD = 56,901.89; Section 3.1), bolometric luminosity, and nickel mass (0.056 $M_\odot$; Section 3.5), the best-fit hydrodynamic model returns a total (kinetic plus thermal) energy of 0.4×10^{51} erg, an initial radius of 4×10^{13} cm (~570 $R_\odot$), and an envelope mass of 8 $M_\odot$ (see Figure 12) for SN 2014cx. Considering a mass of ∼1.5–2.0 $M_\odot$ for the compact remnant star, we estimate that SN 2014cx has an immediate progenitor mass of 9.5–10.0 $M_\odot$ when exploding. The zero-age main-sequence mass should be slightly higher given that the progenitor star suffers some mass loss during the lifetime. These values are consistent with those of a typical RSG with

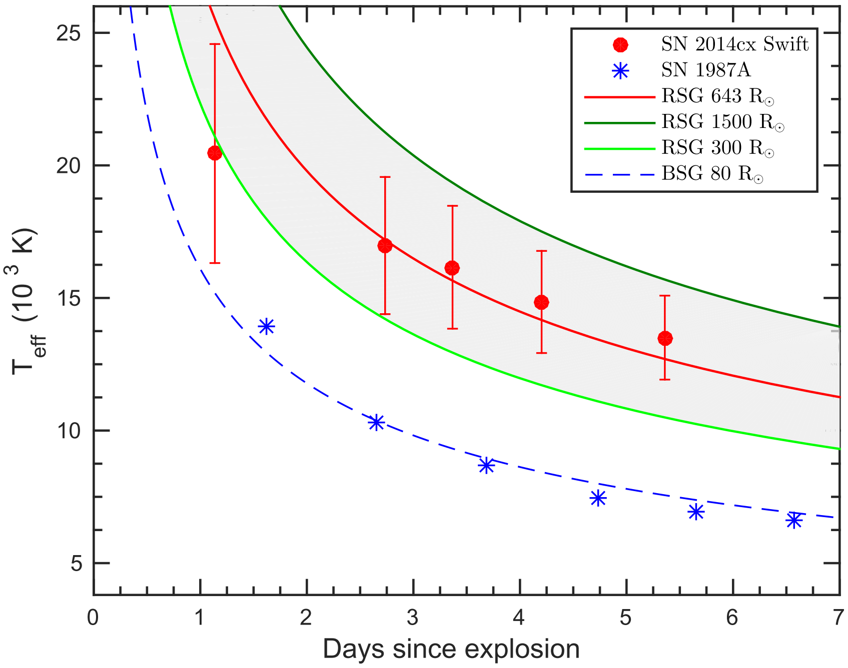

Figure 11. Constraining the progenitor radius using the Rabinak & Waxman (2011) prescription. The red solid line is the best fit for a RSG of 643 $R_{\odot}$, and the blue dashed line is for a BSG of 80 $R_{\odot}$ for SN 1987A.

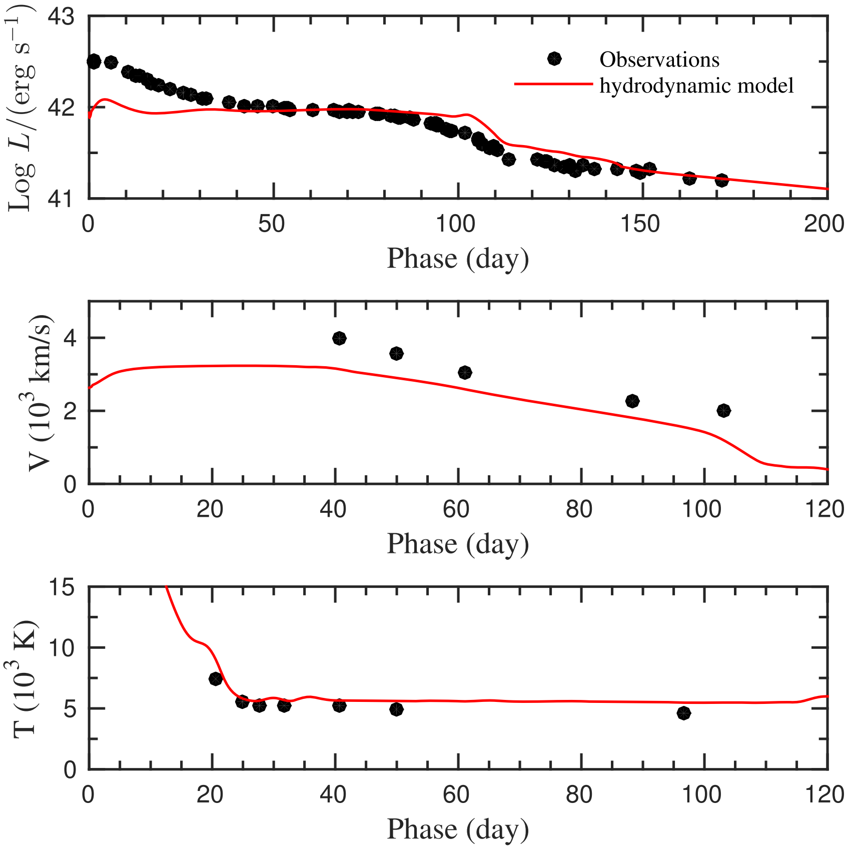

Figure 12. Comparison of the evolution of the main observables of SN 2014cx with the best-fit model computed with the general-relativistic, radiation-hydrodynamics code (total energy $\sim$0.4 × 10^{51} erg, initial radius 4 × 10^{13} cm, envelope mass 8 $M_{\odot}$). Top, middle, and bottom panels show the bolometric light curve, the photospheric velocity, and the photospheric temperature as a function of time, respectively. To estimate the photospheric velocity from observations, we used the value inferred from the Fe II λ5169 line.

relatively low mass. The radius is also in agreement with that estimated from the early temperature as described in Section 5.1 within uncertainties.

We further compare our light curves and spectra with those from Kasen & Woosley (2009), and we found that our parameters generally fall into the range of their Table 2, except that we have a smaller nickel mass (0.056 $M_\odot$ versus 0.1–0.5 $M_\odot$). This difference is likely due to their numerical models using larger main-sequence masses (12–25 $M_\odot$) than our hydrodynamic modeling results (9.5–10.0 $M_\odot$).

The evolutions of three observables (luminosity, velocity, and temperature) and the modeling results are shown in Figure 12. As can be seen, the modeling reasonably matches the observed luminosity/temperature except at early phases where a larger deviation is seen in luminosity. This deviation is likely due to the density profile in the radial direction of the outermost ejecta not being well produced by our simulations (Pumo & Zampieri 2011). In the middle panel of Figure 12, we note that there is also a small ($\lesssim$10%–15%) discrepancy between our best-fit model and the observed photospheric velocity. This discrepancy may be attributed to a systematic shift between the true photospheric velocity and the values estimated from the observed P-Cygni line profiles (Dessart & Hillier 2005). This can be explained with the fact that the optical depth is higher for spectral lines relative to the continuum, which can place the line photosphere at a larger radius (see also Inserra et al. 2013). As discussed in previous work (e.g., Zampieri et al. 2003; Pumo et al. 2011; Huang et al. 2015), the early velocity evolution cannot be reproduced in our simulations and is thus excluded from the fit. The early evolution is caused by the shock-wave propagation in the outermost several percent of the pre-supernova mass. Thus, we suggest that omitting the early stages does not significantly affect our estimates of the parameters of the bulk of the ejecta. However, we are aware that our simplification requires support via detailed modeling of the full data set.

6. DISCUSSION AND SUMMARY

In this paper, we present extensive UV and optical photometry and optical spectroscopy of SN 2014cx in NGC 337, spanning the period from −30 days to +404 days from the maximum light. The explosion time is constrained to be MJD = 56,901.89 with an accuracy of ±0.5 days.

The characteristics of the light curves, such as the rise time, duration of the plateau phase, post-peak decline, and bolometric luminosity, suggest that SN 2014cx is a normal Type IIP supernova. The KAIT unfiltered and LCOGT *r*-band light curves seem to experience two brightening components, with the first likely related to shock breakout of the supernova. The plateau duration is ~100 days, similar to that of our comparison SNe IIP. The value of M_V at mid-plateau phase (~50 day) is -16.48 ± 0.43 mag for SN 2014cx, lying between the luminous SNe IIP (~−17 mag, SN 2004et) and subluminous SNe IIP (~−15 mag, SN 2005cs). The mass of ^{56}Ni, using the tail luminosity and steepness methods, is 0.056 $M_\odot$, similar to that of SN 1999em and SN 2004et.

The spectroscopic evolution of SN 2014cx shares a similarity with the typical Type IIP SNe 1999em and 2004et. The early time spectra exhibit a nearly featureless continuum with only hydrogen Balmer lines and He I visible. As the SN evolves, the continuum becomes redder and the metal lines emerge, becoming the dominant features during the photospheric phase. During the nebular phase, the spectra are dominated by strong emission lines. The continuum at 3800–5000 Å is relatively blue, which might be caused by either late time CSM interaction or a scattered-light echo. The value and evolution of the expansion velocity derived from Fe II λ5169 are similar to those of SN 2004et, but ~1000 km s^{-1} higher than the expansion velocity of SN 1999em.

By modeling the observables of SN 2014cx as derived from our observations, we estimate that this explosion produces a total energy of 0.4 × 10^{51} erg and an ejected mass of ~8.0 $M_\odot$. The progenitor star is calculated to have a radius of 4 × 10^{13} cm (~574 $R_\odot$), which agrees well with that estimated from the early photospheric temperature evolution (643 ± 60 $R_\odot$) and *g*-band rise time–radius relation from SNEC (619 ± 10 $R_\odot$). The values above are consistent with a core-collapse scenario from a typical RSG having an initial mass of 9.5–10 $M_\odot$.

We thank the support of the staffs at Xinglong Station (National Astronomical Observatory of China), Li-Jiang Observatory (Yunnan Astronomical Observatory of China), and Lick Observatory for assistance with the observations. We also acknowledge the use of public data from the *Swift* and Las Cumbres Observatory Global Telescope Network data archives. Some of the data presented herein were obtained at the W. M. Keck Observatory, which is operated as a scientific partnership among the California Institute of Technology, the University of California, and NASA; the observatory was made possible by the generous financial support of the W. M. Keck Foundation. KAIT and its ongoing operation were made possible by donations from Sun Microsystems, Inc., the Hewlett-Packard Company, AutoScope Corporation, Lick Observatory, the U.S. National Science Foundation (NSF), the University of California, the Sylvia & Jim Katzman Foundation, and the TABASGO Foundation. Research at Lick Observatory is partially supported by a generous gift from Google. We thank N. N. Chugai for some useful correspondence.

This work is supported by the Major State Basic Research Development Program (2013CB834903), the National Natural Science Foundation of China (NSFC grants 11178003, 11325313, and 11633002), and the Strategic Priority Research Program of Emergence of Cosmological Structures of the Chinese Academy of Sciences (grant No. XDB09000000). T.-M.Z. is supported by the NSFC (grants 11203034). J.-J.Z. is supported by the NSFC (grants 11403096), the Key Research Program of the CAS (Grant No. KJZD-EW-M06), and the CAS “Light of West China” Program. D.A.H., C.M., and G.H. are supported by NSF grant 1313484. A.V.F.’s group at UC Berkeley is grateful for financial assistance from NSF grant AST-1211916, the TABASGO Foundation, Gary and Cynthia Bengier, and the Christopher R. Redlich Fund. The work of A. V.F. was completed at the Aspen Center for Physics, which is supported by NSF grant PHY-1066293; he thanks the Center for its hospitality during the black holes workshop in 2016 June and July.

REFERENCES

Ahn, C. P., Alexandroff, R., Allende Prieto, C., et al. 2012, ApJS, 203, 21
Anderson, J. P., González-Gaitán, S., Hamuy, M., et al. 2014, ApJ, 786, 67
Andrews, J., Smith, N., Fong, W.-f., & Milne, P. 2015, ATel, 7084, 1

Andrews, J. E., Krafton, K. M., Clayton, G. C., et al. 2016, MNRAS, 457, 3241

Arcavi, I., Gal-Yam, A., Cenko, S. B., et al. 2012, ApJL, 756, L30

Arnett, D. 1996, Supernovae and Nucleosynthesis: An Investigation of the History of Matter, from the Big Bang to the Present, ed. D. Arnett, (Princeton: Princeton Univ. Press)

Barbon, R., Ciatti, F., & Rosino, L. 1979, A&A, 72, 287

Bose, S., Valenti, S., Misra, K., et al. 2015, MNRAS, 450, 2373

Breeveld, A. A., Landsman, W., Holland, S. T., et al. 2011, in AIP Conf. Ser. 1358, An Updated Ultraviolet Calibration for the Swift/UVOT, ed. J. E. McEnery, J. L. Racusin, & N. Gehrels (Melville, NY: AIP), 373

Brown, P. J., Breeveld, A. A., Holland, S., Kuin, P., & Pritchard, T. 2014, Ap&SS, 354, 89

Brown, P. J., Holland, S. T., Immler, S., et al. 2009, AJ, 137, 4517

Brown, T. M., Baliber, N., Bianco, F. B., et al. 2013, PASP, 125, 1031

Cardelli, J. A., Clayton, G. C., & Mathis, J. S. 1989, ApJ, 345, 245

Dall'Ora, M., Botticella, M. T., Pumo, M. L., et al. 2014, ApJ, 787, 139

Dessart, L., & Hillier, D. J. 2005, A&A, 439, 671

Dessart, L., Livne, E., & Waldman, R. 2010, MNRAS, 408, 827

Dhungana, G., Kehoe, R., Vinko, J., et al. 2016, ApJ, 822, 6

Elias-Rosa, N., Tartaglia, L., Cappellaro, E., et al. 2014, ATel, 6440, 1

Elmhamdi, A., Danziger, I. J., Chugai, N., et al. 2003, MNRAS, 338, 939

Falk, S. W., & Arnett, W. D. 1977, ApJS, 33, 515

Faran, T., Poznanski, D., Filippenko, A. V., et al. 2014a, MNRAS, 442, 844

Faran, T., Poznanski, D., Filippenko, A. V., et al. 2014b, MNRAS, 445, 554

Filippenko, A. V. 1997, ARA&A, 35, 309

Filippenko, A. V., Li, W. D., Treffers, R. R., & Modjaz, M. 2001, in IAU Coll. 183, Small Telescope Astronomy on Global Scales, Vol. 246, ed. B. Paczynski, W.-P. Chen, & C. Lemme (San Francisco, CA: ASP), 121

Ganeshalingam, M., Li, W., Filippenko, A. V., et al. 2010, ApJS, 190, 418

Garnavich, P. M., Tucker, B. E., Rest, A., et al. 2016, ApJ, 820, 23

Gezari, S., Jones, D. O., Sanders, N. E., et al. 2015, ApJ, 804, 28

González-Gaitán, S., Tominaga, N., Molina, J., et al. 2015, MNRAS, 451, 2212

Hamuy, M. 2003, ApJ, 582, 905

Heger, A., Fryer, C. L., Woosley, S. E., Langer, N., & Hartmann, D. H. 2003, ApJ, 591, 288

Holoien, T. W.-S., Prieto, J. L., Kochanek, C. S., et al. 2014, ATel, 6436, 1

Horne, K. 1986, PASP, 98, 609

Huang, F., Li, J.-Z., Wang, X.-F., et al. 2012, RAA, 12, 1585

Huang, F., Wang, X., Zhang, J., et al. 2015, ApJ, 807, 59

Inserra, C., Pastorello, A., Turatto, M., et al. 2013, A&A, 555, A142

Inserra, C., Turatto, M., Pastorello, A., et al. 2011, MNRAS, 417, 261

Inserra, C., Turatto, M., Pastorello, A., et al. 2012, MNRAS, 422, 1122

Kasen, D., & Woosley, S. E. 2009, ApJ, 703, 2205

Klein, R. I., & Chevalier, R. A. 1978, ApJL, 223, L109

Leonard, D. C., Filippenko, A. V., Gates, E. L., et al. 2002, PASP, 114, 35

Li, W., Leaman, J., Chornock, R., et al. 2011, MNRAS, 412, 1441

Li, W., Wang, X., Van Dyk, S. D., et al. 2007, ApJ, 661, 1013

Maguire, K., Di Carlo, E., Smartt, S. J., et al. 2010, MNRAS, 404, 981

Monet, D. 1998, USNO-A2.0 (Washington, DC: USNO)

Morozova, V., Piro, A. L., Renzo, M., et al. 2015, ApJ, 814, 63

Morozova, V., Piro, A. L., Renzo, M., & Ott, C. D. 2016, ApJ, 829, 109

Morrell, N., Marion, G. H., Kirshner, R. P., Hsiao, E. Y., & Stritzinger, M. 2014, ATel, 6442, 1

Nadyozhin, D. K. 2003, MNRAS, 346, 97

Nakano, S., Itagaki, K., Yusa, T., et al. 2014, CBET, 3963, 1

Olivares, E. F., Hamuy, M., Pignata, G., et al. 2010, ApJ, 715, 833

Pastorello, A., Pumo, M. L., Navasardyan, H., et al. 2012, A&A, 537, A141

Pastorello, A., Valenti, S., Zampieri, L., et al. 2009, MNRAS, 394, 2266

Patat, F., Barbon, R., Cappellaro, E., & Turatto, M. 1994, A&A, 282, 731

Pumo, M. L., & Zampieri, L. 2011, ApJ, 741, 41

Pumo, M. L., & Zampieri, L. 2013, MNRAS, 434, 3445

Pumo, M. L., Zampieri, L., & Turatto, M. 2010, MSAIS, 14, 123

Quimby, R. M., Wheeler, J. C., Höflich, P., et al. 2007, ApJ, 666, 1093

Rabinak, I., & Waxman, E. 2011, ApJ, 728, 63

Roming, P. W. A., Kennedy, T. E., Mason, K. O., et al. 2005, SSRv, 120, 95

Rubin, A., Gal-Yam, A., De Cia, A., et al. 2016, ApJ, 820, 33

Sahu, D. K., Anupama, G. C., Srividya, S., & Muneer, S. 2006, MNRAS, 372, 1315

Sanders, N. E., Soderberg, A. M., Gezari, S., et al. 2015, ApJ, 799, 208

Schawinski, K., Justham, S., Wolf, C., et al. 2008, Sci, 321, 223

Schlafly, E. F., & Finkbeiner, D. P. 2011, ApJ, 737, 103

Smartt, S. J. 2009, ARA&A, 47, 63

Smartt, S. J., Eldridge, J. J., Crockett, R. M., & Maund, J. R. 2009, MNRAS, 395, 1409

Sorce, J. G., Tully, R. B., Courtois, H. M., et al. 2014, MNRAS, 444, 527

Tomasella, L., Cappellaro, E., Fraser, M., et al. 2013, MNRAS, 434, 1636

Tominaga, N., Blinnikov, S., Baklanov, P., et al. 2009, ApJL, 705, L10

Valenti, S., Howell, D. A., Stritzinger, M. D., et al. 2016, MNRAS, 459, 3939

Valenti, S., Sand, D., Pastorello, A., et al. 2014, MNRAS, 438, L101

Wang, X., Li, W., Filippenko, A. V., et al. 2008, ApJ, 675, 626

Zampieri, L., Pastorello, A., Turatto, M., et al. 2003, MNRAS, 338, 711

The Astrophysical Journal, 819:59 (11pp), 2016 March 1 doi:10.3847/0004-637X/819/1/59

A PAIR OF GIANT PLANETS AROUND THE EVOLVED INTERMEDIATE-MASS STAR HD 47366: MULTIPLE CIRCULAR ORBITS OR A MUTUALLY RETROGRADE CONFIGURATION

Bun'ei Sato[1], Liang Wang[2], Yu-Juan Liu[2], Gang Zhao[2], Masashi Omiya[3], Hiroki Harakawa[3], Makiko Nagasawa[4], Robert A. Wittenmyer[5,6], Paul Butler[7], Nan Song[2], Wei He[2], Fei Zhao[2], Eiji Kambe[8], Kunio Noguchi[3], Hiroyasu Ando[3], Hideyuki Izumiura[8,9], Norio Okada[3], Michitoshi Yoshida[10], Yoichi Takeda[3,9], Yoichi Itoh[11], Eiichiro Kokubo[3,9], and Shigeru Ida[12]

[1] Department of Earth and Planetary Sciences, Tokyo Institute of Technology, 2-12-1 Ookayama, Meguro-ku, Tokyo 152-8551, Japan; satobn@geo.titech.ac.jp
[2] Key Laboratory of Optical Astronomy, National Astronomical Observatories, Chinese Academy of Sciences, Beijing 100012, China
[3] National Astronomical Observatory of Japan, 2-21-1 Osawa, Mitaka, Tokyo 181-8588, Japan
[4] Department of Physics, Kurume University School of Medicine, 67 Asahi-machi, Kurume-city, Fukuoka 830-0011, Japan
[5] School of Physics, University of New South Wales, Sydney 2052, Australia
[6] Australian Centre for Astrobiology, University of New South Wales, Sydney 2052, Australia
[7] Department of Terrestrial Magnetism, Carnegie Institution of Washington, 5241 Broad Branch Road, NW, Washington, DC 20015-1305, USA
[8] Okayama Astrophysical Observatory, National Astronomical Observatory of Japan, Kamogata, Okayama 719-0232, Japan
[9] The Graduate University for Advanced Studies, Shonan Village, Hayama, Kanagawa 240-0193, Japan
[10] Hiroshima Astrophysical Science Center, Hiroshima University, Higashi-Hiroshima, Hiroshima 739-8526, Japan
[11] Nishi-Harima Astronomical Observatory, Center for Astronomy, University of Hyogo, 407-2, Nishigaichi, Sayo, Hyogo 679-5313, Japan
[12] Earth-Life Science Institute, Tokyo Institute of Technology, 2-12-1 Ookayama, Meguro-ku, Tokyo 152-8551, Japan

Received 2015 October 16; accepted 2016 January 16; published 2016 February 26

ABSTRACT

We report the detection of a double planetary system around the evolved intermediate-mass star HD 47366 from precise radial-velocity measurements at the Okayama Astrophysical Observatory, Xinglong Station, and Australian Astronomical Observatory. The star is a K1 giant with a mass of $1.81 \pm 0.13\ M_{\odot}$, a radius of $7.30 \pm 0.33\ R_{\odot}$, and solar metallicity. The planetary system is composed of two giant planets with minimum masses of $1.75^{+0.20}_{-0.17}\ M_{\mathrm{J}}$ and $1.86^{+0.16}_{-0.15}\ M_{\mathrm{J}}$, orbital periods of $363.3^{+2.5}_{-2.4}$ days and $684.7^{+5.0}_{-4.9}$ days, and eccentricities of $0.089^{+0.079}_{-0.060}$ and $0.278^{+0.067}_{-0.094}$, respectively, which are derived by a double Keplerian orbital fit to the radial-velocity data. The system adds to the population of multi-giant-planet systems with relatively small orbital separations, which are preferentially found around evolved intermediate-mass stars. Dynamical stability analysis for the system revealed, however, that the best-fit orbits are unstable in the case of a prograde configuration. The system could be stable if the planets were in 2:1 mean-motion resonance, but this is less likely, considering the observed period ratio and eccentricity. A present possible scenario for the system is that both of the planets have nearly circular orbits, namely the eccentricity of the outer planet is less than ~0.15, which is just within 1.4σ of the best-fit value, or the planets are in a mutually retrograde configuration with a mutual orbital inclination larger than 160°.

Key words: planetary systems – stars: individual (HD 47366) – techniques: radial velocities

1. INTRODUCTION

Evolved stars (giants and subgiants) have been extensively searched for the last 10 years, aiming to explore planets around more massive stars than the Sun and to investigate the orbital evolution of planetary systems during the post-main-sequence phase. Precise radial-velocity surveys have discovered about 120 substellar companions around such evolved stars[13] so far, and they are now known to exhibit statistical properties that are not necessarily similar to those around solar-type stars (e.g., Hatzes et al. 2005, 2006; Setiawan et al. 2005; Lovis & Mayor 2007; de Medeiros et al. 2009; Döllinger et al. 2009; Johnson et al. 2011; Wittenmyer et al. 2011; Omiya et al. 2012; Wang et al. 2012, 2014; Novak et al. 2013; Sato et al. 2013b; Lee et al. 2014; Trifonov et al. 2014; Jones et al. 2015; Reffert et al. 2015). Recently, very-high-precision photometry by the *Kepler* space telescope has succeeded in detecting planetary transits on evolved stars (Batalha et al. 2013). The discoveries include short-period planets and sub-Jupiter-mass ones around giants (Huber et al. 2013; Ciceri et al. 2015; Lillo-Box et al. 2014; Ortiz et al. 2015; Quinn et al. 2015; Sato et al. 2015), which had rarely been found by the ground-based radial-velocity surveys, and also candidates with longer periods, which could be counterparts of those found by the radial-velocity surveys.[14]

Among the planetary systems around evolved stars, multiple-planet systems are of particular interest in terms of the formation and evolution of planetary systems. Figure 1 shows the cumulative number of planet pairs in multiple-planet systems discovered by ground-based, radial-velocity, and transit surveys. The total mass of the planet pair, as well as the log g and mass of the host star, are indicated by the color and size of the symbol, respectively. Interestingly, almost all of the giant-planet pairs with period ratios smaller than two are preferentially found around evolved intermediate-mass stars.[15] For example, 24 Sex (G5 IV; Johnson et al. 2011) and η Cet (K2 III; Trifonov et al. 2014) host double giant-planet systems probably in mean-motion resonances of 2:1, which suggests that these systems have experienced differential convergent

---

[13] Evolved stars here include those with logarithmic surface gravity $\log g < 4.0$. The list of the stars harboring substellar companions is from the NASA Exoplanet Archive.

[14] NASA Exoplanet Archive.

[15] One exception is the planetary system around the K2.5 V star HD 45364, which consists of two giant planets ($m_b \sin i = 0.187\ M_{\mathrm{J}}$ and $m_c \sin i = 0.658\ M_{\mathrm{J}}$) in 3:2 resonance (Correia et al. 2009).

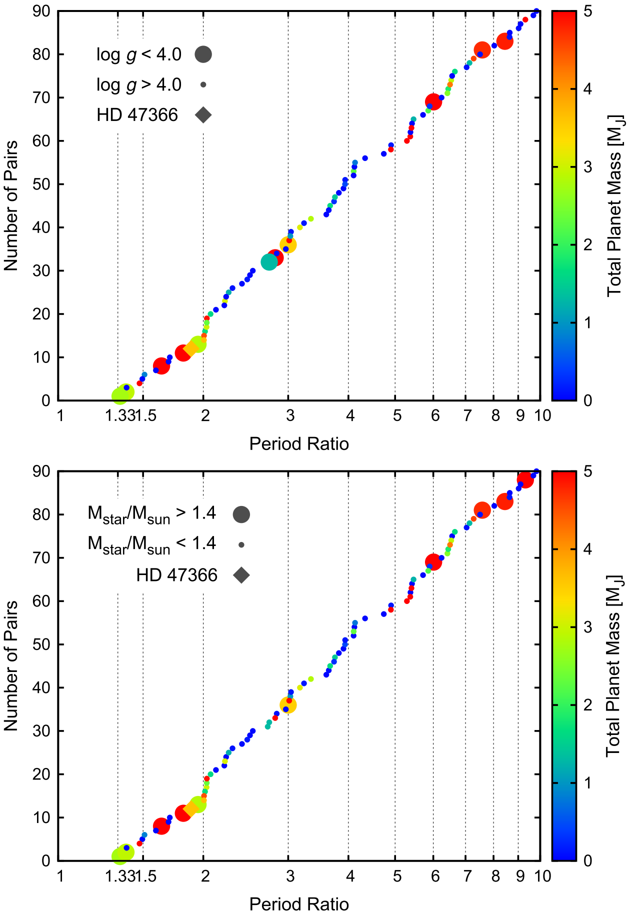

Figure 1. Cumulative number of planet pairs in multiple-planetary systems discovered with ground-based, radial-velocity, and transit surveys. The pairs with period ratios smaller than 10 are plotted. The color indicates the total mass of the planet pair and the symbol size indicates the log g (top) and mass (bottom) of the host star. The data were downloaded from the NASA Exoplanet Archive. Since the ongoing Doppler planet searches target both evolved and intermediate-mass stars at once, the two panels look nearly identical.

orbital migration (e.g., Lee & Peale 2002; Kley et al. 2004). In contrast, double giant-planet systems around HD 200964 (K0 IV; Johnson et al. 2011) and HD 5319 (G5 IV; Robinson et al. 2007; Giguere et al. 2015) are near the 4:3 resonance, which are considered to be difficult to form either via convergent migration, scattering, or in situ formation (Rein et al. 2012). BD+20 2457 (K2 III) hosts two brown dwarfs that are suggested to be near 3:2 resonance (Niedzielski et al. 2009). However, a detailed orbital stability analysis of the system revealed that the best-fit orbits derived by radial-velocity data are unstable, though they would be stable if the two brown dwarfs were mutually in retrograde configuration (Horner et al. 2014). Giant-planet pairs with such small period ratios are rarely found around solar-type stars, though many less massive ones including Neptunes and Super-Earths are found around them.

Here we report the detection of a double giant-planet system around the intermediate-mass giant HD 47366 (K1 III, $M = 1.8\ M_\odot$), which adds to the growing population of multi-planet systems with small period ratios around evolved stars. The discovery was made by Okayama and Xinglong Planet Search Programs (e.g., Wang et al. 2012; Sato et al. 2013b) facilitated by joint precise radial-velocity observations from the Australian Astronomical Observatory (Sato et al. 2013a). The planetary system is intriguing for several reasons: the best-fit Keplerian orbit is unstable, it is near but less likely in 2:1 mean-motion resonance, and could be stable if the orbits are nearly circular or in retrograde configuration.

The rest of the paper is organized as follows. The stellar properties are presented in Section 2 and the observations are described in Section 3. The orbital solution and results of dynamical stability analysis are presented in Sections 4 and 5, respectively. Section 6 is devoted to discussion and summary.

2. STELLAR PROPERTIES

HD 47366 (HIP 31674, BD−12 1566, HR 2437, TYC 5373-2001-1) is listed in the Hipparcos Catalogue (ESA 1997) as a K1 III star, with a visual magnitude of $V = 6.11$ and a color index of $B - V = 0.994$. The *Hipparcos* parallax $\pi = 12.5 \pm 0.42$ mas (van Leeuwen 2007) corresponds to a distance of 80.0 ± 2.7 pc. The reddening $E(B - V) = 0.028$ was obtained from the Galactic dust map of Schlegel et al. (1998), with the correction given by Bonifacio et al. (2000) and a scaling factor of $1 - \exp(-|d \sin b|/h)$, where d is the distance, b is the Galactic latitude, and $h = 125$ pc is the scale height of the reddening layer. The absolute magnitude $M_V = 1.51$ was derived from the distance and the interstellar extinction $A_V = 3.1E(B - V)$. By adopting the broadband photometric color $B - V$ and the estimated metallicity with the empirical calibration relation of Alonso et al. (1999, 2001), we derived the bolometric correction B.C. = −0.309 and the effective temperature $T_{\rm eff} = 4866 \pm 100$ K. We used a high signal-to-noise ratio (S/N ~ 200), iodine-free spectrum taken with HRS to measure the equivalent widths (EWs) of ~30 Fe I lines, to derive the iron abundance [Fe/H]. The line lists as well as their oscillation strengths ($\log gf$) were mainly taken from Hekker & Meléndez (2007), in which iron lines were carefully selected to avoid any blend by atomic or CN lines. The model atmosphere used in this work was interpolated from the line-blanketed, local thermodynamic equilibrium (LTE) ATLAS9-ODFNEW grid (Castelli & Kurucz 2004). The microturbulent velocity $v_{\rm t}$ was obtained by minimizing the trend between the abundances of different Fe I lines and their reduced equivalent widths ($\log({\rm EWs}/\lambda)$). The macroturbulent velocity was estimated with the empirical relations of $v_{\rm macro}$ versus $T_{\rm eff}$ given by Hekker & Meléndez (2007), and the projected rotational velocity ($v \sin i$) was determined with the method of Fekel (1997). The stellar mass, surface gravity ($\log g$), radius, and age were derived using a Bayesian approach with the Geneva database (Lejeune & Schaerer 2001), which includes the post-helium flash phases for stars with $M \geqslant 1.7\,M_\odot$. First, we interpolated an extensive grid of evolutionary tracks, with $\Delta M = 0.05$ within $1.2 \leqslant M/M_\odot \leqslant 3.6$, $\Delta[{\rm Fe/H}] = 0.02$ within $-0.4 \leqslant [{\rm Fe/H}] \leqslant +0.3$, and 500 points in each track. Then, for each data point, we calculated the likelihood functions of $\log L$, $T_{\rm eff}$ and [Fe/H] to match the observed values by assuming Gaussian errors. We adopted uniform prior probabilities of mass and [Fe/H]. It is noted that stars evolving more slowly have a higher probability of being observed. Without correcting this evolution effect, the resulting parameters would bias toward the rapid evolution phases. We therefore weighted the probability of each point along its evolutionary track by the normalized time-step $(a_{i+1,j} - a_{i,j})/(a_{n,j} - a_{a,j})$, where $a_{i,j}$ is the age of

Table 1
Stellar Parameters for HD 47366

Parameter	This Work	Liu et al. (2010)	Mishenina et al. (2006)
Spectral Type	K1 III	⋯	⋯
Hipparcos Parallax π (mas)	12.5 ± 0.42	⋯	⋯
Distance (pc)	80.0 ± 2.7	⋯	⋯
Visual Magnitude V	6.11	⋯	⋯
Color Index $B - V$	0.994 ± 0.002	⋯	⋯
Redenning $E(B - V)$	0.028	⋯	⋯
Interstellar Extinction A_V	0.087	⋯	⋯
Absolute Magnitude M_V	1.51	1.467	1.044
Bolometric Correction B.C.	−0.309	−0.302	⋯
Bolometric Magnitude $M_{\rm bol}$	1.20	1.165	⋯
Effective Temperature $T_{\rm eff}$ (K)	4866 ± 100	4883 ± 100	4772
Surface Gravity $\log g$ (cgs)	2.97 ± 0.06	3.00 ± 0.1	2.60
Metallicity [Fe/H]	−0.02 ± 0.09	−0.10 ± 0.1	−0.16
Microturbulent Velocity $v_{\rm t}$ (km s^{-1})	1.24	1.2 ± 0.2	1.2
Macroturbulent Velocity $v_{\rm macro}$ (km s^{-1})	5.54 ± 0.45	⋯	⋯
Projected Rotational Velocity $v \sin i$ (km s^{-1})	4.3 ± 0.8	⋯	⋯
Luminosity L ($L_\odot$)	26.1 ± 1.8	26.2	38.5
Radius R ($R_\odot$)	7.30 ± 0.33	7.16	9.09
Mass M ($M_\odot$)	1.81 ± 0.13	1.87	1.2
Age (Gyr)	1.61 ± 0.53	⋯	⋯

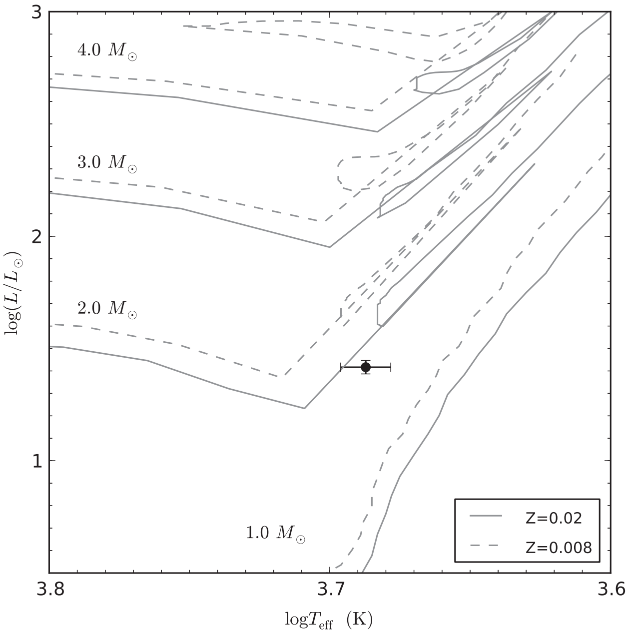

Figure 2. HD 47366 (solid circle) on the H-R diagram. The error bars correspond to the derived uncertainties of $\log L$ and $T_{\rm eff}$. The solid and dashed lines represent the evolutionary tracks from Lejeune & Schaerer (2001) for stars of $M = 1 \sim 4\,M_\odot$ with $Z = 0.02$ (solar metallicity) and $Z = 0.008$, respectively.

the ith interpolated point in the jth track, and $n = 500$ is the number of interpolated points in each track. Eventually, the probability distribution functions (PDFs) of the parameters yield $M = 1.81 \pm 0.13\,M_\odot$, $R = 7.30 \pm 0.33\,R_\odot$, $\log g = 2.97 \pm 0.06$, and age $= 1.61 \pm 0.53$ Gyr. The stellar mass is particularly important to derive the minimum masses of the orbiting planets detected with the Doppler technique. However, previous spectroscopic analyses gave discrepant results ($1.87\,M_\odot$ by Liu et al. 2010; $1.2\,M_\odot$ by Mishenina et al. 2006) for HD 47366, which may be due to the different methods on finding $T_{\rm eff}$ and $\log g$. Our determinations were based on a similar method to that of Liu et al. (2010), but used the Geneva evolutionary tracks, instead of the Y^2 model (Yi et al. 2003), which does not account for the evolutionary phases after the helium-core flash. We found that the probability that the star has passed through the RGB tip and in-core helium burning phase is ~88%. The stellar parameters of HD 47366 are listed in Table 1. In Figure 2, we plotted HD 47366 on the H-R diagram, together with the evolutionary tracks for stars with different masses and metal contents.

The star shows no significant emission in the core of Ca II HK lines, as shown in Figure 3, which suggests that the star is chromospherically inactive. We did not analyze flux variations of Ca II HK lines for the star because of the poor S/N of the core of the lines.

3. OBSERVATIONS

3.1. OAO Observations

Observations of HD 47366 at OAO were made with the 1.88 m reflector and the HIgh Dispersion Echelle Spectrograph (HIDES; Izumiura 1999) from 2006 December to 2014 April. We used both the conventional slit mode (HIDES-S) and the high-efficiency fiber-link mode (HIDES-F) of the spectrograph that became available in 2010 (Kambe et al. 2013). In the case of the HIDES-S, a slit width of the spectrograph was set to 200 μm (0″.76) corresponding to a spectral resolution ($R = \lambda/\Delta\lambda$) of 67,000 by about a 3.3-pixel sampling. In the case of HIDES-F, a width of the image sliced by an image slicer is 1″.05, corresponding to a spectral resolution of $R = 55{,}000$ by a 3.8-pixel sampling. Each observing mode uses its own iodine absorption cell for precise radial-velocity measurements (I$_2$ cell; Kambe et al. 2002, 2013), which provide a fiducial wavelength reference in a wavelength range of 5000–5800 Å. We have obtained a total of 50 and 7 data points of HD 47366 using HIDES-S and HIDES-F mode, respectively. The reduction of echelle data (i.e., bias subtraction, flat-fielding, scattered-light

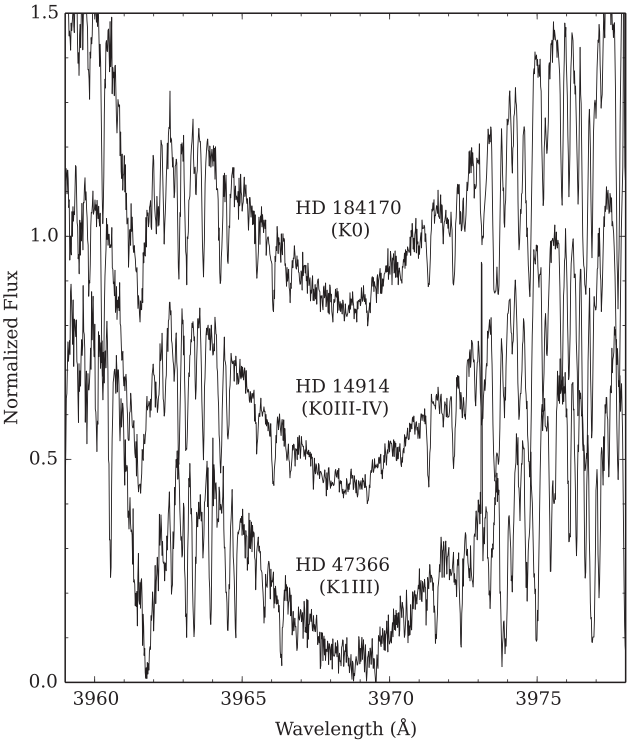

Figure 3. Spectra in the region of Ca II H lines. Stars with similar spectral types to HD 47366 in our sample are also shown. A vertical offset of about 0.4 is added to each spectrum.

subtraction, and spectrum extraction) was performed using the IRAF[16] software package in the standard way.

We performed a radial-velocity analysis following the method of Sato et al. (2002, 2012) and Butler et al. (1996), in which an I_2-superposed spectrum is modeled as a product of a high-resolution I_2 and a stellar template spectrum convolved with a modeled point-spread function (PSF) of the spectrograph. We model the PSF using multiple Gaussian profiles (Valenti et al. 1995) and obtain the stellar spectrum by deconvolving a pure stellar spectrum with the spectrograph PSF estimated from an I_2-superposed B-star spectrum. We obtained a typical measurement error in radial-velocity of about 4–5 m s^{-1} for the star, which was estimated from an ensemble of velocities from each of the ~300 spectral chunks (each ~3 Å long) in every exposure. We listed the derived radial velocities for OAO data in Table 2 together with the estimated uncertainties.

3.2. Xinglong Observations

Observations of HD 47366 at the Xinglong Station started in 2006 November using the 2.16 m reflector and the Coudé Echelle Spectrograph (CES; Zhao & Li 2001). We used the blue-arm, middle focal length camera, and 1 K × 1 K CCD (pixel size of 24 × 24 $\mu\mathrm{m}^2$; hereafter CES-O) of the spectrograph, which covered a wavelength range of 3900–7260 Å with a spectral resolution of 40,000 by 2-pixel sampling. Although a wide wavelength range was obtained with a single exposure, only a wave band of $\Delta\lambda \sim 470$ Å was available for radial-velocity measurements using an I_2 cell because of the small format of the CCD. Radial-velocity analysis for CES data was performed by the optimized method of Sato et al. (2002) for

Table 2
OAO Radial Velocities for HD 47366

JD−2450000	Velocity (m s^{-1})	Uncertainty (m s^{-1})	Mode
4093.18674	11.36	4.59	HIDES-S
4144.11514	−19.66	4.69	HIDES-S
4172.01541	−18.29	3.85	HIDES-S
4467.12999	−4.46	4.31	HIDES-S
4553.97104	−31.25	4.14	HIDES-S
4755.29094	32.92	3.46	HIDES-S
4796.25711	36.33	4.17	HIDES-S
4818.17076	19.49	3.87	HIDES-S
4823.11554	14.96	4.17	HIDES-S
4834.16358	12.38	4.36	HIDES-S
4856.08725	−6.42	3.92	HIDES-S
4863.09739	−6.67	4.41	HIDES-S
4864.03798	−11.43	3.60	HIDES-S
4883.04016	−7.18	4.55	HIDES-S
4923.93523	−17.64	3.73	HIDES-S
5108.31507	40.77	4.18	HIDES-S
5131.32409	47.90	3.57	HIDES-S
5161.34584	39.99	4.64	HIDES-S
5182.16055	11.19	4.10	HIDES-S
5204.11564	−7.29	4.29	HIDES-S
5232.99361	−43.84	3.62	HIDES-S
5267.01163	−60.09	3.57	HIDES-S
5294.93562	−62.39	3.54	HIDES-S
5471.29879	24.76	3.61	HIDES-S
5502.23739	33.89	4.15	HIDES-S
5525.22640	33.98	4.85	HIDES-S
5545.21850	18.86	3.73	HIDES-S
5581.04001	−12.92	3.75	HIDES-S
5611.01311	−8.59	4.13	HIDES-S
5625.02350	−13.62	3.49	HIDES-S
5656.93188	−10.50	3.74	HIDES-S
5854.27845	33.84	3.69	HIDES-S
5877.25348	18.63	5.42	HIDES-S
5882.29779	12.23	3.83	HIDES-S
5922.13357	−12.73	3.88	HIDES-S
5938.09758	−34.44	3.79	HIDES-S
5976.03887	−49.42	4.57	HIDES-S
6010.93116	−64.77	5.74	HIDES-S
6032.96687	−55.43	4.48	HIDES-S
6215.30762	27.47	4.04	HIDES-S
6235.27265	41.83	3.68	HIDES-S
6249.30138	27.36	4.69	HIDES-S
6284.08997	−0.00	4.69	HIDES-S
6552.29701	42.87	5.53	HIDES-S
6577.28414	4.35	4.84	HIDES-S
6578.28739	14.21	4.48	HIDES-S
6578.30265	14.55	4.27	HIDES-S
6579.25810	12.00	5.63	HIDES-S
6618.19944	4.11	3.91	HIDES-S
6753.98409	−63.39	4.45	HIDES-S
6609.21551	21.82	4.04	HIDES-F
6616.27916	33.33	3.44	HIDES-F
6664.09442	−1.41	4.02	HIDES-F
6672.05938	−16.16	3.85	HIDES-F
6697.15561	−9.17	4.70	HIDES-F
6713.98988	−17.94	4.87	HIDES-F
6727.00570	−12.14	3.47	HIDES-F

---

[16] IRAF is distributed by the National Optical Astronomy Observatories, which is operated by the Association of Universities for Research in Astronomy, Inc. under cooperative agreement with the National Science Foundation, USA.

CES (Liu et al. 2008). We took five data points for HD 47366 using CES-O from 2006 November to 2007 December whose radial-velocity uncertainties were better than 25 m s^{-1}. In 2009 March, the old CCD was replaced by a new CCD having a smaller pixel size (2 K × 2 K, 13 × 13 $\mu\mathrm{m}^2$), and it gave a better radial-velocity precision than before, though the wavelength coverage was unchanged (Wang et al. 2012). We made observations of HD 47366 using the new CCD (hereafter CES-N) from 2009 December to 2010 December, and collected a total of 26 data points with a radial-velocity precision of 12–25 m s^{-1} depending on weather conditions.

Since 2011 November, we have observed HD 47366 with the newly developed High Resolution Spectrograph (HRS) attached at the Cassegrain focus of the 2.16 m telescope. The fiber-fed spectrograph is the successor of the CES, giving a higher wavelength resolution and throughput. The single 4 K × 4 K CCD provides a simultaneous wavelength coverage of 3700–9200 Å, and the slit width of 190 μm gives a wavelength resolution of $R = 45{,}000$ with a 3.2-pixel sampling. An iodine cell is installed before the fiber entrance at the Cassegrain focus. We collected a total of 60 observations for the star from 2011 November to 2014 March. Radial-velocity analysis for the HRS data was performed by the same method as Sato et al. (2002, 2012), but optimized for HRS. The resulting measurement errors in radial velocity are ranging from 6 to 20 m s^{-1} depending on weather conditions. The derived radial velocities for Xinglong data are listed in Table 3 together with the estimated uncertainties.

3.3. AAT Observations

Since the inner planet has a period near one year, and HD 47366 is quite far south for OAO, we obtained confirmation observations from the 3.9-m Anglo-Australian Telescope (AAT). This multi-telescope approach was also critical for the confirmation of the 360-day planet HD 4732b (Sato et al. 2013a). The UCLES echelle spectrograph (Diego et al. 1990) delivers a resolving power of $R \sim 45{,}000$ with the 1-arcsecond slit, and has been used for 16 years by the Anglo-Australian Planet Search (e.g., Butler et al. 2001; Tinney et al. 2001; Jones et al. 2010; Wittenmyer et al. 2012b, 2014). Calibration of the spectrograph point-spread function is achieved using an iodine absorption cell temperature-controlled at 60.0 ± 0.1°C. The iodine cell superimposes a forest of narrow absorption lines from 5000 to 6200 Å, allowing for the simultaneous calibration of instrumental drifts as well as a precise wavelength reference (Valenti et al. 1995; Butler et al. 1996). The result is a precision Doppler velocity estimate for each epoch, along with an internal uncertainty estimate, which includes the effects of photon-counting uncertainties, residual errors in the spectrograph PSF model, and variation in the underlying spectrum between the iodine-free template and epoch spectra observed through the iodine cell. HD 47366 was observed at 13 epochs between 2013 March and 2014 April; the AAT velocities are given in Table 4.

4. ORBIT FITTING AND PLANETARY PARAMETERS

The collected radial-velocity data for HD 47366 obviously show a variation with a period near one year. Although the one- year periodicity and the relatively low declination of the star allowed us to cover only half of the cycle, we can clearly see the periodic variation of the velocity amplitude every year,

Table 3
Xinglong Radial Velocities for HD 47366

JD−2450000	Velocity (m s^{-1})	Uncertainty (m s^{-1})	Mode
4046.34259	53.99	27.92	CES-O
4133.12441	53.23	21.39	CES-O
4398.37834	101.38	17.20	CES-O
4459.23135	117.08	30.81	CES-O
4459.24962	32.80	27.00	CES-O
5172.26505	96.73	19.05	CES-N
5172.28626	76.60	15.71	CES-N
5172.30759	51.67	14.37	CES-N
5173.27944	45.82	15.67	CES-N
5173.30065	56.52	16.41	CES-N
5173.32198	65.67	17.79	CES-N
5173.34310	65.70	14.76	CES-N
5226.05844	−45.55	24.43	CES-N
5226.10875	−20.17	22.59	CES-N
5227.08807	−26.57	11.76	CES-N
5227.10979	−46.69	13.18	CES-N
5227.13103	−12.38	14.99	CES-N
5281.99890	−14.95	13.80	CES-N
5282.00964	−22.57	15.56	CES-N
5282.02035	−61.02	17.25	CES-N
5282.98558	−45.16	16.54	CES-N
5283.00671	−59.43	16.13	CES-N
5283.02782	−52.03	15.03	CES-N
5283.98000	−51.62	13.79	CES-N
5284.00528	−29.21	20.65	CES-N
5284.02646	−48.95	20.95	CES-N
5284.04756	−6.26	21.05	CES-N
5520.33128	39.59	17.73	CES-N
5520.35299	21.56	16.20	CES-N
5552.23941	34.69	14.87	CES-N
5552.26341	24.93	21.94	CES-N
5878.34042	43.36	13.50	HRS
5878.36563	33.75	13.50	HRS
5878.38866	−0.73	16.05	HRS
5878.41177	42.81	16.18	HRS
5879.29416	4.27	19.96	HRS
5905.20117	23.16	11.56	HRS
5905.22422	14.68	12.04	HRS
5905.24720	36.90	14.27	HRS
5905.27024	48.98	15.64	HRS
5907.26067	1.38	8.18	HRS
5907.28402	−8.44	9.30	HRS
5907.30698	8.20	10.15	HRS
5907.32995	7.82	9.57	HRS
5936.13872	−29.36	10.11	HRS
5936.16225	−35.52	10.34	HRS
5936.18572	−32.01	10.67	HRS
5936.20863	−22.04	11.92	HRS
5959.11008	−30.57	22.97	HRS
5959.13303	−43.36	20.46	HRS
5959.15600	−43.22	18.84	HRS
5959.17896	−62.76	24.07	HRS
5960.09450	−49.14	13.67	HRS
5960.11747	−39.46	15.51	HRS
5966.04907	−39.47	19.32	HRS
5966.07211	−31.79	20.95	HRS
5966.09510	−79.17	17.80	HRS
5966.11809	−67.76	17.67	HRS
5997.97169	−66.24	10.18	HRS
5997.99495	−52.05	11.16	HRS
5998.01824	−47.66	11.05	HRS
5998.04152	−60.49	10.68	HRS
6199.33390	51.35	6.54	HRS

Table 3
(Continued)

JD−2450000	Velocity (m s^{-1})	Uncertainty (m s^{-1})	Mode
6199.35708	45.59	7.80	HRS
6232.33343	54.89	5.89	HRS
6232.35667	61.48	6.12	HRS
6287.18192	30.60	9.50	HRS
6287.20515	35.52	10.34	HRS
6287.22838	32.06	9.39	HRS
6287.25312	47.44	11.03	HRS
6318.08350	31.16	11.25	HRS
6318.10670	13.27	11.99	HRS
6318.13045	21.01	12.00	HRS
6318.15375	25.07	11.17	HRS
6344.02830	11.76	8.52	HRS
6344.05152	23.29	9.47	HRS
6344.07471	22.34	9.87	HRS
6583.31389	22.42	10.63	HRS
6583.33707	35.39	11.03	HRS
6583.36032	20.96	11.67	HRS
6611.28853	18.21	7.27	HRS
6611.31171	20.81	8.39	HRS
6611.33507	7.72	8.55	HRS
6645.18797	−18.03	12.37	HRS
6645.21133	9.17	12.68	HRS
6645.23463	−12.05	15.41	HRS
6645.25792	−22.92	16.31	HRS
6701.05113	−50.92	11.31	HRS
6701.07444	−55.62	15.95	HRS
6728.98753	−39.22	16.13	HRS
6729.01088	−50.79	19.71	HRS

Table 4
AAT Radial Velocities for HD 47366

JD−2450000	Velocity (m s^{-1})	Uncertainty(m s^{-1})
6374.88737	−4.3	1.2
6375.91758	1.9	1.1
6376.93270	0.0	1.1
6377.98528	−2.0	1.2
6399.91709	13.0	1.4
6526.29116	70.0	1.4
6529.31433	85.4	1.5
6555.29760	63.2	1.5
6556.21605	67.5	1.5
6686.00004	−17.2	1.6
6744.92245	−42.0	1.5
6747.92675	−46.0	1.6
6764.87970	−40.9	1.3

indicating the existence of a second period near two years. Thus we performed the least-squares orbital fitting by a double Keplerian model. The orbital parameters and the uncertainties were derived using the Bayesian Markov Chain Monte Carlo (MCMC) method (e.g., Ford 2005; Gregory 2005; Ford & Gregory 2007), following the analysis in Sato et al. (2013b). We took account of velocity offsets ΔRV of HIDES-F, CES-O, CES-N, HRS, and AAT data relative to HIDES-S data as free parameters in the orbital fitting. Extra Gaussian noises s for each of the six data sets were also incorporated as free parameters, though those for CES-O (s_3) and HRS (s_5) are fixed to 0 since their rms scatters to the best-fit orbit are comparable to their measurement errors. We generated five independent chains having 10^7 points with acceptance rates of about 25%, the first 10% of which were discarded, and confirmed that each parameter was sufficiently converged based on the Gelman-Rubbin statistic (Gelman & Rubin 1992). We derived the median value of the merged posterior PDF for each parameter and set a 1σ uncertainty as the range between 15.87% and 84.13% of the PDF.

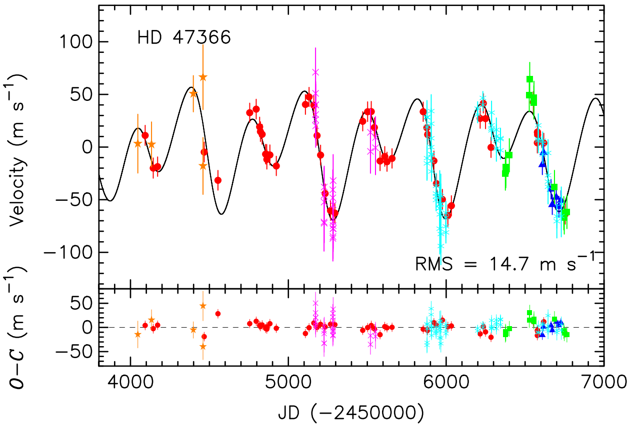

Figure 4. Upper: radial velocities of HD 47366 obtained with HIDES-S (red), HIDES-F (blue), CES-O (brown), CES-N (magenta), HRS (cyan), and AAT (green). The error bar for each point includes the extra Gaussian noise. The double Keplerian model for the radial velocities is shown by the solid line. Bottom: residuals to the Keplerian fit.

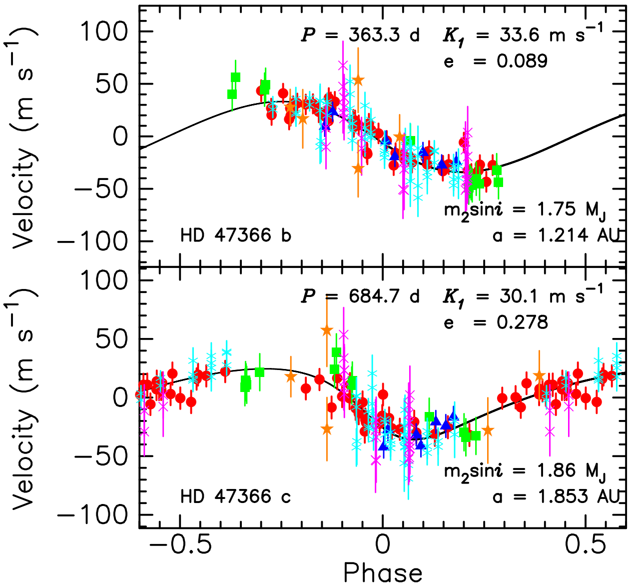

Figure 5. Phased radial velocities and the Keplerian models for the inner (upper panel; signal of the outer planet is removed) and the outer (bottom panel; signal of the inner planet is removed) planet. The error bar for each point includes the extra Gaussian noise. The symbols are the same as those in Figure 4.

In Figures 4 and 5, we plot the derived Keplerian orbits together with the radial-velocity points and their measurement errors including the extra Gaussian noises. The inner planet (planet b) has orbital parameters of a period of $P_b = 363.3^{+2.5}_{-2.4}$ days, an eccentricity of $e_b = 0.089^{+0.079}_{-0.060}$, a minimum mass of $m_b \sin i = 1.75^{+0.20}_{-0.17}$ $M_{\rm J}$, and a semimajor axis of $a_b = 1.214^{+0.030}_{-0.029}$ au, and the outer planet (planet c) has $P_c = 684.7^{+5.0}_{-4.9}$ days, $e_c = 0.278^{+0.067}_{-0.094}$, $m_c \sin i = 1.86^{+0.16}_{-0.15}$ $M_{\rm J}$,

Table 5
Orbital Parameters for HD 47366

Parameter	HD 47366 b	HD 47366 c
Period P (days)	$363.3^{+2.5}_{-2.4}$	$684.7^{+5.0}_{-4.9}$
RV semiamplitude K_1 (m s^{-1})	$33.6^{+3.6}_{-2.8}$	$30.1^{+2.1}_{-2.0}$
Eccentricity e	$0.089^{+0.079}_{-0.060}$	$0.278^{+0.067}_{-0.094}$
Longitude of periastron ω (deg)	100^{+100}_{-71}	132^{+17}_{-20}
Periastron passage T_p (JD−2450000)	122^{+71}_{-55}	445^{+55}_{-62}
Minimum mass $m_2 \sin i$ (M_J)	$1.75^{+0.20}_{-0.17}$	$1.86^{+0.16}_{-0.15}$
Semimajor axis a (au)	$1.214^{+0.030}_{-0.029}$	$1.853^{+0.045}_{-0.045}$
Semimajor axis ratio a_b/a_c	$0.6555^{+0.0041}_{-0.0043}$	
Extra Gaussian noises for HIDES-S s_1 (m s^{-1})	$8.4^{+1.4}_{-1.2}$	
Extra Gaussian noises for HIDES-F s_2 (m s^{-1})	$8.5^{+4.7}_{-3.1}$	
Extra Gaussian noises for CES-O s_3 (m s^{-1})	0 (fixed)	
Extra Gaussian noises for CES-N s_4 (m s^{-1})	$13.1^{+5.8}_{-7.1}$	
Extra Gaussian noises for HRS s_5 (m s^{-1})	0 (fixed)	
Extra Gaussian noises for AAT s_6 (m s^{-1})	$15.8^{+5.6}_{-4.5}$	
Velocity offset of HIDES-F ΔRV_{2-1} (m s^{-1})	$38.3^{+5.2}_{-5.2}$	
Velocity offset of CES-O ΔRV_{3-1} (m s^{-1})	50^{+11}_{-11}	
Velocity offset of CES-N ΔRV_{4-1} (m s^{-1})	$25.3^{+4.7}_{-4.7}$	
Velocity offset of HRS ΔRV_{5-1} (m s^{-1})	$14.5^{+2.4}_{-2.5}$	
Velocity offset of AAT ΔRV_{6-1} (m s^{-1})	$20.5^{+5.6}_{-5.3}$	
Number of data of HIDES-S N_1	50	
Number of data of HIDES-F N_2	7	
Number of data of CES-O N_3	5	
Number of data of CES-N N_4	26	
Number of data of HRS N_5	60	
Number of data of AAT N_6	13	
rms (m s^{-1})	14.7	

Note. Velocity offsets are the values relative to HIDES-S data.

and $a_c = 1.853^{+0.045}_{-0.045}$ au. The obtained parameters are listed in Table 5.

The *Hipparcos* satellite made a total of 158 photometric observations for HD 47366 from 1990 March to 1993 March, and revealed photometric stability for the star down to $\sigma_{\rm HIP} = 0.007$ mag, though the *Hipparcos* observations were not contemporaneous with the radial-velocity observations. Figure 6 shows the generalized Lomb–Scargle periodogram (Zechmeister & Kürster 2009) of the *Hipparcos* photometric data of the star. We did not find any clue that the radial-velocity variations correlate with the brightness variations of the star. Furthermore, the rotational period of the star can be estimated to be shorter than about 86 days based on its radius $R = 7.3\ R_\odot$ and its projected rotational velocity $v \sin i = 4.3$ km s^{-1} (see Table 1). This is much shorter than either the 363-day or the 685-day periods observed in radial velocity. Thus the rotational modulation of spots on the stellar surface is not considered to be a viable explanation for the observed radial-velocity variations.

We also performed a spectral line shape analysis for the star, following the method in Sato et al. (2007). Cross-correlation profiles between pairs of stellar templates, each of which were extracted from five I$_2$-superposed spectra at phases of velocity ∼30 m s^{-1} (phase 1), ∼−10 m s^{-1} (phase 2), and ∼−50 m s^{-1} (phase 3) by using the method of Sato et al. (2002), were derived for about 110 spectral segments (4–5 Å width each). Three bisector quantities of the cross-correlation profiles, BVS, BVC, and BVD, were then calculated, which are the velocity difference between the two flux levels of the bisector, the difference of the BVS of the upper and lower halves of the bisector, and the average of the bisector at three flux levels, respectively. The flux levels of 25%, 50%, and 75% of each cross-correlation profile were used to calculate the above three bisector quantities. As a result, we obtained BVS = 6.6 ± 5.5 m s^{-1}, BVC = −2.5 ± 3.0 m s^{-1}, and BVD = −86.1 ± 10.8 m s^{-1} for the cross-correlation profile between phases 1 and 3, and BVS = −4.1 ± 4.9 m s^{-1}, BVC = 3.1 ± 2.6 m s^{-1}, and BVD = −35.1 ± 11.6 m s^{-1} for the one between phases 2 and 3. The BVD values are consistent with the velocity differences between the phases, and the BVS and BVC values are much smaller than the BVD values. Therefore, we conclude that the observed radial-velocity variations did not originate from the distortion of the spectral lines, but from their parallel shifts, as expected for orbital motion.

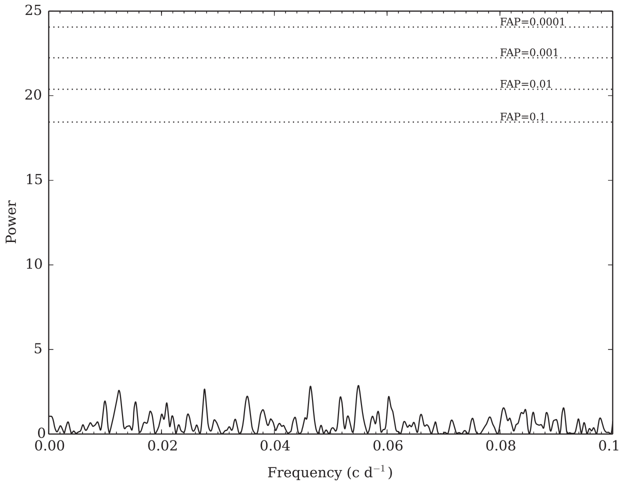

Figure 6. Generalized Lomb–Scargle periodogram of the *Hipparcos* photometric data of HD 47366. The dotted lines indicate False Alarm Probability (FAP) levels.

5. DYNAMICAL STABILITY

The orbital parameters obtained in Section 4 were derived by fitting a double Keplerian model to the radial-velocity data, which does not guarantee that the orbits are stable over long periods of time. In order to investigate the orbital stability of the system and to further constrain orbital parameters, we performed a dynamical analysis of the system. We used a fourth-order Hermite scheme for the numerical integration (Kokubo et al. 1998).

Figure 7 shows the lifetime of the system, calculated by the 10^6-year integrations. The lifetime here is defined as the time elapsing before the semimajor axis of one planet deviates by 10% from its initial value. All of the initial orbital parameters for the orbital integrations are fixed to the best-fit ones derived in Section 4 except for those shown in each axis of each panel. Figures 7(a)–(c) shows the lifetime of the system in the (a_c, e_c), (a_c, ω_c), and (ω_c, e_c) planes, respectively. In the panels, prograde and edge-on orbits ($i_b = i_c = 90°$) are assumed. The dashed line in panel (*a*) shows the orbit-crossing boundary where the apocenter distance of planet b is equal to the pericenter distance of planet c. The planets b and c actually have almost crossing orbits with each other in the case of the best-fit orbits (marked by a red cross in each panel), and, as shown in the figure, they are unstable. Orbits above the boundary line easily become unstable within 1000 years. Stable orbits appearing above the boundary are in the 2:1 mean-

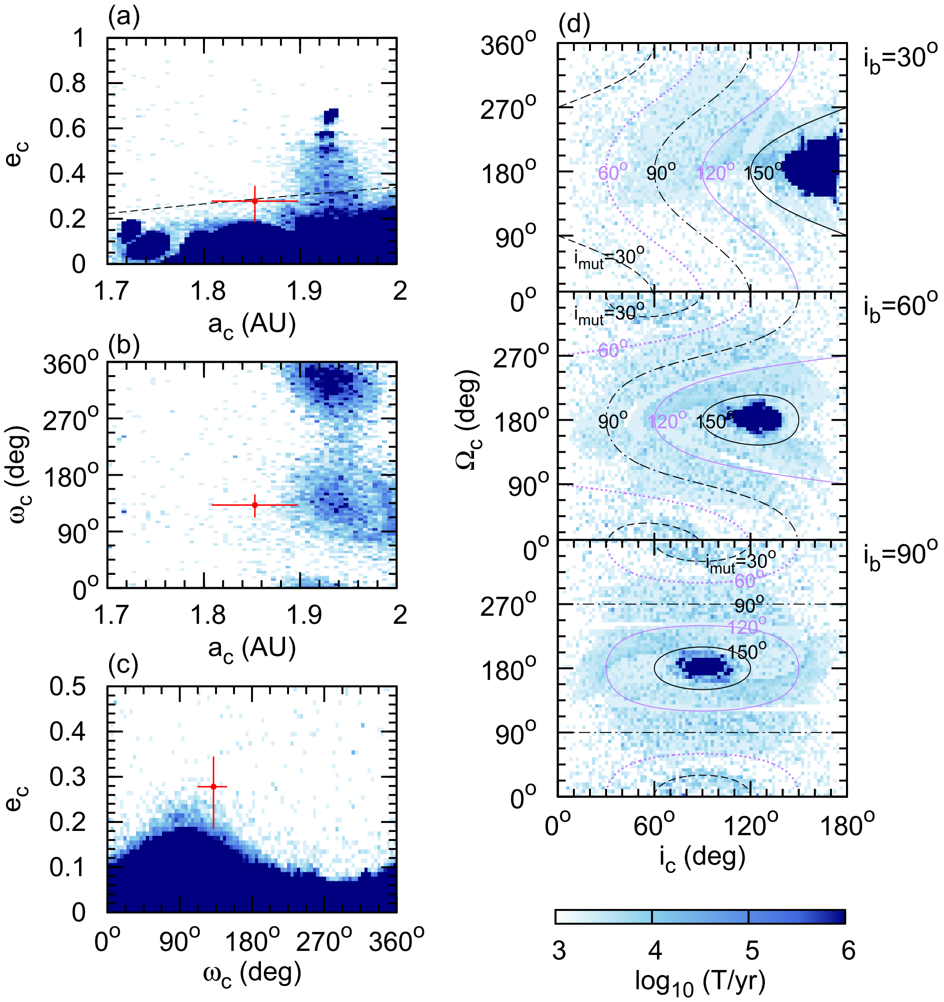

Figure 7. Lifetime of the system. The time elapsing before the semimajor axis of one planet deviates by 10% from its initial value is shown. Since the extent of our numerical integrations is 10^6 years, the lifetime of 10^6 years here means that the system is stable over 10^6 years (dark-blue regions). The red cross represents the best-fitted a_c and e_c to the radial-velocity data with their 1σ errors. (a) The diagram of e_c vs. a_c. (b) The diagram of argument of pericenter ω_c vs. semimajor axis. (c) The e_c–ω_c diagram. (d) The diagram of longitude of ascending node Ω_c vs. inclination from the line of sight i_c, together with the contours of the mutual inclination. From top to bottom, the cases for $i_b = 30°$, $60°$, and $90°$ are shown. The absolute masses of planets b and c are inversely proportional to $\sin i_b$ and $\sin i_c$, respectively.

motion resonance. If a_c is near 1.93 au with an appropriate argument of pericenter, the orbits are stable with up to $e_c \sim 0.7$ over 10^6 years thanks to the resonance, though this a_c value is beyond the 3σ range of $a_b/a_c (=0.6555^{+0.0041}_{-0.0043})$ that is well determined by our radial-velocity data (panel (b)). On the other hand, if e_c is smaller than ~0.15 (1.4σ away from the best-fit value), the orbits are also stable even with the best-fit a_c (1.85 au) in prograde configuration (panel (c)).

If the mutual inclination $i_{\rm mut}$ between the two planets is higher than 160°, the orbit becomes stable in a wider parameter range. Figure 7(d) shows the stability map in the plane of inclination (i_c) and the ascending node (Ω_c) of planet c (ascending node of planet b is set to $\Omega_b = 0$). The mutual inclination of planets depends on i_b, i_c, and $\Omega_c - \Omega_b$ as $\cos i_{\rm mut} = \cos i_b \cos i_c + \sin i_b \sin i_c \cos(\Omega_c - \Omega_b)$, and its contours are shown by black or purple lines in the figure. Since the absolute masses of the planets depend on the angle from the line of sight, the cases of three different inclinations for planet b, $i_b = 30°$, $60°$, and $90°$, are shown. The absolute mass of planet c is also changed according to i_c. The absolute masses of planets b and c are inversely proportional to $\sin i_b$ and $\sin i_c$, respectively. As seen in the figure, the orbits with $i_{\rm mut} \sim 180°$ (i.e., mutually retrograde) are stable in all cases. This is because planet encounters occur in a shorter time with higher mutual velocities in the retrograde system compared to the prograde system. This is similar to the case of the two brown-dwarf candidates orbiting BD+20 2457, in which the system is unstable for the prograde orbits, while it is stable for the retrograde orbits (Horner et al. 2014).

Figure 8 shows the 7×10^4 year evolution of the system. The upper panel shows the evolution of the coplanar retrograde system with the best-fit orbital parameters derived in Section 4. Although the outer planet violates the orbit of the inner planet, they are stable over 10^6 years. The bottom panel shows a prograde case with the same orbital parameters except assuming $e_{\rm c,ini} = 0$. As seen in the figure, if the eccentricity of the outer planet is small, the system can keep stable orbits, while the system with the outer planet in eccentric orbit quickly causes orbital crossing and becomes unstable (see Figure 7).

Figure 9 shows maps of the stability index $D = |\langle n_2 \rangle - \langle n_1 \rangle|$ for the system. From a 5000-year numerical

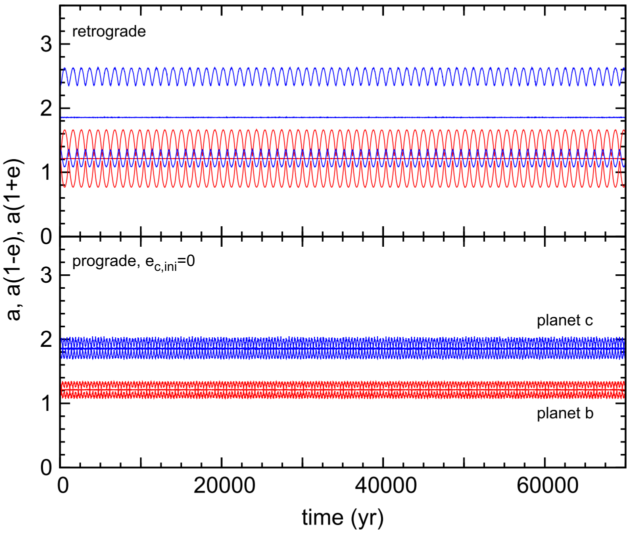

Figure 8. Evolution of semimajor axis, pericenter distance, and apocenter distance of planets b (red lines) and c (blue lines) assuming $i_b = i_c = 90°$. Top: retrograde coplanar case with best-fitting orbital elements. Bottom: prograde coplanar case, but $e_c = 0$ is assumed.

integration, we obtain an average of mean motion $\langle n_1 \rangle$ of planet c and subtract it from an average of mean motion $\langle n_2 \rangle$ obtained in the next 5000-year orbit (see Couetdic et al. 2010 for the details of the stability analysis). The left and right panels are the maps for prograde and retrograde configuration, respectively. From a comparison with panel (*a*) of Figure 7, we find that the system is regular when $\log_{10} D \leqslant -3$. In the case of the retrograde orbit, the orbit is stable even if the eccentricity of the planet c exceeds the orbit-crossing boundary (dashed line) by ~0.1.

6. DISCUSSION AND SUMMARY

We have reported the detection of a double giant-planet system around the K1 giant HD 47366 ($M_\star = 1.81 \pm 0.13\ M_\odot$, $R_\star = 7.30 \pm 0.33\ R_\odot$) from precise radial-velocity measurements at OAO, Xinglong, and AAT. The inner (planet b) and outer planets (planet c) have minimum masses of $1.75^{+0.20}_{-0.17}\ M_\mathrm{J}$ and $1.86^{+0.16}_{-0.15}\ M_\mathrm{J}$, semimajor axes of $1.214^{+0.030}_{-0.029}$ au and $1.853^{+0.045}_{-0.045}$ au, and eccentricities of $0.089^{+0.079}_{-0.060}$ and $0.278^{+0.067}_{-0.094}$, respectively, which were derived by fitting a double Keplerian model to the radial-velocity data. The period ratio of the two planets is slightly smaller than 2, and thus the system adds to the growing population of such multi-giant-planet systems with small orbital separation around evolved intermediate-mass stars.

The dynamical analysis of the system revealed, however, that the best-fit orbits in prograde configuration are unstable. We found that it is stable in the following cases: (1) the two planets are in the 2:1 mean-motion resonance, (2) the eccentricity of planet c is less than ~0.15, (3) the mutual inclination the two planets is larger than 160° (i.e., retrograde configuration).

If the two planets are in the stable 2:1 resonance, the ratio of the semimajor axis should be $a_b/a_c \sim 0.63$ ($a_c \sim 1.93$ au) and the eccentricity of planet c should be $0.5 \lesssim e_c \lesssim 0.7$ or $0 \leqslant e_c \lesssim 0.2$ (see Section 5 and the darkest-blue regions in panel (a) of Figure 7). On the other hand, a_b/a_c is well determined from our observations to be $a_b/a_c = 0.6555^{+0.0041}_{-0.0043}$ and e_c is determined to be $e_c = 0.278^{+0.067}_{-0.094}$. Both of these values deviate from those for the high-eccentricity case with more than 3σ, and thus from the view point of the observational data, it is less likely that the planets are in the high-eccentricity resonance. We cannot completely reject the possibility of the low-eccentricity case. However, considering the semimajor-axis ratio, it is also less likely that the planets are in the resonance.

It is more plausible that the eccentricity of planet c is less than ~0.15. The value is just 1.4σ from the best-fit value, and the best-fit orbit is consistent with a circular one to the 3σ level. Thus, it is reasonable to think that the two planets actually have nearly circular orbits and thus they are stable. In this case, the period ratio of the planets is slightly smaller than 2, and they are not in 2:1 resonance.

The third possibility is the most extreme one. Basically, we cannot determine the inclination or the ascending node of a planetary orbit by radial-velocity measurements, and thus we cannot discriminate between prograde and retrograde orbits observationally. Gayon & Bois (2008) and Gayon-Markt & Bois (2009) studied mutually retrograde configurations for some multi-planet systems around solar-type stars and showed that the configurations are dynamically stable and consistent with the radial-velocity observations. Recently, Horner et al. (2014) studied the dynamical stability of a double brown-dwarf system around the giant BD+20 2457 (Niedzielski et al. 2009), and showed that the prograde orbits best-fitted to the radial-velocity data are unstable, while those in retrograde configuration are stable. The HD 47366 system is similar to the case of the BD+20 2457 system. Our dynamical analysis showed that the coplanar retrograde configuration for the HD 47366 system is stable in a wider range of orbital parameters including the eccentric ones which are unstable for prograde configuration (see Figure 8). Confirmation of the high eccentricity of the outer planet by continuous observations will strongly support the retrograde hypothesis for the HD 47366 system, though the formation mechanism of such a mutually retrograde system is largely unknown. In any of the above cases, the planetary orbits can be altered by the close encounter of the planets in a relatively short period of time, and thus more detailed dynamical modeling for the observed radial-velocity variations is necessary in order to provide a definitive orbital solution.

The stellar and planetary parameters of HD 47366 system are similar to those of the η Cet system; two massive planets ($m_b \sin i = 2.6\ M_\mathrm{J}$, $m_c \sin i = 3.3\ M_\mathrm{J}$), with periods of $P_b = 407$ days and $P_c = 740$ days and eccentricities of $e_b = 0.12$ and $e_c = 0.08$ orbit around a K giant star with a mass of $1.7\,M_\odot$ and a radius of $14.3\,R_\odot$ (Trifonov et al. 2014). Trifonov et al. (2014) revealed that, for a coplanar configuration, the system can be stable by being trapped in an anti-aligned 2:1 mean-motion resonance in a region with moderate e_b eccentricity, which lies about 1σ away from the best-fit Keplerian orbits. A much larger non-resonant stable region also exists in low-eccentricity parameter space, though it appears to be much farther from the best fit than the 2:1 resonant region. This is in contrast with the case of HD 47366 in which low eccentricities of the planets are more plausible than 2:1 resonant configuration. Another possible 2:1 resonant system around an evolved star is 24 Sex, in which two massive planets ($m_b \sin i = 1.99\ M_\mathrm{J}$, $m_c \sin i = 0.86\ M_\mathrm{J}$), with periods of $P_b = 452.8$ days and $P_c = 883.0$ days and eccentricities of $e_b = 0.09$ and $e_c = 0.29$ orbit around a G-type subgiant with a

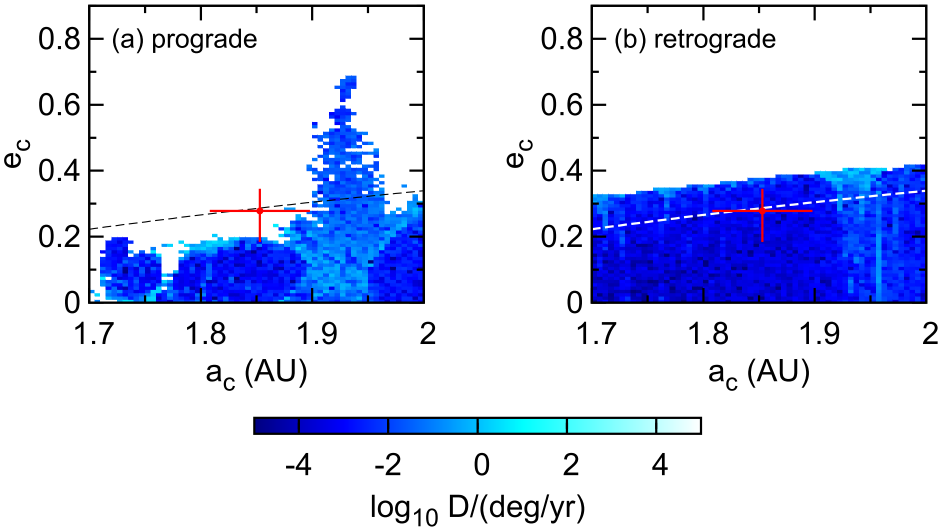

Figure 9. Mean motion diffusion D (stability index) of the HD 47366 system. The best-fit orbital parameters are used as the initial parameters for the orbital integrations except for the semimajor axis and eccentricity of planet c, whose best-fitted values are marked by red crosses with their 1σ errors. The absolute mass of planets used in the simulations are $m_b = 1.75\ M_J$ and $m_c = 1.86\ M_J$ ($i_b = i_c = 90°$). The dashed lines show the orbit-crossing boundary where the apocenter distance of planet b is equal to the pericenter distance of planet c. (a) Prograde coplanar configuration. (b) Retrograde coplanar configuration.

mass of 1.54 $M_\odot$ and a radius of 4.9 $R_\odot$ (Johnson et al. 2011). The period ratio of the planets is the closest to two of the three systems. Wittenmyer et al. (2012a) revealed that the best-fit orbit of the system is mutually crossing and it is only dynamically feasible if the planets are in 2:1 resonance, which can protect them from close encounters. As described, all of the above three systems are near the 2:1 resonance, but they show different properties in their orbital configuration. Further analysis and comparison of the systems would help us understand the dynamics of planetary systems in more detail.

It is unknown why multi-giant-planet systems with small orbital separations are preferentially found around evolved intermediate-mass stars (see Figure 1). It may be a primordial property of planets around intermediate-mass stars that could be an outcome of planet formation or an acquired one as a result of orbital evolution caused by stellar evolution (stellar tide and mass loss) of central stars. In the case of HD 47366, if the star is a helium-core burning star that has passed through the RGB tip (see Section 2), the planetary orbits could have been migrated outward by ~10% (~0.1 au) during the RGB phase because of the effect of mass loss of the central star (Kunitomo et al. 2011; Villaver et al. 2014). However, the effect works for both of the two planets and thus it could not result in making the orbital separation smaller. The star might have harbored a third planet that was engulfed and possibly partially responsible for the current orbital configuration, though the star does not exhibit a possible signature of the planet engulfment such as an overabundance of lithium (e.g., Siess & Livio 1999; Adamow et al. 2012), Liu et al. (2014) obtained the lithium abundance of[17] $A(\mathrm{Li}) = 0.38$ for HD 47366, suggesting that the star is an Li-depleted giant. Considering also that many of the systems with small orbital separation are found around less evolved subgiants, the effect of stellar evolution may be less significant compared to that of stellar mass. Unfortunately, the ongoing Doppler planet searches cannot clearly discriminate between the above two factors, stellar mass and stellar evolution, because the targets of the searches are both evolved and intermediate-mass stars. Investigating planets around intermediate-mass, main-sequence stars or those around evolved low-mass (~1 $M_\odot$) stars would help clarify each effect separately.

This research is based on data collected at the Okayama Astrophysical Observatory (OAO), which is operated by National Astronomical Observatory of Japan, Xinglong Station, which is operated by the National Astronomical Observatory of China, and at the Australian Astronomical Observatory. We are grateful to all the staff members of the observatories for their support during the observations. This work was partially Supported by the Open Project Program of the Key Laboratory of Optical Astronomy, National Astronomical Observatories, Chinese Academy of Sciences. We thank students of Tokyo Institute of Technology and Kobe University for their kind help with the observations at OAO. B. S. was partially supported by MEXT's program "Promotion of Environmental Improvement for Independence of Young Researchers" under the Special Coordination Funds for Promoting Science and Technology, and by Grant-in-Aid for Young Scientists (B) 17740106 and 20740101 and Grant-in-Aid for Scientific Research (C) 23540263 from the Japan Society for the Promotion of Science (JSPS). M.N. is supported by Grant-in-Aid for Young Scientists (B) 21740324 and H.I. is supported by Grant-In-Aid for Scientific Research (A) 23244038 from JSPS. This work was partially funded by the National Natural Science Foundation of China under grants 111173031, 1233004, and 11390371, as well as the Strategic Priority Research Program "The Emergence of Cosmological Structures" of the Chinese Academy of Sciences, grant No. XDB09000000, and by the JSPS under Grant-in-Aid for Scientific Research (B) 17340056 (H.A.) and grant 08032011-000184 in the framework of the Joint Research Project between China and Japan. This research has made use of the SIMBAD database, operated at CDS, Strasbourg, France.

---

[17] $A(\mathrm{Li}) = \log n_{\mathrm{Li}}/n_{\mathrm{H}} + 12$.

REFERENCES

Adamow, M., Niedzielski, A., Villaver, E., Nowak, G., & Wolszczan, A. 2012, ApJ, 754, 15
Alonso, A., Arribas, S., & Martínez-Roger, C. 1999, A&AS, 140, 261
Alonso, A., Arribas, S., & Martínez-Roger, C. 2001, A&A, 376, 1039
Batalha, N. M., Rowe, J. F., Bryson, S. T., et al. 2013, ApJS, 204, 24
Bonifacio, P., Monai, S., & Beers, T. C. 2000, AJ, 120, 2065
Butler, R. P., Marcy, G. W., Williams, E., et al. 1996, PASP, 108, 500
Butler, R. P., Tinney, C. G., Marcy, G. W., et al. 2001, ApJ, 555, 410
Castelli, F., & Kurucz, R. L. 2004, arXiv:astro-ph/0405087
Ciceri, S., Lillo-Box, J., Southworth, J., et al. 2015, A&A, 573, L5
Correia, A. C. M., Udry, S., Mayor, M., et al. 2009, A&A, 496, 521
Couetdic, J., Laskar, J., Correia, A. C. M., Mayor, M., Udry, S., et al. 2010, A&A, 519, A10
de Medeiros, J. R., Setiawan, J., Hatzes, A. P., et al. 2009, A&A, 504, 617
Diego, F., Charalambous, A., Fish, A. C., & Walker, D. D. 1990, Proc. SPIE, 1235, 562
Döllinger, M. P., Hatzes, A. P., Pasquini, L., Guenther, E. W., & Hartmann, M. 2009, A&A, 505, 1311
ESA 1997, A&A, 394, 5
Fekel, F. C. 1997, PASP, 109, 514
Ford, E. B. 2005, AJ, 129, 1706
Ford, E. B., & Gregory, P. C. 2007, in ASP Conf. Proc. 371, Statistical Challenges in Modern Astronomy IV, ed. G. J. Babu, & E. D. Feigelson (San Francisco, CA: ASP), 189
Gayon, J., & Bois, E. 2008, A&A, 482, 665
Gayon-Markt, J., & Bois, E. 2009, MNRAS, 399, 137
Gelman, A., & Rubin, D. B. 1992, StaSc, 7, 457
Giguere, M. J., Fischer, D. A., Payne, M. J., et al. 2015, ApJ, 799, 89
Gregory, P. C. 2005, ApJ, 631, 1198
Hatzes, A. P., Guenther, E. W., Endl, M., et al. 2005, A&A, 437, 743
Hatzes, A. P., Cochran, W. D., Endl, M., et al. 2006, A&A, 457, 335
Hekker, S., & Meléndez, J. 2007, A&A, 475, 1003
Horner, J., Wittenmyer, R. A., Hinse, T. C., & Marchall, J. P. 2014, MNRAS, 439, 1176
Huber, D., Carter, J. A., Barbieri, M., et al. 2013, Sci, 342, 331
Izumiura, H. 1999 in Observational Astrophysics in Asia and its Future, 4th East Asian Meeting on Astronomy (4th EAMA), ed. P. S. Chen (Kunming: Yunnan Univ., Chinese Academy of Sciences), 77
Johnson, J. A., Payne, M., Howard, A. W., et al. 2011, AJ, 141, 16
Jones, H. R. A., Butler, R. P., Tinney, C. G., et al. 2010, MNRAS, 403, 1703
Jones, M. I., Jenkins, J. S., Rojo, P., Melo, C. H. F., & Bluhm, P. 2015, A&A, 573, AA3
Kambe, E., Sato, B., Takeda, Y., et al. 2002, PASJ, 54, 865
Kambe, E., Yoshida, M., Izumiura, H., et al. 2013, PASJ, 65, 15
Kley, W., Peitz, J., & Bryden, G. 2004, A&A, 414, 735
Kokubo, E., Yoshinaga, K., & Makino, J. 1998, MNRAS, 297, 1067
Kunitomo, M., Ikoma, M., Sato, B., Katsuta, Y., & Ida, S. 2011, ApJ, 737, 66
Lee, B.-C., Han, I., Park, M.-G., et al. 2014, A&A, 566, 67
Lee, M. H., & Peale, S. J. 2002, ApJ, 567, 596
Lejeune, T., & Schaerer, D. 2001, A&A, 366, 538
Lillo-Box, J., Barrado, D., Moya, A., et al. 2014, A&A, 562, 109
Liu, Y.-J., Sato, B., Takeda, Y., Ando, H., & Zhao, G. 2010, PASJ, 62, 1071
Liu, Y.-J., Tan, K.-F., Wang, L., et al. 2014, ApJ, 785, 94
Liu, Y.-J., Sato, B., Zhao, G., et al. 2008, ApJ, 672, 553
Lovis, C., & Mayor, M. 2007, A&A, 472, 657
Mishenina, T. V., Bienaymé, O., Gorbaneva, T. I., et al. 2006, A&A, 456, 1109
Niedzielski, A., Nowak, G., Adamow, M., & Wolszczan, A. 2009b, ApJ, 707, 768
Novak, G., Niedzielski, A., Wolszczan, A., Adamów, M., & Maciejewski, G. 2013, ApJ, 770, 53
Omiya, M., Han, I., Izumiura, H., et al. 2012, PASJ, 64, 34
Ortiz, M., Gandolfi, D., Reffert, S., et al. 2015, A&A, 573, L6
Quinn, S. N., White, T. R., Latham, D. W., et al. 2015, ApJ, 803, 49
Reffert, S., Bergmann, C., Quirrenbach, A., Trifonov, T., & Künstler, A. 2015, A&A, 574, A116
Rein, H., Payne, M. J., Veras, D., & Ford, E. B. 2012, MNRAS, 426, 187
Robinson, S. E., Laughlin, G., Vogt, S. S., et al. 2007, ApJ, 670, 1391
Sato, B., Kambe, E., Takeda, Y., Izumiura, H., & Ando, H. 2002, PASJ, 54, 873
Sato, B., Izumiura, H., Toyota, E., et al. 2007, ApJ, 661, 527
Sato, B., Omiya, M., Harakawa, H., et al. 2012, PASJ, 64, 135
Sato, B., Omiya, M., Wittenmyer, R. A., et al. 2013a, ApJ, 762, 9
Sato, B., Omiya, M., Harakawa, H., et al. 2013b, PASJ, 65, 85
Sato, B., Hirano, T., Omiya, M., et al. 2015, ApJ, 802, 57
Schlegel, D. J., Finkbeiner, D. P., & Davis, M. 1998, ApJ, 500, 525
Setiawan, J., Rodmann, J., da Silva, L., et al. 2005, A&A, 437, 31
Siess, L., & Livio, M. 1999, MNRAS, 308, 1133
Tinney, C. G., Butler, R. P., Marcy, G. W., et al. 2001, ApJ, 551, 507
Trifonov, T., Reffert, S., Tan, X., Lee, M. H., & Quirrenbach, A. 2014, A&A, 568, 64
Valenti, J. A., Butler, R. P., & Marcy, G. W. 1995, PASP, 107, 966
van Leeuwen, F. 2007, A&A, 474, 653
Villaver, E., Livio, M., Mustill, A. J., & Siess, L. 2014, ApJ, 794, 3
Wang, L., Sato, B., Zhao, G., et al. 2012, RAA, 12, 84
Wang, L., Sato, B., Omiya, M., et al. 2014, PASJ, 66, 118
Wittenmyer, R. A., Endl, M., Wang, L., et al. 2011, ApJ, 743, 184
Wittenmyer, R. A., Horner, J., & Tinney, C. G. 2012a, ApJ, 761, 165
Wittenmyer, R. A., Horner, J., Tinney, C. G., et al. 2014, ApJ, 783, 103
Wittenmyer, R. A., Horner, J., Tuomi, M., et al. 2012b, ApJ, 753, 169
Yi, S. K., Kim, Y.-C., & Demarque, P. 2003, ApJS, 144, 259
Zechmeister, M., & Kürster, M. 2009, A&A, 496, 577
Zhao, G., & Li, H.-B. 2001, ChJAA, 1, 555

The Astrophysical Journal, 823:36 (10pp), 2016 May 20 doi:10.3847/0004-637X/823/1/36

A NON-LTE STUDY OF SILICON ABUNDANCES IN GIANT STARS FROM THE Si I INFRARED LINES IN THE *zJ*-BAND[*]

Kefeng Tan[1], Jianrong Shi[1], Masahide Takada-Hidai[2], Yoichi Takeda[3], and Gang Zhao[1]
[1] Key Laboratory of Optical Astronomy, National Astronomical Observatories, Chinese Academy of Sciences, Beijing 100012, China; tan@nao.cas.cn
[2] Liberal Arts Education Center, Tokai University, 4-1-1 Kitakaname, Hiratsuka, Kanagawa 259-1292, Japan
[3] National Astronomical Observatory of Japan, 2-21-1 Osawa, Mitaka, Tokyo 181-8588, Japan

Received 2015 July 15; accepted 2016 March 18; published 2016 May 19

ABSTRACT

We investigate the feasibility of Si I infrared (IR) lines as Si abundance indicators for giant stars. We find that Si abundances obtained from the Si I IR lines based on the local thermodynamic equilibrium (LTE) analysis show large line-to-line scatter (mean value of 0.13 dex), and are higher than those from the optical lines. However, when non-LTE effects are taken into account, the line-to-line scatter reduces significantly (mean value of 0.06 dex), and the Si abundances are consistent with those from the optical lines. The typical average non-LTE correction of [Si/Fe] for our sample stars is about −0.35 dex. Our results demonstrate that the Si I IR lines could be reliable abundance indicators, provided that the non-LTE effects are properly taken into account.

Key words: Galaxy: evolution – stars: abundances – stars: atmospheres – stars: late-type

1. INTRODUCTION

The chemical composition of stellar photospheres is a very important tool for investigating the origins of elements, as well as the chemical evolution of galaxies. During the past few decades, stellar abundances[4] have mainly been determined from optical spectra due to both historical and technical reasons. Though visible light can easily penetrate the atmosphere of the Earth, it is subject to the obscuring of interstellar dust and gas. This makes it difficult to utilize optical spectra to investigate the chemical abundances of stars suffering from heavy interstellar extinction, such as stars in the inner Galactic disk and in the Galactic bulge. In this regard, infrared (IR) spectroscopy is more promising, as it is much less affected by interstellar extinction. The ongoing Apache Point Observatory Galactic Evolution Experiment (APOGEE; Majewski et al. 2015) is such an attempt to use high-resolution and high signal-to-noise ratio (S/N) IR spectroscopy to penetrate the dust that obscures significant fractions of the disk and bulge of the Galaxy. Furthermore, IR spectroscopy could even be used to investigate the chemical abundances of stars beyond our Galaxy. Due to their large luminosities and peak fluxes in the IR, red supergiant (RSG) stars are ideal tracers of the chemical abundances of the external galaxies out to large distances (Patrick et al. 2015). This has been verified by chemical abundance analysis of RSG stars in the Magellanic Clouds (Davies et al. 2015), in NGC 6822 (Patrick et al. 2015), and in the Sculptor Galaxy (Gazak et al. 2015) using the medium-resolution ($R \sim 3000$–8000) spectra in the *J*-band obtained by the X-shooter (Vernet et al. 2011) and *K*-band Multi-Object Spectrograph (KMOS; Sharples et al. 2013) mounted on the Very Large Telescope. Evans et al. (2011) showed by simulations that with future instruments, quantitative IR spectroscopy could even be performed for RSG stars to tens of megaparsecs. Due to the aforementioned advantages, IR spectroscopy will play a more important role in chemical abundance analysis with existing and forthcoming IR instruments (such as Keck/MOSFIRE, VLT/KMOS, TMT/IRMS, E-ELT/EAGLE, etc.).

In addition to the advantages mentioned above, sometimes IR lines can be better abundance indicators than optical lines. This is the case for silicon (Si) in very metal-poor stars. Si is attributed as an α-element, which are made during oxygen and neon burning in massive stars, and later ejected to the interstellar medium by SNe II, according to Woosley & Weaver (1995). SNe Ia may also produce some Si, as suggested by Tsujimoto et al. (1995). Therefore, Si abundances in metal-poor stars could be used to test the SNe and Galactic chemical evolution models. Unfortunately, the optical Si I lines are very weak in very metal-poor stars, so the two strong lines at 3905 and 4102 Å in the near-ultraviolet (NUV) are usually employed to derive Si abundances. However, both of these lines have defects in abundance determinations. The Si I 3905 Å line is blended by a CH line. Though this CH feature may be weak in dwarf stars with relatively high temperatures (Cohen et al. 2004), it could be very strong in cool giant stars (Cayrel et al. 2004). The Si I 4102 Å line falls in the wing of the Hδ line, which makes it uneasy to derive accurate Si abundances. In such a situation, the Si I IR lines could be a better alternative to derive Si abundances. There are tens of Si I IR lines that are much stronger than the optical lines and they suffer much less from the problem of blending or continuum normalization compared to the 3905/4102 Å lines. For example, Jönsson et al. (2011) determined Si abundances for 10 metal-poor giant stars using three Si I IR lines at 10371, 10844, and 10883 Å. However, their analysis was performed under the assumption of local thermodynamic equilibrium (LTE), as there was no calculation for the non-LTE effects of the Si I IR lines at that time. Later, Shi et al. (2012) investigated the non-LTE effects of the Si I IR lines in nearby stars (most of which were dwarf stars), and found that the non-LTE effects are important even for metal-rich stars (>0.1 dex). Bergemann et al. (2013) presented theoretical calculations for the non-LTE effects of four Si I lines in the *J*-band for RSG stars. Their results show

---

[*] Based on data collected at the Subaru Telescope, which is operated by the National Astronomical Observatory of Japan; based on observations made with ESO telescopes at the La Silla Paranal Observatory under programme IDs 266.D-5655(A) and 084.D-0912(A); based on observations carried out at the National Astronomical Observatories (Xinglong, China).

[4] We follow the classical notation $[A/B] = \log(N_A/N_B)_\star - \log(N_A/N_B)_\odot$ in this work.

Table 1
Sample Stars and Their Stellar Parameters

Star	$T_{\rm eff}$ (K)	log g (cgs)	[Fe/H] (dex)	ξ (km s^{-1})	References	σ_t (K)	σ_g (cgs)	σ_m (dex)	σ_v (km s^{-1})	References/Note
Arcturus	4281	1.72	−0.55	1.5	(a)	20	0.08	0.07	0.25	(a)
HD 83240	4682	2.45	−0.02	1.3	(b)	84	0.27	0.01	0.03	(b), (l)
BD +23°3130	5000	2.20	−2.60	1.4	(c)	71	0.22	0.14	0.28	[a]
BD −16°251	4825	1.50	−2.91	1.8	(d)	71	0.01	0.07	0.28	(d), (i)
BD −18°5550	4750	1.40	−3.06	1.8	(d)	124	0.00	0.04	0.00	(d), (f)
HD 6268	4735	1.61	−2.30	2.1	(e)	25	0.01	0.45	0.35	(e), (f)
HD 13979	5075	1.90	−2.26	1.3	(f)	71	0.22	0.14	0.28	[a]
HD 108317	5310	2.77	−2.35	1.9	(g)	100	0.15	0.09	0.46	(c), (f), (g), (h), (i)
HD 115444	4721	1.74	−2.71	2.0	(h)	32	0.52	0.12	0.32	(e), (h), (i)
HD 121135	4934	1.91	−1.37	1.6	(h)	6	0.29	0.03	0.28	(f), (h)
HD 126587	4700	1.05	−3.16	1.7	(i)	18	0.88	0.25	0.11	(c), (i)
HD 166161	5350	2.56	−1.22	2.3	(h)	100	0.22	0.14	0.18	(f), (h), (i)
HD 186478	4730	1.50	−2.42	1.8	(i)	76	0.08	0.18	0.10	(d), (f), (h), (i)
HD 195636	5370	2.40	−2.77	1.5	(j)	71	0.22	0.14	0.28	[a]
HD 204543	4672	1.49	−1.72	2.0	(h)	16	0.47	0.21	0.00	(f), (h), (i)
HD 216143	4525	1.77	−1.92	1.9	(e)	8	0.51	0.06	0.48	(c), (e), (f), (g)
HD 221170	4560	1.37	−2.00	1.6	(e)	74	0.22	0.14	0.52	(c), (e), (f), (g), (h)
HE 1523−0901	4630	1.00	−2.95	2.6	(k)	71	0.22	0.14	0.28	[a]

Notes. From left to right: Star ID, effective temperature, surface gravity, metallicity, microturbulent velocity, reference for stellar parameters, adopted uncertainty for effective temperature, surface gravity, metallicity, and microturbulent velocity, references or notes about the calculation of the uncertainty of stellar parameters. For stars with multiple independent measurements of stellar parameters in the references, the standard deviations between different studies were adopted as the uncertainties; for the other stars please see the note in the end of the table.

[a] Only single independent measurement of stellar parameters that was available in the references; the median value of the errors of the 12 stars with multiple independent measurements of stellar parameters was adopted for the uncertainties.

References. (a) Takeda et al. (2009), (b) Mishenina et al. (2006), (c) Fulbright (2000), (d) Cayrel et al. (2004), (e) Saito et al. (2009), (f) Burris et al. (2000), (g) Takada-Hidai et al. (2005), (h) Simmerer et al. (2004), (i) Hansen & Primas (2011), (j) Carney et al. (2003), (k) Frebel et al. (2007), (l) Da Silva et al. (2011).

that the non-LTE abundance correction varies smoothly between −0.4 and −0.1 dex for stars with effective temperatures between 3400 and 4400 K.

Considering that Shi et al. (2012) mainly concentrated on main-sequence stars, while Bergemann et al. (2013) focused on theoretical non-LTE effects, we decided to perform a practical investigation of the non-LTE effects of 16 Si I IR lines in giant stars based on observational spectra. In particular, the atomic data and model atom of Shi et al. (2012) were calibrated by requiring that consistent Si abundances could be obtained from different Si I IR lines, as well as from the optical lines for the Sun, and it is necessary to check whether these still hold true for giant stars. In the next section, we briefly describe the observational data used in this work. Section 3 presents our method of non-LTE calculations and the test of its validity for giants. In Section 4, we apply our method to a sample of metal-poor giant stars and compare our results with the theoretical chemical evolution models of Si. In the last section we briefly summarize our results and conclusions.

2. OBSERVATIONAL DATA

The sample analyzed in this work is comprised of 16 metal-poor giant program stars, as shown in Table 1. These stars were originally observed by Takeda & Takada-Hidai (2011, 2012) in 2009 and 2011 for the purpose of determining sulfur (S) abundances using the S I IR triplet lines. The spectra were obtained using the IR Camera and Spectrograph (IRCS; Kobayashi et al. 2000) in combination with the 188-element curvature-based adaptive optics system (AO188) mounted on the Subaru Telescope. With a resolution of about 20,000, the spectra cover a wavelength range of 1.01–1.19 μm, including several Si I lines that are not (severely) blended. For most of the stars, the S/Ns of the spectra are higher than 100. The spectra were reduced following the standard procedure using the "echelle" package of IRAF.[5] For more details about the observation and data reduction, please refer to Takeda & Takada-Hidai (2011, 2012).

As mentioned in the introduction, one of our aims is to check whether we could obtain consistent Si abundances from the IR and the optical lines in giant stars. Unfortunately, the optical Si I lines are too weak to give very accurate abundances for our sample stars. So we included another two giant stars (Arcturus and HD 83240) as benchmark stars. The optical Si I lines in these two stars are stronger compared to the 16 sample stars, which permits us to check whether abundances from the optical and the IR lines are in reasonable agreement. Additionally, these two stars have archival IR spectra with very high quality, which we could use to obtain very accurate Si abundances to investigate whether different IR lines produce consistent results. For Arcturus, the optical spectra were adopted from the Visible and Near IR Atlas of the Arcturus Spectrum 3727–9300 Å by Hinkle et al. (2000), and the IR spectra were adopted from the IR Atlas of the Arcturus Spectrum, 0.9–5.3 μm by Hinkle et al. (1995). The typical spectral resolutions of the optical and IR spectra of Arcturus are 150,000 and 100,000, respectively. For HD 83240, the optical spectra were adopted from the UVES-POP library (Bagnulo et al. 2003), and the IR spectra were adopted from the

---

[5] IRAF is distributed by the National Optical Astronomy Observatories, which are operated by the Association of Universities for Research in Astronomy, Inc., under cooperative agreement with the National Science Foundation.

Table 2
Atomic Data of the Si I Lines (Adopted from Shi et al. 2008) Used for Abundance Determination

Line (Å)	Transition	EP (eV)	log gf	log C_6
5690.43	$4s\,^3P^o_1 - 5p\,^3P_1$	4.707	−1.73	−30.294
5701.11	$4s\,^3P^o_1 - 5p\,^3P_0$	4.707	−1.95	−30.294
6142.49	$3p^3\,^3D^o_3 - 5f\,^3D_3$	5.619	−1.47	−29.869
6145.02	$3p^3\,^3D^o_2 - 5f\,^3G_3$	5.616	−1.38	−29.869
10288.90	$4s\,^3P^o_0 - 4p\,^3S_1$	4.920	−1.65	−30.661
10371.30	$4s\,^3P^o_1 - 4p\,^3S_1$	4.707	−0.85	−30.659
10585.17	$4s\,^3P^o_2 - 4p\,^3S_1$	4.954	−0.14	−30.659
10603.45	$4s\,^3P^o_1 - 4p\,^3P_2$	4.707	−0.34	−30.677
10627.66	$4p\,^1P_1 - 4d\,^3P^o_2$	5.863	−0.39	−30.692
10661.00	$4s\,^3P^o_0 - 4p\,^3P_1$	4.920	−0.28	−30.687
10689.73	$4p\,^3D_1 - 4d\,^3F^o_2$	5.954	−0.08	−29.964
10694.27	$4p\,^3D_2 - 4d\,^3F^o_3$	5.964	0.06	−29.944
10727.43	$4p\,^3D_3 - 4d\,^3F^o_4$	5.984	0.25	−29.907
10749.40	$4s\,^3P^o_1 - 4p\,^3P_1$	4.707	−0.20	−30.689
10784.57	$4p\,^3D_2 - 4d\,^3F^o_2$	5.964	−0.69	−29.965
10786.88	$4s\,^3P^o_1 - 4p\,^3P_0$	4.707	−0.34	−30.691
10827.10	$4s\,^3P^o_2 - 4p\,^3P_2$	4.954	0.21	−30.677
10843.87	$4p\,^1P_1 - 4d\,^1D^o_2$	5.863	−0.08	−30.145
10882.83	$4p\,^3D_3 - 4d\,^3F^o_3$	5.984	−0.66	−29.945
10979.34	$4s\,^3P^o_2 - 4p\,^3P_1$	4.954	−0.55	−30.688

Note. From left to right: wavelength, lower and upper levels of the transition, excitation potential (EP) of the lower level, oscillator strength, van der Waals damping constant.

CRIRES-POP library (Lebzelter et al. 2012). The typical spectral resolution of the optical and the IR spectra of HD 83240 are 80,000 and 96,000, respectively.

3. METHOD OF NON-LTE CALCULATIONS AND VALIDITY TEST

3.1. *Method of Non-LTE Calculations*

In this work, we used the same method of non-LTE calculations as Shi et al. (2008, 2009, 2011, 2012). Here, we only give a brief description of the method. The key for non-LTE calculations is the atomic model. The Si atomic model adopted here includes 132 terms of Si I, 41 terms of Si II, and the ground state of Si III. In addition to the radiative bound–bound and bound–free transitions, excitation and ionization induced by inelastic collisions with electrons and hydrogen atoms were also taken into account. The atomic data of the spectral lines used for Si abundance determination are given in Table 2. The data were adopted from Shi et al. (2008), where the van der Waals damping constants were computed according to the interpolation tables of Anstee & O'Mara (1991, 1995), and the oscillator strengths were derived by requiring the solar Si abundance $\log(N_{\rm Si}/N_{\rm H}) + 12$ to be 7.5. As for the stellar model atmosphere, we used the revised version of the opacity sampling model MAFAGS-OS (Grupp 2004; Grupp et al. 2009), which is under the one-dimensional (1D) and LTE assumption. The coupled radiative transfer and statistical equilibrium equations were solved with a revised version of the DETAIL program (Butler & Giddings 1985). Chemical abundances were derived by spectrum synthesis using the IDL/FORTRAN-based software package Spectrum Investigation Utility (SIU) developed by Dr. J. Reetz. SIU is an advanced software package that could perform spectrum displaying, continuum normalization, radial velocity correlation/correction, spectrum synthesis (in LTE or non-LTE based on the 1D-LTE model atmosphere MAFAGS-OS mentioned above), etc., interactively. All of the input parameters, such as the abundance for each element, macroturbulence, rotation, and instrument broadening, could be adjusted interactively, and the synthetic spectrum could be displayed on screen in real time. In most cases, the external broadening of line profiles caused by macroturbulence, rotation, and the instrument could be approximated using a simple Gaussian function.

3.2. *Validity Test for Giants with Benchmark Stars*

The above method of non-LTE calculations has been proven to be applicable for dwarf stars by Shi et al. (2012). In this section we will test whether it is also valid for giant stars.

3.2.1. *Stellar Parameters and Uncertainties*

For Arcturus, we adopted the stellar parameters ($T_{\rm eff} = 4281$ K, $\log g = 1.72$, $[{\rm Fe/H}] = -0.55$, $\xi = 1.5\,{\rm km\,s^{-1}}$) from Takeda & Takada-Hidai (2011). They were determined by Takeda et al. (2009) in a fully spectroscopic way, i.e., $T_{\rm eff}$ from excitation equilibrium of Fe I, $\log g$ from ionization equilibrium between Fe I and Fe II, [Fe/H] from Fe I, and ξ from abundance-independence of equivalent width (EW). We noticed that Ramírez & Allende Prieto (2011) also investigated the stellar parameters and abundances of Arcturus using high-quality data and methods that minimize model uncertainties. They determined the effective temperature using model atmosphere fits to the observed spectral energy distribution from the blue to the mid-IR, and the surface gravity using the trigonometric parallax. Their stellar parameters ($T_{\rm eff} = 4286 \pm 30$ K, $\log g = 1.66 \pm 0.05$, $[{\rm Fe/H}] = -0.52 \pm 0.04$, $\xi = 1.74\,{\rm km\,s^{-1}}$) are in excellent agreement with those adopted in this work. Recently, Heiter et al. (2015) presented fundamental determinations of $T_{\rm eff}$ and $\log g$ for 34 *Gaia* FGK benchmark stars. Their determinations were based on the angular diameters, bolometric fluxes, distances, and masses, which are independent of spectroscopy and atmospheric models. They gave a $T_{\rm eff}$ of 4286 ± 35 K and a $\log g$ of 1.64 ± 0.09 for Arcturus. And the [Fe/H] of this star was determined to be -0.52 ± 0.08 (after correction for non-LTE effects) in another work (Jofré et al. 2014) in the *Gaia* FGK benchmark stars series. These values agree well with the two sets of stellar parameters mentioned above, and the offsets between different studies are well within the typical uncertainties of stellar parameters ($\Delta T_{\rm eff} = 20$ K, $\Delta \log g = 0.08$, $\Delta[{\rm Fe/H}] = 0.07$, and $\Delta\xi = 0.25\,{\rm km\,s^{-1}}$) given by Takeda et al. (2009). Actually, our calculations show that such differences in stellar parameters had a very small effect on the Si abundance ($\Delta[{\rm Si/Fe}] \sim 0.04$ dex).

For HD 83240, we adopted the stellar parameters ($T_{\rm eff} = 4682$ K, $\log g = 2.45$, $[{\rm Fe/H}] = -0.02$, $\xi = 1.3\,{\rm km\,s^{-1}}$) from Mishenina et al. (2006). The effective temperature was determined with very high accuracy ($\sigma = 10$–15 K) using the line depth ratios of several iron-peak elements (such as Si, Ti, V, Cr, Fe, and Ni). The surface gravity was derived using two methods, i.e., iron ionization equilibrium and wing fitting of the Ca I 6162 Å line, and both methods give the same result. The metallicity was determined from Fe I lines. We note that according to the investigation of Lind et al. (2012), non-LTE

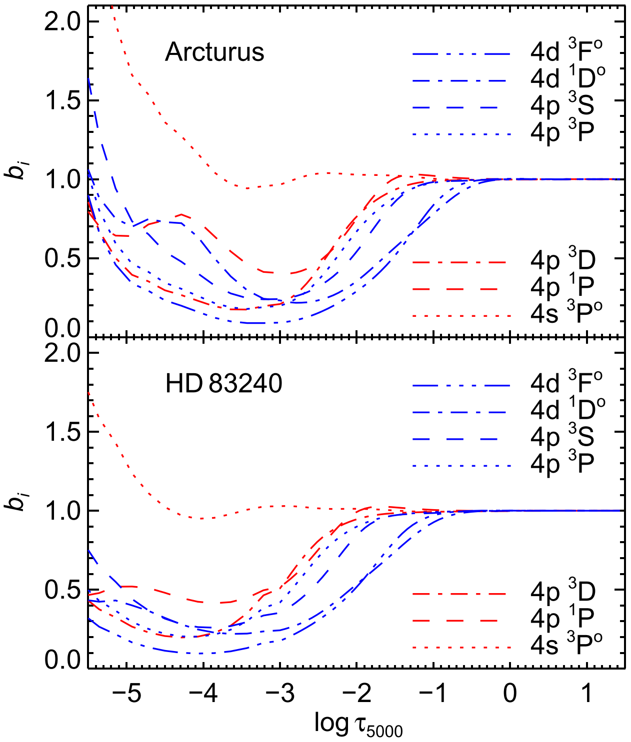

Figure 1. Departure coefficients for the populations of seven selected levels of Si I as a function of continuum optical depth at 5000 Å for Arcturus and HD 83240. The red and the blue lines represent the lower andupper levels, respectively, of the IR transitions used to determine Si abundances in this work.

effects of Fe I are negligible for cool ($T_{\rm eff} < 5000$ K) stars with solar metallicity ([Fe/H] ∼ 0), such as HD 83240. The microturbulent velocity was calculated so that iron abundances do not depend on the EWs. Da Silva et al. (2011) gave different stellar parameters for HD 83240 ($T_{\rm eff} = 4801 \pm 89$ K, $\log g = 2.83 \pm 0.23$, $[{\rm Fe/H}] = -0.03 \pm 0.08$, $\xi = 1.26 \pm 0.09$ km s^{-1}) based on the traditional spectroscopic method, i.e., excitation equilibrium of Fe I and ionization equilibrium between Fe I and Fe II. Their effective temperature is marginally consistent with that of Mishenina et al. (2006) considering the uncertainty, but their surface gravity shows a relatively large discrepancy. Nevertheless, the adoption of stellar parameters for HD 83240 does not affect our validity test because the differences in the Si abundance determined using the above two sets of stellar parameters is only 0.03 dex.

3.2.2. Non-LTE Line Formation Results

With the stellar parameters we could calculate the level populations in statistical equilibrium. Figure 1 shows the departure coefficients $b_i = n_i^{\text{non-LTE}}/n_i^{\text{LTE}}$ for the populations of the seven Si I levels that produce the IR transitions used to determine Si abundances in this work for the two benchmark stars. The red lines represent the lower levels, while the blue lines are the upper levels. It can be seen that within $\log \tau_{5000} = -3 \ldots -2$, where the Si I IR lines are formed, the departure coefficients of the lower levels (denoted with b_i) are higher than those of the upper levels (denoted with b_j). This means that the line source function S_{ij} is smaller than the local Planck function $B_\nu(T)$ because $S_{ij}/B_\nu(T) \sim b_j/b_i < 1$. As a result, the Si I IR lines are stronger in non-LTE than in LTE, and hence the non-LTE abundance corrections should be negative.

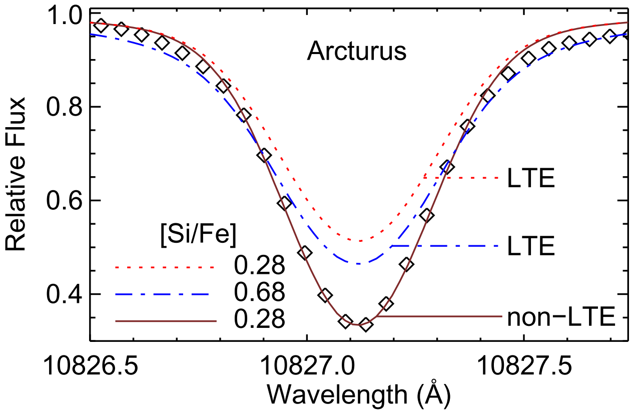

Figure 2. Spectrum synthesis of the Si I 10827 Å line for Arcturus. The diamonds are the observed spectra; the lines are the synthetic spectra in LTE or non-LTE with different [Si/Fe] (see the legend for details).

In combination with the calculated populations for the individual levels, Si abundances were then derived via spectrum synthesis of the individual Si I lines. We note here that, due to the enhanced absorption in the line cores in non-LTE, some of the Si I IR lines are so strong (EW $\gtrsim$ 150 mÅ) that their observed line profiles could only be reproduced in non-LTE. As an example, Figure 2 shows the spectrum synthesis of the strongest Si I IR line (10827 Å with a EW of 318.3 mÅ) in Arcturus. The solid line shows the best fit to the observed line profile in non-LTE with a [Si/Fe] of 0.28 dex. The dotted line is produced with the same [Si/Fe] but in LTE, which is much weaker in the core of the line. No matter how we adjusted the Si abundance, the observed line profile cannot be reproduced in LTE. In this case, the LTE abundance was derived by simply increasing the [Si/Fe] until the observed EW was reproduced. This led to a [Si/Fe] of 0.68 dex, for which the line profile is shown as a dash–dotted line in Figure 2. It can be seen that the core of the line is still much shallower, while the wing is obviously deeper compared to the observed spectra.

Table 3 gives the [Si/Fe] determined from the individual optical and IR lines for the two benchmark stars. EWs for the individual lines are also given. As can be seen in Table 3, for both Arcturus and HD 83240, the optical lines are insensitive to the non-LTE effects. This is because these lines are mainly formed in the inner regions of the photospheres ($\log \tau_{5000} > -2$), where the physical conditions are close to LTE. However, as we mentioned above, the regions of line formation for the IR lines are shifted outward to $\log \tau_{5000} = -3 \ldots -2$, where the line source function differs from the local Planck function, and thus the non-LTE effects cannot be neglected. Figure 3 shows the non-LTE correction of [Si/Fe] for the individual Si I IR lines as a function of EW and EP for the two benchmark stars. It can be seen that the non-LTE abundance correction varies between ∼−0.5 dex and ∼−0.05 dex. Though the non-LTE abundance correction seems to be independent of EP, it is correlated with the EW of the line. In general, stronger lines show larger non-LTE effects, while weaker lines show smaller non-LTE effects. Figure 4 shows the [Si/Fe] derived from the individual Si I IR lines as a function of EW and EP for the two benchmark stars. It is obvious that for both Arcturus and HD 83240, the LTE Si

Table 3
EWs (in mÅ) and [Si/Fe] for the Individual Si I Lines of the Benchmark Stars

Line	Arcturus			HD 83240		
(Å)	EW	LTE	non-LTE	EW	LTE	non-LTE
5690.43	59.1	0.29	0.29	63.3	−0.09	−0.09
5701.11	48.5	0.31	0.31	54.1	−0.04	−0.04
6142.49	31.2	0.29	0.29	41.4	−0.02	−0.02
6145.05	33.6	0.28	0.28	44.6	−0.02	−0.02
mean		0.29	0.29		−0.04	−0.04
σ		0.01	0.01		0.03	0.03
10288.90	82.3	0.40	0.25	91.8	−0.01	−0.07
10371.30	160.9	0.66	0.26	169.1	0.23	−0.06
10585.17	257.1	0.76	0.30	279.5	0.31	−0.01
10603.45	216.8	0.68	0.23	233.0	0.24	−0.06
10627.66	102.4	0.59	0.18	121.0	0.24	−0.11
10661.00	226.8	0.74	0.28	241.2	0.27	−0.02
10689.73	126.5	0.66	0.30	⋯	⋯	⋯
10694.27	135.0	0.66	0.26	162.6	0.26	−0.02
10727.43	153.3	0.68	0.25	179.4	0.26	−0.06
10749.40	237.0	0.68	0.22	263.1	0.29	−0.03
10784.57	68.4	0.44	0.29	⋯	⋯	⋯
10786.88	223.0	0.70	0.24	236.6	0.26	−0.06
10827.10	318.3	0.68	0.28	364.4	0.32	−0.01
10843.87	141.6	0.72	0.24	164.2	0.36	−0.07
10882.83	64.0	0.36	0.22	82.6	0.01	−0.08
10979.34	197.7	0.68	0.25	207.5	0.24	−0.06
mean		0.63	0.25		0.23	−0.05
σ		0.12	0.03		0.11	0.03

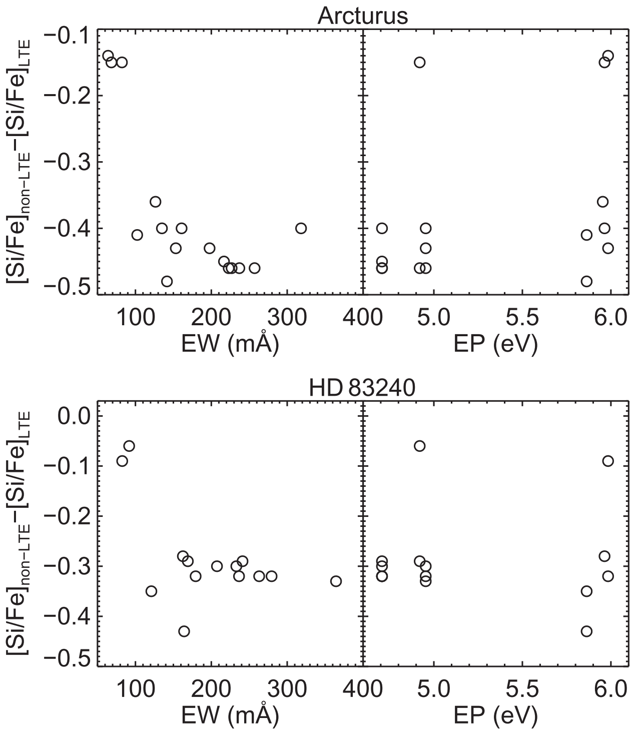

Figure 3. The non-LTE correction of [Si/Fe] for the individual Si I IR lines as a function of EW and EP for Arcturus and HD 83240.

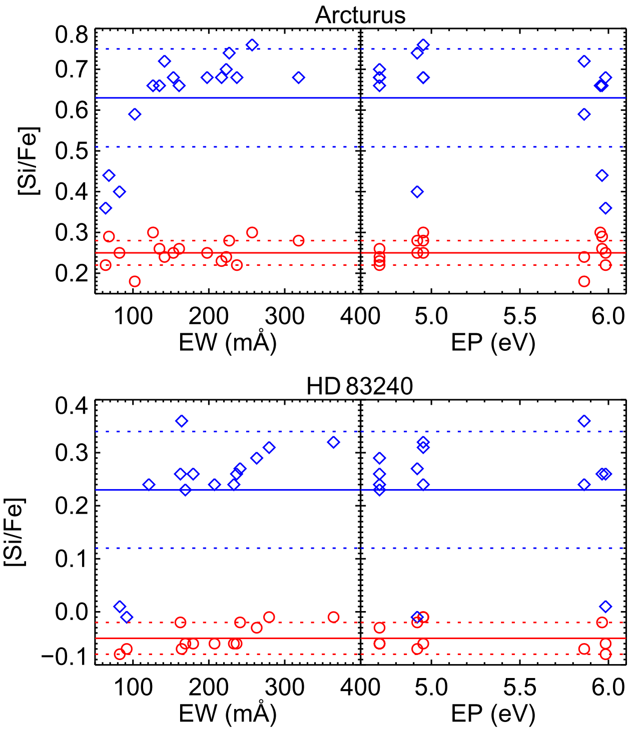

Figure 4. [Si/Fe] from the individual Si I IR lines as a function of EW and EP for Arcturus and HD 83240. The blue and the red are the LTE and the non-LTE results, respectively. The solid lines represent the average values, and the dotted lines indicate the 1σ lower and upper limits for the line-to-line scatter.

abundances from the IR lines show large line-to-line scatter, but when the non-LTE effects are taken into account, the scatter reduces significantly. Moreover, the average non-LTE Si abundances from the IR lines agree well with those from the optical lines, whereas the LTE results are significantly higher. In a word, our method of non-LTE calculations produces consistent Si abundances from the optical and the IR lines for the two benchmark stars.

We were aware that the two benchmark stars we selected are relatively metal-rich, and it is difficult to justify that our method works also for very metal-poor stars. Unfortunately, in the publicly available archival database, we were not able to find any very metal-poor giant star with high-quality IR spectra in the wavelength range studied in this work. However, in a previous study, Shi et al. (2012) investigated Si abundances for a well-studied very metal-poor giant HD 122563 based on the IR spectra of medium quality ($R\sim$ 20,000, S/N $\sim$ 100). The stellar parameters they adopted ($T_{\text{eff}}=4600$ K, $\log g=1.5$, $[\mathrm{Fe/H}]=-2.53$) are in reasonable agreement with the fundamental determinations ($T_{\text{eff}}=4587\pm60$ K, $\log g=1.61\pm0.07$, $[\mathrm{Fe/H}]=-2.64\pm0.22$) of Heiter et al. (2015). The Si abundance determined from the IR spectra ($[\mathrm{Si/Fe}]_{\text{non-LTE}}=0.20\pm0.01$) agrees well with that from the 3905 and 4102 Å lines ($[\mathrm{Si/Fe}]_{\text{non-LTE}}=0.22\pm0.05$). Moreover, Jofré et al. (2015) determined Si abundance for HD 122563 using five optical lines[6] by spectrum synthesis. They adopted the stellar parameters from Heiter et al. (2015), and their Si abundance ($[\mathrm{Si/Fe}]_{\text{non-LTE}}=0.28\pm0.09$) is consistent with those from Shi et al. (2012). Since we used exactly the same method as Shi et al. (2012), it is fair to say that our method works also for very metal-poor giant stars.

---

[6] These lines are very weak; their EWs vary between 1 and 7 mÅ according to Jofré et al. (2015).

4. APPLICATION TO METAL-POOR GIANT STARS

In this section, we applied the above method of non-LTE calculations to a sample of 16 metal-poor giant stars.

4.1. Stellar Parameters and Uncertainties

The narrow wavelength range of our IR spectra prevented us from determining stellar parameters for the sample stars by ourselves. So we adopted the stellar parameters from Takeda & Takada-Hidai (2011, 2012), which were taken from nine published studies[7] (see Table 1 for details). Among these studies, different methods have been employed to determine stellar parameters. For example, some studies derive $T_{\rm eff}$ based on spectroscopic method (Fulbright 2000; Simmerer et al. 2004; Hansen & Primas 2011), while the others are based on photometric calibrations; some studies determine $\log g$ using the parallaxes (Simmerer et al. 2004; Takada-Hidai et al. 2005; Saito et al. 2009), while the others utilize the ionization equilibrium between Fe I and Fe II. Therefore, it is not surprising that differences in stellar parameters exist between different studies. Even with the same method, the adoption of different calibrations or line lists by different studies may lead to different results (see the comparison of stellar parameters from different methods for the FGK stars in the *Gaia*-ESO survey by Smiljanic et al. 2014). In the nine studies where we took the stellar parameters, 12 out of 16 sample stars have multiple independent measurements of stellar parameters. We found that for some stars the uncertainties of stellar parameters given by the original studies cannot interpret the large differences between different studies. Therefore, for these 12 stars, we took the standard deviations of stellar parameters between different studies as the uncertainties, which are given in columns 7–10 of Table 1. For the 4 remaining stars (BD +23°3130, HD 13979, HD 195636, and HE 1523−0901) with only single measurements of stellar parameters, the median value of the errors of the above 12 stars was adopted.

4.2. Si Abundances and Uncertainties

Si abundances of the sample stars were derived by spectrum synthesis of the individual Si I IR lines. Figure 5 shows the spectrum synthesis of the strong Si I 10585 Å line for two program stars HD 126587 and HD 166161. HD 126587 is the most metal-poor star in our sample, while HD 166161 has the highest effective temperature and surface gravity. It can be seen that for both of these two stars, the Si I 10585 Å lines are strong enough (EW > 60 mÅ) to be used to determine Si abundances. Table 4 gives the [Si/Fe] determined from the individual Si I IR lines for the sample stars. The EW for each line is also given.

We were aware that stellar parameters for the sample stars were adopted from different studies, and the effect of inhomogeneous stellar parameters on Si abundances needs to be properly estimated. To do this, for the 12 stars with multiple determinations of stellar parameters, we calculated Si abundances from different stellar parameters and took the standard deviations as the uncertainties of Si abundances caused by stellar parameters. For the remaining four stars with only single measurements of stellar parameters, the median value of the errors (0.12 dex) of the above 12 stars was adopted as the uncertainties caused by stellar parameters. The total errors of [Si/Fe] were then calculated by adding the line-to-line scatters and the errors introduced by stellar parameters in quadrature. Table 5 gives the average [Si/Fe] from the Si I IR lines, as well as the associated uncertainties for all the stars investigated in this work.

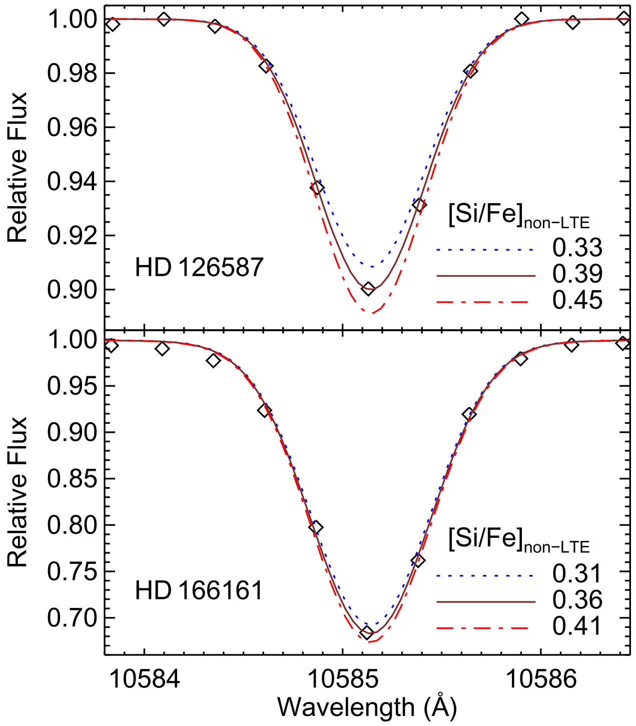

Figure 5. Spectrum synthesis of the Si I 10585 Å line for HD 126587 and HD 166161. The diamonds are the observed spectra; the lines are the synthetic spectra in non-LTE with different [Si/Fe] (see the legend for details).

4.3. Non-LTE Effects of the Si I IR Lines

Figure 6 shows the non-LTE correction of [Si/Fe] for the individual Si I IR lines as a function of EW for the sample stars. It can be seen that the non-LTE effects are significant for all the stars. Additionally, the non-LTE abundance corrections differ from line to line; in general, stronger lines show larger non-LTE effects (up to ~0.8 dex), while weaker lines show smaller non-LTE effects (as low as ~0.1 dex). Overall, the non-LTE abundance corrections show linear correlations with the line strengths for all the stars with similar slopes. But the intercepts of the linear relationships are not necessarily the same; they are dependent on the stellar parameters, especially the surface gravity (see the discussions below). We also explored the dependency of the non-LTE effects on the stellar parameters, and the results are plotted in Figure 7. It can be seen that the non-LTE abundance corrections are all negative within the range of stellar parameters investigated. Moreover, the non-LTE abundance corrections are more sensitive to surface gravity than effective temperature and metallicity. Stars with lower surface gravity show larger non-LTE effects, while stars with higher gravity show smaller non-LTE effects. Figure 8 shows the line-to-line scatter of [Si/Fe] for the sample stars. It can be seen that, for a given star, the LTE Si abundances show relatively large line-to-line scatter. However, when the non-LTE effects are considered, the scatter reduces significantly,

---

[7] It is impossible to find independent measurements of stellar parameters for all the sample stars in any single study.

Table 4
EWs (in mÅ) and [Si/Fe] for the Individual Si I IR Lines of the 16 Metal-poor Giant Stars

Star	10371	10585	10603	10627	10661	10689	10694	10727	10749	10784	10786	10827	10843	10979
BD +23°3130	23.1	77.1	54.2	⋯	54.0	⋯	⋯	⋯	65.7	⋯	55.0	114.4	⋯	39.7
	0.38	0.58	0.40	⋯	0.38	⋯	⋯	⋯	0.41	⋯	0.40	0.69	⋯	0.37
	0.16	0.16	0.14	⋯	0.12	⋯	⋯	⋯	0.11	⋯	0.13	0.14	⋯	0.16
BD −16°251	27.5	84.5	57.2	⋯	60.9	⋯	⋯	⋯	66.7	⋯	62.0	126.7	⋯	⋯
	0.68	0.83	0.63	⋯	0.66	⋯	⋯	⋯	0.60	⋯	0.67	1.00	⋯	⋯
	0.39	0.35	0.27	⋯	0.29	⋯	⋯	⋯	0.21	⋯	0.30	0.29	⋯	⋯
BD −18°5550	24.3	79.4	47.9	⋯	⋯	⋯	⋯	⋯	70.6	⋯	49.5	110.9	⋯	⋯
	0.72	0.87	0.60	⋯	⋯	⋯	⋯	⋯	0.76	⋯	0.61	0.88	⋯	⋯
	0.43	0.41	0.26	⋯	⋯	⋯	⋯	⋯	0.34	⋯	0.26	0.26	⋯	⋯
HD 6268	59.7	125.4	86.4	13.8	98.4	26.3	35.1	41.4	107.0	⋯	89.9	158.8	⋯	⋯
	0.50	0.61	0.30	0.26	0.42	0.37	0.41	0.34	0.39	⋯	0.31	0.57	⋯	⋯
	0.27	0.11	0.03	0.21	0.11	0.21	0.24	0.16	0.04	⋯	0.04	0.00	⋯	⋯
HD 13979	⋯	92.3	57.0	⋯	64.1	⋯	23.3	29.5	73.2	⋯	58.9	120.8	⋯	43.3
	⋯	0.57	0.18	⋯	0.27	⋯	0.28	0.25	0.28	⋯	0.19	0.60	⋯	0.14
	⋯	0.06	−0.07	⋯	−0.01	⋯	0.09	0.04	−0.05	⋯	−0.07	−0.02	⋯	−0.04
HD 108317	33.7	99.4	65.7	⋯	71.7	⋯	⋯	41.2	87.1	⋯	72.9	125.9	⋯	44.4
	0.49	0.69	0.43	⋯	0.49	⋯	⋯	0.58	0.53	⋯	0.49	0.60	⋯	0.33
	0.29	0.26	0.19	⋯	0.23	⋯	⋯	0.39	0.23	⋯	0.24	0.12	⋯	0.16
HD 115444	21.7	76.6	46.9	⋯	54.8	⋯	⋯	⋯	58.3	⋯	58.7	100.7	⋯	⋯
	0.29	0.43	0.21	⋯	0.30	⋯	⋯	⋯	0.16	⋯	0.35	0.31	⋯	⋯
	0.09	0.08	−0.01	⋯	0.06	⋯	⋯	⋯	−0.04	⋯	0.10	−0.09	⋯	⋯
HD 121135	115.6	218.9	172.4	70.2	186.1	97.4	114.1	129.6	194.9	34.9	185.8	⋯	118.0	⋯
	0.55	1.06	0.76	0.48	0.88	0.62	0.71	0.74	0.83	0.32	0.88	⋯	0.79	⋯
	0.21	0.36	0.21	0.23	0.30	0.33	0.36	0.32	0.23	0.24	0.29	⋯	0.36	⋯
HD 126587	⋯	69.1	48.7	⋯	52.0	⋯	⋯	⋯	53.4	⋯	48.5	114.3	⋯	⋯
	⋯	0.82	0.70	⋯	0.73	⋯	⋯	⋯	0.61	⋯	0.68	1.05	⋯	⋯
	⋯	0.39	0.33	⋯	0.35	⋯	⋯	⋯	0.23	⋯	0.31	0.36	⋯	⋯
HD 166161	143.9	243.0	204.1	83.2	206.3	111.6	128.9	151.6	221.3	45.6	189.7	288.0	133.2	193.2
	0.76	1.01	0.86	0.54	0.86	0.61	0.68	0.74	0.84	0.44	0.68	0.88	0.74	0.91
	0.40	0.36	0.36	0.36	0.35	0.36	0.37	0.36	0.31	0.36	0.23	0.29	0.41	0.46
HD 186478	48.7	125.2	87.4	⋯	96.6	⋯	⋯	45.4	103.4	⋯	89.8	159.1	⋯	⋯
	0.50	0.82	0.49	⋯	0.59	⋯	⋯	0.55	0.52	⋯	0.49	0.85	⋯	⋯
	0.26	0.25	0.16	⋯	0.22	⋯	⋯	0.33	0.14	⋯	0.16	0.16	⋯	⋯
HD 195636	⋯	65.4	40.9	⋯	44.4	⋯	⋯	⋯	⋯	⋯	⋯	⋯	⋯	⋯
	⋯	0.75	0.54	⋯	0.58	⋯	⋯	⋯	⋯	⋯	⋯	⋯	⋯	⋯
	⋯	0.32	0.23	⋯	0.26	⋯	⋯	⋯	⋯	⋯	⋯	⋯	⋯	⋯
HD 204543	100.3	216.3	165.0	45.5	181.1	66.5	73.4	104.0	173.0	⋯	157.9	237.7	89.2	⋯
	0.43	1.09	0.69	0.34	0.86	0.41	0.38	0.58	0.62	⋯	0.56	0.84	0.58	⋯
	0.15	0.32	0.16	0.16	0.26	0.21	0.16	0.26	0.06	⋯	0.08	0.10	0.30	⋯
HD 216143	64.4	145.5	111.6	⋯	121.0	⋯	47.6	61.2	131.9	⋯	115.4	183.5	40.2	⋯
	0.17	0.46	0.21	⋯	0.31	⋯	0.25	0.27	0.31	⋯	0.24	0.47	0.14	⋯
	0.01	0.00	−0.05	⋯	0.01	⋯	0.10	0.09	−0.04	⋯	−0.04	−0.07	0.00	⋯
HD 221170	83.4	168.9	126.8	31.7	134.9	48.6	57.5	74.1	155.0	⋯	129.8	201.1	57.1	⋯
	0.50	0.94	0.58	0.37	0.66	0.44	0.46	0.51	0.78	⋯	0.58	0.86	0.45	⋯
	0.23	0.26	0.13	0.22	0.18	0.26	0.25	0.26	0.21	⋯	0.13	0.16	0.26	⋯
HE 1523−0901	23.6	83.1	62.9	⋯	73.1	⋯	⋯	⋯	81.4	⋯	67.2	127.3	⋯	⋯
	0.51	0.62	0.56	⋯	0.65	⋯	⋯	⋯	0.61	⋯	0.59	0.68	⋯	⋯
	0.26	0.24	0.24	⋯	0.31	⋯	⋯	⋯	0.24	⋯	0.26	0.14	⋯	⋯

Note. For each star, the first row is the EW; the second and the third rows are the LTE and the non-LTE [Si/Fe], respectively.

though for some stars it is still relatively large compared to the benchmark stars. This could be partly due to the quality of the spectra (lower resolution and lower S/N compared to the spectra of the benchmark stars) used for abundance determination. Figure 9 shows [Si/Fe] as a function of effective temperature and surface gravity. The results from Shi et al. (2012), which are based on the same IR lines and the same method, are also plotted. It can be seen that [Si/Fe] derived from the Si I IR lines based on the non-LTE analysis is independent of $T_{\rm eff}$ and $\log g$.

4.4. Comparison with Other Studies

Shi et al. (2012) investigated the non-LTE effects of the Si I IR lines for 15 nearby stars. Their sample is mostly dwarf stars, and there is only one giant star (HD 122563), for which the average non-LTE correction of [Si/Fe] is −0.26 dex. This is consistent with the results of our sample stars with similar stellar parameters.

Bergemann et al. (2013) calculated the non-LTE effects of four Si I IR lines for RSG stars with effective temperatures between 3400 and 4400 K. Unfortunately, we are not able to

Table 5
Si Abundances and Uncertainties for All the Sample Stars

Star	[Si/Fe]		$\sigma_{\rm line}$		$\sigma_{\rm par}$	$\sigma_{\rm total}$	
	LTE	non-LTE	LTE	non-LTE		LTE	non-LTE
Arcturus	0.63	0.25	0.12	0.03	0.03	0.12	0.04
HD 83240	0.23	−0.05	0.11	0.03	0.02	0.11	0.04
BD +23°3130	0.45	0.14	0.12	0.02	0.12	0.17	0.12
BD −16°251	0.72	0.30	0.14	0.06	0.01	0.14	0.06
BD −18°5550	0.74	0.33	0.12	0.08	0.06	0.13	0.10
HD 6268	0.41	0.13	0.11	0.09	0.44	0.45	0.45
HD 13979	0.31	−0.01	0.17	0.06	0.12	0.21	0.13
HD 108317	0.51	0.23	0.10	0.08	0.07	0.12	0.11
HD 115444	0.29	0.03	0.09	0.07	0.12	0.15	0.14
HD 121135	0.72	0.29	0.20	0.06	0.05	0.21	0.08
HD 126587	0.77	0.33	0.16	0.06	0.12	0.20	0.13
HD 166161	0.75	0.36	0.15	0.05	0.14	0.21	0.15
HD 186478	0.60	0.21	0.15	0.07	0.16	0.22	0.17
HD 195636	0.62	0.27	0.11	0.05	0.12	0.16	0.13
HD 204543	0.62	0.19	0.22	0.09	0.07	0.23	0.11
HD 216143	0.28	0.00	0.11	0.06	0.11	0.16	0.13
HD 221170	0.59	0.21	0.18	0.05	0.16	0.24	0.17
HE 1523−0901	0.60	0.24	0.06	0.05	0.12	0.13	0.13

Note. The total errors ($\sigma_{\rm total}$) were calculated by adding the line-to-line scatters ($\sigma_{\rm line}$) and the errors introduced by stellar parameters ($\sigma_{\rm par}$) in quadrature.

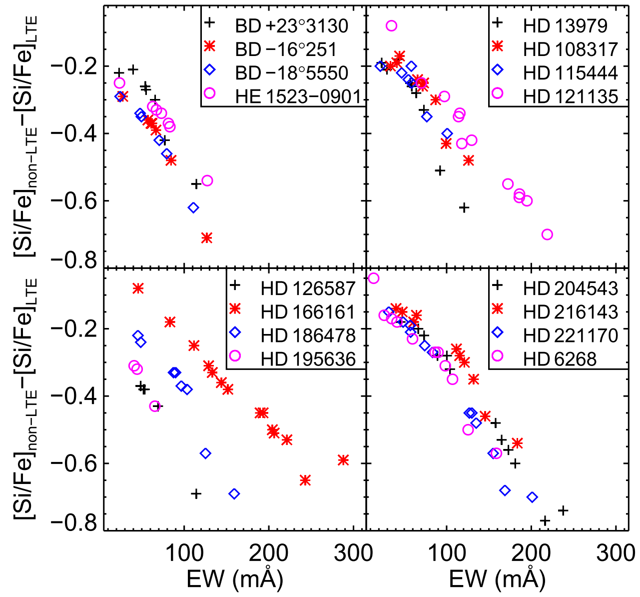

Figure 6. The non-LTE correction of [Si/Fe] for the individual Si I IR lines as a function of EW for the 16 metal-poor giant stars.

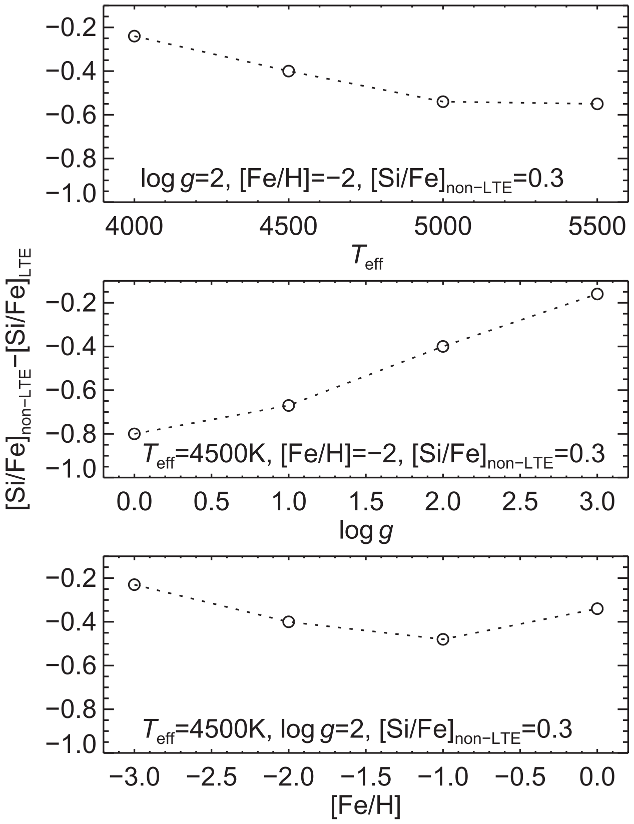

Figure 7. The non-LTE correction of [Si/Fe] for the Si I 10603 Å line as a function of stellar parameters.

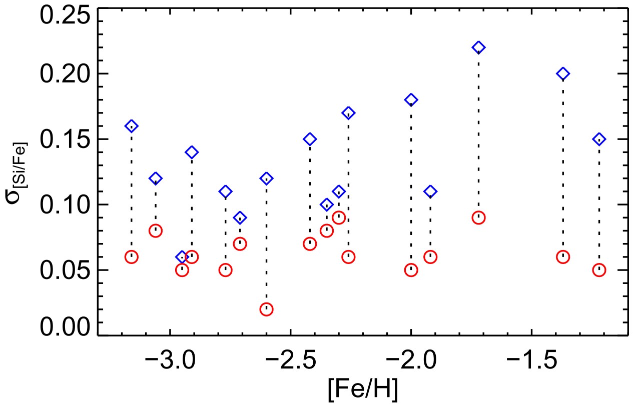

Figure 8. The line-to-line scatter of [Si/Fe] for the 16 metal-poor giant stars. The diamonds and the circles are the LTE and the non-LTE results, respectively.

compare our results directly with those of Bergemann et al. (2013) because the Si I IR lines they investigated are different from those in this work. Nevertheless, their results also show a negative non-LTE abundance correction, though the magnitude of correction (−0.4 … −0.1 dex) is lower than our results. This should be mainly due to the fact that Bergemann et al. (2013) adopted stronger inelastic collisions with neutral hydrogen, which leads to smaller non-LTE effects.

4.5. Implications for the Chemical Evolution of Si

As we mentioned in the introduction, Si abundances could be used to test the SNe and Galactic chemical evolution models. Several previous studies on stellar abundances have investigated the relationship between [Si/Fe] and [Fe/H] (Fulbright 2000; Cayrel et al. 2004; Shi et al. 2009; etc.). While it is generally accepted that [Si/Fe] decreases with [Fe/H] from [Fe/H] ∼ −1 to [Fe/H] ∼ 0, the behavior of [Si/Fe] below [Fe/H] ∼ −1 is still controversial. One reason for this is the

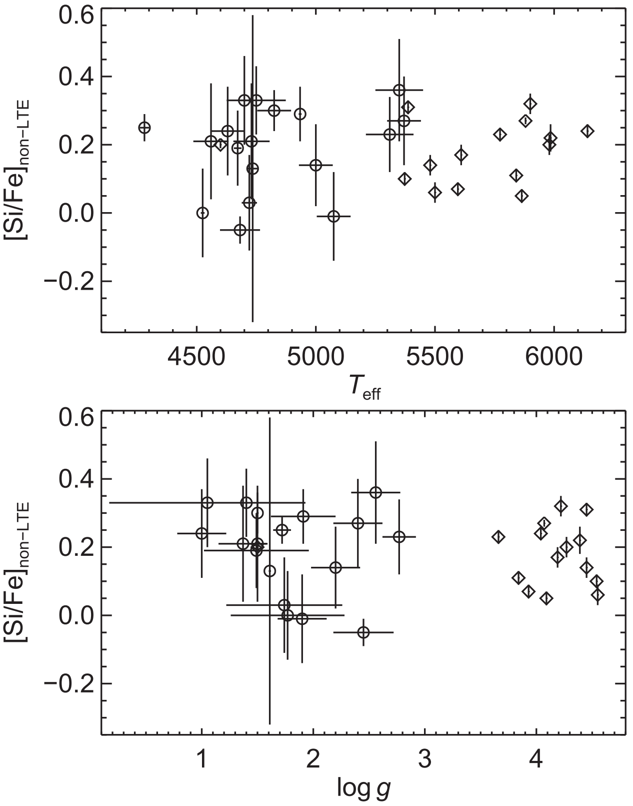

Figure 9. [Si/Fe] derived in non-LTE as a function of effective temperature and surface gravity. The circles are our results; the diamonds are the results from Shi et al. (2012).

significant scatter of [Si/Fe] (ranging from −0.2 to 0.9 dex; see Figure 1 of Shi et al. 2009) below [Fe/H] ∼ −1. The dispersion could be due to either the cosmic scatter or the uncertainties in abundance determinations or both. Fulbright (2000) determined Si abundances in LTE for 168 stars (−3 < [Fe/H] < 0) using 12 Si I lines between 5600 and 7100 Å. Their results showed a decreasing trend of [Si/Fe] with increasing [Fe/H]. Cayrel et al. (2004) performed abundance analysis for 35 very metal-poor stars. Their Si abundances were derived in LTE using the Si I 4102 Å line. The results indicated a slightly increasing trend of [Si/Fe] from [Fe/H] ∼ −4 to [Fe/H] ∼ −2. Shi et al. (2009, 2011) determined Si abundances in non-LTE for 79 stars based on 11 Si I lines between 3900 and 6300 Å, as well as two Si II lines (6347/6371 Å). Their results suggested a flat trend of [Si/Fe] from [Fe/H] ∼ −3 to [Fe/H] ∼ −1, and then a decreasing trend above [Fe/H] ∼ −1. The trend between [Si/Fe] and [Fe/H] derived in this work is shown in Figure 10. The results from Shi et al. (2012), which are obtained using the same IR lines and the same method, are also plotted. All the stars in our sample are giants, while most of the stars from Shi et al. (2012) are dwarfs (only one giant). It can be seen that there is no difference in [Si/Fe] between giants and dwarfs in the common metallicity range. As shown in Figure 10, the combination of our results with those from Shi et al. (2012) suggests that [Si/Fe] decreases with increasing [Fe/H] in general, though there seems to be a bump around [Fe/H] ∼ −1.

There are several Galactic chemical evolution models referring to Si in the literature (Timmes et al. 1995; Samland 1998; Kobayashi et al. 2011; etc.). The chemical evolution calculation of Timmes et al. (1995) predicted that [Si/Fe] increases with [Fe/H] from [Fe/H] ∼ −3 to [Fe/H] ∼ −2, and then decreases with [Fe/H] until [Fe/H] ∼ −0.8. Samland (1998) predicted a constant ratio of [Si/Fe] in the early Galaxy and then a decreasing trend with increasing [Fe/H] due to the contribution of SNe Ia. Kobayashi et al. (2011) presented the evolution of elements (from C to Zn) using chemical evolution models with updated yields of asymptotic giant branch (AGB) stars and core-collapse SNe. Their results showed that [Si/Fe] gradually decreases with [Fe/H] from [Fe/H] ∼ −4 to [Fe/H] ∼ −1. Above [Fe/H] ∼ −1, [Si/Fe] decreases more rapidly with increasing [Fe/H] due to the contribution of SNe Ia. Interestingly, if the effects of rotating massive stars at $Z = 0$ (in addition to hypernovae, SNe II, SNe Ia, and AGB stars) are taken into account, the [Si/Fe] versus [Fe/H] trend that they predicted also shows a small bump around [Fe/H] ∼ −1. Such bumps are also predicted for other α-elements, such as S, Ca, and Ti. Therefore, our observational results are most consistent with the predictions of Kobayashi et al. (2011). However, due to the inhomogeneous stellar parameters and small number of sample stars, we are not able to make any conclusive remarks on the Galactic chemical evolution of Si.

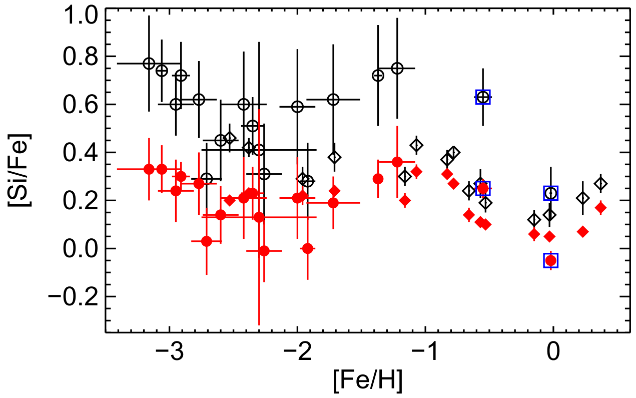

Figure 10. [Si/Fe] as a function of [Fe/H]. Our results are plotted as circles; the results from Shi et al. (2012) are plotted as diamonds. Open and filled symbols correspond to the LTE and the non-LTE abundances, respectively. The results for the two benchmark stars are marked with squares.

5. SUMMARY

As an important α-element, Si is believed to be mainly produced by SNe II, but it is not clear whether SNe Ia also produces some Si. Therefore, Si abundances could be used to test the SNe and Galactic chemical evolution models. Unfortunately, the optical Si I lines are very weak in very metal-poor stars, and the NUV Si I lines are either blended or very difficult to normalize. In this regard, the Si I IR lines could be better abundance indicators because they are usually much stronger than the optical lines and they suffer much less from the problem of blending or continuum normalization compared to the NUV lines. However, LTE is not a realistic approximation for the line formation of the Si I IR lines, so we have investigated the non-LTE effects of the Si I IR lines in giant stars. The main results can be summarized as follows.

1. Si abundances based on the LTE analysis of the Si I IR lines are overestimated (with a typical value of ∼0.35 dex

for giant stars), and thus are higher than those from the optical lines, which are insensitive to the non-LTE effects. However, when our non-LTE calculations are applied, Si abundances from the optical and the IR lines are consistent.

2. The non-LTE effects of the Si I infrared lines differ from line to line. In general, stronger lines show larger non-LTE effects (up to ~0.8 dex), while weaker lines show smaller non-LTE effects (as low as ~0.1 dex). Therefore, it is not surprising that Si abundances based on the LTE analysis of the Si I IR lines show large line-to-line scatter (mean value of 0.13 dex), and when our non-LTE calculations are applied, the scatter reduces significantly (mean value of 0.06 dex).
3. The non-LTE effects of the Si I infrared lines are dependent on stellar parameters, among which the surface gravity plays a dominant role. Giant stars show larger non-LTE effects (typical value of ~0.35 dex), while dwarf stars show smaller non-LTE effects (typical value of ~0.1 dex).

Therefore, the Si I IR lines could be reliable abundance indicators provided that the non-LTE effects are properly taken into account. Our results are a reminder that one should be very careful when using the IR lines to determine chemical abundances under the assumption of LTE. In particular, the APOGEE/APOGEE-2 project will provide high-resolution and high S/N ratio spectra in the *H*-band for about 400,000 stars, a project from which abundances of up to 15 chemical species could be obtained. Investigating the non-LTE effects for the *H*-band spectra lines for these elements is of great importance for improving the accuracy of abundance determinations.

We are grateful to the anonymous referee for the valuable suggestions and comments that improved the paper substantially. This work is supported by the National Nature Science Foundation of China under grant Nos. 11103034, 11321064, 11233004, 11390371, 11473033, 11428308, 11273002, U1331120, and U1331122, and by the National Basic Research Program of China under grant No. 2014CB845701. This research has made use of the SIMBAD database, operated at CDS, Strasbourg, France, and the NASA's Astrophysics Data System.

REFERENCES

Anstee, S. D., & O'Mara, B. J. 1991, MNRAS, 253, 549
Anstee, S. D., & O'Mara, B. J. 1995, MNRAS, 276, 859
Bagnulo, S., Jehin, E., Ledoux, C., et al. 2003, Msngr, 114, 10
Bergemann, M., Kudritzki, R.-P., Würl, M., et al. 2013, ApJ, 764, 115
Burris, D. L., Pilachowski, C. A., Armandroff, T. E., et al. 2000, ApJ, 544, 302
Butler, K., & Giddings, J. R. 1985, Newsletter on Analysis of Astronomical Spectra No. 9 (London: Univ. London)
Carney, B. W., Latham, D. W., Stefanik, R. P., et al. 2003, AJ, 125, 293
Cayrel, R., Depagne, E., Spite, M., et al. 2004, A&A, 416, 1117
Cohen, J. G., Christlieb, N., McWilliam, A., et al. 2004, ApJ, 612, 1107
Da Silva, R., Milone, A. C., & Reddy, B. E. 2011, A&A, 526, A71
Davies, B., Kudritzki, R.-P., Gazak, Z., et al. 2015, ApJ, 806, 21
Evans, C. J., Davies, B., Kudritzki, R.-P., et al. 2011, A&A, 527, 50
Frebel, A., Christlieb, N., Norris, J. E., et al. 2007, ApJ, 660, 117
Fulbright, J. P. 2000, AJ, 120, 1841
Gazak, J. Z., Kudritzki, R., Evans, C., et al. 2015, ApJ, 805, 182
Grupp, F. 2004, A&A, 420, 289
Grupp, F., Kurucz, R. L., & Tan, K. 2009, A&A, 503, 177
Hansen, C. J., & Primas, F. 2011, A&A, 525, L5
Heiter, U., Jofré, P., Gustafsson, B., et al. 2015, A&A, 582, A49
Hinkle, K., Wallace, L., & Livingston, W. 1995, PASP, 107, 1042
Hinkle, K., Wallace, L., Valenti, J., & Harmer, D. (ed.) 2000, Visible and Near IR Atlas of the Arcturus Spectrum 3727–9300 Å (ASP: San Francisco, CA)
Jofré, P., Heiter, U., Soubiran, C., et al. 2014, A&A, 564, A133
Jofré, P., Heiter, U., Soubiran, C., et al. 2015, A&A, 582, A81
Jönsson, H., Ryde, N., Nissen, P. E., et al. 2011, A&A, 530, A144
Kobayashi, C., Karakas, A. I., & Umeda, H. 2011, MNRAS, 414, 3231
Kobayashi, N., Tokunaga, A. T., Terada, H., et al. 2000, Proc. SPIE, 4008, 1056
Lebzelter, T., Seifahrt, A., Uttenthaler, S., et al. 2012, A&A, 539, A10
Lind, K., Bergemann, M., & Asplund, M. 2012, MNRAS, 427, 50
Majewski, S. R., Schiavon, R. P., Frinchaboy, P. M., et al. 2015, arXiv:1509.05420
Mishenina, T. V., Bienaymé, O., Gorbaneva, T. I., et al. 2006, A&A, 456, 1109
Patrick, L. R., Evans, C. J., Davies, B., et al. 2015, ApJ, 803, 14
Ramírez, I., & Allende Prieto, C. 2011, ApJ, 743, 135
Saito, Y.-J., Takada-Hidai, M., Honda, S., et al. 2009, PASJ, 61, 549
Samland, M. 1998, ApJ, 496, 155
Sharples, R., Bender, R., Agudo Berbel, A., et al. 2013, Msngr, 151, 21
Shi, J. R., Gehren, T., Butler, K., et al. 2008, A&A, 486, 303
Shi, J. R., Gehren, T., Mashonkina, L., et al. 2009, A&A, 503, 533
Shi, J. R., Gehren, T., & Zhao, G. 2011, A&A, 534, A103
Shi, J. R., Takada-Hidai, M., Takeda, Y., et al. 2012, ApJ, 755, 36
Simmerer, J., Sneden, C., Cowan, J. J., et al. 2004, ApJ, 617, 1091
Smiljanic, R., Korn, A. J., Bergemann, M., et al. 2014, A&A, 570, A122
Takada-Hidai, M., Saito, Y., Takeda, Y., et al. 2005, PASJ, 57, 347
Takeda, Y., Kaneko, H., Matsumoto, N., et al. 2009, PASJ, 61, 563
Takeda, Y., & Takada-Hidai, M. 2011, PASJ, 63, S537
Takeda, Y., & Takada-Hidai, M. 2012, PASJ, 64, 42
Timmes, F. X., Woosley, S. E., & Weaver, T. A. 1995, ApJS, 98, 617
Tsujimoto, T., Nomoto, K., Yoshii, Y., et al. 1995, MNRAS, 277, 945
Vernet, J., Dekker, H., D'Odorico, S., et al. 2011, A&A, 536, A105
Woosley, S. E., & Weaver, T. A. 1995, ApJS, 101, 181

The Astrophysical Journal, 819:24 (15pp), 2016 March 1 doi:10.3847/0004-637X/819/1/24

A SURVEY OF LUMINOUS HIGH-REDSHIFT QUASARS WITH SDSS AND *WISE*. I. TARGET SELECTION AND OPTICAL SPECTROSCOPY

Feige Wang[1,2], Xue-Bing Wu[1,3], Xiaohui Fan[2,3], Jinyi Yang[1,2], Weimin Yi[4,5], Fuyan Bian[6,10], Ian D. McGreer[2], Qian Yang[1,2], Yanli Ai[7], Xiaoyi Dong[1], Wenwen Zuo[8], Linhua Jiang[3], Richard Green[2], Shu Wang[1], Zheng Cai[2,9], Ran Wang[3], and Minghao Yue[1]

[1] Department of Astronomy, School of Physics, Peking University, Beijing 100871, China; feige.wang@pku.edu.cn
[2] Steward Observatory, University of Arizona, 933 North Cherry Avenue, Tucson, AZ 85721, USA
[3] Kavli Institute for Astronomy and Astrophysics, Peking University, Beijing 100871, China
[4] Yunnan Observatories, Chinese Academy of Sciences, Kunming 650011, China
[5] Key Laboratory for the Structure and Evolution of Celestial Objects, Chinese Academy of Sciences, Kunming 650011, China
[6] Research School of Astronomy and Astrophysics, Australian National University, Weston Creek, ACT 2611, Australia
[7] School of Physics and Astronomy, Sun Yat-Sen University, Guangzhou 510275, China
[8] Shanghai Astronomical Observatory, Chinese Academy of Sciences, Shanghai 200030, China
[9] UCO/Lick Observatory, University of California, 1156 High Street, Santa Cruz, CA 95064, USA

Received 2015 November 16; accepted 2016 January 6; published 2016 February 24

ABSTRACT

High-redshift quasars are important tracers of structure and evolution in the early universe. However, they are very rare and difficult to find when using color selection because of contamination from late-type dwarfs. High-redshift quasar surveys based on only optical colors suffer from incompleteness and low identification efficiency, especially at $z \gtrsim 4.5$. We have developed a new method to select $4.7 \lesssim z \lesssim 5.4$ quasars with both high efficiency and completeness by combining optical and mid-IR *Wide-field Infrared Survey Explorer* (*WISE*) photometric data, and are conducting a luminous $z \sim 5$ quasar survey in the whole Sloan Digital Sky Survey (SDSS) footprint. We have spectroscopically observed 99 out of 110 candidates with z-band magnitudes brighter than 19.5, and 64 (64.6%) of them are quasars with redshifts of $4.4 \lesssim z \lesssim 5.5$ and absolute magnitudes of $-29 \lesssim M_{1450} \lesssim -26.4$. In addition, we also observed 14 fainter candidates selected with the same criteria and identified 8 (57.1%) of them as quasars with $4.7 < z < 5.4$. Among 72 newly identified quasars, 12 of them are at $5.2 < z < 5.7$, which leads to an increase of ∼36% of the number of known quasars at this redshift range. More importantly, our identifications doubled the number of quasars with $M_{1450} < -27.5$ at $z > 4.5$, which will set strong constraints on the bright end of the quasar luminosity function. We also expand our method to select quasars at $z \gtrsim 5.7$. In this paper we report the discovery of four new luminous $z \gtrsim 5.7$ quasars based on SDSS–*WISE* selection.

Key words: galaxies: active – galaxies: high-redshift – quasars: emission lines – quasars: general

Supporting material: machine-readable tables

1. INTRODUCTION

As the most luminous non-transient objects that can be observed in the early universe, high-redshift quasars are important tracers to study early structure formation and the history of cosmic reionization (e.g., Fan et al. 2006a). In addition, understanding the evolution of quasars from the early universe to the present epoch allows us to study the accretion history of supermassive black holes (SMBHs). However, high-redshift quasar searches are highly challenging due to their low spatial density and a high rate of contamination from cool dwarfs when using the traditional multicolor selection method.

With the increasing number of large surveys such as the 2dF Quasar Redshift Survey (2QZ; Croom et al. 2001) and the Sloan Digital Sky Survey (SDSS; York et al. 2000), the number of known quasars has been increasing rapidly. The 2QZ identified more than 23,000 $B < 21$ quasars (Croom et al. 2004). The first two phases of the SDSS spectroscopically identified more than 100,000 quasars (Schneider et al. 2010) and the Baryonic Oscillation Spectroscopic Survey (BOSS; Dawson et al. 2013), which is the third phase of SDSS (SDSS-III; Eisenstein et al. 2011), spectroscopically identified more than 300,000 quasars (e.g., Pâris et al. 2012, 2014) selected by using the extreme deconvolution method (Bovy et al. 2011; DiPompeo et al. 2015). However, most of these quasars are selected based on optical colors only and mostly at lower redshift ($z \lesssim 3.5$). Based on SDSS $g - r/r - i$ and $r - i/i - z$ colors, several hundred $z \geqslant 4$ quasars and some $z \geqslant 5$ quasars have been discovered (Fan et al. 1999, 2000a, 2001b; Zheng et al. 2000; Anderson et al. 2001; Schneider et al. 2001; Chiu et al. 2005). These quasar surveys have to make a very strict $r - i/i - z$ cut and suffer from low completeness to avoid the strong contamination of late-type stars. Nonetheless, the success rate of finding $z \gtrsim 4.5$ quasars in automated spectroscopic surveys remains quite low. For example, the overall success rate of finding $z \gtrsim 4.5$ quasars in the SDSS quasar survey is less than 10%.

Cool et al. (2006) discovered three $z > 5$ quasars in the AGN and Galaxy Evolution Survey (AGES; Kochanek et al. 2012) with targets selected from *Spitzer Space Telescope* mid-infrared photometry. The combination of optical and near-IR colors can improve the success rate and completeness of selecting high-redshift quasars. McGreer et al. (2013) identified 73 $4.7 \leqslant z \leqslant 5.1$ quasars out of 92 candidates by adding near-IR J-band photometry. However, this method can be applied only to a narrow redshift range (McGreer et al. 2013).

Spectroscopic followup of SDSS i-dropout objects has identified more than 30 luminous $z > 5.7$ quasars (Fan

---

[10] Stromlo Fellow.

et al. 2000b, 2001a, 2003, 2004, 2006b; Jiang et al. 2008, 2009, 2015). The Canada–France High-z Quasar Survey (CFHQS) has found 20 fainter $z > 5.7$ quasars based on multicolor optical imaging at the Canada–France–Hawaii Telescope (CFHT; Willott et al. 2007, 2009, 2010a, 2010b). The Panoramic Survey Telescope & Rapid Response System 1 (Pan-STARRS1, PS1 Kaiser et al. 2002, 2010) high-redshift quasar survey has discovered more than ten $z > 5.7$ quasars (Morganson et al. 2012; Bañados et al. 2014). Recently, Bañados et al. (2015) improved the efficiency for selecting $z \sim 6$ quasars by matching Pan-STARRS1 and Faint Images of the Radio Sky at Twenty Centimeters (FIRST, Becker et al. 1995) and Carnall et al. (2015) obtained a cleaner $z \gtrsim 5.7$ candidate sample by matching optical photometry from the Very Large Telescope Survey Telescope ATLAS survey (Shanks et al. 2015) and *Wide-field Infrared Survey Explorer* (*WISE*) photometry. However, these methods can be used to select only $z < 6.5$ quasars. The first $z > 6.5$ quasar, ULAS J112001.48+064124.3 at $z = 7.1$, was discovered in the United Kingdom Infrared Deep Sky Survey (UKIDSS) Large Area Survey (LAS; Lawrence et al. 2007) by Mortlock et al. (2011). Recently, six more $z > 6.5$ quasars (Venemans et al. 2013, 2015) were discovered in the Visible and Infrared Survey Telescope for Astronomy (VISTA) Kilo-Degree Infrared Galaxy survey (VIKING; Arnaboldi et al. 2007) and Pan-STARRS1 survey. To date, although more than 300,000 quasars are known, among them are about 170 quasars at $z > 5$, ~60 quasars at $z > 6$ and one quasar at $z > 7$. In addition there is an obvious gap of known quasars at $5.2 \lesssim z \lesssim 5.7$, which is caused by their optical colors being very similar to those of late-type stars, especially M dwarfs. This redshift distribution gap of known quasars poses challenges for the studies of the high-redshift quasar luminosity function (QLF), the black hole mass function (BHMF) and the properties of the post-reionziation intergalactic medium (IGM).

NASA's *WISE* (Wright et al. 2010) mapped the sky at 3.4, 4.6, 12, and 22 μm (*W*1, *W*2, *W*3, and *W*4) with an angular resolution of 6.1, 6.4, 6.5, and 12.0 arcsec and 5σ photometric sensitivity better than 0.08, 0.11, 1, and 6 mJy (corresponding to 16.5, 15.5, 11.2, and 7.9 Vega magnitudes) in these four bands, respectively. The *WISE* All-Sky Data Release[11] includes all data taken during the *WISE* full cryogenic mission phase from 2010 January 7 to August 6 and consists of over 563 million objects. Recently the ALLWISE[12] program combined data from the *WISE* cryogenic and NEOWISE (Mainzer et al. 2011) post-cryogenic survey phases to form the most comprehensive view of the full mid-infrared sky. The ALLWISE photometric catalog includes over 747 million objects with enhanced photometric sensitivity and accuracy and improved astrometric precision compared to the *WISE* All-Sky Data Release.

In this paper we present a new robust method for selecting luminous high-redshift quasars by combining ALLWISE and SDSS photometric data and provide the results of optical spectroscopy followup observations. This paper is organized as follows. In Section 2 we summarize the ALLWISE detection rate of high-redshift quasars and the $W1-W2$ colors of high-redshift quasars and late-type stars. In Section 3 we describe our target selection and spectroscopic observations. In Section 4 we present our spectroscopic quasar sample and in Section 5 we discuss the pros and cons of our selection method and compare with the SDSS high-redshift quasar selection method. In Section 6 we extend our selection method to $z \gtrsim 5.7$ quasars and present the discovery of four new quasars at $z > 5.7$ and in Section 7 we give a brief summary. Throughout the paper, SDSS magnitudes are reported on the asinh system (Lupton et al. 1999), and *WISE* magnitudes are on the Vega system. We adopt a standard ΛCDM cosmology with Hubble constant $H_0 = 70\ \mathrm{km\ s^{-1}\ Mpc^{-1}}$, and density parameters $\Omega_M = 0.3$ and $\Omega_\Lambda = 0.7$.

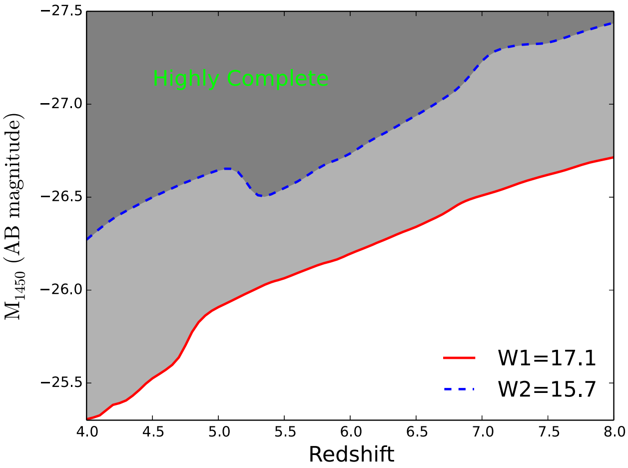

Figure 1. M_{1450} as a function of redshift for a type I quasar template from Glikman et al. (2006). The red solid line denotes $W1 = 17.1$ and the blue dashed line denotes $W2 = 15.7$, which are the 95% completeness limits of the ALLWISE catalog. ALLWISE is a promising data set for finding high-redshift quasars with high luminosity (e.g., $M_{1450} \lesssim -26.5$ at $z \lesssim 6$ and $M_{1450} \lesssim -27.0$ at $z \lesssim 7$).

2. WISE PHOTOMETRY OF PUBLISHED HIGH-REDSHIFT QUASARS

Wu et al. (2012) first studied SDSS quasars in the *WISE* preliminary data release[13] sky coverage and found that *WISE* can detect more than 50% of the SDSS quasars with $i < 20.5$ and $W1-W2 > 0.57$ and can separate late-type stars and quasars efficiently. Remarkably, this method has been used in the Large Sky Area Multi-object Fiber Spectroscopic Telescope (LAMOST) Quasar Survey and has discovered several thousand new quasars mainly at $z \lesssim 4.0$ (Ai et al. 2016). The depth of ALLWISE has improved from the early catalogs, due to the stacking of multiple epoch photometry; the 95% completeness limits of ALLWISE *W*1 and *W*2 are at about 17.1 (44 μJy) and 15.7 (88 μJy) magnitude.[14]

Figure 1 shows the absolute magnitudes at 1450 Å of a low redshift type I quasar template (Glikman et al. 2006) as a function of redshift at the ALLWISE *W*1 and *W*2 magnitude limits. It is clear that the ALLWISE data set has a high completeness of detecting luminous high-redshift quasars (e.g., $M_{1450} \lesssim -26.5$ at $z \lesssim 6$ and $M_{1450} \lesssim -27.0$ at $z \lesssim 7$) and is a highly valuable data set for finding luminous high-redshift quasars when combined with other optical sky surveys such as SDSS, PanSTARRS, SkyMapper, DES, VST ATLAS,

---

[11] http://wise2.ipac.caltech.edu/docs/release/allsky/

[12] http://wise2.ipac.caltech.edu/docs/release/allwise/

[13] http://wise2.ipac.caltech.edu/docs/release/prelim/

[14] http://wise2.ipac.caltech.edu/docs/release/allwise/expsup/

Table 1
Optical and *WISE* Photometry of 725 Published $z > 4.5$ Quasars

Name	Redshift	Ref	r	σ_r	i	σ_i	z	σ_z	Opt	$W1$	σ_{W1}	$W2$	σ_{W2}	*WISE*
J000239.39+255034.80	5.800	16	23.09	0.32	21.51	0.11	18.96	0.05	DR10	16.16	0.06	15.54	0.13	AW
J000552.34–000655.80	5.850	16	24.97	0.51	22.98	0.28	20.41	0.13	DR10	17.30	0.16	17.04	99.0	AW
J000651.61–620803.70	4.510	51	18.29	99.0	99.0	99.0	99.0	99.0	REF	15.20	0.03	14.61	0.04	AW
J000749.17+004119.61	4.780	DR12	21.36	0.06	19.97	0.03	19.84	0.08	DR10	16.85	0.11	16.41	0.26	AW
J000825.77–062604.60	5.929	24	23.91	0.59	23.55	0.63	20.01	0.14	DR10	16.81	0.11	15.68	0.14	AW
J001115.24+144601.80	4.964	DR12	19.48	0.02	18.17	0.02	18.03	0.03	DR10	15.29	0.04	14.69	0.06	AW
J001207.79+094720.23	4.745	DR12	21.40	0.07	19.81	0.04	19.86	0.10	DR10	16.26	0.07	15.80	0.17	AW
J001529.86–004904.30	4.930	32	22.59	0.15	20.99	0.05	20.56	0.12	DR10	99.0	99.0	99.0	99.0	99
J001714.68–100055.43	5.011	DR7	21.23	0.06	19.45	0.03	19.55	0.09	DR10	15.94	0.06	15.17	0.09	AW
J002208.00–150539.76	4.528	50	19.39	0.03	18.75	0.02	18.54	0.04	DR10	15.54	0.05	15.11	0.10	AW

Note. Table 1 is available in its entirety in the electronic edition of the journal. The first 10 rows are shown here for guidance regarding its form and content. The names here are in the format of JHHMMSS.SS+/–DDMMSS.SS. The Ref column lists the reference for each quasar and the Opt column lists the references for the optical magnitudes. Most optical magnitudes are from the SDSS DR10 photometric catalog and are Galactic extinction corrected SDSS PSF asinh magnitudes ($z_{AB} = z_{\mathrm{SDSS}} + 0.02$ mag). The optical magnitudes come from the reference paper and are in the AB system if the quasar does not have SDSS DR 10 photometry. The *WISE* column lists the flag from the *WISE* data: AW = ALLWISE catalog, AWR = ALLWISE Reject catalog, AS = ALL-SKY *WISE* catalog, ASR = ALL-SKY *WISE* Reject catalog, and 99 means no detection in any *WISE* catalog. This table only includes quasars that were published before 2015 July.

(This table is available in its entirety in machine-readable form.)

DECaLS, and LSST as well as with near-IR surveys such as UKIDSS-LAS, UKIDSSS-UHS, and VISTA-VHS.

We collected 725 published quasars at $z > 4.5$ from the SDSS quasar catalogs and the literature (Table 1). We cross-matched these high-redshift quasars with the ALLWISE source catalog using a position offset within 2″ and found that 530 (73.1%) of them were detected in the ALLWISE $W1$ band, 505 (69.7%) in the $W2$ band, 261 (36.0%) in the $W3$ band, and 94 (13.0%) in the $W4$ band. In Figure 2 we show the redshift and z-band magnitude distribution of these quasars as well as the dependence of the ALLWISE detection rate on the redshift and magnitude. The ALLWISE data set detected $\gtrsim$50% of the known quasars over almost all redshifts and $\gtrsim$95% of the known quasars with $z \lesssim 19.5$. This is consistent with what we find in Figure 1. In particular, 34 of 50 (68%) published $z \geqslant 6$ quasars are detected by the ALLWISE data set, which is higher than the result reported in previous studies on the *WISE* All-Sky detection rate (17/31, 55%) of $z > 6$ quasars based on a smaller sample (Blain et al. 2013). Note that the drop in the detection rate at the brightest end is caused by the fact that one of three quasars in the brightest bin is blended by a nearby bright star in the ALLWISE image.

Due to their red optical colors, late-type stars (especially M dwarfs) are the most serious contaminants in selecting $z \sim 5$ quasar candidates using optical colors (e.g., Fan et al. 1999). Wu et al. (2012) studied the color distributions of *WISE*-detected quasars and stars with SDSS spectroscopy and found that both normal and late-type stars can be well rejected with $W1$–$W2$ >0.57 (see Figure 6 in Wu et al. 2012). Figure 3 shows the $W1$–$W2$ color of quasars as a function of redshift. To have a clear view of the color-redshift track, we plot quasars with both $W1$ and $W2$ having a signal-to-noise ratio great than five as blue points and quasars with only $W1$ at the five sigma level as open black cycles in Figure 3. To get a more reasonable statistics of known quasars, we only count quasars detected by ALLWISE with both $W1$ and $W2$ at the five sigma level in the lower panel in Figure 3. Clearly most high-redshift quasars, especially $z > 4.7$ quasars, have a red $W1$–$W2$ color. There are ~41% of $z < 4.7$ quasars having red $W1$–$W2$ colors with $W1$–$W2 > 0.5$, ~68% of $4.7 < z < 5.0$ quasars with $W1$–$W2$ > 0.5, and ~92% of $z > 5.0$ quasars with $W1$–$W2 > 0.5$. Because *WISE* data have a high detection rate of luminous high-redshift quasars and can provide an effective way of separating quasars and late-type stars, we are conducting a luminous quasar survey at $z \gtrsim 4.7$ by combing SDSS and ALLWISE photometry. Note that there is a glaring gap of known quasars at $5.2 < z < 5.7$ which can be seen in both Figures 1 and 3. This is because

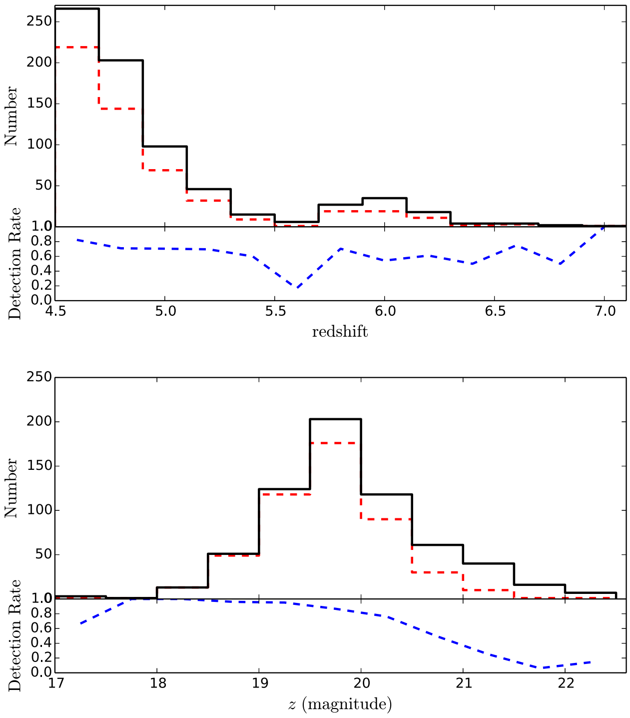

Figure 2. Upper panel: the black solid line denotes the redshift histogram of all published $z > 4.5$ quasars, while the red dashed line is the redshift histogram of the ALLWISE-detected $z > 4.5$ quasars. The ratio between them (blue dashed line) is also plotted as a function of redshift. Note that the drop in the detection rate at $z \sim 5.5$ is mainly affected by the statistic error because of the small number of objects in the bin. Lower panel: the black solid line denotes the SDSS z-band magnitude histogram of $z \geqslant 4.5$ quasars with SDSS detections, while the red dashed line is the z-band magnitude histogram of the ALLWISE-detected $z \geqslant 4.5$ quasars. The ratio between them is also plotted as a function of magnitude.

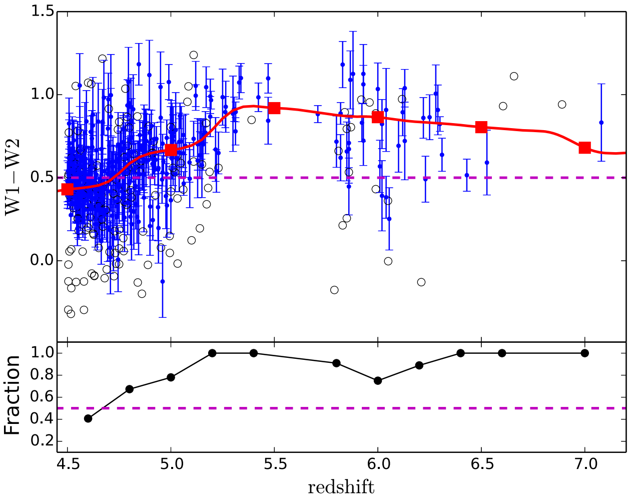

Figure 3. Upper: the $W1$–$W2$ vs. redshift diagram. The purple dashed line represents $W1$–$W2$ $= 0.5$. The red solid line represents the color-z relation predicted using the quasar template from Glikman et al. (2006). The solid squares from left to right mark the color tracks for quasars from $z = 5.0$ to $z = 7.0$ in steps of $\Delta z = 0.5$. The blue points represent $z \geqslant 4.5$ quasars detected by ALLWISE with both $W1$ and $W2$ at the 5σ level. The black open cycles denote $z \geqslant 4.5$ quasars detected by ALLWISE with only $W1$ at the 5σ level. Lower: the fraction of $z > 4.5$ quasars with $W1$–$W2 > 0.5$ as a function of redshift. Note that we only consider quasars detected by ALLWISE with both $W1$ and $W2$ at the 5σ level here. The purple dashed line denotes a fraction of 50%. We calculated the fraction using a redshift bin of 0.2. Note that the bins at $z \sim 5.6$ and $z \sim 6.8$ are not plotted due to no available data. The drop of the fraction at $z \sim 6$ is partly because of the large uncertainties of *WISE* photometry for faint high-redshift quasars.

quasar colors are very similar to those of M dwarfs and hard to distinguish in both optical and near-IR wavelengths. Benefiting from the different $W1$–$W2$ colors of quasars and M dwarfs, we expect that we can select $z > 5.2$ quasars more effectively by combining SDSS and ALLWISE photometry than previous quasar selection methods.

3. TARGET SELECTION AND SPECTROSCOPIC OBSERVATIONS

3.1. Target Selection

At $z \sim 5$, most quasars are undetectable in the u band and g band because of the presence of Lyman limit systems (LLSs), which are optically thick to the continuum radiation from quasars (Fan et al. 1999). Meanwhile the Lyman series line absorptions and Lyman continuum absorptions begin to dominate in the r band and Lyα emission moves to the i band. The $r - i/i - z$ color–color diagram was often used to select $z \sim 5$ quasar candidates in previous studies (Fan et al. 1999; Richards et al. 2002; McGreer et al. 2013). In Figure 4 we show the $r - i/i - z$ colors of stars and 274 SDSS and BOSS $4.7 \leqslant z < 5.6$ quasars (Schneider et al. 2010; Pâris et al. 2014) as well as different $z \sim 5$ quasar selection criteria (Richards et al. 2002; McGreer et al. 2013). The optical color selection limits shown here (cyan and orange dashed lines) are effective for quasars at $z \lesssim 5.1$, but the selection becomes very incomplete for quasars at $z \gtrsim 5.1$ when they enter the M star locus on the $r - i/i - z$ color–color diagram (Richards et al. 2002; McGreer et al. 2013). This is consistent with the color-redshift tracks (green solid line) derived from the $z \sim 5$ quasar composite spectrum constructed from BOSS quasar spectra using a median algorithm by us. As we discussed in Section 2, $W1$–$W2$ can be used to reject M type stars effectively and the addition of *WISE* photometry will allow us to loosen the typical $r - i/i - z$ cuts to reach higher redshift while still being able to reject most late-type star contaminants. Following are our selection criteria:

$$u > 22.3,\ z < 20.2 \tag{1}$$

$$g > 24.0 \text{ or } g - r > 1.8 \tag{2}$$

$$r - i > 1.0 \tag{3}$$

$$i - z < 0.72 \tag{4}$$

$$i - z < 0.625 \times (r - i) - 0.3 \tag{5}$$

$$z - W1 > 2.5 \tag{6}$$

$$W1 - W2 > 0.5 \tag{7}$$

$$W1 < 17.0,\ \sigma_{W2} < 0.2 \tag{8}$$

$$z - W1 > 2.8 \text{ or } W1 - W2 > 0.7, \text{ if } i - z > 0.4, \tag{9}$$

where optical magnitudes are Galactic extinction corrected SDSS point-spread function asinh magnitudes and the $W1$ and $W2$ magnitudes are Vega-based magnitudes. The u-band and g-band cuts are the typical magnitude limits for dropout bands (Fan et al. 1999). The z-band magnitude cut is to ensure the accuracy of the z-band photometry since the 5σ detection of the SDSS z band for point sources with $1''$ image quality is about 20.5. The spectral energy distributions of $z \gtrsim 4.5$ quasars are mainly dominated by a power-law spectrum with a slope around $\alpha_\nu \sim -0.5$ (Vanden Berk et al. 2001), which is flatter than that of M dwarfs. This difference leads to a redder z−$W1$ color for quasars than for M dwarfs (Equation (6)). As we discussed in the last section, the $W1$–$W2$ color can separate quasars and late-type stars very efficiently; here, we require $W1$–$W2$ > 0.5 (Equation (7)). We use the magnitude or photometric error cuts of the ALLWISE photometric data (Equation (8)) to ensure the accuracy of the $W1$–$W2$ color. Considering the serious contamination and redder $W1$–$W2$ colors for $z \gtrsim 5.2$ quasars (Figure 3), we also require a more strict z−$W1$ and $W1$–$W2$ color accuracy for candidates with $i - z > 0.4$ (Equation (9)). Although using Equation (9) leads to a lower completeness of selecting $z \gtrsim 5.2$ quasars, it helps to reduce star contamination significantly. The color distribution of quasars in the color–color diagrams are broader than that derived from composite quasar spectra. This is not only because of the magnitude uncertainties but also because of the broad distributions of quasar emission line strength and continuum slopes. The z band covers the rest-frame UV continuum (~1300–1700 Å), but the $W1$ band covers the rest-frame optical-continuum (~5000–6500 Å). There is a break of the continuum slope at around 5500 Å (Vanden Berk et al. 2001; Glikman et al. 2006) and the distributions of the continuum slopes at UV and optical wavelengths are broad (e.g., Shen et al. 2011). In addition, as the Hα emission contributes significantly to the flux in *WISE* $W1$ and $W2$ bands, the different strength of the Hα emission will also cause some scatters of the z−$W1$ colors. So the large scatter of z−$W1$ colors is not only affected by the *WISE* magnitude uncertainties but also by the broad distributions of the UV and optical-continuum slopes and the strength of the emission lines.

The purple dashed lines in Figures 4 and 5 denote our color–color selection criteria (Equations (5)–(7)). Apparently, our

Table 2
Observational Information of 72 Newly Identified $z \sim 5$ Quasars

Name	Telescope	Grating	Slit	Redshift	Date	Exposure (s)
J000754.08–031730.82	ANU	R3000	1.0	4.76	20141016	1800
J000851.43+361613.49	LJT	G12	1.8	5.17	20131127	2100
J002526.84–014532.51	MMT	270 gpm	1.0	5.07	20140110	600
J003941.03+202554.85	216	G4	2.3	4.61	20141117	3600
J004508.81+374334.91	LJT	G5	1.8	4.62	20141003	1800
J005527.18+122840.67	LJT	G3	1.8	4.70	20131125	1800
J011614.30+053817.70	Bok	R400	2.5	5.33	20141028	2100
J012026.86+223058.55	MMT	270 gpm	1.5	4.59	20140110	600
J012220.29+345658.43	LJT	G5	1.8	4.85	20140121	1800
J012247.35+121624.06	LJT	G5	1.8	4.79	20141024	2400
J013127.34–032100.19	LJT	G3	1.8	5.18	20131125	1500
J013224.89–030718.45	ANU	R3000	1.0	4.83	20150720	1200
J013238.33+292602.57	Bok	R400	2.5	4.45	20141030	2400
J014741.53–030247.88	216	G4	2.3	4.75	20141117	1800
J015533.28+041506.74	Bok	R400	2.5	5.37	20141028	2400
J015618.99–044139.88	MMT	270 gpm	1.5	4.94	20140110	600
J020139.04+032204.73	216	G4	2.3	4.57	20141117	3600
J021624.16+230409.47	Bok	R400	2.5	5.26	20141030	3000
J021736.76+470826.48	MMT	270 gpm	1.0	4.81	20140108	600
J022055.59+473319.34	216	G4	2.3	4.82	20141116	3600
J022112.62–034252.26	LJT	G3	1.8	5.02	20131125	2700
J024601.95+035054.12	LJT	G5	1.8	4.96	20140121	1800
J024643.78+061045.74	Bok	R400	2.5	4.57	20141028	2100
J025121.33+033317.42	LJT	G3	1.8	5.00	20131125	2400
J030642.51+185315.85	LJT	G3	1.8	5.36	20131125	1320
J032407.69+042613.29	Bok	R400	2.5	4.72	20141028	2100
J045427.96–050049.38	Bok	R400	2.5	4.93	20141117	1500
J065330.25+152604.71	MMT	270 gpm	1.0	4.90	20140109	600
J073231.28+325618.33	MMT	270 gpm	1.0	4.76	20150509	300
J074749.18+115352.46	LJT	G3	1.8	5.26	20131127	2100
J075332.01+101511.68	Bok	R400	2.5	4.89	20141111	2400
J080306.19+403958.96	Bok	R400	2.5	4.79	20141118	2400
J083832.31–044017.47	LJT	G12	1.8	4.75	20140225	1800
J085942.62+443115.97	MMT	270 gpm	1.0	4.57	20150314	200
J111700.43–111930.63	LJT	G5	1.8	4.40	20150221	1800
J120829.27+394339.72	MMT	270 gpm	1.0	4.94	20120527	300
J122342.16+183955.39	MMT	270 gpm	1.0	4.55	20150508	300
J133257.45+220835.91	MMT	270 gpm	1.0	5.11	20140109	600
J143704.81+070807.71	LJT	G5	1.8	4.93	20150214	1800
J152302.90+591633.04	216/MMT	270 gpm	1.0	5.11	20150314	600
J155657.36–172107.55	LJT	G5	1.8	4.75	20150228	1500
J160111.16–182835.08	MMT	270 gpm	1.0	5.06	20150508	300
J162045.64+520246.65	MMT	270 gpm	1.5	4.79	20130418	900
J162315.28+470559.90	LJT	G5	1.8	5.13	20140405	2100
J162838.83+063859.14	MMT	270 gpm	1.0	4.85	20150313	500
J163810.39+150058.26	MMT	270 gpm	1.0	4.76	20140514	900
J165635.46+454113.55	LJT	G5	1.8	5.34	20141001	1800
J175114.57+595941.47	216	G10	2.3	4.83	20140507	3600
J175244.10+503633.05	MMT	270 gpm	1.5	5.02	20130418	900
J205442.21+022952.02	MMT	270 gpm	1.0	4.56	20150508	300
J211105.62–015604.14	LJT	G5	1.8	4.85	20140708	1547
J215216.10+104052.44	LJT	G5	1.8	4.79	20141001	1200
J220106.63+030207.71	LJT	G5	1.8	5.06	20141001	1500
J220226.77+150952.38	216	G4	2.3	5.07	20141117	3000
J220710.12–041656.28	LJT	G5	1.8	5.53	20141022	2400
J221232.06+021200.09	LJT	G5	1.8	4.61	20141023	2400
J221921.74+144126.31	LJT	G5	1.8	4.59	20141025	2400
J222514.38+033012.50	Bok	R400	2.5	5.24	20141029	2400
J222612.41–061807.29	LJT	G5	1.8	5.08	20141001	1500
J225257.46+204625.22	LJT	G5	1.8	4.91	20141001	1500
J232939.30+300350.78	LJT	G5	1.8	5.24	20141022	2100
J233048.79+292301.05	LJT	G5	1.8	4.79	20141023	2400
J234241.13+434047.46	LJT	G5	1.8	4.99	20141025	2400
J234433.50+165316.48	LJT	G5	1.8	5.00	20140930	1500

Table 2
(Continued)

Name	Telescope	Grating	Slit	Redshift	Date	Exposure (s)
J003125.86+071036.92	LJT	G3	1.8	5.33	20131126	3000
J011546.27–025312.24	LJT	G5	1.8	5.07	20141123	3600
J024152.92+043553.46	LJT	G12	1.8	5.22	20131129	2100
J081248.82+044056.54	Bok	R400	2.5	5.29	20141030	3000
J132319.69+291755.75	LJT	G12	1.8	4.92	20140223	2100
J151901.27+042348.60	MMT	270 gpm	1.0	4.94	20150316	600
J165951.03+323928.63	LJT	G12	1.8	5.17	20140226	2400
J215904.97+050745.76	LJT	G5	1.8	4.71	20141017	1800

Note. The sources in the first part are from our main sample and those in the second part are from our fainter supplementary sample.

(This table is available in machine-readable form.)

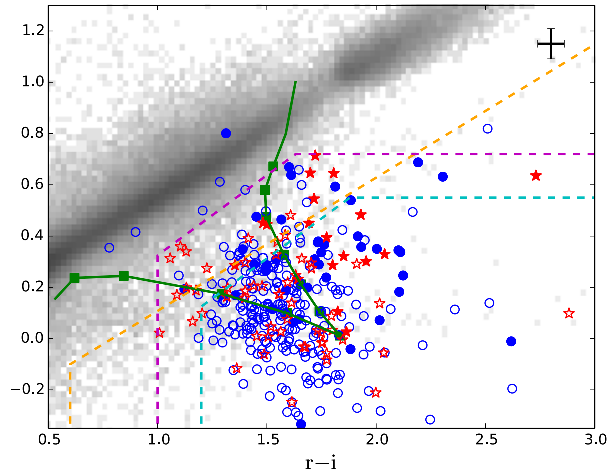

Figure 4. $i - z$ vs. $r - i$ color–color diagram. The purple dashed line represents our selection criteria for quasar candidates. The orange dashed line represents the SDSS $z > 4.5$ quasar selection criteria (Richards et al. 2002) and the cyan dashed line denotes $4.7 \lesssim z \lesssim 5.1$ quasar selection criteria (McGreer et al. 2013). The green solid line represents the color-z relation predicted using $z \sim 5.0$ SDSS quasar composite spectra. The solid squares mark the color tracks for quasars from $z = 4.4$ to $z = 5.4$ in steps of $\Delta z = 0.1$. The gray map denotes SDSS stars, the blue open cycles denote SDSS $4.7 \leqslant z < 5.1$ quasars, the blue solid circles denote SDSS $5.1 \leqslant z < 5.6$ quasars. The red open stars denote our newly discovered quasars with $z < 5.1$ and the red solid stars denote our newly discovered quasars with $5.1 \leqslant z < 5.6$. Typical error bars are shown in the upper right-hand corner.

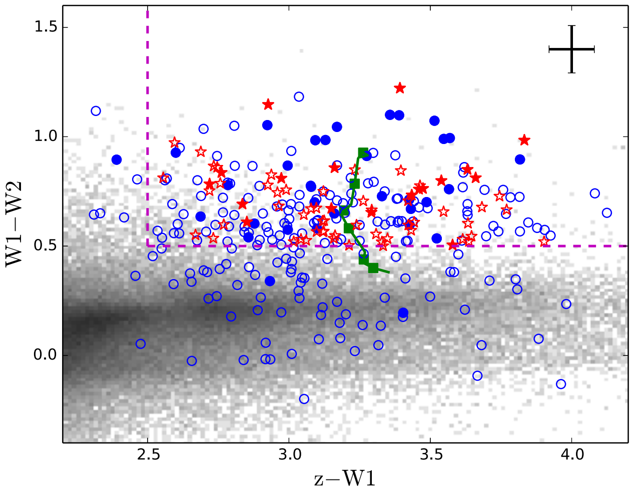

Figure 5. z–$W1$ vs. $W1$–$W2$ color–color diagram. The purple dashed line represents our selection criteria for quasar candidates. The green solid line represents the color-z relation predicted using quasar composite spectra (Glikman et al. 2006). The solid squares mark the color tracks for quasars from $z = 4.4$ to $z = 5.4$ in steps of $\Delta z = 0.2$. Other symbols have the same meaning as in Figure 4.

$r - i/i - z$ selection criteria are much looser than those of other studies (the region between the purple dashed line and the orange dashed line) which will improve the completeness of $z \gtrsim 5.1$ quasars. Among 274 SDSS and BOSS $4.7 \leqslant z < 5.6$ quasars 22 of them (blue crosses between the purple dashed line and the orange dashed line in Figure 4) satisfy our $r - i/i - z$ cuts but not the cuts in Richards et al. (2002) and seven (~32%) of them with $z > 5.1$. Except for the one that was not detected by ALLWISE, the other six $z > 5.1$ quasars also satisfy our z–$W1/W1$–$W2$ selection criteria shown in Figure 5. Therefore we can expect to improve the completeness of selecting $z \gtrsim 5.1$ quasars with our method by combining SDSS and ALLWISE.

We started our quasar candidate selection from a catalog of SDSS Data Release 10 (DR10) primary point sources. Applying the optical magnitude and color cuts (Equations (1)–(5)) using SDSS-III DR10 Query/CasJobs[15] results in 457,930 point sources. We then cross-identified these sources with the ALLWISE source catalog using a position offset within 2″; this reduced our candidate list to 80,404 sources with ALLWISE detections. We selected our candidates using Equations (6)–(9) which resulted in 1262 candidates. As we discussed in Section 2, the ALLWISE data base has a high completeness for finding quasars with z-band magnitudes brighter than 19.5. Limiting candidates to $z \leqslant 19.5$ reduces our candidate list to 420 objects. Before conducting spectroscopic observations we visually inspected images of these 420 candidates and removed 231 candidates with suspicious detections, such as those close to very bright stars or binaries. This list of 189 objects is our primary $z \sim 5$ quasar candidate sample. Removing 78 previously known quasars and one known dwarf results in a total of 110 candidates that required spectroscopic followup observations. We have obtained spectra for 99 of these candidates and also re-identified one known quasar (J022112.62–034252.26, See Table 3) that was not published at the time of observations. In addition to our primary sample at $z \leqslant 19.5$, we also include candidates fainter than 19.5 as a supplementary sample and observed several of them during our spectroscopic runs as a test for our ability to find fainter quasars using SDSS/*WISE* selection.

---

[15] http://skyserver.sdss.org/casjobs/

Table 3
Photometric Properties of 72 New Identified $z \sim 5$ Quasars

Name	Redshift	m_{1450}	M_{1450}	r	σ_r	i	σ_i	z	σ_z	$W1$	σ_{W1}	$W2$	σ_{W2}
J000754.08–031730.82	4.76	19.77	−26.54	21.64	0.08	19.63	0.03	19.49	0.07	16.26	0.07	15.41	0.11
J000851.43+361613.49	5.17	19.12	−27.34	21.45	0.08	19.50	0.02	19.20	0.05	16.05	0.05	15.37	0.09
J002526.84–014532.51	5.07	17.79	−28.63	19.58	0.02	18.03	0.02	17.85	0.02	14.80	0.03	14.16	0.05
J003941.03+202554.85	4.61	19.26	−27.00	20.51	0.05	18.96	0.03	18.78	0.05	14.88	0.03	14.36	0.05
J004508.81+374334.91	4.62	19.40	−26.87	20.43	0.04	19.37	0.03	19.06	0.08	15.98	0.05	15.31	0.08
J005527.18+122840.67	4.70	18.85	−27.45	20.23	0.03	18.71	0.02	18.66	0.04	15.45	0.05	14.95	0.09
J011614.30+053817.70	5.33	18.84	−27.66	21.57	0.09	19.87	0.03	19.22	0.06	16.37	0.07	15.76	0.13
J012026.86+223058.55	4.59	19.38	−26.88	20.58	0.04	19.38	0.02	19.28	0.06	16.73	0.09	15.91	0.17
J012220.29+345658.43	4.85	19.63	−26.72	21.30	0.07	19.45	0.03	19.45	0.07	16.52	0.07	15.69	0.12
J012247.35+121624.06	4.79	19.54	−26.79	22.25	0.14	19.37	0.03	19.27	0.06	15.59	0.05	14.91	0.07
J013127.34–032100.19	5.18	18.09	−28.37	20.15	0.04	18.46	0.02	18.01	0.03	14.58	0.03	13.84	0.04
J013224.89–030718.45	4.83	19.74	−26.60	21.36	0.06	19.73	0.03	19.49	0.06	16.72	0.09	16.12	0.17
J013238.33+292602.57	4.45	19.64	−26.57	20.73	0.06	19.64	0.03	19.47	0.08	16.50	0.07	15.82	0.13
J014741.53–030247.88	4.75	18.55	−27.77	20.08	0.03	18.53	0.02	18.21	0.02	14.86	0.03	14.32	0.05
J015533.28+041506.74	5.37	19.48	−27.03	21.70	0.10	19.97	0.03	19.26	0.06	16.33	0.07	15.19	0.10
J015618.99–044139.88	4.94	19.21	−27.17	20.77	0.04	19.10	0.02	19.13	0.05	15.36	0.04	14.69	0.06
J020139.04+032204.73	4.57	19.15	−27.10	20.25	0.03	19.09	0.02	19.02	0.04	15.38	0.04	14.83	0.07
J021624.16+230409.47	5.26	19.30	−27.18	21.26	0.06	19.78	0.03	19.32	0.06	16.56	0.08	15.73	0.15
J021736.76+470826.48	4.81	19.31	−27.03	20.55	0.05	18.96	0.02	18.88	0.05	15.76	0.05	15.14	0.08
J022055.59+473319.34	4.82	18.56	−27.78	20.07	0.03	18.34	0.01	18.31	0.03	15.19	0.04	14.62	0.06
J022112.62–034252.26[a]	5.02	19.96	−26.45	20.86	0.05	19.25	0.04	19.50	0.07	16.38	0.06	15.63	0.11
J024601.95+035054.12	4.96	19.46	−26.93	21.05	0.05	19.28	0.02	19.36	0.05	16.67	0.07	15.74	0.14
J024643.78+061045.74	4.57	19.06	−27.19	20.22	0.03	19.05	0.02	18.86	0.06	15.42	0.04	14.81	0.07
J025121.33+033317.42	5.00	19.58	−26.82	20.80	0.04	19.04	0.03	19.06	0.05	15.64	0.04	14.93	0.07
J030642.51+185315.85	5.36	17.59	−28.92	19.89	0.03	17.96	0.01	17.47	0.02	14.31	0.03	13.46	0.04
J032407.69+042613.29	4.72	19.19	−27.12	20.39	0.04	19.03	0.02	19.15	0.06	15.72	0.05	15.13	0.09
J045427.96–050049.38	4.93	18.84	−27.54	19.91	0.03	18.59	0.03	18.39	0.03	15.09	0.03	14.53	0.05
J065330.25+152604.71	4.90	19.35	−27.02	21.27	0.06	19.48	0.02	19.39	0.07	16.65	0.11	15.79	0.16
J073231.28+325618.33	4.76	18.78	−27.53	20.26	0.03	18.82	0.01	18.62	0.03	15.46	0.04	14.92	0.08
J074749.18+115352.46	5.26	18.51	−27.97	20.44	0.03	18.67	0.02	18.27	0.03	14.64	0.03	13.79	0.04
J075332.01+101511.68	4.89	19.79	−26.57	21.14	0.04	19.39	0.02	19.37	0.06	16.31	0.08	15.78	0.15
J080306.19+403958.96	4.79	19.17	−27.15	20.58	0.04	18.88	0.02	18.60	0.03	15.28	0.04	14.76	0.06
J083832.31–044017.47	4.75	19.37	−26.94	21.20	0.06	19.62	0.03	19.21	0.07	15.58	0.04	15.06	0.08
J085942.62+443115.97	4.57	18.66	−27.59	19.67	0.02	18.66	0.03	18.64	0.04	15.60	0.05	15.06	0.08
J111700.43–111930.63	4.40	18.61	−27.58	19.75	0.02	18.65	0.02	18.29	0.03	15.19	0.04	14.63	0.06
J120829.27+394339.72	4.94	19.20	−27.18	20.79	0.06	19.04	0.02	19.06	0.05	15.80	0.05	15.09	0.08
J122342.16+183955.39	4.55	18.90	−27.34	20.52	0.04	18.97	0.02	18.59	0.04	14.98	0.03	14.45	0.05
J133257.45+220835.91	5.11	19.11	−27.32	21.12	0.04	19.26	0.02	19.23	0.04	15.69	0.05	14.89	0.06
J143704.81+070807.71	4.93	19.35	−27.03	20.62	0.04	19.17	0.02	19.16	0.05	16.14	0.06	15.62	0.12
J152302.90+591633.04	5.11	19.10	−27.33	21.39	0.06	19.54	0.02	19.22	0.05	15.64	0.03	15.13	0.05
J155657.36–172107.55	4.75	18.47	−27.85	19.94	0.04	18.43	0.02	18.43	0.05	15.09	0.04	14.59	0.06
J160111.16–182835.08	5.06	18.96	−27.46	20.98	0.15	19.37	0.05	18.89	0.09	15.65	0.05	15.05	0.08
J162045.64+520246.65	4.79	19.09	−27.24	20.77	0.04	18.97	0.02	18.94	0.04	15.30	0.03	14.70	0.04
J162315.28+470559.90	5.13	18.89	−27.55	20.87	0.05	19.52	0.03	19.23	0.07	15.57	0.03	14.76	0.05
J162838.83+063859.14	4.85	19.37	−26.98	20.88	0.04	19.56	0.02	19.40	0.05	16.68	0.09	15.93	0.17
J163810.39+150058.26	4.76	18.81	−27.50	20.53	0.04	18.83	0.02	18.53	0.04	15.10	0.04	14.53	0.05
J165635.46+454113.55	5.34	18.94	−27.57	21.51	0.06	19.70	0.02	19.06	0.04	16.22	0.28	15.53	0.07
J175114.57+595941.47	4.83	19.03	−27.17	20.75	0.04	19.09	0.02	18.78	0.04	15.66	0.03	15.09	0.05
J175244.10+503633.05	5.02	18.97	−27.43	20.85	0.04	18.82	0.02	18.87	0.05	15.13	0.03	14.40	0.03
J205442.21+022952.02	4.56	19.15	−27.10	20.33	0.03	19.20	0.02	19.00	0.05	16.33	0.07	15.78	0.14
J211105.62–015604.14	4.85	18.21	−28.14	19.78	0.02	18.11	0.02	18.14	0.03	15.02	0.04	14.41	0.05
J215216.10+104052.44	4.79	18.37	−27.96	19.97	0.03	18.36	0.02	18.22	0.03	14.67	0.03	14.02	0.04
J220106.63+030207.71	5.06	18.90	−27.52	20.58	0.03	19.11	0.02	18.90	0.04	15.98	0.06	15.20	0.10
J220226.77+150952.38	5.07	18.48	−27.95	20.28	0.03	18.69	0.02	18.47	0.03	15.74	0.05	15.20	0.08
J220710.12–041656.28	5.53	18.86	−27.70	22.32	0.24	19.59	0.03	18.95	0.06	15.12	0.04	14.14	0.05
J221232.06+021200.09	4.61	19.83	−26.43	20.90	0.03	19.68	0.03	19.41	0.05	16.65	0.08	15.86	0.14
J221921.74+144126.31	4.59	19.69	−26.57	20.66	0.05	19.53	0.03	19.19	0.06	16.20	0.08	15.45	0.12
J222514.38+033012.50	5.24	19.38	−27.10	21.74	0.14	20.02	0.05	19.47	0.10	16.50	0.08	15.69	0.13
J222612.41–061807.29	5.08	18.66	−27.76	20.32	0.04	18.76	0.02	18.73	0.05	15.64	0.05	14.96	0.09
J225257.46+204625.22	4.91	19.44	−26.93	20.65	0.04	19.16	0.02	19.23	0.06	16.27	0.06	15.52	0.10
J232939.30+300350.78	5.24	18.83	−27.65	20.87	0.05	19.37	0.02	18.93	0.04	16.21	0.06	15.43	0.10
J233048.79+292301.05	4.79	19.73	−26.59	20.93	0.05	19.53	0.02	19.37	0.06	16.77	0.10	15.80	0.13
J234241.13+434047.46	4.99	19.54	−26.86	21.17	0.06	19.26	0.02	18.97	0.05	15.57	0.04	14.73	0.06
J234433.50+165316.48	5.00	18.54	−27.86	20.23	0.03	18.46	0.02	18.52	0.03	15.22	0.04	14.56	0.06

Table 3
(Continued)

Name	Redshift	m_{1450}	M_{1450}	r	σ_r	i	σ_i	z	σ_z	$W1$	σ_{W1}	$W2$	σ_{W2}
J003125.86+071036.92	5.33	20.21	−26.29	22.46	0.15	20.42	0.04	20.09	0.09	16.70	0.10	15.48	0.12
J011546.27–025312.24	5.07	19.56	−26.86	21.28	0.06	19.88	0.03	19.58	0.07	16.42	0.08	15.87	0.17
J024152.92+043553.46	5.22	19.40	−27.07	21.42	0.08	19.78	0.03	19.55	0.08	16.26	0.06	15.60	0.13
J081248.82+044056.54	5.29	19.77	−26.72	21.85	0.11	20.05	0.04	19.77	0.10	16.31	0.07	15.55	0.14
J132319.69+291755.75	4.92	20.16	−26.22	21.74	0.10	19.74	0.04	19.95	0.11	16.65	0.11	15.61	0.15
J151901.27+042348.60	4.94	19.79	−26.59	21.63	0.06	20.22	0.03	19.83	0.08	16.37	0.06	15.59	0.10
J165951.03+323928.63	5.17	19.80	−26.65	21.82	0.07	20.00	0.02	19.89	0.07	16.42	0.06	15.66	0.10
J215904.97+050745.76	4.71	20.24	−26.06	21.14	0.06	19.74	0.03	19.55	0.08	16.81	0.10	15.95	0.17

Notes. The sources in the first part are from our main sample and those in the second part are from our fainter supplementary sample.
[a] This quasar was also independently discovered by SDSS DR12 (I. Pâris et al. 2015, in preparation).

(This table is available in machine-readable form.)

3.2. *Spectroscopic Observations*

Optical spectroscopic observations to identify these quasar candidates were carried out using several facilities: the Lijiang 2.4 m telescope (LJT) and the Xinglong 2.16 m telescope in China; the Kitt Peak 2.3 m Bok telescope and the 6.5 m MMT telescope in the U.S.; and the 2.3 m ANU telescope in Australia. We have observed 99 candidates from our main sample and 64 (64.6%) of them are high-redshift quasars with a redshift of $4.4 \lesssim z \lesssim 5.5$. We also observed 14 fainter candidates from our fainter candidates sample and 8 (57.1%) of them are quasars at $4.7 < z < 5.4$. One of our candidates (J135457.62+314851.4) in our bright main sample was identified to be a low redshift low-ionization broad absorption line quasar (FeLoBAL QSO). However, we can not give the accurate redshift due to strong iron absorptions. The other 40 spectroscopic observed candidates were not quasars and were either identified as cool dwarfs or had relative low S/N and could only be ruled out as quasars. Table 2 lists the observational information of the 72 new identified quasars.

The Lijiang 2.4 m telescope is located at Lijiang Observatory, Yunnan Observatories, Chinese Academy of Sciences (CAS). It is equipped with the Yunnan Faint Object Spectrograph and Camera (YFOSC) which can take spectra followed by photometric images with a very short switching time. We observed 48 candidates by using the YFOSC with a 2k × 4k CCD detector and three different grisms based on the brightness of our candidates. We used Grism 3 (G3) with dispersion of 172 Å mm^{-1} and wavelength coverage from 3200 to 9200 Å to observe the brightest candidates; Grism 5 (G5) with dispersion of 185 Å mm^{-1} and wavelength coverage from 5000 to 9800 Å to observe fainter candidates; and Grism 12 (G12) with dispersion of 900 Å mm^{-1} and wavelength coverage from 5600 to 9900 Å to observe the faintest candidates in our sample. We used a 1.″8 slit for all three grisms. This slit yields a resolution of $R \sim 670$, $R \sim 550$, and $R \sim 160$ for the G3, G5, and G12 grisms, respectively.

We observed 35 candidates using the Red Channel spectrograph (Schmidt et al. 1989) on the MMT 6.5 m telescope. We used the 270 l mm^{-1} grating centered at 7500 Å, providing coverage from 5500 to 9700 Å. We used the 1.″0 or 1.″5 slits based on the seeing, providing resolutions of $R \sim 640$ and $R \sim 430$, respectively.

We observed 16 candidates using the Boller and Chivens Spectrograph (B&C) on Steward Observatory's 2.3 m Bok Telescope at Kitt Peak with the G400 Grating and 2.″5 slit which gave a resolution of $R \sim 450$ and ∼3400 Å wavelength coverage.

We observed eight candidates using the BAO Faint Object Spectrograph and Camera (BFOSC) on the 2.16 m optical telescope at the Xinglong station of the National Astronomical Observatories, Chinese Academy of Sciences (NAOC). We used the G4 or G10 gratings with dispersion of 198 Å mm^{-1} and 392 Å mm^{-1}, respectively. The wavelength coverage of these two gratings is 4000–7800 Å and 4300–9000 Å with spectral resolutions of $R \sim 330$ and $R \sim 110$ with a 2.″3 slit, respectively. Note that we also re-observed one of the candidates (J1523+5916) using the MMT.

We also used the Wide Field Spectrograph (WiFeS; Dopita et al. 2007, 2010), an integral-field double-beam image-slicing spectrograph on the ANU 2.3 m Telescope at Siding Spring Observatory, to observe seven of our quasar candidates. They were observed using Grating R3000 on WiFeS which gives a resolution of $R = 3000$ at wavelengths between 5300 and 9800 Å.

All spectra taken by the 2.4 m telescope, 2.16 m telescope, 2.3 m Bok telescope, and MMT telescope were reduced using standard IRAF routines. The WiFeS data were reduced using a python based pipeline PyWiFeS (Childress et al. 2014). The flux calibrations of all spectra were obtained from standard star observations on the same night and scaled to SDSS *i*-band magnitudes for absolute flux calibrations.

4. RESULTS

4.1. *Discovery of 72 New Quasars at $z \sim 5$*

We have spectroscopically observed 99 candidates with *z*-band magnitudes brighter than 19.5, and 64 (64.6%) of them are quasars with redshifts of $4.4 \lesssim z \lesssim 5.5$ and absolute magnitudes of $-29.0 \lesssim M_{1450} \lesssim -26.4$. We also observed 14 fainter candidates selected with the same selection criteria and identified 8 (57.1%) fainter $z \sim 5$ quasars with $4.7 < z < 5.4$ and absolute magnitude of $-27.1 \lesssim M_{1450} \lesssim -26.1$. Table 4 lists the redshifts and SDSS + *WISE* photometry of the 72 newly discovered quasars and Figure 5 shows the optical spectra of these new quasars. The redshifts of these quasars were measured from Lyα, N v, O i/Si ii, C ii, Si iv, and C iv emission lines (any available). We used a visual recognition assistant for quasar spectra software (ASERA; Yuan et al. 2013), which is an interactive semi-automated toolkit allowing the user to visualize observed spectra and measure the redshifts by fitting the observed spectra to the SDSS quasar

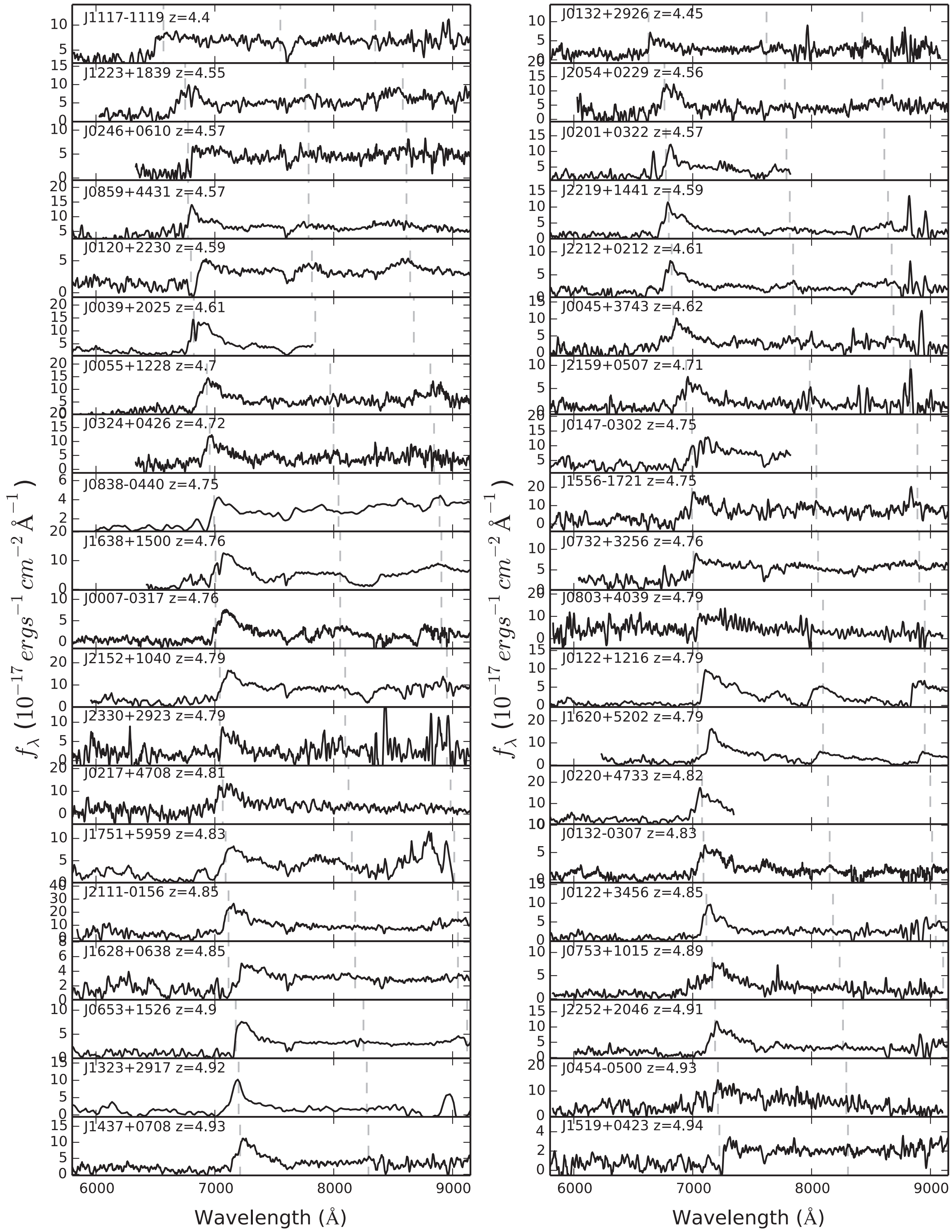

Figure 6. Spectra of 72 newly discovered quasars. We smoothed the spectra by different size boxcars for spectra taken by different instruments. The spectra taken by WiFeS were smoothed to $R \sim 200$. The spectra taken by G3 were smoothed to $R \sim 100$. The spectra taken by G5 were smoothed to $R \sim 110$. The MMT/270 gpm spectra were smoothed to $R \sim 130$ and $R \sim 90$ for those using the 1″.0 and 1″.5 slits, respectively. The spectra taken by R400 were smoothed to $R \sim 90$ and the spectra taken by G12 were smoothed to $R \sim 50$. We present the spectra with the nominal flux calibrations obtained from standard star observations and scaled to the SDSS *i*-band magnitude. The vertical gray lines mark the locations of typical emission lines: in order, Lyα, Si iv, and C iv.

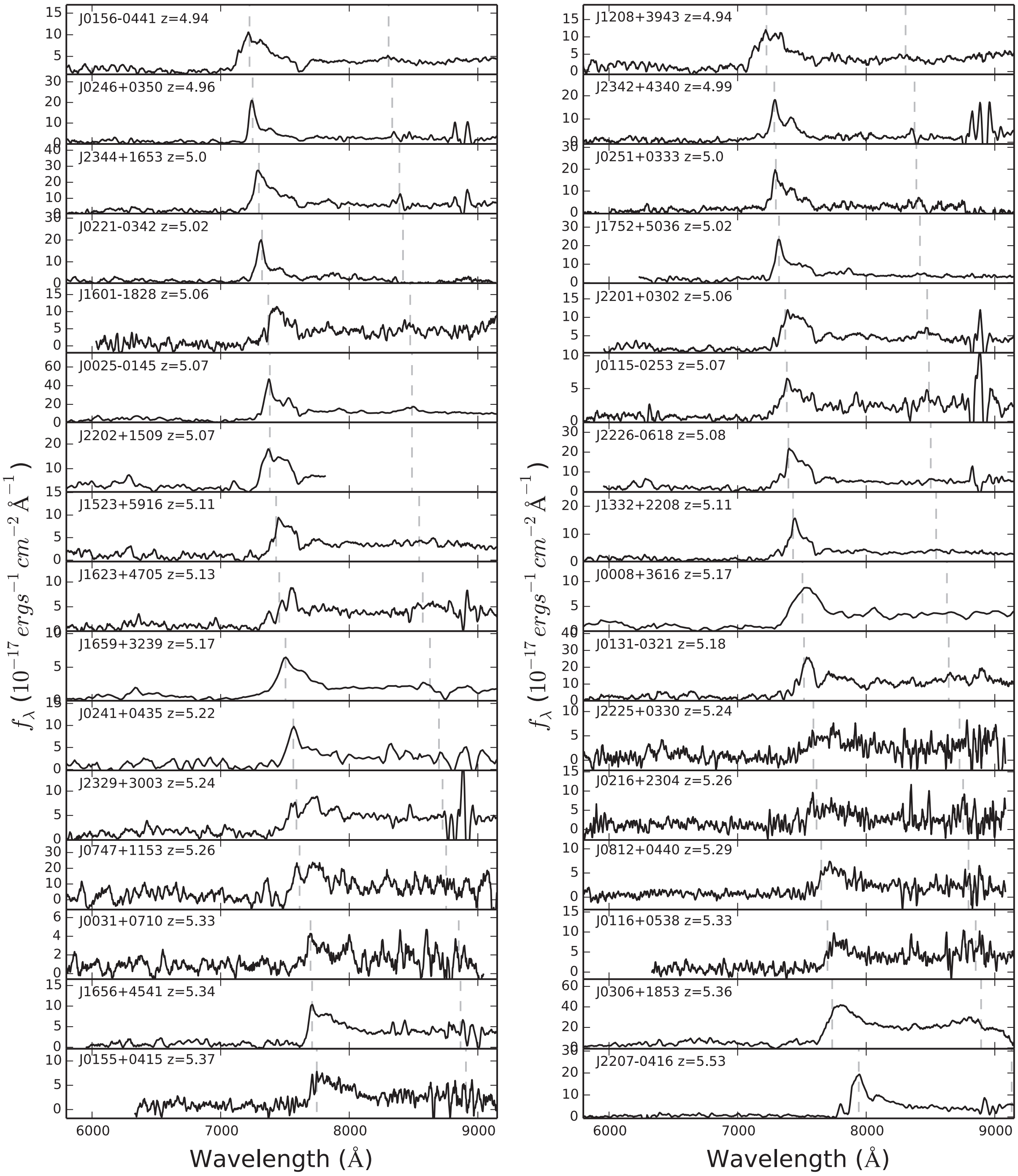

Figure 6. (Continued.)

Table 4
Photometry of Four $z > 5.7$ Quasars Selected by Our Method

Name	Redshift	m_{1450}	M_{1450}	i	σ_i	z	σ_z	$W1$	σ_{W1}	$W2$	σ_{W2}
J010013.02+280225.8[a]	6.30 ± 0.01	17.51	−29.26	20.84	0.06	18.33	0.03	14.46	0.03	13.64	0.03
J154552.08+602824.0	5.78 ± 0.03	19.26	−27.37	21.27	0.07	19.09	0.05	16.00	0.04	15.16	0.05
J232514.24+262847.6	5.77 ± 0.05	19.64	−26.98	21.62	0.17	19.41	0.10	16.19	0.06	15.41	0.10
J235632.44–062259.2	6.15 ± 0.02	19.89	−26.85	22.55	0.35	19.78	0.11	16.56	0.10	15.70	0.20

Note.
[a] See Wu et al. (2015) for details.

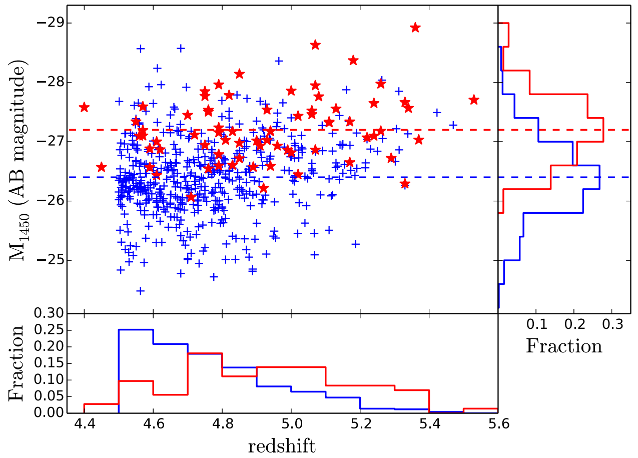

Figure 7. Upper panel: the M_{1450} vs. redshift diagram. The small blue crosses denote SDSS $z \geqslant 4.5$ quasars and the red stars denote our newly discovered quasars. The M_{1450} are AB magnitudes of quasars at 1450 Å. Lower panel: the redshift distributions of newly identified quasars and known $z \geqslant 4.5$ quasars. Our method improves the completeness of selecting quasars at $z > 5.0$, which is consistent with the prediction from the color-z relation shown in Figure 3. Right panel: the distribution of M_{1450}. Apparently our newly discovered quasars are systematically brighter than SDSS quasars and improved the completeness of luminous $z \sim 5$ quasars in the SDSS footprint.

template (Vanden Berk et al. 2001) and interactively accessing related spectral line information. The redshift error measured based on this method mainly depends on the quality of the observed spectra and line properties. Due to the low resolution and strong absorptions blueward of Lyα, the typical redshift error is about 0.05 for our newly discovered quasars. However, the redshift error could be up to 0.1 for objects with relatively low S/N spectra. Our quasar sample spans a redshift range of $4.40 \leqslant z \leqslant 5.53$ and the redshift distribution of these newly identified quasars is shown in the lower panel of Figure 7. As we discussed in Section 2 there is a gap in the previously published quasar redshift distribution at $5.2 < z < 5.7$ with only 33 published quasars at this redshift due to low identification efficiency; 17 of them were identified by the SDSS quasar survey. Among the 72 newly identified quasars, 12 of them are at $5.2 < z < 5.7$, which represents an increase of ∼36% in the number of known quasars in this difficult redshift range.

In Table 3 columns m_{1450} and M_{1450} list the apparent and absolute AB magnitudes of the continuum at rest-frame 1450 Å, respectively. They were calculated by fitting a power-law continuum $f_\nu \sim \nu^{\alpha_\nu}$ to the spectrum of each quasar. As many spectra of our newly discovered quasars do not have enough continuum coverage to reliably measure the slopes of the continua, we assumed that the slope is consistent with the average quasar UV continuum slope $\alpha_\nu = -0.5$ (Vanden Berk et al. 2001). The power-law continuum was then normalized to match visually identified continuum windows that contain minimal contribution from quasar emission lines and from sky OH lines. Figure 7 shows the absolute magnitude at rest-frame 1450 Å and the redshift distribution of our 72 newly discovered quasars and the published SDSS $z \geqslant 4.5$ quasars. The red stars are our newly discovered quasars and the blue crosses denote SDSS quasars. The red and blue dashed lines in Figure 7 denote the mean absolute magnitude of our new quasars ($\overline{M}_{1450} = -27.2$) and the SDSS quasars ($\overline{M}_{1450} = -26.4$), respectively. Our newly discovered quasars are systematically brighter than SDSS quasars and improved the completeness of luminous $z \sim 5$ quasars in the SDSS footprint. More importantly, 24 of our newly discovered quasars have $M_{1450} < -27.5$ and doubled the number of known quasars (26 $z > 4.5$ SDSS quasars) in this brightness range in the SDSS footprint. In particular, 22 of our new quasars are at $z > 4.7$ with $M_{1450} < -27.5$ compared with only 13 previously published SDSS quasars in this redshift/luminosity range.

4.2. Notes on Individual Objects

SDSS J013127.34–032100.1 ($z = 5.19$). The radio loudness defined as the ratio of the rest-frame flux densities in the radio (5 GHz) to optical bands (4400 Å) bands (Kellermann et al. 1989). J0131–0321 is a radio-loud quasar with radio loudness of about 100. J0131–0321 is the most luminous $z \gtrsim 5$ radio-loud quasar known, with a SDSS z-band magnitude of 18.01 ± 0.03 and with $M_{1450} = -28.29$. The observational properties of this quasar are discussed in detail in a separate paper (Yi et al. 2014).

SDSS J022112.62–034252.26 ($z = 5.02$). J0221–0342 was independently discovered by the BOSS quasar survey and published in the DR12 quasar catalog (I. Pâris et al. 2016, in preparation).

SDSS J030642.51+185315.8 ($z = 5.36$). J0306+1853 is the most luminous $z \gtrsim 5$ quasar known to date, with $M_{1450} = -28.92$. A more detailed analysis of this quasar is in Wang et al. (2015).

SDSS J220710.12–041656.28 ($z = 5.53$). J2207–0416 is the most distant quasar discovered in our $z \sim 5$ main sample. Note that due to the extremely similar optical-to-IR colors of $z \sim 5.5$ quasars and M dwarfs, there are only two known $z \sim 5.5$ quasars published before: RD J030117+002025 at $z = 5.50$ (Stern et al. 2000) and NDWFS J142729.7+352209 at $z = 5.53$ (Cool et al. 2006).

5. DISCUSSION

5.1. Comparison with SDSS $z \sim 5$ Quasar Selection

The SDSS quasar surveys provided the largest quasar sample selected based on SDSS u, g, r, i, z photometry and have discovered ∼500 quasars at $z > 4.5$ (e.g., Schneider et al. 2010; Pâris et al. 2012, 2014). The primary method for selecting $z > 4.5$ quasars in the SDSS quasar surveys is based on the $r - i/i - z$ color–color diagram (Fan et al. 1999; Richards et al. 2002). Since the third stage of the SDSS (BOSS) high-redshift quasar survey mainly focused on fainter targets, here we compare our selection only to the first two stages of SDSS high-redshift quasar selection. There are 392 $z > 4.5$ quasars in the SDSS DR7 quasar catalog (Schneider et al. 2010). Three hundred and fifty-six of them have counterparts within 2″ in the ALLWISE catalog and 126 (32%) of them satisfy our selection criteria (also including those with z-band magnitudes fainter than 19.5). Figure 8 shows 392 SDSS high-z quasars: red circles denote quasars that satisfy our selection criteria and blue crosses denote quasars that do not satisfy our selection criteria. Clearly quasars that are not selected by our method are mainly objects with $z \lesssim 4.7$ quasars or with fainter magnitudes. As Figure 3 shows, about 60% of quasars at $z \lesssim 4.7$ have $W1$–$W2$ <0.5 which is the reason why our method is not sensitive to $z \lesssim 4.7$ quasars.

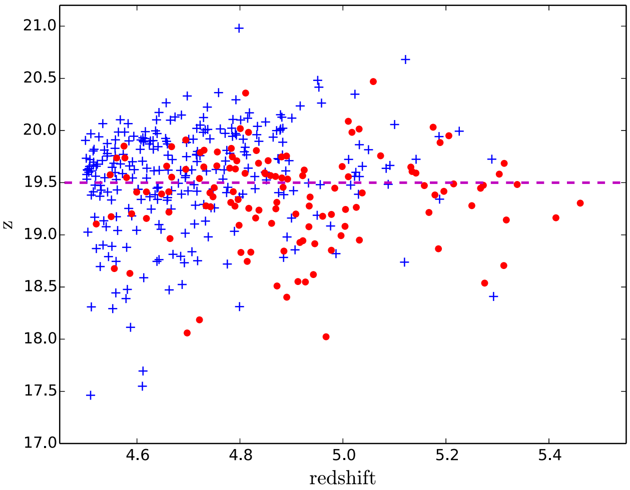

Figure 8. Redshift vs. z-band magnitude diagram of SDSS DR7 $z > 4.5$ quasars. The red circles denote quasars that satisfy our selection method while blue crosses denote quasars that do not satisfy our selection method. The purple line represents z-band magnitudes equal to 19.5.

All our targets are within the SDSS footprint, therefore we examined the 72 newly discovered quasars against the SDSS high-redshift quasar selection criteria presented in Richards et al. (2002). There are three reasons that they are not in the SDSS quasar catalogs: (1) 38 of them are not in the SDSS DR7 photometry sky coverage and thus not in the SDSS main spectroscopy survey region; (2) 25 new quasars have the quasar target flag set by the latest SDSS target selection pipeline but were not observed either because these candidates are at the edge of SDSS main spectroscopy survey or the fields of these candidates were observed at the early stage of the SDSS (e.g., SDSS EDR and DR1) when a preliminary version of the selection pipeline was used (Richards et al. 2002), and (3) The other nine new quasars were not targeted by SDSS altogether. These nine quasars were rejected by the photometric flags (e.g., BLENDED, INTERP_CENTER, CHILD, and FAMILY). Although the SDSS high-redshift quasar target selection method can recover many of these newly discovered quasars, the efficiency (less than 10%) of the SDSS target selection is much lower than that (~60%) of our method by combining SDSS and ALLWISE colors. In addition, our method improved both the completeness and efficiency for selecting $z \gtrsim 5.1$ quasars (the region between the purple dashed line and the orange dashed line in Figure 4).

5.2. *Efficiency and Completeness of Our Quasar Selection*

In our spectroscopic observations ~60% of our candidates are real high-redshift quasars, which is a relatively high efficiency for selecting high-redshift quasars. Although our optical color cuts are very sensitive to $4.5 \lesssim z \lesssim 5.4$ (Figure 4), quasars at $z \lesssim 4.7$ have a bluer $W1$–$W2$ color and lead to a lower completeness of our selection method in this redshift range (Figures 3 and 8). At $z \sim 5$, the *WISE* $W1$ and $W2$ bands only cover quasar rest-frame optical emission (shorter than 1μm), which is not significantly polluted by the hot dust (e.g., Leipski et al. 2014). The $W1$–$W2$ color changes a lot from redshift 4.5 to 5.5 as the Hα emission line moves from $W1$ to $W2$. More than half of the quasars at $z \lesssim 4.7$ have a bluer $W1$–$W2$ with $W1$–$W2 < 0.5$. At this redshift range, the Hα emission line redshifts into the $W1$ band. Quasars with weaker Hα emission lines or a redder continuum will prefer redder $W1$–$W2$ colors and quasars with stronger Hα emission lines or a bluer continuum will show bluer $W1$–$W2$ colors. So our $W1$–$W2$ cut will bias to quasars with weaker Hα emissions or a redder continuum at $z \lesssim 4.7$. At $z \gtrsim 4.7$ the Hα emission line moves out from $W1$ band and the $W1$–$W2$ colors change to be redder and our $W1$–$W2$ cut will not bias to quasars emission line and continuum properties significantly. Overall, our selection method can select luminous quasars at $4.7 \lesssim z \lesssim 5.4$ with both high efficiency and relatively high completeness (e.g., Figure 7). Benefiting from this we will be able to study the QLF at $z \sim 5$, especially at the bright end of the QLF, and do detailed statistics on quasar properties based on a complete sample of SDSS–*WISE* selected $z \sim 5$ quasars in the near future (J. Yang et al. 2016, in preparation). More detailed analysis of the completeness of our quasar sample will be discussed in the QLF paper.

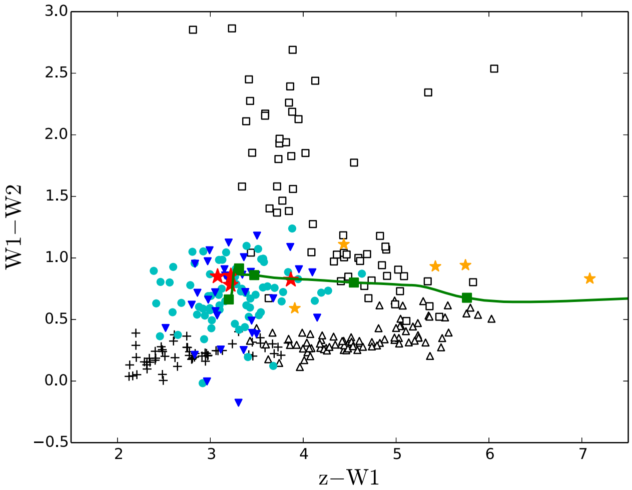

Figure 9. z–$W1$ vs. $W1$–$W2$ color–color diagram. The green solid line represents the color-z relation predicted using quasar composite spectra. The green solid squares mark the color tracks for quasars from $z = 5.0$ to $z = 7.0$ in steps of $\Delta z = 0.5$. The cyan circles denote $5 \leqslant z < 5.5$ quasars, the blue triangles denote $5.5 \leqslant z < 6.5$ quasars, and the orange stars denote $z \geqslant 6.5$ quasars. The red stars represent our four newly discovered $z \gtrsim 5.7$ quasars. The black crosses, open triangles, and open squares are M, L, and T dwarfs, respectively, from Kirkpatrick et al. (2011).

Although ALLWISE has whole-sky coverage, SDSS is limited to only one quarter of the sky. New optical sky surveys are providing coverage of the entire high galactic latitude sky: the PAN-STARRS-1 survey (Kaiser et al. 2002, 2010) has a much larger sky coverage and a slightly deeper depth in red filters than SDSS and it has a y-band filter that covers the 9200 Å $< \lambda <$ 10500 Å range, allowing quasar selection to $z \sim 7$. Combining PAN-STARRS with ALLWISE photometry will provide a much more comprehensive way to find luminous high-redshift quasars. Many other ongoing large-area optical sky surveys including SkyMapper, VST ATLAS, DECaLS, BASS, and DES will enable a complete all-sky survey of luminous high-redshift quasars by combining them with the ALLWISE photometry.

6. OPTICAL SURVEYS PLUS *WISE* FOR FINDING LUMINOUS $z \gtrsim 5.7$ QUASARS

As Figure 3 shows, quasars at $4.7 \lesssim z \lesssim 7$ have relatively redder $W1$–$W2$ colors which are useful for rejecting late-type

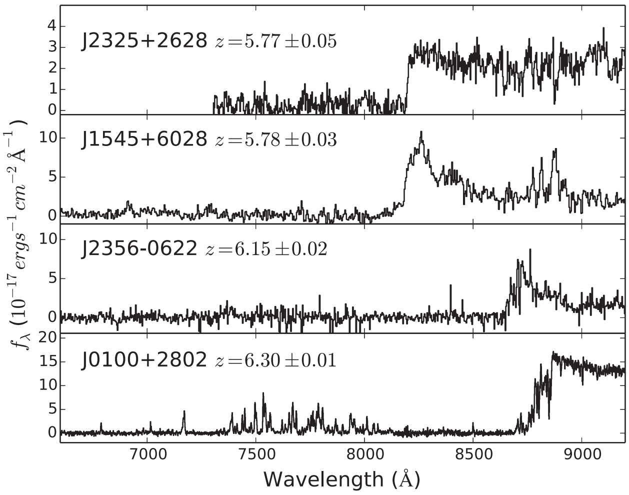

Figure 10. Optical spectra of four $z \gtrsim 5.7$ quasars discovered by using the method described in Section 6. J0100+2802 is the most luminous quasar at $z > 5$ known to date and has been reported in Wu et al. (2015).

star contamination. Figure 9 shows the known $z > 5.0$ quasars (Table 1 and references therein) and M, L, and T dwarfs (Kirkpatrick et al. 2011) on the $z{-}W1/W1{-}W2$ color–color diagram. The cyan cycles denote $5.0 < z < 5.5$ quasars, the blue triangles represent $5.5 < z < 6.5$ quasars, and the orange stars represent $z > 6.5$ quasars. Clearly the optical plus *WISE* photometric selection method can separate quasars from contaminants at redshifts up to $z \lesssim 6.4$, the upper redshift limit of optical surveys. However, the L and T dwarfs begin to overlap with $z \gtrsim 6.5$ quasars in this color–color diagram which is a limit for finding quasars at this redshift range. It could be improved by combining near-infrared photometry (e.g., *Y*-band and *J*-band) as L and T dwarfs have redder $Y - J$ colors than that of $z \gtrsim 6.5$ quasars (Venemans et al. 2013). Actually, Carnall et al. (2015) have used a similar method ($z{-}W2/W1{-}W2$) to search for $z > 5.7$ quasars in the VST ATLAS survey and have identified two new $z > 6$ luminous quasars in the ATLAS survey area.

Motivated by the high detection rate of luminous high-redshift quasars as described in Section 2 (e.g., $M_{1450} \lesssim -26.5$ at $z \lesssim 6$ and $M_{1450} \lesssim -27.0$ at $z \lesssim 7$), we also search for luminous $z \gtrsim 5.7$ quasars by combining the *i*-dropout technique (e.g., Fan et al. 2001b; Willott et al. 2007; Jiang et al. 2008; Bañados et al. 2014) and $z{-}W1/W1{-}W2$ colors mentioned above. This method can be used to reject superposed objects without any photometric followup observations and can reject the majority of contaminants (mainly L and T dwarfs). We selected about 20 *i*-dropouts with $z_{AB} < 19.8$ in the SDSS area. Before doing spectroscopy we visually compared the spectra energy distribution (SED) of these candidates with type 1 quasar composite SED (Richards et al. 2006) to rank the priority.

We have observed four candidates with the highest priority and have identified four $z \gtrsim 5.7$ quasars: J010013.02+280225.8 at $z = 6.30 \pm 0.01$ (Wu et al. 2015), J235632.44–062259.2 at $z = 6.15 \pm 0.02$, J154552.08+602824.0 at $z = 5.78 \pm 0.03$, and J232514.24+262847.6 at $z = 5.77 \pm 0.05$. Table 4 lists the photometric and redshift information for these four quasars and Figure 10 shows their optical spectra. The spectrum of J0100+2802 was obtained with LBT/MODS spectrograph (Pogge et al. 2010) and the redshift determined from Mg II emission line in the near-IR spectrum (Wu et al. 2015). J0100+2802 is the most luminous $z > 6$ quasar ever known and hosts a 12 billion solar black hole in its center (Wu et al. 2015). We observed J1545+6028 with the G5 grating on the LJT 2.4 m telescope with a 3600-s exposure on 2014 April 5. This quasar was not targeted by SDSS main $z \sim 6$ quasar survey as its $i - z = 2.18$ does not satisfy their $i - z$ cut (Fan et al. 2001a). The spectrum of J2325+2628 was obtained with MMT Red Channel on 2015 May 9. We used the 27 gpm grating centered at 8500 Å and a 1."0 slit. The MMT spectrum shows that J2325+2628 is a weak-line emission quasar (WLQ) and with the current S/N there are no clear emission lines. The redshift of J2325+2628 was estimated by fitting the continuum to the composite spectra (Vanden Berk et al. 2001). Although this quasar has SDSS photometry data and satisfy SDSS $z \gtrsim 5.7$ selection criteria, it does not fall in the SDSS $z \gtrsim 5.7$ quasar survey region. We observed J2356–0622 with ANU WiFeS with a 30-minute exposure on 2015 May 15. However, the target was only marginally detected due to the cloudy weather and it was hard to confirm that it is a high-redshift quasar. A further one-hour exposure was obtained with WiFeS on 20 July, which confirmed J2356–0622 as a quasar at $z = 6.15$. J2356–0622 is the faintest $z > 5.7$ quasar in our sample with $M_{1450} = -26.85$. This quasar has a bad SDSS photometry flag (maybe a cosmic ray) and was not selected by SDSS. The redshifts of J1545+6028 and J2356–0622 were determined by using ASERA to visually fit the Lyα, N V emission lines, and the position of Lyα drop.

Although we have identified four $z \sim 6$ quasars with our method, we still cannot give an accurate success rate for finding $z \gtrsim 5.7$ quasars as we only observed very few candidates with highest priority. We are still working on the spectroscopy observations and will also extend our method to the ongoing DECam legacy survey (DECaLS) and the unblurred coadds of the *WISE* Imaging (unWISE; Lang 2014) to find fainter $z \gtrsim 5.7$ quasars.

7. SUMMARY

The SDSS spectroscopic surveys have discovered the majority of quasars known to date. However, they have a lower degree of completeness at high redshift (e.g., $z \gtrsim 4.5$). Even with additional efforts aimed at finding high-redshift quasars by using SDSS and other photometric data (e.g., Fan et al. 1999, 2000b; Willott et al. 2007; Jiang et al. 2008; Mortlock et al. 2011; McGreer et al. 2013; Venemans et al. 2013), there is an obvious gap for quasars at $5.2 < z < 5.7$. Up to now about 300,000 quasars have been spectroscopically identified, but only ~700 quasars at $z \geqslant 4.5$, ~ 30 quasars at $5.2 < z < 5.7$ and ~90 quasars at $z \geqslant 5.7$.

ALLWISE has a high detection rate of known high-redshift quasars, especially in the two bluest *WISE* bands. The $W1{-}W2$ color can be used to reject late-type stars efficiently. We have developed a new method by combining optical and *WISE* colors that yields a much higher selection efficiency for finding luminous high-redshift quasars than by using only optical colors. We have assembled a sample of $z \sim 5.0$ quasar candidates using SDSS and ALLWISE photometric data and have spectroscopically identified 72 new $z \sim 5.0$ quasars, with 12 quasars at $z \geqslant 5.2$, allowing us to begin filling the gap at $5.2 < z < 5.7$. Our current spectroscopic observations have led to an increase of ~36% of quasars at $5.2 < z < 5.7$. However, this gap is still far from being filled as our method only focus on quasars at $z \lesssim 5.4$. A lot of work still needs to be done to find more quasars at this redshift range. Our new quasar sample is about 0.8 mag brighter than SDSS $z \sim 5$ quasars and is expected to set strong constraints on the bright end of the $z \sim 5$ QLF (J. Yang et al. 2016, in preparation; Paper II), the massive end of the BHMF with future near-IR spectroscopy (Paper III), and the high-redshift IGM through future high-resolution quasar absorption spectra. Moreover, our method can also be used to find quasars with redshifts up to $z \lesssim 6.4$ and we have identified four quasars with redshifts beyond 5.7.

F. W. and X-B. W. thank the support from the NSFC grants No.11373008 and 11533001, the Strategic Priority Research Program "The Emergence of Cosmological Structures" of the Chinese Academy of Sciences, grant No. XDB09000000, and the National Key Basic Research Program of China 2014CB845700. F. W. thanks the financial support from the program of China Scholarships Council No. 201406010031 during his visit to the University of Arizona. X. F. and I. D. M. thank the support from the US NSF grant AST 11-07682. This research uses data obtained through the Telescope Access Program (TAP), which has been funded by the Strategic Priority Research Program "The Emergence of Cosmological Structures" (grant No. XDB09000000), National Astronomical Observatories, Chinese Academy of Sciences, and the Special Fund for Astronomy from the Ministry of Finance. We acknowledge the support of the staff of the Lijiang 2.4 m telescope. Funding for the telescope has been provided by CAS and the People's Government of Yunnan Province. We acknowledge the use of the MMT Observatory, a joint facility of the Smithsonian Institution and the University of Arizona. We acknowledge the use of the Bok telescope and ANU 2.3 m telescope. We acknowledge the use of Xinglong 2.16 m telescope. This work was partially supported by the Open Project Program of the Key Laboratory of Optical Astronomy, National Astronomical Observatories, Chinese Academy of Sciences.

We acknowledge the use of SDSS photometric data. Funding for SDSS-III has been provided by the Alfred P. Sloan Foundation, the Participating Institutions of the SDSS, the National Science Foundation, and the U.S. Department of Energy Office of Science. The SDSS-III Web site is http://www.sdss3.org/. SDSS-III is managed by the Astrophysical Research Consortium for the Participating Institutions of the SDSS-III Collaboration including the University of Arizona, the Brazilian Participation Group, Brookhaven National Laboratory, the University of Cambridge, Carnegie Mellon University, the University of Florida, the French Participation Group, the German Participation Group, Harvard University, the Instituto de Astrofisica de Canarias, the Michigan State/Notre Dame/JINA Participation Group, Johns Hopkins University, the Lawrence Berkeley National Laboratory, the Max Planck Institute for Astrophysics, the Max Planck Institute for Extraterrestrial Physics, New Mexico State University, New York University, Ohio State University, the Pennsylvania State University, the University of Portsmouth, Princeton University, the Spanish Participation Group, the University of Tokyo, the University of Utah, Vanderbilt University, the University of Virginia, the University of Washington, and Yale University. This publication makes use of data products from the *Wide-field Infrared Survey Explorer*, which is a joint project of the University of California, Los Angeles, and the Jet Propulsion Laboratory/California Institute of Technology as well as NEOWISE, which is a project of the Jet Propulsion Laboratory/California Institute of Technology. *WISE* and NEOWISE are funded by the National Aeronautics and Space Administration.

Facilities: Sloan (SDSS), *WISE*, 2.4 m/YNAO (YFOSC), MMT (Red Channel spectrograph), 2.16 m/NAOC (BFOSC), 2.3 m/ANU (WiFeS).

REFERENCES

Ai, Y., Wu, X.-B., Yang, J., et al. 2016, AJ, 151, 24
Anderson, S. F., Fan, X., Richards, G. T., et al. 2001, AJ, 122, 503
Arnaboldi, M., Neeser, M. J., Parker, L. C., et al. 2007, Msngr, 127, 28
Bañados, E., Venemans, B. P., Morganson, E., et al. 2014, AJ, 148, 14
Bañados, E., Venemans, B. P., Morganson, E., et al. 2015, ApJ, 804, 118
Becker, R. H., White, R. L., & Helfand, D. J. 1995, ApJ, 450, 559
Blain, A. W., Assef, R., Stern, D., et al. 2013, ApJ, 778, 113
Bovy, J., Hennawi, J. F., Hogg, D. W., et al. 2011, ApJ, 729, 141
Carnall, A. C., Shanks, T., Chehade, B., et al. 2015, MNRAS, 451, L16
Childress, M. J., Vogt, F. P. A., Nielsen, J., & Sharp, R. G. 2014, Ap&SS, 349, 617
Chiu, K., Zheng, W., Schneider, D. P., et al. 2005, AJ, 130, 13
Cool, R. J., Kochanek, C. S., Eisenstein, D. J., et al. 2006, AJ, 132, 823
Croom, S. M., Smith, R. J., Boyle, B. J., et al. 2001, MNRAS, 322, L29
Croom, S. M., Smith, R. J., Boyle, B. J., et al. 2004, MNRAS, 349, 1397
Dawson, K. S., Schlegel, D. J., Ahn, C. P., et al. 2013, AJ, 145, 10
DiPompeo, M. A., Bovy, J., Myers, A. D., & Lang, D. 2015, MNRAS, 452, 3124
Dopita, M., Hart, J., McGregor, P., et al. 2007, Ap&SS, 310, 255
Dopita, M., Rhee, J., Farage, C., et al. 2010, Ap&SS, 327, 245
Eisenstein, D. J., Weinberg, D. H., Agol, E., et al. 2011, AJ, 142, 72
Fan, X., Carilli, C. L., & Keating, B. 2006a, ARA&A, 44, 415
Fan, X., Hennawi, J. F., Richards, G. T., et al. 2004, AJ, 128, 515
Fan, X., Narayanan, V. K., Lupton, R. H., et al. 2001a, AJ, 122, 2833
Fan, X., Strauss, M. A., Richards, G. T., et al. 2001b, AJ, 121, 31
Fan, X., Strauss, M. A., Richards, G. T., et al. 2006b, AJ, 131, 1203
Fan, X., Strauss, M. A., Schneider, D. P., et al. 1999, AJ, 118, 1
Fan, X., Strauss, M. A., Schneider, D. P., et al. 2000a, AJ, 119, 1
Fan, X., Strauss, M. A., Schneider, D. P., et al. 2003, AJ, 125, 1649
Fan, X., White, R. L., Davis, M., et al. 2000b, AJ, 120, 1167
Glikman, E., Helfand, D. J., & White, R. L. 2006, ApJ, 640, 579
Jiang, L., Fan, X., Annis, J., et al. 2008, AJ, 135, 1057
Jiang, L., Fan, X., Bian, F., et al. 2009, AJ, 138, 305
Jiang, L., McGreer, I. D., Fan, X., et al. 2015, AJ, 149, 188
Kaiser, N., Aussel, H., Burke, B. E., et al. 2002, Proc. SPIE, 4836, 154
Kaiser, N., Burgett, W., Chambers, K., et al. 2010, Proc. SPIE, 7733, 77330E
Kellermann, K. I., Sramek, R., Schmidt, M., Shaffer, D. B., & Green, R. 1989, AJ, 98, 1195
Kirkpatrick, J. D., Cushing, M. C., Gelino, C. R., et al. 2011, ApJS, 197, 19
Kochanek, C. S., Eisenstein, D. J., Cool, R. J., et al. 2012, ApJS, 200, 8
Lang, D. 2014, AJ, 147, 108
Lawrence, A., Warren, S. J., Almaini, O., et al. 2007, MNRAS, 379, 1599
Leipski, C., Meisenheimer, K., Walter, F., et al. 2014, ApJ, 785, 154
Lupton, R. H., Gunn, J. E., & Szalay, A. S. 1999, AJ, 118, 1406
Mainzer, A., Bauer, J., Grav, T., et al. 2011, ApJ, 731, 53
McGreer, I. D., Jiang, L., Fan, X., et al. 2013, ApJ, 768, 105
Morganson, E., De Rosa, G., Decarli, R., et al. 2012, AJ, 143, 142
Mortlock, D. J., Warren, S. J., Venemans, B. P., et al. 2011, Natur, 474, 616
Pâris, I., Petitjean, P., Aubourg, É., et al. 2012, A&A, 548, A66
Pâris, I., Petitjean, P., Aubourg, É., et al. 2014, A&A, 563, A54
Pogge, R. W., Atwood, B., Brewer, D. F., et al. 2010, Proc. SPIE, 7735, 77350A
Richards, G. T., Fan, X., Newberg, H. J., et al. 2002, AJ, 123, 2945
Richards, G. T., Lacy, M., Storrie-Lombardi, L. J., et al. 2006, ApJS, 166, 470
Schmidt, G. D., Weymann, R. J., & Foltz, C. B. 1989, PASP, 101, 713
Schneider, D. P., Fan, X., Strauss, M. A., et al. 2001, AJ, 121, 1232
Schneider, D. P., Richards, G. T., Hall, P. B., et al. 2010, AJ, 139, 2360
Shanks, T., Metcalfe, N., Chehade, B., et al. 2015, MNRAS, 451, 4238
Shen, Y., Richards, G. T., Strauss, M. A., et al. 2011, ApJS, 194, 45
Stern, D., Spinrad, H., Eisenhardt, P., et al. 2000, ApJL, 533, L75
Vanden Berk, D. E., Richards, G. T., Bauer, A., et al. 2001, AJ, 122, 549
Venemans, B. P., Bañados, E., Decarli, R., et al. 2015, ApJL, 801, L11

Venemans, B. P., Findlay, J. R., Sutherland, W. J., et al. 2013, ApJ, 779, 24
Wang, F., Wu, X.-B., Fan, X., et al. 2015, ApJL, 807, L9
Willott, C. J., Albert, L., Arzoumanian, D., et al. 2010a, AJ, 140, 546
Willott, C. J., Delorme, P., Omont, A., et al. 2007, AJ, 134, 2435
Willott, C. J., Delorme, P., Reylé, C., et al. 2009, AJ, 137, 3541
Willott, C. J., Delorme, P., Reylé, C., et al. 2010b, AJ, 139, 906
Wright, E. L., Eisenhardt, P. R. M., Mainzer, A. K., et al. 2010, AJ, 140, 1868
Wu, X.-B., Hao, G., Jia, Z., Zhang, Y., & Peng, N. 2012, AJ, 144, 49
Wu, X.-B., Wang, F., Fan, X., et al. 2015, Natur, 518, 512
Yi, W.-M., Wang, F., Wu, X.-B., et al. 2014, ApJL, 795, L29
York, D. G., Adelman, J., Anderson, J. E., Jr., et al. 2000, AJ, 120, 1579
Yuan, H., Zhang, H., Zhang, Y., et al. 2013, A&C, 3, 65
Zheng, W., Tsvetanov, Z. I., Schneider, D. P., et al. 2000, AJ, 120, 1607

THE ASTROPHYSICAL JOURNAL, 829:33 (13pp), 2016 September 20
doi:10.3847/0004-637X/829/1/33

A SURVEY OF LUMINOUS HIGH-REDSHIFT QUASARS WITH SDSS AND *WISE*. II. THE BRIGHT END OF THE QUASAR LUMINOSITY FUNCTION AT $z \sim 5$

JINYI YANG[1,2], FEIGE WANG[1,2], XUE-BING WU[1,3], XIAOHUI FAN[2,3], IAN D. MCGREER[2],
FUYAN BIAN[4,9], WEIMIN YI[5,6], QIAN YANG[1,2], YANLI AI[7], XIAOYI DONG[1], WENWEN ZUO[8],
RICHARD GREEN[2], LINHUA JIANG[3], SHU WANG[1], RAN WANG[3], AND MINGHAO YUE[1]
[1] Department of Astronomy, School of Physics, Peking University, Beijing 100871, China
[2] Steward Observatory, University of Arizona, 933 North Cherry Avenue, Tucson, AZ 85721, USA
[3] Kavli Institute for Astronomy and Astrophysics, Peking University, Beijing 100871, China
[4] Research School of Astronomy and Astrophysics, Australian National University, Weston Creek, ACT 2611, Australia
[5] Yunnan Observatories, Chinese Academy of Sciences, Kunming 650011, China
[6] Key Laboratory for the Structure and Evolution of Celestial Objects, Chinese Academy of Sciences, Kunming 650011, China
[7] School of Astronomy and Space Science, Sun Yat-Sen University, Guangzhou 510275, China
[8] Shanghai Astronomical Observatory, Chinese Academy of Sciences, Shanghai 200030, China

Received 2016 February 14; revised 2016 June 25; accepted 2016 July 14; published 2016 September 20

ABSTRACT

This is the second paper in a series on a new luminous $z \sim 5$ quasar survey using optical and near-infrared colors. Here we present a new determination of the bright end of the quasar luminosity function (QLF) at $z \sim 5$. Combining our 45 new quasars with previously known quasars that satisfy our selections, we construct the largest uniform luminous $z \sim 5$ quasar sample to date, with 99 quasars in the range of $4.7 \leqslant z < 5.4$ and $-29 < M_{1450} \leqslant -26.8$, within the Sloan Digital Sky Survey (SDSS) footprint. We use a modified $1/V_{\rm a}$ method including flux limit correction to derive a binned QLF, and we model the parametric QLF using maximum likelihood estimation. With the faint-end slope of the QLF fixed as $\alpha = -2.03$ from previous deeper samples, the best fit of our QLF gives a flatter bright end slope $\beta = -3.58 \pm 0.24$ and a fainter break magnitude $M^*_{1450} = -26.98 \pm 0.23$ than previous studies at similar redshift. Combined with previous work at lower and higher redshifts, our result is consistent with a luminosity evolution and density evolution model. Using the best-fit QLF, the contribution of quasars to the ionizing background at $z \sim 5$ is found to be 18%–45% with a clumping factor C of 2–5. Our sample suggests an evolution of radio loud fraction with optical luminosity but no obvious evolution with redshift.

Key words: galaxies: active – galaxies: high-redshift – quasars: general

1. INTRODUCTION

Quasars comprise the most luminous class of non-transient objects in the universe. Characterizing their population and evolution is the critical tool to directly constrain the formation and evolution of supermassive black holes (SMBHs) across cosmic time. The fundamental way to characterize these objects is through the evolution of their number densities with luminosity and redshift, namely the quasar luminosity function (QLF). The QLF and its cosmological evolution have been a key focus of quasar studies for half a century. Schmidt (1968) first determined the evolution of the quasar population and found the first evidence for a significant increase of the quasar number density with redshift in both radio and optical bands. More recently, based on measurements of the QLF from several successful surveys, such as the 2dF Quasar Redshift Survey (Boyle et al. 2000; Croom et al. 2004), COMBO-17 (Wolf et al. 2003), the 2dF-SDSS LRG and QSO survey (2SLAQ; Richards et al. 2005), the SDSS Faint Quasar Survey (Jiang et al. 2006), the VIMOS-VLT Deep Survey (VVDS; Bongiorno et al. 2007), SDSS and 2SLAQ (Croom et al. 2009), and BOSS DR9 (Ross et al. 2013), the QLF, especially in optical bands, has been well characterized at low to intermediate redshifts. The QLF can be parameterized with a double power-law shape and pure luminosity evolution for quasars at redshifts up to $z = 2$ (Boyle et al. 2000; Croom et al. 2004). The bright end slope at low redshift, the effect of "cosmic downsizing," and the density peak of quasars at $2 < z < 3$ (Brown et al. 2006; Jiang et al. 2006; Richards et al. 2006; Croom et al. 2009) have been confirmed by many subsequent investigations. The measurements based on large samples from BOSS yield a QLF evolution best fit by a luminosity evolution and density evolution (LEDE) model at $2 < z < 3.5$ (Ross et al. 2013). In their work, the bright end slope does not evolve with redshift and is different from the result of Richards et al. (2006), which suggested a flatter bright end slope at high redshift than that at low redshift. To better determine the evolution of QLF parameters, a wider redshift range is needed.

Toward higher redshift, quasars are important tracers of the structure and evolution of the early universe, the evolution of the intergalactic medium (IGM), the growth of SMBHs and co-evolution of SMBHs and host galaxies at early epochs. Observations of the Gunn–Peterson effect using absorption spectra of quasars at $z \gtrsim 5.7$ have established $z \sim 6$ as the end of cosmic reionization, when the IGM is rapidly transforming from largely neutral to completely ionized (Fan et al. 2006). Becker et al. (2015) find evidence for UV background fluctuations at $z \sim 5.7$ in excess of predictions from a single mean-free-path model, which indicates that reionization is not fully complete at that redshift. McGreer et al. (2015) suggest that reionization is just completing at $z \sim 6$, possibly with a tail to $z \sim 5.5$. Therefore, in the post-reionization epoch, the QLF at $z \gtrsim 5$ is needed to estimate the contribution of quasars to the ionizing background during and after the reionization epoch.

---

[9] Stromlo Fellow.

Although quasars are not likely to be the dominant source of ionizing photons (Fan et al. 2001a; Willott et al. 2010; McGreer et al. 2013), their exact contribution is still highly uncertain. In addition, $z \sim 5$ quasar absorption spectra can be used to constrain the physical conditions of the IGM in this key redshift range, and provide the basic boundary conditions for models of reionization, such as the evolution of IGM temperature, photon mean-free path, metallicity and the impact of helium reionization (Bolton et al. 2012).

However, high-redshift quasars are very rare, especially at $z > 5$. Although more than 300,000 quasars are known, only ~200 of them are at $z > 5$. Therefore, QLF measurements at high redshift still have large uncertainties. From the combination of SDSS DR7 quasars and the Stripe 82 (S82) faint quasar sample, McGreer et al. (2013) provided the most complete measurement of the $z \sim 5$ QLF so far, especially at the faint end. A factor of two greater decrease in the number density of luminous quasars from $z = 5$ to 6 than that from $z = 4$ to 5 was claimed (McGreer et al. 2013, hereafter M13). However, their work focused on the faint end; there are only eight quasars with $M_{1450} < -27.3$ in the sample.

A survey described in this series of papers is aimed at finding more luminous quasars at $4.7 < z < 5.5$, which allows a better determination of the bright end QLF and a better constraint on the quasar evolution model at high redshift. Wang et al. (2016, hereafter Paper I) presented a new selection using SDSS and the *Wide-field Infrared Survey Explorer* (*WISE*) optical/NIR colors. In this follow-up paper, we report our measurement of the bright end $z \sim 5$ QLF using the quasar sample selected by the method presented in Paper I. The outline of our paper is as follows. In Section 2, we briefly review the quasar candidate selection and the spectroscopic observations of these candidates. The survey completeness will be presented in Section 3. In this section, we use a quasar color model (M13) to quantify our selection completeness and to correct the incompleteness due to the ALLWISE detection flux limit and spectral coverage. We then calculate the binned luminosity function and fit our data using a maximum likelihood estimator in Section 4. We also study the evolution of the QLF and compare our results with previous work in this section. In Section 5, we discuss the contribution of $z \sim 5$ quasars to the ionizing background and the radio loud fraction of our quasar sample. We summarize our main results in Section 6. In this paper, we adopt a ΛCDM cosmology with parameters $\Omega_\Lambda = 0.728$, $\Omega_m = 0.272$, $\Omega_b = 0.0456$, and $H_0 = 70$ km s^{-1} Mpc^{-1} (Komatsu et al. 2009) for direct comparison with the result in M13. Photometric data from the SDSS are in the SDSS photometric system (Lupton et al. 1999), which is almost identical to the AB system at bright magnitudes; photometric data from ALLWISE are in the Vega system. All SDSS data shown in this paper are corrected for Galactic extinction.

2. A LARGE SAMPLE OF LUMINOUS QUASARS AT $z \sim 5$

2.1. Quasar Selection and Spectroscopic Observations

Our SDSS+*WISE* selection technique and spectroscopic follow-up observations were discussed in detail in Paper I. Here we briefly review the basic steps. At $z \sim 5$, most quasars are undetectable in the u band and g band because of the presence of strong Lyman limit systems, which are optically thick to the UV continuum radiation from quasars (Fan et al. 1999). The Lyα absorption systems also begin to dominate in the r band and Lyα emission moves to the i band. Therefore, the $r - i/i - z$ color–color diagram was often used to select $z \sim 5$ quasar candidates in previous studies (Fan et al. 1999; Richards et al. 2002; M13). However, with increasing redshift, the $i - z$ color also becomes increasingly red and most $z > 5.1$ quasars enter the M star locus in the $r - i/i - z$ color–color diagram, which makes it difficult to find $z > 5.1$ quasars with only the optical colors. Therefore, we added near-infrared colors from *WISE* photometry data in our selection. We used typical u, g drop-out methods but more relaxed $r - i/i - z$ cuts to select candidates from the SDSS DR10 database. Then we cross-matched our candidates with the ALLWISE database using a 2″ match radius and used z-$W1/W1$-$W2$ cuts to remove more star contaminations by the following criteria. The exact selection criteria are given in Paper I.

$$z - W1 > 2.5 \tag{1}$$

$$W1 - W2 > 0.5 \tag{2}$$

$$W1 < 17.0,\ \sigma_{W2} < 0.2 \tag{3}$$

$$z - W1 > 2.8 \text{ or } W1 - W2 > 0.7, \text{ if } i - z > 0.4. \tag{4}$$

We constructed our main luminous quasar candidate sample by limiting the SDSS z-band magnitudes to brighter than 19.5, and selected a total of 420 luminous $z \sim 5$ quasar candidates. We removed 78 known quasars, one known dwarf and 231 candidates with suspicious detections, such as multiple peaked objects or being affected by bright star artifacts. We visually inspected images of each candidate and removed those 231 candidates. We selected 110 candidates with high image quality as our main candidate sample. Our spectroscopic follow-up campaign started in 2013 October. We observed 99 candidates from our main sample with the Lijiang 2.4 m telescope (LJT) and Xinglong 2.16 m telescope in China, the Kitt Peak 2.3 m Bok telescope and 6.5 m MMT telescope in the U.S., as well as the 2.3 m ANU telescope in Australia. 64 (64.6%) candidates have been identified as high-redshift quasars in the redshift range $4.4 \lesssim z \lesssim 5.5$. As discussed in Paper I, due to the serious contamination from M-type stars, there is a gap in the previously published quasar redshift distribution at $5.2 < z < 5.7$ with only 33 published quasars in this redshift range. Among our 64 newly identified quasars from main candidates sample, 9 quasars are at $5.2 < z < 5.7$, which represents an increase of 27% in the number of known quasars in this redshift range. The details of spectroscopic observation and data reduction are also given in Paper I.

2.2. Quasar Sample

The redshifts of newly identified quasars are measured from Lyα, N V, O I/Si II, C II, Si IV, and C IV emission lines (any available) by an eye-recognition assistant for quasar spectra software (ASERA; Yuan et al. 2013). The typical redshift error is about 0.05 for Lyα-based redshift measurement and will be less for that based on more emission lines. We calculate M_{1450} in the AB system by fitting a power-law continuum $f_\nu \sim \nu^{\alpha_\nu}$ to the spectrum for each quasar. We assume an average quasar UV continuum slope of $\alpha_\nu = -0.5$ (Vanden Berk et al. 2001; see details in Paper I). Our 64 new quasars from the luminous quasar candidate sample are within the absolute magnitude range $-29 < M_{1450} < -26.4$. We calculate M_{1450} for previous known quasars using the same method. The known quasars are from the SDSS DR7 and DR12 quasar catalogs (Schneider

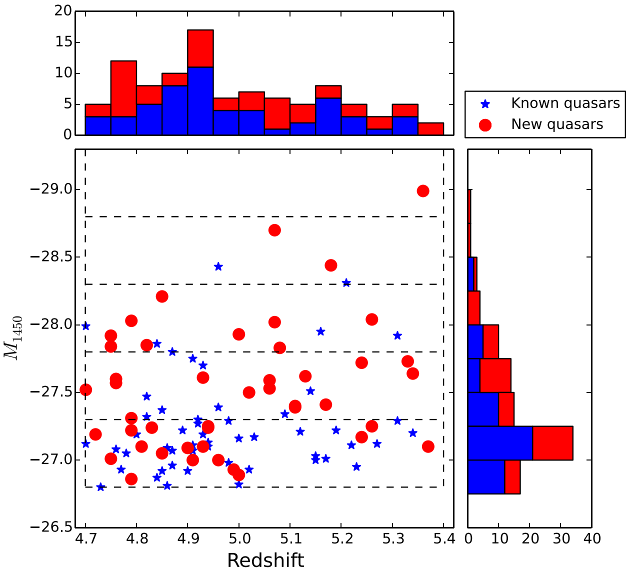

Figure 1. Redshift and M_{1450} distributions of both our newly identified luminous quasars (red dots) and known quasars (blue stars) at $4.7 \lesssim z \lesssim 5.4$ and $-29.3 \lesssim M_{1450} \lesssim -26.8$. The known quasars are from the SDSS DR7 and DR12 quasar catalogs (Schneider et al. 2010; Pâris et al. 2016; McGreer et al. 2009; Schneider et al. 1991). This is the sample used for QLF measurement. The dashed lines represent the redshift and magnitude bins for determining the binned QLF. We use only one redshift bin.

et al. 2010; Pâris et al. 2016; McGreer et al. 2013; Schneider et al. 1991). When we removed the known quasars from our quasar candidate sample, we missed two known quasars. These two quasars from McGreer et al. (2009) and Schneider et al. (1991) were also spectroscopically observed by us, and thus we use our new spectra to do the M_{1450} calculation.

For the QLF determination, we define our sample of $z \sim 5$ luminous quasars as follows.

1. Quasars in the redshift range $4.7 \leqslant z < 5.4$. Our selection criteria yield low completeness at redshifts lower than 4.7 or higher than 5.4. The former is caused by the drop of $W1 - W2$ color (See Figure 3 in Paper I), and the latter is caused by our $r - i/i - z$ limit. Therefore, we restrict our sample to the range of $4.7 \leqslant z < 5.4$ (see details in Section 3.2).
2. Quasars in the luminosity range of $M_{1450} \leqslant -26.8$. Our selection criteria yield a low completeness in the region with $z > 5$ and $-26.8 < M_{1450} < -26.4$. The mean completeness in this region is ~4%. That is caused by our SDSS magnitude limit of $z < 19.5$. Therefore, we limit our sample to $M_{1450} \leqslant -26.8$.
3. Our selection covers the whole SDSS footprint without masked regions, which is a 14,555 square degree field.

Based on the criteria above, there are 45 newly identified quasars in the sample of Paper I and another 54 previously known quasars that satisfy our selection criteria. This is the final complete $z \sim 5$ luminous quasar sample that we will use to determine the $z \sim 5$ QLF. Figure 1 shows the redshift and M_{1450} distributions of both our newly identified luminous quasars and known quasars. Three of our new quasars are more luminous than any previously known quasars at $z > 5$. It is obvious that our discovery significantly expands the $z \sim 5$ luminous quasar sample. Table 1 lists all 99 quasars in our sample used for the QLF determination.

3. SURVEY COMPLETENESS

In this section, we will discuss the incompleteness corrections. We limit our candidates to be brighter than 19.5 mag in the SDSS z band, the ALLWISE detection is not deep enough for all quasars in this magnitude range and its depth highly depends on sky position. Therefore, we first model the ALLWISE incompleteness caused by survey depth. We then correct for the incompleteness of our SDSS-ALLWISE color–color selection. Besides, there are 11 candidates that have not been observed, which leads to an incompleteness. For photometric completeness, we visually inspected images of each candidate. To see how many quasars will be missed in this step, we randomly selected 2000 SDSS images of point sources in the same magnitude range as our quasar candidates. We divided them into four groups and visually inspected the images. The fraction of rejected images is 2%–4% in each group. It is difficult to obtain a more accurate value of this incompleteness and this effect is much smaller than the error of QLF, thus image selection is not included in our incompleteness correction.

3.1. Model ALLWISE Incompleteness

The magnitude limit of our main sample is SDSS $z = 19.5$, which is much brighter than the flux limit (5σ) of the SDSS survey. Therefore, within our magnitude limit, the SDSS detections can be considered as complete. Our survey adds ALLWISE $W1$ and $W2$ photometric data into the selection, and thus we need to consider the detection incompleteness caused by the shallower ALLWISE detection limit. We correct this by using the ALLWISE detection completeness from the Explanatory Supplement to the AllWISE Data Release Products[10], which is a function of frame coverage and flux in $W1$ and $W2$ bands respectively. Figure 2 represents the empirical models of 2D detection completeness in $W1$ and $W2$ bands. As shown, our sample limited with $W1 < 17$ and $\sigma_{W2} < 0.2$ will be effected slightly by the detection incompleteness at the faint end.

The ALLWISE coverage depends on the sky position. To take the position-dependence into account on completeness correction, we mapped the ALLWISE spatial surveying depth within the SDSS footprint. We first randomly generated ~1,220,000 positions in the whole SDSS footprint and derived the ALLWISE coverage map in the SDSS footprint by matching($1'$) positions to the nearest ALLWISE sources. A detection with coverage ⩽5 could be contaminated by random pixel variations such as cosmic rays because they are at or below the threshold for ALLWISE statistically viable outlier detection and rejection. So we removed all positions with frame coverage ⩽5. There are only 269 (0.02%) positions with coverage ⩽5. Figure 3 shows the distributions of $W1/W2$ frame coverages in the whole SDSS footprint. The average coverage is 36 in both $W1$ and $W2$ bands. The 10% and 90% tile coverage in $W1/W2$ band are 23/22 and 56/56. We use our ALLWISE coverage map to correct the detection incompleteness (see details in Section 3.2).

---

[10] http://wise2.ipac.caltech.edu/docs/release/allwise/

Table 1

$z \sim 5$ Quasar Sample Used for QLF Measurement

Name	$r_{\rm SDSS}$	$i_{\rm SDSS}$	$z_{\rm SDSS}$	$W1$	$W2$	Redshift	M_{1450}	Notes[a]
J000851.43+361613.49	21.45 ± 0.08	19.50 ± 0.02	19.20 ± 0.05	16.05 ± 0.05	15.37 ± 0.09	5.17	−27.41	Paper I
J001115.24+144601.80	19.48 ± 0.02	18.17 ± 0.02	18.03 ± 0.03	15.29 ± 0.04	14.69 ± 0.06	4.96	−28.43	DR12
J002526.84−014532.51	19.58 ± 0.02	18.03 ± 0.02	17.85 ± 0.02	14.80 ± 0.03	14.16 ± 0.05	5.07	−28.70	Paper I
J005527.19+122840.67	20.23 ± 0.03	18.71 ± 0.02	18.66 ± 0.04	15.45 ± 0.05	14.95 ± 0.09	4.70	−27.52	Paper I
J011614.30+053817.70	21.57 ± 0.09	19.87 ± 0.03	19.22 ± 0.06	16.37 ± 0.07	15.76 ± 0.13	5.33	−27.73	Paper I
J012247.35+121624.06	22.25 ± 0.14	19.37 ± 0.03	19.27 ± 0.06	15.59 ± 0.05	14.91 ± 0.07	4.79	−26.86	Paper I
J013127.34−032100.19	20.15 ± 0.04	18.46 ± 0.02	18.01 ± 0.03	14.58 ± 0.03	13.84 ± 0.04	5.18	−28.44	Paper I
J014741.53−030247.88	20.08 ± 0.03	18.53 ± 0.02	18.21 ± 0.02	14.86 ± 0.03	14.32 ± 0.05	4.75	−27.84	Paper I
J015533.28+041506.74	21.70 ± 0.10	19.97 ± 0.03	19.26 ± 0.06	16.33 ± 0.07	15.19 ± 0.10	5.37	−27.10	Paper I
J015618.99−044139.88	20.77 ± 0.04	19.10 ± 0.02	19.13 ± 0.05	15.36 ± 0.04	14.69 ± 0.06	4.94	−27.24	Paper I
J021624.16+230409.47	21.26 ± 0.06	19.78 ± 0.03	19.32 ± 0.06	16.56 ± 0.08	15.73 ± 0.15	5.26	−27.25	Paper I
J021736.76+470826.48	20.55 ± 0.05	18.96 ± 0.02	18.88 ± 0.05	15.76 ± 0.05	15.14 ± 0.08	4.81	−27.10	Paper I
J022055.59+473319.34	20.07 ± 0.03	18.34 ± 0.01	18.31 ± 0.03	15.19 ± 0.04	14.62 ± 0.06	4.82	−27.85	Paper I
J024601.95+035054.12	21.05 ± 0.05	19.28 ± 0.02	19.36 ± 0.05	16.67 ± 0.07	15.74 ± 0.14	4.96	−27.00	Paper I
J025121.33+033317.42	20.80 ± 0.04	19.04 ± 0.03	19.06 ± 0.05	15.64 ± 0.04	14.93 ± 0.07	5.00	−26.89	Paper I
J030642.51+185315.85	19.89 ± 0.03	17.96 ± 0.01	17.47 ± 0.02	14.31 ± 0.03	13.46 ± 0.04	5.36	−28.99	Paper I
J032407.69+042613.29	20.39 ± 0.04	19.03 ± 0.02	19.15 ± 0.06	15.72 ± 0.05	15.13 ± 0.09	4.72	−27.19	Paper I
J045427.96−050049.38	19.91 ± 0.03	18.59 ± 0.03	18.39 ± 0.03	15.09 ± 0.03	14.53 ± 0.05	4.93	−27.61	Paper I
J065330.25+152604.71	21.27 ± 0.06	19.48 ± 0.02	19.39 ± 0.07	16.65 ± 0.11	15.79 ± 0.16	4.90	−27.09	Paper I
J073103.13+445949.43	20.66 ± 0.04	19.06 ± 0.02	19.07 ± 0.05	15.82 ± 0.05	15.30 ± 0.09	4.98	−27.29	DR12
J073231.28+325618.33	20.26 ± 0.03	18.82 ± 0.01	18.62 ± 0.03	15.46 ± 0.04	14.92 ± 0.08	4.76	−27.60	Paper I
J074154.72+252029.65[b]	20.49 ± 0.03	18.45 ± 0.02	18.36 ± 0.02	14.78 ± 0.03	13.81 ± 0.04	5.21	−28.31	McGreer2009
J074749.18+115352.46	20.44 ± 0.03	18.67 ± 0.02	18.27 ± 0.03	14.64 ± 0.03	13.79 ± 0.04	5.26	−28.04	Paper I
J075907.58+180054.71	20.95 ± 0.04	19.12 ± 0.02	19.11 ± 0.04	16.07 ± 0.07	15.39 ± 0.11	4.78	−27.05	DR12
J080306.19+403958.96	20.58 ± 0.04	18.88 ± 0.02	18.60 ± 0.03	15.28 ± 0.04	14.76 ± 0.06	4.79	−27.22	Paper I
J081333.33+350810.78	20.49 ± 0.03	18.97 ± 0.02	18.94 ± 0.04	15.79 ± 0.05	15.06 ± 0.08	4.92	−27.27	DR12
J082454.02+130216.98	21.36 ± 0.06	19.90 ± 0.03	19.43 ± 0.07	16.43 ± 0.08	15.86 ± 0.18	5.15	−27.03	DR12
J083832.31−044017.47	21.20 ± 0.06	19.62 ± 0.03	19.21 ± 0.07	15.58 ± 0.04	15.06 ± 0.08	4.75	−27.01	Paper I
J084631.53+241108.37	20.76 ± 0.03	19.15 ± 0.02	19.27 ± 0.04	15.66 ± 0.05	15.14 ± 0.12	4.73	−26.80	DR12
J085430.37+205650.84	21.99 ± 0.10	19.37 ± 0.03	19.38 ± 0.06	16.21 ± 0.07	15.17 ± 0.10	5.17	−27.01	DR12
J091543.64+492416.65	20.93 ± 0.05	19.57 ± 0.02	19.40 ± 0.06	16.41 ± 0.07	15.54 ± 0.10	5.19	−27.22	DR12
J094108.36+594725.76	20.56 ± 0.04	19.27 ± 0.02	19.28 ± 0.06	16.44 ± 0.06	15.88 ± 0.13	4.86	−26.81	DR12
J095707.68+061059.55	20.60 ± 0.03	19.21 ± 0.02	18.87 ± 0.04	16.18 ± 0.07	15.54 ± 0.13	5.14	−27.51	DR12
J100416.13+434739.12	20.95 ± 0.05	19.38 ± 0.02	19.31 ± 0.06	16.64 ± 0.08	16.11 ± 0.18	4.84	−26.87	DR12
J102622.88+471907.19	20.17 ± 0.03	18.73 ± 0.01	18.62 ± 0.04	15.58 ± 0.04	14.85 ± 0.06	4.93	−27.62	DR12
J104041.10+162233.87	20.50 ± 0.03	18.82 ± 0.07	18.75 ± 0.04	16.14 ± 0.06	15.19 ± 0.12	4.80	−27.19	DR12
J104242.41+310713.20	20.37 ± 0.04	18.98 ± 0.02	18.96 ± 0.05	16.18 ± 0.06	15.59 ± 0.12	4.70	−27.12	DR12
J104325.56+404849.49	20.70 ± 0.04	19.02 ± 0.02	19.09 ± 0.04	15.87 ± 0.05	15.06 ± 0.08	4.91	−27.07	DR12
J105020.41+262002.33	20.74 ± 0.04	19.39 ± 0.02	19.34 ± 0.06	16.38 ± 0.07	15.70 ± 0.14	4.86	−27.09	DR12
J105123.04+354534.31	20.23 ± 0.03	18.42 ± 0.02	18.56 ± 0.04	15.46 ± 0.04	14.84 ± 0.06	4.91	−27.75	DR12
J105322.99+580412.13	21.51 ± 0.05	19.80 ± 0.02	19.49 ± 0.05	16.89 ± 0.09	15.96 ± 0.13	5.27	−27.12	DR12
J112857.85+575909.84	20.89 ± 0.05	19.50 ± 0.03	19.20 ± 0.06	16.64 ± 0.08	15.84 ± 0.14	5.00	−27.16	DR12
J112956.09−014212.44	21.94 ± 0.11	19.58 ± 0.02	19.47 ± 0.07	15.11 ± 0.04	14.44 ± 0.05	4.87	−26.96	DR12
J113246.50+120901.70	21.25 ± 0.08	19.68 ± 0.04	19.21 ± 0.06	16.14 ± 0.07	15.37 ± 0.11	5.17	−27.41	DR7
J114657.79+403708.67	20.95 ± 0.05	19.38 ± 0.03	19.25 ± 0.05	16.03 ± 0.06	15.29 ± 0.09	4.98	−26.98	DR12
J120055.62+181733.01	21.25 ± 0.08	19.62 ± 0.03	19.44 ± 0.08	16.55 ± 0.08	15.77 ± 0.13	5.00	−26.82	DR12
J120441.73−002149.63	20.74 ± 0.04	19.21 ± 0.02	18.93 ± 0.04	15.94 ± 0.06	15.34 ± 0.11	5.09	−27.34	DR12
J120829.27+394339.72	20.79 ± 0.06	19.04 ± 0.02	19.06 ± 0.05	15.80 ± 0.05	15.09 ± 0.08	4.94	−27.25	Paper I
J120952.73+183147.21	21.57 ± 0.11	19.80 ± 0.04	19.44 ± 0.08	16.11 ± 0.06	15.38 ± 0.10	5.15	−27.00	DR12
J124942.12+334953.85[c]	20.48 ± 0.04	19.14 ± 0.02	19.08 ± 0.05	16.23 ± 0.06	15.46 ± 0.09	4.93	−27.19	Schnider1991
J125353.35+104603.19	20.95 ± 0.04	19.37 ± 0.02	19.21 ± 0.05	15.33 ± 0.04	14.75 ± 0.07	4.91	−27.11	DR12
J131234.08+230716.36	20.74 ± 0.04	19.30 ± 0.02	18.97 ± 0.04	15.89 ± 0.05	15.28 ± 0.08	4.89	−27.22	DR12
J131814.03+341805.64	20.59 ± 0.03	19.05 ± 0.02	18.83 ± 0.04	15.20 ± 0.03	14.54 ± 0.05	4.82	−27.32	DR7
J133257.45+220835.91	21.12 ± 0.04	19.26 ± 0.02	19.23 ± 0.04	15.69 ± 0.05	14.89 ± 0.06	5.11	−27.39	Paper I
J134015.03+392630.70	21.19 ± 0.04	19.39 ± 0.02	19.19 ± 0.05	16.09 ± 0.05	15.48 ± 0.08	5.03	−27.17	DR12
J134040.24+281328.16	21.91 ± 0.10	20.02 ± 0.03	19.48 ± 0.08	16.13 ± 0.06	15.03 ± 0.07	5.34	−27.20	DR7
J134154.02+351005.71	21.32 ± 0.05	19.68 ± 0.02	19.45 ± 0.05	16.29 ± 0.06	15.64 ± 0.11	5.23	−26.95	DR12
J134408.62+152125.05	21.01 ± 0.06	19.40 ± 0.02	19.37 ± 0.06	16.20 ± 0.06	15.68 ± 0.13	4.87	−27.07	DR12
J134819.88+181925.82	20.80 ± 0.04	19.15 ± 0.02	19.18 ± 0.05	16.13 ± 0.06	15.57 ± 0.11	4.94	−27.10	DR12
J140404.65+031403.85	20.93 ± 0.06	19.52 ± 0.03	19.26 ± 0.07	16.09 ± 0.05	15.38 ± 0.09	4.90	−26.92	DR12
J141839.99+314244.07	21.54 ± 0.06	19.69 ± 0.03	19.27 ± 0.06	15.78 ± 0.04	15.11 ± 0.07	4.85	−26.92	DR12
J142325.92+130300.71	21.17 ± 0.05	19.67 ± 0.02	19.39 ± 0.08	15.98 ± 0.05	15.46 ± 0.09	5.02	−26.93	DR12
J142526.10+082718.46	20.54 ± 0.03	18.77 ± 0.02	18.92 ± 0.04	15.96 ± 0.04	15.41 ± 0.08	4.94	−27.13	DR12
J142634.33+204336.38	20.66 ± 0.03	19.13 ± 0.02	18.84 ± 0.04	15.59 ± 0.04	14.99 ± 0.06	4.82	−27.47	DR12

Table 1
(Continued)

Name	$r_{\rm SDSS}$	$i_{\rm SDSS}$	$z_{\rm SDSS}$	$W1$	$W2$	Redshift	M_{1450}	Notes[a]
J143605.00+213239.25	21.55 ± 0.07	19.95 ± 0.03	19.28 ± 0.06	16.42 ± 0.06	15.88 ± 0.11	5.22	−27.11	DR12
J143704.82+070807.72	20.62 ± 0.04	19.17 ± 0.02	19.16 ± 0.05	16.14 ± 0.06	15.62 ± 0.12	4.93	−27.10	Paper I
J143751.83+232313.35	21.19 ± 0.06	19.45 ± 0.02	19.16 ± 0.06	15.89 ± 0.04	14.97 ± 0.06	5.31	−27.29	DR12
J144350.67+362315.14	22.35 ± 0.14	20.15 ± 0.03	19.47 ± 0.06	15.90 ± 0.04	14.90 ± 0.05	5.12	−27.21	DR12
J152302.90+591633.05	21.39 ± 0.06	19.54 ± 0.02	19.22 ± 0.05	15.64 ± 0.03	15.13 ± 0.05	5.11	−27.40	Paper I
J153650.26+500810.33	20.18 ± 0.03	18.48 ± 0.02	18.51 ± 0.03	15.13 ± 0.03	14.52 ± 0.04	4.93	−27.70	DR12
J155657.36−172107.56	19.94 ± 0.04	18.43 ± 0.02	18.43 ± 0.05	15.09 ± 0.04	14.59 ± 0.06	4.75	−27.92	Paper I
J160111.17−182835.09	20.98 ± 0.15	19.37 ± 0.05	18.89 ± 0.09	15.65 ± 0.05	15.05 ± 0.08	5.06	−27.53	Paper I
J160734.23+160417.44	20.53 ± 0.03	19.15 ± 0.02	19.09 ± 0.06	16.09 ± 0.06	15.43 ± 0.09	4.76	−27.08	DR12
J161622.11+050127.71	20.16 ± 0.03	18.67 ± 0.02	18.59 ± 0.04	15.90 ± 0.06	15.17 ± 0.09	4.87	−27.80	DR7
J162045.64+520246.65	20.77 ± 0.04	18.97 ± 0.02	18.94 ± 0.04	15.30 ± 0.03	14.70 ± 0.04	4.79	−27.31	Paper I
J162315.28+470559.90	20.87 ± 0.05	19.52 ± 0.03	19.23 ± 0.07	15.57 ± 0.03	14.76 ± 0.05	5.13	−27.62	Paper I
J162623.38+484136.47	20.06 ± 0.02	18.50 ± 0.01	18.40 ± 0.03	15.51 ± 0.04	15.01 ± 0.05	4.84	−27.86	DR12
J162626.50+275132.50	21.47 ± 0.06	19.17 ± 0.02	18.53 ± 0.03	14.97 ± 0.03	14.21 ± 0.04	5.16	−27.95	DR12
J162838.84+063859.15	20.88 ± 0.04	19.56 ± 0.02	19.40 ± 0.05	16.68 ± 0.09	15.93 ± 0.17	4.85	−27.05	Paper I
J163810.39+150058.26	20.53 ± 0.04	18.83 ± 0.02	18.53 ± 0.04	15.10 ± 0.04	14.53 ± 0.05	4.76	−27.57	Paper I
J165354.62+405402.21	20.50 ± 0.03	18.59 ± 0.01	18.86 ± 0.05	15.42 ± 0.03	14.72 ± 0.05	4.96	−27.39	DR12
J165436.85+222733.80	19.74 ± 0.02	18.17 ± 0.01	18.08 ± 0.03	15.14 ± 0.04	14.58 ± 0.05	4.70	−27.99	DR12
J165635.46+454113.55	21.51 ± 0.06	19.70 ± 0.02	19.06 ± 0.04	16.22 ± 0.28	15.53 ± 0.07	5.34	−27.64	Paper I
J165902.12+270935.19	20.95 ± 0.07	19.34 ± 0.03	18.70 ± 0.04	15.92 ± 0.05	15.14 ± 0.07	5.31	−27.92	DR7
J173744.87+582829.66	20.79 ± 0.05	19.27 ± 0.02	19.15 ± 0.06	16.17 ± 0.05	15.56 ± 0.07	4.92	−27.30	DR7
J175114.57+595941.47	20.75 ± 0.04	19.09 ± 0.02	18.78 ± 0.04	15.66 ± 0.03	15.09 ± 0.05	4.83	−27.24	Paper I
J175244.10+503633.05	20.85 ± 0.04	18.82 ± 0.02	18.87 ± 0.05	15.13 ± 0.03	14.40 ± 0.03	5.02	−27.50	Paper I
J211105.62−015604.14	19.78 ± 0.02	18.11 ± 0.02	18.14 ± 0.03	15.02 ± 0.04	14.41 ± 0.05	4.85	−28.21	Paper I
J215216.10+104052.44	19.97 ± 0.03	18.36 ± 0.02	18.22 ± 0.03	14.67 ± 0.03	14.02 ± 0.04	4.79	−28.03	Paper I
J220008.67+001744.93	20.68 ± 0.04	19.09 ± 0.02	19.29 ± 0.06	16.20 ± 0.07	15.48 ± 0.13	4.77	−26.93	DR12
J220106.63+030207.71	20.58 ± 0.03	19.11 ± 0.02	18.90 ± 0.04	15.98 ± 0.06	15.20 ± 0.10	5.06	−27.59	Paper I
J220226.77+150952.38	20.28 ± 0.03	18.69 ± 0.02	18.47 ± 0.03	15.74 ± 0.05	15.20 ± 0.08	5.07	−28.02	Paper I
J222509.19−001406.82	20.46 ± 0.04	19.01 ± 0.03	18.71 ± 0.04	15.93 ± 0.05	15.41 ± 0.11	4.85	−27.37	DR12
J222514.38+033012.50	21.74 ± 0.14	20.02 ± 0.05	19.47 ± 0.10	16.50 ± 0.08	15.69 ± 0.13	5.24	−27.17	Paper I
J222612.41−061807.29	20.32 ± 0.04	18.76 ± 0.02	18.73 ± 0.05	15.64 ± 0.05	14.96 ± 0.09	5.08	−27.83	Paper I
J225257.46+204625.22	20.65 ± 0.04	19.16 ± 0.02	19.23 ± 0.06	16.27 ± 0.06	15.52 ± 0.10	4.91	−27.00	Paper I
J232939.30+300350.78	20.87 ± 0.05	19.37 ± 0.02	18.93 ± 0.04	16.21 ± 0.06	15.43 ± 0.10	5.24	−27.72	Paper I
J234241.13+434047.46	21.17 ± 0.06	19.26 ± 0.02	18.97 ± 0.05	15.57 ± 0.04	14.73 ± 0.06	4.99	−26.93	Paper I
J234433.50+165316.48	20.23 ± 0.03	18.46 ± 0.02	18.52 ± 0.03	15.22 ± 0.04	14.56 ± 0.06	5.00	−27.93	Paper I

Notes.

[a] Quasars from the SDSS DR7 and DR12 quasar catalogs are labeled as "DR7" and "DR12." Quasars newly identified by us are labeled as "Paper I." Two quasars from McGreer et al. (2009) and Schneider et al. (1991) were also spectroscopically observed by us and we use our new spectra to do the M_{1450} calculation. See the details for our newly observed quasars in Paper I. All M_{1450} values are corrected using our adopted cosmology.

[b] This quasar discovered by McGreer et al. (2009) using the radio-selection method was also observed by us and we use the new spectra for the M_{1450} calculation.

[c] This quasar discovered by Schneider et al. (1991) was also observed by us and we use the new spectra for the M_{1450} calculation.

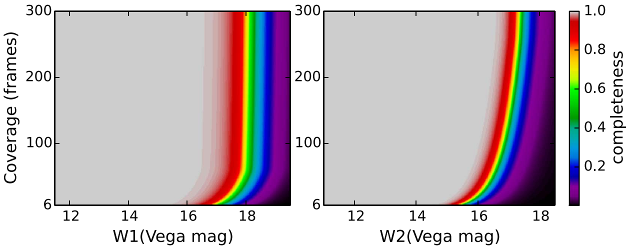

Figure 2. Empirical models of 2D detection completeness in ALLWISE $W1$ and $W2$ bands, which is from the Explanatory Supplement to the AllWISE Data Release Products. Our sample limited with $W1 < 17$ and $\sigma_{W2} < 0.2$ will be effected slightly by the detection incompleteness at the faint end.

ALLWISE coverage also affects the photometric errors of detected sources. The photometric error in $W1/W2$ will be a function of magnitude and coverage. We used all point sources in our ALLWISE sources sample discussed above to model the empirical magnitude–coverage–magnitude error relations for the ALLWISE $W1$ and $W2$ bands. The ALLWISE sensitivity improves approximately as the square root of the depth of coverage, $\sigma \propto 1/\sqrt{N_{\rm cov}}$, $N_{\rm cov}$ is the number of frame coverage. Considering this, we first eliminated the effect of coverage on magnitude errors and then fit the relations between $W1/W2$ magnitude and coverage-corrected magnitude error. Based on the *WISE* all-sky magnitude-error relation (Wright et al. 2010),

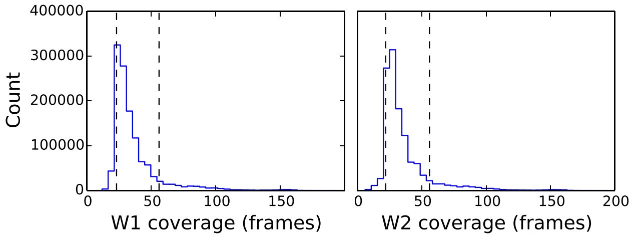

Figure 3. Distributions of $W1/W2$ frame coverages in the whole SDSS footprint. Dashed lines show the 10% and 90% tile ALLWISE coverage.

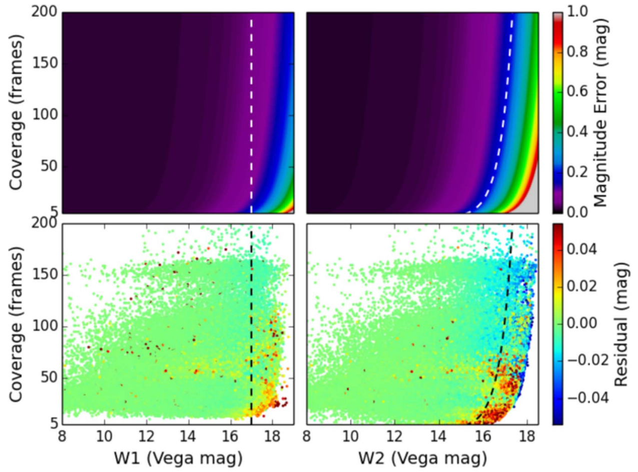

Figure 4. Top: the magnitude–coverage–magnitude error relations for the ALLWISE *W*1 and *W*2 bands. Bottom: the residuals of magnitude error, observed data minus model fitted. The dashed lines denote our *W*1 and *W*2 magnitude limit ($W1 < 17$, $\sigma_{W2} < 0.2$). Our model reproduced the ALLWISE photometric errors in SDSS footprint well.

the final ALLWISE magnitude–coverage–error relation we obtained is

$$\sigma(m, N_{\rm cov}) = a + [2.5/\ln(10)]n/10^{-0.4m}/\sqrt{N_{\rm cov}}\ . \qquad (5)$$

Where m is the magnitude in $W1/W2$. Constant a is basic photometric error, equal to 0.01 in WLSE all-sky photometry (Wright et al. 2010). We found that a should be 0.022 for *W*1 and 0.019 for *W*2 in ALLWISE photometry. The best-fitted parameter n is 6.43e–8 for *W*1, 2.71e–7 for *W*2. Figure 4 shows our empirical model compared with observed data.

3.2. Selection Function of Color–Color Selection

To estimate the completeness of our selection criteria, we generate a sample of simulated quasars following the procedure in Fan (1999). M13 updated the spectral model of Fan (1999) and applied it to higher redshift, assuming that the quasar spectral energy distributions do not evolve with redshift (Kuhn et al. 2001; Yip et al. 2004; Jiang et al. 2006). We extend this model toward redder wavelengths to cover the ALLWISE *W*1, *W*2 bands for quasars at $z = 4$–6 (I. D. McGreer et al. 2016, in preparation). The quasar spectrum from M13 is modeled as a power-law continuum with a break at 1100 Å. For redder wavelength coverage, we added three new breaks at 5700, 10850, and 22300 Å. The slope (α_ν) from 5700 to 10850 Å follows a Gaussian distribution of $\mu(\alpha) = -0.48$ and $\sigma(\alpha) = 0.3$; the middle range has a slope with the distribution of $\mu(\alpha) = -1.74$ and $\sigma(\alpha) = 0.3$; and at the red end, the slope distribution has $\mu(\alpha) = -1.17$ and $\sigma(\alpha) = 0.3$ (Glikman et al. 2006). The parameters of emission lines are derived from the composite quasar spectra (Glikman et al. 2006). Although the composite spectrum from Glikman et al. (2006) is constructed from fainter lower redshift quasars, it does not have obvious difference with composite spectra built from luminous quasars at high redshift (e.g., Selsing et al. 2016). It is the only one we know that can cover both *W*1 and *W*2 bands in the redshift range of our simulation ($4 < z < 6$). The IGM absorption model is the same as M13, which extends the Ly$_\alpha$ forest model based on the work of Worseck & Prochaska (2011) to higher redshift by using the observed number densities of high column density systems (Songaila & Cowie 2010). Compared to M13, we have made minor modifications for Fe emission. We use the template from Vestergaard & Wilkes (2001) for wavelengths shorter than 2200 Å. For 2200–3500 Å, we use the template from Tsuzuki et al. (2006), which separates the Fe II emission from the Mg II λ2798 line. A template from Boroson & Green (1992) covering 3500–7500 Å is also added.

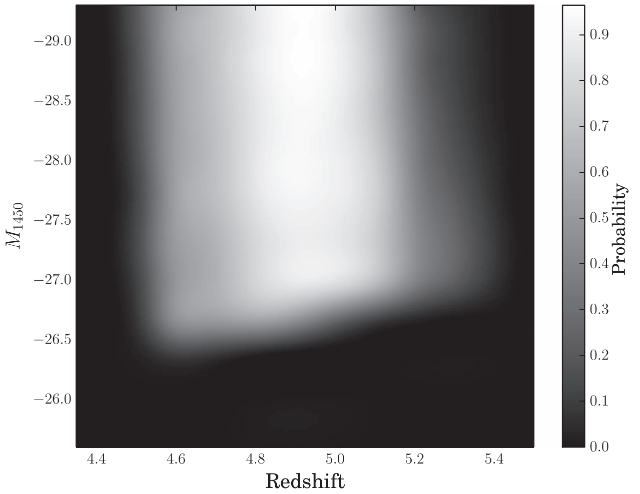

Figure 5. Selection function of our survey ($z_{\rm SDSS} < 19.5$) based on position-dependent ALLWISE coverage. The probability is the fraction of simulated quasars, which can be selected by our selection criteria in each (M_{1450}, z) bin.

Based on this model, we generate a sample of simulated quasars and then calculate the selection function of our color–color selection. We construct a grid of quasars in the redshift range of $4 < z < 6$ and the luminosity range of $-29.5 < M_{1450} < -25.5$. A total of 314,000 simulated quasars has been generated and evenly distributed in the (M_{1450}, z) space. There are ~200 quasars in each (M_{1450}, z) bin with $\Delta M = 0.1$ and $\Delta z = 0.05$. We assign optical photometric errors, which are from the SDSS main survey, and photometric uncertainties of the *W*1 and *W*2 bands using the empirical magnitude–coverage–error relations discussed above. We added the ALLWISE detection completeness into the selection probability calculation.

We calculate the ALLWISE detection probability by randomly choosing a unique sky position from our 1,220,000 positions for each simulated quasar, and thus obtained an ALLWISE detection probability of each simulated quasar based on its frame's coverage and *W*1 and *W*2 magnitude. For each (M_{1450}, z) bin ($\Delta M = 0.1$ and $\Delta z = 0.05$) discussed above, we obtain a mean detection probability. Then we calculate the fraction of simulated quasars selected by our selection criteria in each (M_{1450}, z) bin as the selection probability, shown in Figure 5.

As shown in Figure 5, after relaxing the traditional $r - i/i - z$ color cut and adding the $W1 - W2$ color, our color selection criteria show a high completeness at $4.8 < z < 5.2$ and extend the selection region to $z \sim 5.4$. Within the central bright region ($4.8 < z < 5.2$ and $M_{1450} < -26.8$), the mean completeness reaches 78%. Extended to the range of $4.7 < z < 5.4$, the mean completeness is ~60%. At a redshift lower than 4.5 or higher than 5.4, the completeness is below than 5%. At $z < 4.7$, the $W1 - W2$ color becomes bluer; our $W1 - W2 > 0.5$ cut will miss some quasars at $z < 4.7$ (see

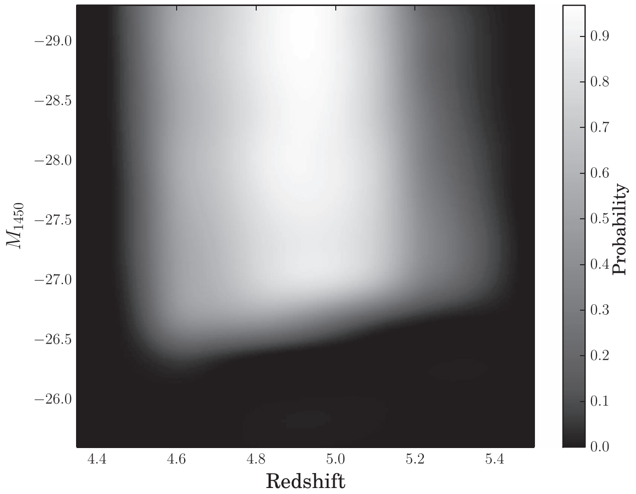

Figure 6. Selection function of our survey ($z_{\rm SDSS} < 19.5$) using 10% tile ALLWISE coverage, $N_{\rm cov} = 23$ for $W1$, $N_{\rm cov} = 22$ for $W2$. Comparing with Figure 5, the change of probability is small.

Figure 3 in Paper I). However, the exact completeness is more sensitive to the assumption we made about the rest-frame optical continuum of high-redshift quasars at $4.5 < z < 4.7$ due to the fast change of $W1 - W2$ color here. The uncertainty of the simulation in this redshift range is higher than that at $z > 4.7$. Therefore, we restrict our quasar sample for the QLF calculation to $z \geqslant 4.7$. At $5.2 < z < 5.4$, although the completeness becomes lower, our selection has explored a higher redshift range with higher completeness than previous works at $z \sim 5$. Thus, we limit our sample with $z < 5.4$.

To see how the ALLWISE coverage affects our selection function, we also calculate the selection function by assuming a fixed number of coverage, 10% tile ALLWISE coverage ($N_{\rm cov} = 23$ for $W1$, $N_{\rm cov} = 22$ for $W2$), shown in Figure 6. The difference in the selection function between using 10% tile coverage and position-dependent coverage is less than 5% at $M_{1450} < -27$ and increases to ∼10% at $M_{1450} < -26.8$, to 15%–20% at a fainter range. We also compare the QLF result base on 10% tile coverage and position-dependent coverage. The change of the parameters of best-fitted QLFs is ∼0.05, much smaller than error bars. We use the position-dependent coverage selection function to calculate the parametric QLF. When we calculate the selection probability of each quasar in our sample for a binned QLF measurement, we use the real ALLWISE coverage to calculate the ALLWISE detection completeness of each quasar. The agreement between binned QLF and best-fit parametric QLF (See Sections 4.1 and 4.2) shows that our ALLWISE coverage model and the selection function using mean detection incompleteness are reasonable.

3.3. Spectroscopic Incompleteness

We spectroscopically observed 99 out of 110 candidates. The spectroscopic completeness reaches 100% at $z_{\rm SDSS} \leqslant 19$; at the fainter end, the completeness is lower but it still has a high value around 80%. The histogram of our observed and unobserved candidates is shown in Figure 7. The completeness is a function of z-band magnitude. We use this function to correct the incompleteness from spectral coverage, assuming the probability of an unobserved candidate to be a quasar is the same as in the observed sample. As shown, the quasar fraction in our unknown candidate sample becomes lower at the faint end. That is caused by the fact that there are more known quasars at $z_{\rm SDSS} > 19$, and these known quasars are not plotted in this figure.

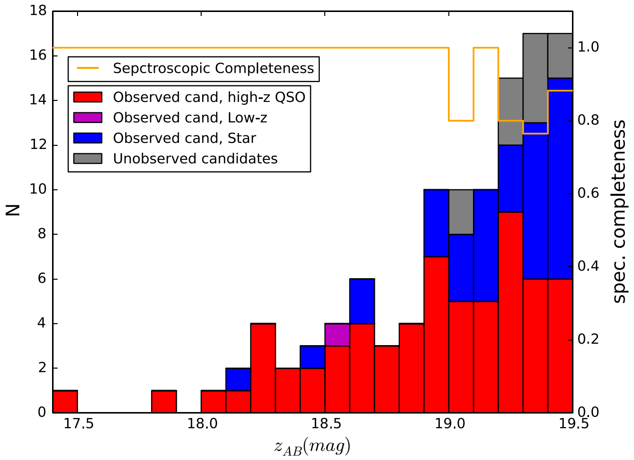

Figure 7. Spectroscopic incompleteness of our 110 $z \sim 5$ quasar candidates. The orange line denotes the spectroscopic incompleteness as a function of z-band magnitude. The histogram is divided into several components filled by different colors and represents newly identified high-redshift quasars (red), low-redshift quasars (purple), stars (blue), and unobserved candidates (gray).

Table 2
Binned QLF

M_{1450}	N	$N_{\rm cor}$	logΦ	$\Delta\Phi$[a]
−28.99[b]	1	18.2	−9.48	0.33
−28.55	4	7.7	−9.86	0.08
−28.05	14	24.4	−9.36	0.15
−27.55	26	44.4	−9.09	0.19
−27.05	54	103.1	−8.70	0.32

Notes.
[a] $\Delta\Phi$ is in units of 10^{-9} Mpc^{-3} mag^{-1}.
[b] Within the brightest magnitude bin, there is only one quasar. Therefore, we use its M_{1450} as the M_{1450} of this bin.

4. A NEW DETERMINATION OF THE QLF AT Z ∼ 5

4.1. Binned QLF

To compute the binned QLF, we divide our sample into several bins. Due to the narrow redshift interval of our sample, we only use one redshift bin and do not include any evolution with redshift. We then divide our sample into 5 mag bins with $\Delta M_{1450} = 0.5$ mag over the magnitude range $-26.8 < M_{1450} < -29.3$ (see Figure 1). We calculate the binned luminosity function by using the Page & Carrera (2000) modification of the $1/V_{\rm a}$ method (Schmidt 1968; Avni & Bahcall 1980) for flux limit correction. The final selection function is applied after all incompleteness corrections have been applied for each quasar. The result for the binned QLF and number counts are listed in Table 2. In the table, the number counts and corrected number counts derived by applying all incompleteness corrections are denoted as N and $N_{\rm cor}$ respectively. The result is also displayed in Figure 8 as red squares together with the binned QLF data from the SDSS main (black) and Stripe 82 (blue) samples in M13 for comparison. Data from M13 have been corrected to $z = 5.05$ by using the quasar redshift evolution at high

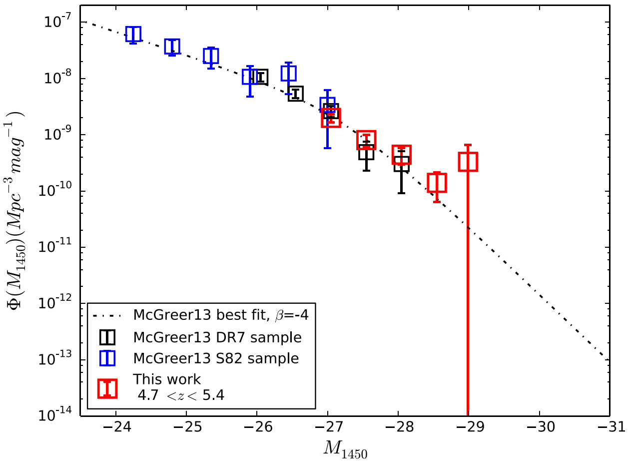

Figure 8. Binned QLF at $z = 5.05$ ($4.7 \leqslant z < 5.4$). The red squares represent our binned QLF data. The blue and black squares denote the binned QLF data from the Stripe 82 sample and the SDSS main sample in M13. These data have been corrected to $z = 5.05$ by using the redshift evolution proposed by Fan et al. (2001b). The black dashed–dotted line shows the best fitting QLF from M13 with the bright end slope $\beta = -4$.

redshifts according to Fan et al. (2001b). Compared to previous results, our binned QLF has more luminous quasars and extends the measurement of the $z \sim 5$ QLF to $M_{1450} = -29$, and thus gives a smaller error bar in each bin at $M_{1450} < -27.05$. Our data show a similar result, but suggest a higher value at the bright end. The binned QLF in the brightest bin has a large error bar due to the fact that there is only one quasar in this bin.

4.2. Maximum Likelihood Fitting

The binned QLF result, while non-parametric, is dependent on the choice of binning. Here we derive a parametric QLF by performing a maximum likelihood fit for each quasar in the sample. We model the QLF using the most common double power-law form (Boyle et al. 2000):

$$\Phi(M, z) = \frac{\Phi^*(z)}{10^{0.4(\alpha+1)(M-M^*)} + 10^{0.4(\beta+1)(M-M^*)}}, \quad (6)$$

where α and β are the faint end and the bright end slopes, M^* is the break magnitude, and $\Phi^*(z)$ is the normalization. These four parameters have been suggested to evolve with redshift. Following previous work, we adopt the rapid decline in quasar number density at high redshift from Fan et al. (2001b) as the QLF evolution within our narrow redshift interval, $\Phi^*(z) = \Phi^*(z = 6) \times 10^{k(z-6)}$, where $k = -0.47$ (Fan et al. 2001b).[11] Here we also normalize Φ^* to $z = 6$ for easier comparison to the higher redshift results.

Due to the fact that our quasar sample covers the magnitude range of $M_{1450} \leqslant -26.8$, and the break magnitude given by M13 is around −26 to −27, our sample cannot be used to constrain the faint end slope. For measurement of the break magnitude M^*, we combine our luminous quasar sample with the S82 and DR7 quasar samples from M13 and then carry out parametric fits for the QLF for all observed quasars in the combined sample. The DR7 sample has a large number of overlaps with our luminous quasar sample. Therefore, we select DR7 quasars only in the magnitude range $-26.8 < M_{1450} < -25.8$ to construct the combined sample. For the S82 and DR7 samples, we use the same incompleteness corrections as in M13. We use maximum likelihood estimation to derive the fit. The maximum likelihood fit (Marshall et al. 1983) for a luminosity function aims to minimize the log likelihood function S, which is equal to $-2\ln L$, where L is the likelihood function:

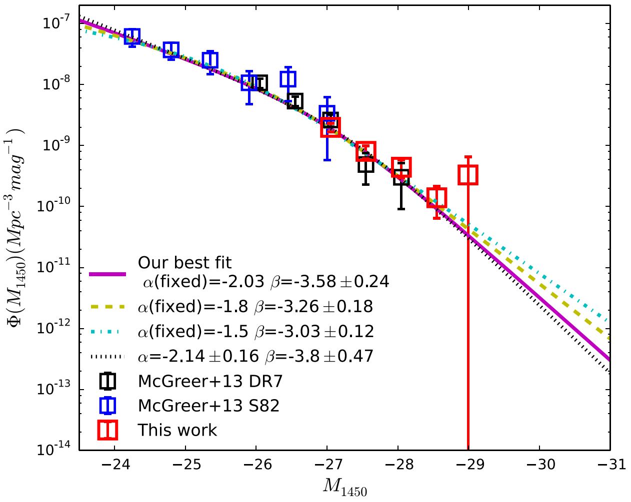

Figure 9. Double power-law fits using maximum likelihood fitting compared with the binned QLF data from the S82 sample, the DR7 sample, and our luminous quasar sample. The results based on fixed α and on four free parameters are plotted for comparison. We fix the faint-end slope α at −2.03 (purple line), −1.8 (yellow dashed line), and −1.5 (cyan dotted–dashed line) and do the fits respectively. Then we also allow all four parameters to be free (Green dashed line). When we change the faint-end slope α from −2.03 to −1.8 and −1.5, the bright end slope β is flattened, but it only changes a little. The break magnitude becomes fainter following the change of β. When we allow all four parameters to be free, we get a steeper bright end slope $\beta = -3.80$.

$$S = -2\sum_{i}^{N} \ln[\Phi(M_i, z_i)] + 2\int\!\!\int \Phi(M, z)p(M, z)\frac{dV}{dz}dMdz, \quad (7)$$

where the first term is the sum over all observed quasars in the sample, and the second term is integrated over the full range of absolute magnitude and redshift of the sample (Marshall et al. 1983; Fan et al. 2001a); $p(M, z)$ is the probability for a quasar to be observed by the survey at given absolute magnitude M_{1450} and redshift z. It includes all incompleteness corrections discussed above. The second term represents the total number of expected quasars in the survey with a given luminosity function, and provides the normalization for the likelihood function. The confidence intervals are determined from the likelihood function by assuming a χ^2 distribution of ΔS (=S $-S_{\rm min}$) (Lampton et al. 1976).

We first fix the faint-end slope α to be −2.03, as given by M13. We find the luminosity function parameters to be log $\Phi^*(z = 6) = -8.82 \pm 0.15$, $M^*_{1450} = -26.98 \pm 0.23$ and $\beta = -3.58 \pm 0.24$. This result is plotted in Figure 9 and shows excellent agreement with our binned QLF. In order to

---

[11] To see how the results depend on $\Phi^*(z)$ evolution, we varied the value of k from −0.3 to −0.7. We find that the form of $\Phi^*(z)$ evolution has little effect on the other parameters when doing the fits. The changes are within 1σ. Furthermore, due to the narrow redshift range we used, the log($\Phi^*(z)$) is also affected only slightly by varying the form of the evolution.

Table 3
Parameters of Fits

α	β	M^*_{1450}	$\log\Phi^*(z=6)$
-2.03	-3.58 ± 0.24	-26.98 ± 0.23	-8.82 ± 0.15
-1.80	-3.26 ± 0.18	-26.28 ± 0.29	-8.35 ± 0.17
-1.50	-3.03 ± 0.12	-25.56 ± 0.29	-7.94 ± 0.15
-2.14 ± 0.16	-3.80 ± 0.47	-27.32 ± 0.53	-9.07 ± 0.40

Note. We fix the faint slope α to be -2.03, -1.8, and -1.5 respectively. Then we allow all four parameters to be free. $\alpha = -2.03$ is measured from the combination of the SDSS S82 and DR7 samples in M13. We adopt the result with fixed $\alpha = -2.03$ as our best fit.

investigate how the different values of α affect our result, we also assume the faint-end slope α to be -1.8, similar to what was measured from quasar samples at $z \geqslant 4$ (Glikman et al. 2010; Willott et al. 2010; Masters et al. 2012; McGreer et al. 2013), and to -1.5, typical for lower redshift measurements at $z \lesssim 3$ (Croom et al. 2009). The values of parameters assuming different faint-end slopes are listed in Table 3. When we change the faint-end slope α from -2.03 to -1.8 and -1.5, the bright end slope β is flattened but only at the $\lesssim 1\sigma$ level. The break magnitude becomes fainter more significantly following the change of β. If we allow all four parameters to be unconstrained, we derive a steeper bright end slope $\beta = -3.80$ and a very bright break magnitude of $M^*_{1450} = -27.33$ with significantly larger error bars. Allowing all parameters to be free has many degeneracies, which is why the uncertainty ranges are larger. In this case, the faint-end slope α also becomes steeper ($\alpha = -2.15$). We need more data to better constrain a four-parameter fit, especially for $M_{1450} < -28.3$. Considering that $\alpha = -2.03$ derived by M13 is a strong constraint on the faint-end slope, we adopt the result based on fixed $\alpha = -2.03$ as our best fit. The fitted QLFs for different cases are plotted in Figure 9.

We calculate the confidence regions to investigate the degeneracy between the bright end slope and break magnitude; the results are shown in Figure 10. The regions filled with different colors illustrate 1σ (68.3%), 2σ (95.4%), and 3σ (99.7%) regions, respectively. We generate the probability contours by calculating $S_{\min}$ for each (M_{1450}, β) point and allowing $\log\Phi(z=6)^*$ to be free at each point with the fixed $\alpha = -2.03$. Figure 10 shows that our data constrain β to the range of $-4.83 < \beta < -2.78$ at 95% confidence; this is flatter than the result from M13, which shows $\beta < -3.1$ at 95% confidence, although the best fit from M13, $\beta = -4$, lies within our 2σ region.

We compare the parameters of our result with previous work at different redshifts to study the evolution of the QLF. In Figure 11, we plot the evolution of the normalization Φ^*, the break magnitude M^*_{1450}, and the bright end slope β with redshift. Ross et al. (2013) measured the QLF at $2.2 < z < 3.5$ using the BOSS DR9 quasar sample and concluded that the QLF can be described well by an LEDE model at this redshift range. In this model, the evolutions of normalization and break luminosity with redshift are expressed in a log–linear relation, and slopes of the double power law are fixed. M13 add a point at $z = 4.9$ and combine the result from Masters et al. (2012) at $z = 4$ and the result from Willott et al. (2010) at $z = 6$ to modify this model. They found that the slope of the normalization evolution was steeper ($c1 = -0.7$) and the slope of the break magnitude evolution was shallower ($c_2 = -0.55$). Now

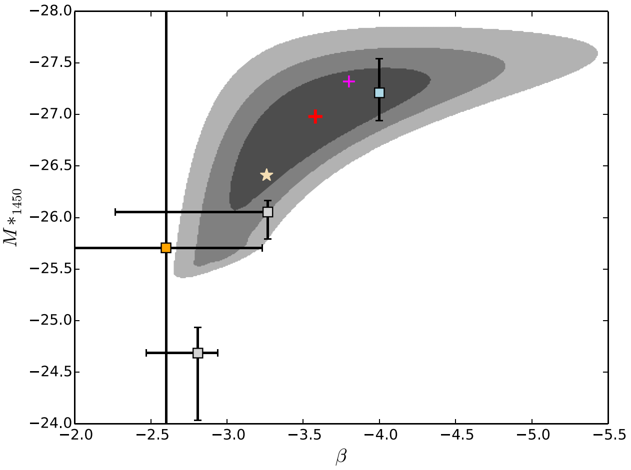

Figure 10. Confidence region for β and M^*_{1450}. The regions filled with different shades of gray denote 1σ (68.3%), 2σ (95.4%), and 3σ (99.7%) regions, respectively. For comparison, we plot our best-fit result (red cross) and the result of the four-parameter fit (magenta cross) together with the best fit from other work. The light blue square denotes the best fit from M13 at $z \sim 5$. The white star shows the result from Willott et al. (2010) for fixed $\alpha = -1.8$ (uncertainties of the fit were not reported) at $z \sim 6$. The yellow square represents the best fit from Masters et al. (2012), which used the faint quasar sample in the COSMOS field in conjunction with the bright quasar sample from Richards et al. (2006) to model a double power-law QLF at $z \sim 4$. We also plot the points (gray squares) to show the best fits for binned data in the $z = 2.2$ (left) and 3.4 (right) redshift bins from the BOSS S82 sample (Ross et al. 2013). All data have been corrected to our adopted cosmology.

we add our new measurement at $z = 5.05$ and the point at $z = 6$ from Kashikawa et al. (2015) in case 1. The result from Kashikawa et al. (2015) includes the discovery of new faint $z \sim 6$ quasars and places stronger constraints on the faint-end slope and break magnitude of the $z \sim 6$ QLF. Then we use all of these points to fit the LEDE model.

$$\log[\Phi^*(z)] = \log[\Phi^*(z = 2.2)] + c_1(z - 2.2), \tag{8}$$

$$M^*_{i,2}(z) = M^*_{i,2}(z = 2.2) + c_2(z - 2.2), \tag{9}$$

where $M_{i,2} \equiv M_i(z = 2) = M_{1450} - 1.486$ is the absolute i-band magnitude at $z = 2$ (Richards et al. 2006), corresponding to rest-frame ~2600 Å in the assumption of a spectral index of $\alpha_\nu = -0.5$. We obtain values of $\log\ \Phi^*(z = 2.2) = -5.87 \pm 0.07$ and $c1 = -0.81 \pm 0.03$; $M^*_{i,2}(z = 2.2) = -26.68 \pm 0.15$ and $c2 = -0.50 \pm 0.08$. Note that the errors of parameters are standard deviation errors of fit. We only use these points without uncertainties to do the fit because the uncertainties of the best fit in Willott et al. (2010) are not reported. The real errors should be larger than the fitting errors explored here. Our result is consistent with the LEDE model but prefers a steeper slope of $\log\Phi^*(z)$ evolution and a flatter slope of the break magnitude evolution.[12]

---

[12] Our results can also be compared to Figure 19 of M13; however, the BOSS data used in M13 were based on a pre-publication analysis of the DR9 sample, and were later updated in Ross et al. (2013). Here we use the final version of the BOSS data from that work.

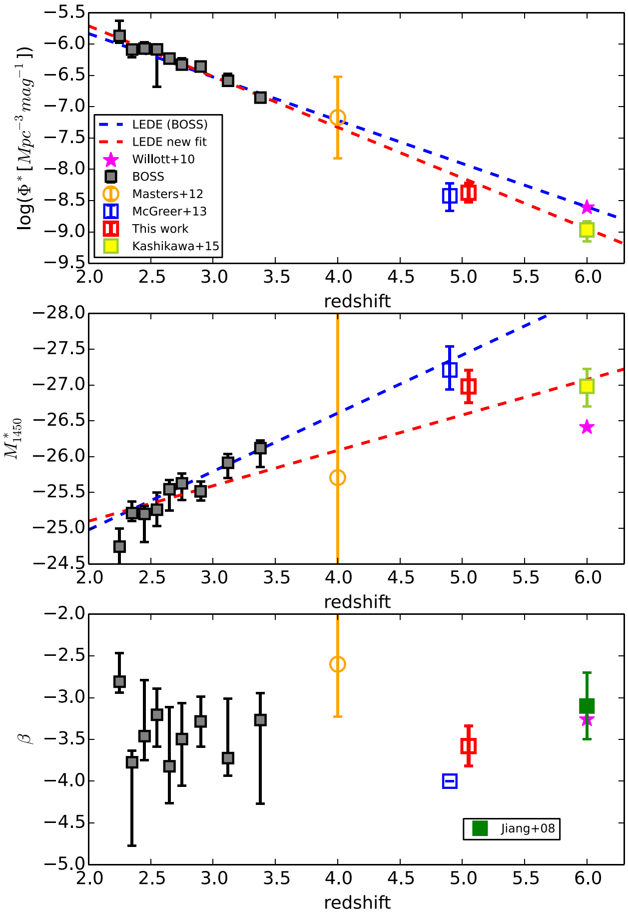

Figure 11. Evolution of QLF parameters: normalization Φ^* (upper), break magnitude M^*_{1450} (middle), and the bright end slope β (bottom). We compare our best-fit QLF parameters with previous results at similar and different redshifts to show the evolution of parameters from redshift of $z \sim 2$ to 6. The gray squares at $2.2 < z < 3.5$ are the best fits for each redshift bin from the BOSS DR9 QLF, which were measured by using a sample of ~6000 variability-selected quasars in Stripe 82 (Ross et al. 2013). The orange circle is the best fit from Masters et al. (2012) at $z = 4$. The blue square represents the best fit from M13 at $z = 4.9$, and our best fit at $z = 5.05$ is plotted as a red square. At $z = 6$, in the Φ^* and M^*_{1450} plots, we plot the result from Willott et al. (2010) with $\alpha = -1.8$ (magenta star) and Kashikawa et al. (2015) in their case 1 fits (yellow square). In the β − redshift plot, we plot the result from Willott et al. (2010) and the single power-law fit of Jiang et al. (2008) at $z = 6$ because Kashikawa et al. (2015) fit their data with a fixed bright end slope. The blue dashed lines in the Φ^* and M^*_{1450} plots represent the LEDE model from Ross et al. (2013). The red dashed lines are our new fits. All data have been corrected to our adopted cosmology.

5. DISCUSSION

5.1. Contribution to the Ionizing Background

Previous measurements of the QLF at $z = 5$ and 6 have shown evidence that quasars cannot produce the entire required ionizing photon background (M13; Meiksin 2005; Bolton & Haehnelt 2007; Willott et al. 2010; Kashikawa et al. 2015) at those redshifts. It is suggested that quasars can contribute ~30%–70% of the ionizing photons required to maintain full ionization at $z = 5$ (M13), and produce about several percent to 15% at $z = 6$ (Willott et al. 2010; Kashikawa et al. 2015), depending on the assumed IGM clumping factor C. Here we update the quasar contribution to the high-redshift ionizing background using our new QLF at $z \sim 5$.

We calculate the comoving emissivity of quasars at the Lyman limit by $\epsilon(z) = \int \phi(L_\nu, z) L_\nu dL_\nu$ erg s^{-1} Hz^{-1} Mpc^{-3}, assuming the escape fraction of ionizing radiation from quasars $f = 1$. We integrate our parametric QLF $\Phi(M_{1450}, z)$ and then convert it into emissivity at $\lambda = 912$ Å. For the conversion, we adopt the UV slopes from Stevans et al. (2014), who suggest a gradual break wavelength at 1000 Å, with the index $\alpha_\nu = -1.41$ in the extreme ultraviolet and a spectral index $\alpha_\nu = -0.83$ at wavelengths above the break. By integrating our best-fit QLF to $M_{1450} = -20$, we derive an ionizing photon density $\dot{N}_Q = 6.06 \times 10^{49}$ Mpc^{-3} s^{-1}. When we use the QLF result with a fixed faint-end slope of $\alpha = -1.8$, the photon number density changes to $\dot{N}_Q = 4.73 \times 10^{49}$ Mpc^{-3} s^{-1}. Using the QLF generated from the four-parameter fit, we get $\dot{N}_Q = 7.37 \times 10^{49}$ Mpc^{-3} s^{-1}. The change of ionizing photon density is dominated by the change of the break magnitude M^*_{1450} and the faint-end slope α. Luminous quasars make little contribution to the ionizing background, so a survey of faint quasars is required to give a more accurate measurement.

The required number of photons to balance hydrogen recombination and maintain full ionization was estimated by Madau et al. (1999) as a function of redshift. The number of required photons at $z = 5$ is $\dot{N}_{\rm ion} = 3.38 \times 10^{50}(C/5)$ Mpc^{-3} s^{-1} in our adopted cosmology. The clumping factor C is crucial to estimate the contribution of quasars to the ionizing background. Madau et al. (1999) considered a recombination-dominated IGM and suggested a high value for the clumping factor $C = 30$. Recent work provides a lower clumping factor $C < 10$. Meiksin (2005) suggests that $C \approx 5$ and a $C \approx 2$–3 at $z = 6$ is suggested by some reionization models (McQuinn et al. 2011; Finlator et al. 2012; Shull et al. 2012). For $C = 2$, based on the result from our best-fit QLF, quasars are estimated to provide ~45% of the required photons; while for $C = 5$, the fraction changes to 18%. This result agrees with previous work, suggesting that quasars may play some role in maintaining ionization at $z \sim 5$ but have low possibilities of being the dominant source of ionizing photons (M13).

5.2. Radio-loud Fraction

Traditionally, quasars have been divided into two populations, radio-loud and radio-quiet (Kellermann et al. 1989). The similarity and difference between the evolution of radio-loud and radio-quiet quasars are thought to be related to black-hole mass, accretion, and spin. (Rees et al. 1982; Wilson & Colbert 1995; Laor 2000). The radio-loud fraction (RLF) has been suggested to evolve with optical luminosity and redshift by some work (e.g., Padovani 1993; La Franca et al. 1994; Hooper et al. 1995; Jiang et al. 2007; Kratzer & Richards 2015). In contrast to this, no evolution of the RLF is also found (e.g., Goldschmidt et al. 1999; Stern et al. 2000; Ivezić et al. 2002; Cirasuolo et al. 2003). Our luminous quasar sample is selected only by optical and near-infrared colors and thus it can be considered to be an unbiased sample for the study of the RLF.

We cross-match all 99 quasars in our sample with catalogs from Faint Images of the Radio Sky at Twenty-cm (FIRST; Becker et al. 1995) and the NRAO VLA Sky Survey (NVSS; Condon et al. 1998) and find 8 quasars with radio detections. We use 3″ matching radius for FIRST data, and 5″ for NVSS due to the lower resolution of NVSS. We calculate the radio loudness for these 8 quasars by assuming an optical spectral

Table 4
Radio Detection and Radio Loudness

Name	z	m_{1450}	$f_{1.4\,\mathrm{GHz,FIRST}}$[a]	$f_{\mathrm{err},F}$	$f_{1.4\,\mathrm{GHz,NVSS}}$	$f_{\mathrm{err},N}$	$f_{\nu,2500}$	$f_{\nu,4400}$	$f_{\nu,5\,\mathrm{GHz}}$	R_{2500}	R_{4400}	M_{2500}[b]
J0011+1446	4.96	18.03	23.96	0.146	35.8	1.5	0.0491	0.0651	5.1933	105.8	79.7	−28.65
J0131−0321	5.18	18.09	32.83	0.123	31.4	1.0	0.0448	0.0594	6.9880	156.0	117.6	−28.66
J0741+2520	5.21	18.22	2.07	0.141	⋯	⋯	0.0396	0.0525	0.4395	11.1	8.4	−28.54
J0813+3508	4.92	19.17	20.04	0.156	35.6	1.1	0.0173	0.0229	4.3583	252.0	189.9	−27.50
J1146+4037	4.98	19.48	12.45	0.146	12.5	0.5	0.0129	0.0171	2.6940	209.3	157.8	−27.21
J1318+3418	4.82	19.09	3.73	0.148	3.5	0.4	0.0189	0.0251	0.8181	43.2	32.6	−27.54
J2329+3003[c]	5.24	18.83	⋯	⋯	4.9	0.4	0.0224	0.0298	1.0380	46.2	34.9	−27.94
J2344+1653	5.00	18.54	⋯	⋯	15.3	0.6	0.0305	0.0404	3.3052	108.4	81.7	−28.15

Notes.
[a] Flux density and flux density error are in units of mJy.
[b] Data in this table are calculated based on cosmology $H_0 = 70\ \mathrm{km\ s^{-1}\ Mpc^{-1}}$, $\Omega_m = 0.3$, and $\Omega_\Lambda = 0.7$.
[c] The two objects only detected by NVSS without FIRST detection are not covered by the FIRST footprint.

index of −0.5 and radio spectral index of −0.5 ($f_\nu \propto \nu^\alpha$) and list them in Table 4. To compare with previous work at higher redshifts (Bañados et al. 2015), we adopt the radio/optical flux density ratio $R_{4400} = f_{\nu,5\,\mathrm{GHz}}/f_{\nu,4400\,\text{Å}}$ (Kellermann et al. 1989) and the criterion $R > 10$ for the definition of a radio loud quasar, where $f_{\nu,5\,\mathrm{GHz}}$ is the radio flux density at rest-frame 5 GHz, and $f_{\nu,4400\,\text{Å}}$ is the optical flux density at rest-frame 4400 Å. There are 7 quasars considered to be radio loud quasars among the 99 quasars. Therefore, we find a radio loud fraction RLF ~ 7.1%. Considering FIRST with its 1mJy flux limit and NVSS with its 2.5 mJy flux limit are not deep enough to detect all radio loud quasars, especially for quasars at $z_{\mathrm{SDSS}} > 19$, 7.1% is a lower limit. This result shows agreement with the result from Bañados et al. (2015), which constrains the RLF at $z \sim 6$ to be $8.1^{+5.0}_{-3.2}\%$. We also do the calculation using a radio spectral index of −0.75. The radio loudness based on $\alpha = -0.5$ to −0.75 increases 12%–15%. The radio loud fraction has no change.

Jiang et al. (2007) suggest that the RLF is a function of absolute magnitude M_{2500} and redshift at $z < 4$, and give the best fit for the function. To compare with Jiang et al. (2007), we also calculate the radio/optical flux density ratio $R_{2500} = f_{\nu,5\,\mathrm{GHz}}/f_{\nu,2500\,\text{Å}}$, where $f_{\nu,2500\,\text{Å}}$ is the optical flux density at rest-frame 2500 Å. We convert M_{1450} to M_{2500} by $M_{2500} = M_{1450} - 0.3$ on the assumption of an optical spectral index of approximately −0.5. For comparison, here we use the same cosmology as Jiang et al. (2007), which is $H_0 = 70\ \mathrm{km\ s^{-1}\ Mpc^{-1}}$, $\Omega_m = 0.3$, and $\Omega_\Lambda = 0.7$. Our sample covers magnitudes of $-27.03 < M_{2500} < -29.22$. Due to the fact that there are only 8 quasars with radio detection covering a narrow redshift range, we use only one redshift bin and roughly divide our sample into two magnitude bins, one for $M_{2500} < -28$ and the other one for $M_{2500} > -28$. Here we use $R > 30$ as the definition of the radio loud quasar so that FIRST with limiting flux of ~1 mJy will be deep enough for our quasar sample. NVSS, with an ~2.5 mJy flux limit, is still not deep enough and is able to detect radio-loud quasars ($R > 30$) at $z \sim 5$ only down to $M_{2500} \sim -27.7$. Therefore, we calculate the RLF for quasars within the area covered by FIRST and NVSS, respectively. In the bright magnitude bin, there are 13 quasars in the FIRST coverage and 19 quasars in the NVSS coverage. In the faint bin, there are 68 quasars in the FIRST coverage and 80 quasars in the NVSS coverage. The details and radio loudness of radio detected quasars are given in Table 4. We compare our result with the RLF evolution function $\log(\mathrm{RLF}/(1\text{-}\mathrm{RLF})) = -0.218 - 2.096\log(1 + z) - 0.203(M_{2500} + 26)$ from Jiang et al. (2007). As shown in Figure 12, our points show an evolution of the RLF with magnitude, but prefer a higher RLF at $z \sim 5$ than the prediction. Our result suggests that the RLF may evolve with optical luminosity, but it may not decline as rapidly with increasing redshift as measured in Jiang et al. (2007) at high redshift, though this could be affected by the small number of radio-loud quasars in our sample.

6. CONCLUSION

We establish a highly effective $z \sim 5$ quasar selection method based on SDSS and ALLWISE optical/near-infrared colors. We relax the traditional $r - i/i - z$ color limit by including color cuts in the ALLWISE $W1$ and $W2$ data. We selected 110 quasar candidates that satisfied our selection criteria with good optical image quality and obtained spectroscopic observations for 99 candidates. 64 new quasars have been discovered in the redshift range of $4.4 < z < 5.5$ and magnitude range of $-29 < M_{1450} < -26.4$. We restrict our luminous quasar sample to $4.7 \leqslant z < 5.4$ and $M_{1450} \leqslant -26.8$ for the QLF calculation. Combining all previously known quasars in this range, we construct the largest luminous quasar sample at $z \sim 5$ and determine the QLF, covering a sky area of 14,555 deg^2. Here we list our main conclusions.

1. Within the redshift range of $4.7 \leqslant z < 5.4$ and magnitude range of $M_{1450} \leqslant -26.8$, there are 45 newly identified quasars and 54 known quasars. Our new discovery successfully extends the population of luminous quasars at $z \sim 5$, especially at $M_{1450} \leqslant -27.3$, where we discovered 27 new quasars and increased the number of known quasars by a factor of 1.5 in this luminosity range. Our final sample, including 99 quasars, is the largest sample of luminous $z \sim 5$ quasars (Figure 1).
2. We derive the selection function of our color–color selection by using 311,000 simulated quasars in the redshift range of $z = 4$–6 and luminosity range of $-29.5 < M_{1450} < -25.5$. The selection function shows that by relaxing the traditional $r - i/i - z$ color cut and adding the $W1 - W2$ color, our color selection criteria extend the selection fuction to a higher redshift $z \sim 5.4$ than previous work (Figure 5).
3. Using this sample, we calculate the binned QLF and fit the parametric QLF by using maximum likelihood fitting at $z = 5.05$ (Figures 8 and 9). For the parametric QLF,

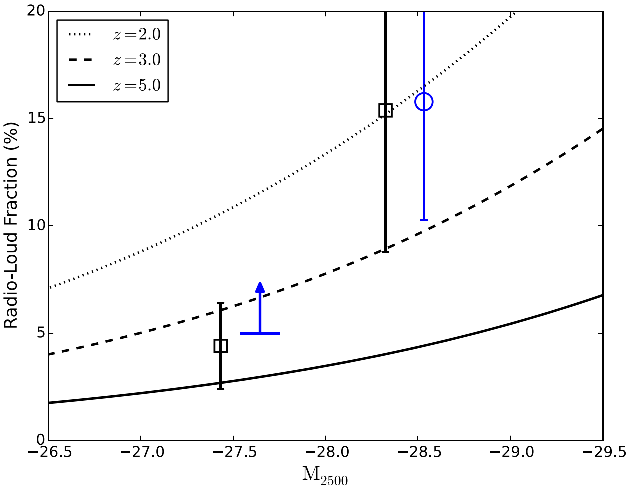

Figure 12. RLF in each magnitude bin compared with the evolution function from Jiang et al. (2007). The dotted, dashed, and solid lines show the predicted RLF at $z = 2$, 3, and 5 from Jiang et al. (2007). The black squares represent the RLF in the FIRST area, and the blue circle and blue arrow denote the result from quasars within the NVSS area. In the faint magnitude bin, the RLF based on NVSS data is a lower limit. To show the points clearly, we shift the NVSS points by −0.2 mag. The uncertainties of RLF is estimated by assuming a poisson distribution of the number of quasars in each bin.

we fix the faint-end slope $\alpha = -2.03$, which is measured by using the S82 and DR7 quasar samples (M13), and find the best-fit result of the bright end slope $\beta = -3.58 \pm 0.25$ and break magnitude of $M^{*}_{1450} = -26.99 \pm 0.23$.

4. We compare parameters of our best-fit QLF with previous work at different redshifts and use all points to fit an LEDE model. Our result is consistent with the previous LEDE model but prefers a steeper slope of $\log \Phi^{*}(z)$ evolution and a flatter slope of break magnitude evolution. The comparison for β shows no clear evolution with redshift (Figure 11).
5. We calculate the contribution of quasars to the ionizing background at $z \sim 5$ based on our QLF. Integrating our best-fit QLF, we find that quasars are able to provide ~18%–45% of the required photons based on a clumping factor of $C \sim 2$–5.
6. We use FIRST and NVSS data to calculate the radio loud fraction of our sample and give a lower limit for the RLF of ~7.1%, which agrees with the result at $z \sim 6$ of Bañados et al. (2015). In comparison to the predicted evolution function of the RLF with M_{2500} and z proposed by Jiang et al. (2007), our result shows evolution with optical luminosity but no obvious evolution with redshift (Figure 12).

We thank the referee for providing constructive comments and suggestions. J.Y., F.W., and X.-B.W. are thankful for support by NSFC grant Nos.11373008 and 11533001, the Strategic Priority Research Program "The Emergence of Cosmological Structures" of the Chinese Academy of Sciences, grant No. XDB09000000, and the National Key Basic Research Program of China 2014CB845700, and support from the Ministry of Science and Technology of China under grant 2016YFA0400703. J.Y., X.F., and I.D.M. acknowledge the support from the US NSF grant AST 11-07682. Funding for the Lijiang 2.4 m telescope is provided by Chinese Academy of Sciences and the People's Government of Yunnan Province. This research uses data obtained through the Telescope Access Program (TAP), which has been funded by the Strategic Priority Research Program "The Emergence of Cosmological Structures" (grant No. XDB09000000), National Astronomical Observatories, Chinese Academy of Sciences, and the Special Fund for Astronomy from the Ministry of Finance in China. We acknowledge the use of the Lijiang 2.4 m telescope, the MMT 6.5 m telescope, the Bok telescope, the ANU 2.3 m telescope, and the Xinglong 2.16 m telescope. We acknowledge the support of the staff of the Xinglong 2.16 m telescope. This work was partially supported by the Open Project Program of the Key Laboratory of Optical Astronomy, National Astronomical Observatories, Chinese Academy of Sciences.

We acknowledge the use of SDSS photometric data. Funding for SDSS-III has been provided by the Alfred P. Sloan Foundation, the Participating Institutions, the National Science Foundation, and the U.S. Department of Energy Office of Science. The SDSS-III Web site is http://www.sdss3.org/. SDSS-III is managed by the Astrophysical Research Consortium for the Participating Institutions of the SDSS-III Collaboration including the University of Arizona, the Brazilian Participation Group, Brookhaven National Laboratory, University of Cambridge, Carnegie Mellon University, University of Florida, the French Participation Group, the German Participation Group, Harvard University, the Instituto de Astrofisica de Canarias, the Michigan State/Notre Dame/JINA Participation Group, Johns Hopkins University, Lawrence Berkeley National Laboratory, Max Planck Institute for Astrophysics, Max Planck Institute for Extraterrestrial Physics, New Mexico State University, New York University, Ohio State University, Pennsylvania State University, University of Portsmouth, Princeton University, the Spanish Participation Group, University of Tokyo, University of Utah, Vanderbilt University, University of Virginia, University of Washington, and Yale University. This publication makes use of data products from the *Wide-field Infrared Survey Explorer*, which is a joint project of the University of California, Los Angeles, and the Jet Propulsion Laboratory/California Institute of Technology, and NEOWISE, which is a project of the Jet Propulsion Laboratory/California Institute of Technology. *WISE* and NEOWISE are funded by the National Aeronautics and Space Administration.

Facilities: Sloan (SDSS), *WISE*, 2.4 m/YAO (YFOSC), MMT (Red Channel spectrograph), 2.16 m/NAOC (BFOSC), 2.3 m/ANU (WiFeS), Bok/Steward Observatory(B&C).

REFERENCES

Avni, Y., & Bahcall, J. N. 1980, ApJ, 235, 694
Bañados, E., Venemans, B. P., Morganson, E., et al. 2015, ApJ, 804, 118
Becker, G. D., Bolton, J. S., Madau, P., et al. 2015, MNRAS, 447, 3402
Becker, R. H., White, R. L., & Helfand, D. J. 1995, ApJ, 450, 559
Bolton, J. S., Becker, G. D., Raskutti, S., et al. 2012, MNRAS, 419, 2880
Bolton, J. S., & Haehnelt, M. G. 2007, MNRAS, 382, 325
Bongiorno, A., Zamorani, G., Gavignaud, I., et al. 2007, A&A, 472, 443
Boroson, T. A., & Green, R. F. 1992, ApJS, 80, 109
Boyle, B. J., Shanks, T., Croom, S. M., et al. 2000, MNRAS, 317, 1014
Brown, M. J. I., Brand, K., Dey, A., et al. 2006, ApJ, 638, 88
Cirasuolo, M., Magliocchetti, M., Celotti, A., & Danese, L. 2003, MNRAS, 341, 993
Condon, J. J., Cotton, W. D., Greisen, E. W., et al. 1998, AJ, 115, 1693
Croom, S. M., Richards, G. T., Shanks, T., et al. 2009, MNRAS, 399, 1755
Croom, S. M., Smith, R. J., Boyle, B. J., et al. 2004, MNRAS, 349, 1397
Fan, X. 1999, AJ, 117, 2528

Fan, X., Carilli, C. L., & Keating, B. 2006, ARA&A, 44, 415
Fan, X., Narayanan, V. K., Lupton, R. H., et al. 2001a, AJ, 122, 2833
Fan, X., Strauss, M. A., Schneider, D. P., et al. 1999, AJ, 118, 1
Fan, X., Strauss, M. A., Schneider, D. P., et al. 2001b, AJ, 121, 54
Finlator, K., Oh, S. P., Özel, F., & Davé, R. 2012, MNRAS, 427, 2464
Glikman, E., Bogosavljević, M., Djorgovski, S. G., et al. 2010, ApJ, 710, 1498
Glikman, E., Helfand, D. J., & White, R. L. 2006, ApJ, 640, 579
Goldschmidt, P., Kukula, M. J., Miller, L., & Dunlop, J. S. 1999, ApJ, 511, 612
Hooper, E. J., Impey, C. D., Foltz, C. B., & Hewett, P. C. 1995, ApJ, 445, 62
Ivezić, Ž, Menou, K., Knapp, G. R., et al. 2002, AJ, 124, 2364
Jiang, L., Fan, X., Annis, J., et al. 2008, AJ, 135, 1057
Jiang, L., Fan, X., Cool, R. J., et al. 2006, AJ, 131, 2788
Jiang, L., Fan, X., Ivezić, Ž, et al. 2007, ApJ, 656, 680
Kashikawa, N., Ishizaki, Y., Willott, C. J., et al. 2015, ApJ, 798, 28
Kellermann, K. I., Sramek, R., Schmidt, M., Shaffer, D. B., & Green, R. 1989, AJ, 98, 1195
Komatsu, E., Dunkley, J., Nolta, M. R., et al. 2009, ApJS, 180, 330
Kratzer, R. M., & Richards, G. T. 2015, AJ, 149, 61
Kuhn, O., Elvis, M., Bechtold, J., & Elston, R. 2001, ApJS, 136, 225
La Franca, F., Gregorini, L., Cristiani, S., de Ruiter, H., & Owen, F. 1994, AJ, 108, 1548
Lampton, M., Margon, B., & Bowyer, S. 1976, ApJ, 208, 177
Laor, A. 2000, ApJL, 543, L111
Lupton, R. H., Gunn, J. E., & Szalay, A. S. 1999, AJ, 118, 1406
Madau, P., Haardt, F., & Rees, M. J. 1999, ApJ, 514, 648
Marshall, H. L., Tananbaum, H., Avni, Y., & Zamorani, G. 1983, ApJ, 269, 35
Masters, D., Capak, P., Salvato, M., et al. 2012, ApJ, 755, 169
McGreer, I. D., Helfand, D. J., & White, R. L. 2009, AJ, 138, 1925
McGreer, I. D., Jiang, L., Fan, X., et al. 2013, ApJ, 768, 105
McGreer, I. D., Mesinger, A., & D'Odorico, V. 2015, MNRAS, 447, 499
McQuinn, M., Oh, S. P., & Faucher-Giguère, C.-A. 2011, ApJ, 743, 82
Meiksin, A. 2005, MNRAS, 356, 596
Padovani, P. 1993, MNRAS, 263, 461
Page, M. J., & Carrera, F. J. 2000, MNRAS, 311, 433
Pãris, I., Petitjean, P., & Ross, N. P. 2016, arXiv:1608.06483
Rees, M. J., Begelman, M. C., Blandford, R. D., & Phinney, E. S. 1982, Natur, 295, 17
Richards, G. T., Croom, S. M., Anderson, S. F., et al. 2005, MNRAS, 360, 839
Richards, G. T., Fan, X., Newberg, H. J., et al. 2002, AJ, 123, 2945
Richards, G. T., Strauss, M. A., Fan, X., et al. 2006, AJ, 131, 2766
Ross, N. P., McGreer, I. D., White, M., et al. 2013, ApJ, 773, 14
Schmidt, M. 1968, ApJ, 151, 393
Schneider, D. P., Richards, G. T., Hall, P. B., et al. 2010, AJ, 139, 2360
Schneider, D. P., Schmidt, M., & Gunn, J. E. 1991, AJ, 102, 837
Selsing, J., Fynbo, J. P. U., Christensen, L., & Krogager, J.-K. 2016, A&A, 585, A87
Shull, J. M., Harness, A., Trenti, M., & Smith, B. D. 2012, ApJ, 747, 100
Songaila, A., & Cowie, L. L. 2010, ApJ, 721, 1448
Stern, D., Djorgovski, S. G., Perley, R. A., de Carvalho, R. R., & Wall, J. V. 2000, AJ, 119, 1526
Stevans, M. L., Shull, J. M., Danforth, C. W., & Tilton, E. M. 2014, ApJ, 794, 75
Tsuzuki, Y., Kawara, K., Yoshii, Y., et al. 2006, ApJ, 650, 57
Vanden Berk, D. E., Richards, G. T., Bauer, A., et al. 2001, AJ, 122, 549
Vestergaard, M., & Wilkes, B. J. 2001, ApJS, 134, 1
Wang, F., Wu, X.-B., Fan, X., et al. 2016, ApJ, 819, 24 (Paper I)
Willott, C. J., Delorme, P., Reylé, C., et al. 2010, AJ, 139, 906
Wilson, A. S., & Colbert, E. J. M. 1995, ApJ, 438, 62
Wolf, C., Wisotzki, L., Borch, A., et al. 2003, A&A, 408, 499
Worseck, G., & Prochaska, J. X. 2011, ApJ, 728, 23
Wright, E. L., Eisenhardt, P. R. M., Mainzer, A. K., et al. 2010, AJ, 140, 1868
Yip, C. W., Connolaly, A. J., Vanden Berk, D. E., et al. 2004, AJ, 128, 2603
Yuan, H., Zhang, H., Zhang, Y., et al. 2013, A&C, 3, 65

The Astrophysical Journal, 817:114 (13pp), 2016 February 1
doi:10.3847/0004-637X/817/2/114

A LUMINOUS PECULIAR TYPE IA SUPERNOVA SN 2011HR: MORE LIKE SN 1991T OR SN 2007if?

Ju-Jia Zhang[1,2,3], Xiao-Feng Wang[3], Michele Sasdelli[4,5], Tian-Meng Zhang[6], Zheng-Wei Liu[7], Paolo A. Mazzali[4,5], Xiang-Cun Meng[1,2], Keiichi Maeda[8,9], Jun-Cheng Chen[3], Fang Huang[3], Xu-Lin Zhao[3], Kai-Cheng Zhang[3], Qian Zhai[1,2,10], Elena Pian[11,12], Bo Wang[1,2], Liang Chang[1,2], Wei-Min Yi[1,2], Chuan-Jun Wang[1,2,10], Xue-Li Wang[1,2], Yu-Xin Xin[1,2], Jian-Guo Wang[1,2], Bao-Li Lun[1,2], Xiang-Ming Zheng[1,2], Xi-Liang Zhang[1,2], Yu-Feng Fan[1,2], and Jin-Ming Bai[1,2]

[1] Yunnan Observatories (YNAO), Chinese Academy of Sciences, Kunming 650011, China; jujia@ynao.ac.cn
[2] Key Laboratory for the Structure and Evolution of Celestial Objects, Chinese Academy of Sciences, Kunming 650011, China
[3] Physics Department and Tsinghua Center for Astrophysics (THCA), Tsinghua University, Beijing 100084, China; wang_xf@mail.tsinghua.edu.cn
[4] Astrophysics Research Institute, Liverpool John Moores University, Liverpool Science Park, 146 Brownlow Hill, Liverpool L3 5RF, UK
[5] Max-Planck Institute fur Astrophysics, D-85748 Garching, Germany
[6] National Astronomical Observatories of China (NAOC), Chinese Academy of Sciences, Beijing 100012, China
[7] Argelander-Institut für Astronomie, Auf dem Hügel 71, D-53121, Bonn, Germany
[8] Department of Astronomy, Kyoto University, Kyoto, 606-8502, Japan
[9] Kavli Institute for the Physics and Mathematics of the Universe (WPI), University of Tokyo, 5-1-5 Kashiwanoha, Kashiwa, Chiba 277-8583, Japan
[10] University of Chinese Academy of Sciences, Beijing 100049, China
[11] INAF-IASF-Bo, via Gobetti, 101, I-40129 Bologna, Italy
[12] Scuola Normale Superiore, Piazza dei Cavalieri 7, I-56126 Pisa, Italy

Received 2015 September 8; accepted 2015 December 12; published 2016 January 26

ABSTRACT

Photometric and spectroscopic observations of a slowly declining, luminous Type Ia supernova (SN Ia) SN 2011hr in the starburst galaxy NGC 2691 are presented. SN 2011hr is found to peak at $M_B = -19.84 \pm 0.40$ mag, with a postmaximum decline rate $\Delta m_{15}(B) = 0.92 \pm 0.03$ mag. From the maximum-light bolometric luminosity, $L = (2.30 \pm 0.90) \times 10^{43}$ erg s^{-1}, we estimate the mass of synthesized ^{56}Ni in SN 2011hr to be $M(^{56}\mathrm{Ni}) = 1.11 \pm 0.43\,M_\odot$. SN 2011hr appears more luminous than SN 1991T at around maximum light, and the absorption features from its intermediate-mass elements (IMEs) are noticeably weaker than those of the latter at similar phases. Spectral modeling suggests that SN 2011hr has IMEs of $\sim 0.07\,M_\odot$ in the outer ejecta, which is much lower than the typical value of normal SNe Ia (i.e., 0.3–0.4 $M_\odot$) and is also lower than the value of SN 1991T (i.e., $\sim 0.18\,M_\odot$). These results indicate that SN 2011hr may arise from a Chandrasekhar-mass white dwarf progenitor that experienced a more efficient burning process in the explosion. Nevertheless, it is still possible that SN 2011hr may serve as a transitional object connecting the SN 1991T-like SNe Ia with a superluminous subclass like SN 2007if given that the latter also shows very weak IMEs at all phases.

Key words: galaxies: individual (NGC 2691) – supernovae: general – supernovae: individual (SN 2011hr, SN 1991T, SN 2007if)

1. INTRODUCTION

Type Ia supernovae (SNe Ia), one of the most luminous stellar explosions, could explode within a similar mechanism: complete explosive destruction of a carbon–oxygen white dwarf (C–O WD) reaching the Chandrasekhar-mass limit (i.e., $\sim 1.4\,M_\odot$ for the C–O WD without rotation), most likely via accretion in a binary system, although other channels have been proposed (see, e.g., the review by Maoz et al. 2014). They show strikingly similar photometric and spectroscopic behavior in the optical (i.e., Suntzeff 1996; Filippenko 1997), and the remaining scatter can be better understood in terms of an empirical relation between light-curve width (i.e., $\Delta m_{15}(B)$) and luminosity (i.e., width–luminosity relation [WLR]; Phillips 1993). Based on that relation, SNe Ia have been successfully applied as luminosity distance indicators for measuring the expansion history of the universe (Riess et al. 1998; Schmidt et al. 1998; Perlmutter et al. 1999).

Observationally, SNe Ia could be divided into several different subclasses according to their spectral characteristics (Benetti 2005; Branch et al. 2009; Wang et al. 2009a). For example, SN 1991T (Filippenko et al. 1992b; Phillips et al. 1992) is spectroscopically different from the bulk of SNe Ia, lying at the luminous end of luminosity distribution. Its featureless spectra at early phase are characterized by appearances of strong Fe III lines and weak or absent lines of intermediate-mass elements (IMEs; e.g., Si II, S II, and Ca II), which are usually strong in the spectra of normal SNe Ia. It had a slowly declining light curve (e.g., $\Delta m_{15}(B) = 0.94$; Lira et al. 1998) and is ∼0.6 mag more luminous than normal ones (Filippenko et al. 1992b). However, Gibson & Stetson (2001) suggested that SN 1991T is indistinguishable from normal SNe Ia in luminosity. Altavilla et al. (2004) also showed that SN 1991T fits in the WLR and that its peculiarities are only spectroscopic. Through modeling of a series of early spectra, Mazzali et al. (1995) found that the absence of Fe II, Si II, and Ca II lines and the presence of strong Fe III lines are due to the low abundance of IMEs and the high ionization caused by the high luminosity. Superluminous SNe Ia such as SN 2003fg (Howell et al. 2006), SN 2006gz (Hichen et al. 2007), SN 2007if (Scalzo et al. 2010), and SN 2009dc (Taubenberger et al. 2010; Silverman et al. 2011; Hachinger et al. 2012) are called super-Chandrasekhar (SC) SN Ia candidates. These SNe Ia are required to have progenitor masses exceeding the Chandrasekhar-mass limit if their luminosities are entirely attributed to the radioactive decay of ^{56}Ni.

In this paper, we present observations of SN 2011hr (R. A. = $08^{\mathrm{h}}54^{\mathrm{m}}46\overset{\mathrm{s}}{.}03$, decl. = $+39^\circ32'16\overset{''}{.}1$), which was discovered on UT 2011 November 8.54 (UT time is used throughout this paper) by the Katzman Automatic Imaging Telescope, Lick Observatory, USA (Nayak et al. 2011). The supernova is located $3\farcs4$ west and $3\farcs7$ north of the center of NGC 2691, which is equivalent to a projected distance ~1.5 kpc using the distance of the host adopted in this paper (i.e., $D \approx 60.0$ Mpc). Two days after the discovery, an optical spectrum was taken with the Li-Jiang 2.4 m telescope (hereafter LJT) of Yunnan observatories (YNAO), China, showing that it was a young SN 1991T-like SN Ia at about 10 days before maximum light, with prominent iron lines in the spectrum (Zhang et al. 2011). A follow-up photometric and spectroscopic observing campaign was immediately established for SN 2011hr.

This paper is organized as follows. Photometric observations and data reductions are described in Section 2, where the light and color curves are investigated. Section 3 presents the spectroscopic observations. In Section 4 we derive the bolometric luminosity and the mass of ^{56}Ni synthesized in the explosion, and we model the early-time spectra using abundance tomography. Moreover, a possible explosion mechanism is also discussed in this section. A brief summary is given in Section 5.

2. PHOTOMETRY

2.1. Observations and Data Reduction

The photometric observations of SN 2011hr were performed in broad *UBVRI* bands with the Tsinghua-NAOC 0.8 m telescope (hereafter TNT; Wang et al. 2008; Huang et al. 2012) at Xing-Long Observatory of NAOC. This telescope is equipped with a 1340 × 1300 CCD (PI VersArray: 1300B), providing a field of view (FOV) of $11\farcm5 \times 11\farcm2$ with a spatial resolution of $\sim 0\farcs52$ pixel^{-1}. The typical exposure times are 180 s in the *BVRI* bands and 300 s in the *U* band when taking images of SN 2011hr. These images have typical FWHM of about $2\farcs5$. The CCD images were reduced using standard IRAF routines. The data collections started from $t \approx -14$ days and lasted until $t \approx +70$ days relative to the *B*-band maximum light. All CCD images were reduced using the IRAF[13] standard procedure.

Since SN 2011hr exploded near the center of its host galaxy, the step of subtracting the galaxy template from the SN images is necessary for accurate photometry, in particular when the SN became faint and/or the images were taken under poor seeing conditions. Higher-quality template images were obtained with the TNT on 2013 May 11, when the SN was sufficiently faint. Using the galaxy-subtracted images, we measured the instrumental magnitudes of the SN and the local standard stars (labeled in Figure 1) by aperture photometry, performed using the IRAF DAOPHOT package (Stetson 1987). The radius for the photometric aperture is set as 2.0 times the FWHM; the sky background light was determined from the median counts at a radius that is 5.0 times the FWHM. Twelve local standard stars in the field of SN 2011hr are labeled in Figure 1. We transformed the instrumental magnitudes of these reference stars to the standard Johnson *UBV* (Johnson et al. 1966) and Kron–Cousins *RI* (Cousins 1981) systems through the following transforming equations (Huang et al. 2012):

$$\begin{aligned} U &= u + 0.22(U - B), && (1) \\ B &= b + 0.15(B - V), && (2) \\ V &= v - 0.06(B - V), && (3) \\ R &= r - 0.10(V - R), && (4) \\ I &= i + 0.02(V - I), && (5) \end{aligned}$$

where *UBVRI* represent the magnitudes in the standard system and *ubvri* represent the instrumental magnitudes. The color term coefficient was determined by observing Landolt (1992) standards on photometric nights. The magnitudes of these reference stars are listed in Table 1, and they are then used to convert the photometry of SN 2011hr to the standard *UBVRI* magnitudes as shown in Table 2.

2.2. Light Curves

Figure 2 displays the *UBVRI*-band light curves of SN 2011hr (see details in Table 2). Some basic photometric parameters such as the maximum-light dates, peak magnitudes, and magnitude decline rates (Δm_{15}; Phillips 1993) can be derived from a polynomial fit to the observed light curves, which are listed in Table 3. We find that SN 2011hr reached a *B*-band maximum brightness of 14.95 ± 0.03 mag on JD $2{,}455{,}889.62 \pm 0.30$ (2011 November 23.12), with a decline rate $\Delta m_{15}(B) = 0.92 \pm 0.03$ mag. The slower decline rate suggests that SN 2011hr should be intrinsically luminous if it follows the WLR (e.g., Phillips 1993; Riess et al. 1996; Goldhaber et al. 2001; Guy et al. 2005); see also Table 3 and detailed discussion in Section 2.5. After correcting for a Galactic reddening of $E(B - V) = 0.02$ mag (Schlegel et al. 1998), the color index $B_{\rm max} - V_{\rm max}$ becomes 0.23 ± 0.04 mag. On the other hand, the corresponding color index is about 0.13 ± 0.03 mag for SN 1991T. This suggests that both SN 2011hr and SN 1991T suffer a significant host-galaxy reddening assuming that their intrinsic colors are comparable to that established for normal SNe Ia (e.g., Phillips et al. 1999; Wang et al. 2009b); see also Sections 2.3 and 2.4.

Overplotted in Figure 2 are the light curves of other well-observed SNe, including overluminous SN Ia SN 1991T ($\Delta m_{15} = 0.94$ mag; Sasdelli et al. 2014 and therein), SN 1999aa ($\Delta m_{15}(B) = 0.83$ mag; Jha et al. 2006), the "golden standard" SN Ia SN 2005cf ($\Delta m_{15}(B) = 1.05$ mag; Wang et al. 2009b), the superluminous SN 2007if ($\Delta m_{15}(B) = 0.71$; Scalzo et al. 2010) and SN 2009dc ($\Delta m_{15}(B) = 0.71$; Taubenberger et al. 2010). In general, SN 2011hr shows a close resemblance to SN 1991T in *UBVRI*-band photometry. Compared to SN 2011hr/SN 1991T, the superluminous object SN 2009dc shows apparently broader light curves, especially in the redder bands, where its secondary maximum/shoulder feature is more prominent. Note that another so-called superluminous SN Ia, SN 2007if, is found to be more similar in morphology to SN 2011hr/SN 1991T.

2.3. Color Curves

Figure 3 shows the color curves of SN 2011hr. Overplotted are the color curves of SN 1991T, SN 1999aa, SN 2005cf, SN 2007if, and SN 2009dc. All of these color curves (including those of SN 2011hr) are corrected for the reddening of the Milky Way and the host galaxy. The reddening of SN 2011hr is discussed in the following section.

---

[13] IRAF, the Image Reduction and Analysis Facility, is distributed by the National Optical Astronomy Observatory, which is operated by the Association of Universities for Research in Astronomy (AURA), Inc., under cooperative agreement with the National Science Foundation (NSF).

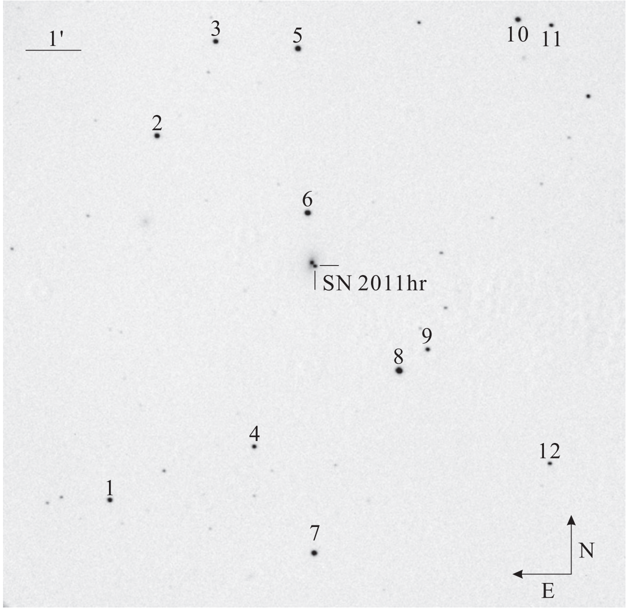

Figure 1. *R*-band image of SN 2011hr, which was taken on 2011 November 14.81 with the Tsinghua-NAOC 0.8 m telescope. The mean FWHM of this image is 2.″60 under the scale of 0.″52 pixel^{-1}. The supernova and reference stars are marked. North is up, and east is to the left.

Table 1
Magnitudes of the Photometric Standards in the Field of SN 2011hr

Star	*U*(mag)	*B*(mag)	*V*(mag)	*R*(mag)	*I*(mag)
1	16.01(03)	15.27(02)	14.50(03)	14.00(02)	13.66(02)
2	14.15(02)	14.15(02)	13.78(02)	13.48(02)	13.32(01)
3	17.03(04)	15.66(02)	14.58(03)	13.79(02)	13.33(01)
4	17.99(04)	16.61(03)	15.31(03)	14.39(02)	13.72(02)
5	16.06(03)	14.81(02)	13.88(02)	13.22(02)	12.88(01)
6	16.27(03)	14.96(03)	13.71(02)	12.99(02)	12.46(01)
7	14.36(03)	14.26(02)	13.67(02)	13.35(02)	13.17(02)
8	13.94(02)	13.47(01)	12.76(01)	12.40(01)	12.15(01)
9	15.91(03)	15.53(02)	14.91(03)	14.52(02)	14.26(02)
10	16.57(04)	15.67(03)	14.44(03)	13.48(03)	12.76(03)
11	17.30(05)	16.28(04)	15.38(04)	14.70(04)	14.39(04)
12	16.41(03)	16.13(02)	15.39(03)	14.96(03)	14.67(02)

Note. Uncertainties, in units of 0.01 mag, are 1σ. Figure 1 shows a finding chart of SN 2011hr and the comparison stars.

At early time, the $U-B$ colors of the luminous/super-luminous SNe Ia (including SN 2011hr) show distinct behavior compared to the normal SN 2005cf. The former group tends to become progressively redder after explosion, while SN 2005cf shows a "red–blue–red" evolutionary trend at a similar phase. At around maximum light, the $B-V$ color of SN 2011hr and SN 1991T is redder than that of other comparison SNe Ia. SN 2011hr and SN 1991T are also found to be redder by 0.1–0.2 mag than predicted by the Lira–Phillips relation (Phillips et al. 1999; see solid line in Figure 3). Among our comparison sample, SN 2009dc shows the bluest $U-B$ and $B-V$ colors at $t < +35$ days, while it (and SN 2007if) shows redder $V-R$ and $V-I$ colors. Large scatter can be seen in the $V-I$ color, where the strength of the Ca II near-IR (NIR) triplet could have a dominant effect. In general, SN 2011hr shows a color evolution that is quite similar to that of SN 1991T and SN 2007if at all phases.

2.4. Extinction

The Milky Way reddening of SN 2011hr is $E(B-V)_{\rm Gal} = 0.02$ mag (Schlegel et al. 1998), corresponding to an extinction of 0.06 mag adopting the standard Galactic reddening law (i.e., $R_V = 3.1$; Cardelli et al. 1989). The reddening due to the host galaxy can be estimated by several empirical methods. For instance, a comparison of the late-time $B-V$ color with that predicted by the Lira–Phillips relation (Phillips et al. 1999) gives a host-galaxy reddening of $E(B-V)_{\rm host} = 0.29 \pm 0.07$ mag for SN 2011hr. The peak $B_{\rm max}-V_{\rm max}$ color has also been used as a better reddening indicator for SNe Ia (Phillips et al. 1999; Wang et al. 2009b), based on its dependence on $\Delta m_{15}(B)$. For SN 2011hr, the observed peak $B-V$ color is 0.23 ± 0.04 mag, which suggests a host-galaxy reddening of $E(B-V) = 0.32 \pm 0.06$ mag. However, a scatter of about 0.1 mag might exist for the above estimates considering that such overluminous SNe Ia may have intrinsically different colors relative to the normal SNe Ia.

The low-resolution spectra of SN 2011hr show prominent signatures of Na I D absorption, for which the equivalent width (EW) of this absorption can be derived by using a double-Gaussian fit as shown in Figure 4. The best fit yields EW (Na I D) $= 1.42 \pm 0.02$ Å with $\mathrm{EW}_{\rm D1} = 0.84 \pm 0.01$ Å and $\mathrm{EW}_{\rm D2} = 0.58 \pm 0.01$ Å. Based on an empirical correlation between reddening and the EW of Na I D, namely, $E(B-V) = 0.16\,\mathrm{EW} - 0.01$ [Å] (Turatto et al. 2003), we estimate $E(B-V)_{\rm host}$ to be 0.22 ± 0.10 mag for SN 2011hr, which is consistent with the result derived from the photometric $B-V$ color within 1σ error.

Combining the results from both photometry and Na I D absorption, a host-galaxy reddening of $E(B-V)_{\rm host} = 0.25 \pm 0.10$ can be obtained for SN 2011hr. On the other hand, the spectral modeling presented in Section 4.3 suggests a moderate host-galaxy reddening, i.e., $E(B-V)_{\rm host} = 0.15$ mag, which seems to be more reasonable as it matches the observed colors. Therefore, a mean value $E(B-V)_{\rm total} = 0.22 \pm 0.05$ mag is adopted as the total reddening of SN 2011hr in this paper.

2.5. Distance

The actual luminosity of SN 2011hr is affected by the uncertainty in the distance to the SN. Table 4 lists the measurements obtained using different methods. One can see that these measurements show significant dispersion. For example, the distance derived from the redshift of the host galaxy NGC 2691 and the Hubble flow is 59.3 ± 4.0 Mpc (Mould et al. 2000), which agrees with the result from the Tully–Fisher relation (60.2 ± 10.0 Mpc; Theureau et al. 2007). These two values are larger than the luminosity distance derived for the SN using the original Phillips (1993) relation but close to that derived from the modified relation for 91T-like events in Blondin et al. (2012), as listed in Table 4.

On the other hand, we can also estimate the distance to SN 2011hr based on its NIR magnitude, since the *JHK*-band luminosities of SNe Ia are relatively insensitive to the reddening and are more uniform around the peak compared to the corresponding values in the optical bands (Meikle 2000; Krisciunas et al. 2004; Barone-Nugent et al. 2012). Additionally, some peculiar SNe Ia such as SN 1999aa, SN 1999ac, and SN 1999aw are found to have normal luminosities in the NIR bands (Krisciunas et al. 2004), though they appear somewhat

Table 2
The *UBV RI* Photometry of SN 2011hr

MJD	Epoch[a]	*U* (mag)	*B* (mag)	*V* (mag)	*R* (mag)	*I* (mag)
55,874.04	−15.08	⋯	⋯	⋯	16.90(20)	⋯
55,875.08	−14.04	⋯	⋯	⋯	17.10(20)	⋯
55,875.34	−13.78	16.17(08)	16.90(03)	16.71(02)	16.53(02)	16.43(02)
55,876.36	−12.76	⋯	16.47(02)	16.24(01)	15.98(02)	16.01(01)
55,878.32	−10.80	⋯	15.91(02)	15.71(04)	15.59(02)	15.41(01)
55,879.30	−9.82	15.00(05)	15.60(02)	15.38(02)	15.33(01)	15.24(01)
55,880.31	−8.81	14.89(05)	15.41(02)	15.22(01)	15.10(01)	15.15(03)
55,890.31	1.19	14.71(03)	14.97(02)	14.76(01)	14.63(01)	14.84(01)
55,892.31	3.19	14.82(03)	15.01(02)	14.73(01)	14.62(01)	14.83(01)
55,899.36	10.24	15.33(04)	15.40(02)	14.97(05)	14.93(01)	15.27(04)
55,904.33	15.21	16.03(08)	15.93(02)	15.26(01)	15.12(04)	15.24(03)
55,905.33	16.21	⋯	⋯	15.29(05)	15.18(04)	15.23(05)
55,906.31	17.19	16.28(05)	16.06(03)	15.36(02)	15.22(03)	15.28(01)
55,907.33	18.21	16.45(06)	16.18(04)	15.43(01)	15.32(01)	15.26(01)
55,910.35	21.23	⋯	⋯	15.54(04)	15.47(06)	15.24(05)
55,911.33	22.21	17.00(05)	16.69(02)	15.59(05)	15.51(04)	15.25(04)
55,912.33	23.21	17.07(05)	16.79(05)	15.63(01)	15.47(01)	15.19(03)
55,915.26	26.14	17.37(05)	17.01(03)	15.81(01)	15.43(01)	15.22(04)
55,916.31	27.19	17.38(05)	17.18(02)	15.84(05)	15.52(02)	15.26(02)
55,917.33	28.21	17.47(09)	17.18(02)	15.89(05)	15.59(01)	15.29(03)
55,918.31	29.19	17.54(06)	17.21(07)	15.94(01)	15.51(01)	15.26(04)
55,919.25	30.13	17.58(10)	17.31(02)	15.99(01)	15.51(01)	15.26(03)
55,920.39	31.27	17.61(05)	17.37(01)	16.06(05)	15.60(01)	15.29(02)
55,927.23	38.11	18.02(06)	17.65(07)	16.28(05)	15.93(05)	15.55(05)
55,929.24	40.12	18.13(06)	17.77(08)	16.42(05)	16.03(05)	15.64(06)
55,930.17	41.05	18.18(10)	17.78(04)	16.49(05)	16.11(04)	15.68(08)
55,931.21	42.09	18.20(09)	17.82(04)	16.53(04)	16.13(02)	15.78(02)
55,932.21	43.09	18.23(06)	17.88(05)	16.55(04)	16.23(01)	15.84(03)
55,935.19	46.07	18.26(07)	17.96(04)	16.69(04)	16.39(01)	16.04(02)
55,936.20	47.08	18.32(05)	17.88(03)	16.74(05)	16.42(04)	16.17(05)
55,937.11	47.99	⋯	⋯	⋯	16.48(03)	⋯
55,938.21	49.09	18.31(09)	17.92(04)	16.76(05)	16.51(05)	16.19(03)
55,939.25	50.13	18.34(10)	17.95(03)	16.82(04)	16.52(08)	16.35(02)
55,941.08	51.96	18.46(08)	18.01(03)	16.92(05)	16.55(03)	16.39(06)
55,954.12	65.00	18.56(10)	18.11(03)	17.21(02)	16.91(05)	16.87(05)
55,955.30	66.18	18.62(12)	18.12(07)	17.28(04)	17.04(05)	⋯
55,956.08	66.96	18.63(12)	18.19(08)	17.31(05)	17.08(05)	16.99(07)
55,958.06	68.94	⋯	⋯	17.34(07)	17.14(06)	⋯
55,959.10	69.98	⋯	18.27(08)	17.36(07)	17.21(08)	⋯

Note. Uncertainties, in units of 0.01 mag, are 1σ; MJD = JD − 2,400,000.5.
[a] Relative to the epoch of *B*-band maximum on 2011 November 23.49, JD 2,455,889.62.

peculiar in optical bands. Based on the NIR photometry of 13 SNe Ia (including SN 2011hr), Weyant et al. (2014) estimated their mean absolute peak magnitude as -18.31 ± 0.02 mag in the *H* band. Taking the observed *H*-band peak magnitude of 15.02 ± 0.20 mag for SN 2011hr (Weyant et al. 2014) and assuming that it has a similar absolute *H*-band magnitude, we get a distance modulus $m - M = 33.20 \pm 0.20$ mag or $D = 43.7 \pm 5.0$ Mpc. This estimate is much smaller than the Tully–Fisher distance and that inferred from the Hubble flow. Note, however, that the dispersion of the sample from Weyant et al. (2014) will decrease significantly from $\sigma_{\rm H} = 0.23$ mag to ~0.18 mag if SN 2011hr was excluded in the analysis. This is due to the fact that SN 2011hr is actually more luminous than normal SNe Ia by ~0.7 mag in the *H* band.

As the distance derived from Hubble expansion is independent of corrections for reddening and agrees well with the estimate from the Tully–Fisher relation, a distance of $D = 60.0 \pm 6.0$ Mpc is thus adopted for SN 2011hr in this paper.

3. SPECTROSCOPY

3.1. Observations and Data Reduction

A journal of spectroscopic observation of SN 2011hr is given in Table 5. A total of 11 low-resolution spectra were obtained with the LJT, the Yunnan Faint Object Spectrograph and Camera (YFOSC; Zhang et al. 2014), the Xing-Long 2.16 m telescope (hereafter XLT), and the Beijing Faint Object Spectrograph and Camera (BFOSC). During our spectral observations, the typical FWHM was about 1″.5 at Lijiang Observatory and about 2″.5 at Xinglong Observatory. All spectra were reduced using standard IRAF routines. Flux calibration was done using spectrophotometric flux standard stars observed at a similar airmass on the same night. The spectra were further corrected for the atmospheric absorption and telluric lines at the site. Synthetic photometry computed using Bessell (1992) passbands was introduced to check the spectroscopic flux calibration, while the spectral fluxes were

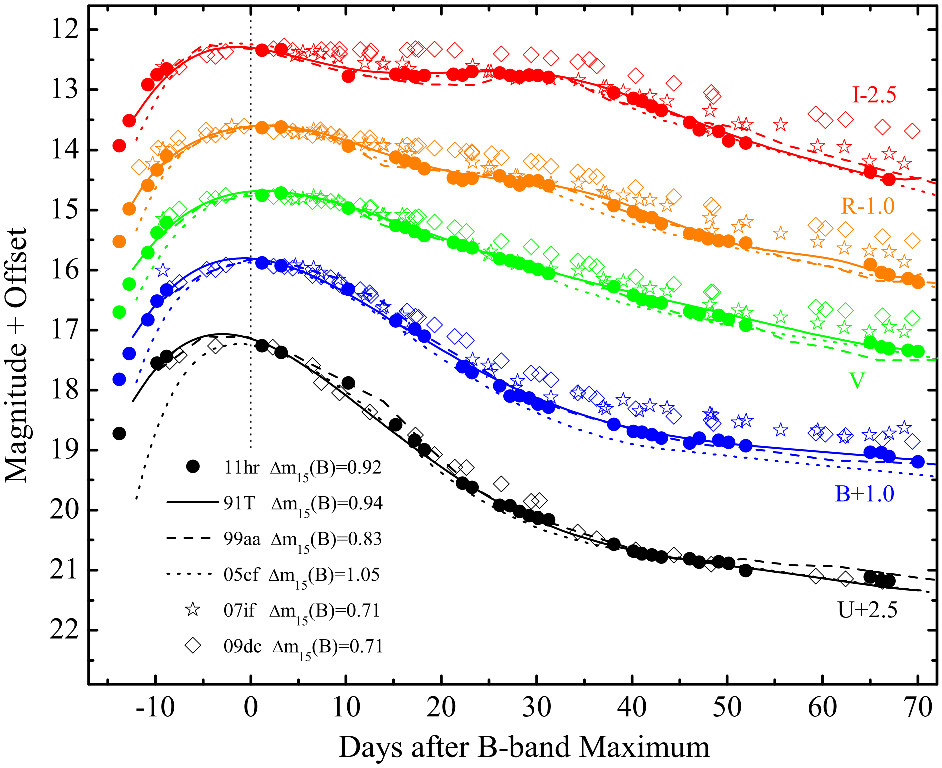

Figure 2. *UBVRI*-band light curves of SN 2011hr, compared with those of SN 1991T, SN 1999aa, SN 2005cf, SN 2007if, and SN 2009dc (see text for references). The light curves of SN 2011hr are shifted vertically by numbers as indicated in the plot, and those of the comparison SNe are normalized to the peak magnitudes of SN 2011hr. The light curves of SN 1991T, SN 1999aa, and SN 2005cf have been slightly smoothed with a low-order polynomial for a better display.

Table 3
Light-curve Parameters of SN 2011hr

Band	λ_{mid} (Å)	$t_{\rm max}$[a] (−2455000.5)	$m_{\rm peak}$[b] (mag)	Δm_{15}[b] (mag)	$M_{\rm peak}$[b] (mag)
U	3650	887.39(50)	14.63(03)	1.04(05)	−20.34(45)
B	4450	889.12(30)	14.95(02)	0.92(03)	−19.84(40)
V	5500	889.95(30)	14.70(03)	0.59(03)	−19.87(35)
R	6450	890.01(30)	14.62(02)	0.53(05)	−19.81(30)
I	7870	890.10(40)	14.70(03)	0.45(05)	−19.57(30)

Notes.
[a] 1σ uncertainties, in units of 0.01 days.
[b] 1σ uncertainties, in units of 0.01 mag.

adjusted to match the contemporaneous photometry. Figure 4 shows the complete spectral evolution of SN 2011hr.

3.2. Temporal Evolution of the Spectra

The spectra of SN 2011hr are described in more detail and compared to those of SN 1991T, SN 1999aa, SN 2005cf, SN 2007if, and SN 2009dc at different epochs in this section; see Figures 5, 6, and 7. All of these spectra have been corrected for redshift and reddening. The line identifications labeled in these figures are based on the modeling results for SN 1991T (Mazzali et al. 1995). The spectra of SN 2011hr have been corrected for the contamination of host-galaxy emission lines by using the spectrum taken at the site of SN 2011hr (with the LJT and YFOSC) at ~500 days after maximum light.

3.2.1. The Early Phase

Figure 5 displays the spectra at $t < -7$ days. At this phase, the spectra usually carry the signature of the ejecta materials in the outermost layers and show mainly lines of IMEs for normal SNe Ia. The spectra of SN 2011hr are rather similar to those of 91T-like events, which are characterized by a blue continuum and prominent Fe III/Fe II lines. Two main absorption features in SN 2011hr and SN 1991T are multiplets of Fe III or Fe II lines at 4404 and 5129 Å. By contrast, lines from IMEs (e.g., Si II, S II, and O I) are very weak, which is a common characteristic of 91T-like SNe Ia. Lines of Si III are also present in the spectra. This peculiar phenomenon is due to a combination of high photospheric temperature and low abundance of light elements in the ejecta (Mazzali et al. 1995; Sasdelli et al. 2014).

A notable difference between SN 2011hr and SN 1991T is the absorption near 3900 Å at $t \approx -10$ and -8 days. Such a feature could be a blend of Fe III λ4006 and Ni II λ4067. The spectrum of SN 1999aa at $t \approx -9$ days shows both strong Fe III lines and also a strong Ca II H&K feature, while the absorption of Si II λ6355 is weaker in this object. Spectral databases of SNe Ia (e.g., Blondin et al. 2012; Silverman et al. 2012) indicate that most SNe show strong Ca II absorption from very early phases to 4–5 months after explosion. However, as shown in Figure 8, the Ca II lines in the spectra of SN 2011hr are even weaker than those of SN 1991T at some phases after maximum light.

At $t < -7$ days, the spectrum of SN 2007if is also featureless and dominated by lines of doubly ionized Fe and Si. Ca II absorptions are also very weak at this phase. Note that the Fe III lines are weaker in SN 2007if compared to those in SN 2011hr at this phase. In SN 2007if, a weak absorption on

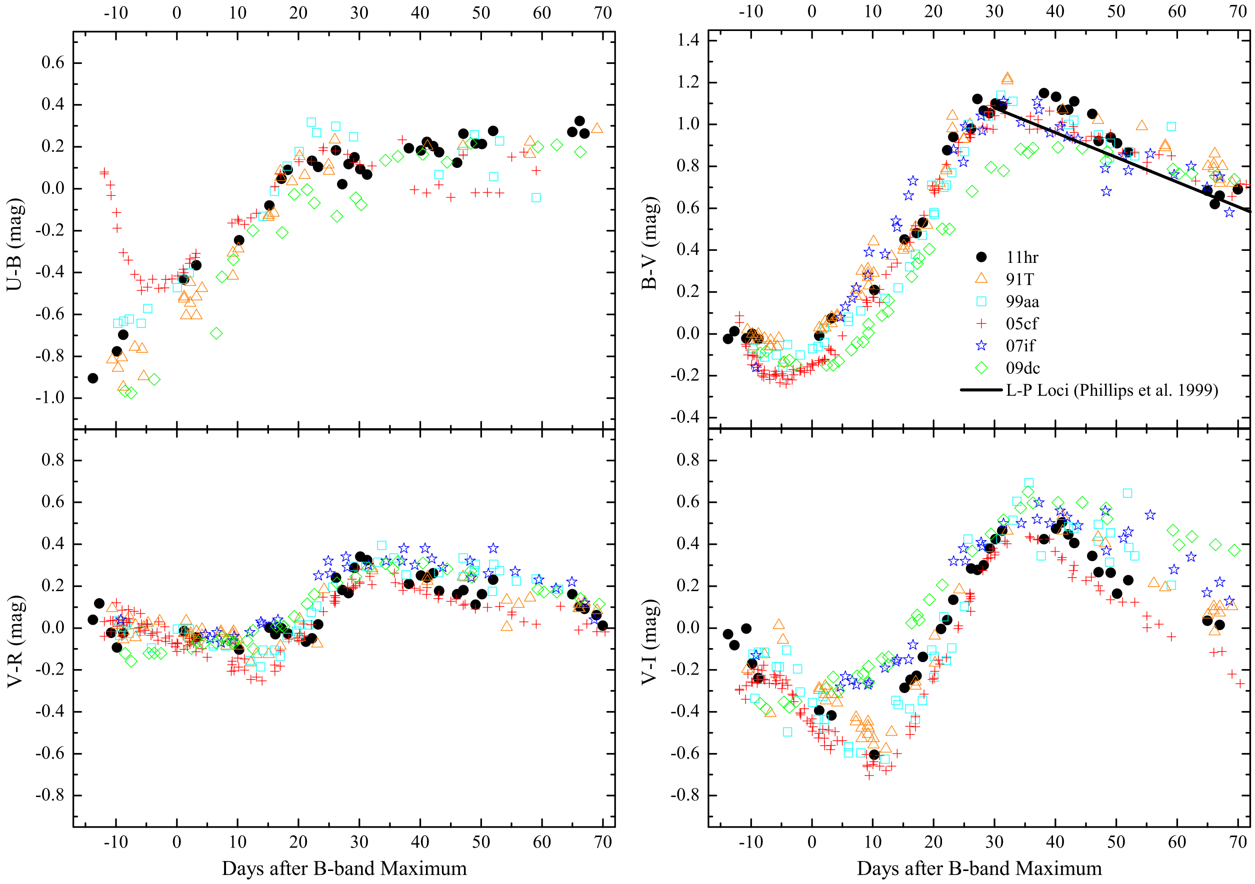

Figure 3. Optical color curves of SN 2011hr, in comparison with those of SN 1991T, SN 1999aa, SN 2005cf, SN 2007if, and SN 2009dc. See text for details.

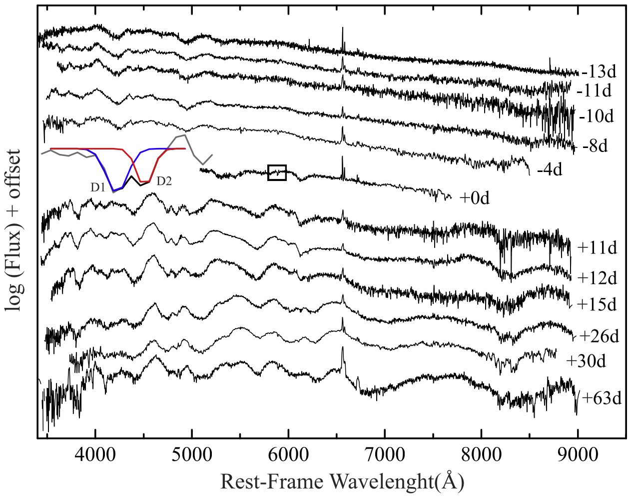

Figure 4. Optical spectral evolution of SN 2011hr. The spectra have been corrected for the redshift of the host galaxy ($v_{\rm hel} = 4137$ km s^{-1}) and telluric lines. They have been shifted vertically by arbitrary amounts for clarity. The numbers on the right-hand side mark the epochs of the spectra in days since the *B*-band maximum. The Na I D absorption of the host galaxy in the $t \approx +0$ day spectrum is indicated with a box, and the blow-up of this absorption is also shown on the left.

Table 4
Distances to SN 2011hr and NGC 2691

Method	Details	Results (Mpc)
Hubble flow[a]	4269 km s^{-1}	59.3 ± 4
Tully–Fisher[b]	*JHK* bands	60.2 ± 10
Phillips relation[c]	$E(B - V) = 0.17$	48.24 ± 8
Phillips relation[d]	$E(B - V) = 0.17$	56.58 ± 4
NIR luminous[e]	*H* band	43.7 ± 5

Notes.

[a] Corrected for Virgo infall, GA, and Shapley (Mould et al. 2000), on the scale of $H_0 = 72$ km s^{-1} Mpc^{-1}.

[b] Mean distance from estimates in the *JHK* bands (Theureau et al. 2007; Tully et al. 2009).

[c] $\Delta m_{15}(B) = 0.92$; Phillips (1993).

[d] Modified Phillips (1993) relation in Figure 13 of Blondin et al. (2012) for 91T-like events.

[e] Weyant et al. (2014).

the red side of the weak Si II λ6355 could be due to absorption from C II λ6580. The spectrum of SN 2009dc at $t \approx -9$ days is characterized by prominent C II λ6580 absorption, which is comparable in strength to the Si II λ6355. However, there is no evidence that such a strong C II feature is present in the early-time spectra of SN 2011hr, which shows differences from superluminous SNe Ia.

Figure 9 compares the Fe III features of SN 2011hr, SN 1991T, and SN 1999aa. Some Fe lines, identified by modeling performed in Section 4.3, are marked at a velocity of ~12,000 km s^{-1}. The absorption feature shown in the left panel of the plot is a blend of Fe III λ4397, λ4421, and λ4432 and is represented as Fe III (A). The feature shown in the right panel is a multiplet of Fe III λ5082, λ5129, and

Table 5
Journal of Spectroscopic Observations of SN 2011hr

Date	MJD (−2,400,000.5)	Epoch[a] (days)	Res. (Å pixel^{-1})	Range (Å)	Slit Width (pixel)	Exp. time (s)	Telescope (+Instrument)
2011 Nov 10	55,875.90	−13.22	1.5	5000–9800	2.8	1200	LJT YFSOC
2011 Nov 10	55,875.92	−13.20	1.8	3340–7680	2.8	1200	LJT YFSOC
2011 Nov 12	55,877.85	−11.27	2.9	3500–8890	4.2	1200	LJT YFSOC
2011 Nov 13	55,878.85	−10.27	1.5	5000–9800	4.2	1200	LJT YFSOC
2011 Nov 13	55,878.87	−10.25	1.8	3340–7680	4.2	1200	LJT YFSOC
2011 Nov 13	55,878.89	−10.23	2.9	3500–8890	4.2	1200	LJT YFSOC
2011 Nov 15	55,880.82	−8.30	2.9	3500–8890	4.2	1200	LJT YFSOC
2011 Nov 19	55,884.84	−4.28	4.1	3580–8565	3.0	3600	XLT BFOSC
2011 Nov 23	55,888.82	−0.30	2.1	5080–7690	3.0	1800	XLT BFOSC
2011 Dec 04	55,899.91	+10.79	2.9	3500–8890	6.4	900	LJT YFSOC
2011 Dec 05	55,900.93	+11.81	2.9	3500–8890	6.4	900	LJT YFSOC
2011 Dec 08	55,903.81	14.69	2.9	3500–8890	6.4	900	LJT YFSOC
2011 Dec 19	55,914.78	25.66	2.9	3500–8890	6.4	900	LJT YFSOC
2011 Dec 23	55,918.57	29.45	4.1	3780–8900	6.0	2700	XLT BFOSC
2012 Jan 25	55,951.76	62.64	2.9	3500–8890	6.4	3000	LJT YFSOC

Note. Journal of spectroscopic observations of SN 2011hr.
[a] Relative to *B*-band maximum on 2011 November 22.3, JD 2,455,889.62.

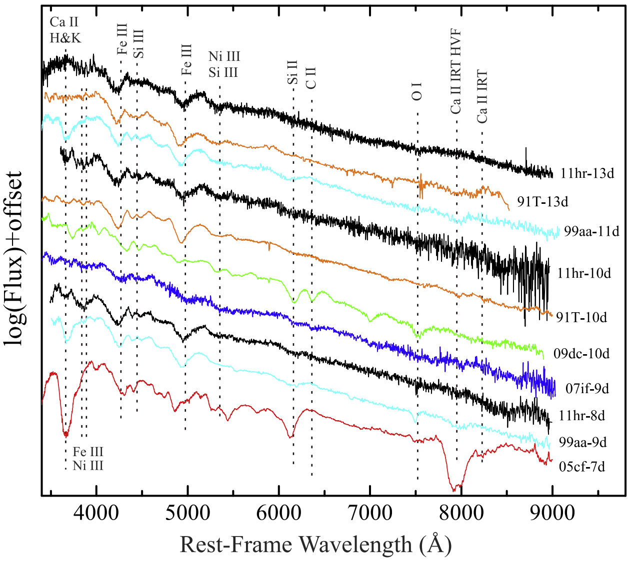

Figure 5. Spectra of SN 2011hr at $t < -7$ days before the *B*-band maximum light. Overplotted are the spectra of SN 1991T (Filippenko et al. 1992b), SN 1999aa (Garavini et al. 2004), and SN 2005cf (Wang et al. 2009b) at comparable phases. The spectra of SN 2011hr are corrected for contaminations of the host galaxy.

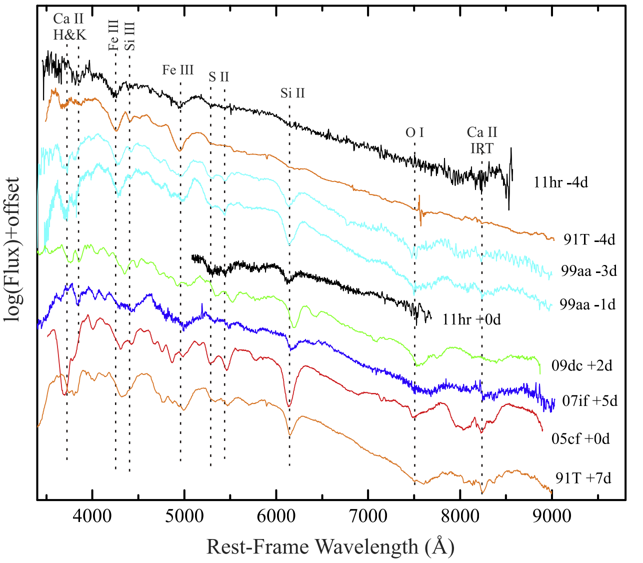

Figure 6. Spectra of SN 2011hr at around maximum light, compared to those of the same SNe Ia as in Figure 5.

λ5158 and is represented as Fe III (B). For the Fe III (A) feature, the three SNe Ia show similarities in the line strength, velocity, and shape at $t \approx -13$ days. For the Fe III (B) feature, SN 2011hr appears weaker than SN 1991T and SN 1999aa on the blue side of the absorption, which is more significant at earlier phases. It is unlikely that this difference is due to the absorption of Fe III λ5082 alone.

3.2.2. The Maximum-light Phase

Figure 6 shows the spectra at around maximum light. At $t \approx -4$ days, the Fe II/Fe III lines appear shallower and wider in SN 2011hr compared to SN 1991T. At this phase, the S II features at ∼5300 Å and ∼5450 Å start to emerge in the spectra of SN 2011hr and SN 1991T. These lines are useful to follow the shift of the ionization state of IMEs from doubly to singly ionized species. S II features in the spectra of SN 2011hr and SN 1991T are weaker than in SN 1999aa, suggesting a relatively lower ionization state for the latter. Moreover, the Fe III (B) absorption in SN 1999aa may be blended with the Fe II lines, suggesting a lower ionization. In SN 2011hr, the weak absorption near 6150 Å is likely to be Si II λ6355, which may indicate a lower ejecta velocity (see also Figure 10). In other SNe Ia, this Si II feature is stronger at similar phases.

At $t \approx 0$ days, Si II λ6355 finally develops in SN 2011hr, but it does not become as strong as normal SNe Ia. The EW of this line is ∼34 Å for SN 2011hr, which is only slightly larger than SN 2007if (i.e., ∼25 Å) and smaller than SN 1991T (i.e., ∼48 Å), SN 1999aa (i.e., ∼56 Å), SN 2005cf (i.e., ∼85 Å), and SN 2009dc (i.e., ∼51 Å) at similar phases. At this phase, the

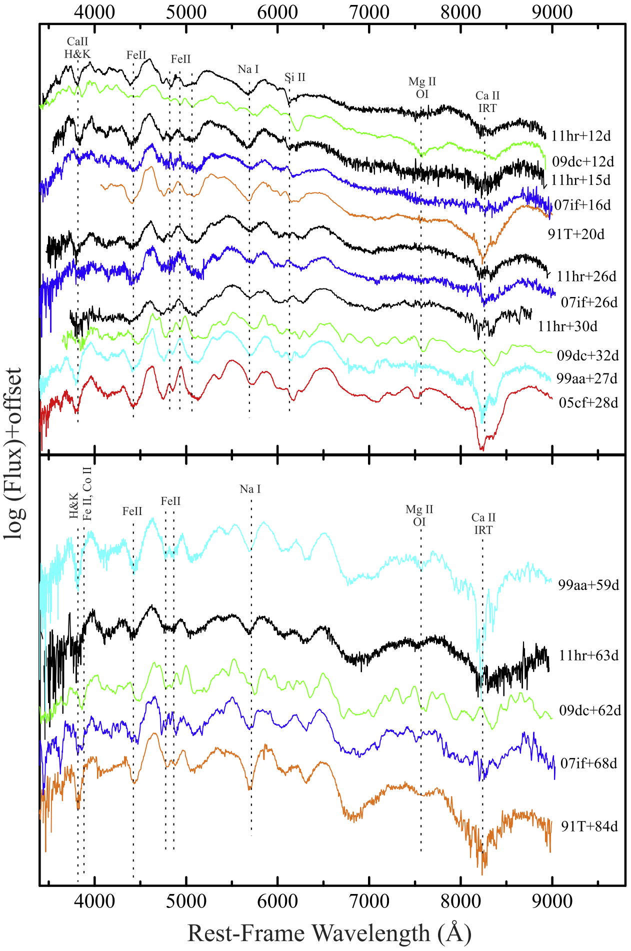

Figure 7. Postmaximum spectra of SN 2011hr, compared to the same SNe as in Figure 5. The spectrum of SN 2007if at $t \approx +68$ is smoothed with a box of 10 (~24 Å). The spectrum of SN 1999aa at $t \approx +59$ days is from Silverman et al. (2012).

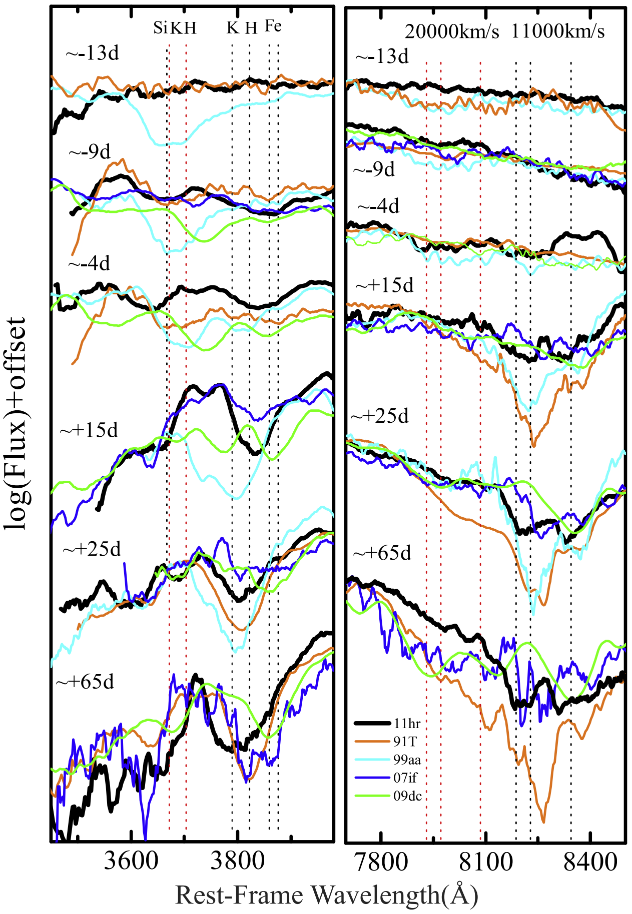

Figure 8. Evolution of the Ca II absorption in the spectra of SN 2011hr, SN 1991T, SN 1999aa, SN 2007if, and SN 2009dc at selected epochs. Left panel: evolution of Ca II H&K and Si II λ3860. Right panel: evolution of Ca II NIR triplet. The positions of Ca II H&K, Si III λ3807, Fe II, and the Ca II NIR triplet lines at different velocities (black dotted lines mark the line positions with $v = 11{,}000$ km s^{-1}, and red dotted lines mark the positions with $v = 20{,}000$ km s^{-1}) are shown to guide the eyes. All spectra are smoothed with a boxcar of 10 (i.e., ~20–30 Å). See Figures 5, 6, and 7 for the exact phase of each spectrum.

"W"-shaped feature of S II lines becomes noticeable in SN 2011hr. The presence of the S II lines indicates that SN 2011hr originated from a thermonuclear runaway. Inspection of Figure 6 reveals that there is no clear signature of O I λ7773 absorption in SN 2011hr and SN 1991T near maximum light. However, this feature becomes obvious in the spectra of other SNe Ia at this phase.

3.2.3. The Postmaximum Phase

The postmaximum spectra of SN 2011hr are compared with those of other SNe Ia in Figure 7. At about 2 weeks after maximum light, the spectrum of SN 2011hr is dominated by lines of iron and sodium, and the Si II λ6355 absorption is still very weak and the O I λ7773 line is almost undetectable at this phase. SN 2007if exhibits similar features in the comparable-phase spectra, while SN 2009dc shows stronger absorptions of Si II λ6355 and O I λ7773 but has lower expansion velocities. Moreover, the Ca II NIR triplets of SN 2011hr, SN 2007if, and SN 2009dc are all weak compared to SN 1991T.

At $t \approx +26$ days, the spectra of SN 2011hr and SN 2007if become more similar. For normal SNe Ia at this phase, the absorption of the Ca II NIR triplet usually evolves to become the strongest feature in the spectra. However, such a line

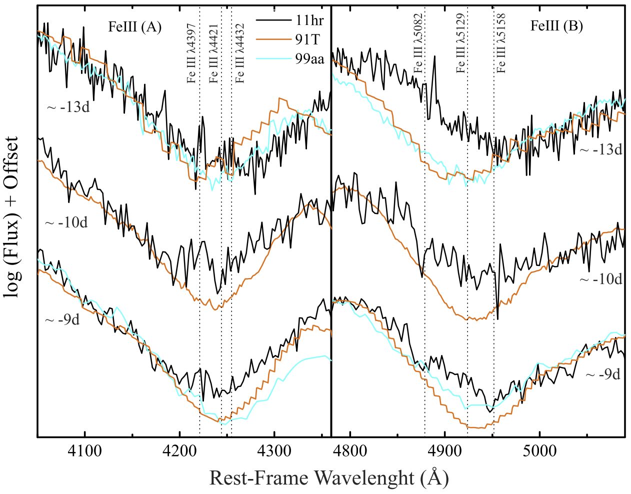

Figure 9. Absorption lines of Fe III in the spectra of SN 2011hr, SN 1991T, and SN 1999aa at early phases. The positions of these lines at a velocity of 12,000 km s^{-1} are marked to guide the eyes.

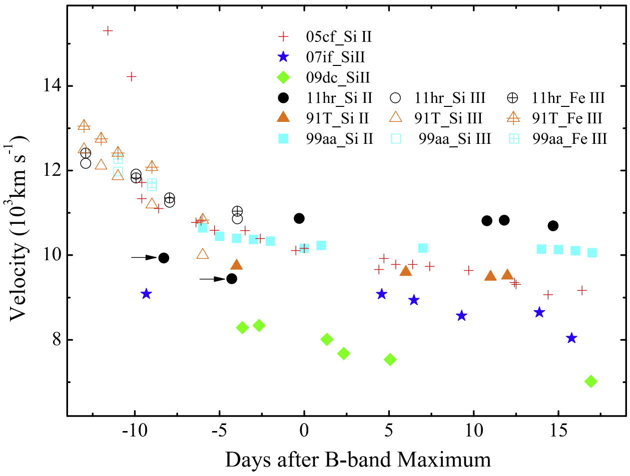

Figure 10. Ejecta velocity evolution of SN 2011hr, SN 1991T, SN 1999aa, SN 2005cf, SN 2007if, and SN 2009dc, as inferred from absorption minima of Si ii λ6355, Si iii λ4565, and Fe iii λλ4400, 5100 lines.

feature is still rather weak in SN 2011hr, SN 2007if, and SN 2009dc. At this phase, SN 1991T and SN 1999aa show absorption of the Ca ii NIR triplet that is as strong as that seen in normal SNe Ia. At 2–3 months later, absorption of the Ca ii NIR triplet grows in strength in SN 2011hr, SN 2007if, and SN 2009dc, but it is still significantly weaker compared to that seen in SN 1991T and SN 1999aa. The postmaximum spectra of SN 2011hr show distinct behavior relative to normal SNe Ia but are overall very similar to those of SN 2007if, including the velocity and strength of different species.

3.3. *Velocities of the Ejecta*

Figure 10 shows the ejecta velocity of SN 2011hr measured via the absorption feature of Fe iii before maximum light and Si ii λ6355 after the peak. The absorption near 4300 and 5000 Å is produced by blends of Fe iii lines, with rest wavelengths marked in Figure 5. A mean wavelength is adopted for each feature in the velocity estimation. The position of the blueshifted absorption minimum was measured using both the Gaussian fit and the direct measurement of the center of the absorption, and the results are averaged. The results for the two groups of Fe iii lines are also averaged in this figure. The first two points of Si ii λ6355 of SN 2011hr are derived from center of the minor absorption around 6200 Å, which are ~1000 km s^{-1} lower than the measurement at $t \approx +0$ days. This might suggest that this feature is not due to Si ii λ6355, but it is more likely that the Si ii line grows in strength and velocity owing to recombination and that its optical depth at higher velocities increases with time in spite of decreasing density. The Si ii λ6355 velocity near maximum light is estimated as $v = 10.88 \pm 0.15 \times 10^3$ km s^{-1} for SN 2011hr, which is closer to that of SN 1991T and SN 1999aa. SN 2007if and SN 2009dc have lower velocities, which suggests that they may have different ejecta structures.

The velocity gradient of SN 2011hr, derived from absorption of Si ii λ6355 during the period from $t \approx +0$ to $t \approx +15$ days, is 9 ± 10 km s^{-1}day^{-1}. This is comparable to that of SN 1999aa, SN 1991T, and SN 2007if, which places SN 2011hr in the low-velocity gradient (LVG) category of SNe Ia according to the classification scheme of Benetti (2005). After maximum light, SN 2011hr shows a higher Si ii velocity relative to the comparison SNe Ia, indicating that the inner boundary of the Si shell is located at higher velocities. If the inner layers are dominated by Fe-group elements (Mazzali et al. 2007), this implies that SN 2011hr produced more ^{56}Ni than the normal SNe Ia.

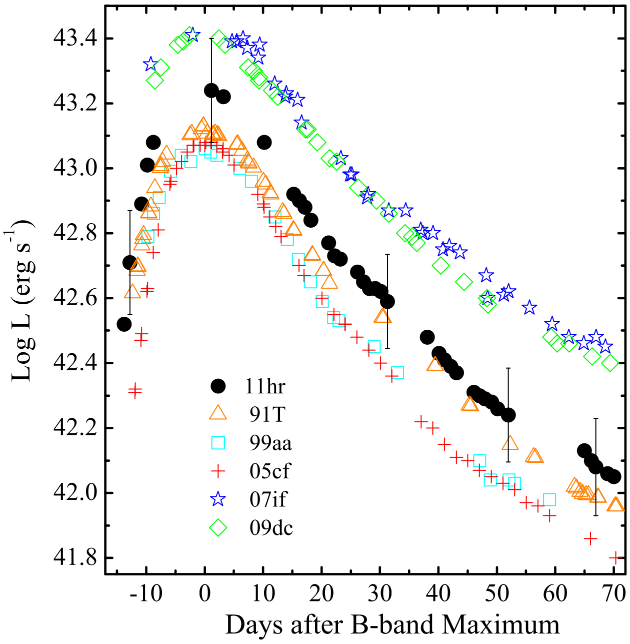

Figure 11. Quasi-bolometric light curves of SN 2011hr derived from the *UBVRI* photometry, compared with those of SN 1991T, SN 1999aa, SN 2005cf, SN 2007if, and SN 2009dc.

4. DISCUSSION

4.1. *Quasi-bolometric Luminosity*

Figure 11 displays the quasi-bolometric light curves of SN 2011hr derived from the *UBVRI* photometry, compared to those of SN 1991T (Sasdelli et al. 2014), SN 1999aa (Jha et al. 2006), SN 2005cf (Wang et al. 2009b), SN 2007if (Scalzo et al. 2010), and SN 2009dc (Taubenberger et al. 2010). Note that the brightness of SN 2011hr is located at the middle of SN 1991T/SN 1999aa and SN 2007if/SN 2009dc. However, the bolometric light curve of SN 2011hr is similar to that of SN 1991T and SN 1999aa in morphology. The superluminous SN 2007if and SN 2009dc show apparently wider light curves. These suggest that SN 2011hr may have a somewhat different explosion mechanism from these superluminous SNe Ia, although it shares some spectroscopic properties with SN 2007if.

To estimate the ^{56}Ni mass synthesized in the explosion of SN 2011hr, we need to calculate its generic bolometric luminosity at maximum light. The UV emission of SN 2011hr was estimated by assuming that it has a similar ratio of UV to *B*-band flux as the well-sampled 99aa-like event iPTF14bdn (Smitka et al. 2015), while the NIR contribution was extrapolated based on its *J* & *H*-band photometry published by Weyant et al. (2014). The peak "*uvoir*" bolometric luminosity is thus estimated to be $(2.30 \pm 0.90) \times 10^{43}$ erg s^{-1}. Applying a t^2 model to the observed *R*-band light curve yields an explosion time of MJD = 55,869.7 ± 1.0 and a rise time of 19.4 ± 1.0 days in

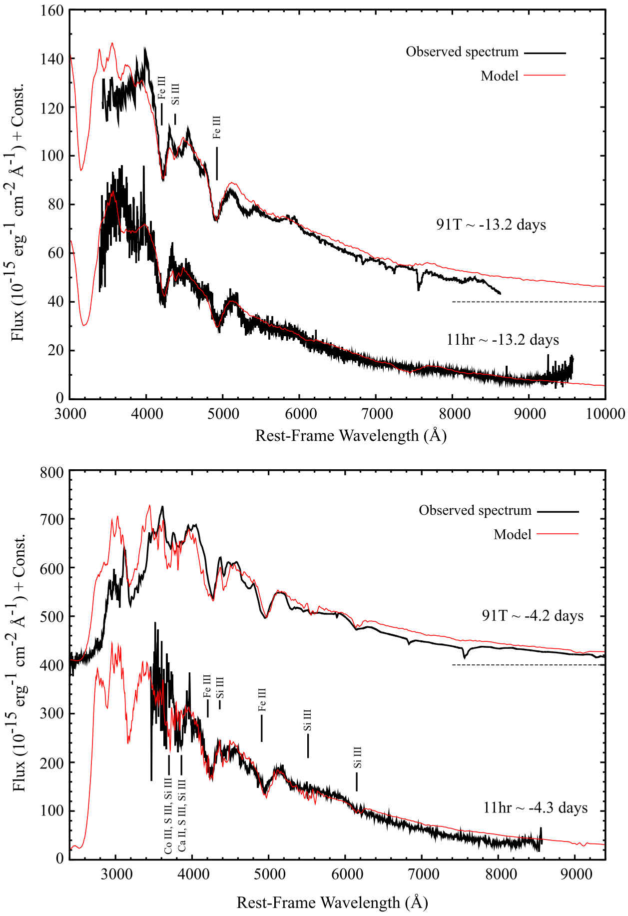

Figure 12. Synthetic spectra are compared with the observed spectra of SN 2011hr at −13.2 and −4.3 days. At the top of each panel, the model and the observed spectrum of SN 1991T at the same epoch from Sasdelli et al. (2014) are shown for comparison. To allow the comparison between these two SNe, the flux of SN 2011hr has been scaled by putting it at the same distance as SN 1991T. The spectra are in rest frame and corrected for reddening by the amount assumed during the modeling.

B band, which is close to the estimate derived from the spectral modeling (i.e., ∼20 days in the *B* band; see discussions in Section 4.1). Considering the UV contribution, the bolometric curve of SN 2011hr reaches its peak at about 1.4 days earlier than in *B* band; a rise time of 18.0 ± 1.0 days is thus adopted for SN 2011hr in the following analysis. Based on these parameters, we estimate that the ^{56}Ni mass synthesized in the explosion of SN 2011hr is $M(^{56}\mathrm{Ni}) = 1.11 \pm 0.43\ M_{\odot}$ according to the Arnett law (Arnett 1982; Stritzinger & Leibundgut 2005). This value is larger than that obtained for SN 1991T ($M(^{56}\mathrm{Ni}) = 0.82\ M_{\odot}$), SN 1999aa ($M(^{56}\mathrm{Ni}) = 0.72\ M_{\odot}$), and SN 2005cf ($M(^{56}\mathrm{Ni}) = 0.75\ M_{\odot}$). The ^{56}Ni masses inferred for SN 2007if and SN 2009dc (with a similar method) are much larger, which are close to 2.0 $M_{\odot}$. An accurate determination of the ^{56}Ni mass could be also obtained using nebular spectra (Mazzali et al. 2007), but no late-time spectra are available for SN 2011hr.

4.2. Explosion Models

Our observations indicate that SN 2011hr is an overluminous SN Ia. Both the SC-mass and the Chandrasekhar-mass scenario have been proposed to explain observational features of overluminous SNe Ia. Yoon & Langer (2005) suggested that the WDs may accrete mass from a nondegenerate or another WD companion star and grow in mass to values exceeding the Chandrasekhar-mass limit (which can reach a mass of $\gtrsim 2.0\,M_{\odot}$ if the WD is in differential rotation). Thermonuclear explosions of rapidly rotating WDs have been suggested to account for production of superluminous SNe Ia in terms of both burning products and explosion kinematics by Pfannes et al. (2010a, 2010b). Also, they find that a rotating WD that detonates has an ejecta velocity compatible with that of a normal SN Ia. Meanwhile, Pfannes et al. (2010a, 2010b) also showed that a significant amount of IMEs are produced for rotating SC-mass WDs. Inspection of Figure 6 reveals that SN 2011hr has rather weak absorption features of Si II, Ca II, and O I, unlike the 91T-like and normal SNe Ia. These results indicate that the IMEs (especially Ca) are apparently less abundant in SN 2011hr, which seems to be inconsistent with the predictions of rotating SC-mass WDs (see Pfannes et al. 2010a, 2010b).

Alternatively, SN 2011hr may be an energetic explosion of a Chandrasekhar-mass WD. For instance, the Chandrasekhar-mass model with a high kinetic energy in Iwamoto et al. (1999) may be a good candidate for producing overluminous SNe Ia, which will be addressed in Section 4.3. The gravitationally confined detonation (GCD) of near-Chandrasekhar-mass WDs may be an alternative scenario to explain the overluminous SNe Ia. The GCD model has been studied by different groups (e.g., Plewa et al. 2004, 2007; Meakin et al. 2009; Jordan et al. 2012). On one hand, it has been shown that the GCD model may provide explanations for overluminous SN 1991T-like events because it can produce a large mass of ^{56}Ni that can even exceed 1.0 $M_{\odot}$. On the other hand, GCD models naturally produce chemically mixed compositions and thus are proposed to explain the high-velocity Fe-group elements observed in early-time spectra of some overluminous 91T-like SNe. Unfortunately, to date, no detailed radiative transfer calculations have yet been performed to compare with the observations of overluminous SNe Ia.

Finally, we point out that the absence of C and O lines in the early-time spectra of SN 2011hr suggests that SN 2011hr is unlikely to be the result of the merger of two WDs (i.e., the so-called violent merger model within the double-degenerate scenario).

4.3. Abundance Tomography of SN 2011hr

To set further constraints on the possible progenitor scenario, we modeled the early spectra of SN 2011hr using a well-tested Monte Carlo code that was initially developed by Mazzali & Lucy (1993) and later improved by Lucy (1999) and Mazzali (2000) by including the photon branching. The code assumes a photosphere with a scaled blackbody emission. This approximation is valid when the inner part of the ejecta that encloses most of the radioactive materials is optically thick. To model the spectra, we adopt a technique called "abundance tomography" (Stehle et al. 2005; Mazzali et al. 2008; Tanaka et al. 2011; Ashall et al. 2014; Sasdelli et al. 2014). As shown in previous sections, there are some uncertainties in determinations of the distance and host-galaxy reddening for SN 2011hr. A higher luminosity may require an SC-mass progenitor, e.g., $M(^{56}\mathrm{Ni}) = 1.61\ M_{\odot}$ if $E(B - V) = 0.27$ and $D = 66$ Mpc. We want to investigate whether a Chandrasekhar-mass scenario is still viable for SN 2011hr, or whether it can only be

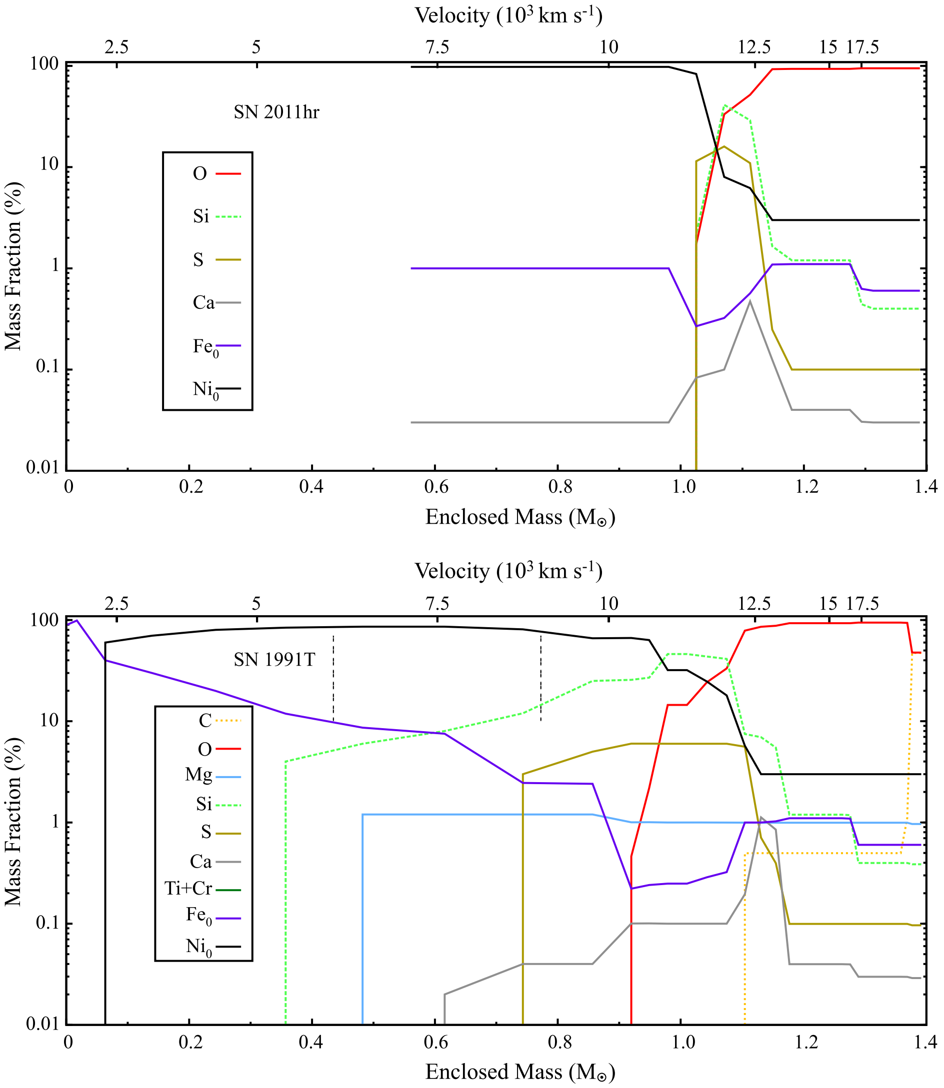

Figure 13. Abundance distribution of the outer ejecta inferred for SN 2011hr and SN 1991T. SN 2011hr (top panel) has a thinner layer of IMEs above a large amount of ^{56}Ni. Only the outer layers can be probed with the photospheric method adopted here. The abundances of SN 1991T (bottom panel) are taken from Figure 5 of Sasdelli et al. (2014).

explained with an SC-mass model. For our investigation, we use the density profile of the energetic WDD3 model from Iwamoto et al. (1999). This should be a good choice for SN 2011hr, which shows lines with relatively higher velocities.

We fit the luminosity of SN 2011hr from spectral modeling. This is an independent estimate of the distance and the extinction. We follow the same method as that described in Sasdelli et al. (2014) to study the luminosity of SN 1991T, which is an ideal SN for a comparative study with SN 2011hr. Similarly to SN 1991T, the time at which the recombination from Si III into Si II happens can place a tight constraint on the luminosity. For SN 2011hr, this transition happens at a couple of days later than SN 1991T. Figure 12 displays the comparison of the modeled spectra of SN 2011hr at $t \approx -13$ days and -4 days, respectively. The observed and modeled spectra of SN 1991T are also shown as references. The distance adopted for SN 2011hr is $D = 60$ Mpc (i.e., $m - M = 33.89$). In addition to the Milky Way reddening of $E(B - V) = 0.02$, we use a reddening $E(B - V) = 0.15$ for the host galaxy. A larger reddening is disfavored by the synthetic color from the model spectrum.

Compared to SN 1991T, the Fe III features at 4200 and 4900 Å are less pronounced in SN 2011hr. The modeling analysis shows that this can be explained with an ionization effect, as a consequence of the fact that the temperature of SN 2011hr is higher than that of SN 1991T. The Si II line at 6100 Å first appears at around the *B*-band maximum light, ~4 days later than in SN 1991T. Again, this can also be due to an ionization effect caused by the higher luminosity of SN 2011hr. On the other hand, the Si III λ4450 line is weaker than in SN 1991T despite a larger fraction of Si III because of a lower Si abundance. Si is the dominant element only within 11,500 and 12,000 km s^{-1}. SN 2011hr has an abundance profile qualitatively similar to SN 1991T, but likely representing a more extreme case (i.e., Figure 13). The interface between the ^{56}Ni-dominated interior and the layer dominated by IMEs is thinner in SN 2011hr compared to that seen in SN 1991T. The ^{56}Ni fraction exceeds 90% up to velocities as high as ~11,500 km s^{-1}. This matches the lowest velocities of Si II measured in the spectra. The layer dominated by Si and other IMEs is also thinner than in SN 1991T, and their total mass is just 0.07 $M_\odot$, while in SN 1991T the IME mass is 0.18 $M_\odot$ (Sasdelli et al. 2014). We could recap the properties of SN 2011hr as "more 91T-like than SN 1991T itself."

The modeling result shows that the luminosity of SN 2011hr is higher than SN 1991T by about 20%. This requires a ^{56}Ni mass of about 0.94 $M_\odot$. The luminosity of SN 2011hr is at the brightest end of SNe Ia, which requires a large amount of ^{56}Ni, but this is balanced by a lower mass of IMEs. The model does not require a mass larger than the Chandrasekhar mass, and instead it suggests that a scenario with an efficiently burned Chandrasekhar mass is also possible to produce such an overluminous SN Ia.

5. CONCLUSION

We have presented extensive observations and studies of the luminous (e.g., $M_{\max}(B) = -19.84 \pm 0.40$ mag), spectroscopically peculiar SN Ia SN 2011hr. It exhibits light-curve evolution that is similar to SN 1991T, with a postmaximum decline rate $\Delta m_{15}(B) = 0.92 \pm 0.03$ mag. The spectra of SN 2011hr are characterized by strong Fe-group lines and weak absorptions of IMEs, showing close resemblances to that of SN 2007if at all phases. Note, however, that the absence of C II absorption in the early-time spectra of SN 2011hr suggests that there should be differences between these two SNe Ia. Moreover, SN 2011hr has narrower light-curve peaks and its light curves decline more rapidly at late phases compared to SN 2007if. Overall, SN 2011hr shows more similarities with SN 1991T in morphology of the light curves, while it bears more common features with SN 2007if in the spectral evolution.

Computing the detailed abundance distribution of the IMEs and iron-group elements helps further reveal the nature of this peculiar SN Ia. Mapping the abundances in the outer ejecta with the abundance tomography method, we found that a lower mass of IMEs (i.e., 0.07 $M_\odot$) and a larger mass of ^{56}Ni (i.e., ~0.94 $M_\odot$ by spectral modeling or ~1.11 $M_\odot$ by Arnett law) can be inferred for SN 2011hr. The corresponding values inferred for SN 1991T are ~0.18 $M_\odot$ for IMEs and ~0.78 $M_\odot$ for ^{56}Ni. Our models suggest that a very efficiently burned Chandrasekhar-mass progenitor is the favored scenario for this overluminous SN Ia. The weaker absorptions of the IMEs might indicate a lower abundance of these elements in the outer ejecta. Nevertheless, the presence of similar features in SN 2011hr and SN 2007if may indicate that SN 2011hr represents a transitional object linking 91T-like SNe Ia to some superluminous SNe Ia.

We acknowledge the support of the staff of the Li-Jiang 2.4 m telescope (LJT), Xing-Long 2.16 m telescope, and Tsinghua-NAOC 0.8 m telescope (TNT). Funding for the LJT has been provided by the Chinese Academy of Sciences (CAS) and the People's Government of Yunnan Province. The TNT is owned by Tsinghua University and jointly operated by the National Astronomical Observatory (NAOC) of the CAS. Financial support for this work has been provided by the National Science Foundation of China (NSFC, grants 11403096, 11178003, 11325313, 11133006, 11361140347, 11203034, 11473063, 11322327, 11103072, 11203078, 11303085, 11203070 and 11103078); the Major State Basic Research Development Program (2013CB834903); the Strategic Priority Research Program "The Emergence of Cosmological Structures" of the CAS (grant No. XDB09000000); the Key Research Program of the CAS (Grant NO. KJZD-EW-M06); the Western Light Youth Project; the Youth Innovation Promotion Association of the CAS; the Open Project Program of the Key Laboratory of Optical Astronomy, NAOC, CAS; and the key Laboratory for Research in Galaxies and Cosmology of the CAS.

REFERENCES

Altavilla, G., Fiorentino, G., Marconi, G., et al. 2004, MNRAS, 349, 1344
Arnett, W. D. 1982, ApJ, 253, 785
Ashall, C., Mazzali, P., Bersier, D., et al. 2014, MNRAS, 445, 4427
Barbon, R., Benetti, S., Rosino, L., Cappellaro, E., & Turatto, M. 1990, A&A, 237, 79
Barone-Nugent, R. L., Lidman, C., Wyithe, J. S. B., et al. 2012, MNRAS, 425, 1007
Benetti, S. 2005, ApJ, 623, 1011
Bessell, M. S. 1990, PASP, 102, 1181
Blondin, S., Matheson, T., Kirshner, R. P., et al. 2012, AJ, 143, 126
Blondin, S., & Tonry, J. L. 2007, ApJ, 666, 1024
Branch, D., Dang, L. C., & Baron, E. 2009, PASP, 121, 238
Branch, D., Baron, E., Hall, N., et al. 2005, PASP, 117, 545
Branch, D., Dang, L. C., Hall, N., et al. 2006, PASP, 118, 560
Brown, P. J., Kuin, P., Scalzo, R., et al. 2014, ApJ, 787, 29
Cardelli, J. A., Clayton, G. C., & Mathis, J. S. 1989, ApJ, 345, 245
Childress, M. J., Filippenko, A. V., Ganeshalingam, M., et al. 2014, MNRAS, 437, 338
Childress, M. J., Scalzo, R. A., Sim, S., et al. 2013, ApJ, 770, 29
Cousins, A. 1981, SAAOC, 6, 4
Dilday, B., Howell, D. A., Cenko, S. B., et al. 2012, Sci, 337, 942
Fan, Y. F., Bai, J. M., Zhang, J. J., et al. 2015, RAA, 15, 918
Filippenko, A. V. 1997, ARA&A, 35, 309
Filippenko, A. V., Richmond, M. W., Branch, D., et al. 1992a, AJ, 104, 1543
Filippenko, A. V., Richmond, M. W., Michael, W., et al. 1992b, ApJL, 384, L15
Fisher, A., Branch, D., Hatano, K., & Baron, E. 1999, MNRAS, 304, 67
Fitzpatrick, E. L., & Massa, D. 2007, ApJ, 663, 320
Foley, R. J., Challis, P. J., Chornock, R., et al. 2013, ApJ, 767, 57
Garavini, G., Folatelli, G., Goobar, A., et al. 2004, AJ, 128, 387
Gibson, B. K., & Stetson, P. B. 2001, ApJL, 547, L103
Goldhaber, G., Groom, D. E., Kim, A., et al. 2001, ApJ, 558, 359
Guy, J., Astier, P., Nobili, S., et al. 2005, A&A, 443, 781
Hachinger, S., Mazzali, P. A., Taubenberger, S., et al. 2012, MNRAS, 427, 2057
Hamuy, M., Phillips, M. M., Suntzeff, N. B., et al. 1996, AJ, 12, 2438
Hicken, M., Garnavich, P. M., Prieto, J. L., et al. 2007, ApJL, 669, L17
Hicken, M., Wood-Vasey, W. M., Blondin, S., et al. 2009, ApJ, 700, 1097
Hillebrandt, W., Sim, S. A., & Röpke, F. K. 2007, A&A, 465, 17
Howell, D., Sullivan, M., Nugent, P. E., et al. 2006, Natur, 443, 308
Huang, F., Li, J. Z., Wang, X. F., et al. 2012, RAA, 11, 1585
Iwamoto, K., Brachwitz, F., Nomoto, K., et al. 1999, ApJS, 125, 439
Jha, S., Krishner, R. P., Challis, P., et al. 2006, AJ, 131, 527
Johnson, H., Iriarte, B., Mitchell, R., & Wisniewskj, W. 1966, CoLPL, 4, 99
Jordan, G. C., IV, Graziani, C., Fisher, R. T., et al. 2012, ApJ, 759, 53
Krisciunas, K., Phillips, M. M., & Suntzeff, N. B. 2004, ApJL, 602, L81
Landolt, A. V. 1992, AJ, 104, 340
Li, W., Filippenko, A., Ryan, C., et al. 2003, PASP, 115, 453
Lira, P., Suntzeff, N. B., Phillips, M. M., et al. 1998, AJ, 115, 234
Lucy, L. B. 1999, A&A, 345, 211
Maeda, K., Leloudas, G., Taubenberger, S., et al. 2011, MNRAS, 413, 3075
Maeda, K., Benetti, S., Stritzinger, M., et al. 2010, Natur, 466, 82
Maoz, D., Mannucci, F., & Nelemans, G. 2014, ARA&A, 52, 107
Marion, G. H., Vinko, J., Wheeler, J. C., et al. 2013, ApJ, 777, 40
Maund, J., Hörflich, P., Patat, F., et al. 2010, ApJL, 725, L167
Mazzali, P. A. 2000, A&A, 363, 705
Mazzali, P. A., Benetti, S., Altavilla, G., et al. 2005, ApJL, 623, L37
Mazzali, P. A., Danziger, I. J., & Turatto, M. 1995, A&A, 297, 509
Mazzali, P. A., & Lucy, L. B. 1993, A&A, 279, 447
Mazzali, P. A., Röpke, F. K., Benetti, S., & Hillebrandt, W. 2007, Sci, 315, 825
Mazzali, P. A., Sauer, D. N., Pastorello, A., Benetti, S., & Hillebrandt, W. 2008, MNRAS, 386, 1897
Meakin, C. A., Seitenzahl, I., Townsley, D., et al. 2009, ApJ, 693, 1188
Meikle, W. P. S. 2000, MNRAS, 314, 782

Mould, J. R., Huchra, J. P., Freedman, W.L., et al. 2000, ApJ, 529, 786
Nayak, I., Cenko, S. B., & Filippenko, A. V. 2011, CEBT, 2837
O'Donnell, J. E. 1994, ApJ, 422, 158
Perlmutter, S., Aldering, G., Goldhaber, G., et al. 1999, ApJ, 517, 565
Pfannes, J. M. M., Niemeyer, J. C., & Schmidt, W. 2010a, A&A, 509, 75
Pfannes, J. M. M., Niemeyer, J. C., Schmidt, W., & Klingenberg, C. 2010b, A&A, 509, 74
Phillips, M. 1993, ApJL, 413, L105
Phillips, M., Lira, R., Suntzeff, N. B., et al. 1999, AJ, 118, 1766
Phillips, M., Simon, J., Morrell, N., et al. 2013, ApJ, 779, 38
Phillips, M., Wells, L. A., Suntzeff, N. B., et al. 1992, AJ, 103, 1632
Plewa, T., Calder, A. C., Lamb, D. Q., et al. 2004, ApJL, 612, L37
Plewa, T. 2007, ApJ, 657, 942
Poznanski, D., Ganeshalingam, M., Silverman, J. M., & Filippenko, A. V. 2011, MNRAS, 415, L81
Riess, A., Filippenko, A. V., Challis, P., et al. 1998, AJ, 116, 1009
Riess, A., Press, W., & Kirshner, R. 1996, ApJ, 473, 88
Ruiz-Lapuente, P., Cappellaro, E., Turatto, M., et al. 1992, ApJL, 387, L33
Sasdelli, M., Mazzali, P. A., Pian, E., et al. 2014, MNRAS, 445, 711
Scalzo, R., Aldering, G., Antilogus, P., et al. 2010, ApJ, 713, 1073
Schlegel, D., Finkbeiner, D., & Davis, M. 1998, ApJ, 500, 525
Schmidt, B., Suntzeff, N., Phillips, M., et al. 1998, ApJ, 507, 46
Silverman, J., Foley, R. J., Filippenko, A. V., et al. 2012, MNRAS, 425, 1789
Silverman, J., Ganeshalingam, M., Li, W., et al. 2011, MNRAS, 410, 585
Sim, S., Sauer, D. N., Röpke, F. K., & Hillebrandt, W. 2007, MNRAS, 378, 2
Smitka, M. T., Brown, P. J., Suntzeff, N. B., et al. 2015, ApJ, 813, 30
Stehle, M., Mazzali, P. A., Benetti, S., & Hillebrandt, W. 2005, MNRAS, 360, 1231
Stetson, P. 1987, PASP, 99, 191
Stritzinger, M., & Leibundgut, B. 2005, A&A, 431, 423
Suntzeff, N. 1996, in Supernovae and Supernova Remnants, ed. R. McCray, & Z. Wang (Cambridge: Cambridge Univ. Press), 41
Tanaka, M., Mazzali, P. A., Stanishev, V., et al. 2011, MNRAS, 410, 1725
Taubenberger, S., Benetti, S., Childress, M., et al. 2010, MNRAS, 412, 2735
Theureau, G., Hanski, M. O., Coudreau, N., et al. 2007, A&A, 465, 71
Tully, R. B., Rizzi, L., Shaya, E., et al. 2009, AJ, 138, 323
Turatto, M., Benetti, S., & Cappellaro, E. 2003, in From Twilight to Highlight: The Physics of Supernovae, ed. B. Leibundgut, & W. Hillebrandt (Berlin: Springer), 200
Wang, X., Filippenko, A. V., Ganeshalingam, M., et al. 2009a, ApJL, 699, L139
Wang, X., Li, W., Filippenko, A., et al. 2009b, ApJ, 697, 380
Wang, X., Li, W., Filippenko, A. V., et al. 2008, ApJ, 675, 626
Wang, X., Wang, L., Filippenko, A., et al. 2013, Sci, 340, 170
Wang, X. F., Wang, L. F., Filippenko, A. V., et al. 2012, ApJ, 749, 126
Weyant, A., Michael, W., Allen, L., et al. 2014, ApJ, 784, 105
Yoon, S. C., & Langer, N. 2005, A&A, 435, 967
Zhang, J. J., Wang, X. F., Bai, J. M., et al. 2014, AJ, 148, 1
Zhang, T. M., Zhang, J. J., & Wang, X. F. 2011, CEBT, 2901

The Astrophysical Journal, 833:137 (15pp), 2016 December 20 doi:10.3847/1538-4357/833/2/137

NLTE ANALYSIS OF HIGH-RESOLUTION *H*-BAND SPECTRA. I. NEUTRAL SILICON[*]

Junbo Zhang[1,2], Jianrong Shi[1,2], Kaike Pan[3], Carlos Allende Prieto[4,5], and Chao Liu[1]
[1] Key Laboratory of Optical Astronomy, National Astronomical Observatories, Chinese Academy of Sciences, A20 Datun Road, Chaoyang District, Beijing 100012, China
[2] School of Astronomy and Space Science, University of Chinese Academy of Sciences, Beijing 100049, China; sjr@bao.ac.cn
[3] Apache Point Observatory and New Mexico State University, P.O. Box 59, Sunspot, NM, 88349-0059, USA
[4] Instituto de Astrofísica de Canarias, E-38205 La Laguna, Tenerife, Spain
[5] Departamento de Astrofísica, Universidad de La Laguna, E-38206 La Laguna, Tenerife, Spain

Received 2016 February 26; revised 2016 October 13; accepted 2016 October 14; published 2016 December 13

ABSTRACT

We investigated the reliability of our silicon atomic model and the influence of non-local thermodynamical equilibrium (NLTE) on the formation of neutral silicon (Si I) lines in the near-infrared (near-IR) *H*-band. We derived the differential Si abundances for 13 sample stars with high-resolution *H*-band spectra from the Apache Point Observatory Galactic Evolution Experiment (APOGEE), as well as from optical spectra, both under local thermodynamical equilibrium (LTE) and NLTE conditions. We found that the differences between the Si abundances derived from the *H*-band and from optical lines for the same stars are less than 0.1 dex when the NLTE effects are included, and that NLTE reduces the line-to-line scatter in the *H*-band spectra for most sample stars. These results suggest that our Si atomic model is appropriate for studying the formation of *H*-band Si lines. Our calculations show that the NLTE corrections of the Si I *H*-band lines are negative, i.e., the final Si abundances will be overestimated in LTE. The corrections for strong lines depend on surface gravity, and tend to be larger for giants, reaching ∼−0.2 dex in our sample, and up to ∼−0.4 dex in extreme cases of APOGEE targets. Thus, the NLTE effects should be included in deriving silicon abundances from *H*-band Si I lines, especially for the cases where only strong lines are available.

Key words: line: formation – line: profiles – stars: abundances – stars: atmospheres

1. INTRODUCTION

Silicon is an important α-element mainly produced during oxygen and neon burning, and is returned to the interstellar medium by Type II supernovae (SNe II; Woosley & Weaver 1995). SNe Ia may also produce a small fraction of silicon (Tsujimoto et al. 1995). Silicon is an important element of the interstellar dust, one of the main electron contributors (only next to Fe and Mg) in the atmospheres of late-type stars (Holweger 1973; Wedemeyer 2001). The silicon abundance is often used as a tracer to explore the formation and evolution of the solar system (Johnson et al. 2011; Zambardi et al. 2013) and to study the Galactic structure, chemical enrichment history, and the origin of the Galaxy in many studies. For example, the silicon abundance, combined with other α-elements, is often adopted as an indicator to distinguish stars from different populations, namely thick- and thin-disk populations (Lee et al. 2011). A series of studies, e.g., Bensby et al. (2005, 2014), Reddy et al. (2003, 2006), Nissen & Schuster (2010), and Zhang et al. (2011), have observed many high-resolution spectra and have derived accurate silicon abundances. Compared with different Galactic evolution models, e.g., Samland (1998), Goswami & Prantzos (2000), Romano et al. (2010) and Kobayashi et al. (2011), these abundances can help astronomers to understand the chemical enrichment history and the origin of the Galaxy. Thus, an accurate measurement of silicon abundances is necessary for many astrophysical applications.

Kamp (1973, 1978, 1982) calculated theoretical equivalent widths and profiles for silicon lines in both local thermodynamical equilibrium (LTE) and nonlocal thermodynamical equilibrium (NLTE) and compared them with observational data of a dozen early-type stars. The results indicate that the NLTE calculations provided better agreement with observations. The deviations from LTE on Si abundances in the photospheres of the Sun and Vega have been investigated by Wedemeyer (2001), who found that the mean NLTE correction for Si was ∼−0.01 dex for the Sun, and ∼−0.054 dex for Vega. This indicated that the NLTE effects on the Si abundance in the Sun could be neglected, which was confirmed by Shi et al. (2008). Later on, Shi et al. (2009, 2011) systematically investigated the NLTE effects on the derived silicon abundances in the atmospheres of metal-poor stars based on visible lines, and found that the NLTE effects are large for the two strong UV lines at 3905 and 4103 Å, especially for warm metal-poor stars. Shi et al. (2012) extended the study to the near-IR *J*-band Si lines, and found that the NLTE effects depend on surface gravities becoming higher for giants. Recently, Bergemann et al. (2013) investigated the NLTE effects on the *J*-band Si lines for red supergiants, and confirmed that Si abundance based on NLTE is significantly lower than that from LTE.

Until very recently, almost all observed high-resolution spectra are from UV, optical, and near-IR *J* bands, therefore previous studies on NLTE Si abundance are for spectral lines in these three bands. The situation has changed since the Apache Point Observatory Galactic Evolution Experiment (APOGEE) survey[6] (Majewski et al. 2015) (as part of SDSS-III, Eisenstein et al. 2011) started to take high-resolution IR *H*-band spectra

---

[*] Based on observations collected with the 2.16 m telescope at Xinglong station, National Astronomical Observatories, Chinese Academy of Sciences, the 2.2 m telescope at the Calar Alto Observatory, the 1.88 m reflector at the Okayama Astrophysical Observatory, the Kitt Peak coudé feed telescope, and the McMath-Pierce solar telescope and the coudé focus of the Mayall 4 m reflector at Kitt Peak.

[6] http://www.sdss.org/surveys/apogee

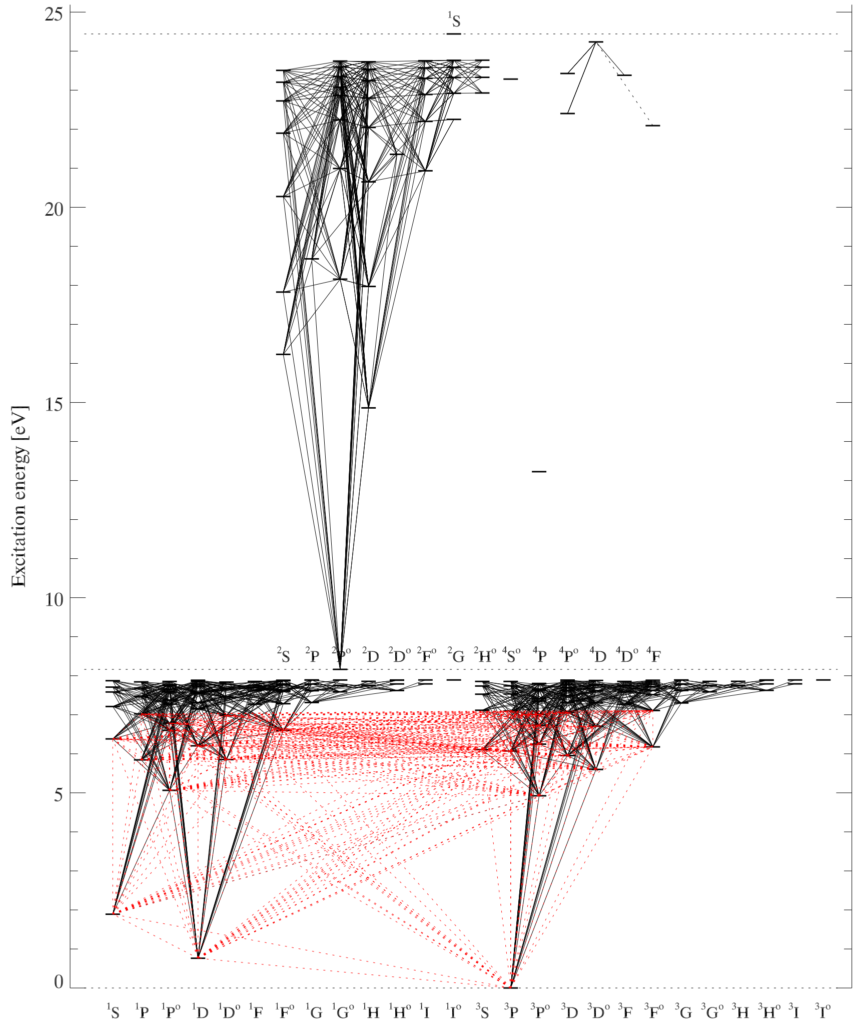

Figure 1. Grotrian diagram of the silicon model atom. Si II quartets are neglected. Allowed transitions are plotted as black continuous lines, the forbidden Si I 4103 Å line is a black dotted line. Transitions of Si I between 26 low-lying energy terms presented by Belyaev et al. (2014) are shown with red dotted lines.

for several hundred thousands stars. Thus, it is highly desirable to extend the NLTE investigations to the *H* band, where there are a dozen Si I lines that are clearly seen in APOGEE spectra.

Since 2011, the APOGEE survey employs a fiber spectrograph that simultaneously records 300 spectra in the *H* band between 1.51 and 1.70 μm at a spectral resolution of $R \sim 22{,}500$. Detailed information about the instrument was provided by Wilson et al. (2010). Taking advantage of the reduced effect of extinction in the IR *H* band, APOGEE has observed ~150,000 stars, predominantly red giants in all major Galactic components that are accessible from the Apache Point Observatory (APO) (Holtzman et al. 2015; Majewski et al. 2015). The spectra have been included in the SDSS Data Release 10 (DR10) (Ahn et al. 2014) and SDSS Data Release 12 (DR12) (Alam et al. 2015). The data provide a promising way to trace and explore the formation history of the Galaxy, and they are revolutionizing our knowledge on the kinematical and chemical enrichment history of all Galactic stellar populations.

The APOGEE Stellar Parameters and Chemical Abundances Pipeline (ASPCAP) provides the physical and chemical parameters for the APOGEE stars (García Pérez et al. 2016). In addition to the stellar parameters, i.e., the effective temperature ($T_{\rm eff}$), surface gravity ($\log g$), and metallicity ([M/H]), ASPCAP delivers individual chemical abundances for 15 elements. The accuracy of these derived stellar fundamental parameters and chemical compositions may be compromised. NLTE effects are enhanced by the characteristic low densities found in the atmospheres of giants and the absolute reduction in collision rates, which affects the atomic populations (Mészáros et al. 2013). Hawkins et al. (2016) have performed an independent procedure to determine the chemical abundances of the APOGEE + *Kepler* stellar sample (APO-KASC), and they inferred that the discrepant phenomenon for some elements is likely due to the NLTE effects. As part of a series of studies on the NLTE analysis of *H*-band lines for several important elements, e.g., Na, Mg, Al, Si, K, Ca, and Fe, this work aims to validate the Si atomic model and to investigate how the abundances derived from the Si *H*-band transitions are affected by departures from LTE.

This paper is organized as follows. In Section 2 we briefly introduce our adopted Si model atom and NLTE calculation

Table 1
Characteristics of the Observed Optical Spectra

Star	V_{mag}[a] (mag)	Telescope/Spectrograph	Observing Run, Observer	Spectral Range (Å)	R	S/N
Arcturus	−0.05	KPCFT/ES	1998–99, K. Hinkle et al.	3727–9300	150,000	~1000
HD 87	5.55	1.88 m/HIDES	2007 Jul, Anonymous[b]	5000–6200	67,000	⩾150
HD 6582	5.17	2.2 m/FOCES	1995 Sep, K. Fuhrmann	4000–7000	35,000	⩾150
HD 6920	5.67	2.2 m/FOCES	1997 Feb, K. Fuhrmann	4000–9000	60,000	~200
HD 22675	5.86	1.88 m/HIDES	2010 Jan, B. Sato	4000–7540	67,000	~300
HD 31501	8.15	2.16 m/CES	2008 Jan, J. R. Shi	5600–8800	40,000	⩾150
HD 58367	4.99	1.88 m/HIDES	2004 Feb, Anonymous[b]	5000–6200	67,000	⩾150
HD 67447	5.34	2.16 m/FOES	2015 Jan, J. B. Zhang	3900–7260	50,000	⩾150
HD 102870	3.59	2.2 m/FOCES	1997 May, K. Fuhrmann	4000–9000	60,000	~200
HD 103095	6.42	2.2 m/FOCES	2000 May, K. Fuhrmann	4000–9000	60,000	~200
HD 121370	2.68	2.2 m/FOCES	1998 Dec, K. Fuhrmann	4000–9000	60,000	~200
HD 148816	7.27	2.2 m/FOCES	2001 Aug, T. Gehren	4000–9000	60,000	~200
HD 177249	5.51	1.88 m/HIDES	2004 Nov, Anonymous[b]	5000–6200	67,000	~300

Notes.
[a] Visual magnitudes are derived from the *Hipparcos* Main Catalogue (ESA 1997) through VizieR (http://vizier.u-strasbg.fr/viz-bin/VizieR).
[b] Spectra were provided by Y. Takeda, B. Sato, and Y. J. Liu et al. The observer written in the spectra header is anonymous, and it is difficult for us to identify the actual observers.

codes, while the selection of the sample stars and the observed spectra are described in Section 3. The stellar parameters of our sample stars are determined in Section 4, and the Si abundances derived from both the *H*-band and optical lines for the sample stars under LTE and NLTE analyses are presented in Section 5. Finally, the conclusions are given in Section 6.

2. METHOD OF NLTE CALCULATIONS

2.1. Model Atom of Silicon

The Si atomic model that we used here is similar to that of Shi et al. (2008), which includes the most important 132 terms of Si I, 41 terms of Si II, and the Si III ground state. The radiative data are taken from Nahar & Pradhan (1993). Lacking accurate values for inelastic collisions with neutral hydrogen, Shi et al. (2008) suggested $S_{\mathrm{H}} = 0.1$ by fitting solar strong infrared Si I lines. Fortunately, Belyaev et al. (2014) calculated the cross sections and rate coefficients for inelastic processes in Si + H and Si^{+} + H^{-} collisions for all transitions between 26 low-lying states plus the ionic state. We revised the Si atomic model by including all cross sections from Belyaev et al. (2014) whenever available; otherwise, $S_{\mathrm{H}} = 0.1$ was adopted. The Grotrian diagram of the silicon model atom with the transitions between 26 low-lying energy terms relative to Belyaev et al. (2014) is shown in Figure 1. In this work, we also calculated the NLTE line profiles for the Sun and Arcturus with four different collision treatments, i.e., the Drawin recipe with $S_{\mathrm{H}} = 0.0$, 0.1, and 1.0, and the treatment from Belyaev et al. (2014). The results are depicted in Figures 3 and 4, respectively. Our adopted stellar parameters for the Sun are $T_{\mathrm{eff}} = 5777$ K, [Fe/H] = 0.0 dex, $\log g = 4.44$ dex, and $\xi_t = 0.9\ \mathrm{km\ s^{-1}}$. As shown in these two groups of figures, the calculated NLTE line profiles with $S_{\mathrm{H}} = 0.1$ and the treatment from Belyaev et al. (2014) can fit the observed spectral lines well for both the Sun and Arcturus; for the strong lines at 15888 and 16680 Å, the synthetic line profiles with $S_{\mathrm{H}} = 1.0$ are shallower than the observed lines, while those with $S_{\mathrm{H}} = 0.0$ are slightly deeper, with the same silicon abundance.

2.2. Model Atmospheres

We adopted MARCS atmospheric models,[7] described in detail by Gustafsson et al. (2008). The MARCS models come in two types, the plane-parallel and the spherically symmetric model atmospheres. The models with low surface gravities ($-1.0 \leqslant \log g \leqslant 3.5$) are calculated in spherical geometry, while the plane-parallel models are adopted for stars with $3.0 \leqslant \log g \leqslant 5.5$. Gustafsson et al. (2008) suggested that sphericity effects are generally important for the temperature structures of low-gravity stars. In this paper, spherical model atmospheres are used for stars with $\log g \leqslant 3.5$, and plane-parallel model atmospheres for the other stars. They are interpolated with a FORTRAN-based routine coded by Thomas Masseron.[8]

The main characteristics of the MARCS model atmospheres are summarized below (Gustafsson et al. 2008).

1. The basic chemical composition of the Sun in model atmospheres is that listed by Grevesse et al. (2007). The adopted solar Si abundance is 7.51 dex, which is the Si abundance based on a three-dimensional (3D) LTE and also the meteoritic Si abundance. Amarsi & Asplund (2016) recently based on 3D NLTE calculations and also found the same solar Si abundance.
2. The α-enhancement is included.

$$[\alpha/\mathrm{Fe}] = \begin{cases} 0.4 \cdot |[\mathrm{Fe/H}]| & \text{if } -1.0 < [\mathrm{Fe/H}] < 0.0 \\ 0.4 & \text{if } [\mathrm{Fe/H}] \leqslant -1.0 \end{cases}.$$

3. The adopted mixing-length parameter l/H_{P} is 1.5 (Henyey et al. 1965).

2.3. Statistical Equilibrium Codes

A revised DETAIL program of Butler & Giddings (1985) was adopted to solve the coupled statistical equilibrium and the radiative transfer equations. This program is based on an

---

[7] http://marcs.astro.uu.se
[8] http://marcs.astro.uu.se/software.php

Table 2
Comparison of Stellar Parameters with Other Studies

Star	$T_{\rm eff}$ (K)	log g (cgs)	[Fe/H]	ξ_t (km s^{-1})	Reference[a]
Arcturus	4275	1.67	−0.58	1.60	This study
	4286	1.66	−0.52	1.74	RAM11
	4286	1.66	−0.48	1.74	SHE15
HD 87	5053	2.71	−0.10	1.35	This study
	5072	2.63	−0.10	1.35	TAK08
HD 6582	5390	4.42	−0.81	0.90	This study
	5387	4.45	−0.83	0.89	FUH98
HD 6920	5845	3.45	−0.06	1.40	This study
	5838	3.48	−0.05	1.35	FUH98
HD 22675	4901	2.76	−0.05	1.30	This study
	4878	2.50[b]	−0.06	1.29	TAK08
		2.66[c]	…		…
HD 31501	5320	4.45	−0.40	1.00	This study
	5326	4.41	−0.38	1.00	WAN09
HD 58367	4932	1.79	−0.18	2.00	This study
	4911	1.76	−0.14	2.04	TAK08
HD 67447	4933	2.17	−0.05	2.12	This study
	4974	2.12	−0.06	2.12	TAK08
HD 102870	6070	4.08	0.20	1.20	This study
	6085	4.04	0.14	1.38	FUH98
	6060	4.11	0.18	1.20	MAS11
HD 103095	5085	4.65	−1.35	0.80	This study
	5110	4.66	−1.35	0.85	FUH98
	5070	4.69	−1.35	0.80	MAS07
HD 121370	6020	3.80	0.28	1.40	This study
	6023	3.76	0.28	1.40	FUH98
HD 148816	5830	4.10	−0.73	1.40	This study
	5823	4.13	−0.73	1.40	NIS10
HD 177249	5273	2.66	0.03	1.65	This study
	5251	2.55[b]	0.00	1.65	TAK08
	…	2.62[c]	…	…	TAK08

Notes. Underlines mean that the stars are discussed in detail in Section 4.
[a] RAM11: Ramírez & Allende Prieto (2011), SHE15: Sheminova (2015), TAK08: Takeda et al. (2008), FUH98: Fuhrmann (1998), WAN09: Wang et al. (2009), MAS11: Mashonkina et al. (2011), MAS07: Mashonkina et al. (2007), NIS10: Nissen & Schuster (2010).
[b] log g, derived from the spectroscopic method.
[c] log g, derived from the parallax and evolution-track method.

accelerated lambda iteration scheme, following the approach described by Rybicki & Hummer (1991, 1992). In this paper, departure coefficients were computed with DETAIL and then fed to the spectrum synthesis software package Spectrum Investigation Utility (SIU), developed by Reetz (1991), to derive chemical abundances.

3. THE SAMPLE STARS AND THEIR SPECTRA

3.1. Sample Selection

Although Shi et al. (2012) have demonstrated that their Si atomic model could provide consistent silicon abundances for the optical and infrared J-band spectra, we would like to check whether the atomic model can also be applied to the H-band Si I lines. We selected 13 FGK dwarfs and giants as sample stars for this test according to the following criteria: 1) they must have available high-resolution ($R > 20{,}000$) and high signal-to-noise ratio (S/N > 100) spectra both in the optical and H bands and 2) the selected stars should be representative of the typical stellar parameter range of the FGK stars ($T_{\rm eff} \sim 4000$–6500 K, log $g \sim 0.0$–5.0, and [M/H] ~ -2.0–0.5 dex). The final stellar parameters of sample stars span from 4275 to 6070 K for $T_{\rm eff}$, from 1.67 to 4.65 for log g, and from −1.35 to 0.28 dex for [Fe/H]. However, there are no very metal-poor stars ([Fe/H] < −1.5 dex) in our sample because the Si lines in the APOGEE spectra are weak for such stars. The IR and optical data are described in the following subsections.

3.2. Infrared H-band Spectra

The IR H-band spectra of our 13 sample stars are from the New Mexico State University (NMSU) 1m+APOGEE observations, and they are included in SDSS DR12. The 1m +APOGEE configuration is designed to observe nearby bright stars and to provide an improved calibration for the main APOGEE survey (Holtzman et al. 2015). A bundle of ten fibers was installed connecting the APOGEE instrument to the NMSU 1 m telescope. This configuration provides one science fiber and nine sky fibers per observation. Bright stars with a magnitude of $0 < H < 8$ are observed in this configuration in dark time when the APOGEE instrument is not connected with the Sloan 2.5 m telescope. The spectra taken with the NMSU 1m+APOGEE are reduced and analyzed with the same software employed by the main survey (Nidever et al. 2015). We refer the reader to Feuillet et al. (2016) for more details. Since all 13 selected stars are bright, the S/N of APOGEE spectra of these stars are very high (e.g., S/N ⩾ 400 for Arcturus). As mentioned earlier, the resolution is about 22,500.

The high-resolution ($R \sim 500{,}000$) solar infrared spectrum from the Kurucz website[9] was adopted in this study. It was obtained by James Brault at Kitt Peak and reduced by Robert L. Kurucz. We also employed the spectrum of Arcturus from the NOAO science archives,[10] which was recorded with the Fourier transform spectrometer (FTS, Hall et al. 1979) operated at the coudé focus of the Mayall 4 m reflector at Kitt Peak. The detailed description of the observation was presented by Hinkle et al. (1995). The high-resolution (∼100,000) and high S/N spectrum of Arcturus facilitates identifying the continuum, and is most efficient in recognizing blending lines.

3.3. Optical Spectra

We adopted the optical solar spectrum of Kurucz et al. (1984). Six of our sample stars (HD 6582, HD 6920, HD 102870, HD 103095, HD 121370, and HD 148816) were observed with the fiber-coupled Cassegrain échelle spectrograph (FOCES; Pfeiffer et al. 1998) on the 2.2 m telescope at the Calar Alto Observatory. Spectra of HD 87, HD 22675, HD 58367, and HD 177249 were taken with the High Dispersion Échelle Spectrograph (HIDES) on the coudé focus of the 1.88 m reflector at the Okayama Astrophysical Observatory (Izumiura 2003). The optical spectrum of Arcturus was obtained with the échelle spectrograph (ES) on the Kitt Peak coudé feed telescope (KPCFT), with a typical resolving power of 150,000 and a S/N of about 1000 (Hinkle et al. 2000, 2005). Both HD 31501 and HD 67447 were observed using the 2.16 m telescope at Xinglong station, but with different spectrographs: for HD 31501 it was the Coudé Échelle Spectrograph (CES; Zhao & Li 2001), and for HD 67447 with the fiber optics échelle spectrograph (FOES). The detailed

---

[9] http://kurucz.harvard.edu/sun/irradiance2008/
[10] http://ast.noao.edu/data/other

Table 3
Atomic Data of the Silicon Optical and *H*-band Lines, the Derived LTE and NLTE Solar Silicon Abundance Based on Log *gf* from References and the NLTE Corrections for the Solar Silicon Lines

λ (Å)	Transition	χ (eV)	log C_6	log *gf*	Reference	log $\varepsilon_\odot$Si LTE (dex)	log $\varepsilon_\odot$Si NLTE (dex)	log gf' LTE	log gf' NLTE	$\Delta_\odot$ (dex)
5701.104	$4s\ ^3P^o_1-5p\ ^3P_0$	4.930	−30.094	−2.05	GAR73, KEL08	7.60	7.60	−1.96	−1.96	0.00
5772.146	$4s\ ^1P^o_1-5p\ ^1S_0$	5.082	−30.087	−1.75	GAR73, KEL08	7.64	7.63	−1.62	−1.63	−0.01
6142.483	$3p^3\ ^3D^o_1-5f\ ^3D_3$	5.619	−29.669	−1.30	KUR07	7.37	7.37	−1.44	−1.44	0.00
6145.016	$3p^3\ ^3D^o_2-5f\ ^3G_3$	5.616	−29.669	−1.31	KUR07	7.45	7.45	−1.37	−1.37	0.00
6155.134	$3p^3\ ^3D^o_3-5f\ ^3G_4$	5.619	−29.669	−0.76	KUR07	7.50	7.49	−0.77	−0.78	−0.01
6237.319	$3p^3\ ^3D^o_1-5f\ ^3F_2$	5.614	−29.669	−0.98	KUR07	7.43	7.43	−1.06	−1.06	0.00
6243.815	$3p^3\ ^3D^o_2-5f\ ^3F_3$	5.616	−29.669	−1.24	KUR07	7.49	7.49	−1.26	−1.26	0.00
6244.466	$3p^3\ ^3D^o_2-5f\ ^1D_2$	5.616	−29.669	−1.09	KUR07	7.35	7.35	−1.25	−1.25	0.00
mean	…	…	…	…	…	7.48	7.48	…	…	…
σ	…	…	…	…	…	0.10	0.10	…	…	…
15888.440	$4s\ ^1\ P^o_1-4p\ ^1P_1$	5.082	−30.638	0.06	KUR07	7.58	7.57	0.13	0.12	−0.01
16380.177	$4p\ ^1\ P_1-3d\ ^1P^o_1$	5.863	−30.495	−0.47	KUR07	7.03	7.03	−0.95	−0.95	0.00
16680.810	$4p\ ^3D_3-3d\ ^3D^o_3$	5.984	−30.357	−0.14	KUR07	7.48	7.45	−0.17	−0.20	−0.03
16828.158	$4p\ ^3D_3-3d\ ^3D^o_2$	5.984	−30.357	−1.03	KUR07	7.41	7.41	−1.13	−1.13	0.00
mean	…	…	…	…	…	7.37	7.36	…	…	…
σ	…	…	…	…	…	0.24	0.24	…	…	…

Note. References to the log *gf* values are GAR73: Garz (1973), KEL08: Kelleher & Podobedova (2008) and KUR07: Kurucz (2007). The log C_6 values were calculated according to Anstee & O'Mara (1991, 1995) and Barklem et al. (2000). σ refers to the statistical error. The log gf' denotes that the *gf*-values were derived from the solar fits.

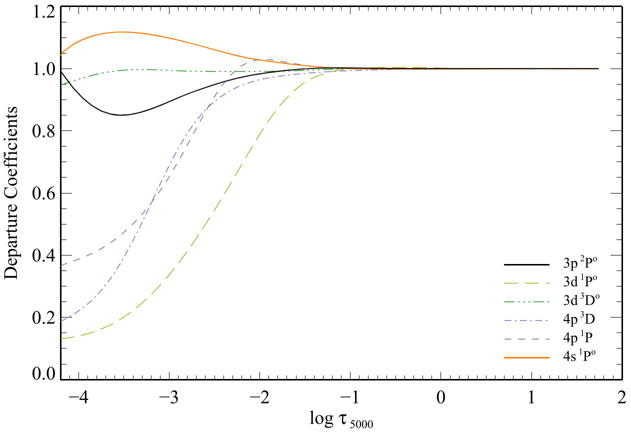

Figure 2. Departure coefficients $b_i = N_i^{\rm NLTE}/N_i^{\rm LTE}$ as a function of the standard optical depth for HD 87.

observational information for the sample stars is listed in Table 1 (except for the Sun). It is worthwhile noting that all optical spectra have a resolving power better than 35,000 and a S/N $\geqslant$ 150.

4. STELLAR PARAMETERS

The stellar parameters of all 13 stars were determined via the spectroscopic approach. Specifically, the effective temperature and surface gravity were determined by fulfilling the excitation equilibrium of Fe I and the ionization equilibrium of Fe I and Fe II, respectively; the microturbulence velocity was determined by forcing [Fe/H] from different Fe I lines to be independent of their equivalent widths. Table 8 gives the equivalent widths for our sample stars.

This process of determining stellar parameters is an iterative procedure. A set of initial parameters is needed to begin with. The initial temperature was derived from the Balmer lines (H_α and H_β) (Fuhrmann 1998) when these lines were available. Otherwise, it was obtained based on the color index ($b-y$ or $V-K$) employing the calibration given by Alonso et al. (1996, 1999, 2001). The initial surface gravity was estimated using the parallax method. There are 30 Fe I and 6 Fe II optical lines included in our analysis. The line data as well as the equivalent widths for the solar iron lines are listed in Table 6. Departures from LTE have been considered when determining the iron abundance based on the iron model atom from Mashonkina et al. (2011), and for the Sun and our sample stars, they are small, lower than 0.05 dex. In Table 6 we also present the solar LTE and NLTE iron abundances based on the oscillator strength (log *gf*) values recommended by the VALD3 database.[11] According to this table, the iron abundances derived from Fe I lines are 7.56 ± 0.13 dex in LTE and 7.60 ± 0.13 dex in NLTE, while they are 7.49 ± 0.04 dex from Fe II lines in both cases. The statistical error for the Sun is uncomfortably large, up to 0.13 dex, thus we derived the empirical log *gf* by fitting the solar spectrum and present the log *gf* values derived from the NLTE solar fits in this table. The values of log C_6 were calculated referring to Anstee & O'Mara (1991, 1995) and Barklem et al. (2000). Based on multiple iterative processes, we estimate that the typical uncertainties of $T_{\rm eff}$, $\log g$, [Fe/H], and ξ_t are ±80 K, ±0.1 dex, ±0.08 dex, and 0.2 km s^{-1}, respectively.

---

[11] http://vald.astro.uu.se

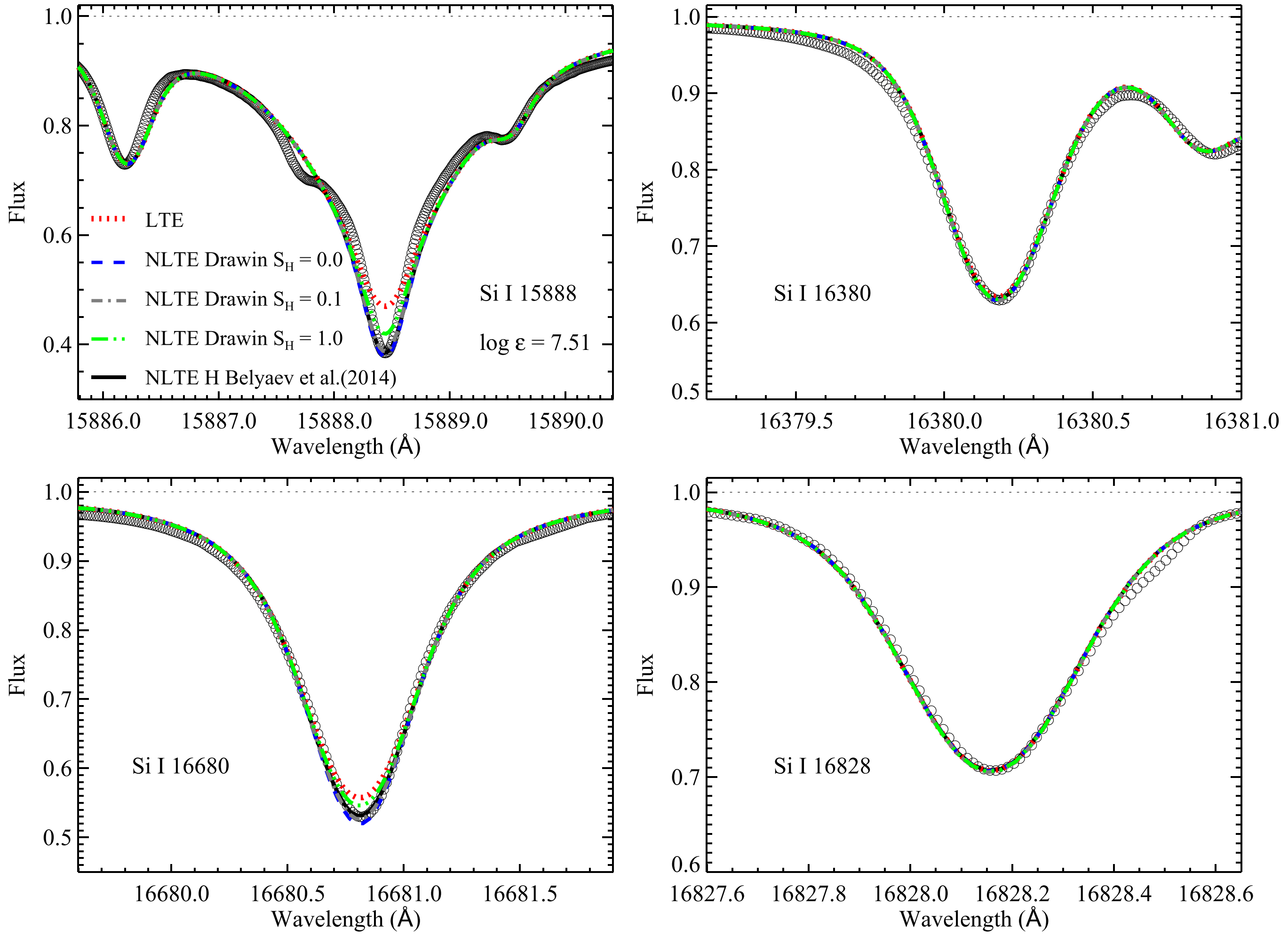

Figure 3. *H*-band solar Si I line profiles. The NLTE profiles with rates of collisions with hydrogen from Belyaev et al. (2014) and the Drawin recipe with $S_H = 0.0$, 0.1, 1.0, and LTE profiles compared with the observed spectrum (open circles), where the NLTE profiles with the Belyaev et al. (2014) treatment refer to the best fits.

The final derived stellar parameters, along with stellar parameters for the same stars from the literature, are presented in Table 2. Our derived values are consistent with those from literature, except $\log g$ for HD 22675 and HD 177249. Our newly derived $\log g$ values for the two stars are 0.26 and 0.11, respectively, higher than those determined by Takeda et al. (2008). We note that our spectroscopic $\log g$ values agree well with those from the parallax method derived by Takeda et al. (2008). This may indicate that our spectroscopic surface gravities for these two stars are more accurate than those from Takeda et al. (2008).

5. NLTE CALCULATIONS FOR SAMPLE STARS

5.1. Line Data

5.1.1. Infrared Atomic Line Data in the H band

Initially, we found 11 Si I lines in the *H*-band APOGEE spectra. A further investigation reveals that seven of them are very weak or heavily blended. As a result, only four lines were employed in this study. The details about them are presented in Table 3. The transitions are taken from the NIST database.[12] The van der Waals damping constants ($\log C_6$) are extracted from Meléndez & Barbuy (1999) , who calculated C_6 based on the quantum-mechanical approximate cross sections provided by Anstee & O'Mara (1995); Barklem & O'Mara (1997) and Barklem et al. (1998). We derived the solar LTE and NLTE Si abundances using the *gf*-values referring to the references and found that the statistic errors are very large in both LTE and NLTE. In order to reduced the importance of oscillator strengths, therefore, we performed a line-to-line differential analysis and the *gf*-values derived from the LTE and NLTE solar spectrum fits are also listed in Table 3.

5.1.2. Optical Atomic Line Data

We started with the same set of neutral Si optical lines used by Shi et al. (2009). An examination shows that the line at 3905 Å is severely blended with a CH line, and the line at 4103 Å falls in the wing of H_δ, while the line at 5690 Å is blended with an iron line. These three transitions were excluded from our Si abundance analysis. The adopted eight Si I lines and line data are listed in Table 3. We also derived the solar Si abundance based on optical lines using the $\log gf$ values from references. Although the mean Si abundance is consistent with the previous studies, the statistic error is also

---

[12] http://physics.nist.gov/

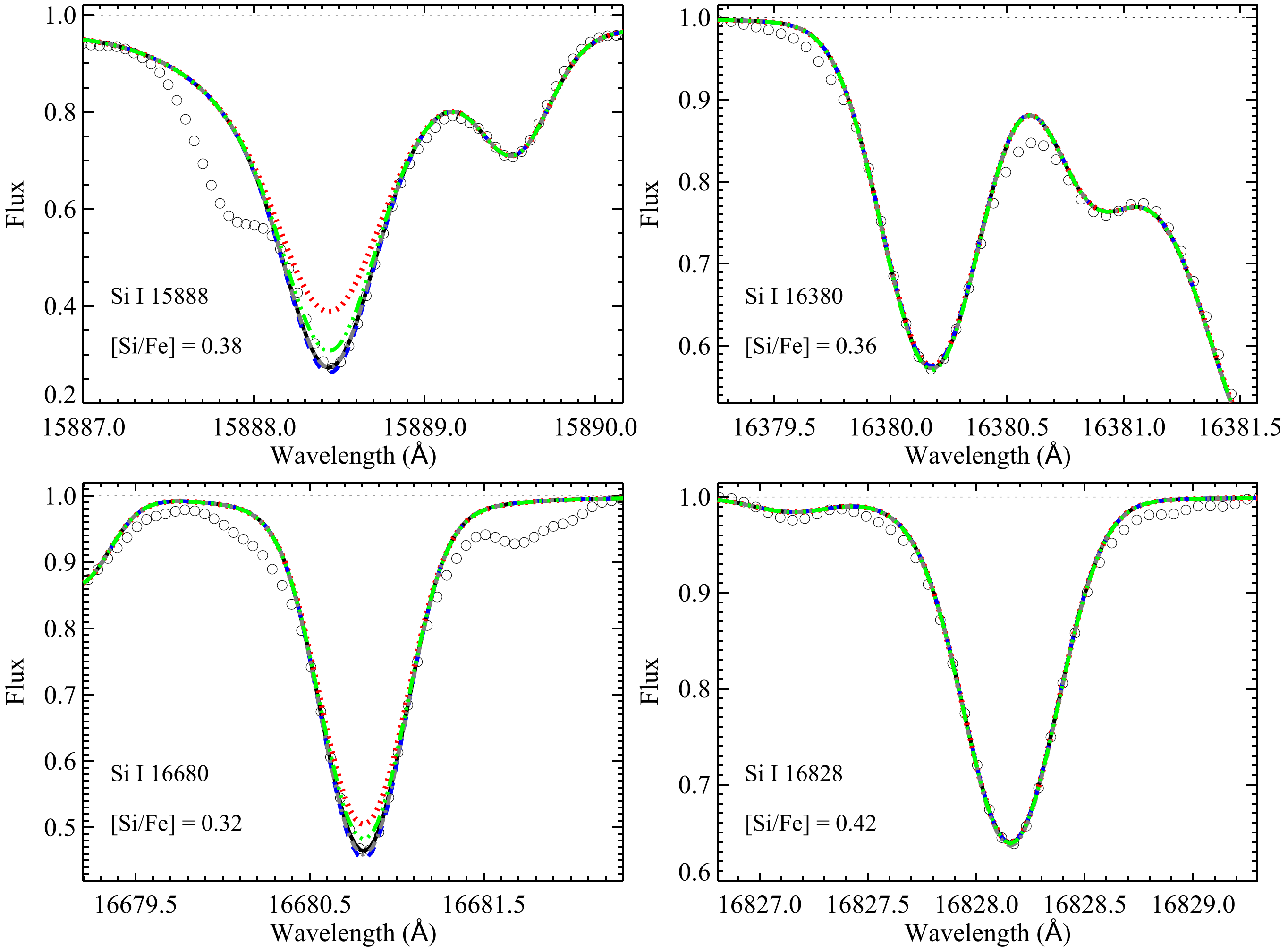

Figure 4. Similar to Figure 3, the NLTE and LTE profiles for Arcturus. Here the observed spectrum is from Hinkle et al. (1995).

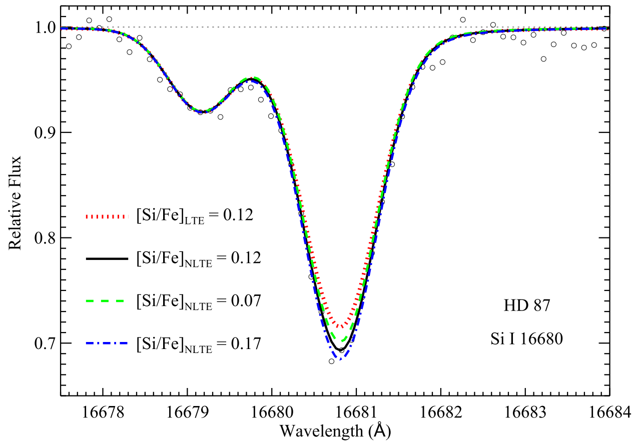

Figure 5. Spectrum synthesis of the Si I 16680 Å line for HD 87. The open circles are the observed spectrum. The black solid line is the best-fitting NLTE line profile, and the red dotted curve is the LTE profile with the same Si abundance. The other two lines are the synthetic spectra in NLTE with different [Si/Fe] (see the legend for details).

not satisfying, up to 0.1 dex. To be consistent with the situation for infrared lines, we also present the *gf*-values determined from the solar spectrum fitting. The C_6 values were calculated according to Anstee & O'Mara (1991, 1995) and Barklem et al. (2000).

5.2. NLTE Effects

5.2.1. Departures form LTE for the Si I H-band Lines

In Figure 2 we present the departure coefficients (b_i) for the relevant Si I levels for H-band transitions and Si II ground state as a function of the optical depth at $\lambda = 5000$ Å (τ_{5000}) for the model atmosphere of HD 87. Here, the departure coefficients (b_i) are defined as $b_i = n_i^{\mathrm{NLTE}}/n_i^{\mathrm{LTE}}$, where n_i^{NLTE} and n_i^{LTE} represent the statistical equilibrium (NLTE) and thermal (LTE) atomic level number densities, respectively. It is found that the departure coefficients for the level $3d\ ^3\mathrm{D}^0$ of Si I are near their thermal value ($b_i \sim 1$) and the level $4s\ ^1\mathrm{P}^0$ is overpopulated, while the other excitation levels, $4p\ ^1\mathrm{P}$, $4p\ ^3\mathrm{D}$, and $3d\ ^1\mathrm{P}^\mathrm{o}$ are underpopulated as a result of photon loss (see Figure 2 for details).

As the first test of our atomic model, we have analyzed optical lines for the Sun. We confirmed that the NLTE corrections for optical silicon lines are negligible (Shi et al. 2008; Wedemeyer 2001; Bergemann et al. 2013). For the investigated four H-band Si lines, we found that the derived NLTE effects are also minor, and the largest effect is 0.03 dex

Table 4
Stellar [Si/Fe] for the Individual Si I H-band Lines under LTE and NLTE Analyses

	15888 (Å)		16380 (Å)		16680 (Å)		16828 (Å)		$\sigma_{\rm line}$	
Star	LTE	NLTE	LTE	NLTE	LTE	NLTE	LTE	NLTE	LTE	NLTE
Arcturus[a]	0.49	0.38	0.37	0.36	0.43	0.32	0.43	0.42	0.06	0.05
Arcturus[b]	0.50	0.38	0.34	0.33	0.44	0.34	0.44	0.43	0.08	0.06
HD 87	0.19	0.08	0.15	0.14	0.23	0.12	0.15	0.15	0.05	0.04
HD 6582	0.22	0.19	0.26	0.25	0.26	0.25	⋯	⋯	0.03	0.04
HD 6920	0.11	−0.01	−0.04	−0.05	0.10	−0.01	⋯	⋯	0.10	0.03
HD 22675	0.12	0.02	0.07	0.06	0.15	0.06	⋯	⋯	0.05	0.03
HD 31501	0.13	0.09	0.16	0.15	0.21	0.19	⋯	⋯	0.05	0.07
HD 58367	0.26	0.03	0.04	0.04	0.31	0.13	0.12	0.13	0.16	0.07
HD 67447	0.25	0.08	0.05	0.04	0.22	0.07	0.10	0.10	0.12	0.03
HD 102870	−0.02	−0.09	−0.07	−0.08	−0.04	−0.09	−0.08	−0.08	0.04	0.01
HD 103095	0.26	0.24	0.36	0.36	0.35	0.35	⋯	⋯	0.07	0.08
HD 121370	0.11	0.02	0.15	0.14	0.22	0.14	0.14	0.14	0.06	0.06
HD 148816	0.30	0.24	0.21	0.20	0.27	0.23	⋯	⋯	0.06	0.03
HD 177249	0.20	0.07	⋯	⋯	0.20	0.06	0.08	0.08	0.08	0.01

Notes. $\sigma_{\rm line}$ denotes the mean line-to-line scatter.

[a] The H-band spectrum of Arcturus is from Hinkle et al. (1995).

[b] The H-band spectrum of Arcturus is from the NMSU 1m+APOGEE.

Table 5
Stellar Silicon LTE and NLTE Abundances

Star	$T_{\rm eff}$	log g	[Fe/H]	ξ_t	[Si $\rm I_{LTE}$/Fe](ir)	[Si $\rm I_{NLTE}$/Fe](ir)	$\Delta_{\rm ir}$	[Si $\rm I_{LTE}$/Fe](opt)	[Si $\rm I_{NLTE}$/Fe](opt)	$\Delta_{\rm opt}$
Arcturus[a]	4275	1.67	−0.58	1.60	0.43 ± 0.05	0.37 ± 0.04	−0.06	0.35 ± 0.03	0.29 ± 0.02	−0.06
Arcturus[b]	4275	1.67	−0.58	1.60	0.43 ± 0.07	0.37 ± 0.05	−0.06	⋯	⋯	⋯
HD 87	5053	2.71	−0.10	1.35	0.18 ± 0.04	0.12 ± 0.03	−0.06	0.15 ± 0.03	0.12 ± 0.01	−0.03
HD 6582	5390	4.42	−0.81	0.90	0.25 ± 0.02	0.23 ± 0.03	−0.02	0.27 ± 0.02	0.27 ± 0.02	0.00
HD 6920	5845	3.45	−0.06	1.40	0.06 ± 0.08	−0.02 ± 0.02	−0.08	0.05 ± 0.05	0.02 ± 0.03	−0.03
HD 22675	4901	2.76	−0.05	1.30	0.11 ± 0.04	0.05 ± 0.02	−0.06	0.11 ± 0.04	0.07 ± 0.02	−0.04
HD 31501	5320	4.45	−0.40	1.00	0.17 ± 0.04	0.14 ± 0.05	−0.03	0.22 ± 0.02	0.21 ± 0.02	−0.01
HD 58367	4932	1.79	−0.18	2.00	0.18 ± 0.12	0.08 ± 0.06	−0.10	0.16 ± 0.05	0.13 ± 0.02	−0.03
HD 67447	4933	2.17	−0.05	2.12	0.16 ± 0.10	0.07 ± 0.02	−0.09	0.12 ± 0.04	0.08 ± 0.02	−0.04
HD 102870	6070	4.08	0.20	1.20	−0.05 ± 0.03	−0.09 ± 0.01	−0.04	−0.07 ± 0.02	−0.08 ± 0.02	−0.01
HD 103095	5085	4.65	−1.35	0.80	0.32 ± 0.06	0.32 ± 0.07	0.00	0.30 ± 0.04	0.30 ± 0.04	0.00
HD 121370	6020	3.80	0.28	1.40	0.16 ± 0.05	0.11 ± 0.06	−0.05	0.22 ± 0.05	0.19 ± 0.03	−0.03
HD 148816	5830	4.10	−0.73	1.40	0.26 ± 0.05	0.22 ± 0.02	−0.04	0.18 ± 0.03	0.18 ± 0.03	0.00
HD 177249	5273	2.66	0.03	1.65	0.16 ± 0.07	0.07 ± 0.01	−0.09	0.05 ± 0.04	0.03 ± 0.02	−0.02

Notes. $\Delta_{\rm ir}$ and $\Delta_{\rm opt}$ stand for the NLTE effects ($\Delta = \log \varepsilon_{\rm NLTE} - \log \varepsilon_{\rm LTE}$) derived from IR and optical spectra, respectively.

[a] The H-band spectrum of Arcturus is from Hinkle et al. (1995).

[b] The H-band spectrum of Arcturus is from the NMSU 1m+APOGEE.

(see Table 3). A comparison between the calculated H-band line profiles and the observed solar spectrum is shown in Figure 3. In this figure, the NLTE (black solid) lines agree well with the observed spectrum for the strong lines at 15888 and 16680 Å, while the LTE (red dotted) line profiles are weaker. This issue is more obvious for Arcturus, as presented in Figure 4. Figure 5 gives the synthetic profiles at 16680 Å under LTE and NLTE for HD 87. The black solid line denotes the best fit to the observed spectrum in NLTE with a [Si/Fe] of 0.12 dex. The red dotted curve is produced with the same [Si/Fe] in LTE, which is shallower in the line core.

In Table 4 we present the Si abundances derived from the individual H-band lines and the mean line-to-line scatter under NLTE and LTE for all sample stars. As indicated in this table, relative to LTE, NLTE obviously reduces the line-to-line scatter in the derived abundances for some stars. Taking HD 67447 as an example, the mean line-to-line scatter is reduced from 0.12 in LTE to 0.03 dex in NLTE. Table 5 gives the mean abundances along with the standard deviation. As shown in this table, the largest standard deviation in LTE is 0.12 dex, but it decreases to 0.07 dex when the NLTE effects are considered.

According to Table 4, the NLTE effects differ from line to line, and they are larger for strong lines. In our four H-band lines, NLTE effects are relatively strong for the Si I lines at 15888 and 16680 Å, while they are weaker for the others. Table 5 also shows the mean NLTE corrections for individual stars, and the NLTE effects range from −0.1 to 0.0 dex.

Table 6
Line Data, Iron Abundances Derived from the Solar Spectrum, and Equivalent Widths of the Solar Lines

λ (Å)	χ (eV)	log C_6	log *gf*	Reference	log $\varepsilon_\odot$Fe LTE (dex)	log $\varepsilon_\odot$Fe NLTE (dex)	log gf'	EW (mÅ)
Fe I								
4661.534	4.558	−29.481	−1.27	FUH88	7.57	7.61	−1.16	40.5
4808.149	3.251	−31.464	−2.79	FUH88	7.66	7.70	−2.59	29.5
4885.430	3.882	−30.173	−1.02	KUR14	7.49	7.55	−0.97	91.3
5223.186	3.635	−31.165	−1.78	BRI91	7.05	7.09	−2.19	31.0
5242.497	3.634	−31.248	−0.97	BRI91	7.56	7.52	−0.95	90.3
5379.579	4.154	−31.242	−1.51	BRI91	7.57	7.57	−1.44	63.5
5398.279	4.371	−30.155	−0.67	FUH88	7.55	7.59	−0.58	78.8
5522.449	4.217	−30.457	−1.55	FUH88	7.63	7.68	−1.37	44.9
5546.506	4.434	−30.356	−1.31	FUH88	7.68	7.74	−1.07	52.7
5618.633	4.386	−30.475	−1.28	BRI91	7.49	7.55	−1.23	52.2
5651.469	4.386	−30.264	−2.00	FUH88	7.77	7.78	−1.72	19.5
5679.023	4.186	−30.040	−0.92	FUH88	7.72	7.78	−0.64	65.0
5793.915	4.220	−30.505	−1.70	FUH88	7.58	7.63	−1.57	35.5
5853.148	1.485	−31.586	−5.28	FUH88	7.64	7.67	−5.11	8.1
5855.077	4.608	−30.189	−1.48	BAR94	7.43	7.48	−1.50	23.3
5929.677	4.548	−30.305	−1.41	FUH88	7.71	7.77	−1.14	41.7
6024.058	4.548	−30.358	−0.12	FUH88	7.66	7.70	0.08	127.5
6078.491	4.796	−29.749	−0.32	KUR14	7.47	7.52	−0.30	84.6
6079.009	4.652	−30.237	−1.12	FUH88	7.64	7.70	−0.92	48.8
6151.623	2.176	−31.538	−3.30	FUH88	7.53	7.55	−3.25	51.6
6173.335	2.223	−31.523	−2.88	FUH88	7.56	7.58	−2.80	70.1
6200.321	2.608	−31.279	−2.44	FUH88	7.59	7.59	−2.35	75.2
6240.646	2.223	−31.450	−3.23	BAR91	7.44	7.46	−3.27	48.7
6322.686	2.588	−31.296	−2.43	FUH88	7.60	7.60	−2.33	77.6
6335.331	2.198	−31.546	−2.18	BRI91	7.46	7.46	−2.22	103.3
6481.877	2.279	−31.420	−2.98	FUH88	7.58	7.60	−2.88	65.7
6593.871	2.433	−31.375	−2.42	FUH88	7.62	7.63	−2.29	98.7
6726.666	4.607	−30.256	−1.09	KUR14	7.56	7.63	−0.96	50.2
6839.831	2.559	−31.346	−3.45	FUH88	7.55	7.58	−3.37	30.3
6857.250	4.076	−30.895	−2.15	FUH88	7.56	7.61	−2.04	23.4
mean	…	…	…	…	7.56	7.60	…	…
σ	…	…	…	…	0.13	0.13	…	…
Fe II								
4508.288	2.856	−31.971	−2.25	RYA99	7.48	7.48	−2.27	77.6
5264.808	3.230	−31.977	−3.12	RYA99	7.53	7.53	−3.09	103.3
5414.073	3.221	−31.976	−3.54	RYA99	7.45	7.45	−3.60	65.7
5991.376	3.153	−31.983	−3.54	BLA80	7.43	7.43	−3.61	98.7
6149.258	3.889	−32.048	−2.72	BLA80	7.49	7.49	−2.73	50.2
6456.383	3.903	−31.979	−2.10	BLA80	7.54	7.54	−2.07	30.3
mean	…	…	…	…	7.49	7.49	…	…
σ	…	…	…	…	0.04	0.04	…	…

Note. References to the log *gf* values are FUH88: Fuhr et al. (1988), KUR14: Kurucz (2014), BRI91: O'Brian et al. (1991), BAR94: Bard & Kock (1994), BAR91: Bard et al. (1991), RYA99: Ryabchikova et al. (1999) and BLA80: Blackwell et al. (1980). The log C_6 values were calculated according to Anstee & O'Mara (1991, 1995) and Barklem et al. (2000). σ refers to the statistical error. The log gf' denotes that the *gf*-values were derived from the NLTE solar fits.

To explore the dependency of the NLTE corrections on stellar parameters, we plot the difference of the [Si/Fe] derived under NLTE and LTE assumptions for the strong silicon lines (15888 and 16680 Å) as functions of metallicity, effective temperature, and surface gravity in Figure 6. It can be seen that the NLTE corrections of the *H*-band lines are negative, which means that the Si abundances would be overestimated under LTE. The NLTE effects, on the other hand, are very sensitive to the surface gravity, the absolute corrections increase with the decreasing surface gravity, and the largest correction reaches $\sim$0.2 dex for HD 58367. Since surface gravity effects dominate, we do not see clear trends in the NLTE corrections with metallicity and effective temperature in these figures. In order to investigate the NLTE corrections for APOGEE data in extreme cases, we calculated the NLTE and LTE line profiles of the Si I line at 15888 Å with parameters $T_{\rm eff} = 5000$ K, [Fe/H] = 0.0 dex, $\log g = 0.5$, $\xi_t = 2.0\ {\rm km\ s^{-1}}$. As shown in Figure 7, when [Si/Fe] under NLTE and LTE shares the same value, namely [Si/Fe] = 0.0 dex, the two profiles are different. By increasing [Si/Fe], the line cores of LTE spectra tend to be deeper, and until [Si/Fe] reaches 0.39 dex, the LTE profile best fits the synthetic NLTE profile. That is to say that in this extreme case, the NLTE correction can reach ~ -0.4 dex.

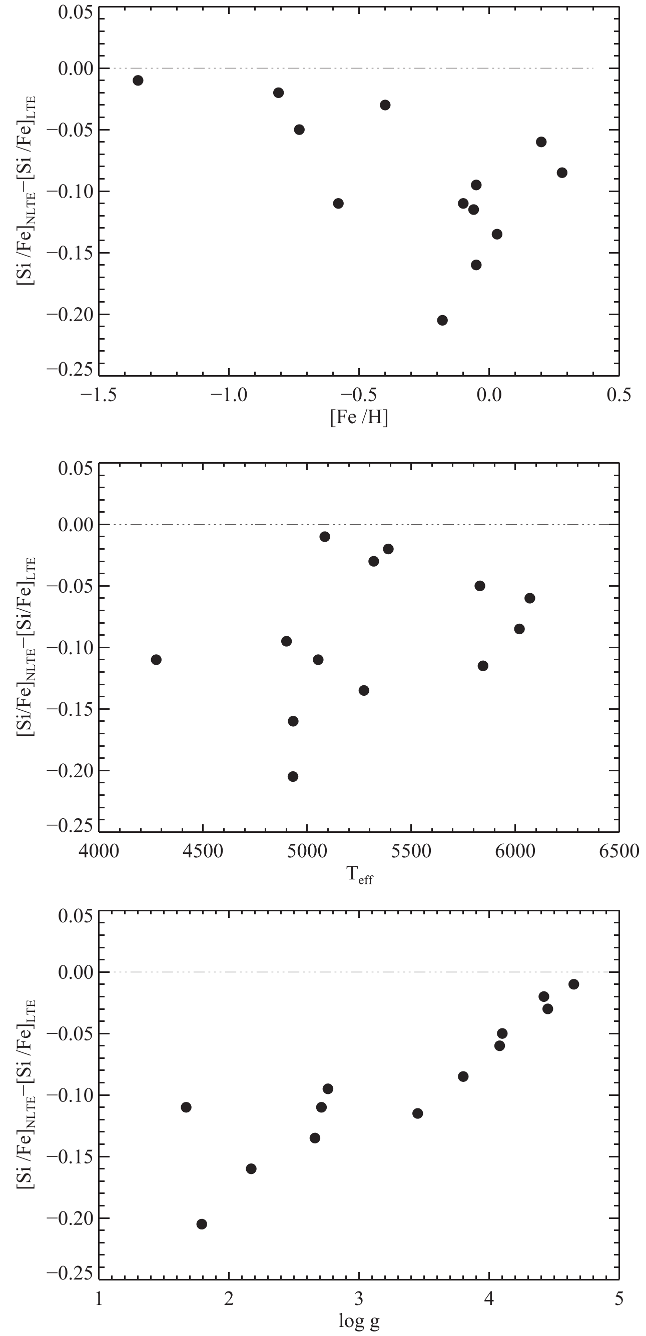

Figure 6. The mean NLTE corrections for the two strong Si i lines at 15888 and 16680 Å as functions of [Fe/H], $T_{\rm eff}$, and log g, respectively (from top to bottom).

To test whether consistent abundances are obtained from spectra acquired with different telescopes or instruments, we derived the Si abundance of Arcturus with the spectrum from Hinkle et al. (1995) ($R \sim$ 100,000) and the 1m+APOGEE spectrum ($R \sim$ 22,500). Figure 8 shows the best-fitting NLTE profiles for the two observed spectra. The left panel shows the Arcturus spectrum from Hinkle et al. (1995), while the right panel is for the 1m+APOGEE spectrum. Their results for individual lines are listed in Table 4, and the mean values for each line are collected in Table 5. The difference of abundances derived from individual lines between the two spectra is negligible, ⩽0.02 dex. A consistent Si abundance is acquired for the same object from different telescopes or instruments.

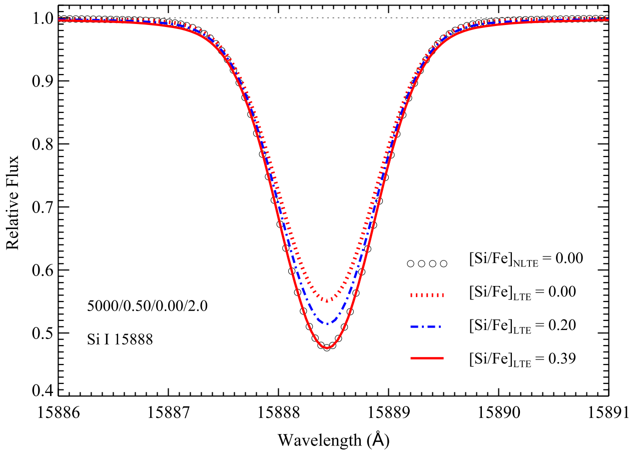

Figure 7. The LTE and NLTE synthetic spectra of Si i 15888 Å line with different [Si/Fe] values and the same parameters of $T_{\rm eff}$ = 5000 K, log g = 0.5, and [Fe/H] = 0.0, ξ_t = 2.0. [Si/Fe] = 0.00, 0.20, and 0.39 dex for the LTE line profiles, while [Si/Fe] = 0.00 for the NLTE calculation.

5.2.2. Departures form LTE for Si i *Optical Lines*

We investigated the eight Si i optical lines described in Section 5.1.2 for our sample stars. The mean Si abundances under LTE and NLTE are presented in Table 5. As shown in this table, the standard deviations are very small, lower than 0.05 dex for both LTE and NLTE abundances; the net NLTE correction for a given star is minor, with an absolute value lower than 0.06 dex. Although the mean NLTE corrections are small, the NLTE effects are necessary for the strongest investigated Si i lines, e.g., the largest NLTE correction for the line at 6155 Å reaches ~0.1 dex in our sample according to Table 7. The corrections could be greater in extreme cases.

5.2.3. Comparison with the Optical Results and Discussions

For our sample stars, the differences between the mean Si abundances derived from IR and from optical spectra are shown against the metallicity in Figure 9. In this figure, open circles denote the differences in LTE, while filled circles indicate the NLTE results. The differences between LTE and NLTE are evidently small (lower than 0.1 dex), and the derived Si abundances from the H-band spectral lines agree better with those from optical lines in NLTE than in LTE. Since the NLTE effects are larger for strong lines, it is interesting to see whether the Si abundances derived when only H-band strong lines at 15888 and 16680 Å are available are still consistent with those from optical lines. The differences between the abundances derived from the two strong H-band lines and from optical lines are depicted in Figure 10. Similar to Figure 9, the NLTE Si abundances from the strong H-band lines are consistent with those from optical lines, while the differences become as large as 0.2 dex in LTE.

6. CONCLUSIONS

The main purpose of this work is to test the validity of the Si atomic model for the H-band line formation and to investigate

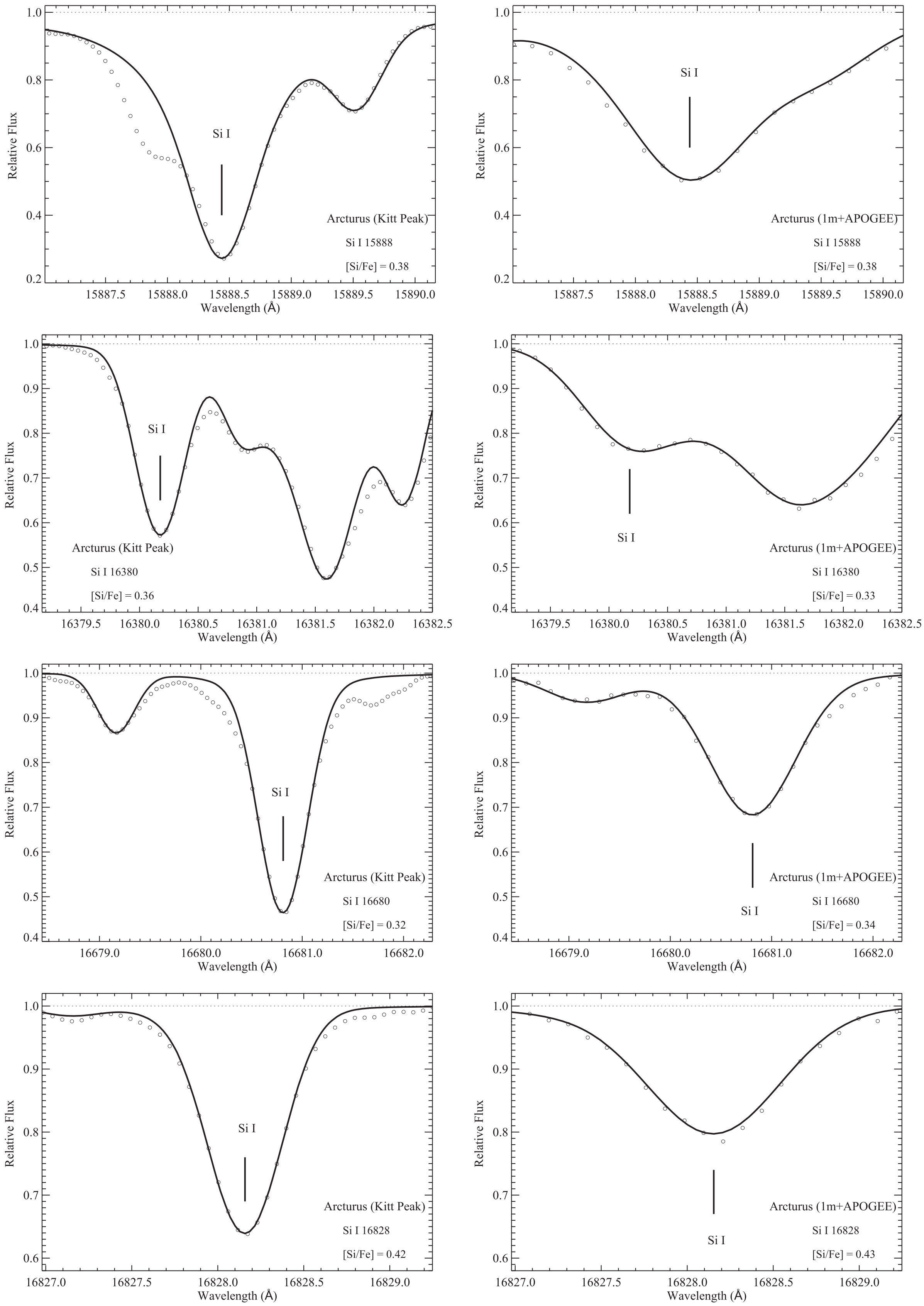

Figure 8. The best-fitting NLTE profiles (solid lines) of the four investigated Si I lines in the Kitt Peak (Hinkle et al. 1995) and 1m+APOGEE observed spectra of Arcturus (open circles). The left panel shows the spectrum of Arcturus from Hinkle et al. (1995), while the right panel is for the 1m+APOGEE spectrum.

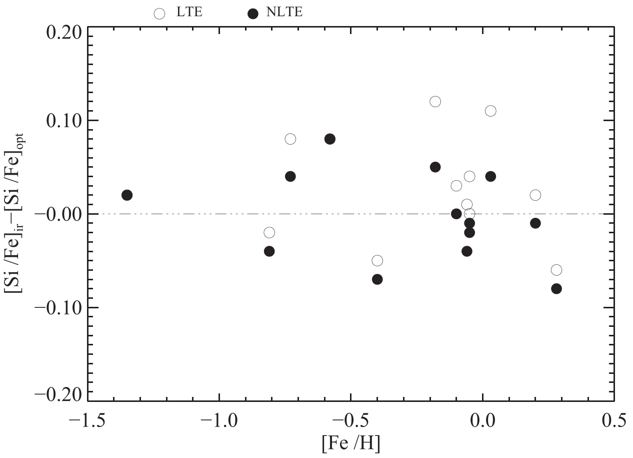

Figure 9. The difference between the mean Si abundances derived from IR and optical lines under LTE (open circles) and NLTE (filled circles) assumptions.

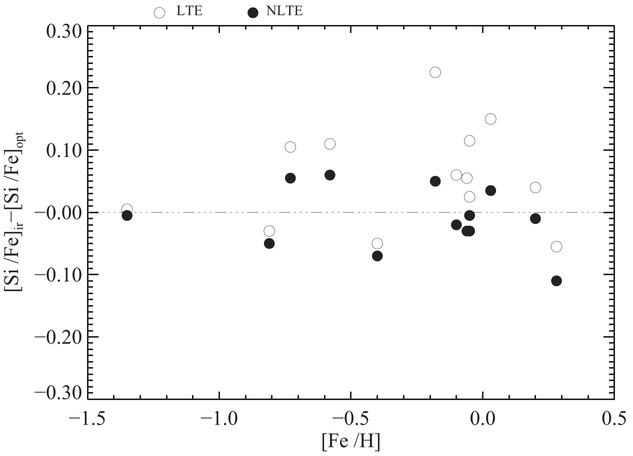

Figure 10. The difference between the Si abundances derived from the two strong Si I lines at 15888 and 16680 Å and the optical lines under LTE (open circles) and NLTE (filled circles).

the NLTE effects on Si spectral lines based on high S/N IR *H*-band spectra. A sample of 13 FGK dwarfs and giants was selected, and the Si abundances were derived from both *H*-band and optical lines under LTE and NLTE.

After careful analyses, we list our conclusions below.

1. With a NLTE analysis, the absolute differences between the mean Si abundances from the *H*-band and from optical lines are lower than 0.1 dex for the sample stars, which suggests that our Si atomic model can be applied to investigate the formation of the *H*-band Si I lines.
2. The NLTE effects differ from line to line. The strong Si I lines at 15888 and 16680 Å need large NLTE corrections, while the other two lines show weaker NLTE effects. Thus, it is not surprising that the NLTE silicon abundance shows a smaller line-to-line scatter than the LTE abundance for some stars in this analysis. The NLTE corrections reach ~−0.2 dex for the strongest Si I line in our sample. It can be up to ~−0.4 dex for the extreme cases of APOGEE targets ($\log g \sim 0.5$). This shows that it should be considered in the abundance analysis, especially for the cases where only strong lines are available.
3. The NLTE effects are sensitive to the surface gravity, and increase with decreasing surface gravities.
4. The NLTE corrections for the investigated *H*-band lines are negative, which means that the Si abundances derived with a LTE assumption are overestimated.

To the best of our knowledge, this work is the first NLTE investigation of the *H*-band Si spectral lines. The NLTE corrections of strong lines range from −0.2 to −0.1 dex for giant stars in our sample. In extreme cases of APOGEE targets, the correction could be up to −0.4 dex. Thus they may have a significant impact on the Si abundances derived from APOGEE observations. Motivated by these results, the APOGEE team is planning to pursue more extended NLTE calculations in the coming years.

This research is supported by National Key Basic Research Program of China 2014CB845700, and by the National Natural Science Foundation of China under grant Nos. 11321064, 11233004, 11390371, 11473033, 11428308, U1331122. C.A.P. is thankful to the Spanish MINECO for support through grant AYA2014-56359-P.

We acknowledge the support of the staff of the Xinglong 2.16 m telescope. This work was partially supported by the Open Project Program of the Key Laboratory of Optical Astronomy, National Astronomical Observatories, Chinese Academy of Sciences. We thank Yoichi Takeda, Bun'ei Sato, and Yujuan Liu for providing us the optical data. The authors thank the anonymous referee for comments that helped to improve the manuscript.

This research uses services or data provided by the NOAO Science Archive. NOAO is operated by the Association of Universities for Research in Astronomy (AURA), Inc. under a cooperative agreement with the National Science Foundation.

This work has made use of the VALD database, operated at Uppsala University, the Institute of Astronomy RAS in Moscow, and the University of Vienna.

Funding for SDSS-III has been provided by the Alfred P. Sloan Foundation, the Participating Institutions, the National Science Foundation, and the U.S. Department of Energy Office of Science. The SDSS-III website is http://www.sdss3.org/.

SDSS-III is managed by the Astrophysical Research Consortium for the Participating Institutions of the SDSS-III Collaboration including the University of Arizona, the Brazilian Participation Group, Brookhaven National Laboratory, Carnegie Mellon University, University of Florida, the French Participation Group, the German Participation Group, Harvard University, the Instituto de Astrofisica de Canarias, the Michigan State/Notre Dame/JINA Participation Group, Johns Hopkins University, Lawrence Berkeley National Laboratory, Max Planck Institute for Astrophysics, Max Planck Institute for Extraterrestrial Physics, New Mexico State University, New York University, Ohio State University, Pennsylvania State University, University of Portsmouth, Princeton University, the Spanish Participation Group, University of Tokyo, University of Utah, Vanderbilt University, University of Virginia, University of Washington, and Yale University.

APPENDIX

Table 7
Silicon Relative to Iron Abundances Based on Optical Si I Lines under LTE and NLTE Analyses

	5701 (Å)		5772 (Å)		6142 (Å)		6145 (Å)		6155 (Å)		6237 (Å)		6243 (Å)		6244 (Å)	
Star	LTE	NLTE	LTE	NLTE	LTE	NLTE	LTE	NLTE	LTE	NLTE	LTE	NLTE	LTE	NLTE	LTE	NLTE
Arcturus	0.32	0.27	⋯	⋯	0.31	0.28	⋯	⋯	0.38	0.28	0.36	0.30	0.36	0.32	⋯	⋯
HD 87	0.15	0.12	0.19	0.13	0.12	0.11	0.14	0.13	0.13	0.13	⋯	⋯	⋯	⋯	⋯	⋯
HD 6582	0.27	0.27	0.27	0.26	⋯	⋯	0.27	0.27	0.26	0.25	0.23	0.23	0.31	0.31	0.27	0.27
HD 6920	⋯	⋯	0.06	0.03	⋯	⋯	0.00	−0.01	0.10	0.05	⋯	⋯	⋯	⋯	⋯	⋯
HD 22675	0.11	0.08	0.14	0.07	0.07	0.05	0.08	0.06	0.17	0.10	⋯	⋯	⋯	⋯	⋯	⋯
HD 31501	0.21	0.20	⋯	⋯	0.18	0.18	0.23	0.22	0.22	0.20	⋯	⋯	0.25	0.24	0.22	0.21
HD 58367	0.15	0.11	⋯	⋯	0.11	0.11	0.13	0.13	0.23	0.15	⋯	⋯	⋯	⋯	⋯	⋯
HD 67447	0.11	0.07	0.15	0.08	0.06	0.05	0.10	0.09	0.17	0.08	0.15	0.10	0.08	0.06	0.13	0.09
HD 102870	−0.09	−0.10	−0.05	−0.07	−0.08	−0.08	−0.06	−0.06	−0.03	−0.05	−0.09	−0.10	−0.07	−0.07	−0.09	−0.09
HD 103095	0.36	0.35	⋯	⋯	⋯	⋯	⋯	⋯	0.25	0.25	0.30	0.30	0.32	0.32	0.28	0.28
HD 121370	⋯	⋯	0.21	0.18	0.17	0.17	0.17	0.17	0.29	0.23	0.24	0.21	⋯	⋯	⋯	⋯
HD 148816	⋯	⋯	0.18	0.17	0.14	0.14	0.23	0.23	0.17	0.16	0.17	0.17	0.18	0.18	0.19	0.19
HD 177249	0.04	0.02	⋯	⋯	0.05	0.05	0.02	0.02	0.13	0.07	⋯	⋯	⋯	⋯	⋯	⋯

Table 8
Equivalent Widths of Neutral Iron Lines for Sample Stars

λ (Å)	Arcturus	HD 87	HD 6582	HD 6920	HD 22675	HD 31501	HD 58367	HD 67447	HD 102870	HD 103095	HD 121370	HD 148816	HD 177249
4661.534	···	···	18.0	39.8	···	···	···	89.5	40.4	8.0	48.7	10.4	···
4808.149	···	···	11.5	25.6	···	···	···	72.4	28.8	8.4	37.1	7.1	···
4885.430	···	···	55.7	75.3	···	···	···	126.2	77.8	38.1	87.9	37.7	···
5223.186	64.3	52.0	14.7	32.5	61.5	···	···	67.8	30.7	8.7	37.3	7.2	···
5242.497	117.5	115.9	63.6	92.2	120.9	···	146.5	146.4	92.0	54.9	108.0	54.8	121.6
5379.579	90.9	87.5	38.1	59.5	93.8	···	111.4	114.7	63.7	22.4	76.1	27.7	93.4
5398.279	91.1	94.7	48.3	71.0	104.2	···	116.8	124.5	78.9	33.2	88.7	38.5	102.9
5522.449	61.0	66.2	20.1	41.5	71.1	···	78.8	84.3	44.1	10.6	57.0	14.3	69.8
5546.506	72.2	75.1	26.0	51.0	81.7	···	91.6	100.4	53.4	14.1	68.8	17.7	80.4
5618.633	71.0	69.4	27.4	50.3	76.0	42.3	88.9	93.6	53.2	12.3	65.3	18.4	77.6
5651.469	32.2	33.5	6.6	18.8	39.7	14.6	45.7	45.1	19.2	···	27.3	···	35.8
5679.023	70.0	76.4	32.8	61.2	81.9	53.7	87.9	97.2	60.8	17.1	72.0	24.0	81.5
5793.915	53.6	58.6	12.9	29.8	62.1	28.1	70.0	84.6	34.4	6.1	45.9	9.3	72.0
5853.148	···	···	···	···	44.2	12.0	45.1	51.5	6.0	···	10.5	···	27.4
5855.077	34.2	39.9	7.8	22.0	43.9	17.5	···	49.5	23.0	···	31.2	5.3	39.2
5929.677	54.7	63.3	16.3	···	67.6	37.7	73.9	78.0	40.4	17.0	50.9	17.0	63.4
6024.058	116.8	125.7	87.0	107.5	132.6	120.1	···	156.0	114.0	70.3	124.7	66.7	135.0
6078.491	81.2	93.8	47.5	76.6	99.0	81.2	···	117.0	82.5	29.5	92.8	35.2	99.2
6079.009	58.3	62.9	19.3	40.7	69.7	41.6	80.0	85.4	48.9	9.2	54.2	13.7	70.1
6151.623	114.6	88.1	31.3	47.5	97.9	51.4	117.4	122.1	45.4	21.4	54.7	17.4	91.5
6173.335	133.0	109.5	48.3	70.3	119.9	52.3	146.8	148.9	66.0	40.0	78.0	33.7	115.1
6200.321	132.7	111.0	52.2	73.0	121.7	74.2	140.3	148.0	78.8	41.4	87.1	34.5	116.4
6240.646	114.7	···	29.8	43.7	···	52.3	···	127.4	43.2	19.8	55.2	16.5	···
6322.686	140.7	···	53.8	76.8	···	76.7	···	150.6	73.0	44.3	91.0	40.6	···
6335.331	132.6	···	85.1	103.5	···	109.1	···	196.0	98.4	79.2	115.3	66.2	···
6481.877	···	···	···	63.9	···	72.4	···	142.9	62.4	34.1	76.6	27.5	···
6593.871	···	···	68.8	89.1	···	90.6	···	177.7	93.9	61.3	101.1	55.4	···
6726.666	···	···	19.8	50.0	···	42.1	···	86.6	49.6	9.8	62.8	15.3	···
6839.831	···	···	15.3	···	···	32.2	···	94.5	28.9	8.2	43.5	7.2	···
6857.250	···	···	···	···	···	18.8	···	55.3	···	···	···	5.9	···

Note. Strongly blended lines and lines with poor S/N were rejected when we determined the stellar parameters for a given star.

REFERENCES

Ahn, C. P., Alexandroff, R., Allende Prieto, C., et al. 2014, ApJS, 211, 17
Alam, S., Albareti, F. D., Allende Prieto, C., et al. 2015, ApJS, 219, 12
Alonso, A., Arribas, S., & Martínez-Roger, C. 1996, A&A, 313, 873
Alonso, A., Arribas, S., & Martínez-Roger, C. 1999, A&AS, 140, 261
Alonso, A., Arribas, S., & Martínez-Roger, C. 2001, A&A, 376, 1039
Amarsi, A. M., & Asplund, M. 2016, arXiv:1609.07283
Anstee, S. D., & O'Mara, B. J. 1991, MNRAS, 253, 549
Anstee, S. D., & O'Mara, B. J. 1995, MNRAS, 276, 859
Bard, A., Kock, A., & Kock, M. 1991, A&A, 248, 315
Bard, A., & Kock, M. 1994, A&A, 282, 1014
Barklem, P. S., & O'Mara, B. J. 1997, MNRAS, 290, 102
Barklem, P. S., O'Mara, B. J., & Ross, J. E. 1998, MNRAS, 296, 1057
Barklem, P. S., Piskunov, N., & O'Mara, B. J. 2000, A&AS, 142, 467
Belyaev, A. K., Yakovleva, S. A., & Barklem, P. S. 2014, A&A, 572, A103
Bensby, T., Feltzing, S., Lundström, I., et al. 2005, A&A, 433, 185
Bensby, T., Feltzing, S., & Oey, M. S. 2014, A&A, 562, A71
Bergemann, M., Kudritzki, R. P., Würl, M., et al. 2013, ApJ, 764, 115
Blackwell, D. E., Shallis, M. J., & Simmons, G. J. 1980, A&A, 81, 340
Butler, K., & Giddings, J. 1985, Newsletter on the Analysis of Astronomical Spectra (Univ. London)
Eisenstein, D. J., Weinberg, D. H., Agol, E., et al. 2011, AJ, 142, 72
Feuillet, D. K., Bovy, J., Holtzman, J., et al. 2016, ApJ, 817, 40
Fuhr, J. R., Martin, G. A., & Wiese, W. L. 1988, JPCRD, 17, 4
Fuhrmann, K. 1998, A&A, 338, 161
García Pérez, A. E., Allende Prieto, C., Holtzman, J. A., et al. 2016, AJ, 151, 144
Garz, T. 1973, A&A, 26, 471
Goswami, A., & Prantzos, N. 2000, A&A, 359, 191
Grevesse, N., Asplund, M., & Sauval, A. J. 2007, SSRv, 130, 105
Gustafsson, B., Edvardsson, B., Eriksson, K., et al. 2008, A&A, 486, 951
Hall, D. N. B., Ridgway, S. T., Bell, E. A., et al. 1979, Proc. SPIE, 172, 121
Hawkins, K., Masseron, T., Jofre, P., et al. 2016, arXiv:1604.08800
Henyey, L., Vardya, M. S., & Bodenheimer, P. 1965, ApJ, 142, 841
Hinkle, K., & Wallace, L. 2005, in ASP Conf. Ser. 336, Cosmic Abundances as Records of Stellar Evolution and Nucleosynthesis, ed. T. G. Barnes, III & F. N. Bash (San Francisco, CA: ASP), 321
Hinkle, K., Wallace, L., & Livingston, W. 1995, PASP, 107, 1042
Hinkle, K., Wallace, L., Valenti, J., et al. 2000, Visible and Near Infrared Atlas of the Arcturus Spectrum 3727-9300 Å (San Francisco, CA: ASP)
Holtzman, J. A., Shetrone, M., Johnson, J. A., et al. 2015, AJ, 150, 148
Holweger, H. 1973, A&A, 26, 275
Izumiura, H. 2003, AstHe, 96, 291
Johnson, T. V., Mousis, O., Lunine, J. I., & Madhusudhan, N. , 2011, LPICo, 1639, 9011
Kamp, L. W. 1973, ApJ, 180, 447
Kamp, L. W. 1978, ApJ, 36, 143
Kamp, L. W. 1982, ApJ, 48, 415
Kelleher, D. E., & Podobedova, L. I. 2008, JPCRD, 37, 1285
Kobayashi, C., Karakas, A. I., & Umeda, H. 2011, MNRAS, 414, 3231
Kurucz, R. L. 2007, Robert L. Kurucz Online Database of Observed and Predicted Atomic Transitions, http://kurucz.harvard.edu
Kurucz, R. L. 2014, Robert L. Kurucz Online Database of Observed and Predicted Atomic Transitions, http://kurucz.harvard.edu
Kurucz, R. L., Furenlid, I., Brault, J., et al. 1984, Solar Flux Atlas from 296 to 1300 nm (Sunspot, NM: National Solar Observatory)
Lee, Y. S., Beers, T. C., An, D., et al. 2011, ApJ, 738, 187
Majewski, S. R., Schiavon, R. P., Allende Prieto, C., et al. 2015, arXiv:1509.05420
Mashonkina, L., Gehren, T., Shi, J. R., et al. 2011, A&A, 528, A87
Mashonkina, L., Korn, A. J., & Przybilla, N. 2007, A&A, 461, 261
Meléndez, J., & Barbuy, B. 1999, ApJS, 124, 527
Mészáros, S., Holtzman, J., García Pérez, A. E., et al. 2013, AJ, 146, 133
Nahar, S. N., & Pradhan, A. K. 1993, JPhB, 26, 1109
Nidever, D. L., Holtzman, J. A., Allende Prieto, C., et al. 2015, AJ, 150, 173
Nissen, P. E., & Schuster, W. J. 2010, A&A, 511, L10
O'Brian, T. R., Wickliffe, M. E., Lawler, J. E., et al. 1991, JOSAB, 8, 1185
Pfeiffer, M. J., Frank, C., Baumüller, D., et al. 1998, A&AS, 130, 381
Ramírez, I., & Allende Prieto, C. 2011, ApJ, 743, 135
Reddy, B. E., Lambert, D. L., & Allende Prieto, C. 2006, MNRAS, 367, 1329
Reddy, B. E., Tomkin, J., Lambert, D. L., et al. 2003, MNRAS, 340, 304
Reetz, J. K. 1991, Diploma thesis, Universität München
Romano, D., Karakas, A. I., Tosi, M., et al. 2010, A&A, 522, A32
Ryabchikova, T. A., Piskunov, N. E., Stempels, H. C., et al. 1999, PhST, 83, 162
Rybicki, G. B., & Hummer, D. G. 1991, A&A, 245, 171
Rybicki, G. B., & Hummer, D. G. 1992, A&A, 262, 209
Samland, M. 1998, ApJ, 496, 155
Sheminova, V. A. 2015, KPCB, 31, 172
Shi, J. R., Gehren, T., Butler, K., et al. 2008, A&A, 486, 303
Shi, J. R., Gehren, T., Mashonkina, L., et al. 2009, A&A, 503, 533
Shi, J. R., Gehren, T., & Zhao, G. 2011, A&A, 534, A103
Shi, J. R., Takada-Hidai, M., Takeda, Y., et al. 2012, ApJ, 755, 36
Takeda, Y., Sato, B., & Murata, D. 2008, PASJ, 60, 781
Tsujimoto, T., Nomoto, K., Yoshii, Y., et al. 1995, MNRAS, 277, 945
Wang, X. M., Shi, J. R., & Zhao, G. 2009, MNRAS, 399, 1264
Wedemeyer, S. 2001, A&A, 2001, 998
Wilson, J. C., Hearty, F., Skrutskie, M. F., et al. 2010, Proc. SPIE, 7735, 77351C
Woosley, S. E., & Weaver, T. A. 1995, ApJS, 101, 181
Zambardi, T., Poitrasson, F., Corgne, A., et al. 2013, GeCoA, 121, 67
Zhang, L., Karlsson, T., Christlieb, N., et al. 2011, A&A, 528, A92
Zhao, G., & Li, H. B. 2001, ChJAA, 1, 555

The Astrophysical Journal, 820:67 (17pp), 2016 March 20 doi:10.3847/0004-637X/820/1/67

OPTICAL OBSERVATIONS OF THE TYPE IA SUPERNOVA SN 2011fe IN M101 FOR NEARLY 500 DAYS

Kaicheng Zhang[1], Xiaofeng Wang[1], JuJia Zhang[2,3], Tianmeng Zhang[4], Mohan Ganeshalingam[5], Weidong Li[5,8], Alexei V. Filippenko[5], Xulin Zhao[1], Weikang Zheng[5], Jinming Bai[2,3], Jia Chen[1], Juncheng Chen[1], Fang Huang[1,6], Jun Mo[1], Liming Rui[1], Hao Song[1], Hanna Sai[1], Wenxiong Li[1], Lifan Wang[7], and Chao Wu[4]

[1] Physics Department and Tsinghua Center for Astrophysics (THCA), Tsinghua University, Beijing, 100084, China; wang_xf@mail.tsinghua.edu.cn

[2] Yunnan Astronomical Observatory of China, Chinese Academy of Sciences, Kunming, 650011, China

[3] Key Laboratory for the Structure and Evolution of Celestial Objects, Chinese Academy of Sciences, Kunming 650011, China

[4] National Astronomical Observatory of China, Chinese Academy of Sciences, Beijing, 100012, China

[5] Department of Astronomy, University of California, Berkeley, CA 94720-3411, USA

[6] Astronomy Department, Beijing Normal University, Beijing, 100875, China

[7] Physics and Astronomy Department, Texas A&M University, College Station, TX 77843, USA

Received 2015 December 10; accepted 2016 February 9; published 2016 March 21

ABSTRACT

We present well-sampled optical observations of the bright Type Ia supernova (SN Ia) SN 2011fe in M101. Our data, starting from ~16 days before maximum light and extending to ~463 days after maximum, provide an unprecedented time series of spectra and photometry for a normal SN Ia. Fitting the early-time rising light curve, we find that the luminosity evolution of SN 2011fe follows a t^n law, with the index n being close to 2.0 in the *VRI* bands but slightly larger in the *U* and *B* bands. Combining the published ultraviolet (UV) and near-infrared (NIR) photometry, we derive the contribution of UV/NIR emission relative to the optical. SN 2011fe is found to have stronger UV emission and reaches its UV peak a few days earlier than other SNe Ia with similar $\Delta m_{15}(B)$, suggestive of less trapping of high-energy photons in the ejecta. Moreover, the *U*-band light curve shows a notably faster decline at late phases ($t \approx$ 100–300 days), which also suggests that the ejecta may be relatively transparent to UV photons. These results favor the notion that SN 2011fe might have a progenitor system with relatively lower metallicity. On the other hand, the early-phase spectra exhibit prominent high-velocity features (HVFs) of O i λ7773 and the Ca ii NIR triplet, but only barely detectable in Si ii 6355. This difference can be caused by either an ionization/temperature effect or an abundance enhancement scenario for the formation of HVFs; it suggests that the photospheric temperature of SN 2011fe is intrinsically low, perhaps owing to incomplete burning during the explosion of the white dwarf.

Key words: supernovae: general – supernovae: individual (SN 2011fe)

1. INTRODUCTION

SN 2011fe/PTF11kly was discovered in the nearby spiral galaxy M101 by the Palomar Transient Factory on 2011 August 24.167 (UT dates are used throughout this paper), and it was classified as a normal Type Ia supernova (SN Ia; Nugent et al. 2011). SN 2011fe is one of the nearest SNe Ia discovered over the past three decades, with a Cepheid-based distance of about 6.4 ± 0.5 Mpc ($\mu = 29.04 \pm 0.19$ mag; Shappee & Stanek 2011). It is also one of the earliest detected SNe Ia, within a few hours after the explosion (Nugent et al. 2011). Thus, the discovery of this object provides a rare opportunity to study the properties of a normal SN Ia at both very early and very late phases.

There are two competing scenarios for the progenitors of SNe Ia. One is a system consisting of a single white dwarf (WD) and a nondegenerate companion (Whelan & Iben 1973); the other is a system consisting of two WDs (Iben & Tutukov 1984). The fact that these explosions are linked to their birth environments suggests that SNe Ia may arise from multiple classes of binary evolution (e.g., Wang et al. 2013). The early discovery of SN 2011fe leads to tight constraints on the nature of the progenitor of this particular SN Ia.

The pre-explosion *Hubble Space Telescope* image of SN 2011fe ruled out luminous red giants and almost all helium stars as the mass-donating companion to the exploding WD (Li et al. 2011). Based on the early-time photometry of SN 2011fe, Bloom et al. (2012) set a limit on the initial radius of the primary star, $R_p \lesssim 0.02\,R_\odot$, as well as a limit on the size of the companion star, $R_c \lesssim 0.1\,R_\odot$. These studies suggest that for SN 2011fe, the companion star of the exploding WD is relatively compact, favoring a double-degenerate progenitor system. Using *Swift* Ultraviolet/Optical Telescope (UVOT) observations, Brown et al. (2012) fit the *Swift* UV light curves with the fireball model and concluded that there was no shock interaction with a nondegenerate companion. Similar conclusions were obtained from the analysis of radio and X-ray data (Chomiuk et al. 2012; Horesh et al. 2012). Based on deep Expanded Very Large Array radio observations, Chomiuk et al. (2012) constrained the density of the circumstellar material (CSM) and the mass-loss rate from the progenitor system, and they ruled out much of the parameter space associated with single-degenerate progenitor models for SN 2011fe. Horesh et al. (2012) used radio and X-ray observations of SN 2011fe to set a limit on the pre-explosion mass-loss rate of $\dot{M} \lesssim 10^{-8}(w/100\ \mathrm{km\,s^{-1}})M_\odot\ \mathrm{yr}^{-1}$ for the progenitor system. They found that their data modestly disfavor the symbiotic progenitor model, which involves a red giant donor, but they cannot eliminate systems with an accreting main-sequence or subgiant star. Furthermore, the nondetection of hydrogen-rich material in the ejecta of SN 2011fe (i.e., with an upper limit of 0.001–0.003 $M_\odot$), inferred from its nebular spectra, further ruled out the possibility of having a hydrogen-rich star as the

---

[8] Deceased 2011 December 12.

Table 1
Photometric Standards in the SN 2011fe Field[a]

Star	α(J2000)	δ(J2000)	U (mag[b])	B (mag)	V (mag)	R (mag)	I (mag)
1	$14^{h}03^{m}22^{s}.39$	$+54^\circ15'35''.9$	17.369(139)	16.142(023)	14.861(015)	14.007(008)	13.290(011)
2	14:03:23.75	+54:14:32.6	16.023(111)	16.077(019)	15.452(017)	15.089(012)	14.700(011)
3	14:03:24.91	+54:13:57.2	16.840(020)	16.858(007)	16.151(009)	15.877(013)	15.499(018)
4	14:03:15.81	+54:15:44.8	17.636(120)	17.165(027)	16.487(014)	16.116(018)	15.707(016)
5	14:03:13.66	+54:15:43.3	15.111(085)	14.778(020)	13.849(010)	13.319(008)	12.781(011)
6	14:03:05.82	+54:17:25.3	16.901(030)	16.779(019)	16.120(013)	15.659(007)	15.248(008)
7	14:02:57.09	+54:16:41.0	16.510(072)	16.596(024)	16.090(007)	15.743(005)	15.379(007)
8	14:02:54.12	+54:16:29.0	14.683(079)	14.608(019)	14.005(009)	13.653(010)	13.296(012)
9	14:02:36.29	+54:18:54.3	18.287(100)	17.027(038)	15.663(035)	14.750(023)	13.985(021)

Notes.
[a] See Figure 1 for a chart of SN 2011fe and the comparison stars.
[b] Uncertainties, in units of 0.001 mag, are 1σ.

donor of the exploding WD (Shappee et al. 2013; Graham et al. 2015b; Lundqvist et al. 2015).

Besides studies of the progenitor itself, there are also many investigations of the observed properties of SN 2011fe. Richmond & Smith (2012) present *BVRI* photometry of SN 2011fe covering phases from t = 2.9 to 182 days after the explosion, finding a light-curve decline of $\Delta m_{15}(B) = 1.21 \pm 0.03$ mag. Munari et al. (2013) also published BVR_CI_C light curves of SN 2011fe. Near-infrared (NIR) observations of SN 2011fe starting from 14 days before *B*-band maximum were obtained by Matheson et al. (2012), who also derived the Cepheid distance to M101 based on these data.

Studies of the earliest spectra were given by Parrent et al. (2012), Pereira et al. (2013), and Patat et al. (2013). Parrent et al. (2012) examined the high-velocity features (HVFs) and evolution of unburned material (carbon and oxygen) in the spectra. Pereira et al. (2013) presented spectrophotometric observations of SN 2011fe and explored the unburned carbon features in the spectra. Patat et al. (2013) studied the reddening along the line of sight toward SN 2011fe and concluded that this SN Ia exploded in a “clean” environment. Multiple spectropolarimetric observations reveal that SN 2011fe has a low degree of continuum polarization, 0.2%–0.4% (Smith et al. 2011), indicating that the explosion was symmetric overall. The very late-time evolution of this object was recently reported by Taubenberger et al. (2015) and Graham et al. (2015b), based on optical spectra taken ~1000 days after the explosion.

In this paper, we present extensive photometry and spectroscopy covering phases from 16 days before to 463 days after *B*-band maximum light. Notwithstanding all the published data on SN 2011fe, our observations presented here are still a significant contribution to the literature and will aid future studies of SN 2011fe. With these data, we set better constraints on the explosion and progenitor properties of SN 2011fe. The observations are described in Section 2, light curves are presented in Section 3, and our spectra are shown in Section 4. A discussion is given in Section 5, and we conclude in Section 6.

2. OBSERVATIONS

2.1. Optical Photometry

The optical photometry presented here was obtained with the 0.8 m Tsinghua-NAOC Telescope (TNT; Wang et al. 2008; Huang et al. 2012), the 2.4 m Lijiang Telescope (LJT; Fan et al. 2015) of Yunnan Astronomical Observatory (YNAO), and the 0.76 m Katzman Automatic Imaging Telescope (KAIT; Filippenko et al. 2001). All of the data were reduced with standard IRAF routines. The instrumental magnitudes were converted to those of the Johnson *UBV* (Johnson et al. 1966) and Kron–Cousins *RI* (Cousins 1981) systems, based on transformation correlations established through observations performed on photometric nights. The *UBVRI* magnitudes of nine standard stars are listed in Table 1 (see Figure 1 for the finder chart). The final flux-calibrated *UBVRI* magnitudes of SN 2011fe are listed in Table 2.

2.2. Optical Spectroscopy

Our optical spectra of SN 2011fe were obtained by the 2.16 m telescope at Xinglong Observatory of NAOC and the 2.4 m LJT of YNAO; see Table 3 for the journal of observations. All spectra were reduced using standard IRAF routines and flux-calibrated with spectrophotometric standard stars. The spectra were corrected for continuum atmospheric extinction at the two observatories, and telluric absorption lines were removed from the data.

3. LIGHT AND COLOR CURVES OF SN 2011fe

Figure 2 shows the *UBVRI*-band light curves of SN 2011fe from our observations; overplotted are the UV and NIR data (Brown et al. 2012; Matheson et al. 2012). The light curves resemble those of normal SNe Ia, with a “shoulder” in the *R* band and a prominent secondary maximum in the *I* and NIR bands. For SN 2011fe, the peaks of the NIR and UV light curves appeared slightly earlier than in the *B* band. Details of the light curves are described in the following subsections.

3.1. The Light Curves

A polynomial fit to the near-maximum light curves reveals that SN 2011fe reached a *B*-band maximum of $B_{\rm max} = 9.96 \pm 0.03$ mag on JD 2,455,814.98 ± 0.03 and a *V*-band maximum of $V_{\rm max} = 9.99 \pm 0.02$ mag on JD 2,455,816.92 ± 0.03, very close to $B_{\rm max} = 9.94 \pm 0.01$ mag on JD 2,455,815.01 ± 0.06 and $V_{\rm max} = 9.98 \pm 0.02$ mag on JD 2,455,816.75 ± 0.06 as given by Pereira et al. (2013). We also derived the luminosity decline parameter $\Delta m_{15}(B) = 1.18 \pm 0.03$ mag and $B_{\rm max} - V_{\rm max} = -0.03 \pm 0.04$ mag, consistent with the values obtained by Richmond & Smith (2012). From an empirical relation between intrinsic $B_{\rm max} - V_{\rm max}$ color and $\Delta m_{15}(B)$ (Phillips et al. 1999;

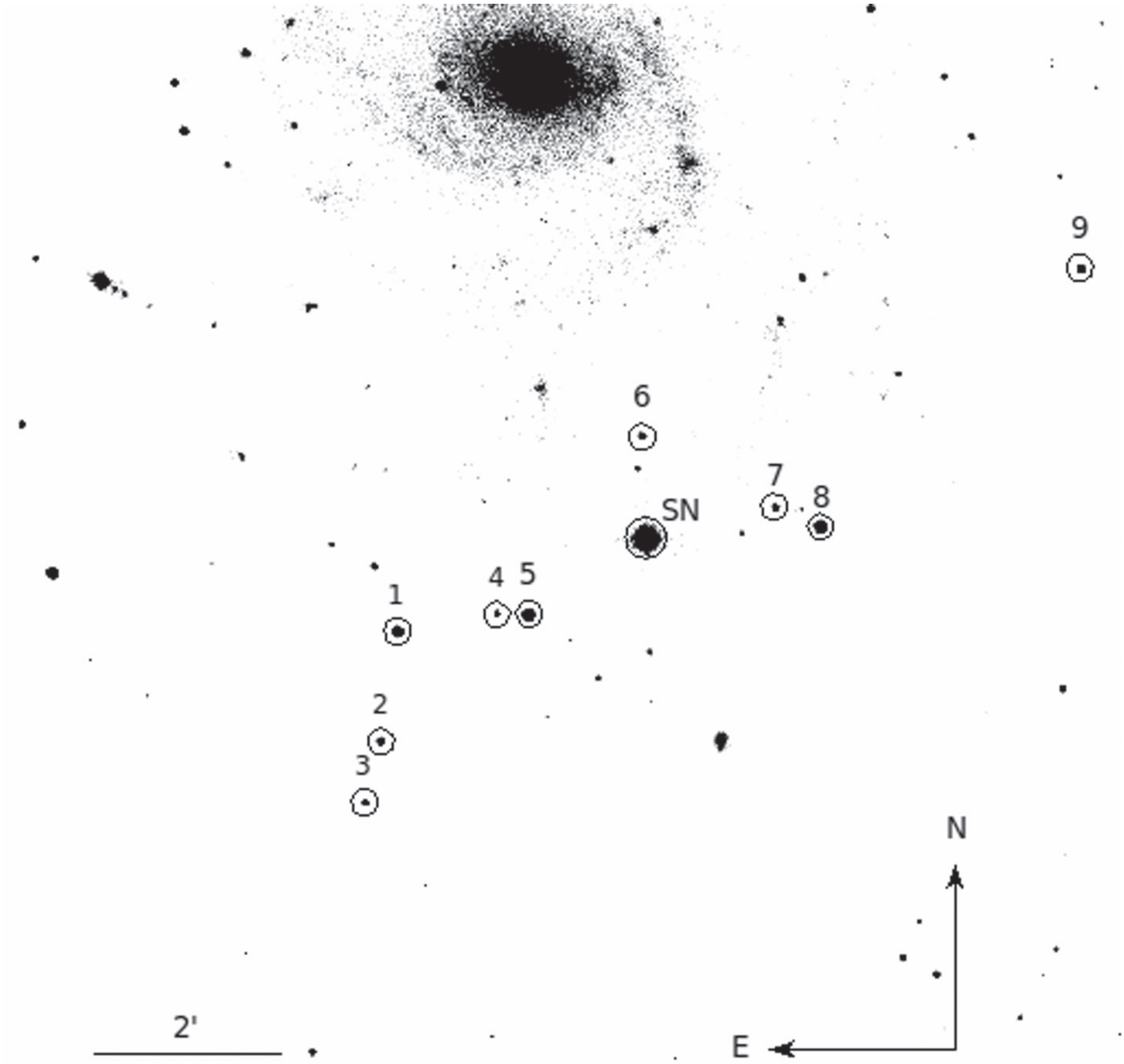

Figure 1. SN 2011fe in M101. This is an *R*-band image taken with the TNT 0.8 m telescope on 2011 September 20. The supernova and nine local reference stars are marked. North is up and east is to the left.

Wang et al. 2009b), we can deduce $(B_{\max} - V_{\max})_0 = -0.07 \pm 0.02$ mag for SN 2011fe. With the removal of the Galactic component, $E(B - V)_{\rm MW} = 0.008$ mag (Schlafly & Finkbeiner 2011), we get $E(B - V)_{\rm host} = 0.032 \pm 0.045$ mag. Pereira et al. (2013) estimated the host-galaxy reddening as $E(B - V)_{\rm host} = 0.026 \pm 0.036$ mag from the photometric method and $E(B - V)_{\rm host} = 0.014 \pm 0.003$ mag from spectral data, while Tammann & Reindl (2011) obtained $E(B - V)_{\rm host} = 0.030 \pm 0.060$ mag. Our result is consistent with these estimates within the quoted errors. Adopting a Cepheid distance modulus of $\mu = 29.04 \pm 0.19$ mag (6.4 Mpc; Shappee & Stanek 2011) and correcting for the Galactic and host-galaxy extinction with $R_V = 3.1$, we derive absolute B and V magnitudes of $M_B = -19.24 \pm 0.19$ mag and $M_V = -19.17 \pm 0.19$ mag. Detailed photometric parameters of SN 2011fe are listed in Table 4.

Figure 3 shows comparisons of the near-maximum-light UV and optical light curves of SN 2011fe with those of well-observed normal SNe Ia such as SN 2003du ($\Delta m_{15}(B) = 1.02$ mag; Stanishev et al. 2007), SN 2003hv ($\Delta m_{15}(B) = 1.61$ mag; Leloudas et al. 2009), SN 2005cf ($\Delta m_{15}(B) = 1.07$ mag; Wang et al. 2009b), SN 2011by ($\Delta m_{15}(B) = 1.16$ mag; Graham et al. 2015a; H. Song et al. 2016, in preparation), and SN 2012cg ($\Delta m_{15}(B) = 1.04$ mag; Munari et al. 2013; Marion et al. 2015). It is readily seen that the light curves of our comparison samples are similar around maximum light, except for SN 2003hv, which exhibits a faster decline. Closer inspection reveals a faster rise in all bands for SN 2011fe compared with SN

Table 2
Optical Photometry of SN 2011fe

JD[a]	Phase[b]	U (mag)[c]	B (mag)	V (mag)	R (mag)	I (mag)	Telescope
5798.17	−16.31	15.013(086)	15.185(030)	14.797(021)	14.740(020)	14.848(030)	KAIT
5798.53	−15.95	14.534(014)	14.743(013)	14.325(019)	14.260(024)	14.248(052)	LJT
5799.16	−15.32	13.894(044)	14.027(030)	13.685(020)	13.641(020)	13.745(030)	KAIT
5799.53	−14.95	13.572(036)	13.687(019)	13.410(020)	13.367(025)	13.333(040)	LJT
5800.17	−14.31	13.138(084)	13.225(030)	12.943(020)	12.921(020)	12.991(030)	KAIT
5800.53	−13.95	12.855(017)	12.940(019)	12.768(020)	12.710(025)	12.645(041)	LJT
5801.50	−12.98	⋯	12.470(012)	12.370(011)	12.266(017)	12.221(023)	TNT
5801.52	−12.96	12.201(017)	12.410(017)	12.242(021)	12.183(025)	12.121(046)	LJT
5802.15	−12.33	11.951(072)	12.022(030)	11.996(020)	11.938(020)	11.914(030)	KAIT
5802.52	−11.96	11.621(019)	11.890(017)	11.837(022)	11.748(024)	11.678(051)	LJT
5803.15	−11.33	11.371(046)	11.624(030)	11.590(020)	11.464(020)	11.500(030)	KAIT
5803.52	−10.96	11.094(024)	11.454(015)	11.460(020)	11.353(025)	11.293(048)	LJT
5804.15	−10.33	10.988(019)	11.216(030)	11.236(021)	11.136(020)	11.129(030)	KAIT
5804.53	−9.95	10.688(019)	11.142(016)	11.152(022)	11.039(024)	10.995(059)	LJT
5805.15	−9.33	10.557(015)	10.943(030)	11.002(020)	10.854(020)	10.900(030)	KAIT
5805.51	−8.97	⋯	10.929(011)	10.972(021)	10.835(014)	10.878(023)	TNT
5805.52	−8.96	10.400(038)	10.861(014)	10.903(020)	10.788(025)	10.763(050)	LJT
5806.14	−8.34	10.379(017)	10.743(030)	10.697(020)	10.688(020)	10.666(030)	KAIT
5806.51	−7.97	⋯	10.750(010)	10.744(013)	10.651(035)	10.734(066)	TNT
5806.52	−7.96	10.190(028)	10.662(025)	10.628(022)	10.581(025)	10.553(043)	LJT
5807.14	−7.34	10.160(088)	10.519(030)	10.559(020)	10.460(020)	10.519(030)	KAIT
5807.54	−6.94	9.940(018)	10.473(021)	10.504(023)	10.423(029)	10.443(044)	LJT
5808.14	−6.34	9.852(093)	10.396(030)	10.426(020)	10.338(020)	10.425(030)	KAIT
5808.50	−5.98	⋯	10.412(009)	10.475(021)	10.347(009)	10.403(021)	TNT
5808.52	−5.96	⋯	⋯	⋯	⋯	10.342(060)	LJT
5809.14	−5.34	⋯	10.252(030)	10.323(021)	10.226(020)	10.346(030)	KAIT
5809.52	−4.96	9.714(054)	10.214(014)	10.216(023)	10.185(026)	10.240(048)	LJT
5809.52	−4.96	⋯	10.281(010)	10.372(034)	10.271(021)	10.313(043)	TNT
5810.14	−4.34	9.607(147)	10.171(030)	10.212(020)	10.167(020)	10.270(030)	KAIT
5811.14	−3.34	9.516(115)	10.082(030)	10.124(020)	10.079(020)	10.251(030)	KAIT
5812.14	−2.34	9.527(028)	10.017(030)	10.079(020)	10.057(020)	10.228(030)	KAIT
5813.14	−1.34	9.545(088)	9.969(030)	9.996(020)	10.020(020)	10.243(030)	KAIT
5815.13	0.65	9.505(092)	9.991(030)	9.998(020)	10.034(020)	10.321(030)	KAIT
5816.13	1.65	9.570(014)	9.987(030)	10.015(021)	10.047(020)	10.360(030)	KAIT
5817.13	2.65	9.589(070)	10.034(030)	9.984(020)	10.004(020)	10.410(030)	KAIT
5817.51	3.03	9.772(013)	10.095(028)	9.998(020)	10.028(025)	10.311(042)	LJT
5818.13	3.65	9.631(144)	10.108(030)	9.983(020)	10.062(020)	10.439(030)	KAIT
5819.13	4.65	9.613(025)	10.117(030)	10.025(020)	10.081(020)	10.501(030)	KAIT
5820.13	5.65	9.754(100)	⋯	⋯	⋯	⋯	KAIT
5821.12	6.64	9.800(040)	10.188(030)	10.107(021)	10.187(020)	10.594(030)	KAIT
5822.12	7.64	9.958(075)	10.324(030)	10.117(020)	⋯	⋯	KAIT
5823.52	9.04	10.224(019)	10.447(015)	10.184(023)	10.351(027)	10.667(047)	LJT
5824.49	10.01	10.404(045)	10.627(010)	10.356(015)	10.564(012)	10.875(025)	TNT
5825.49	11.01	10.564(043)	10.667(010)	10.471(017)	10.650(010)	10.969(026)	TNT
5826.49	12.01	10.676(041)	10.800(009)	10.456(012)	10.636(011)	10.956(025)	TNT
5827.47	12.99	10.840(051)	10.933(011)	10.474(017)	10.692(014)	10.969(020)	TNT
5828.48	14.00	10.939(042)	11.039(009)	10.558(011)	10.731(016)	10.978(018)	TNT
5829.46	14.98	11.207(194)	11.138(008)	10.632(037)	10.763(028)	10.935(022)	TNT
5830.47	15.99	11.228(068)	11.311(021)	10.701(022)	10.827(032)	10.923(031)	TNT
5832.50	18.02	11.425(013)	11.328(026)	10.759(032)	10.715(026)	10.716(064)	LJT
5833.46	18.98	⋯	11.637(012)	10.807(025)	10.814(012)	10.851(030)	TNT
5834.45	19.97	⋯	11.814(024)	10.866(025)	10.830(019)	10.866(027)	TNT
5835.45	20.97	11.527(573)	11.918(008)	10.952(046)	10.786(042)	10.852(066)	TNT
5836.45	21.97	12.200(044)	12.001(013)	11.011(023)	10.859(017)	10.827(043)	TNT
5837.45	22.97	12.126(065)	12.155(009)	11.023(037)	10.851(013)	10.787(019)	TNT
5839.45	24.97	12.663(068)	12.243(009)	11.196(027)	10.920(017)	10.743(035)	TNT
5840.45	25.97	12.637(042)	12.310(010)	11.234(021)	10.949(013)	10.749(024)	TNT
5841.48	27.00	⋯	12.422(011)	11.305(050)	11.032(035)	10.747(025)	TNT
5847.44	32.96	⋯	12.888(016)	11.679(054)	11.348(050)	11.056(095)	TNT
5848.45	33.97	12.938(058)	12.942(013)	11.749(010)	11.457(024)	11.089(023)	TNT
5850.44	35.96	13.152(065)	13.045(013)	11.854(022)	11.598(022)	11.237(025)	TNT
5851.44	36.96	13.091(060)	13.048(026)	11.930(012)	11.646(020)	11.310(023)	TNT
5852.45	37.97	13.309(042)	13.106(017)	11.948(013)	11.677(015)	11.365(028)	TNT
5858.43	43.95	13.358(064)	13.281(009)	12.152(019)	11.936(013)	11.686(022)	TNT

Table 2
(Continued)

JD[a]	Phase[b]	U (mag)[c]	B (mag)	V (mag)	R (mag)	I (mag)	Telescope
5891.90	77.42	⋯	13.747(009)	13.078(010)	13.031(010)	13.119(021)	TNT
5894.87	80.39	14.305(050)	13.791(008)	13.157(017)	13.114(014)	13.218(021)	TNT
5906.89	92.41	14.728(044)	13.941(011)	13.451(010)	13.497(011)	13.645(020)	TNT
5908.91	94.43	14.700(048)	13.956(011)	13.466(015)	13.555(012)	13.707(020)	TNT
5910.93	96.45	14.837(053)	13.962(009)	13.547(008)	13.621(015)	13.777(022)	TNT
5911.86	97.38	14.958(055)	14.007(011)	13.592(011)	13.653(011)	13.815(021)	TNT
5912.93	98.45	15.056(043)	14.035(011)	13.601(011)	13.684(012)	13.862(019)	TNT
5913.86	99.38	15.217(105)	14.030(011)	13.631(019)	13.767(044)	13.848(078)	TNT
5914.91	100.43	14.954(049)	14.036(011)	13.647(008)	13.751(011)	13.920(023)	TNT
5916.91	102.43	15.230(045)	14.076(011)	13.689(008)	13.803(011)	13.973(018)	TNT
5917.90	103.42	15.117(042)	14.096(009)	13.712(008)	13.847(009)	13.989(020)	TNT
5918.91	104.43	15.219(042)	14.101(009)	13.728(006)	13.862(010)	14.036(019)	TNT
5926.92	112.44	15.399(043)	14.226(012)	13.916(009)	⋯	14.266(021)	TNT
5928.88	114.40	15.593(046)	14.268(010)	13.955(009)	14.122(014)	14.296(021)	TNT
5929.84	115.36	15.557(046)	14.278(012)	13.975(010)	14.201(009)	14.314(022)	TNT
5934.85	120.37	15.768(048)	14.359(015)	14.108(010)	14.390(011)	14.522(018)	TNT
5936.91	122.43	15.940(050)	14.423(015)	14.156(010)	14.418(011)	14.515(021)	TNT
5937.92	123.44	15.883(048)	14.426(012)	14.195(009)	14.496(011)	14.598(019)	TNT
5938.94	124.46	⋯	14.419(016)	14.200(021)	14.479(016)	14.410(047)	TNT
5954.92	140.44	16.606(051)	14.673(012)	14.481(012)	14.849(017)	14.833(027)	TNT
5960.73	146.25	16.828(048)	14.736(014)	14.597(013)	15.075(016)	14.980(027)	TNT
5965.84	151.36	16.537(059)	14.857(011)	14.711(013)	15.208(013)	15.175(023)	TNT
5966.93	152.45	⋯	14.885(022)	14.795(021)	15.142(028)	15.119(037)	TNT
5967.90	153.42	16.728(085)	14.860(013)	14.781(013)	15.234(012)	15.155(022)	TNT
5968.86	154.38	16.700(065)	14.857(013)	14.782(013)	15.276(012)	15.187(025)	TNT
5971.89	157.41	17.024(056)	14.911(013)	14.856(014)	15.284(017)	15.252(023)	TNT
5972.89	158.41	17.024(048)	14.918(010)	14.821(012)	15.297(019)	15.197(027)	TNT
5979.85	165.37	17.228(050)	15.056(013)	14.900(011)	15.511(024)	15.282(029)	TNT
5981.87	167.39	17.503(050)	15.067(015)	15.009(013)	15.516(018)	15.297(031)	TNT
5982.84	168.36	17.248(061)	15.073(017)	14.990(017)	15.574(023)	15.371(037)	TNT
5983.83	169.35	17.328(057)	15.062(016)	15.037(019)	15.596(015)	15.356(030)	TNT
5985.88	171.40	17.274(077)	15.125(013)	15.112(011)	15.699(014)	15.520(024)	TNT
5992.84	178.36	17.729(078)	15.229(020)	15.144(013)	15.761(023)	15.588(027)	TNT
5994.86	180.38	17.248(097)	15.421(041)	15.176(036)	16.037(076)	15.558(081)	TNT
5996.87	182.39	18.076(099)	15.287(039)	15.182(031)	15.810(051)	15.619(056)	TNT
5998.85	184.37	17.510(081)	15.327(014)	15.282(011)	15.950(014)	15.672(022)	TNT
5999.87	185.39	17.681(055)	15.322(018)	15.247(016)	15.859(021)	15.722(041)	TNT
6010.82	196.34	18.074(062)	15.477(014)	15.500(013)	16.201(017)	15.798(025)	TNT
6011.79	197.31	⋯	15.478(011)	15.523(013)	16.215(018)	15.943(032)	TNT
6012.72	198.24	⋯	15.474(018)	15.505(014)	16.092(033)	15.789(056)	TNT
6015.77	201.29	18.008(055)	15.531(012)	15.539(013)	16.223(018)	15.821(028)	TNT
6020.80	206.32	17.974(081)	15.676(012)	15.666(015)	16.355(025)	16.057(029)	TNT
6021.71	207.23	⋯	15.653(020)	15.672(019)	16.490(028)	15.909(028)	TNT
6029.75	215.27	18.140(065)	15.784(013)	15.785(012)	16.511(015)	16.153(021)	TNT
6042.81	228.33	18.581(081)	15.930(012)	15.993(013)	16.762(016)	16.249(023)	TNT
6050.62	236.14	18.052(278)	16.094(033)	16.102(035)	16.909(066)	16.363(051)	TNT
6062.55	248.07	19.014(159)	16.242(018)	16.281(018)	17.105(027)	16.505(032)	TNT
6069.62	255.14	⋯	16.304(038)	16.374(019)	16.968(077)	⋯	TNT
6071.61	257.13	⋯	16.357(013)	16.419(013)	17.247(028)	16.529(038)	TNT
6077.52	263.04	⋯	16.588(114)	16.443(043)	17.325(065)	16.855(087)	TNT
6090.72	276.24	⋯	16.588(034)	16.673(033)	17.399(077)	16.709(088)	TNT
6108.53	294.05	⋯	17.318(139)	17.234(082)	17.850(117)	16.937(061)	TNT
6137.54	323.06	⋯	17.651(101)	17.430(071)	18.258(090)	17.145(059)	TNT
6160.59	346.11	⋯	17.918(140)	17.814(107)	18.051(155)	18.096(260)	TNT
6277.56	463.08	⋯	⋯	19.360(040)	20.100(060)	18.930(030)	LJT

Notes.
[a] 2,450,000.5 has been subtracted from the Julian Date.
[b] Relative to the epoch of B-band maximum (JD = 2,455,814.98).
[c] Uncertainties, in units of 0.001 mag, are 1σ.

2011by, although these two SNe Ia have similar values of $\Delta m_{15}(B)$.

Figure 4 shows comparisons of the late-time light curves over the period from $t \approx +70$ to $+500$ days relative to B-band maximum. One can see that large differences emerge in the U band; SN 2011fe declined more rapidly than SN 2003du and even the fast decliner SN 2003hv. Past about 70 days after maximum light, the U-band decay rate of SN 2011fe is

Table 3
Journal of Spectroscopic Observations of SN 2011fe

UT Date	JD[a]	Phase[b]	Exp.(s)	Telescope + Instrument	Range (Å)
2011 Aug 25	5798.55	−16	2 × 1800	YNAO 2.4 m+YFOSC (G8+G14)	3500–9000
2011 Aug 26	5809.54	−15	2 × 1800	YNAO 2.4 m+YFOSC (G8+G14)	3500–9000
2011 Aug 27	5800.53	−14	2 × 1200	YNAO 2.4 m+YFOSC (G8+G14)	3500–9000
2011 Aug 28	5801.53	−13	2 × 1200	YNAO 2.4 m+YFOSC (G8+G14)	3500–9000
2011 Aug 28	5801.54	−13	1800	BAO 2.16 m+BFOSC (G4)	3400–8500
2011 Aug 29	5802.53	−12	2 × 900	YNAO 2.4 m+YFOSC (G8+G14)	3500–9000
2011 Aug 30	5803.53	−11	2 × 600	YNAO 2.4 m+YFOSC (G8+G14)	3500–9000
2011 Aug 31	5804.54	−10	2 × 600	YNAO 2.4 m+YFOSC (G8+G14)	3500–9000
2011 Sep 1	5805.53	−9	2 × 600	YNAO 2.4 m+YFOSC (G8+G14)	3500–9000
2011 Sep 2	5806.50	−8	1200	BAO 2.16 m+OMR	3400–8750
2011 Sep 2	5806.52	−8	2 × 300	YNAO 2.4 m+YFOSC (G8+G14)	3500–9000
2011 Sep 3	5807.55	−7	2 × 300	YNAO 2.4 m+YFOSC (G8+G14)	3500–9000
2011 Sep 4	5808.55	−6	600	BAO 2.16 m+BFOSC (G4)	4000–6700
2011 Sep 5	5809.53	−5	2 × 300	YNAO 2.4 m+YFOSC (G8+G14)	3500–9000
2011 Sep 5	5809.54	−5	600	BAO 2.16 m+BFOSC (G4)	4000–6700
2011 Sep 13	5817.52	+3	2 × 480	YNAO 2.4 m+YFOSC	3500–9000
2011 Sep 17	5821.48	+7	300	BAO 2.16 m+OMR	4100–6900
2011 Sep 19	5823.48	+9	600	BAO 2.16 m+OMR	5500–6850
2011 Sep 19	5823.52	+9	2 × 300	YNAO 2.4 m+YFOSC (G8+G14)	3500–9000
2011 Sep 28	5832.50	+18	2 × 300	YNAO 2.4 m+YFOSC (G8+G14)	3500–9000
2011 Sep 30	5834.45	+20	1200	BAO 2.16 m+OMR	4500–8900
2011 Oct 3	5837.45	+23	600	BAO 2.16 m+BFOSC (G4)	3400–8700
2011 Oct 6	5840.45	+26	300	BAO 2.16 m+BFOSC (G4)	4000–6700
2011 Dec 3	5898.93	+85	900	YNAO 2.4 m+YFOSC (G3)	3500–9000
2011 Dec 16	5911.88	+97	1800	BAO 2.16 m+BFOSC(G4)	3300–9700
2011 Dec 23	5918.92	+105	1200	BAO 2.16 m+OMR	3800–9000
2011 Dec 31	5926.92	+113	1200	YNAO 2.4 m+YFOSC (G3)	3350–9100
2012 Jan 26	5952.82	+138	1800	YNAO 2.4 m+YFOSC (G3)	3900–9100
2012 Feb 05	5962.89	+148	2700	YNAO 2.4 m+YFOSC (G3)	3700–8300
2012 Feb 24	5981.85	+167	3600	BAO 2.16 m+OMR	3850–8500
2012 Mar 16	6002.71	+188	3000	BAO 2.16 m+OMR	3500–8750
2012 Apr 13	6030.76	+216	3600	BAO 2.16 m+OMR	4550–8200
2012 Apr 30	6047.79	+233	3000	YNAO 2.4 m+YFOSC (G3)	3400–9050
2012 May 23	6070.79	+256	3000	YNAO 2.4 m+YFOSC (G3)	3400–9050
2012 Dec 16	6277.56	+463	3600	YNAO 2.4 m+YFOSC (G3)	3400–9050

Notes.
[a] 2,450,000.5 has been subtracted from the Julian Date.
[b] Relative to the epoch of *B*-band maximum (JD = 2,455,814.98).

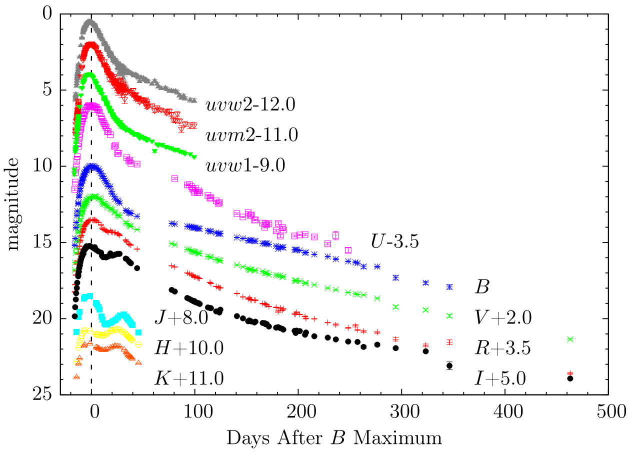

Figure 2. The UV, optical, and NIR light curves of SN 2011fe, with UV data from Brown et al. (2012) and NIR data from Matheson et al. (2012).

Table 4
Photometric Parameters of SN 2011fe

Parameters	Value
$t_{B_{\max}}$ (JD)	2,455,814.48 ± 0.03
$B_{\max}$ (mag)	9.96 ± 0.03
Δm_{15} (mag)	1.18 ± 0.03
$B_{\max} - V_{\max}$ (mag)	−0.03 ± 0.04
Host galaxy	M101
Absolute magnitude *U*	−19.74 ± 0.19
B	−19.24 ± 0.19
V	−19.17 ± 0.19
R	−19.11 ± 0.19
I	−18.85 ± 0.19
$E(B-V)_{\mathrm{MW}}$ (mag)	0.008
$E(B-V)_{\mathrm{host}}$ (mag)	0.032 ± 0.045
Late-time decline rate (mag/100 days) *U*	2.28 ± 0.06
B	1.44 ± 0.02
V	1.51 ± 0.02
R	1.71 ± 0.03
I	1.12 ± 0.04

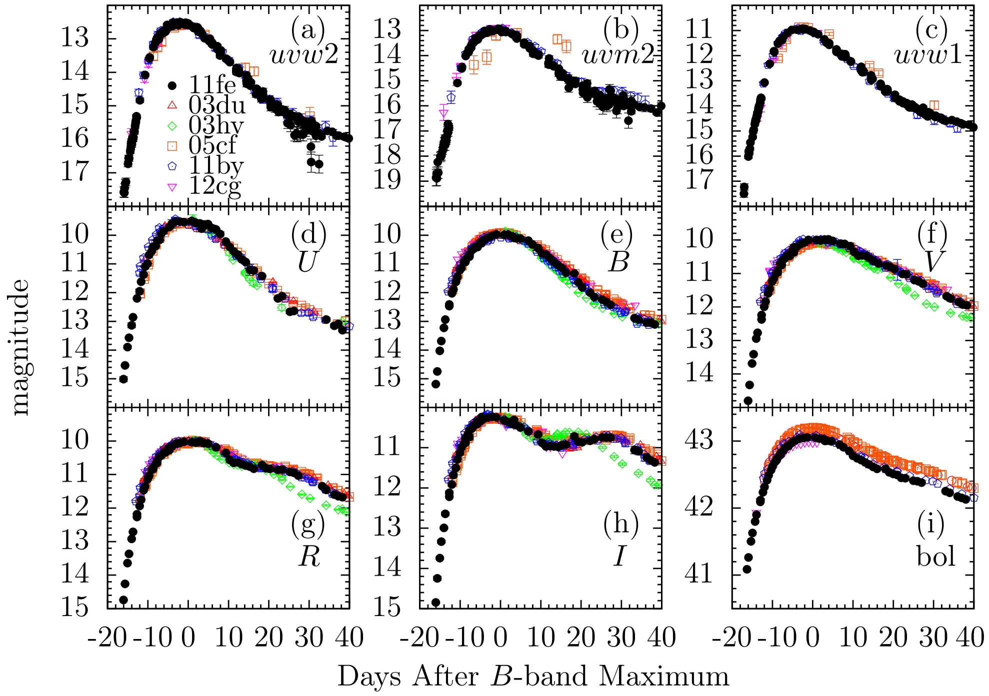

Figure 3. Comparison of the near-maximum-light UV, optical, and bolometric (erg s^{-1}) light curves of SN 2011fe and other well-observed SNe Ia: SN 2003du, SN 2003hv, SN 2005cf, SN 2011by, and SN 2012cg. See text for references.

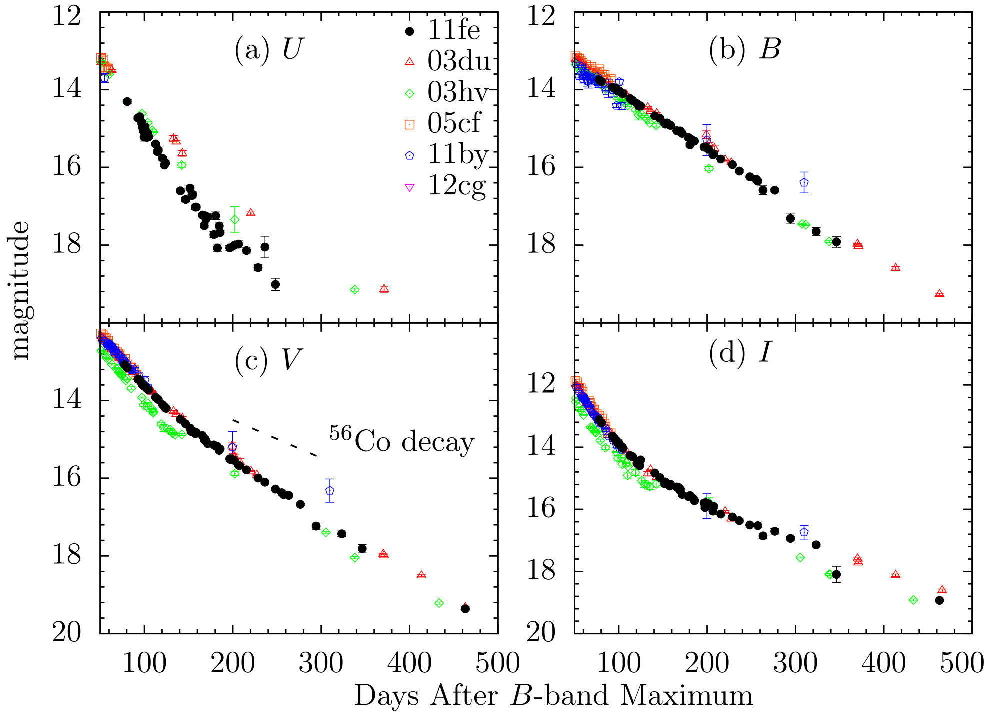

Figure 4. Comparison of the late-time *UBVI* light curves of SN 2011fe and other well-observed SNe Ia: SN 2003du, SN 2003hv, SN 2005cf, SN 2011by, and SN 2012cg. The ^{56}Co → ^{56}Fe decay rate is also plotted. See text for references.

estimated to be 2.28 ± 0.06 mag (100 days)$^{-1}$, while the corresponding decline rates are 1.62 ± 0.12 mag (100 days)$^{-1}$ for SN 2003du (Stanishev et al. 2007) and 1.33 ± 0.24 mag (100 days)$^{-1}$ for SN 2003hv (Leloudas et al. 2009) at comparable phases. Although SN 2003du has small Δm_{15}(B), SN 2011fe still has a much faster decay rate compared to SN 2003hv. The faster decay shown by the *U*-band light curve of SN 2011fe is thus likely caused by its ejecta having a relatively lower opacity in the UV (see also discussion in Section 5.3). Another possible factor is a difference in the magnetic field, which may lead to different amounts of positron trapping.

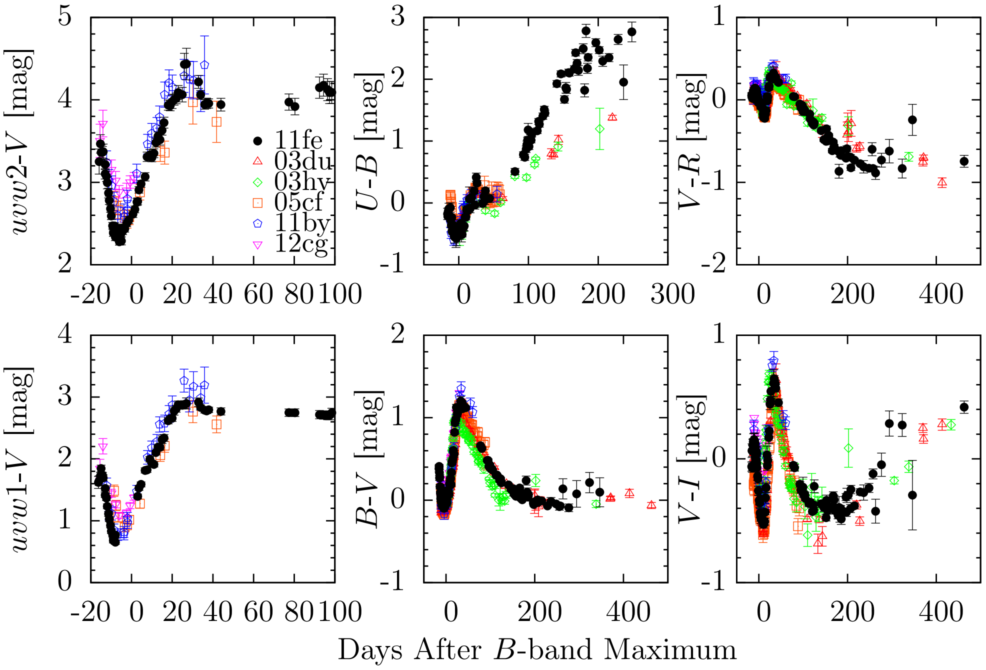

Figure 5. $uvw2 - V$, $uvw1 - V$, $U - B$, $B - V$, $V - R$, and $V - I$ color curves of SN 2011fe compared with those of SN 2003du, SN 2003hv, SN 2005cf, SN 2011by, and SN 2012cg. All of the color curves have been corrected for reddening from the Milky Way and the host galaxies. The data sources are cited in the text.

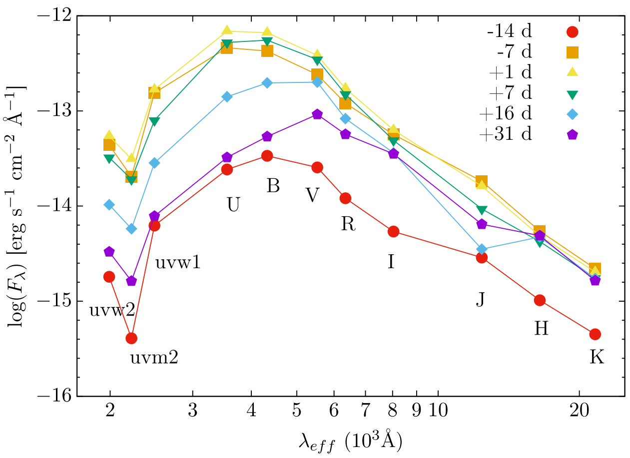

Figure 6. SED of SN 2011fe obtained at $t \approx -14$, -7, $+1$, $+7$, $+16$, and $+31$ days after B-band maximum.

3.2. The Color Curves

Figure 5 shows the color curves of SN 2011fe, including the two UV minus V colors ($uvw2 - V$ and $uvw1 - V$). Overplotted are the color curves of SN 2003du, SN 2003hv, SN 2005cf, SN 2011by, and SN 2012cg. All of the color curves are corrected for reddening in both the Milky Way (Schlafly & Finkbeiner 2011) and the host galaxies.

Inspection of the plot reveals that SN 2011fe has bluer $uvw1 - V$ and $uvw2 - V$ colors than the comparison SNe Ia before maximum light (by ~0.2 mag), consistent with its strong UV emission at early times. On the other hand, the $B - V$, $V - R$, and $V - I$ colors of SN 2011fe exhibit behaviors that are similar to those of the comparison SNe at early phases. The UV and optical color curves commonly showed an initial decline after the explosion, and they reached their minimum values (i.e., bluest colors) around maximum light, followed by an increase toward redder colors until $t \approx +30$ days.

The subsequent evolution of the different color curves shows large scatter. The $uvw1 - V$ and $uvw2 - V$ colors become nearly constant during the period from $t \approx +30$ to $+100$ days. Similarly, the $U - B$ color also showed a plateau feature during this phase, which then became redder in a linear fashion thereafter. At later phases, SN 2011fe is found to be progressively redder than SN 2003du and SN 2003hv in $U - B$, suggesting that its photospheric temperature drops more rapidly than that of SN 2003du and SN 2003hv. Meanwhile, $B - V$, $V - R$, and $V - I$ evolved toward bluer colors (declined by ~1.2 mag) during the period from $t \approx +30$ days to $t \approx +200$ days. At $t \gtrsim +200$ days, the $B - V$ and $V - R$ colors showed a flat evolution while the $V - I$ color gradually became red again.

3.3. The SED and Bolometric Light Curve

Since we have photometry of SN 2011fe in the UV, optical, and NIR bands covering wavelengths of 1600–24000 Å, we can study its spectral energy distribution (SED) evolution by means of photometry. A rough SED can be constructed from the observed fluxes in various passbands at the same or similar epochs. The missing data can be obtained through interpolations of the neighboring data points whenever necessary. The observed fluxes are corrected for the reddening of Milky Way and the host galaxies.

Figure 6 shows the SEDs obtained at $t = -14$, -7, $+1$, $+7$, $+16$, and $+31$ days with respect to B-band maximum. One can see that the SEDs show a prominent deficit in the $uvm2$ band at all of these epochs, explained as line blending caused by iron-peak elements (e.g., Wang et al. 2009b). The SED of SN 2011fe is found to peak in the B band at $t = -14$ days, and it

Table 5
Bolometric Light Curve of SN 2011fe

Phase[a]	log(L) (erg s^{-1})[b]	Phase	log(L) (erg s^{-1})
−16.31	41.09	20	42.51
−16	41.26	21	42.49
−15	41.63	22	42.45
−14	41.90	23	42.45
−13	42.09	25	42.41
−12	42.31	26	42.40
−11	42.49	27	42.38
−10	42.62	33	42.25
−9	42.71	37	42.15
−8	42.79	44	42.03
−7	42.89	49	41.96
−6	42.92	55	41.88
−5	42.99	60	41.82
−4	43.00	64	41.77
−3	43.03	80	41.57
−2	43.05	92	41.45
−1	43.05	97	41.40
1	43.05	104	41.33
2	43.04	114	41.25
3	43.00	120	41.18
4	43.00	123	41.15
5	43.00	140	41.03
7	42.95	151	40.94
8	42.91	158	40.91
9	42.85	165	40.86
10	42.78	171	40.80
11	42.74	178	40.77
12	42.72	185	40.73
13	42.68	196	40.65
14	42.65	206	40.58
15	42.61	215	40.53
16	42.58	228	40.46
18	42.58	236	40.41
19	42.53	248	40.34

Notes.

[a] Relative to the epoch of B-band maximum (JD = 2,455,814.98).

[b] Typical uncertainty is 0.07, dominated by the uncertainty in the distance.

then peaked in the U band at $t = -7$ days and $t = +1$ days. After maximum light, the SED peak shifted quickly toward longer wavelengths. Around 1 month after maximum light, the emission in the H band became stronger than that in the J band, which is likely caused by the recombination of Fe III. Compared to SN 2005cf (see Figure 12 in Wang et al. 2009b), SN 2011fe seems to show a faster decrease in the photospheric temperature.

We constructed the bolometric light curve of SN 2011fe, as listed in Table 5, and compare it with that of SN 2003du, SN 2005cf, SN 2011by, and SN 2012cg, as shown in Figure 7. Owing to the lack of NIR data for SN 2011by, we assume that it has the same NIR/optical ratio ($F_{\rm NIR}/F_{\rm optical}$) as SN 2005cf. With a peak luminosity of $(1.13 \pm 0.07) \times 10^{43}$ erg s^{-1}, we can deduce that the synthesized nickel mass is $M_{\rm Ni} = 0.57\,M_{\odot}$ for SN 2011fe according to the Arnett law (Arnett 1982; Stritzinger & Leibundgut 2005). In Figure 8, we plot the ratio of the UV (1600–3200 Å) and NIR (9000–24000 Å) fluxes to the optical (3200–9000 Å) for SN 2011fe and the comparison sample SN 2005cf, SN 2011by, and SN 2012cg. It can be seen that the UV/optical ratio ($F_{\rm UV}/F_{\rm optical}$) of SN 2011fe is comparable to that of SN 2005cf but apparently higher than that of SN 2011by and SN 2012cg, while the NIR/optical ratio ($F_{\rm NIR}/F_{\rm optical}$) is similar for these three SNe Ia. We noticed that the $F_{\rm UV}/F_{\rm optical}$ ratio of SN 2011fe reached its peak 1 week earlier than that of SN 2005cf and also slightly earlier than that of SN 2012cg, suggestive of a shorter diffusion time for its higher-energy photons. Given a similar ejecta mass and expansion velocity, this difference implies that the ejecta of SN 2011fe have a lower opacity at shorter wavelengths.

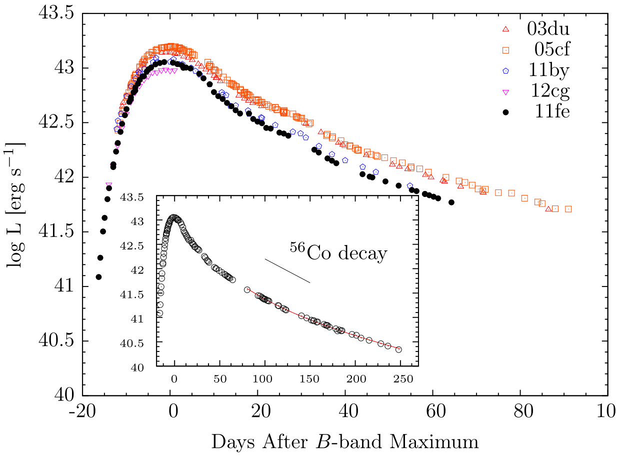

Figure 7. UV through optical bolometric light curve of SN 2011fe compared with those of SN 2003du, SN 2005cf, SN 2011by, and SN 2012cg. The late-time bolometric light curve of SN 2011fe is shown in the inset. The red line is the model described in the text, and the black line shows the $^{56}\mathrm{Co} \rightarrow {}^{56}\mathrm{Fe}$ decay.

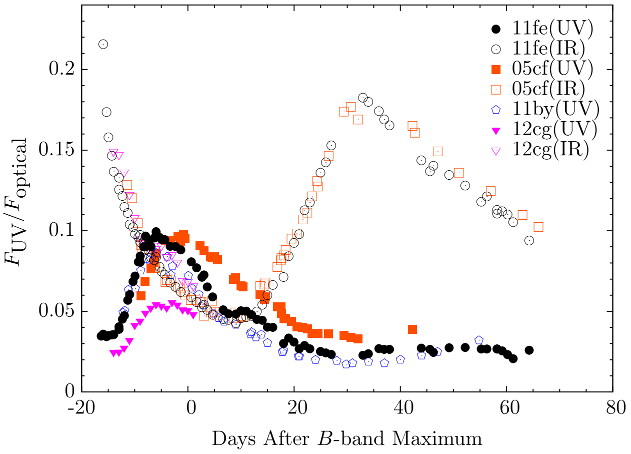

Figure 8. Ratio of the UV (1600–3200 Å) and NIR (9000–24000 Å) fluxes to the optical (3200–9000 Å). Overplotted are the corresponding flux ratios of SN 2005cf, SN 2011by, and SN 2012cg.

4. OPTICAL SPECTRA

We have in total 35 optical spectra of SN 2011fe, obtained with the 2.4 m LJT of YNAO and the 2.16 m telescope of NAOC, spanning from $t = -16$ to $+463$ days with respect to B-band maximum light. Figure 9 shows the complete spectral evolution. Detailed comparisons with some well-observed SNe Ia at different epoches are shown in Figures 10 and 11.

4.1. Temporal Evolution of the Spectra

In Figure 10, we compare the spectra of SN 2011fe with those of SN 2003du (Stanishev et al. 2007), SN 2005cf (Wang

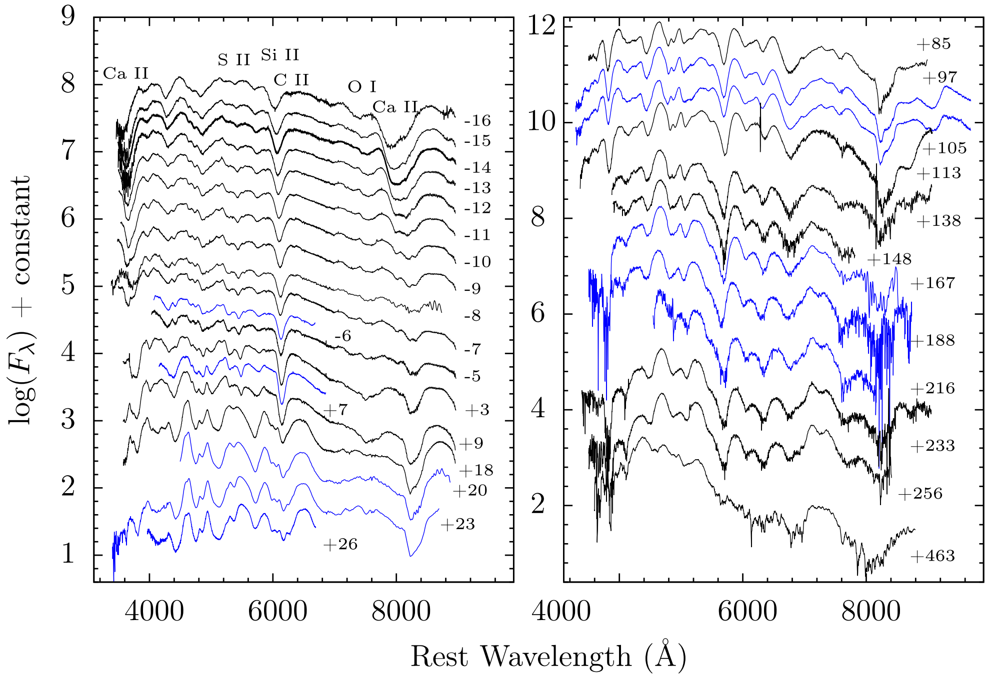

Figure 9. Optical spectra of SN 2011fe. Spectra obtained with the YNAO 2.4 m telescope are shown in black; those obtained with the Xinglong 2.16 m of NAOC are in blue.

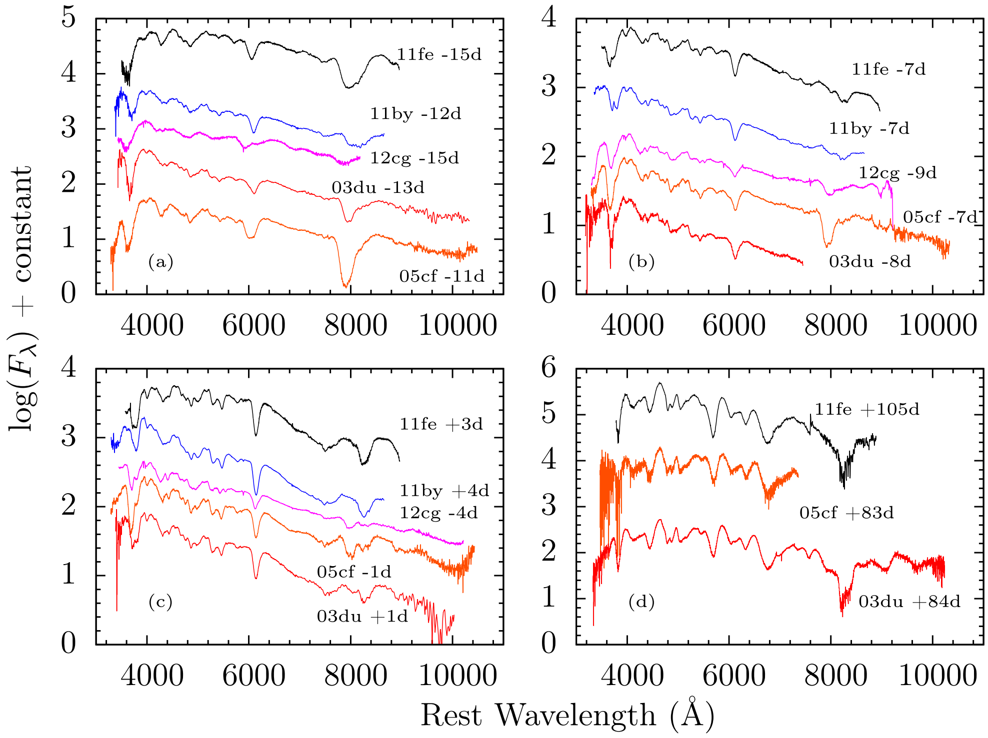

Figure 10. Spectrum of SN 2011fe at $t \approx -15$ days, -7 days, 0 day, and $+3$ months after B-band maximum. The comparable-phase spectra of SN 2003du, SN 2005cf, SN 2011by, and SN 2012cg are overplotted for comparison.

et al. 2009b), SN 2011by (Graham et al. 2015a; H. Song et al. 2016, in preparation), and SN 2012cg (our own unpublished database) at four different epochs ($t \approx -14$ days, -7 days, 0 day, and $+90$ days with respect to B maximum). At these phases (except for $t \approx 3$ months), spectra of SN 2011fe and the comparison sample show large differences in line profiles of some species, in particular the Si II and Ca II absorption.

Figure 10(a) shows the comparison of the spectra at $t \approx -14$ days. To identify the absorption features in the early-time spectra of SN 2011fe, we use SYNAPPS (Thomas et al.

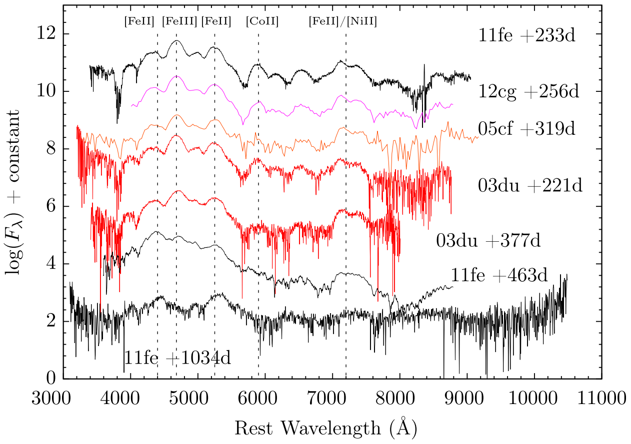

Figure 11. Late-time spectra of SN 2011fe. The nebular spectra of SN 2003du, SN 2005cf, SN 2011by, and SN 2012cg at similar phases are also shown for comparison.

2011) to fit two early-time spectra obtained at $t = -16$ and -12 days, and the results are shown in Figure 12. One can see that the spectral features at these phases are dominated by intermediate-mass elements like calcium, silicon, oxygen, and magnesium, while the Fe II/Fe III absorptions are responsible for the troughs near 4300 and 4800 Å. Note that the fit to the spectrum at $t = -12$ days looks better if Co II and Ni II are included. The notches near 6300 and 7000 Å can be attributed to C II λ6580 and C II λ7234 absorptions, respectively, which have also been identified by Parrent et al. (2012) and Pereira et al. (2013). Weak absorption from C II is also detected in SN 2003du, SN 2005cf, SN 2011by, and SN 2012cg at earlier phases. For the Ca II NIR triplet lines, we found that high-velocity components are needed in order to get a better fit for SN 2011fe. At $t \approx -14$ days, the HVF of Si II λ6355 is found to be very prominent in SN 2005cf and SN 2012cg, while it is weak in SN 2003du and does not seem to exist in SN 2011by and SN 2011fe. On the other hand, SN 2011fe displays two noticeable absorption features at ~7300 and ~7400 Å, and they can be identified as HVF and photospheric components of O I λ7773 at velocities of $\sim 1.8 \times 10^4$ km s^{-1} and $\sim 1.3 \times 10^4$ km s^{-1}, respectively (see Figure 15). Note that such O-HVFs are very weak or undetectable in the earliest spectra of our comparison SNe Ia.

Figure 10(b) shows the comparison at $t \approx -7$ days. The most noticeable change in the spectra is the rapid evolution of the HVFs of O, Si, and Ca. For SN 2011fe and SN 2011by, the Ca-HVFs became almost invisible in the spectrum at this time. In contrast, the Ca-HVFs are still very strong in SN 2005cf and SN 2012cg, and the Si-HVF becomes very weak but still detectable in these SNe Ia. On the other hand, at this phase, the HVF of O I λ7773 still appears to be detectable in SN 2011fe. This indicates that SN 2011fe (and perhaps SN 2011by) has overall weaker Si-HVFs and Ca-HVFs compared to SN 2005cf and SN 2012cg, while it shows prominent O-HVFs.

In Figure 10(c), we compare the near-maximum-light spectra. At $t \approx 0$ day, the spectrum of SN 2011fe has shown some evolution relative to the features exhibited at the earlier epochs, and the photospheric components of the O I λ7773 and Ca II NIR triplet absorption are found to be stronger than in the comparison SNe Ia. For SN 2005cf and SN 2012cg, the HVFs of the Ca II NIR triplet are still dominant over the photospheric components around maximum light.

In Figure 10(d), we compare the spectra at $t \approx 3$ months. With the photosphere receding into the inner region, SN 2011fe and the comparison SNe Ia exhibit quite similar spectral features. The absorption trough from the Ca II NIR triplet is still the dominant feature, and other main lines include Na I, Fe II, and Fe III lines, which develop into a highly similar profile in the nebular phase.

Two late-time nebular spectra, obtained with the YFOSC on day +233 and on day +463, are shown in Figure 11. Overplotted are the late-time spectra of SN 2003du, SN 2005cf, and SN 2012cg. One very late-time spectrum of SN 2011fe, taken on day +1034 (Taubenberger et al. 2015), is also shown for comparison. At such late phases, the spectra are dominated by forbidden lines of singly and doubly ionized iron-group elements, such as the [Fe II] features at ~4400, ~5200, and ~7200 Å, [Fe III] at ~4700 Å, and [Co II] at ~4900 Å. These features are commonly seen in the comparison SNe Ia at similar phases. Combining the spectra at $t \approx +233$, +463, and +1034 days, we notice that the [Fe III] feature at ~4700 Å, [Co II] at ~6000 Å, and [Fe II]/[Ni II] at ~7200 Å tend to become relatively weak with time, while the [Fe II] features at ~4400 and ~5200 Å seem to show the opposite tendency.

4.2. Evolution of Photospheric- and High-velocity Features

The well-sampled spectra of SN 2011fe can also allow us to study the evolution of the photospheric-velocity features (PVFs) and HVFs in the earliest spectra. From the evolution of these line profiles as displayed in Figure 13, one can hardly see the presence of an HVF in Si II λ6355, while the HVFs are obviously seen in the Ca II NIR triplet. Note that our spectral sequence indicates that the O I λ7773 line may have multiple absorptions formed at different velocities, as discussed below. For a thorough analysis of the PVFs and HVFs of Si and Ca in SNe Ia, see Silverman et al. (2015, hereafter S15) and Zhao et al. (2015, hereafter Z15). In this subsection, we analyze the evolution of velocity and pseudo-equivalent width (pEW) of the absorptions of Si II λ6355 and the Ca II NIR triplet for SN 2011fe and compare the results with those from SN 2003du, SN 2005cf, SN 2011by, and SN 2012cg, as shown in Figures 14 and 15.

The velocity measured from the Si II λ6355 absorption in near-maximum-light spectra is 1.04×10^4 km s^{-1} for SN 2011fe, showing that it belongs to the normal-velocity (NV) subclass of SNe Ia in the classification scheme of Wang et al. (2009a). The velocity gradient, measured during the period from $t = 0$ to +10 days, is found to be $\dot{v} = 52.4$ km s^{-1} day^{-1}, suggesting that SN 2011fe can be put into the low-velocity gradient subtype in the classification scheme of Benetti et al. (2005).

As discussed by S15 and Z15, the HVFs are usually prominent in the early-phase spectra. To detect the HVFs of SN 2011fe, we apply a two-component Gaussian function to fit the absorptions from Si II λ6355 and the Ca II NIR triplet in the spectrum at $t = -16$ days. We did not detect any significant HVF in the Si II λ6355 absorption, but there are noticeably strong HVFs in the Ca II NIR triplet. The velocity evolution of the Si II and Ca II absorptions (both PVF and HVF) is shown in Figure 14, where we can see that the Ca-HVFs of SN 2011fe maintain a velocity of $\sim 2.0 \times 10^4$ km s^{-1} during the period from $t = -10$ to -5 days with respect to B

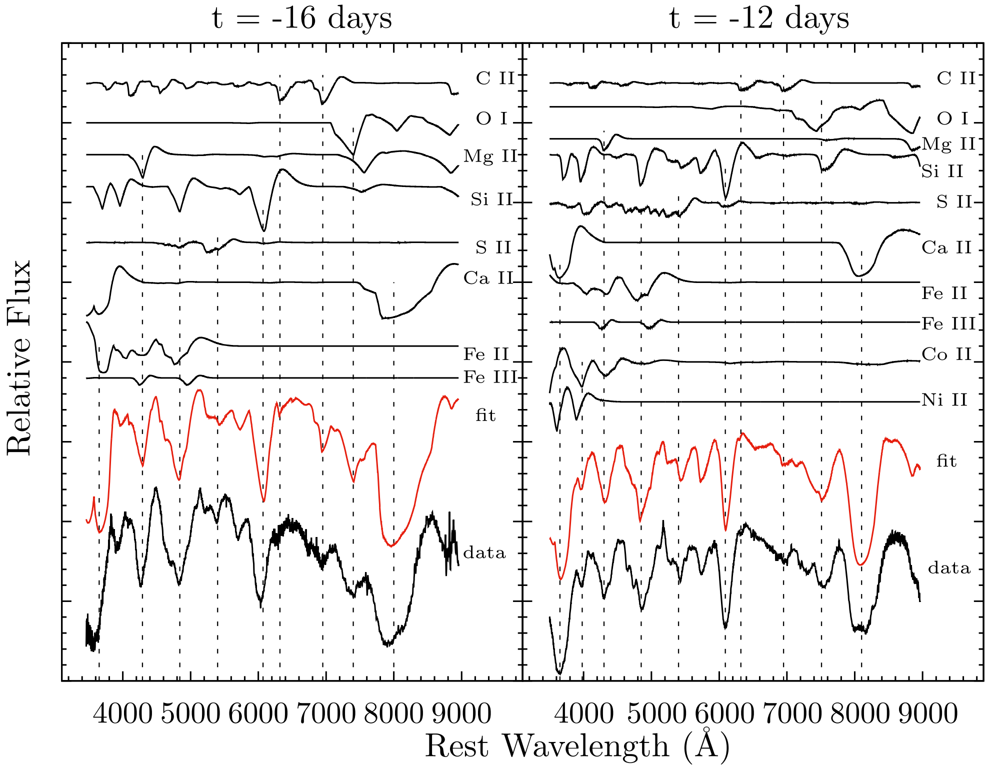

Figure 12. SYNAPPS fit to the spectra at $t = -16$ and -12 days of SN 2011fe. Features from different ions are marked with dashed lines.

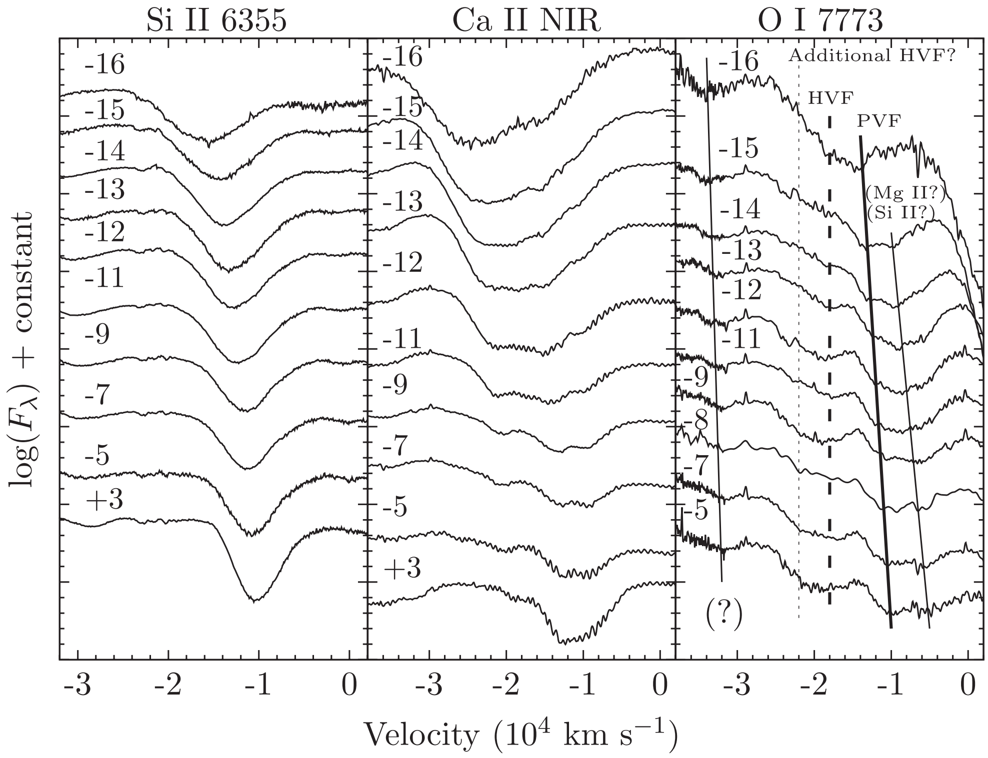

Figure 13. Evolution of Si II λ6355, Ca II NIR, and O I λ7773 lines of SN 2011fe in velocity space. The solid line marks the positions of the photospheric component, the dashed line marks the HVF, and the dotted line marks the position of a possible additional HVF of O I λ7773 identified by X. Zhao et al. (2016, in preparation).

maximum. This velocity plateau can be also seen in the Ca-HVFs of SN 2011by and SN 2012cg.

Figure 15 shows the pEW of Si II λ6355 and the Ca II NIR triplet absorptions. It can be seen that the pEW of the Si-PVF of SN 2011fe reached a minimum at ~-6 days, with a pEW of $\sim$80 Å. A similar trend can be seen in the comparison SNe, of which SN 2012cg has an overall weaker absorption. Our fit to the early-time Si II absorption suggests that the Si-HVF is very

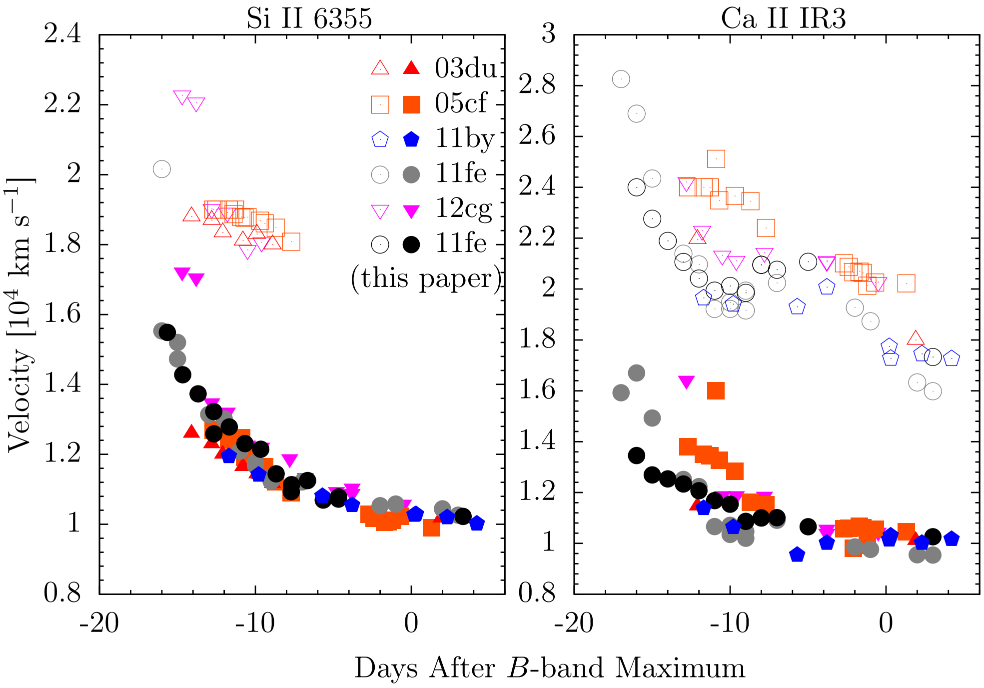

Figure 14. Evolution of the expansion velocity of SN 2011fe as measured from the absorption minima of Si II λ6355 (left panel) and the Ca II NIR triplet (right panel), in comparison with the values of SN 2003du, SN 2005cf, SN 2011by, and SN 2012cg (see text for references). Open symbols represent the HVFs, and filled symbols represent the PVFs.

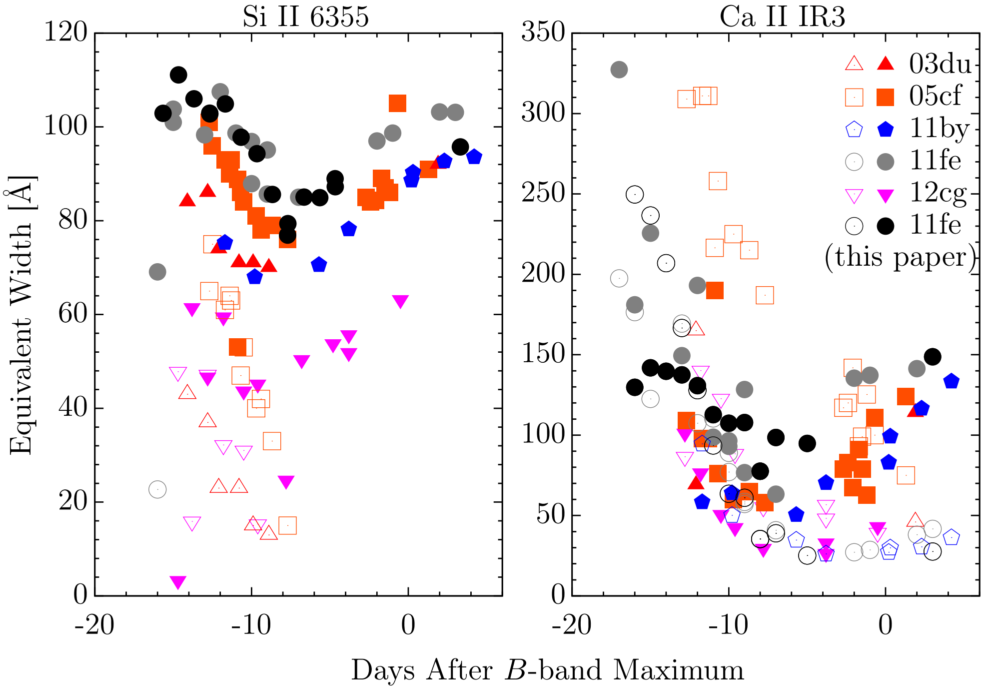

Figure 15. Evolution of the pEW of SN 2011fe as measured from the absorption of Si II λ6355 (left panel) and the Ca II NIR triplet (right panel), compared with the measurements of SN 2003du, SN 2005cf, SN 2011by, and SN 2012cg (see text for references). Open symbols denote the HVFs, and filled symbols denote the PVFs.

weak or does not exist in SN 2011fe, consistent with previous analyses by S15 and Z15. In contrast, the HVFs are clearly detected in the Ca II NIR triplet of SN 2011fe and the four comparison SNe Ia. This is consistent with the statistical result that the Ca-HVFs are more commonly seen in SNe Ia than the Si-HVF. The absorption strength of Ca-HVFs decayed very quickly in SN 2011fe, changing from ~250 Å at $t \approx -16$ days to ~30 Å at $t \approx -5$ days. This is similarly seen in SN 2005cf, SN 2011by, and SN 2012cg.

In addition to the HVFs of the Ca II NIR triplet, the HVF of O I λ7773 can be detected in the earliest spectra of SN 2011fe, as shown in Figure 13. At $t \approx -16$ days, the HVF of O I λ7773 is measured to have a velocity of $\sim 1.8 \times 10^4$ km s^{-1}, and the photospheric component has a velocity of $\sim 1.4 \times 10^4$ km s^{-1}.

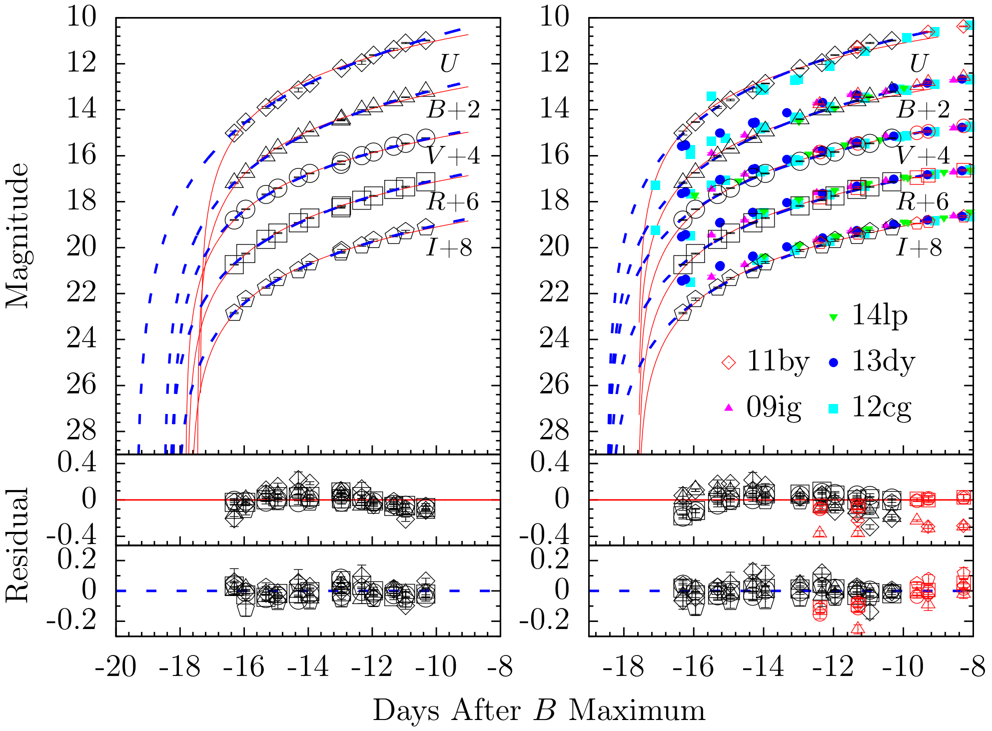

Figure 16. Fit to the early-time *UBVRI* light curves of SN 2011fe. Left panel shows fits to the data with $t < -10$ days; the red line shows the fit with the $(t - t_{\rm first})^2$ model, while the blue line represents the fit with the $(t - t_0)^n$ model. Right panel shows a multiband t^n fitting by forcing all five bands to have the same $t_{\rm first}$; the red line shows the fit with the $(t - t_{\rm first})^2$ model, while the blue dashed line represents the fit with the $(t - t_0)^n$ model. Some SNe Ia with early-time data are also plotted for comparison.

The photospheric velocity is consistent with that from Si II and Ca IIlines. It is interesting to note that a second HVF of O I λ7773 may appear in the earlier spectra of SN 2011fe (see minor absorption marked by the dotted line), which has a velocity of $\sim 2.2 \times 10^4$ km s^{-1} (X. Zhao et al. 2016, in preparation). The presence of oxygen at such a high velocity may naturally explain the formation of Ca-HVFs seen in SN 2011fe. Nugent et al. (2011) noticed that the O-HVF shows a rapid velocity decline from about 18,000 to 14,000 km s^{-1} in the first two spectra (at $t = 1.2$ and 1.5 days after explosion), and they attributed it to geometrical dilution during the early phases. However, it is more likely that the velocity variation they measured is actually related to different components of O I λ7773 absorption. From the SYNAPPS fit as shown in Figure 12, the feature with a velocity of $\sim 0.9 \times 10^4$ to 0.5×10^4 km s^{-1} may be due to the blending of Mg II and Si II. The feature with a velocity of $\sim 3.3 \times 10^4$ km s^{-1} remains unknown to us.

5. DISCUSSION

5.1. The Rising Light Curves

The rising light curves are important, as they can determine the explosion time (Nugent et al. 2011), constrain the radius of the exploding star itself (Piro et al. 2010; Bloom et al. 2012; Piro & Nakar 2013), and test the scenario of luminosity evolution of SNe Ia, as well as other properties of their progenitor systems, such as interaction with a companion star (Kasen 2010). Note that there is a difference between the explosion time and the time when the SN begins to brighten (time of first light, $t_{\rm first}$) because of a possible dark phase immediately after the explosion (Piro & Nakar 2013, 2014); thus, we use $t_{\rm first}$ relative to *B*-band maximum in the following discussion. In the "expanding fireball model," the early-time flux is thought to be $f \propto (t - t_{\rm first})^2$ (Riess et al. 1999; Conley et al. 2006). Assuming a more general form of the fireball model such as $f \propto (t - t_{\rm first})^n$, a recent study using 18 SNe Ia yields a mean (but without stretch correction) rise time of 18.98 ± 0.54 days and a mean index of $n = 2.44 \pm 0.13$ (Firth et al. 2015). Some modified models, such as a broken power law, are also proposed for the luminosity evolution of SNe Ia (e.g., Zheng et al. 2013).

For SN 2011fe, Nugent et al. (2011) obtained a $t_{\rm first}$ of MJD 55796.696 ± 0.003 (t^2) and $55{,}796.687 \pm 0.014$ ($t^{2.01}$). Brown et al. (2012) estimated $t_{\rm first}$ ranging from MJD 55,796.62 to MJD 55,797.07 in different bands, using the earliest data from *Swift* UVOT observations. With a bolometric light curve, Pereira et al. (2013) derived $t_{\rm first}$ as $55{,}796.81 \pm 0.13$ for t^2 evolution and $t_{\rm first} = 55{,}796.47 \pm 0.83$ for t^n, and $n = 2.21 \pm 0.51$.

Our extensive photometric data for SN 2011fe, starting within 1 day after the explosion, also enable better constraints on its luminosity evolution and first-light time. Using the observed data at $t < -10$ days and assuming a model of $f \propto (t - t_{\rm first})^n$ for the rising light curves, we find that the rising rate of the emission flux differs from t^2 evolution in all bands except *V* and *I*, where the flux rises in a manner close to t^2 evolution (i.e., $n = 2.27$ and 2.33). Residuals of the fits are shown in the bottom panels of Figure 16, and the best-fit results are listed in Table 6. From the t^2 fit, we found that the first-light time ranges from -17.37 days (*U* band) to -17.82 days (*V* band), while the corresponding time estimated with the t^n model spans from -18.12 days (*I* band) to -19.37 days (*U* band). In light of the goodness of the fit, one may conclude that

Table 6
Fit Parameters of the Rising Light Curve

Filter	Data Points	$t_{\rm first}(f \propto t^2)$ (days)[a,b]	Reduced χ^2	$t_{\rm first}(f \propto t^n)$ (days)	n	Reduced χ^2
U	12	−17.37(01)	31.61	−19.37(21)	3.42(14)	4.35
B	13	−17.46(01)	19.18	−18.50(11)	2.76(08)	4.76
V	13	−17.82(02)	10.41	−18.24(10)	2.27(06)	9.26
R	13	−17.76(02)	6.98	−18.36(11)	2.39(07)	3.39
I	13	−17.66(02)	3.49	−18.12(14)	2.33(09)	2.26
			Multiband Fitting	*UBVRI* bands		
U	12	−17.59(01)	52.52	−18.18(29)	2.63(16)	10.65
B	12	−17.59(01)	28.52	−18.18(29)	2.56(12)	1.40
V	12	−17.59(01)	18.35	−18.18(29)	2.25(21)	1.50
R	12	−17.59(01)	15.01	−18.18(29)	2.29(34)	1.62
I	12	−17.59(01)	3.91	−18.18(29)	2.37(42)	2.29
Total reduced χ^2	60	−17.59(01)	21.91	−18.18(29)	⋯	3.21
			Multiband Fitting	*BVRI* bands		
B	12	−17.63(01)	38.75	−18.00(16)	2.43(09)	2.23
V	12	−17.63(01)	10.33	−18.00(16)	2.14(07)	1.01
R	12	−17.63(01)	9.12	−18.00(16)	2.17(11)	2.25
I	12	−17.63(01)	3.30	−18.00(16)	2.25(09)	2.24
Total reduced χ^2	48	−17.63(01)	14.30	−18.00(16)	⋯	1.78

Notes.
[a] Relative to the epoch of B-band maximum (JD = 2,455,814.98).
[b] Uncertainties, in units of 0.01, are 1σ.

the rising light curve of SN 2011fe differs from the t^2 evolution, especially in the U and B bands, where a faster rise (and hence a larger index, $n > 2.7$) is needed for a better fit, or the first-light times obtained in the UB bands are smaller than those in the VRI bands.

In principle, the first-light time (or explosion time) derived from different bands should have the same value, but this is not the case either for the t^2 fit or for the t^n fit to the data. We thus refit the multiband light curves of SN 2011fe simultaneously by forcing all the light curves to have the same $t_{\rm first}$. For the t^2 model, the combined fit gives $t_{\rm first} = -17.59 \pm 0.01$ (MJD $55{,}796.89 \pm 0.01$) by using the data at $t < -10$ days, while for the t^n model, the combined fit gives $t_{\rm first} = -18.18 \pm 0.29$ (MJD $55{,}796.30 \pm 0.29$), with n ranging from 2.25 (in the V band) to 2.63 (in the U band). We noticed that the χ^2 for the U-band data is much larger than that for other bands, so we refit the data by restricting only to the *BVRI* bands. We obtained $t_{\rm first} = -17.64 \pm 0.01$ (MJD $55{,}796.84 \pm 0.01$) for the t^2 model and $t_{\rm first} = -18.00 \pm 0.16$ (MJD $55{,}796.48 \pm 0.16$) for the t^n model, with n ranging from 2.14 (in the V band) to 2.43 (in the B band). The detailed results are shown in the right panels of Figure 16 and reported in Table 6. Again, one can see that the indices $n(U)$ and $n(B)$ are larger than the values obtained for the *VRI* bands (which are close to 2).

For comparison, we overplot the *UBVRI*-band fluxes of some SNe Ia with very early-time observations in the right panel of Figure 16, such as SN 2009ig (Foley et al. 2012), SN 2012cg (Marion et al. 2015), SN 2013dy (Zheng et al. 2013), and ASASSN-14lp (Shappee et al. 2015), with the peak flux of each SN normalized to that of SN 2011fe. One can see that all of these comparison SNe Ia clearly exhibit slower rises at early times, while they also have smaller $\Delta m_{15}(B)$ than SN 2011fe. However, comparison of the $\Delta m_{15}(B)$-corrected rise times between different SNe Ia may not make much sense, given that the duration of the very early light curve does not correlate with the light-curve shape and the n index shows a large range for the t^n evolution of different SNe Ia (Firth et al. 2015). Moreover, SN 2009ig and ASASSN-14lp have large photospheric velocities around the time of maximum light (e.g., $v_{\rm Si} \approx 13{,}000\ {\rm km\ s^{-1}}$), and these rapidly expanding SNe Ia usually have shorter rise times compared to their normal counterparts (Zhang et al. 2010; Ganeshalingam et al. 2011); also, the early light curve of SN 2012cg may be affected by interaction with the companion star (Marion et al. 2015). On the other hand, since SN 2011by is considered to be a "twin" of SN 2011fe (Graham et al. 2015a), it is interesting to include it in Figure 16 even though its light curve does not cover the very early phases. As can be seen, SN 2011by is brighter than SN 2011fe at $t \approx -12.5$ days, especially in the B band (see also the residual plot of Figure 16). This likely suggests that SN 2011fe may have an intrinsically faster rise rate compared to SN 2011by, since these two SNe Ia have very similar $\Delta m_{15}(B)$ values, consistent with the argument that the gamma-ray photons from the radioactive decay are less trapped in SN 2011fe and reach its photosphere more easily relative to SN 2011by.

5.2. The Late-time Light Curves

The late-time light curves can be used to constrain the underlying physics for the lingering light, such as radioactive decay of long-lived isotopes (Milne et al. 1999, 2001), interaction with CSM, and light echoes (Li et al. 2002).

Very late-time observations are rare for SNe Ia. SN 2011fe provides us a good opportunity to study the late-time evolution of a normal SN Ia. Based on late-time mid-IR photometry and nebular spectra, McClelland et al. (2013) found that the singly ionized iron-peak elements faded at close to the ^{56}Co radioactive decay rate, while doubly ionized cobalt faded at a rate more than twice the ^{56}Co radioactive decay rate owing to recombination. In Section 3.1, we noticed that SN 2011fe showed an apparently faster decay rate in the *U* band compared to SN 2003du and SN 2003hv, which can also be interpreted as an opacity effect. Alternatively, the SN has a relatively clean environment, and the expanding ejecta do not interact with the CSM expelled from the progenitor.

To obtain better knowledge of the late-time emission, we use our optical light curves to construct the late-time bolometric light curve by assuming that the contribution of NIR-band emission is about 5% and the contribution of the UV-band emission is negligible after $t \approx +80$ days, as adopted in the analysis of SN 2003hv (Leloudas et al. 2009). We fit the bolometric light curve during the phase from $t = +80$ to $+250$ days using a simple model, $L = 1.3 \times M_{\rm Ni}^{-t/111.3}(1 - 0.966e^{-\tau})$. where L is the bolometric luminosity, $M_{\rm Ni}$ is the ^{56}Ni mass, $\tau = (t_1/t)^2$ is the optical depth, and t_1 is the time when the optical depth to the gamma rays becomes unity (e.g., Sollerman et al. 1998; Leloudas et al. 2009), as shown in the subset of Figure 7. We derive $t_1 = 34.5$ days and $M_{\rm Ni} = 0.32\,M_{\odot}$, which is lower than the ^{56}Ni mass obtained with the peak luminosity ($\sim 0.57\,M_{\odot}$). This large difference is perhaps caused by a substantial fraction of the flux being emitted beyond the UV through IR bands, or by positron escape and/or an IR catastrophe (IRC) that occurs in the ejecta at very late phases as suggested by Leloudas et al. (2009). The effect of an IRC in SN 2011fe has been confirmed by Fransson & Jerkstrand (2015) using the spectrum taken at ~1000 days. In comparison, Mazzali et al. (2015) derived the ^{56}Ni mass as $\sim 0.47 \pm 0.05\,M_{\odot}$ and the stable iron mass as $\sim 0.23 \pm 0.03\,M_{\odot}$ for SN 2011fe, based on modeling of the nebular spectra.

5.3. *Progenitor Properties of SN 2011fe*

Although the progenitor properties of SN 2011fe have been thoroughly studied in the literature, our extensive observations presented here still enable us to put useful constraints from a different perspective because the UV- or *U*-band emission may be sensitive to metallicity (e.g., Höflich et al. 1998; Lentz et al. 2000; Sauer et al. 2008). The stronger UV emission and fast-rising evolution seen in SN 2011fe indicate that the ejecta from the exploding WD may have smaller opacity compared to that of some normal SNe Ia (especially its "twin" SN 2011by; Foley & Kirshner 2013; Graham et al. 2015a). This is further supported by the fast decay of the *U*-band light curve seen at late times, which is likely to be the result of less energy trapping in the ejecta.

The unusual behavior of SN 2011fe shown in the UV and *U* bands can be reasonably explained if the progenitor star of SN 2011fe has a lower metallicity than normal. This conclusion is supported by some other evidence and analysis. Assuming that SN 2011fe is in the plane of the galactic disk of M101, and adopting a gas-phase oxygen abundance gradient of Bresolin (2007), Stoll et al. (2011) estimated that the oxygen abundance inferred at the site of SN 2011fe is $12 + \log({\rm O/H}) = 8.45 \pm 0.05$, which is apparently lower than the corresponding solar value. Analysis of the observed UV spectra of SN 2011fe and SN 2011by also suggests that the former has a subsolar progenitor metallicity (Foley & Kirshner 2013; however, see Graham et al. 2015a). The effect of metallicity variations in the progenitor on the synthetic spectra was recently studied by Baron et al. (2015), who found that a delayed-detonation model with a progenitor metallicity of $Z_{\odot}/20$ can fit the spectra of SN 2011fe better than a metallicity of $Z_{\odot}$.

The sign of a metallicity effect on the explosions of SNe Ia has been controversial (e.g., Timmes et al. 2003; Brown et al. 2015; Miles et al. 2015). However, the study of SN 2011fe seems to indicate that the emission of SNe Ia at shorter wavelengths could be enhanced with decreasing metallicity of the progenitors.

6. CONCLUSIONS

In this paper, we present extensive observations of optical photometry and spectroscopy of SN 2011fe. Fitting to the early-time multiband light curves of SN 2011fe with a power-law model ($f \propto (t - t_0)^n$) yields a rise time of 18.00 days, which is consistent with previous results. The best-fit index n is close to 2 in the *VRI* bands, but larger than 2 in the *UB* bands, suggestive of a faster rise at shorter wavelengths. SN 2011fe is also found to have stronger UV emission and reach its UV peak a few days earlier than the comparison SNe Ia such as SN 2005cf and the "twin" SN 2011by. Moreover, the *U*-band light curve shows a remarkably faster decay rate at late times compared to other normal SNe Ia.

The early-time spectra of SN 2011fe resemble those of other normal SNe Ia in many respects, including the presence of C II absorption and the HVFs from the Ca II NIR triplet. Note that no significant HVF is detected in Si II λ6355 absorption even in the extremely early-time spectrum. The HVFs are relatively weak in SN 2011fe compared to other normal SNe Ia with similar $\Delta m_{15}(B)$. On the other hand, the O-HVFs are very prominent in SN 2011fe, strong relative to normal SNe Ia. Moreover, a second HVF at higher velocities (~22,000 km s^{-1}) can be also identified in some of our early-time spectra. The presence of this high-velocity oxygen indicates that the burning of the C+O WD is not complete for SN 2011fe and the corresponding photosphere has a lower temperature. This is consistent with the relatively weak Si-HVF in SN 2011fe, given an ionization (or temperature) effect and/or an abundance enhancement scenario for the formation of HVFs.

These results suggest congruously that the expanding ejecta of the progenitor of SN 2011fe have a lower opacity and hence a lower metallicity. This conclusion is consistent with a recent result obtained through modeling of early-time spectra of SN 2011fe (Baron et al. 2015).

We are grateful to the staffs of the various telescopes and observatories with which data were obtained (Tsinghua-NAOC Telescope, Lijiang Telescope, Xinglong 2.16 m Telescope, KAIT, Yunnan Astronomical Observatory, Lick Observatory). Financial support for this work has been provided by the National Science Foundation of China (NSFC grants 11178003, 11325313, 11403096, 11203034), the Major State Basic Research Development Program (2013CB834903), and the Key Research Program of the Chinese Academy of Sciences (Grant No. KJZD-EW-M06). This work was partially supported by the Open Project Program of the Key Laboratory of Optical Astronomy, National Astronomical Observatories, Chinese Academy of Sciences. A.V.F.'s group at UC Berkeley is grateful for financial assistance from NSF grant AST-1211916, the TABASGO Foundation, and the Christopher R. Redlich Fund. Research at Lick Observatory is partially supported by a generous gift from Google. KAIT and its ongoing operation were made possible by donations from Sun Microsystems, Inc., the Hewlett-Packard Company, AutoScope Corporation, Lick Observatory, the NSF, the University of California, the Sylvia & Jim Katzman Foundation, and the TABASGO Foundation. Funding for the LJT has been provided by the Chinese Academy of Sciences and the People's Government of Yunnan Province.

REFERENCES

Arnett, W. D. 1982, ApJ, 253, 785
Baron, E., Höflich, P., Friesen, B., et al. 2015, MNRAS, 454, 2549
Benetti, S., Cappellaro, E., Mazzali, P. A., et al. 2005, ApJ, 623, 1011
Bloom, J. S., Kasen, D., Shen, K. J., et al. 2012, ApJL, 744, L17
Bresolin, F. 2007, ApJ, 656, 186
Brown, P. J., Baron, E., Milne, P., Roming, P. W. A., & Wang, L. 2015, ApJ, 809, 37
Brown, P. J., Dawson, K. S., de Pasquale, M., et al. 2012, ApJ, 753, 22
Chomiuk, L., Soderberg, A. M., Moe, M., et al. 2012, ApJ, 750, 164
Conley, A., Howell, D. A., Howes, A., et al. 2006, AJ, 132, 1707
Cousins, A. W. J. 1981, SAAOC, 6, 4
Fan, Y.-F., Bai, J.-M., Zhang, J.-J., et al. 2015, RAA, 15, 918
Filippenko, A. V., Li, W. D., Treffers, R. R., & Modjaz, M. 2001, in ASP Conf. Ser. 246, Small-Telescope Astronomy on Global Scales, ed. W. P. Chen, C. Lemme, & B. Paczyński (San Francisco, CA: ASP), 121
Firth, R. E., Sullivan, M., Gal-Yam, A., et al. 2015, MNRAS, 446, 3895
Foley, R. J., Challis, P. J., Filippenko, A. V., et al. 2012, ApJ, 744, 38
Foley, R. J., & Kirshner, R. P. 2013, ApJL, 769, L1
Fransson, C., & Jerkstrand, A. 2015, ApJL, 814, L2
Ganeshalingam, M., Li, W., & Filippenko, A. V. 2011, MNRAS, 416, 2607
Graham, M. L., Foley, R. J., Zheng, W., et al. 2015a, MNRAS, 446, 2073
Graham, M. L., Nugent, P. E., Sullivan, M., et al. 2015b, MNRAS, 454, 1948
Höflich, P., Wheeler, J. C., & Thielemann, F. K. 1998, ApJ, 495, 617
Horesh, A., Kulkarni, S. R., Fox, D. B., et al. 2012, ApJ, 746, 21
Huang, F., Li, J.-Z., Wang, X.-F., et al. 2012, RAA, 12, 1585
Iben, I., Jr., & Tutukov, A. V. 1984, ApJS, 54, 335
Johnson, H. L., Mitchell, R. I., Iriarte, B., & Wisniewski, W. Z. 1966, CoLPL, 4, 99
Kasen, D. 2010, ApJ, 708, 1025
Leloudas, G., Stritzinger, M. D., Sollerman, J., et al. 2009, A&A, 505, 265
Lentz, E. J., Baron, E., Branch, D., Hauschildt, P. H., & Nugent, P. E. 2000, ApJ, 530, 966
Li, W., Bloom, J. S., Podsiadlowski, P., et al. 2011, Natur, 480, 348
Li, W., Filippenko, A. V., Van Dyk, S. D., et al. 2002, PASP, 114, 403
Lundqvist, P., Nyholm, A., Taddia, F., et al. 2015, A&A, 577, A39
Marion, G. H., Brown, P. J., Vinkó, J., et al. 2015, ApJ, in press (arXiv:1507.07261)
Matheson, T., Joyce, R. R., Allen, L. E., et al. 2012, ApJ, 754, 19
Mazzali, P. A., Sullivan, M., Filippenko, A. V., et al. 2015, MNRAS, 450, 2631
McClelland, C. M., Garnavich, P. M., Milne, P. A., Shappee, B. J., & Pogge, R. W. 2013, ApJ, 767, 119
Miles, B. J., van Rossum, D. R., Townsley, D. M., et al. 2015, ApJ, submitted (arXiv:1508.05961)
Milne, P. A., The, L.-S., & Leising, M. D. 1999, ApJS, 124, 503
Milne, P. A., The, L.-S., & Leising, M. D. 2001, ApJ, 559, 1019
Munari, U., Henden, A., Belligoli, R., et al. 2013, NewA, 20, 30
Nugent, P. E., Sullivan, M., Cenko, S. B., et al. 2011, Natur, 480, 344
Parrent, J. T., Howell, D. A., Friesen, B., et al. 2012, ApJL, 752, L26
Patat, F., Cordiner, M. A., Cox, N. L. J., et al. 2013, A&A, 549, A62
Pereira, R., Thomas, R. C., Aldering, G., et al. 2013, A&A, 554, A27
Phillips, M. M., Lira, P., Suntzeff, N. B., et al. 1999, AJ, 118, 1766
Piro, A. L., Chang, P., & Weinberg, N. N. 2010, ApJ, 708, 598
Piro, A. L., & Nakar, E. 2013, ApJ, 769, 67
Piro, A. L., & Nakar, E. 2014, ApJ, 784, 85
Richmond, M. W., & Smith, H. A. 2012, JAVSO, 40, 872
Riess, A. G., Filippenko, A. V., Li, W., et al. 1999, AJ, 118, 2675
Sauer, D. N., Mazzali, P. A., Blondin, S., et al. 2008, MNRAS, 391, 1605
Schlafly, E. F., & Finkbeiner, D. P. 2011, ApJ, 737, 103
Shappee, B. J., Piro, A. L., Holoien, T. W.-S., et al. 2015, ApJ, submitted (arXiv:1507.04257)
Shappee, B. J., & Stanek, K. Z. 2011, ApJ, 733, 124
Shappee, B. J., Stanek, K. Z., Pogge, R. W., & Garnavich, P. M. 2013, ApJL, 762, L5
Silverman, J. M., Vinkó, J., Marion, G. H., et al. 2015, MNRAS, 451, 1973 (S15)
Smith, P. S., Williams, G. G., Smith, N., et al. 2011, ApJL, submitted (arXiv:1111.6626)
Sollerman, J., Leibundgut, B., & Spyromilio, J. 1998, A&A, 337, 207
Stanishev, V., Goobar, A., Benetti, S., et al. 2007, A&A, 469, 645
Stoll, R., Shappee, B., & Stanek, K. Z. 2011, ATel, 3588, 1
Stritzinger, M., & Leibundgut, B. 2005, A&A, 431, 423
Tammann, G. A., & Reindl, B. 2011, ApJL, submitted (arXiv:1112.0439)
Taubenberger, S., Elias-Rosa, N., Kerzendorf, W. E., et al. 2015, MNRAS, 448, L48
Thomas, R. C., Nugent, P. E., & Meza, J. C. 2011, PASP, 123, 237
Timmes, F. X., Brown, E. F., & Truran, J. W. 2003, ApJL, 590, L83
Wang, X., Filippenko, A. V., Ganeshalingam, M., et al. 2009a, ApJL, 699, L139
Wang, X., Li, W., Filippenko, A. V., et al. 2008, ApJ, 675, 626
Wang, X., Li, W., Filippenko, A. V., et al. 2009b, ApJ, 697, 380
Wang, X., Wang, L., Filippenko, A. V., Zhang, T., & Zhao, X. 2013, Sci, 340, 170
Whelan, J., & Iben, I., Jr. 1973, ApJ, 186, 1007
Zhang, T., Wang, X., Li, W., et al. 2010, PASP, 122, 1
Zhao, X., Wang, X., Maeda, K., et al. 2015, ApJS, 220, 20 (Z15)
Zheng, W., Silverman, J. M., Filippenko, A. V., et al. 2013, ApJL, 778, L15

THE ASTROPHYSICAL JOURNAL, 826:211 (20pp), 2016 August 1
doi:10.3847/0004-637X/826/2/211

THE OXYGEN FEATURES IN TYPE Ia SUPERNOVAE AND IMPLICATIONS FOR THE NATURE OF THERMONUCLEAR EXPLOSIONS

XULIN ZHAO[1,2,3], KEIICHI MAEDA[2,4], XIAOFENG WANG[1], LIFAN WANG[5], HANNA SAI[1], JUJIA ZHANG[6,7], TIANMENG ZHANG[8], FANG HUANG[1], AND LIMING RUI[1]
[1] Physics Department and Tsinghua Center for Astrophysics, Tsinghua University, Beijing, 100084, China;
wang_xf@mail.tsinghua.edu.cn, zhaoxl11@mails.tsinghua.edu.cn
[2] Department of Astronomy, Kyoto University, Kitashirakawa-Oiwake-cho, Sakyo-ku, Kyoto 606-8502, Japan; keiichi.maeda@kusastro.kyoto-u.ac.jp
[3] School of Science, Tianjin University of Technology, Tianjin, 300384, China
[4] Kavli Institute for the Physics and Mathematics of the Universe (WPI), University of Tokyo, 5-1-5 Kashiwanoha, Kashiwa, Chiba 277-8583, Japan
[5] Mitchell Institute for Fundamental Physics and Astronomy, Texas A&M University, College Station, TX 77843, USA
[6] Yunnan Observatories, Chinese Academy of Sciences, Kunming, 650216, China
[7] Key Laboratory for the Structure and Evolution of Celestial Objects, Chinese Academy of Sciences, Kunming 650216, China
[8] National Astronomical Observatory of China, Chinese Academy of Sciences, Beijing, 100012, China
Received 2016 January 27; revised 2016 May 11; accepted 2016 May 23; published 2016 August 1

ABSTRACT

The absorption feature O I λ7773 is an important spectral indicator for type Ia supernovae (SNe Ia) that can be used to trace the unburned material in outer layers of the exploding white dwarf (WD). In this work, we use a large sample of SNe Ia to examine this absorption at early phases (i.e., -13 day $\lesssim t \lesssim -7$ day) and make comparisons with the absorption features of Si II λ6355 and the Ca II near-infrared triplet. We show that for a subgroup of spectroscopically normal SNe with normal photospheric velocities (i.e., $v_{\rm si} \lesssim 12{,}500$ km s^{-1} at optical maximum), the line strength of the high velocity feature (HVF) of O I is inversely correlated with that of Si II (or Ca II), and this feature also shows a negative correlation with the luminosity of SNe Ia. This finding, together with other features we find for the O I HVF, reveal that for this subgroup of SNe Ia, explosive oxygen burning occurs in the outermost layer of the SN. Differences in the oxygen burning could lead to the observed diversity, which is in remarkable agreement with the popular delayed-detonation model of Chandrasekhar mass WDs.

Key words: methods: data analysis – supernovae: general – techniques: spectroscopic

1. INTRODUCTION

Type Ia supernovae (SNe Ia) are important in cosmology and astrophysics, not only for the key role they played in the discovery of the accelerating universe (Riess et al. 1998; Perlmutter et al. 1999), but also for their contribution to the production of heavy elements in the universe. However, the nature of their progenitor systems is still controversial (e.g., Maoz et al. 2014, and references therein). It is widely accepted that SNe Ia are the result of a thermonuclear explosion of carbon/oxygen (C/O) white dwarfs (WDs), but there are two major channels proposed so far that could lead to such an explosion. One is the explosion of a WD which accretes hydrogen or helium from its non-degenerate companion (the single degenerate scenario; Whelan & Iben 1973; Nomoto 1982; Nomoto et al. 1997), which is supported by the detection of circumstellar material (CSM) around some SNe Ia (Hamuy et al. 2003; Aldering et al. 2006; Patat et al. 2007; Sternberg et al. 2011; Dilday et al. 2012; Maguire et al. 2013; Silverman et al. 2013). The other is the merger of two WDs (the double degenerate scenario; Iben & Tutukov 1984; Webbink 1984), which has recently received more attention due to the observational findings that no companion signature is found for some SNe Ia, e.g., the nearby object SN 2011fe and some SN remnants such as SN 1006 and SNR 0509-67.5 in the LMC, down to luminosities much fainter than the Sun (Li et al. 2011; Bloom et al. 2012; Brown et al. 2012; Hernández et al. 2012; Schaefer & Pagnotta 2012).

There are also differences in the spectroscopic and photometric properties of SNe Ia, and researchers have considered whether all (or spectroscopically normal) SNe Ia originate in a single evolutionary path or whether there are multiple populations. For example, there is the so-called high velocity (HV) subclass of SNe Ia (Wang et al. 2008; Wang et al. 2009a), with redder peak $B-V$ colors and slower late-time decline rates in bluer bands relative to the normal-velocity (Normal) subclass[9], and it is interesting to explore whether these represent different populations. The observed differences between the HV and Normal SNe Ia could at least partly be attributed to the geometric effect of an asymmetric explosion (Maeda et al. 2010; Maund et al. 2010). However, the observed differences have also been found to be linked to birthplace environments, to some extent (Wang et al. 2013), suggesting that SNe Ia may arise from multiple classes of binary evolution. Taken together, this could mean that there are two populations in the HV subclass, one of which is related to Normal SNe Ia while the other is not.

The other long-standing problem is the physical process of SN Ia explosions (Hillebrandt & Niemeyer 2000). Theoretically, the thermonuclear reaction disrupting the star may propagate at a range of speeds from subsonic deflagration to supersonic detonation (Nomoto et al. 1984; Khokhlov 1991; Fink et al. 2010; Pakmor et al. 2012). The most popular scenario is the delayed-detonation model (Khokhlov 1991), which assumes that a strong detonation unbinds the whole progenitor WD, after a deflagration which produces stable Fe-peak elements near the center of the WD. Another popular model involves the double-detonation mechanism (Livne & Glasner 1990; Fink et al. 2007; Sim et al. 2012; Shen & Bildsten 2014). In this model, explosive He burning is induced

---

[9] This spectroscopic classification is based on the photospheric velocity measured from Si II λ6355 lines in the near-maximum-light spectra (Wang et al. 2009a).

on the WD surface by compressional heating if the accreted He amount is sufficiently large, and this creates a shock wave penetrating into the WD core. Once the shock wave converges near the center, a powerful detonation can be triggered and will lead to an explosion unbinding the whole WD. Existing observational diagnostics offer some clues for the explosion models, but this topic is still controversial.

The high-velocity absorption features (HVFs) can provide evidence of the burning processes in the outer layers of the exploding WD, although their origins are still debated. The HVFs are absorption components that are likely formed in regions lying above the photosphere (Hatano et al. 1999; Mazzali et al. 2005b), with velocities >16,000 km s^{-1}. The HVFs of the Ca II near-infrared (NIR) triplet and Si II 6355 Å in SNe Ia have been systematically examined using both early-phase and near-maximum-light spectra (Maguire et al. 2012; Childress et al. 2014; Silverman et al. 2015; Zhao et al. 2015). These studies indicate that the abundance distributions of Si and Ca are strongly related, likely as a result of the same burning process being responsible for creating Si and Ca. Since Si and Ca are basically produced in the same burning layer, their relative strengths are not expected to be sensitive to the typical burning process they experienced. It is thus interesting to make comparisons with absorption features created by elements whose abundance patterns are different from Si and Ca in different burning layers. C II λ6580 could be an important indicator of unburned fuel in the progenitor and observations of this feature have been discussed in many studies (Parrent et al. 2011; Thomas et al. 2011; Blondin et al. 2012; Folatelli et al. 2012; Silverman & Filippenko 2012; Maguire et al. 2014; Hsiao et al. 2015). However, C II λ6580 absorption is usually very weak and difficult to be quantified in terms of line strength and velocity distribution. The O I λ7773 line, in contrast, is relatively strong but has not been explored so far. Thus, in this paper, we propose using this feature as a tracer of unburned material, although some oxygen is also produced via carbon burning.

The presence of HVFs in O I λ7773 absorption has only been reported in the earliest spectra of SN 2011fe in M101, where it was observed to disappear rapidly (Nugent et al. 2011). Detection of such an O-HVF is critically important, since Si and Ca are produced from O via oxygen burning, and the comparison of the HVFs of O and those of Si and Ca can potentially be used to confirm their associations. In the Si burning layer oxygen is fully consumed; in the O burning layer O, Si, and Ca can have large abundances; in the C burning layer oxygen is abundant, but Si and Ca are under-abundant; and finally, in the unburned layer the ratio of O to Si or Ca is large. Thus, we may obtain information about the typical burning process encountered by the layer producing the HVFs, and hence the still-unclarified origin of the outermost materials in SN Ia.

This paper is organized as follows. In Section 2, our data samples and methods for measuring the spectral parameters are introduced. In Section 3, correlations between the spectroscopic parameters of oxygen (O I λ7773) and those of other elements (Si II λ6355, Ca II NIR triplet, and C II λ6580) are investigated. Correlations between the spectroscopic features of O I λ7773, Si II λ6355, the Ca II NIR triplet, and luminosity indicator Δm_{15}(B) are also examined and analyzed in this section. The origins of HVFs and the constraints on explosion models are discussed in Section 4. A conclusion is given in Section 5.

2. DATA SET AND METHODS OF MEASUREMENT

2.1. Sample

Since the HVFs of SNe Ia are only prominent in their early spectra, we choose a sample with spectroscopic observations at $t \lesssim -7$ day from the B-band maximum light. Our sample is taken from the published spectral data bases of the CfA Supernova Program (Matheson et al. 2008; Blondin et al. 2012), the Berkeley Supernova Program (Silverman et al. 2012a), and the Carnegie Supernova Project (CSP: Folatelli et al. 2013), and the unpublished data set from the Tsinghua Supernova Program.[10] The telluric absorption features were removed from almost all of the spectral samples above using the standard-star spectra obtained with the same slit used for the SN observations. However, this procedure often leaves residuals from the strongest telluric bands near 7620 Å. With the multi-Gaussian fit addressed in the next subsection, we examine the blending of the residual telluric absorption with the O I λ7773 absorption in the spectra of our SN Ia sample. The spectra showing larger degrees of blending between these two absorptions (see Section 2.2) are excluded from our analysis. Moreover, the near-maximum-light Si II λ6355 velocity is also required for further classification of our sample. This leads to a total of 143 early-time spectra (with $t \lesssim -7$ day from the B-band maximum light) that cover the wavelength region of O I λ7773 absorption. These spectra belong to 62 SNe Ia, including 55 spectroscopically normal SNe Ia, two 1991T-like SNe (Filippenko et al. 1992; Phillips et al. 1992), and five 1999aa-like SNe Ia (Li et al. 2001) (hereafter these two subclasses are abbreviated to 91T/99aa-like SNe Ia). The spectroscopically normal objects can be further divided into 42 Normal SNe Ia and 13 HV ones.

The above sample of SNe Ia were largely included in our previous study (Zhao et al. 2015), where their photometric and host-galaxy parameters (i.e., Δm_{15}(B), $B_{\max} - V_{\max}$, spectroscopic subclassification, host-galaxy type, K-band magnitude of the host galaxy, etc.) can be found. The sources of the light curves are from the Harvard CfA Supernova Group (Hicken et al. 2009, 2012), the CSP (Contreras et al. 2010; Stritzinger et al. 2011), the Lick Observatory Supernova Search (Ganeshalingam et al. 2010), and our own database.

2.2. Measurement Procedure

The measurement procedure of O I absorption is similar to that applied to measuring the Si II 6355/5972 and Ca II NIR triplet absorptions (Zhao et al. 2015), but with more Gaussian components being used to fit more absorptions. The absorptions identified around O I λ7773 include three O I components (two HVFs and one photospheric component), three residual telluric components (i.e., at λs 7186, 7606, 7630 Å), and a possible Mg II λ7890 component (with a velocity at 10,000 km s^{-1} ∼ 14,000 km s^{-1}). These absorption components can be represented using the following multi-component Gaussian function:

$$f(\lambda) = \sum_{i=1}^{6} A_i \exp\left(-\frac{(\lambda_i - \lambda_i^0)^2}{2\sigma_i^2}\right) \quad (1)$$

---

[10] This data set contains nearly 1000 spectra for over 200 SNe (L. Rui et al. 2016, in preparation), obtained with the Lijiang 2.4 m telescope (+YFOSC) of Yunnan Astronomical Observatories and the Xinglong 2.16 m telescope (+BFOSC) of the National Astronomical Observatories of China.

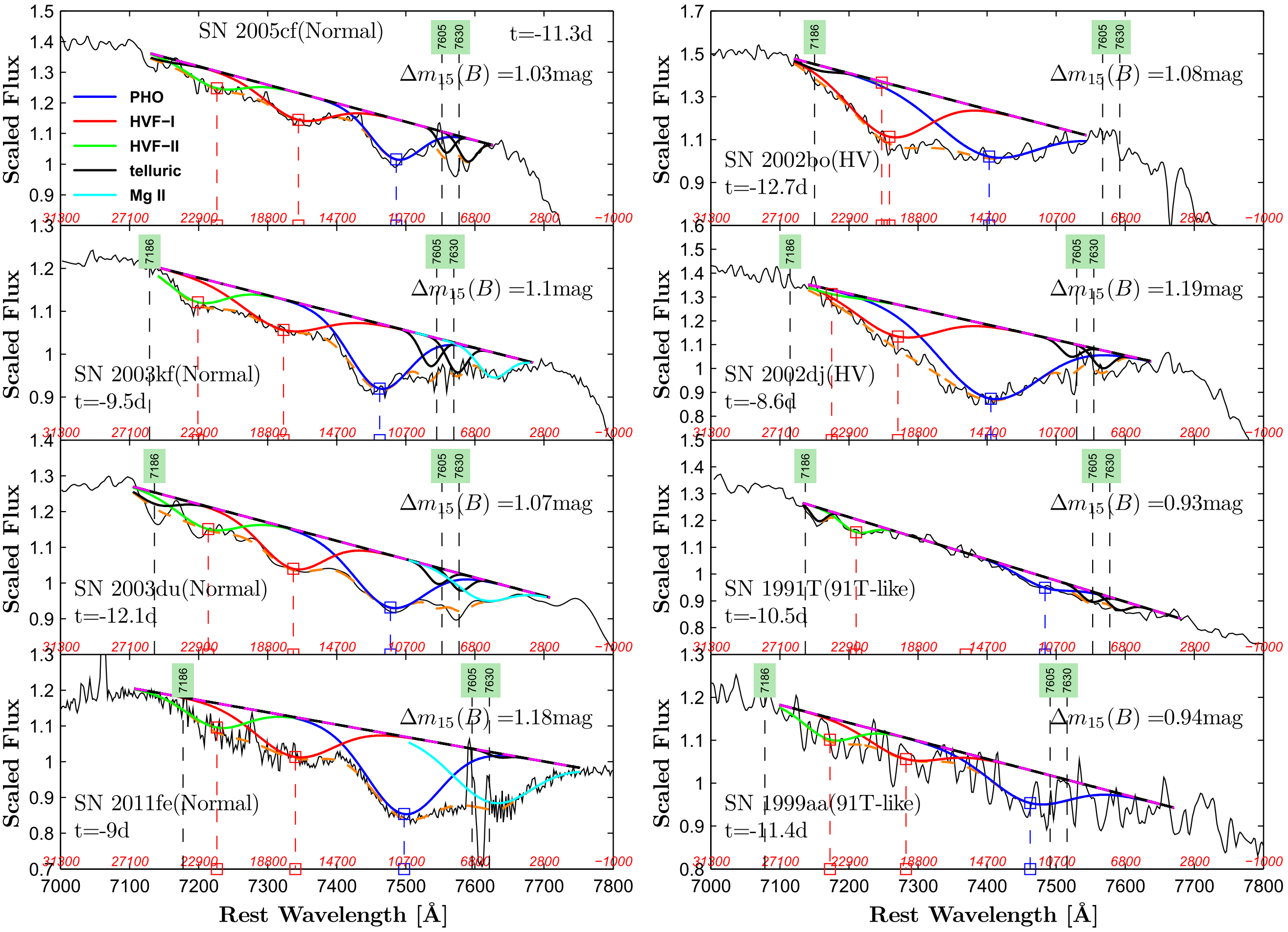

Figure 1. Absorption features of blueshifted O i λ7773, centered near 7300–7500 Å in the optical spectrum, are shown for some representative SNe Ia. The SN name and the phase of the spectrum are shown in each panel. The left panels show the Normal SNe Ia in order of increasing strength (from top to bottom) for O i λ7773 absorption, while the right panels show the HV and 91T/99aa-like SNe Ia. A multi-Gaussian fit is applied to determine different absorption components, with the blue curve representing the photospheric component, the red curve representing the main HVF (HVF-I), and the green curve representing the the additional HVF at higher velocities (HVF-II). The orange curve represents the combined fits. The vertical dashed lines mark the positions of the absorption minima of the photospheric component and the two HVF components. The black dashed lines mark the positions of telluric absorptions (corrected for the redshifts of the SNe) at 7186, 7605, and 7630 Å. The number in brackets represents the B-band magnitude decline rate over the first 15 days after maximum light (see the text for references).

where subscripts $i = 1$–6 denote the photospheric component of O i λ7773, the "main" HVF (hereafter HVF-I), the possible "second" HVF (hereafter HVF-II), and the telluric absorptions at 7168 Å, 7605 Å, and 7630 Å, respectively. In the above equation, A_i is the amplitude (i.e., the maximum absorption), σ_i is the dispersion (i.e., the standard deviation in a normal distribution), and λ_i^0 is the laboratory wavelength of a specific spectral line. Note that the positions of the telluric absorptions (and thereby the λ_i^0) are blueshifted relative to the rest-frame wavelengths because the spectrum was corrected for the redshift of the host galaxy.

In the fitting, the pseudo-continuum is defined as a straight line connecting the line wings on both sides of the absorption, and is determined through repeated visual inspections and careful manual adjustments in order to better counter the noise. As usual, the line strength of an absorption feature is quantified by the pseudo-equivalent width (pEW). From Equation (1), we have:

$$\mathrm{pEW} = \sum \sqrt{2\pi} A_i \sigma_i \tag{2}$$

where the summation is performed for appropriate components.

Before fitting, we smoothed the observed spectrum around the O i λ7773 absorption (i.e., covering the wavelength range from 7000 to 7800 Å) with a locally weighted scatter-plot smoothing method (Cleveland 1979) in order to reduce the effect of noise spikes on the fitting results, as the O i λ7773 line (especially the HVF) is usually weak in early-time spectra of SNe Ia. In our previous work (Zhao et al. 2015), the photospheric velocity of Si ii 5972 was used as an initial condition to constrain that of Si ii λ6355 because the HVF and photospheric component of the latter feature are often seriously blended. In determining the velocity of the O iλ7773 line, however, we did not use the velocity condition from the Si iiλ5972 line or the Ca ii NIR triplet lines because the HVF and photospheric component of the O iλ7773 line are distinctly separated (i.e., by about 6000 km s^{-1}) and their locations can be better determined in early-time spectra, as shown in Figure 1. The only exceptions are for several HV SNe Ia where their HVFs and photospheric components show more severe blending (i.e., SN 2002dj) and the velocity of Si ii λ5972

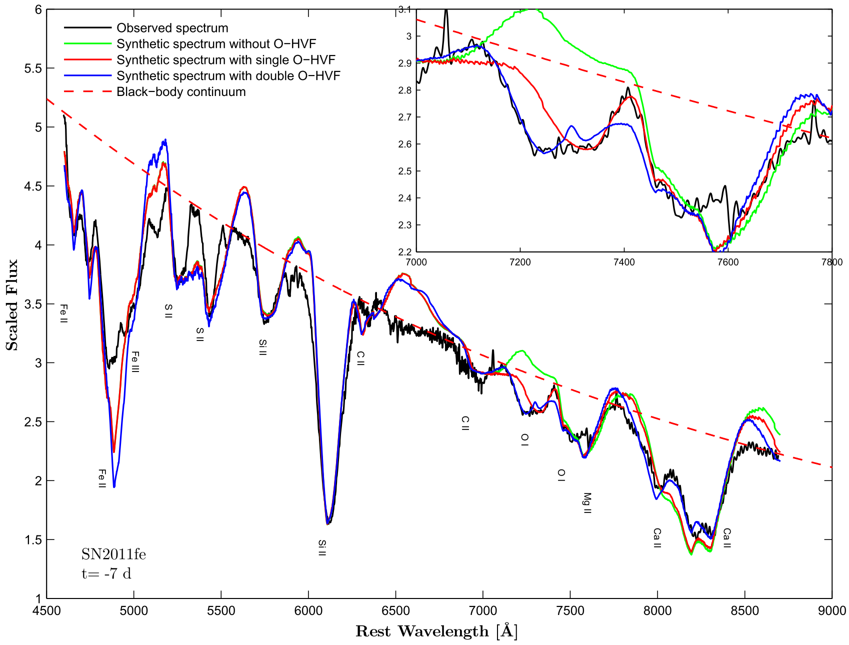

Figure 2. $t = -7$ day spectrum of SN 2011fe is compared with the synthetic spectrum from the SYNOW fit (Fisher et al. 1995). The green curve represents the synthetic spectrum without including the O-HVF; the red curve represents the fit with single O-HVF; the blue curve represents the fit with double O-HVFs at 18,000 km s^{-1} and 22,000 km s^{-1}, respectively.

is used to better locate the photospheric component of O I λ7773.

As most of the published spectral data do not have accompanying flux errors, we adopt the R-squared statistic to fit the parameters of absorption features such as the amplitude A_i, the dispersion σ_i, and velocity of absorption minima v_i^0. This fitting procedure is done through the Curve Fitting Toolbox in Matalab, where regression analysis can be conducted using the library of various models provided. Generally speaking, the fittings were well-performed and objectively determined by the absorption profiles, with the typical R-squared value being 0.97 for our sample. There are several reasons why the multi-Gaussian fitting applied in our analysis can be performed well without over/under-fitting. First, the blending between the HVF and photospheric component of O I λ7773 is much weaker than that seen in Si II λ6355 or the Ca II NIR triplet. Second, the contaminations from residual telluric absorptions are not very serious for our selected sample. For example, the blending ratio between the telluric absorption and the photospheric component of O I λ7773 is overall small for our sample (see discussion below). Third, in most cases, the possible Mg II λ7890 is not strong (with pEW $\lesssim$10 Å) and it is well separated from the photospheric component of O I λ7773.

Figure 1 shows the absorption features centering at O I λ7773 in the $t \approx -10$ day spectra of some representative SNe Ia. A demonstration of applying the multi-Gaussian fit is shown in the plot, where the photospheric absorption of O I λ7773 (at ~12,000 km s^{-1}) is accompanied by two additional absorptions on the blue side. These two absorptions can be attributed to the HVF-I and HVF-II of oxygen at velocities ~18,000 km s^{-1} and ~22,000 km s^{-1}, respectively, and this identification is secured by comparisons with the SYNOW fit as shown in Figure 2 (Fisher et al. 1995). We note that the different absorption components of the O I line are clearly separated from each other for Normal SNe Ia, while the O-HVF absorption tend to blend with the photospheric component in some HV SNe Ia such as SN 2002bo and SN 2002dj.

In this work, errors of spectral fit were retrieved from the Matlab function "confint." This function calculates the confidence bounds of the fitting results using $t\sqrt{((X^T X)^{-1} s^2)}$, where X is the Jacobian of fitted values, X^T is the transpose of X, s^2 is the mean squared error, and t is calculated using the inverse of Student's cumulative distribution function. The errors of A_i and σ_i are then used to compute that of the pEW using Equation (2), and the error of λ_i is converted to that of the line velocity. Since the fitting is applied to the smoothed spectrum, the noise of the original spectrum is further factored into the above errors by taking the residual standard deviation between the original and smoothed data roughly as a 1σ error in the spectral fitting. The typical error from spectral noise is about 3% for our sample and the corresponding error in pEW is about 1.0 Å. An additional velocity error is also considered for the fits to the smoothed spectra, which is taken to be the velocity shift from the Gaussian fits to the smoothed and original spectra[11] or the standard error of these two fits (i.e., 460 km s^{-1} for the photospheric component and 515 km s^{-1} for the HVF for 87 spectra) when the Matlab code fails to fit the original spectra.

Moreover, the photospheric component of O I λ7773 absorption might also be affected by the residual telluric absorptions. To obtain a quantitative estimation of this contamination, we introduce a parameter of blending ratio R_b, which measures the fraction that the line profile of the photospheric component of O I λ7773 is overlapped by the telluric absorption. This ratio is calculated as $\mathrm{pEW}^{\mathrm{telluric}}_{\mathrm{blending}}/\mathrm{pEW}^{\mathrm{O}}_{\mathrm{PHO}}$, where $\mathrm{pEW}^{\mathrm{telluric}}_{\mathrm{blending}}$

---

[11] The fit to the original spectra can be done for 87 spectra (out of 143) for our sample. The resultant velocities (and pEWs) are well consistent with those from fits to the smoothed spectra, with the adjusted R-squared coefficient for linear correlations being 0.91 for the photospheric component and 0.83 for the O-HVF component.

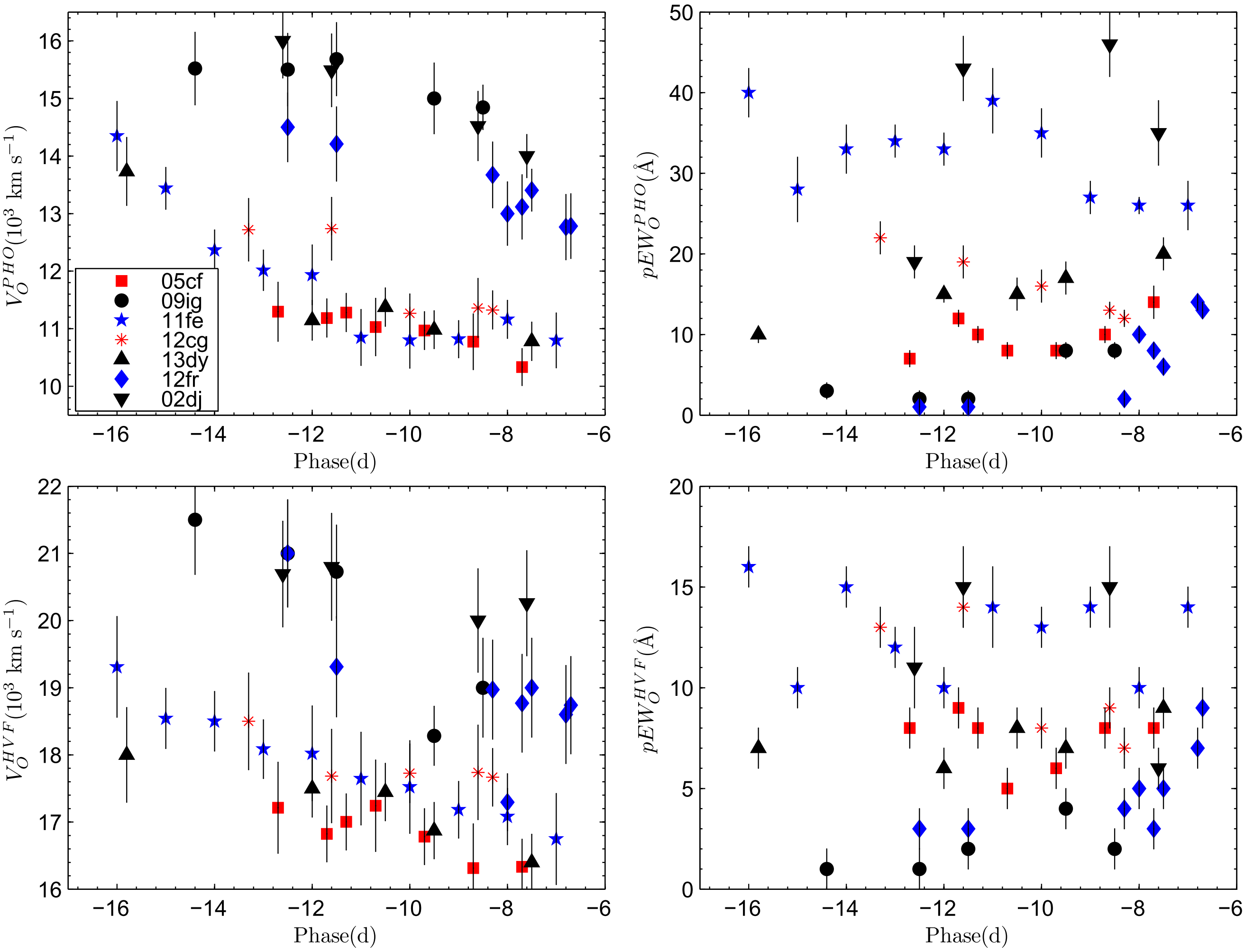

Figure 3. Left panels: evolution of the absorption strength of HVF and the photospheric component of O I λ7773 for some well-observed SNe Ia such as SNe 2002dj, 2005cf, 2009ig, 2011fe, 2012cg, 2012fr, and 2013dy. Right panels: similar evolutions but for the absorption strength of the HVF and photospheric component of the O I line.

represents the pEW of the region of telluric feature that is blended with the photospheric component of O I λ7773, and pEW $^{\text{O}}_{\text{PHO}}$ refers to the pEW of the O photospheric component. The results of this parameter measured for each spectrum of our sample are reported in the last column of Table 2. This blending ratio is, overall, small for our sample, with a mean value of only 3.7%, suggesting that the effect of residual telluric lines is negligible. In addition to the uncertainties listed above, the photospheric component of O I λ7773 could also suffer from blending of an unknown component that could be due to Mg II λ7890 or additional absorption feature of oxygen at lower velocities (i.e., $<$7000 km s^{-1}). However, these two effects are not considered in this work because they are difficult to quantify.

2.3. Temporal Evolution of O I λ7773

The temporal evolution of the line velocity and strength of the O I 7773 absorption is shown in Figure 3 for some well-observed SNe Ia, including SNe 2002dj, 2005cf, 2009ig, 2011fe, 2012fr, and 2013dy (see Table 1 for references). According to the spectroscopic classification as proposed by Wang et al. (2009a), SN 2002dj and SN 2009ig belong to the HV subclass of SNe Ia, while SN 2005cf, SN 2011fe, and SN 2013dy can be put into the Normal subclass. SN 2012cg shares some properties with the SN 1999aa-like subclass, which is characterized by shallow silicon in the spectra (Silverman et al. 2012b; Zhang et al. 2014; Marion et al. 2015). SN 2012fr may lie at the boundary of the above classifications (Zhang et al. 2014).

As shown in the left panels of Figure 3, the O I λ7773 absorptions of different SNe Ia show large differences in the velocity and the velocity evolution for both the HVF and photospheric component. For example, at $t \approx -10$ day, the photospheric velocity measured for our sample has a range from ~11,000 to ~15,000 km s^{-1}, and the velocity of the HVF-I ranges from ~17,000 to ~20,000 km s^{-1}. The O I lines (both the photospheric component and HVF-I) of HV SNe Ia have a velocity that is on average larger than that of the Normal SNe by 3000–4000 km s^{-1} at comparable phases, similar to the case seen in Si II λ6355 (Zhao et al. 2015). Restricting the data to the phases from $t \sim -13$ day to $t \sim -7$ day in the calculation of the velocity gradient, we find that the velocity gradients measured for the photospheric components of SN 2005cf, SN 2011fe, and SN 2013dy are -182, -186, and -100 km s^{-1}day^{-1}, respectively, while the corresponding values obtained for their HVFs are -183, -227, and -263 km s^{-1}day^{-1}. For SN 2002dj, SN 2009ig, SN

Table 1
Velocities and pEWs Near $t \sim -10$ day

SN		O I λ7773						Si II λ6355				Ca II NIR						
	t[a] (day)	V_P[b] (km s^{-1})	W_P[c] (Å)	V_H[d] (km s^{-1})	W_H[e] (Å)	V_S[f] (km s^{-1})	W_S[g] (Å)	V_P[h] (km s^{-1})	W_P[i] (Å)	V_H[j] (km s^{-1})	W_H[k] (Å)	V_P[l] (km s^{-1})	W_P[m] (Å)	V_H[n] (km s^{-1})	W_H[o] (Å)	v_0^{Sip} (km s^{-1})	$\Delta m_{15}(B)$[q] (mag)	Ref.[r]
1991M	−7.8	12501 (562)	40(4)	17000 (675)	27(2)	22969 (841)	3(1)	13384 (624)	118(10)	18000 (766)	1(1)	14672 (345)	129(16)	23788 (495)	96(6)	12511 (434)	1.51(10)	A; B;1
1991T*	−10.5	11362 (331)	4(1)	16000 (643)	1(1)	22539 (504)	2(1)	12500 (582)	17(2)	17000 (735)	1(1)	…	…	…	…	9509 (476)	0.93(05)	A;B;2
1994D	−9.5	12601 (542)	22(2)	17631 (697)	10(1)	21679 (822)	5(1)	12249 (578)	81(6)	18900 (788)	21(1)	12322 (322)	48(5)	23177 (491)	75(7)	11021 (330)	1.37(03)	A;B;3
1997bq	−11.8	13390 (302)	34(3)	18197 (412)	28(4)	22603 (491)	14(2)	16545 (722)	133(10)	21654 (878)	37(3)	15500 (605)	59(5)	24000 (863)	236(24)	13000 (650)	1.01(05)	A;4
1998dm	−10.9	11702 (338)	21(2)	17709 (429)	8(1)	22237 (501)	5(1)	11715 (356)	65(4)	18011 (516)	13(1)	12179 (319)	69(6)	22314 (475)	91(5)	11058 (553)	0.85(05)	A;B;4;5
1998ef	−8.9	11222 (509)	29(4)	16333 (664)	50(5)	21660 (831)	14(1)	14394 (634)	150(12)	18000 (748)	1(1)	11778 (314)	118(12)	21011 (457)	116(12)	13260 (384)	1.30(05)	A; B;4;5
1999aa⋆	−11.4	12216 (539)	11(1)	19535 (750)	6(1)	24103 (889)	4(1)	12457 (590)	40(4)	18869 (791)	1(1)	…	…	…	…	10484 (310)	0.94(01)	A;B;4;5
1999dk	−7.7	13531 (460)	32(2)	18664 (651)	22(4)	23000 (856)	1(1)	13818 (637)	116(9)	18214 (772)	18(2)	14104 (352)	108(9)	22725 (484)	99(5)	12500 (625)	1.15(04)	B;5
1999dq⋆	−9.6	12355 (531)	5(1)	18051 (699)	5(1)	23586 (866)	5(1)	11156 (552)	27(2)	18875 (798)	4(1)	…	…	…	…	10939 (314)	0.96(04)	A;4;5
1999ee	−9.4	13000 (383)	5(1)	18000 (706)	6(1)	23088 (509)	5(1)	10800 (544)	30(2)	17694 (490)	54(3)	…	…	…	…	10189 (332)	0.96(05)	A; B;6
2000dx+	−9.0	12501 (349)	18(1)	17715 (431)	11(1)	22738 (507)	7(1)	13793 (414)	121(6)	19504 (520)	27(3)	…	…	…	…	12500 (625)	…	B;
2000fa	−9.1	12011 (524)	20(2)	20342 (779)	10(1)	26000 (948)	1(1)	13391 (624)	85(7)	20756 (851)	18(2)	12863 (330)	47(5)	23994 (862)	129(13)	12106 (344)	0.91(04)	A;B;4;5
2001el+	−9.0	11701 (347)	12(1)	17847 (437)	8(1)	22760 (506)	4(1)	13428 (368)	84(3)	20088 (511)	39(5)	14003 (338)	68(7)	24553 (499)	223(21)	11715 (346)	1.16(03)	7;8
2002cr	−7.6	9371 (439)	39(3)	16117 (644)	16(2)	20926 (792)	2(1)	10929 (328)	106(8)	16128 (466)	3(1)	…	…	…	…	10017 (292)	1.23(04)	A; B;5
2002cs+	−9.0	14465 (383)	37(4)	19000 (736)	24(2)	23782 (523)	11(2)	14816 (446)	109(9)	19197 (516)	23(1)	13911 (346)	97(5)	21900 (799)	24(3)	13982 (700)	1.03(05)	A;B;4
2002dj	−8.6	14521 (602)	46(4)	20000 (771)	15(2)	24000 (887)	1(1)	15108 (677)	145(11)	21344 (868)	19(2)	14222 (351)	118(11)	23862 (500)	161(9)	13095 (655)	1.19(05)	A;B;5;9
2002er	−8.9	12962 (355)	35(4)	19454 (465)	15(2)	23047 (512)	20(2)	14390 (654)	103(8)	19900 (824)	1(1)	…	…	…	…	11895 (346)	1.23(03)	A;B;5
2003U	−8.8	13054 (555)	51(7)	17403 (738)	21(2)	24105 (891)	1(1)	12985 (388)	121(11)	18000 (766)	2(1)	…	…	…	…	11046 (342)	1.46(10)	A;B;9
2003cg	−8.4	11559 (342)	21(2)	16576 (420)	12(1)	21848 (494)	5(1)	11603 (350)	89(9)	18300 (765)	3(1)	12000 (497)	79(8)	21890 (471)	25(3)	11322 (326)	1.22(10)	A;5;9
2003du	−12.1	11762 (336)	16(2)	17250 (424)	10(1)	22363 (502)	6(1)	12000 (581)	74(6)	18344 (774)	23(2)	11466 (304)	69(6)	21957 (470)	165(16)	10557 (306)	1.07(06)	A;B;5;9

Table 1
(Continued)

SN	t[a] (day)	O I λ7773 V_P[b] (km s^{-1})	W_P[c] (Å)	V_H[d] (km s^{-1})	W_H[e] (Å)	V_S[f] (km s^{-1})	W_S[g] (Å)	Si II λ6355 V_P[h] (km s^{-1})	W_P[i] (Å)	V_H[j] (km s^{-1})	W_H[k] (Å)	Ca II NIR V_P[l] (km s^{-1})	W_P[m] (Å)	V_H[n] (km s^{-1})	W_H[o] (Å)	v_0^{Si}[p] (km s^{-1})	$\Delta m_{15}(B)$[q] (mag)	Ref.[r]
2003ek^{+}	−10.0	12483 (536)	38(4)	20853 (794)	23(3)	26000 (948)	22(2)	11042 (330)	96(5)	18082 (771)	1(1)	⋯	⋯	⋯	⋯	10832 (320)	⋯	A;B;
2003fa*	−9.2	10938 (488)	11(1)	18500 (719)	4(1)	22412 (838)	4(1)	11369 (336)	37(2)	19497 (513)	5(1)	⋯	⋯	⋯	⋯	10357 (518)	0.96(03)	A;B;5;9
2003kc	−11.4	13563 (573)	37(4)	18611 (725)	31(3)	21409 (807)	3(1)	15646 (694)	152(16)	18000 (767)	1(1)	⋯	⋯	⋯	⋯	12723 (608)	1.19(03)	A;B;9
2003kf	−9.5	12240 (535)	15(1)	17860 (710)	9(1)	23000 (856)	5(1)	11998 (358)	75(4)	18200 (771)	12(2)	12340 (323)	45(4)	23590 (496)	82(7)	11444 (573)	1.10(05)	A;B;1
2004dt	−10.8	12157 (335)	43(2)	17362 (418)	64(7)	21983 (494)	28(3)	15000 (750)	137(14)	20162 (1009)	30(3)	12500 (512)	58(6)	21300 (780)	79(5)	14110 (406)	1.14(04)	A;B;C;5;10
2004eo	−11.4	12500 (528)	21(3)	17500 (423)	11(2)	24479 (502)	1(1)	11684 (364)	124(10)	18000 (774)	1(1)	11800 (482)	144(13)	20634 (445)	155(8)	10497 (296)	1.38(03)	A;B;C;5;10
2004ey	−8.2	12114 (523)	18(2)	17930 (698)	13(1)	23000 (856)	2(1)	11759 (352)	88(5)	20188 (532)	6(1)	11474 (308)	59(5)	22386 (477)	81(7)	11220 (324)	0.96(06)	B;C;5;10
2005cf	−10.2	10999 (414)	8(1)	17012 (549)	6(1)	22700 (678)	3(1)	11773 (348)	83(4)	18674 (503)	45(3)	12963 (520)	69(7)	23406 (492)	243(25)	10276 (302)	1.03(01)	A;B;11
2005cg^{+}	−9.0	11555 (509)	15(2)	18000 (704)	5(1)	22210 (831)	2(1)	12137 (366)	49(3)	18661 (806)	30(2)	9906 (283)	32(2)	23239 (489)	115(11)	11590 (342)	⋯	A;
2005el	−8.1	11000 (460)	31(2)	17078 (416)	14(2)	22511 (503)	4(1)	11355 (338)	76(5)	18799 (857)	3(1)	11357 (304)	58(6)	21059 (454)	46(3)	10811 (304)	1.31(06)	A;B;C;5;9;10
2005eu*	−9.1	12447 (535)	5(1)	18782 (728)	2(1)	23200 (862)	4(1)	11161 (324)	42(2)	18300 (774)	1(1)	⋯	⋯	⋯	⋯	11068 (554)	0.94(04)	A;B;5;9
2006X	−11.1	15500 (660)	5(1)	21000 (798)	24(3)	24040 (527)	7(1)	16357 (818)	121(13)	22500 (1125)	73(8)	⋯	⋯	⋯	⋯	15577 (441)	1.17(05)	A;B;C;12
2006ax^{+}	−10.6	11061 (490)	24(2)	16651 (662)	10(2)	22137 (832)	2(1)	12105 (361)	94(5)	18281 (774)	4(1)	11554 (311)	85(9)	20324 (446)	108(6)	10503 (298)	1.02(02)	A;B;C;9;10
2006dd	−12.4	11156 (341)	21(2)	17280 (427)	12(2)	22309 (502)	6(1)	11306 (340)	88(5)	18000 (765)	1(1)	⋯	⋯	⋯	⋯	10500 (525)	1.07(03)	C;13
2006dm	−7.9	10000 (460)	55(6)	16351 (653)	23(3)	21000 (795)	7(1)	12454 (372)	110(6)	18000 (765)	1(1)	⋯	⋯	⋯	⋯	11800 (590)	1.53(06)	B;5
2006dy	−11.8	10556 (491)	38(4)	18317 (722)	8(1)	22949 (842)	2(1)	12363 (370)	110(5)	20000 (827)	10(1)	⋯	⋯	⋯	⋯	10459 (523)	⋯	B;
2006gr	−9.2	13100 (556)	8(1)	19269 (744)	7(1)	23148 (860)	3(1)	13752 (418)	55(3)	20465 (533)	32(3)	10723 (299)	30(3)	23385 (492)	129(13)	11492 (366)	1.03(06)	A;B;5;9
2006kf	−8.3	11991 (460)	64(4)	17418 (673)	21(3)	22152 (830)	6(1)	12953 (390)	128(7)	19239 (518)	4(1)	⋯	⋯	⋯	⋯	11378 (322)	1.48(01)	A;B;C;9;13
2006le	−8.9	12209 (524)	9(1)	18176 (709)	7(1)	23003 (855)	4(1)	12882 (576)	68(5)	20115 (806)	25(4)	11159 (325)	12(2)	24000 (862)	151(13)	11005 (342)	0.89(05)	A;B;5;9
2007F*	−9.7	11868 (518)	6(1)	17995 (702)	2(1)	22964 (843)	2(1)	12055 (348)	71(5)	20372 (513)	10(2)	10617 (296)	41(4)	24000 (861)	106(9)	11254 (324)	1.03(01)	A;B;9

Table 1
(Continued)

		O I $\lambda 7773$						Si II $\lambda 6355$				Ca II NIR						
SN	t[a] (day)	V_P[b] (km s^{-1})	W_P[c] (Å)	V_H[d] (km s^{-1})	W_H[e] (Å)	V_S[f] (km s^{-1})	W_S[g] (Å)	V_P[h] (km s^{-1})	W_P[i] (Å)	V_H[j] (km s^{-1})	W_H[k] (Å)	V_P[l] (km s^{-1})	W_P[m] (Å)	V_H[n] (km s^{-1})	W_H[o] (Å)	v_0^{Si}[p] (km s^{-1})	$\Delta m_{15}(B)$[q] (mag)	Ref.[r]
2007af	−11.3	11183 (496)	35(3)	17000 (674)	19(2)	22091 (829)	1(1)	12629 (632)	113(12)	18300 (915)	1(1)	11647 (318)	93(10)	20725 (454)	151(9)	11007 (315)	1.20(05)	A;B;C;5;9
2007bd	−8.1	11580 (508)	39(4)	17500 (689)	20(2)	24000 (887)	1(1)	13709 (402)	130(6)	18300 (775)	1(1)	12459 (324)	93(10)	21064 (457)	71(4)	12557 (366)	1.24(01)	A;B;C;9
2007bm	−8.2	11246 (507)	36(2)	17170 (676)	12(1)	21473 (813)	5(1)	11145 (334)	89(4)	18300 (774)	1(1)	11064 (301)	85(7)	20297 (444)	41(2)	10500 (525)	1.19(02)	A;B;C;9
2007ca	−10.4	11000 (491)	17(2)	17811 (700)	8(1)	23102 (859)	1(1)	12053 (362)	67(4)	18564 (786)	10(1)	…	…	…	…	11230 (314)	1.10(01)	A;B;C;5;9
2007le	−9.7	14623 (603)	9(1)	20142 (776)	4(1)	24000 (887)	2(1)	13795 (637)	99(8)	21000 (858)	54(4)	14500 (349)	55(6)	26710 (544)	288(29)	12410 (370)	1.01(05)	A;B;C;5
2008ar	−9.1	12207 (529)	13(1)	17145 (674)	7(1)	21673 (819)	3(1)	12187 (336)	93(4)	19000 (492)	37(5)	13247 (312)	58(5)	23921 (681)	185(13)	10634 (316)	1.08(06)	A;B;C;5;14
2008bc	−9.7	14337 (606)	15(2)	19000 (736)	6(1)	23364 (865)	5(1)	12933 (612)	90(6)	19609 (815)	38(3)	11774 (327)	41(3)	24000 (862)	253(11)	11600 (580)	0.93(01)	C;13
2008bf	−9.5	12000 (522)	14(2)	18677 (723)	5(1)	24010 (886)	2(1)	12153 (360)	61(5)	19023 (512)	20(1)	12412 (319)	50(5)	22942 (486)	101(10)	11466 (336)	1.03(07)	A;B;C;5;9
2008hv	−11.3	14314 (375)	36(3)	18500 (721)	9(1)	22505 (503)	2(1)	13735 (424)	105(6)	19241 (518)	41(3)	14062 (347)	95(9)	24000 (863)	257(27)	10926 (312)	1.25(01)	B;C;14
2009aa	−8.7	10381 (481)	28(2)	16824 (683)	13(1)	22255 (829)	1(1)	10513 (316)	80(4)	18300 (774)	1(1)	10516 (294)	85(7)	20889 (454)	23(2)	10000 (500)	1.12(05)	C;13
2009ab	−10.8	11303 (335)	30(2)	17730 (428)	16(2)	23107 (512)	5(1)	10921 (547)	73(8)	18300 (915)	1(1)	…	…	…	…	10839 (306)	1.21(10)	C;13
2009ig	−9.5	15000 (614)	8(1)	18284 (440)	4(1)	22689 (506)	6(1)	14896 (668)	84(6)	22700 (906)	12(1)	…	…	…	…	13400 (670)	0.89(02)	B;15;16
2011by	−12.4	11418 (333)	30(2)	18592 (443)	10(1)	23001 (511)	1(1)	12209 (368)	86(4)	18300 (774)	7(1)	12000 (497)	116(12)	20650 (450)	79(5)	10300 (515)	1.14(03)	D;17
2011df[+]	−9.0	13711 (574)	9(1)	18615 (722)	6(1)	21961 (825)	3(1)	12280 (366)	96(5)	19500 (811)	29(2)	…	…	…	…	11005 (348)	…	D;
2011fe[+]	−10.0	10819 (485)	35(3)	17522 (689)	14(1)	22379 (837)	3(1)	11917 (569)	99(9)	20300 (835)	3(1)	11537 (296)	108(9)	19939 (431)	64(4)	10444 (529)	1.18(03)	D;17,18
2012cg[+]	−10.0	11266 (338)	16(2)	17726 (436)	8(1)	23564 (517)	2(1)	12278 (587)	64(5)	18936 (790)	31(3)	13052 (334)	78(7)	21722 (466)	98(5)	10000 (500)	0.83(05)	D;19;20
2012et[+]	−8.0	13550 (525)	27(3)	18500 (720)	11(2)	23043 (948)	9(1)	14051 (645)	119(9)	18421 (779)	14(1)	…	…	…	…	13053 (408)	1.24(04)	D;
2012fr[+]	−11.5	14208 (645)	1(1)	19312 (747)	3(1)	26000 (948)	2(1)	13400 (576)	40(1)	22507 (857)	109(10)	13000 (528)	9(1)	27000 (547)	150(14)	12200 (611)	0.80(01)	D;21
2013dy[*+]	−10.0	11179 (331)	16(2)	17160 (423)	8(1)	23184 (515)	6(1)	11404 (562)	49(4)	18417 (777)	5(1)	10644 (435)	58(6)	21985 (464)	52(4)	10300 (515)	0.92(01)	D;22,23
2013gs[+]	−9.7	13748 (573)	10(1)	19451 (741)	5(1)	25227 (928)	1(1)	12873 (608)	67(5)	17561 (752)	56(4)	9756 (405)	61(7)	21112 (453)	185(20)	12200 (610)	1.05(01)	D;

Table 1
(Continued)

SN		O I λ7773						Si II λ6355				Ca II NIR						
	t[a] (day)	V_P[b] (km s^{-1})	W_P[c] (Å)	V_H[d] (km s^{-1})	W_H[e] (Å)	V_S[f] (km s^{-1})	W_S[g] (Å)	V_P[h] (km s^{-1})	W_P[i] (Å)	V_H[j] (km s^{-1})	W_H[k] (Å)	V_P[l] (km s^{-1})	W_P[m] (Å)	V_H[n] (km s^{-1})	W_H[o] (Å)	v_0^{Si}[p] (km s^{-1})	$\Delta m_{15}(B)$[q] (mag)	Ref.[r]
2013gy	−9.1	12106 (538)	32(4)	16553 (710)	17(2)	21000 (911)	3(1)	13211 (392)	121(6)	18300 (775)	1(1)	12500 (512)	158(16)	20423 (447)	121(7)	11000 (316)	1.20(01)	D;
2014J^{+}	−10.5	14438 (607)	19(2)	19972 (775)	7(1)	23500 (872)	3(1)	13920 (632)	114(9)	20322 (816)	25(2)	13043 (439)	52(5)	24651 (693)	190(19)	12050 (360)	1.02(01)	D;

Notes. Spectral parameters measured for O I λ7773, Si II λ6355, and the Ca II NIR triplet in the $t \sim -10 \pm 2.5$ day spectra of SNe Ia. Note that the velocity, pEW, photospheric component, HVF-I, and HVF-II are abbreviated to V, W, P, H, and S, respectively. The "*" and "⋆" after the SN names denote the 99aa-like and 91T-like SNe Ia, respectively, while the "+" marks the SNe whose spectra used for the measurements of the Ca II NIR triplet and Si II λ6355 (or O I λ7773) are taken at slightly different epochs. The 1σ uncertainties shown in the brackets are in units of 1 km s^{-1} for velocity, 1 Å for equivalent width, and 0.01 mag for $\Delta m_{15}(B)$, respectively.

References. A—CfA Supernova Program (Matheson et al. 2008; Blondin et al. 2012); B—Berkeley Supernova Program (Silverman et al. 2012a); C—CSP (Folatelli et al. 2013); D—Tsinghua Supernova Program; 1—(Hachinger et al. 2006); 2—(Lira et al. 1998); 3—(Patat et al. 1996); 4—(Jha et al. 2006); 5—(Ganeshalingam et al. 2010); 6—(Stritzinger et al. 2002); 7—(Krisciunas et al. 2003); 8—(Mattila et al. 2005); 9—(Hicken et al. 2009); 10—(Contreras et al. 2010); 11—(Wang et al. 2009a); 12—(Wang et al. 2008); 13—(Stritzinger et al. 2011); 14—(Hicken et al. 2012); 15—(Marion et al. 2013); 16—(Foley et al. 2012); 17 —(Graham et al. 2015); 18—(Zhang et al. 2016); 19—(Marion et al. 2016); 20— (Silverman et al. 2012b); 21—(Zhang et al. 2014); 22—(Zheng et al. 2013); 23—(Zhai et al. 2016).

[a] Days since B-band maximum light.
[b] Velocity of O I λ7773 for the photospheric component.
[c] pEW of O I λ7773 for the photospheric component.
[d] Velocity of O I λ7773 for the HVF-I component.
[e] pEW of O I λ7773 for the HVF-I component.
[f] Velocity of O I λ7773 for the HVF-II component.
[g] pEW of O I λ7773 for the HVF-II component.
[h] Velocity of Si II λ6355 for the photospheric component.
[i] pEW of Si II λ6355 for the photospheric component.
[j] Velocity of Si II λ6355 for the HVF component.
[k] pEW of Si II λ6355 for the HVF component.
[l] Velocity of the Ca II IR triplet for the photospheric component.
[m] pEW of the Ca II IR triplet for the photospheric component.
[n] Velocity of the Ca II IR triplet for the HVF component.
[o] pEW of the Ca II IR triplet for the HVF component.
[p] Velocity of Si II λ6355 measured near maximum light.
[q] Light-curve parameter, B-band light-curve decline rate $\Delta m_{15}(B)$.
[r] References for both spectra and photometry.

2012cg, and SN 2012fr, the velocity gradients of the photospheric components are −379, −199, −329, and −257 km $s^{-1}day^{-1}$, while the corresponding values for the HVFs are −134, −644, −136, and −413 km s^{-1} day^{-1}. The Normal SNe Ia appear to have a relatively uniform velocity evolution compared to other subclasses of SNe Ia. This may enable better extrapolations of absorption velocity to the value at a given phase (i.e., $t \sim -10$ day) for some normal sample when necessary. In contrast, the velocity evolution of SN 2002dj and SN 2009ig shows large scatter for either the HVFs or the photospheric components. This may be caused, to some extent, by the HV SNe Ia suffering more serious line blending and it thus being more difficult to separate the HVFs from the photospheric components.

The strength of the O I λ7773 absorption is plotted as a function of phase in the right panels of Figure 3, which shows even larger scatter than the velocity. One can see that the O I absorptions are found to be strong in some SNe Ia such as SN 2002dj and SN 2011fe, but they are marginally detected in other objects such as SN 2009ig and SN 2012fr. Note, however, that the absorption strength of the O-HVF does not show significant variation with time for our sample, in particular the Normal subsample. This is different from the trend seen in the HVFs of the Si II λ6355 line and the Ca II NIR triplet, which become weaker at a faster rate, perhaps due to having an optically thin environment in their outermost layers (see the references in Zhao et al. 2015).

3. STATISTICAL ANALYSIS

Table 1 lists the line velocities and strengths of O I λ7773, Si II λ6355, the Ca II NIR triplet, and C II λ6580 absorptions obtained at $t \sim -10$ day for 62 SNe Ia. If more than one spectrum is available during the period from $t = -11$ day to $t = -9$ day the median values are presented. The B-band light-curve decline rate $\Delta m_{15}(B)$ (Phillips 1993) is also listed. The detailed results for the measurements of the velocities and pEWs of the O I λ7773 and C II λ6580 absorptions at different phases are tabulated in Tables 2 and 3. Given the uncertainties due to line blending and/or the intrinsically larger scatter in the temporal evolution of O I absorption for HV SNe Ia, we concentrate on the spectroscopically normal SNe Ia with $v_0^{\mathrm{Si}} <$ 12,500 km s^{-1} in the following analysis.

3.1. Expansion Velocity from O I 7773

The velocity distribution of the ejected matter at different layers of the exploding WD can provide strong constraints on its compositional structure. To obtain an overall picture of the velocity distributions of C II λ6580, Si II λ6355, O I λ7773, and the Ca II NIR triplet, we construct the mean spectrum using the spectra of a subsample of Normal SNe Ia whose spectra have a sufficiently high signal-to-noise ratio (S/N) (i.e., S/N $\gtrsim$ 20) and cover phases close to $t = -10$ day. The mean profiles of the above four absorption features are shown in Figure 4, where the Ca II lines are characterized by prominent HVFs at ∼22,000 km s^{-1} and the O I line is characterized by the HVF-I at ∼18,000 km s^{-1} and a possible HVF-II at ∼22,000 km s^{-1}. The small notch on the blue side of the Si II λ6355 absorption corresponds to the HVF of Si formed at a velocity of about 18,000 km s^{-1}. The C II λ6580 absorption does not show any significant signature of an absorption feature at higher velocities. As can be seen, the photospheric components of different species have similar velocities (see the blue dashed line in Figure 4). Note that Figure 4 is constructed for illustrative purpose only.

Figure 5 shows the expansion velocities measured from absorption minima of Si II, Ca II, and C II lines versus that from the O I line. At the photospheric layer, the velocity of the O I line shows a positive correlation with those of the Si II, Ca II, and C II lines; and a linear fit indicates that the O I velocity is slightly lower than the Si II and C II velocities by about 750 km s^{-1}. At the outer layers, the HVF-I of O (O-HVF-I) shows a similar but slightly lower central velocity compared to the Si-HVF; and at the outermost layers, the HVF-II of O has a velocity that is roughly comparable to the Ca-HVFs. This similarity in expansion velocities indicates that the fuel-indicative O and the burned Si (or Ca) are physically connected. The observation results for the small velocity differences between the lines, and the fact that the Ca-HVFs have higher velocities relative to the Si-HVFs, might be well explained by different ionization (or excitation) energies being required to produce the lines of O I λ7773 (i.e., $E_{\mathrm{ex}} = 9.15$ eV), Si II λ6355 (i.e., $E_{\mathrm{ex}} = 8.12$ eV), and the Ca II NIR triplet (i.e., $E_{\mathrm{ex}} = 1.7$ eV). For the relatively low temperature expected for the outermost HVF forming layer, the Ca II NIR triplet is more easily formed and saturated compared to the Si II and O I lines.

3.2. Equivalent Width of O I 7773

The line strength of O I 7773 absorption carries important information on the diversity of SNe Ia. Figures 6 shows the pEW (for the photospheric component and HVF) of O I absorption versus the corresponding velocities, measured from the $t \approx -10$ day spectra of our SN Ia sample. As can be readily seen in these figures, these two quantities do not show significant correlation for the full sample, as indicated by the lower Pearson coefficients. Excluding the HV SNe Ia from the statistical sample, a modest anti-correlation seems to emerge between the pEWs and velocities of O I lines, although there are a few outliers. These results indicate that a smaller amount of oxygen is detected in SNe Ia with relatively larger expansion velocities. Such an inverse relation becomes stronger for the subsample with prominent detection of C II λ6580 absorption, i.e., pEW $\gtrsim$ 1.0 Å at $t \approx -10$ day (see Table 3 for the detailed results of the measurements). The corresponding Pearson coefficients, ρ, are −0.64 and −0.67 for the correlations of the HVFs and photospheric components, respectively. The much tighter pEW–velocity relation for O I λ7773 absorption suggests that the SNe Ia showing prominent carbon in their spectra may form a distinct population with relatively smaller diversity.

We notice that the velocity–pEW correlation seen in O I λ7773 absorption is the opposite to that seen in the Si II λ6355 line (Wang et al. 2009a; Blondin et al. 2012), which directly reflects the different roles that O and Si play in burning in the HVF and photospheric layers. In the right-most panel of Figure 6, we further examine the relation between the absorption strengths of the HVF and the photospheric component of O I λ7773. We find that the pEW of the O-HVF absorption is highly correlated with that of the O photospheric absorption, which has a Pearson coefficient of 0.86. This strong correlation indicates that the O detected at the outermost layers of the ejecta is intrinsic to the SNe, rather than coming from other sources such as CSM, which usually lies far outside the exploding WD and should not have such a strong connection with the photosphere unless CSM properties are

Table 2
Fit Results of O I λ7773

SN	t[a] (day)	V_P[b] (km s^{-1})	W_P[c] (Å)	V_H[d] (km s^{-1})	W_H[e] (Å)	V_S[f] (km s^{-1})	W_S[g] (Å)	R_b[h]
1990N	−13.9	12851(353)	11(2)	17946(419)	12(1)	21349(795)	10(2)	0
1991M	−7.8	12501(562)	40(4)	17000(675)	27(2)	22969(841)	3(1)	0.13
1991T	−10.5	11362(331)	4(1)	16000(643)	1(1)	22539(504)	2(1)	0.06
1994D	−11.1	13119(361)	15(2)	18625(444)	10(1)	21719(486)	2(1)	0
1994D	−9.5	12601(542)	22(2)	17631(697)	10(1)	21679(822)	5(1)	0
1994D	−8.5	12001(507)	26(2)	17785(675)	10(1)	22284(816)	1(1)	0
1997bq	−11.8	13390(302)	34(3)	18197(412)	28(4)	22603(491)	14(2)	0.14
1998dk	−7.1	14496(387)	23(3)	20364(479)	15(2)	23790(527)	3(1)	0.07
1998dm	−10.9	11702(338)	21(2)	17709(429)	8(1)	22237(501)	5(1)	0.08
1998ef	−8.9	11222(509)	29(4)	16333(664)	50(5)	21660(831)	14(1)	0
1999aa	−11.4	12216(539)	11(1)	19535(750)	6(1)	24103(889)	4(1)	0
1999dk	−7.7	13531(460)	32(2)	18664(651)	22(4)	23000(856)	1(1)	0.05
1999dq	−9.6	12355(531)	5(1)	18051(699)	5(1)	23586(866)	5(1)	0
1999ee	−9.4	13000(383)	5(1)	18000(706)	6(1)	23088(509)	5(1)	0.08
1999ee	−7.4	13000(378)	8(1)	18000(705)	7(1)	23025(510)	6(1)	0.12
2000dx	−9	12501(349)	18(1)	17715(431)	11(1)	22738(507)	7(1)	0
2000fa	−9.1	12011(524)	20(2)	20342(779)	10(1)	26000(948)	1(1)	0
2001el	−9	11701(347)	12(1)	17847(437)	8(1)	22760(506)	4(1)	0.09
2002bo	−12.7	14626(603)	31(3)	20507(782)	26(2)	21000(795)	1(1)	0
2002cr	−7.6	9371(439)	39(3)	16117(644)	16(2)	20926(792)	2(1)	0
2002cs	−9	14465(383)	37(4)	19000(736)	24(2)	23782(523)	11(2)	0.02
2002dj	−12.6	16000(645)	19(2)	20693(787)	11(2)	24000(887)	1(1)	0
2002dj	−11.6	15487(632)	43(4)	20799(797)	15(2)	24000(887)	1(1)	0
2002dj	−8.6	14521(602)	46(4)	20000(771)	15(2)	24000(887)	1(1)	0.06
2002dj	−7.6	14000(375)	35(4)	20258(782)	6(1)	24000(887)	2(1)	0.1
2002er	−8.9	12962(355)	35(4)	19454(465)	15(2)	23047(512)	20(2)	0.15
2002er	−7.9	13183(363)	36(3)	20520(596)	15(2)	24000(887)	8(1)	0.09
2003U	−8.8	13054(555)	51(7)	17403(738)	21(2)	24105(891)	1(1)	0
2003cg	−8.4	11559(342)	21(2)	16576(420)	12(1)	21848(494)	5(1)	0.11
2003cg	−7.4	11763(515)	22(2)	16100(647)	8(1)	22572(843)	1(1)	0.08
2003du	−12.1	11762(336)	16(2)	17250(424)	10(1)	22363(502)	6(1)	0.12
2003ek	−10	12483(536)	38(4)	20853(794)	23(3)	26000(948)	22(2)	0
2003fa	−9.2	10938(488)	11(1)	18500(719)	4(1)	22412(838)	4(1)	0
2003fa	−8.8	11009(489)	9(1)	18500(719)	4(1)	22230(833)	3(1)	0
2003kc	−11.4	13563(573)	37(4)	18611(725)	31(3)	21409(807)	3(1)	0
2003kf	−9.5	12240(535)	15(1)	17860(710)	9(1)	23000(856)	5(1)	0.09
2003kf	−8.8	12222(534)	16(2)	17651(702)	9(1)	23000(856)	4(1)	0.08
2004dt	−10.8	12157(335)	43(2)	17362(418)	64(7)	21983(494)	28(3)	0.04
2004dt	−7.8	10325(318)	35(4)	16082(407)	42(4)	21199(484)	20(2)	0
2004eo	−11.4	12500(537)	21(3)	17500(690)	11(2)	24479(948)	1(1)	0.3
2004ey	−8.2	12114(523)	18(2)	17930(698)	13(1)	23000(856)	2(1)	0.05
2005cf	−12.7	11295(513)	7(1)	17213(679)	8(1)	23592(873)	1(1)	0.12
2005cf	−11.7	11186(331)	12(1)	16824(416)	9(1)	22034(494)	4(1)	0.06
2005cf	−11.3	11281(332)	10(1)	17002(418)	8(1)	21877(492)	4(1)	0.05
2005cf	−10.7	11029(498)	8(1)	17242(681)	5(1)	23016(857)	2(1)	0.08
2005cf	−9.7	10968(329)	8(1)	16782(416)	6(1)	22383(499)	3(1)	0.08
2005cf	−8.7	10774(485)	10(1)	16315(658)	8(1)	22081(831)	5(1)	0.1
2005cf	−7.7	10334(322)	14(2)	16334(410)	8(1)	21827(489)	7(1)	0.12
2005cg	−9	11555(509)	15(2)	18000(704)	5(1)	22210(831)	2(1)	0
2005el	−8.1	11000(460)	31(2)	17078(416)	14(2)	22511(503)	4(1)	0.04
2005el	−7.1	11000(480)	31(3)	17171(672)	12(1)	22067(818)	3(1)	0.03
2005el	−6.9	11000(491)	31(3)	16555(418)	12(1)	21000(488)	4(1)	0.02
2005eu	−9.1	12447(535)	5(1)	18782(728)	2(1)	23200(862)	4(1)	0
2006X	−11.1	15500(660)	5(1)	21000(798)	24(3)	24040(527)	7(1)	0
2006X	−6.8	15579(398)	14(1)	20536(474)	24(2)	24008(856)	1(1)	0
2006ax	−10.8	11500(506)	22(2)	16200(650)	9(2)	21410(812)	2(1)	0.03
2006ax	−10.4	10622(474)	25(3)	17102(674)	11(1)	22864(851)	2(1)	0
2006ax	−8.8	10493(466)	16(2)	16630(650)	12(2)	21959(795)	2(1)	0
2006dd	−12.4	11156(341)	21(2)	17280(427)	12(2)	22309(502)	6(1)	0.22
2006dm	−7.9	10000(460)	55(6)	16351(653)	23(3)	21000(795)	7(1)	0
2006dy	−11.8	10556(491)	38(4)	18317(722)	8(1)	22949(842)	2(1)	0.08
2006gr	−9.2	13100(556)	8(1)	19269(744)	7(1)	23148(860)	3(1)	0
2006kf	−8.3	11991(460)	64(4)	17418(673)	21(3)	22152(830)	6(1)	0.04

Table 2
(Continued)

SN	t[a] (day)	V_P[b] (km s^{-1})	W_P[c] (Å)	V_H[d] (km s^{-1})	W_H[e] (Å)	V_S[f] (km s^{-1})	W_S[g] (Å)	R_b[h]
2006le	−8.9	12209(524)	9(1)	18176(709)	7(1)	23003(855)	4(1)	0
2007F	−9.7	11868(518)	6(1)	17995(702)	2(1)	22964(843)	2(1)	0
2007af	−11.3	11183(496)	35(3)	17000(674)	19(2)	22091(829)	1(1)	0.11
2007bd	−8.1	11580(508)	39(4)	17500(689)	20(2)	24000(887)	1(1)	0
2007bm	−8.2	11246(507)	36(2)	17170(676)	12(1)	21473(813)	5(1)	0.06
2007ca	−10.4	11000(491)	17(2)	17811(700)	8(1)	23102(859)	1(1)	0
2007ci	−7.1	11614(509)	50(5)	16000(643)	20(2)	22693(845)	6(1)	0
2007le	−10.4	14623(603)	6(1)	20000(766)	2(1)	24000(887)	2(1)	0
2007le	−9.7	14859(616)	9(1)	20142(776)	4(1)	24000(887)	2(1)	0
2007le	−9.5	14618(602)	15(2)	21000(797)	4(1)	24000(887)	5(1)	0
2008ar	−9.2	12414(535)	11(1)	17264(682)	10(1)	21827(820)	3(1)	0
2008ar	−9.1	12000(522)	14(1)	17026(666)	4(1)	21518(818)	3(1)	0
2008bc	−9.7	14337(606)	15(2)	19000(736)	6(1)	23364(865)	5(1)	0.09
2008bf	−9.5	12000(522)	14(2)	18677(723)	5(1)	24010(886)	2(1)	0
2008hv	−11.3	14314(375)	36(3)	18500(721)	9(1)	22505(503)	2(1)	0.2
2009aa	−8.7	10381(481)	28(2)	16824(683)	13(1)	22255(829)	1(1)	0
2009aa	−7.7	9588(450)	29(3)	16000(643)	16(2)	21621(814)	2(1)	0
2009ab	−10.8	11303(335)	30(2)	17730(428)	16(2)	23107(512)	5(1)	0.21
2009dc	−7	9000(430)	47(5)	16984(673)	14(2)	21000(795)	2(1)	0
2009ig	−14.4	15519(630)	3(1)	21500(813)	1(1)	24145(891)	1(1)	0
2009ig	−12.5	15500(630)	2(1)	21000(797)	1(1)	24192(891)	1(1)	0
2009ig	−11.5	15682(635)	2(1)	20728(694)	2(1)	24000(887)	2(1)	0
2009ig	−9.5	15000(614)	8(1)	18284(440)	4(1)	22689(506)	6(1)	0
2009ig	−8.5	14845(387)	8(1)	19000(736)	2(1)	24000(887)	3(1)	0
2011by	−12.4	11418(333)	30(2)	18592(443)	10(1)	23001(511)	1(1)	0.04
2011by	−7.3	11344(331)	18(1)	17637(430)	12(1)	22110(498)	7(1)	0.03
2011df	−9	13711(574)	9(1)	18615(722)	6(1)	21961(825)	3(1)	0
2011fe	−16	14347(603)	40(3)	19310(749)	16(1)	24242(854)	1(1)	0
2011fe	−15	13439(363)	28(4)	18542(448)	10(1)	23389(518)	3(1)	0
2011fe	−14	12367(350)	33(3)	18500(443)	15(1)	23361(514)	2(1)	0
2011fe	−13	12015(351)	34(2)	18086(437)	12(1)	23451(517)	1(1)	0
2011fe	−12	11936(519)	33(2)	18022(706)	10(1)	22445(840)	3(1)	0
2011fe	−11	10849(486)	39(4)	17647(691)	14(2)	22611(844)	3(1)	0
2011fe	−10	10800(485)	35(3)	17522(689)	13(1)	22379(837)	2(1)	0
2011fe	−9	10819(323)	27(2)	17183(421)	14(1)	21868(492)	6(1)	0
2011fe	−8	11163(331)	26(1)	17082(420)	10(1)	21392(487)	3(1)	0
2011fe	−7	10797(476)	26(3)	16748(678)	14(1)	21663(809)	6(1)	0.01
2012cg	−13.3	12719(544)	22(2)	18500(720)	13(1)	23144(860)	1(1)	0
2012cg	−11.6	12737(544)	19(2)	17685(695)	14(1)	22200(832)	3(1)	0
2012cg	−10	11266(338)	16(2)	17726(436)	8(1)	23564(517)	2(1)	0
2012cg	−8.6	11360(513)	13(1)	17739(703)	9(1)	23356(868)	4(1)	0
2012cg	−8.3	11326(332)	12(1)	17667(429)	7(1)	23038(512)	4(1)	0
2012et	−8	13550(525)	27(3)	18500(720)	11(2)	23043(948)	9(1)	0
2012fr	−12.5	14500(599)	1(1)	21000(797)	3(1)	23269(864)	4(1)	0
2012fr	−11.5	14208(645)	1(1)	19312(747)	3(1)	26000(948)	2(1)	0
2012fr	−8.3	13672(572)	2(1)	18971(737)	4(1)	22325(855)	1(1)	0
2012fr	−8	13000(552)	10(1)	17294(425)	5(1)	21000(795)	2(1)	0
2012fr	−7.7	13116(558)	8(1)	18769(729)	3(1)	23500(871)	2(1)	0
2012fr	−7.5	13406(364)	6(1)	19000(736)	5(1)	23500(871)	3(1)	0
2012fr	−6.8	12766(567)	14(1)	18601(730)	7(1)	25802(944)	1(1)	0.03
2012fr	−6.7	12783(563)	13(1)	18740(724)	9(1)	24251(891)	3(1)	0
2013ah	−7	10083(304)	39(4)	19757(462)	18(2)	26000(948)	11(1)	0
2013dy	−15.8	13732(590)	10(1)	18000(705)	7(1)	21752(806)	1(1)	0
2013dy	−12	11147(347)	15(1)	17500(427)	6(1)	23923(526)	2(1)	0.1
2013dy	−10.5	11375(333)	15(2)	17446(427)	8(1)	23378(517)	6(1)	0.06
2013dy	−9.5	10983(328)	17(2)	16873(419)	7(1)	22990(512)	5(1)	0.09
2013dy	−7.5	10781(333)	20(2)	16400(418)	9(1)	21617(495)	5(1)	0.15
2013gs	−9.7	13748(573)	10(1)	19451(741)	5(1)	25227(928)	1(1)	0
2013gs	−8.4	13500(568)	9(1)	18638(439)	8(1)	25356(546)	2(1)	0.19
2013gs	−7.5	13200(559)	21(2)	19742(759)	9(1)	26000(948)	2(1)	0.03
2013gy	−9.1	12106(538)	32(4)	16553(710)	17(2)	21000(911)	3(1)	0.12
2014J	−11	14952(614)	19(2)	21000(797)	7(1)	24000(887)	2(1)	0
2014J	−10	13923(599)	18(2)	18943(752)	7(1)	23000(857)	4(1)	0

Table 2
(Continued)

SN	t[a] (day)	V_P[b] (km s^{-1})	W_P[c] (Å)	V_H[d] (km s^{-1})	W_H[e] (Å)	V_S[f] (km s^{-1})	W_S[g] (Å)	R_b[h]
2014J	−7.7	13459(379)	23(2)	19514(480)	9(1)	22782(510)	1(1)	0

Notes. Spectral parameters measured for the absorption O i λ7773 in the early spectra of SNe Ia . The abbreviations are similar to those used in Table 1, with V, W, P, H, and S representing the velocity, pEW, photospheric component, HVF-I, and HVF-II, respectively. The 1σ uncertainties shown in the bracket are in units of 1 km s^{-1} and 1 Å for velocity and equivalent width, respectively.

[a] Days since the B-band maximum light.

[b] Velocity of O i λ7773 for the photospheric component.

[c] pEW of O i λ7773 for the photospheric component.

[d] Velocity of O i λ7773 for HVF-I component.

[e] pEW of O i λ7773 for HVF-I component.

[f] Velocity of O i λ7773 for the HVF-II component.

[g] pEW of O i λ7773 for the HVF-II component.

[h] The blending ratio between the telluric lines and the photospheric component of O i λ7773, defined as pEW $^{\rm telluric}_{\rm blending}$/pEW $^{\rm O}_{\rm PHO}$, where pEW $^{\rm telluric}_{\rm blending}$ is the pEW of the telluric absorptions overlapped by the photospheric component of O iλ7773, and pEW $^{\rm O}_{\rm PHO}$ refers to the pEW of the photospheric component of O i λ7773.

Table 3
Fit Results of C ii λ6580

SN	t (day)	V (km s^{-1})	W (Å)	SN	t (day)	V (km s^{-1})	W (Å)	SN	t (day)	V (km s^{-1})	W (Å)
1990N	−13.9	13496(675)	8.2(0.9)	2005cf	−12.5	12048(362)	1.4(1)	2008Z	−9.4	14000(700)	7.1(0.8)
1994D	−9.5	13114(396)	3.9(1)	2005cf	−11.7	11886(362)	1.5(1)	2008bf	−9.5	12917(388)	2.7(1)
1994D	−8.5	13060(382)	4.6(1)	2005el	−8.1	12130(364)	4.2(1)	2009F	−5.8	12145(608)	6.2(0.7)
1998aq	−9.9	12072(604)	3.7(0.4)	2005el	−7.1	11791(352)	4(1)	2009dc	−7	10351(314)	5.7(1)
1998dm	−10.9	12580(629)	1.7(0.2)	2005eu	−9.7	12487(625)	2.6(0.3)	2009ig	−15	9304(466)	0.5(0.1)
1999by	−6.2	10454(523)	1.3(0.2)	2005iq	−6.4	11889(595)	3.2(0.4)	2011by	−10	12821(390)	3.1(1)
1999cp	−12	12688(635)	6.3(0.7)	2006D	−6.3	12010(601)	6.8(0.7)	2011fe	−13	11732(360)	3.2(1)
2002cr	−11.3	11007(330)	2.7(1)	2006ax	−11.1	11326(567)	5.2(0.6)	2011fe	−12	11778(354)	2.1(1)
2002cr	−7.6	10563(316)	2.4(1)	2006dd	−12.4	12436(368)	2.9(1)	2011fe	−11	11402(346)	1.9(1)
2003du	−14.1	12722(382)	2.8(1)	2006dy	−11.8	11914(362)	3.1(1)	2011fe	−10	11285(332)	3.6(1)
2003du	−12.8	12392(372)	3.9(1)	2006gz	−9.6	13622(682)	14.6(1.5)	2011fe	−9	11094(334)	2.1(1)
2003du	−12.1	12311(370)	1.9(1)	2006le	−7.9	12284(615)	3.7(0.4)	2011fe	−7	10792(324)	1.8(1)
2003du	−10.8	12221(366)	2(1)	2007F	−9.7	12640(380)	1.2(1)	2012cg	−10	12668(382)	4.9(1)
2003du	−9.9	12009(360)	2.6(1)	2007af	−11.3	12031(366)	1.2(1)	2012cg	−8.6	12400(595)	3.1(1)
2003du	−8.9	12378(372)	2(1)	2007bm	−9.3	11436(344)	2.3(1)	2012cu	−7	12150(608)	8.1(0.9)
2003kf	−9.4	12878(644)	2.4(0.3)	2007bm	−8.5	11260(342)	1.6(1)	2013dy	−15.8	>13000	>20
2004bw	−10.5	12301(616)	10.5(1.1)	2007le	−10.7	13607(681)	0.6(0.1)	…	…	…	…
2005cf	−12.7	12048(362)	1.4(1)	2008Q	−7.3	14000(700)	6.5(0.7)	…	…	…	…

Note. Spectral parameters measured for C ii λ6580 in early spectra of SNe Ia. Velocity is abbreviated to V and pEW is further abbreviated to W due to limited space. The 1σ uncertainties shown in brackets are in units of 1 km s^{-1} and 1 Å for velocity and equivalent width, respectively.

somehow tied to SN properties. Note that the O-HVF we discuss here refers to the HVF-I marked in Figure 1, and we did not attempt to quantify the correlations of the O-HVF-II with the HVFs of Si (or Ca) because this feature is usually very weak and there are relatively larger uncertainties in measuring its absorption strength.

3.3. Correlations of O i λ7773, Si ii λ6355, and the Ca ii NIR Triplet

In our previous study, the HVFs of both Si ii λ6355 and the Ca ii NIR triplet in SNe Ia were systematically examined using their early-phase spectra. While the photospheric velocities were found to be similar between Si ii λ6355 and the Ca ii NIR triplet, the HVF velocity of the latter is higher than the former by about 4000 km s^{-1}. Similarly, although the Ca ii NIR triplet has a photospheric strength that is roughly comparable to that of Si iiλ6355, its HVF is found to be much stronger (by about six times). Note that these correlations are all positive, meaning that the velocity and strength of these two lines grow/decline in the same direction. These two spectral lines were also found to show similar behaviors as functions of photometric and host-galaxy properties such as $\Delta m_{15}(B)$, $B_{\rm max} - V_{\rm max}$ color, host-galaxy type, etc. (see details in Zhao et al. 2015). These results indicate that the amount of Si and Ca in both the photospheric component and HVF forming regions are strongly connected. However, the ratio of Si to Ca is not sensitive to the different burning processes expected in SNe Ia (which is similar to the unburned solar composition), while the ratio of O to Si (or Ca) is expected to be quite different in different layers.

Figure 7 compares the line strengths of O and Si for our sample of SNe Ia. In the left panel one can see that the photospheric components of O and Si are positively correlated and the Pearson coefficient is 0.69 for the Normal SNe Ia. On average, the pEW of O photospheric absorption is found to be

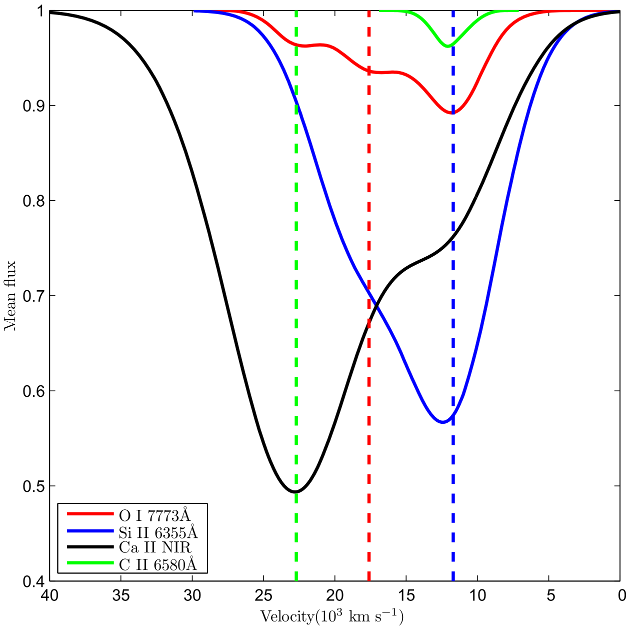

Figure 4. Mean line profiles of the C iiλ6580 (cyan), Si ii λ6355 (blue), O i λ7773 (red), and Ca ii NIR triplet (black) absorption features, obtained with the $t \sim -10$ day spectra of spectroscopically normal SNe Ia, are shown in velocity space. The vertical dashed lines mark the positions of the absorption minima of the HVFs and the photospheric component.

roughly 1/3 times that of Si ii. Inspection of the right panel of Figure 7, however, reveals that there is a distinct anti-correlation between the absorption strengths of the HVFs of Normal SNe Ia, with the Pearson coefficient $\rho = -0.71$ for a linear relation. Assuming a reciprocal correlation for the pEW $^{\rm O}_{\rm HVF}$–pEW$^{\rm Si}_{\rm HVF}$ relation, the Pearson coefficient becomes 0.90. A similar correlation (for the photospheric components) and anti-correlation (for the HVFs) can also be found between the line strengths of the O iλ7773 line and the Ca ii NIR triplet lines, as shown in Figure 8, although both these relations are less significant. Compared to Normal SNe Ia, the HV SNe (i.e., $v_0^{Si} \gtrsim 12{,}500$ km s^{-1}) show large scatter in both Figures 7 and 8, and do not seem to follow well the above relations, in particular the anti-correlation of the HVFs. The spectroscopically peculiar and luminous objects, with weak absorptions of both O and Si, also show obvious deviations in the plots of the HVFs.

The anti pEW $^{\rm O}_{\rm HVF}$–pEW $^{\rm Si}_{\rm HVF}$ correlation indicates that, at the outermost layers of the exploding WD, less O will be detected when Si and Ca are more abundant, and this favors the need for oxygen burning to produce the HVFs. Again the HV subgroup of SNe Ia is found to show larger scatter in this correlation, suggesting that the HVFs may have different origins (see discussions in Section 4).

3.4. Correlation of the Absorption with Peak Luminosity

Since the line velocities and strengths of the O i 7773 absorption feature show a wide range for different SNe Ia, it is necessary to explore the reasons for this diversity. Peak luminosity is an important parameter reflecting the properties of SNe Ia. In Figure 9 the observed features of the O photospheric component and O-HVF (including both line velocity and absorption strength) are plotted against the luminosity-indicator parameter Δm_{15}(B). As can readily be seen, the velocity of the O-HVF shows a modest dependence on Δm_{15}(B), with slower-declining (or more luminous) SNe Ia having larger ejecta velocities at outer layers. This velocity–luminosity relation can be explained if the characteristic velocity is moved toward higher velocities for explosions with more complete burning. Due to the loss of absorbing oxygen material, the strength of the absorption feature could then be weakened for SNe Ia with higher luminosities. This is supported by the prominent pEW–Δm_{15}(B) relation as shown in the right panels of Figure 9, where stronger O i absorptions are found in SNe Ia with lower luminosities. On average, the SNe Ia with $\Delta m_{15}(B) \gtrsim 1.20$ mag have pEWs that are about 2.0 times larger than those with $\Delta m_{15}(B) < 1.20$ mag. The above relations become stronger when the HV SNe Ia are discarded in the analysis.

As a comparison, the correlations of Si-HVF and Ca-HVF (line strength and velocity) with Δm_{15}(B) are also examined in Figure 10. The velocities of Si- and Ca-HVF are also found to be lower for SNe Ia with larger decline rates, which is similar to the behavior shown by the O-HVF. Although the strength of the Si-HVF does not show a strong anti-correlation with Δm_{15}(B), it is clear that stronger Si-HVFs tend to be detected in more luminous SNe Ia (i.e., with $\Delta m_{15}(B) < 1.3$ mag). This tendency is consistent with the earlier result obtained using the relative line strengths of the Si- and Ca-HVFs (Childress et al. 2014; Silverman et al. 2015; Zhao et al. 2015). The correlation between the Si-HVF and Δm_{15}(B) is weaker than that observed between the O-HVF and Δm_{15}(B), which may be due to the fact that not all luminous SNe Ia have prominent Si-HVFs, and also that the line blending of the HVF and the photospheric component is more serious than that for the O i λ7773 absorption. The fact that the Si-HVF and O-HVF show an opposite correlation with Δm_{15} suggests that the ionization effect should not play a key role in forming the HVFs in the outer layers of the ejecta since Si and O have similar ionization energies (see detailed discussions in Section 4.1).

4. DISCUSSION

4.1. Origin of the HVFs

The origin of the HVFs in SNe Ia still remains unclear. It has been suggested that HVFs could be associated with abundance enhancement (AE), density enhancement (DE), or ionization enhancement (IE) in the outermost layers (Gerardy et al. 2004; Mazzali et al. 2005b, 2005a; Blondin et al. 2012). The material producing the HVFs could either be intrinsic to the SNe or from the CSM. The features we investigate in this work, i.e., O i λ7773, Si ii λ6355, and the Ca ii NIR triplet, are suited to probing the density structure (through the pEW), velocity distribution (see Figure 4), and composition (through the pEW) of the ejecta. With this information we may decode the main functions involved in the origin of some HVFs.

Here we briefly summarize the scenarios proposed so far for the formation of HVFs. In the AE scenario, the abundances of Si and Ca are somehow enhanced in the outermost regions of the ejecta. A possible cause is a strong asymmetry in the explosion process (see Maeda et al. 2010 and Seitenzahl et al. 2013 for the single-detonation scenario, or Röpke et al. 2012 for the double-detonation scenario). Alternatively, the abundances could be enhanced by He burning near the WD surface, as suggested by the double-detonation model (e.g., Fink et al. 2007; Woosley & Kasen 2011). In the DE scenario, the HVFs are suggested to originate in a dense shell of

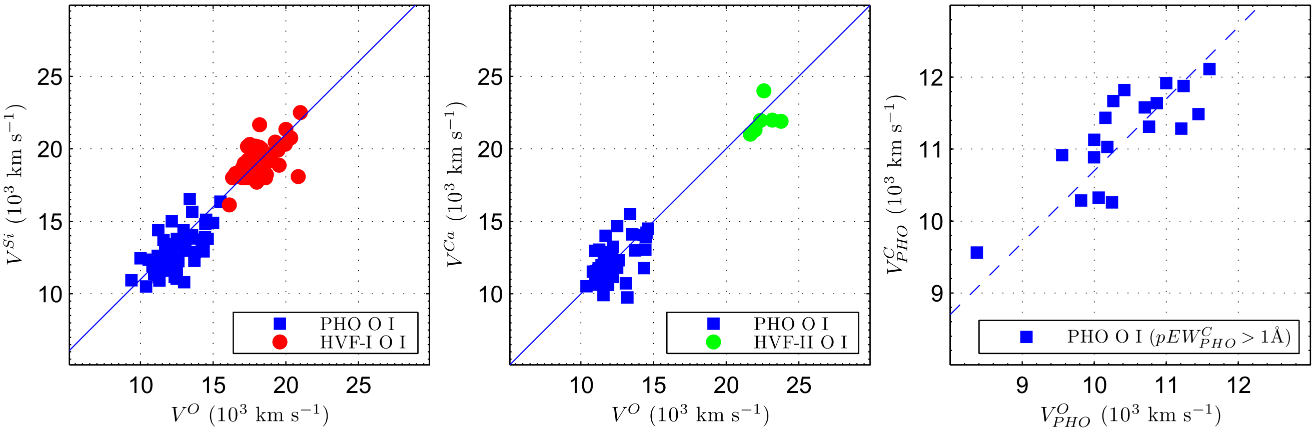

Figure 5. Comparison of velocity inferred from O i line with those from the Si ii, Ca ii, and C ii lines. The blue dots represent the velocities of the photospheric components. The red dots show the Si-HVF and O-HVF-I, while the green dots show the Ca-HVF and the O-HVF-II. Only those spectra with significant detection of the carbon signature are used for comparison with the C ii velocity.

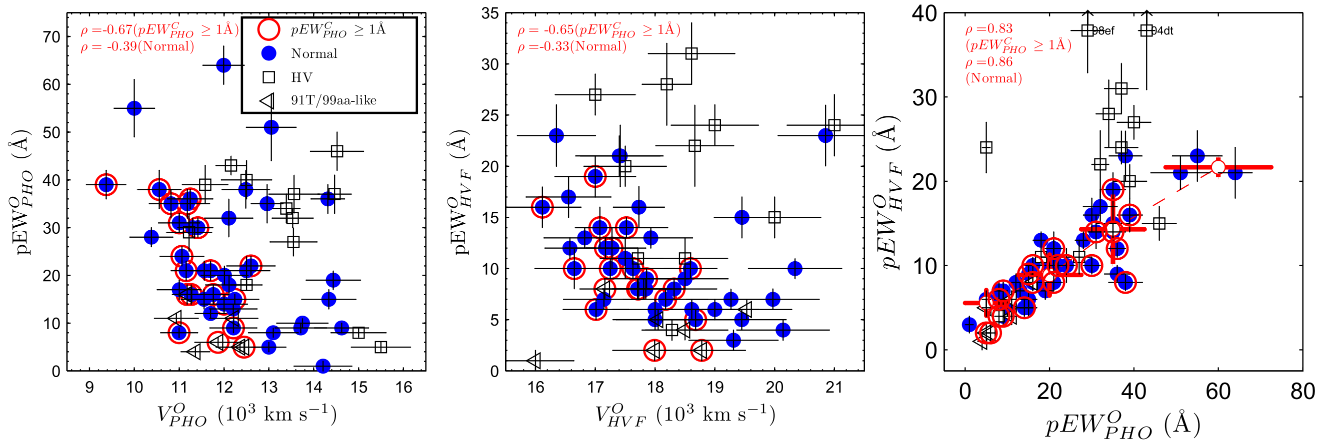

Figure 6. Line strength and velocity of O i λ7773. (a) Comparison between the line strength of the photospheric component of O i λ7773 absorption and the corresponding line velocity. (b) Similar comparison as (a) but for the line strength and velocity of the O-HVF. (c) Comparison of the line strengths between the HVFs and the photospheric components. Blue dots show Normal SNe Ia with $v_0^{\rm Si} < 12{,}500$ km s^{-1} at maximum light. The HV SNe Ia ($v_0^{\rm Si} \gtrsim 12{,}500$ km s^{-1} at maximum light) and the 91T/99aa-like SNe Ia are represented by squares and triangles, respectively. The larger red open circles represent the subsample of SNe Ia showing prominent C ii λ6580 absorption in the early-time spectra, i.e., pEW > 1.0 Å at $t \sim -10$ day.

basically unburned material, formed either at the outermost layer of the ejecta or in the CSM (Gerardy et al. 2004; Mazzali et al. 2005a; Tanaka et al. 2006, 2008; Mulligan & Wheeler 2015). In the IE scenario, a small amount of H in the outermost layer serves as a source of free electrons, which thus suppresses the ionization status of Ca and Si through recombination. This then leads to a larger amount of Ca ii and Si ii, potentially producing HVFs (Mazzali et al. 2005b; Tanaka et al. 2008). This may happen either as a contamination of H in the WD surface before the explosion or due to an interaction between the ejecta and the H-rich CSM, similarly to the DE scenario.

In our previous study (Zhao et al. 2015), the HVF of Si ii λ6355 was compared to that of Ca ii NIR and was found to be much stronger (the difference in strength could be understood as coming from different ionization potentials and oscillator strengths of the two lines). We also found an anti-correlation with Δm_{15}(B), namely slower-declining (or brighter) SNe Ia tend to show more prominent HVFs. In this work, we further examine the behavior and correlations of the fuel-indicative O i λ7773 absorption feature. Here we summarize our findings in relation to the expectations from the DE, AE, and IE scenarios.

1. *Mutual correlations of the velocities of HVFs and their time evolutions.* (a) The velocities of the Si-HVFs are about 4000 km s^{-1} lower than the velocities of the Ca-HVFs, i.e., $v_{\rm HVF}^{\rm Si} - v_{\rm HVF}^{\rm Ca} \approx 4000$ km s^{-1} (see Figure 17 in Zhao et al. 2015). This may not support DE scenario for the origin of HVFs. If the HVFs (of O, Si and Ca) are generated in a dense shell (either the outermost layer of the ejecta or the CSM), their (central) velocities should be roughly the same, regardless of the radiation condition, unless the shell is very thick in radial scale. But such a large-scale DE is not expected in hydrodynamics. Also, the velocities of Si-HVFs are much lower than the expectation from the CSM scenario. As Tanaka et al. (2006) pointed out, dense blobs covering the entire photosphere would result in Si ii λ6355 absorption velocities in excess of 20,000 km s^{-1}, which is, however, observed in only a few (HV) SNe (see also the discussion in Blondin et al. 2012). (b) Similarly, the time evolution of the line velocities of the O-HVFs as seen in Figure 3 may also not support the DE scenario as the origin of HVFs. If the HVFs originate from a dense shell created

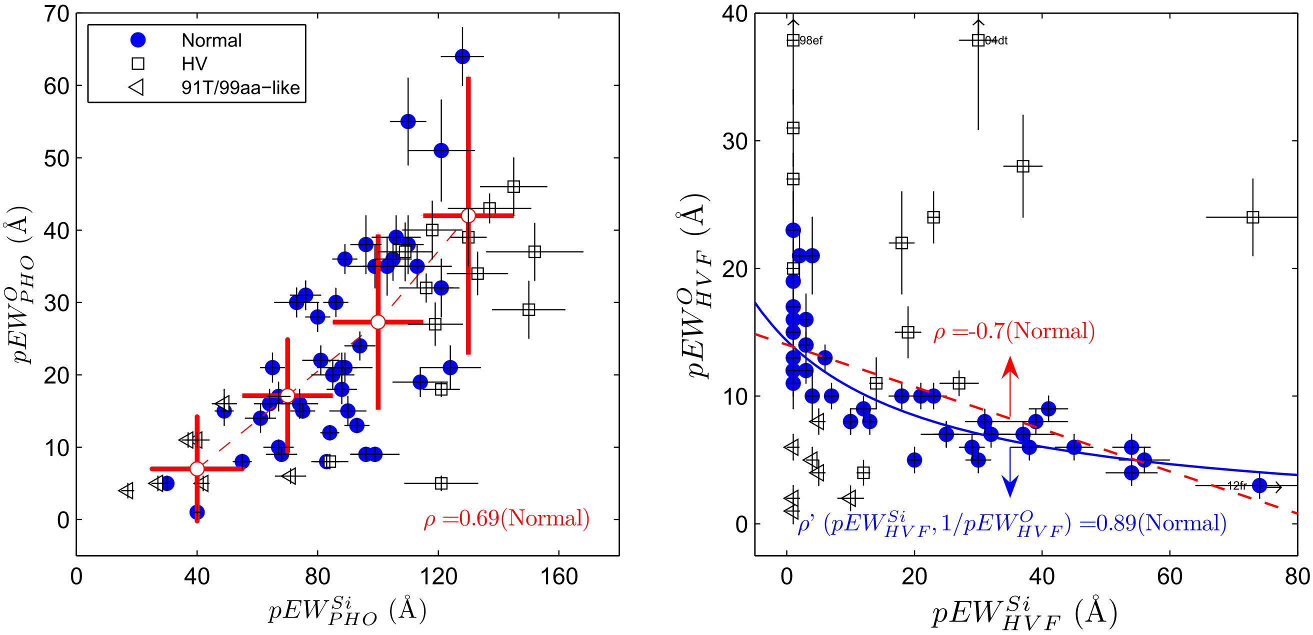

Figure 7. Comparison of the line strength of O I $\lambda7773$ with that of Si II $\lambda6355$ for the photospheric components (left) and the HVFs (left). The symbols are the same as in Figure 6. It is clear that the photospheric components of these two features show a positive correlation (with the Pearson coefficient $\rho = 0.69$) and their HVFs have an inverse correlation (with $\rho = -0.70$ for a linear correlation and $\rho = 0.89$ for a reciprocal correlation) for the subgroup of Normal SNe Ia. The open circles in the left panel represent the mean pEWs of O I $\lambda7773$ in bins of pEWs of Si II $\lambda6355$, and the error bars are the widths of the bins and 1σ dispersion.

by SN–CSM interaction, one would expect a nearly constant velocity of the HVFs as a function of time, since the hydrodynamical interaction is expected to create a geometrically very thin shell in which the velocity variation is at most a few percent (Chevalier 1982). However, the variation in velocity is much larger, as seen in Figure 3, where the typical velocity variation is close to 20% within one week from the earliest detection.

2. *Additional HVFs of O I $\lambda7773$.* As one can see from Figures 1, 2, and 4, the HVF of O I $\lambda7773$ is accompanied by an additional HVF at even higher velocities (i.e., higher by ≈4000 km s^{-1}). Possible explanations for this doublet-HVF includes the following. Explanation A—The O-HVF may be a combination of burned and unburned clumps, where the burned clumps also form the Si- and Ca-HVFs. While the detection of Si- and Ca-HVFs suggests that the burnt clumps are distributed in a large velocity space, at higher velocities the fraction of unburned clumps may be large and then the HVF-II of O I may be dominated by such unburned regions. Given the lower ionization energy for Ca II, HVFs can be still formed for the Ca II NIR triplet at higher velocities where a smaller number of burnt clumps exists, but not for Si II. Explanation B—The HVF-II of O I could be produced from carbon burning initiated by outflowing flames at higher velocities (Mazzali et al. 2005b; Maeda et al. 2008) in an asymmetric explosion or from He burning near the WD surface. The burning may also light up the HVFs of Ca II NIR which has a very low excitation energy at early times. However, these processes will not be the dominant factor affecting the correlation with Δm_{15}(B) because the amount of helium or carbon near the WD surface is small. Explanation C—The HVF-II of O I could be from a shocked CSM, while the HVF-I is from the outer layers of the ejecta.
3. *Slow time evolution in the line strength of O-HVF.* For the Normal SNe Ia, the absorption strength of the O-HVF weakens at a much slower rate (see Figure 3) than the Si-HVF in early phases (see Figure 5 in Zhao et al. 2015). This result cannot be explained by the ionization effect because Si II $\lambda6355$ has an excitation energy even lower than O I $\lambda7773$ (i.e., 8.12 eV versus 9.15 eV). Nor would this be easy to explain with the DE scenario. If the fast weakening of the Si- and Ca-HVFs is caused by the fast decline of density in the HVF layers, then the O-HVF would also quickly weaken for the same reason. The most plausible explanation could be given by a scenario related to AE. If the abundance of O increases toward lower velocities, then the decreasing density as a function of time could be compensated by the increasing abundance, possibly resulting in a slow evolution. In other words, if the main body of the HVF-I forming region is dominated by the burnt material and these clumps indeed become less significant for the lower velocities toward the photosphere, then the observed behavior is reproduced.
4. *Velocity–pEW correlation of O I absorption.* As can be seen from Figure 6, the line strength of O absorption (both the HVF and photospheric component) is decreasing with increasing velocity. This anti-correlation might be explained by the fact that more complete burning of oxygen could release more energy, driving the remaining oxygen shell to move at a higher velocity. The characteristic velocity is then moved toward higher velocities for explosions with more complete burning. Due to the loss of absorbing oxygen material, the strength of the absorption feature could then be weakened for SNe with higher velocities. This inverse correlation is fully in line with the effect from a burning difference. However, it is not clear why this relation is only strong in the SNe Ia

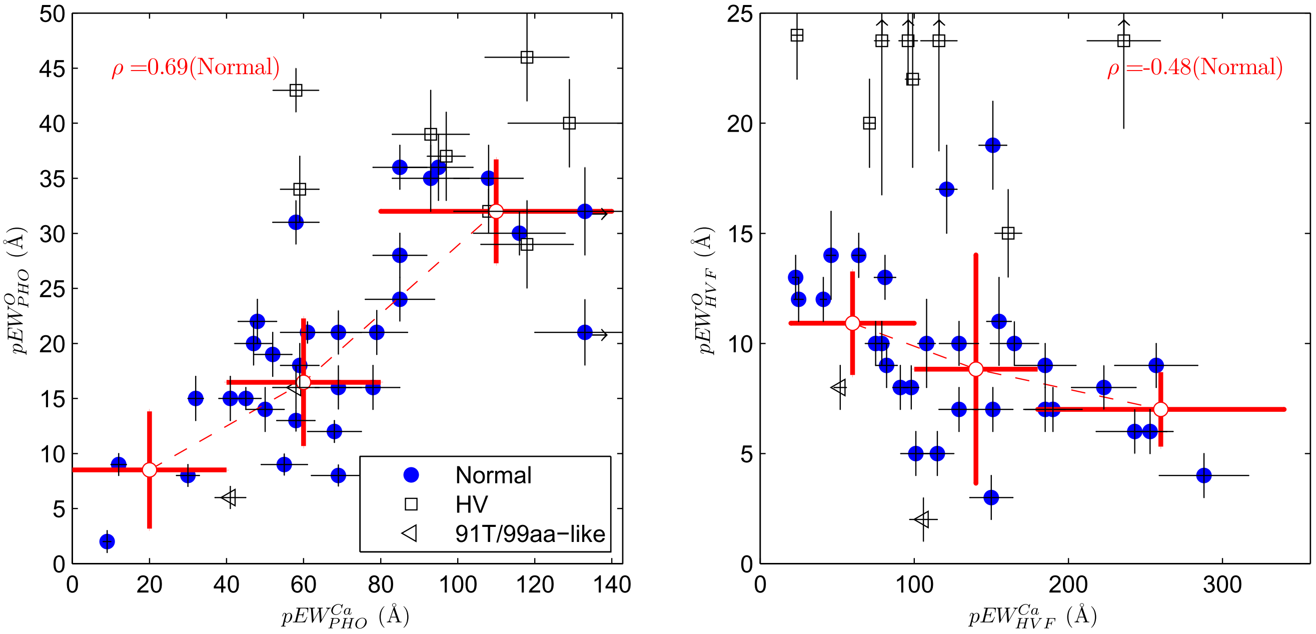

Figure 8. Same as Figure 7 but for a comparison with the Ca II NIR triplet. Similar correlations of the photospheric components and anti-correlations of the HVFs exist between O and Ca, but are less significant compared to those seen between O and Si. The Pearson coefficient is 0.69 for the photospheric component correlation and −0.48 for the HVF anti-correlation. The symbols are the same as indicated in Figure 6.

showing a signature of C II λ6580 absorption. Possibly, this indicates that SNe Ia showing strong C II would form a distinct population.

5. *Correlation and anti-correlation between the absorption strengths of O-HVF and Si- or Ca-HVFs.* From Figures 7 and 8, one can see that there are positive correlations between the photospheric components of O and Si (or Ca) and anti-correlations between their HVFs. These results likely provide evidence that the HVF and photospheric component are created at different characteristic burning layers, which is required in the AE scenario. The HVFs of Si and Ca could be produced from He burning or asymmetric burning in the outermost layers. However, this burning process is not expected to have a significant effect on SN Ia luminosity (or Δm_{15}(B)) due to the small amount of He fuel near the WD surface. Observationally, a SN may show significant deviation from the luminosity–Δm_{15}(B) relation established for SNe Ia (Phillips 1993) if the helium burning plays an important role. On the other hand, this relation seems difficult to explain in the DE scenario, as the density of O is also enhanced in the DE process. This finding does not directly support the IE scenario (as such an effect is not required in the IE), but nor does it reject the IE scenario.
6. *Correlation of O-HVF with* Δm_{15}(B). From Figure 9, one can see that the strength of the O-HVF tends to become stronger for SNe Ia with larger Δm_{15}(B). This tendency is opposite to that seen in the Si-HVF (see Figure 10), where stronger HVFs are only detected in SNe Ia with Δm_{15}(B) $<$ 1.3 mag. Indeed, the behavior of the O-HVF is understandable through general ionization effects. For the SNe Ia with higher luminosities, the outer materials should be at higher ionization stages. This reduces the number of neutral ions, thus depressing the O I line—as is observed. On the other hand, the behavior seen in Si II is difficult to understand solely from this effect—they should also be weakened for higher SN luminosity, but the observations indicate the opposite trend. A larger Si/O pEW ratio is observed in our sample for more luminous SNe Ia, a result which solidly rejects the ionization effect as a possible dominant factor.
7. *Abnormal behavior of HV SNe* Ia. Note, however, that the above conclusion may only apply to SNe Ia with relatively lower expansion velocities (i.e., $v_0^{\rm Si} <$ 12,500 km s^{-1}) since the HV SNe Ia are found to show significant scatter in the mutual correlations and anti-correlations of line strengths between O and Si (or Ca). Large scatter is also seen in the pEW–Δm_{15}(B) correlations (see Figure 9). Thus, an additional mechanism may be needed to explain the formation of the HVFs seen in HV SNe Ia if the measurements of their HVFs are generic. Given that the HVFs of Si in HV SNe have higher velocities than those in Normal SNe, a possible explanation is that the burning effect is weakened as the shells move outward. As an alternative, the HVFs of HV SNe Ia might also arise from the DE of the outer Si shell, perhaps due to CSM interaction. Also, we note that the HV SNe Ia could indeed come from multiple populations, one belonging intrinsically to the same population as Normal SNe (Maeda et al. 2010) and the other exploding in younger environments than Normal SNe (Wang et al. 2013). In this case, it could be natural that the HV SNe show diversity in their HVFs as well. Nevertheless, there remains the caveat that the scatter in the HV SNe Ia could merely arise from the uncertainty in the fitting.

In conclusion, the different behaviors of the HVFs of O and Si (or Ca), in particular the anti-correlations between the HVF strengths, are most naturally explained by a scenario where the HVF regions experience explosive oxygen burning. This result is consistent with, and indeed expected for, the AE scenario.

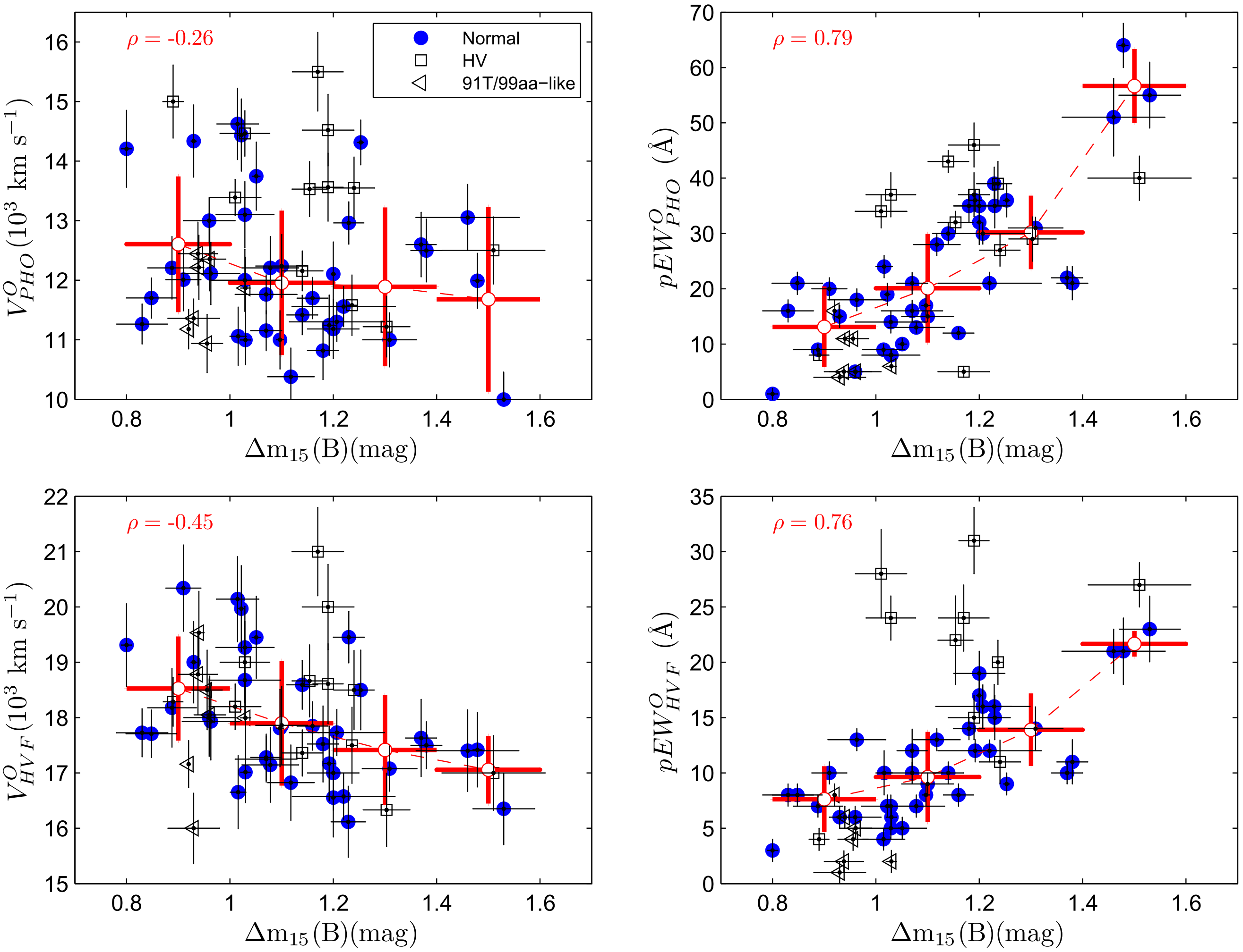

Figure 9. Absorption feature of O I λ7773 as a function of the luminosity indicator Δm_{15}(B) shown for both the photospheric components and the HVFs. SNe Ia with smaller Δm_{15}(B) (or higher luminosity) tend to have larger expansion velocities (left panels) but weaker absorptions (right panels). For the photospheric component (upper panels), the Pearson coefficients of these relations derived for Normal SNe Ia are −0.26 for velocity and 0.79 for line strength. For the HVF, the corresponding coefficients are −0.45 and 0.76 for velocity and line strength, respectively. Red circles represent the mean velocity and the pEWs of O I absorption in bins of Δm_{15}(B), and the error bars represent the width of the bins and 1σ dispersion. The symbols are the same as in Figure 6.

4.2. Constraints on Explosion Models

In addition to clarifying the origin of the HVFs formed at the outermost layers of the exploding WD, our result also places a strong constraint on the still-debated explosion mechanism. The need for the formation of HVFs from nuclear burning leaves us with three possible models: standard delayed detonation (Khokhlov 1991; Gamezo et al. 2005), double detonation through He accretion (Fink et al. 2010; Woosley & Kasen 2011), and the violent merger of two WDs (Pakmor et al. 2011, 2012; Röpke et al. 2012).

It has been suggested that the double-detonation model will mostly produce Fe-peak elements at higher velocities (Woosley & Kasen 2011) rather than intermediate mass elements (IMEs), and C and O will not be present in the He layer. Therefore, this model is not able to explain the HVFs seen at the outermost layers of the ejecta. In the case of violent mergers, the detonation can convert the bulk of the secondary WD to IMEs. The simulation indicates that these IMEs would indeed be left in the low-velocity zone of the ejecta, with typical velocities <20,000 km s^{-1} (Röpke et al. 2012), and no mechanism proposed so far can accelerate the IME-rich region toward higher velocities in this scenario. In addition, for the double-denotation or violent merger models, the "surface" detonation and the resultant HVFs are controlled by the nature of the mass accretion and/or secondary star, while the main features of the SN Ia will be determined by the primary WD. Therefore, it is difficult to understand the luminosity–velocity relation shown in Figures 9 and 10 within the framework of these two models.

On the other hand, the delayed-detonation model has a natural explanation for the observed brighter–faster relation. The diversity of the outer-layer spectral features can be attributed to the difference in the transition density $\rho_{\rm tr}$ from deflagration to detonation in the explosion (Höflich et al. 2002; Woosley et al. 2009). In cases where this transition is delayed, the expansion velocities of the ejecta will decrease and the burned materials like Si (or Ca) will be less abundant at higher velocities because a significant amount of oxygen remains unburned and does not contribute to energy production. This supports the notion that the degree of burning is an important source of spectroscopic diversity among SNe Ia, in addition to progenitor scenarios.

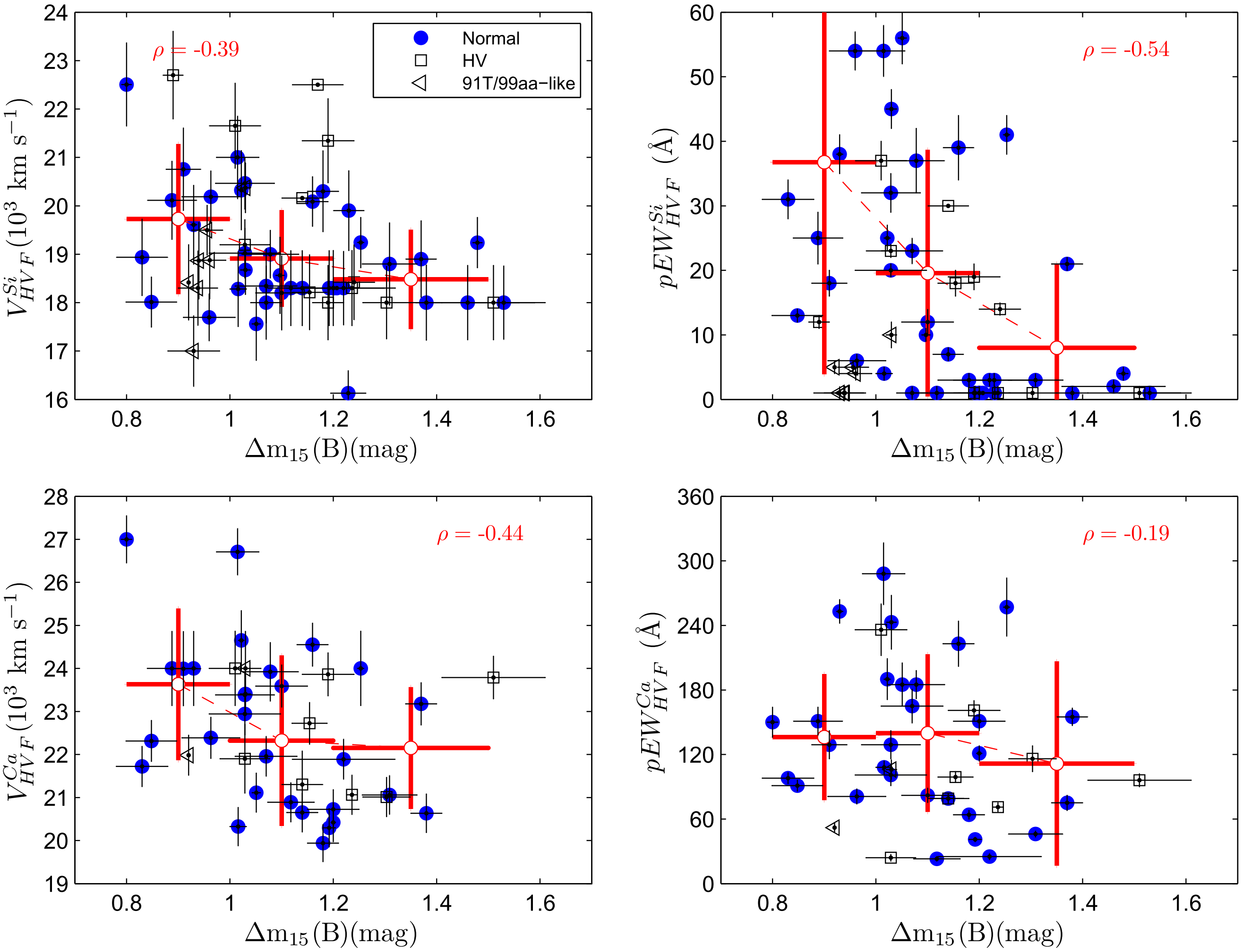

Figure 10. Same as Figure 9 but for correlations of the HVFs of Si II (upper panels) and Ca II (lower panels) with Δm_{15}(B).

In the currently available multi-dimensional simulations for delayed-detonation models, the velocity is still limited to ~20,000 km s^{-1}, but this velocity may be further extended once the outermost region is well resolved, and thus higher resolution simulations may show small clumps (currently not resolved) penetrating into the outermost layer. The observed velocity distributions of O and Si, and the Si/O ratio in the outer layers of the ejecta may be used to constrain the density where the transition from deflagration to detonation occurs through comparisons to the predictions from models (Höflich et al. 2002; Seitenzahl et al. 2013). However, high-resolution simulations are further required to provide a guide to connect the detailed hydrodynamic nature of the explosion and the observed properties we have found in this paper.

5. CONCLUSION

With a large sample of early spectra ($t \leqslant -7$ day), we search for the HVFs in the absorption features of O I λ7773, Si II λ6355, and the Ca II NIR triplet. Double O-HVFs are detected in the early-time spectra of SNe Ia, with velocities comparable to those of the Si-HVFs and Ca-HVFs, respectively. Their mutual correlations and correlations with Δm_{15}(B) are scrutinized.

By comparing the HVFs of O I with those of Si II and Ca II, we attempt to differentiate between various scenarios for the formation of HVFs in the outer layers of the exploding ejecta. From the anti-correlation between the pEWs of the HVF of O I and those of Si II and Ca II, we conclude that oxygen burning is an important contributor to the HVFs of Si and Ca, at least for Normal SNe Ia (see discussion in Section 4.1). This evidence is against the scenario that Si/Ca-HVFs are produced from primordial material (i.e., CSM), while it is in line with the AE scenario. Considering that the HV SNe Ia tend to have distinct explosion environments (Wang et al. 2013; Zhao et al. 2015), and weaker correlations and anti-correlations between O I and Si II (or Ca II), it is possible that the formation of their HVFs is more complicated than that of the Normal counterparts. Indeed the HV subclass may arise from multiple populations, either with a normal-velocity counterpart or without (Maeda et al. 2010; Wang et al. 2013), so this could complicate the analysis of HV SNe Ia. Given that the HVFs of Si in HV SNe Ia have higher velocities than those in Normal SNe Ia, a possible explanation is that the burning effect is weakened as the shells move outward. As an alternative, the HVFs of HV SNe Ia might also arise from the DE of the outer Si shell, perhaps due to CSM interaction.

In addition to distinguishing the origin of the HVFs, the velocities and strengths we have measured for species of C, O, Si, and Ca in this paper could be used to shape a picture of the ejecta, and further constrain the explosion models. The existence of the HVF-I and even the HVF-II of O I λ7773 at higher velocities indicates that the photosphere of SNe Ia is covered by oxygen materials (clumps or a separated shell) from the WD and explosive carbon burning. Current observations suggest that the delayed detonation is the favorable explosion model for at least spectroscopically normal SNe Ia with normal photospheric velocities. Numerical explosion simulations with sufficient resolution are encouraged to focus on the outermost layer to further discriminate the explosion models using the new observational indicators we have found in this paper.

We thank the anonymous referee for suggestive comments to help improve the manuscript. The work is supported by the Major State Basic Research Development Program (2013CB834903), the National Natural Science Foundation of China (NSFC grants 11178003 and 11325313), and China Scholarship Council (CSC 201406210312). The work by K.M. is partly supported by JSPS Grant-in-Aid for Scientific Research (No. 26800100) and by World Premier International Research Center Initiative (WPI Initiative), MEXT, Japan. J.Z. is supported by the Key Research Program of the CAS (grant No. KJZD-EW-M06) and the Western Light Youth Project of CAS. This work was partially supported by the Open Project Program of the Key Laboratory of Optical Astronomy, National Astronomical Observatories, Chinese Academy of Sciences. This research has made use of the CfA Supernova Archive, which is funded in part by the US National Science Foundation through grant AST 0907903. This research has also made use of the Lick Supernova Archive, which is funded in part by the US National Science Foundation.

REFERENCES

Aldering, G., Antilogus, P., Bailey, S., et al. 2006, ApJ, 650, 510
Blondin, S., Matheson, T., Kirshner, R. P., et al. 2012, AJ, 143, 126
Bloom, J. S., Kasen, D., Shen, K. J., et al. 2012, ApJL, 744, L17
Brown, P., Dawson, K. S., Harris, D. W., et al. 2012, ApJ, 749, 18
Chevalier, R. A. 1982, ApJ, 258, 790
Childress, M. J., Filippenko, A. V., Ganeshalingam, M., & Schmidt, B. P. 2014, MNRAS, 437, 338
Cleveland, W. S. 1979, J. Am. Statist., 74, 368
Contreras, C., Hamuy, M., Phillips, M. M., et al. 2010, AJ, 139, 519
Dilday, B., Howell, D. A., Cenko, S. B., et al. 2012, Sci, 337, 942
Filippenko, A. V., Richmond, M. W., Branch, D., et al. 1992, ApJL, 384, L15
Fink, M., Hillebrandt, W., & Röpke, F. K. 2007, A&A, 476, 1133
Fink, M., Röpke, F. K., Hillebrandt, W., et al. 2010, A&A, 514, 53
Fisher, A., Branch, D., Hoflich, P., & Khokhlov, A. 1995, ApJL, 447, L73
Folatelli, G., Morrell, N., Phillips, M. M., et al. 2013, ApJ, 773, 53
Folatelli, G., Phillips, M. M., Morrell, N., et al. 2012, ApJ, 745, 74
Foley, R. J. 2012, ApJ, 744, 38
Gamezo, V. N., Khokhlov, A. M., & Oran, E. S. 2005, ApJ, 623, 337
Ganeshalingam, M., Li, W., Filippenko, A. V., et al. 2010, ApJS, 190, 418
Gerardy, C. L., Höflich, P., Fesen, R. A., et al. 2004, ApJ, 607, 391
Graham, M. L., Foley, R. J., Zheng, W., et al. 2015, MNRAS, 446, 2073
Hachinger, S., Mazzali, P. A., & Benetti, S. 2006, MNRAS, 370, 299
Hamuy, M., Phillips, M. M., Suntzeff, N. B., et al. 2003, Natur, 424, 651
Hatano, K., Branch, D., Fisher, A., Baron, E., & Filippenko, A. V. 1999, ApJ, 525, 881
Hernández, J. I. G., Ruiz-Lapuente, P., Hugo, M. T., et al. 2012, Natur, 489, 533
Hicken, M., Challis, P., Jha, S., et al. 2009, ApJ, 700, 331
Hicken, M., Challis, P., Kirshner, R. P., et al. 2012, ApJS, 200, 12
Hillebrandt, W., & Niemeyer, J. C. 2000, ARA&A, 38, 191
Höflich, P., Gerardy, C., Fesen, R., & Sakai, S. 2002, ApJ, 568, 791
Hsiao, E. Y., Burns, C. R., Contreras, C., et al. 2015, A&A, 578, 9
Iben, I., & Tutukov, A. V. 1984, ApJS, 54, 355
Jha, S., Kirshner, R. P., Challis, P., et al. 2006, AJ, 131, 527
Khokhlov, A. M. 1991, A&A, 245, 114
Krisciunas, K., Suntzeff, N. B., Candia, P., et al. 2003, AJ, 125, 166
Li, W., Bloom, J. S., Podsiadlowski, P., et al. 2011, Natur, 480, 348
Li, W., Filippenko, A. V., Treffers, R. R., et al. 2001, ApJ, 546, 734
Lira, P., Suntzeff, N. B., Phillips, M. M., et al. 1998, AJ, 115, 234
Livne, E., & Glasner, A. S. 1990, ApJ, 361, 244
Maeda, K., Benetti, S., Stritzinger, M., et al. 2010, Natur, 466, 82
Maeda, K., Kawabata, K., Mazzali, P. A., et al. 2008, Sci, 319, 1220
Maguire, K., Sullivan, M., Ellis, R. S., et al. 2012, MNRAS, 426, 2359
Maguire, K., Sullivan, M., Pan, Y.-C., et al. 2014, MNRAS, 444, 3258
Maguire, K., Sullivan, M., Patat, F., et al. 2013, MNRAS, 436, 222
Maoz, D., Mannucci, F., & Nelemans, G. 2014, ARA&A, 52, 107
Marion, G. H., Brown, P. J., Vinkó, J., et al. 2016, ApJ, 820, 92
Marion, G. H., Vinko, J., Wheeler, J. C., et al. 2013, ApJ, 777, 40
Matheson, T., Kirshner, R. P., Challis, P., et al. 2008, AJ, 135, 1598
Mattila, S., Lundqvist, P., Sollerman, J., et al. 2005, A&A, 443, 649
Maund, J. R., Höflich, P., Patat, F., et al. 2010, ApJL, 725, L167
Mazzali, P. A., Benetti, S., Altavilla, G., et al. 2005a, ApJL, 623, L37
Mazzali, P. A., Benetti, S., Stehle, M., et al. 2005b, MNRAS, 357, 200
Mulligan, B. W., & Wheeler, J. C. 2015, arXiv:1505.05145
Nomoto, K. 1982, ApJ, 253, 798
Nomoto, K., Iwamoto, K., & Kishimoto, N. 1997, Sci, 276, 1378
Nomoto, K., Thielemann, F. K., & Yokoi, K. 1984, ApJ, 286, 644
Nugent, P., Sullivan, M., Cenko, S. B., et al. 2011, Natur, 480, 344
Pakmor, R., Hachinger, S., Röpke, F. K., & Hillebrandt, W. 2011, A&A, 528, A117
Pakmor, R., Kromer, M., Taubenberger, S., et al. 2012, ApJ, 747, 10
Parrent, J. T., Thomas, R. C., Fesen, R. A., et al. 2011, ApJ, 732, 30
Patat, F., Chandra, P., Chevalier, R., et al. 2007, Sci., 317, 924
Patat, R., Benetti, S., Cappellaro, E., et al. 1996, MNRAS, 278, 111
Perlmutter, S., Aldering, G., Goldhaber, G., et al. 1999, ApJ, 517, 565
Phillips, M. M. 1993, ApJL, 413, L105
Phillips, M. M., Wells, L. A., Suntzeff, et al. 1992, AJ, 103, 1632
Riess, A. G., Filippenko, A. V., Challis, P., et al. 1998, AJ, 116, 1009
Röpke, F. K., Kromer, M., Seitenzahl, I. R., et al. 2012, ApJL, 750, L19
Schaefer, B. E., & Pagnotta, A. 2012, Natur, 481, 164
Seitenzahl, I. R., Ciaraldi-Schoolmann, F., Röpke, F. K., et al. 2013, MNRAS, 429, 1156
Shen, K. J., & Bildsten, L. 2014, ApJ, 785, 61
Silverman, J. M., & Filippenko, A. V. 2012, MNRAS, 425, 1917
Silverman, J. M., Foley, R. J., Filippenko, A. V., et al. 2012a, MNRAS, 425, 1789
Silverman, J. M., Ganeshalingam, M., Cenko, S. B., et al. 2012b, ApJL, 756, L7
Silverman, J. M., Nugent, P. E., Gal-Yam, A., et al. 2013, ApJS, 207, 3
Silverman, J. M., Vinkó, J., Marion, G. H., et al. 2015, MNRAS, 451, 1973
Sim, S., Fink, M., Kromer, M., et al. 2012, MNRAS, 420, 3003
Sternberg, A., Gal-Yam, A., Simon, J. D., et al. 2011, Sci, 333, 856
Stritzinger, M., Hamuy, M., Suntzeff, N. B., et al. 2011, AJ, 142, 156
Stritzinger, M., Hamuy, M., Suntzeff, N. B., et al. 2002, AJ, 124, 2100
Tanaka, M., Mazzali, P. A., Benetti, S., et al. 2008, ApJ, 677, 448
Tanaka, M., Mazzali, P. A., Maeda, K., & Nomoto, K. 2006, ApJ, 645, 470
Thomas, R. C., Aldering, G., Antilogus, P., et al. 2011, ApJ, 743, 27
Wang, X., Filippenko, A. V., Ganeshalingam, M., et al. 2009a, ApJL, 699, L139
Wang, X., Li, W., Filippenko, A. V., et al. 2009b, ApJ, 697, 380
Wang, X., Li, W., Filippenko, A. V., et al. 2008, ApJ, 675, 626
Wang, X., Wang, L., Filippenko, A. V., Zhang, T., & Zhao, X. 2013, Sci, 340, 170
Webbink, R. F. 1984, ApJ, 277, 355
Whelan, J., & Iben, I. 1973, ApJ, 186, 1007
Woosley, S. E., & Kasen, D. 2011, ApJ, 734, 38
Woosley, S. E., Kerstein, A. R., Sankaran, V., Aspden, A. J., & Röpke, F. K. 2009, ApJ, 704, 255
Zhang, J., Wang, X., Bai, J., et al. 2014, AJ, 148, 1
Zhang, K., Wang, X., Zhang, J. J., et al. 2016, ApJ, 820, 67
Zhai, Q., Zhang, J. J., Wang, X., et al. 2016, AJ, 151, 125
Zhao, X., Wang, X., Maeda, K., et al. 2015, ApJS, 220, 20
Zheng, W., Silverman, J. M., Filippenko, A. V., et al. 2013, ApJ, 778, L15

Monthly Notices
of the
ROYAL ASTRONOMICAL SOCIETY

MNRAS **456,** 314–322 (2016) doi:10.1093/mnras/stv2642

The first Doppler images of the eclipsing binary SZ Piscium

Yue Xiang,[1,2,3⋆] Shenghong Gu,[1,2⋆] A. Collier Cameron,[4] J. R. Barnes[5] and Liyun Zhang[6]

[1] *Yunnan Observatories, Chinese Academy of Sciences, Kunming 650011, China*
[2] *Key Laboratory for the Structure and Evolution of Celestial Objects, Chinese Academy of Sciences, Kunming 650011, China*
[3] *University of Chinese Academy of Sciences, Beijing 100049, China*
[4] *School of Physics and Astronomy, University of St Andrews, Fife KY16 9SS, UK*
[5] *Department of Physical Sciences, The Open University, Walton Hall, Milton Keynes MK7 6AA, UK*
[6] *Department of Physics, College of Science, Guizhou University and NAOC-GZU-Sponsored Center for Astronomy, Guizhou University, Guiyang 550025, China*

Accepted 2015 November 9. Received 2015 November 9; in original form 2015 July 3

ABSTRACT

We present the first Doppler images of the active eclipsing binary system SZ Psc, based on the high-resolution spectral data sets obtained in 2004 November and 2006 September–December. The least-squares deconvolution technique was applied to derive high signal-to-noise profiles from the observed spectra of SZ Psc. Absorption features contributed by a third component of the system were detected in the LSD profiles at all observed phases. We estimated the mass and period of the third component to be about 0.9 $M_{\odot}$ and 1283 ± 10 d, respectively. After removing the contribution of the third body from the least-squares deconvolved profiles, we derived the surface maps of SZ Psc. The resulting Doppler images indicate significant star-spot activities on the surface of the K subgiant component. The distributions of star-spots are more complex than that revealed by previous photometric studies. The cooler K component exhibited pronounced high-latitude spots as well as numerous low- and intermediate-latitude spot groups during the entire observing seasons, but did not show any large, stable polar cap, different from many other active RS CVn-type binaries.

Key words: stars: activity – binaries: eclipsing – stars: imaging – stars: individual: SZ Psc – starspots.

1 INTRODUCTION

SZ Psc is a double-lined partial eclipsing binary composed of an F8V hotter and a K1IV cooler component, with an orbital period of about 3.97 d. The cooler component is larger and more massive than the hotter one and has filled 85 per cent of its Roche lobe (Popper 1988). The rotation of the hotter component is several times slower than its synchronous value, while the cooler component shows synchronous rotation (Eaton & Henry 2007; Glazunova et al. 2008). SZ Psc is very active and classified as a member of RS CVn-type stars (Hall 1976). It shows strong chromospheric emission lines attributed to its cooler component (Ramsey & Nations 1981; Popper 1988; Doyle et al. 1994; Frasca & Catalano 1994). Star-spot activities on the K star were also revealed by many photometric studies (Eaton & Hall 1979; Lanza et al. 2001; Kang et al. 2003; Eaton & Henry 2007). The orbital period of SZ Psc is not constant (Jakate et al. 1976; Tunca 1984; Kalimeris et al. 1995), which is similar to those of many other active binary systems. Kalimeris et al. (1995) derived a periodicity of 56 yr and an amplitude of 4.3×10^{-4} d for the period change of the system. They suggested that it can be explained by a combination of the magnetic activity and the stellar wind.

SZ Psc is suspected to be a triple system. Eaton & Henry (2007) revealed that the systemic velocity of the binary is changing with time, which indicates a third component in SZ Psc. They suggested an amplitude less than 8 km s^{-1} and a period of 1143 or 1530 d for the systemic velocity and thus inferred that the third component is a cool dwarf with a mass of about 0.9–1.0 $M_{\odot}$. They also found weak features in the Na I D lines probably contributed by the third component and estimated its contribution to be about 3–4 per cent of the brightness of SZ Psc. So far, the physical properties of the third component and the outer orbit of SZ Psc are still poorly known.

Zhang & Gu (2008) analysed several chromospheric activity indicators using the spectral subtraction technique and revealed the rotational modulation of the activity on the cooler component of SZ Psc. In addition, they found absorption features in the H_{α} profiles of SZ Psc probably accounted for by prominence-like material around

---

⋆ E-mail: xy@ynao.ac.cn (YX); shenghonggu@ynao.ac.cn (SG)

Published by Oxford University Press on behalf of the Royal Astronomical Society

the K star or mass transfer between two components. Using higher time-resolved spectra, Cao & Gu (2012) also detected absorption features in the Hα profiles, which indicate prominence activity on the cooler component. Their calculation shows that the distance of the prominence from the K star's rotation axis exceeded the Roche lobe of the K star.

Lanza et al. (2001) derived surface images of both components of SZ Psc from long-term photometric observations. They revealed the presence of several active regions on the surface of the cooler component of SZ Psc. One of them is stable and facing the hotter component. Kang et al. (2003) derived unique solutions from light curves with good phase sampling using the star-spot model and revealed that the variations of the shape of light curves are mainly accounted for by spot evolution and migration on the K star of SZ Psc. Eaton & Henry (2007) suggested that the cooler component have many small star-spots rather than a few large ones, because its line profiles lack large distortions.

In order to investigate the star-spot activities on active close binaries, we have carried out a series of high-resolution spectroscopic observations on targets with various stellar parameters and evolutionary stages (Gu et al. 2003; Xiang et al. 2014, 2015). In this work, we have derived the surface images of the K subgiant component of SZ Psc for 2004 November, 2006 September, October, November and December, through the Doppler imaging technique. To our knowledge, there is no Doppler image for SZ Psc before, which could offer us a more detailed distribution of star-spots than light-curve modelling. We shall describe the observations and data reduction in Section 2. The Doppler images will be given and discussed in Section 3 and 4, respectively. In Section 5, we shall summarize this work.

2 OBSERVATIONS AND DATA REDUCTION

The observations of SZ Psc were carried out on 2004 November 20–27, 2006 September 01–06, 2006 October 28–30, 2006 November 28–December 01 and 2006 December 07–11, using the Coudé echelle spectrograph (Zhao & Li 2001) mounted on the 2.16m telescope at the Xinglong station of the National Astronomical Observatories of China. In all observations, a 1024 × 1024 pixel TEK CCD detector was deployed to record the data. As results, the spectral region was about 5600–9000 Å and the resolution was R = 37 000. The observations are the same as that of Zhang & Gu (2008), but the number of spectra we used is more. Their work aimed to investigate chromospheric activities of the cooler component by analysing several indicators, so the data obtained at the eclipsing phases were omitted and some spectra were combined to improve the signal-to-noise ratios. In our case, since the imaging code can handle the eclipse and we can obtain enough S/N for a single observation through the least-squares deconvolution (LSD) calculation, we used all of available spectral data to derive Doppler images for SZ Psc.

The observing log, including the UT date, Heliocentric Julian date, exposure time, is given in Table 1, which is available online. In the next section, we will use the spectral data obtained on 2006 October 28, 29 and 30 to show signatures of the third component, but the last two spectra observed on 2006 October 28 will be excluded because the lines of the F star and the third component nearly coincided.

Apart from SZ Psc, we also observed three slowly-rotating, inactive template stars, HR 6669 (F8V), HR 7948 (K1IV) and HR 248 (M0III), by using the same instrument setup as SZ Psc, to mimic the local intensity profiles of the photosphere and star-spot for each component of SZ Psc, which are required for the two-temperature model of our imaging code.

Table 1. The observing log. The full version of this table is only available online.

UT date	HJD 2450000+	Exp. (s)	S/N Input	S/N LSD
2004-11-20	3330.1055	2400	141	1911
2004-11-20	3330.1365	2400	134	1818
2004-11-21	3331.1073	2400	87	1180
2004-11-27	3337.1254	2400	103	1407
2006-09-01	3980.1557	1800	55	750
2006-09-01	3980.1769	1800	62	847

The spectroscopic data were reduced using the IRAF[1] package in a standard way. The reduction procedure included image trimming, bias subtraction, flat-field dividing, scatter light subtraction, cosmic ray removal, 1D spectrum extraction, wavelength calibration and continuum fitting. The wavelength calibration was carried out using the comparison spectra of the ThAr lamp taken at each night.

Since star-spot signatures are very small, we enhanced the S/N of the observed profiles by applying the LSD (Donati et al. 1997) technique, which combines all available atomic lines in one observed spectrum into a single mean profile. We derived the line list, which contained central wavelength and line depth, for the model atmosphere with $T_{\rm eff} = 5000$ K, from the Vienna Atomic Line Database (VALD; Kupka et al. 1999). The wavelength regions of strong telluric and chromospheric lines were excluded from the line list to prevent their influence. Then we calculated the LSD profile from each observed spectrum with the line list. In the LSD calculations we set the increment per pixel to 4.1 km s^{-1}, according to the resolution power of our spectral data. We list the peak S/N of the observed spectra and the S/N of the corresponding LSD profiles in Table 1. The S/N gain is around 14 for our observations. To correct the errors in radial velocity caused by the instrumental shift, we take advantage of the telluric lines in the spectra, which have negligible velocities, as described by Collier Cameron (1999). An LSD profile was derived using the list of telluric lines for each spectrum; the first one in each observing run was used as the template. Then the shift derived from the cross-correlation between the telluric LSD profile and the template was corrected. As demonstrated by Donati et al. (2003), this method can provide a precision better than 0.1 km s^{-1}.

The spectra of the template stars of the photospheres and star-spots were also deconvolved in the same manner to produce the lookup tables. The linear limb-darkening coefficients for *UBVRI* passbands derived by Claret & Bloemen (2011) were used to obtain the values at the centroidal wavelength of the LSD profile for the photospheres and star-spots. Then 30 limb angles were used for producing the lookup tables.

---

[1] IRAF is distributed by the National Optical Astronomy Observatory, which is operated by the Association of Universities for Research in Astronomy (AURA) under cooperative agreement with the National Science Foundation.

3 DOPPLER IMAGING

3.1 The third component

The LSD profiles of SZ Psc with high S/N offer us an opportunity to detect the spectral line of the third body directly. For example, we select the LSD profiles of the 2006 October data set at the orbital phases when the absorption lines of the F star and the possible third one are not blurred seriously, and plot them as well as the corresponding calculated profiles that represent the immaculate photospheres of the binary in Fig. 1. As shown in this figure, the possible line of the third star was blurred by the highly rotational broadened profile of the cooler component, which is deformed by the star-spots significantly, at all observed phases. According to Eaton & Henry (2007), the period of the triple system is very long, thus we may expect that the velocity of the third body changed little in one observing run relative to the resolution of our spectral data (4.1 km s^{-1}). On the other hand, the deformation of profiles caused by star-spots is changing with orbital phase. Therefore we derive the mean of the residuals between the observed and the calculated profiles to reduce the effect of star-spot distortions. The result is shown in the bottom panel of Fig. 1. As seen in the figure, clear absorption features were detected in the LSD profiles of SZ Psc, which confirmed that SZ Psc is a triple system.

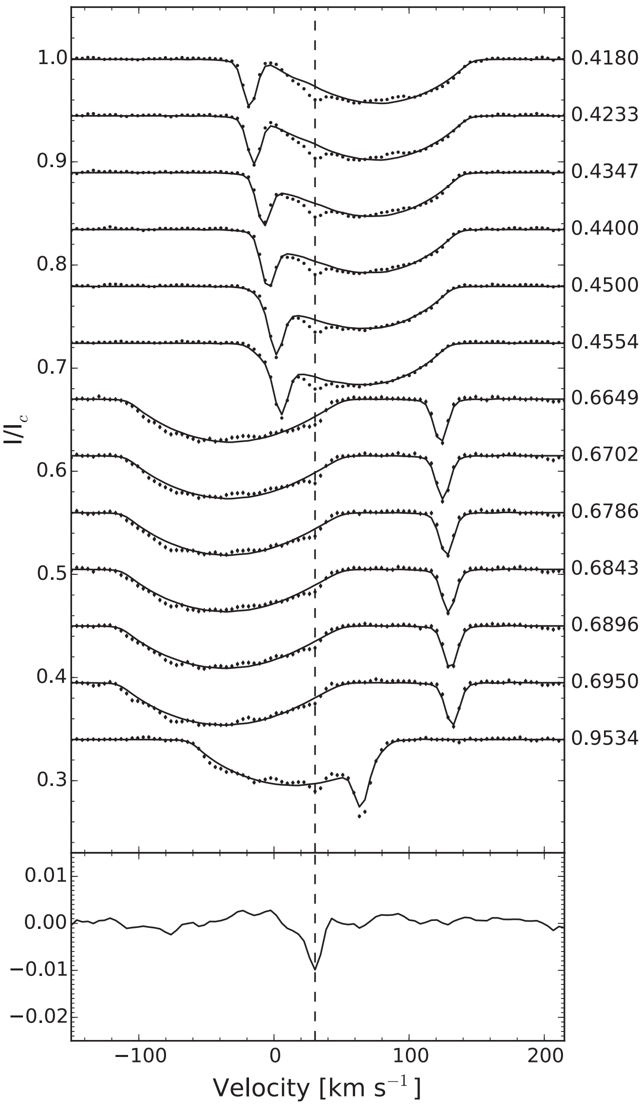

Figure 1. The upper panel shows observed LSD profiles (dots) and calculated profiles of immaculate photosphere (solid lines). The spectra at the orbital phases when the lines of the hotter component and the third one were not blurred significantly were selected. The lower panel shows the mean residual between observed and calculated profiles. The vertical dashed line shows the positions of the absorption features, which are probably contributed by the third component of SZ Psc.

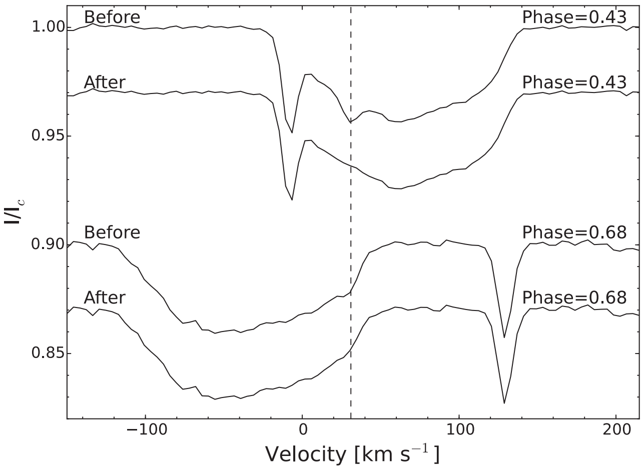

Figure 2. Examples for removing the contribution of the third component. The dashed line shows the position of the profile of the third component.

Table 2. The radial velocities of the third star and the binary system, derived from five observing runs. The errors are 0.4 and 0.6 km s^{-1}, respectively.

Date	RV$_{\rm third}$ km s^{-1}	γ km s^{-1}
2004 Nov.	19.0	8.5
2006 Sept.	3.1	12.7
2006 Oct.	8.4	11.3
2006 Nov.	11.4	10.2
2006 Dec.	12.9	9.7

Since the weak features may produce the same effect as star-spot distortions, we subtracted the contribution of the third component assuming a Gaussian profile. First, we estimated the radial velocity of the third body by cross-correlating the residuals with the template telluric profile for each observing run. In our case, we assumed that the intrinsic velocity of the third body was fixed in one observing run and only changed the velocity depending on the heliocentric motion for each observed phase. Then we created a Gaussian profile and multiply it by a factor depending on the brightness of the binary system at different phases. We also used imaging code to fine tune the profile by minimizing χ^2 as described in the next subsection. Examples for removing the contribution of the third component are shown in Fig. 2. The radial velocity of the third star determined for each observing run is given in the second column of Table 2.

3.2 System parameters

Accurate stellar parameters are required to derive reliable Doppler images and prevent from reconstructing artefacts (Collier Cameron & Unruh 1994), especially for eclipsing binary systems (Vincent, Piskunov & Tuominen 1993). It has been demonstrated that the imaging code can be used to determine stellar parameters for both

Table 3. Adopted stellar parameters of SZ Psc for Doppler imaging. The F hotter component is defined as the primary and the K cooler star is the secondary.

Parameter	Value	Ref.
$q = M_2/M_1$	1.40	a
K_1 (km s^{-1})	103.98	a
K_2 (km s^{-1})	74.2	a
i (°)	69.75	a
T_0 (HJD)	2449 284.4483	a
P (d)	3.96 566 356	a
$v \sin i_1$ (km s^{-1})	3.0 ± 0.6	DOTS
$v \sin i_2$ (km s^{-1})	67.7 ± 1.0	DOTS
$T_{\mathrm{eff},1}$ (K)	6090	b
$T_{\mathrm{eff},2}$ (K)	4910	b
albedo$_1$	1.0	b
albedo$_2$	0.3	b

Notes. References: a. Eaton & Henry (2007); b. Lanza et al. (2001).

of single and binary stars (Barnes et al. 1998, 2004). Fine tuning stellar parameters can be achieved by performing a fixed number of maximum entropy iterations with various combinations of parameters and then finding the best-fitting values that leads to a minimum χ^2. The advantage of this method is that the effect of star-spot distortions on parameter determinations is removed (Barnes et al. 2005).

In our case, first, we took the improved parameters, such as the radial velocity curve amplitudes of the F hotter (K_1) and the K cooler (K_2) components, the inclination of the orbital axis (i), the conjunction time (T_0; the hotter component is behind) and the orbital period (P), from the paper by Eaton & Henry (2007), who used both of the photometric and spectroscopic data; we did not change these values in the following steps. Then we used χ^2 minimization method to determine the projected rotational velocity ($v \sin i$) of each component, from the combined data set of 2006 November and December; and the systematic radial velocity of the binary (γ), from each data set. We list the final adopted values for imaging SZ Psc in Table 3, except for the values of γ for five observing runs, which are given in the third column of Table 2 for comparison. The rotational velocity of the cooler component we derived is obviously lower than that (80 km s^{-1}) determined by Eaton & Henry (2007) but very close to the value (70 km s^{-1}) derived by Strassmeier et al. (1993) and Glazunova et al. (2008).

3.3 Results

We used the imaging code Doppler Tomography of Stars (DOTS; Collier Cameron 1992; Collier Cameron 1997) to perform the maximum entropy regularized iterations to each data set. Minor modifications were made on the imaging code to take into account the non-synchronous rotation of the hotter component of SZ Psc. The vertexes of the surface grid of the hotter component were shifted in each observed phase and given new radial velocities when projected on to the view plane, depending on the rotational velocity of the F star. The observed LSD profiles and the corresponding maximum entropy solutions are plotted in Figs 3 and 4; the Mercator projection of each resulting surface image for the cooler component of SZ Psc is presented in Fig. 5. Note that phase 0.5 on the cooler component faces the hotter component in our images.

In 2004 November, the cooler component of SZ Psc showed significant low-latitude spot patterns around phases 0.15, 0.4 and a pronounced high-latitude spot around phase 0. The image of 2006 September shows an extended intermediate-latitude spot in phase 0.9–1.1. Meanwhile, low latitudes also show the presence of several active regions around phases 0.1 and 0.35. In 2006 October, a pronounced low-latitude spot group appeared between phases 0.6 and 0.7. The image of 2006 November–December indicates pronounced high-latitude spot patterns located at phases 0.1 and 0.75. Besides, there are several low- and intermediate-latitude spot groups around phases 0, 0.25, 0.4, 0.55 and 0.9. In order to show the relationship between the star-spot distribution and the relative positions of two components of SZ Psc clearly, we present the images of the binary system at phases 0, 0.25, 0.5 and 0.75, of one orbital cycle in Fig. 6, using the Doppler image of 2006 November–December. In this figure, we can also see the non-synchronous rotation of the F star from its star-spot rotation. Since the rotational velocity of the hotter component is very small, the spots on it are hardly resolved and mainly produce the changes of the line strength of the F star at different orbital phases.

Poor phase sampling may lead to artefacts in the reconstructed images. Hence, we tested for the reliability of our Doppler images, as discussed in Appendix A (online only). The results indicate that arc-shaped features in all of the surface images of the K star are spurious, especially for large phase gaps, where show pronounced arc-shaped artefacts (e.g. the prominent features at phases 0.4 and 0.8 in 2006 September). In addition, star-spots at unobserved phases may be absent in the reconstructed images.

4 DISCUSSION

We have presented the first Doppler images of the cooler component of SZ Psc for 2004 November and 2006 September–December. The surface images indicate significant star-spot activities for all of the observing seasons. Star-spots on the surface of the cooler component were located at various latitudes and longitudes. The presence of pronounced high-latitude or polar spots was revealed by all of our Doppler images. However, the surface maps do not show large polar cap on the cooler component during our observations, which is commonly found on many other active RS CVn-type binaries (Strassmeier 2009). On the other hand, low-to-mid latitudes of the cooler component of SZ Psc also exhibited numerous star-spot groups during the observations. It should be noted that the smearing and vertical elongation of the star-spot features near the equator of the star is due to the poor latitude discrimination of Doppler imaging around the equator, which will be worse on stars with high inclination and poor phase sampling (Collier Cameron & Unruh 1994; Barnes et al. 2004). The test reconstructions in Appendix A indicate that the lack of a high-latitude spot around phase 0–0.1 in October is most likely due to the phasing, and not to spot evolution. Besides, the high-latitude spot at phase 0.7 is a real feature.

Rapidly rotating cool stars with convective envelop always exhibit star-spot activities. The presence of star-spots in polar regions of rapidly rotating Sun-like stars, which is not shown on the Sun, is predicted by various numerical simulations (Granzer et al. 2000; Mackay et al. 2004). Their results suggested that the Coriolis force and the meridional advection are playing important role in locations of star-spots on rapid rotators. The K star in SZ Psc has a high rotational velocity and shows pronounced high-latitude and polar star-spots, which is consistent with the results of these models. The simulations of the generation and transport of the flux performed by Işık, Schmitt & Schüssler (2011) revealed coexistence of high- and low-latitude star-spot activities on rapidly rotating main-sequence stars. However, their simulations did not show low-latitude features on K-type subgiants, which have been detected by various observations. They suggested that a possible reason is different

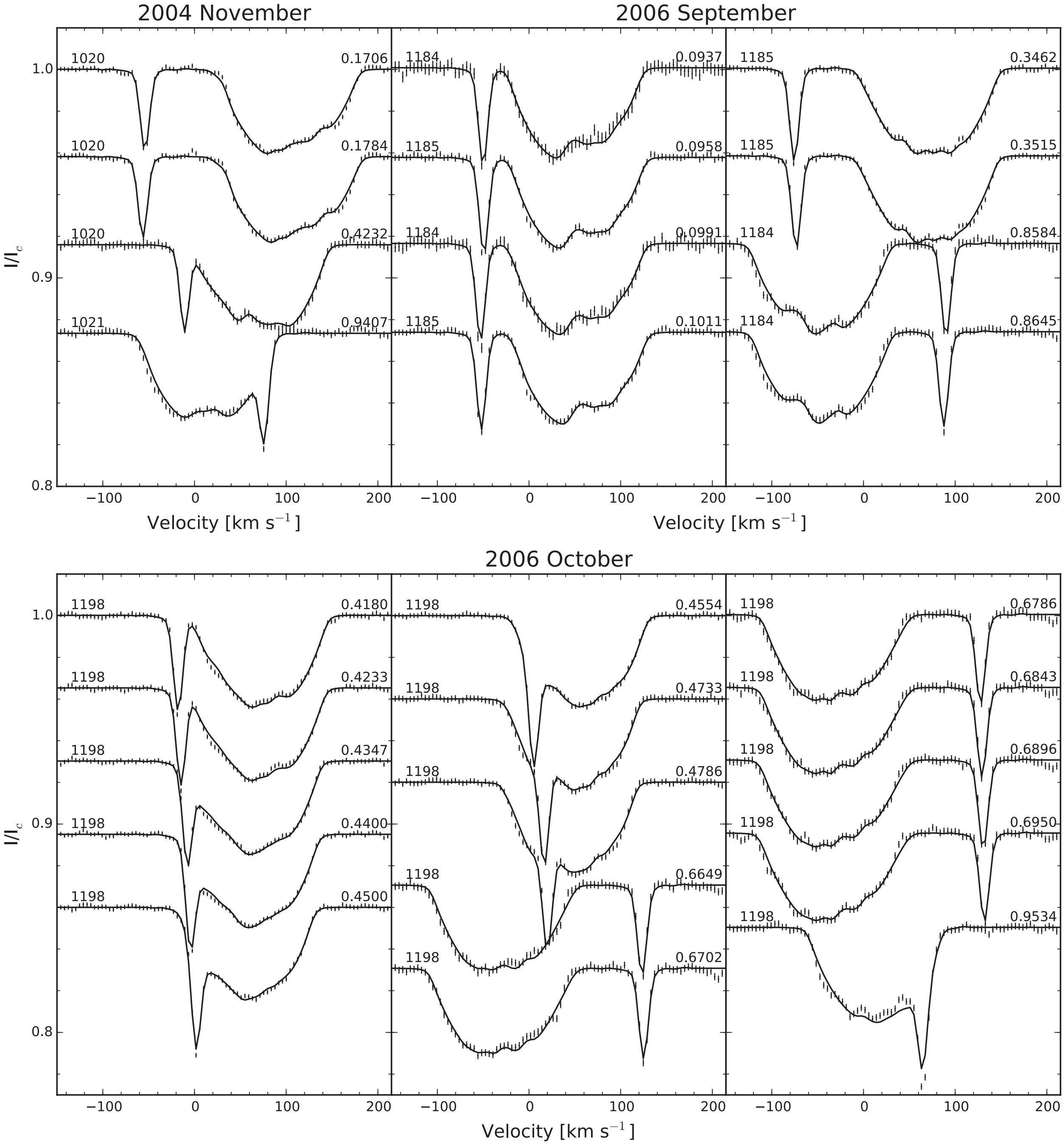

Figure 3. The observed LSD profiles (dots with error bars) and the maximum entropy solutions (solid lines) for 2004 November, 2006 September and 2006 October. The rotation number and orbital phase are marked at the left- and right-hand sides of each profile, respectively.

meridional flow profiles on these stars, which may produce equatorward transport.

Star-spot activities of SZ Psc have been investigated via light-curve modelling by many authors. Their results indicate the spottedness on the surface of the cooler component of SZ Psc in all observing seasons. However, most of these studies only revealed 1–3 large spots on the cooler component for fitting the light curves due to less constraint on spot locations provided by photometric data. The doppler imaging technique can offer us a more detailed distribution of star-spots on the cooler component of SZ Psc. As shown in Figs 5 and 6, our new surface images reveal more complex structure of star-spots on the K subgiant component. A number of star-spot groups are found to be located at various longitudes during our observations. This is very consistent with the result of Eaton & Henry (2007), who found that there should be more than 15 small star-spots on the K star to fit line profile distortions and light curves.

From long-term photometric observations, Lanza et al. (2001) derived spot maps of both components and found several active longitudes on the cooler component. They also revealed two active regions on each component of SZ Psc, facing the other star; the one on the cooler component was long-lived and compact. Our Doppler images also revealed non-uniform longitudinal spot distribution on the cooler component, where star-spots were concentrated in several

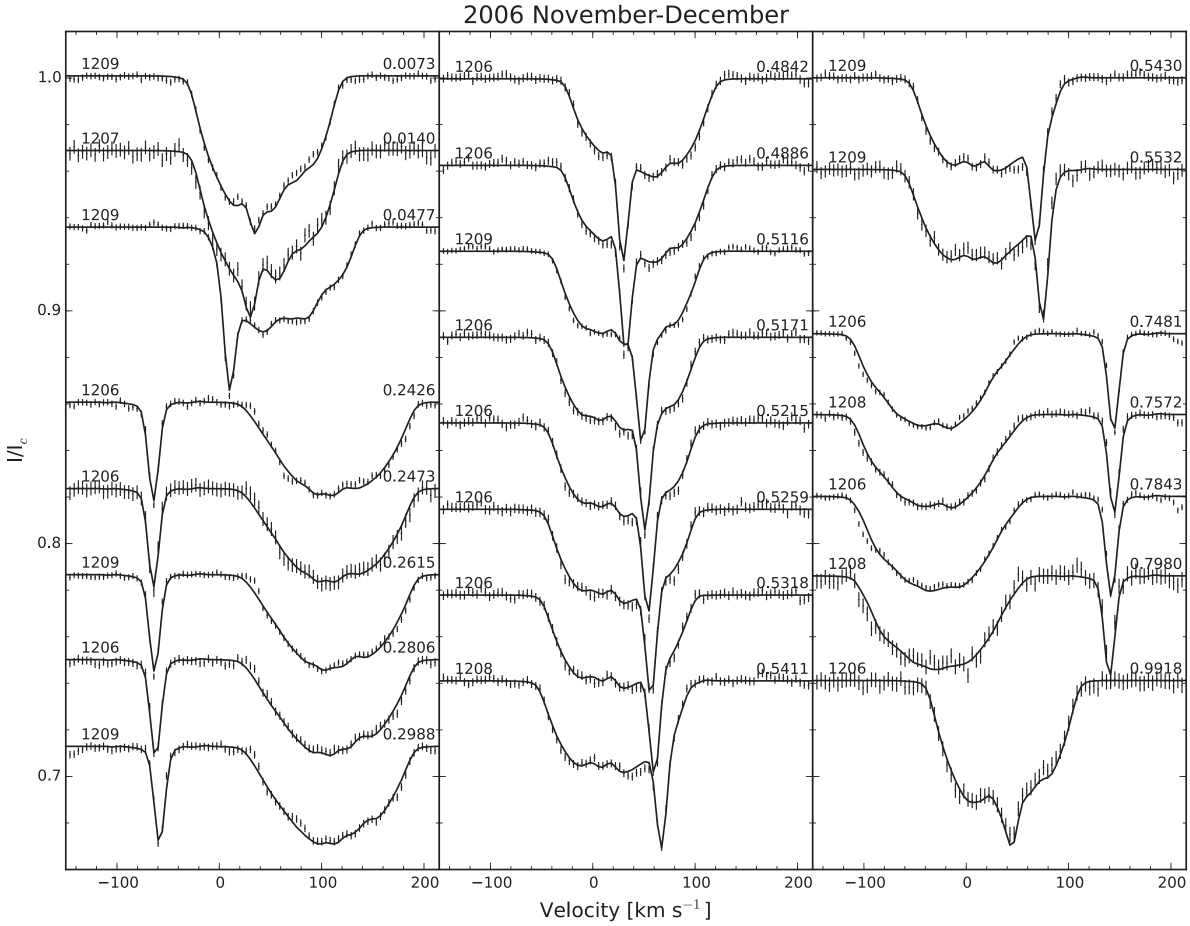

Figure 4. Same as Fig. 3, but for 2006 November–December.

active longitudes, but we do not find any stable active region around the sub-stellar point of the K star during our observations. However, the high-latitude spot around phase 0 seemed to be persistent in most of our images, except for 2006 October, when there is no observation around that phase (see also Fig. A1). The images do not show a clear relationship between the positions of star-spots and the stars. This is different from that on another active binary ER Vul, where low- and intermediate-latitude active regions of two components were always located at the hemispheres facing each other probably due to the tidal interactions (Xiang et al. 2015). As shown in Fig. 6, we also find that the hotter component may exhibit star-spot activity, which is consistent with the results of Lanza et al. (2001). However, due to the low rotational velocity and the non-synchronous rotation of the hotter component, we cannot derive a reliable distribution of star-spots on this star and do not know how the locations of its star-spots are related to the position of the cooler component yet.

The observations in 2006 spanning about three months provide some clues of migrations and evolutions of individual star-spots. As shown in Fig. 5, the low-latitude star-spot groups around phases 0.1 and 0.35 in September seem to migrate to phases 0 and 0.25 three months later. Besides, the pronounced low-latitude spot group around phase 0.65 in October was faded out in December. However, the different phase coverage also results in different spot patterns, especially for high-latitude features. Hence, further Doppler images with complete phase coverage are needed to confirm spot migration and evolution on the cooler component of SZ Psc. Kang et al. (2003) suggested that migrations and evolutions of star-spots are mainly responsible for the shape changes of the light curves of SZ Psc. Using a two-spot model, they fitted the light curves of SZ Psc obtained in 1978–1981 and found two spots on the cooler component had respectively migrated 65° and 170° in longitude during the observations. However, the two-spot model does not offer any information of individual star-spots and thus it is not sure that their results can be attributed to star-spot migrations.

Previously, Zhang & Gu (2008) investigated the chromospheric activity indicators, such as He I D_3, Na I doublet, Hα, Ca II IRT, using the same spectral data sets as ours. The results showed rotational modulation of the chromospheric activity for SZ Psc in 2006. They found that the equivalent widths of several chromospheric lines reached their maximum values at phases 0.25 and 0.75, which indicates two active longitudes on the surface of the cooler component. The emission lines were also strong at phase 0.09. The longitude distribution of star-spots revealed by the 2006 images seems to match the rotational modulation of the chromospheric activity. However, since Zhang & Gu (2008) combined all data spanning about three months, from 2006 September to December, evolutions of star-spots might take place during the observations.

We also compare the star-spot activities of SZ Psc with that of other similar binary systems. The K1 subgiant component of the well-studied RS CVn-type binary HR 1099 has an orbital period of about 2.8 d. Vogt et al. (1999) derived Doppler images for HR 1099 from the observing runs between 1981 and 1992. They found the presence of polar cap in the entire observations, which suggests a large, stable polar spot with lifetime longer than 11 yr.

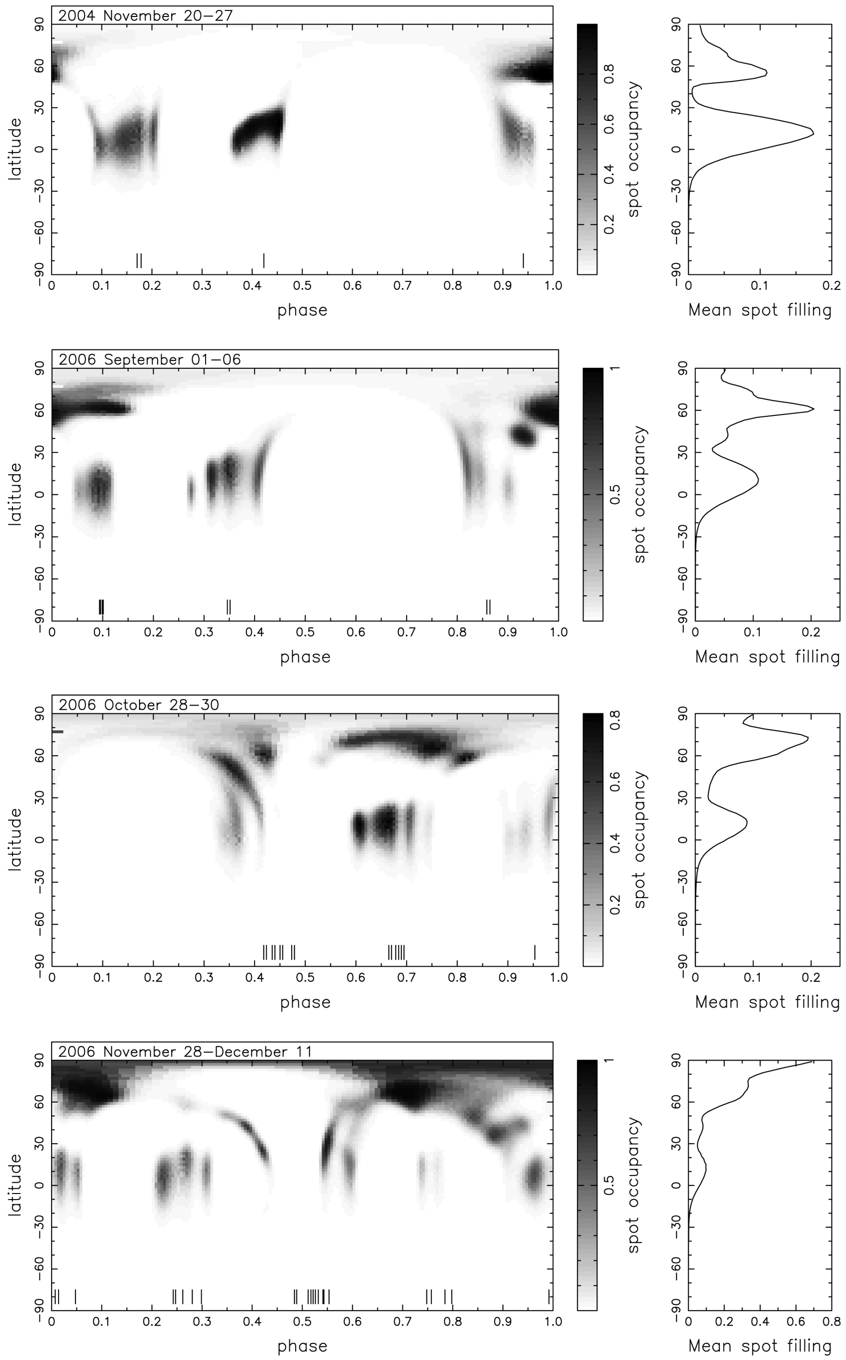

Figure 5. Mercator projection of reconstructed images of 2004 November, 2006 September, 2006 October, and 2006 November–December (from top to bottom). Observing phases are marked by ticks. Mean spot filling factor as a function of latitude is also plotted at the right-hand side of each surface image.

Our Doppler images of SZ Psc do not show any large polar cap spots which are comparable to that on HR 1099, but show several high-latitude or polar spots on SZ Psc instead. From consecutive Doppler images, Vogt et al. (1999) and Strassmeier & Bartus (2000) revealed a complicated behaviour of star-spots on the surface of HR 1099, where several spots at low-to-mid latitudes were migrating in both latitude and longitude and merged with a high-latitude one eventually.

Another similar RS CVn-type system II Peg, which consists of a K2 subgiant and an unseen M dwarf, is one of the most active binaries. The K star exhibits similar latitude distribution of star-spots to SZ Psc, although its rotational velocity is relatively slow (22.6 km s^{-1}). The presence of high-latitude and polar star-spots as well as low-latitude active regions on the surface of II Peg was revealed by many Doppler images for various observing seasons (Gu et al. 2003; Kochukhov et al. 2013; Xiang et al. 2014). Berdyugina et al. (1998) revealed two long-lived active longitudes, which were separated by half of the rotational period and showed persistent longitudinal migrations. Berdyugina, Ilyin & Tuominen (1999) found the strong correlation between the star-spot locations and the strength of the chromospheric emission lines and thus inferred a two-component structure in its chromosphere.

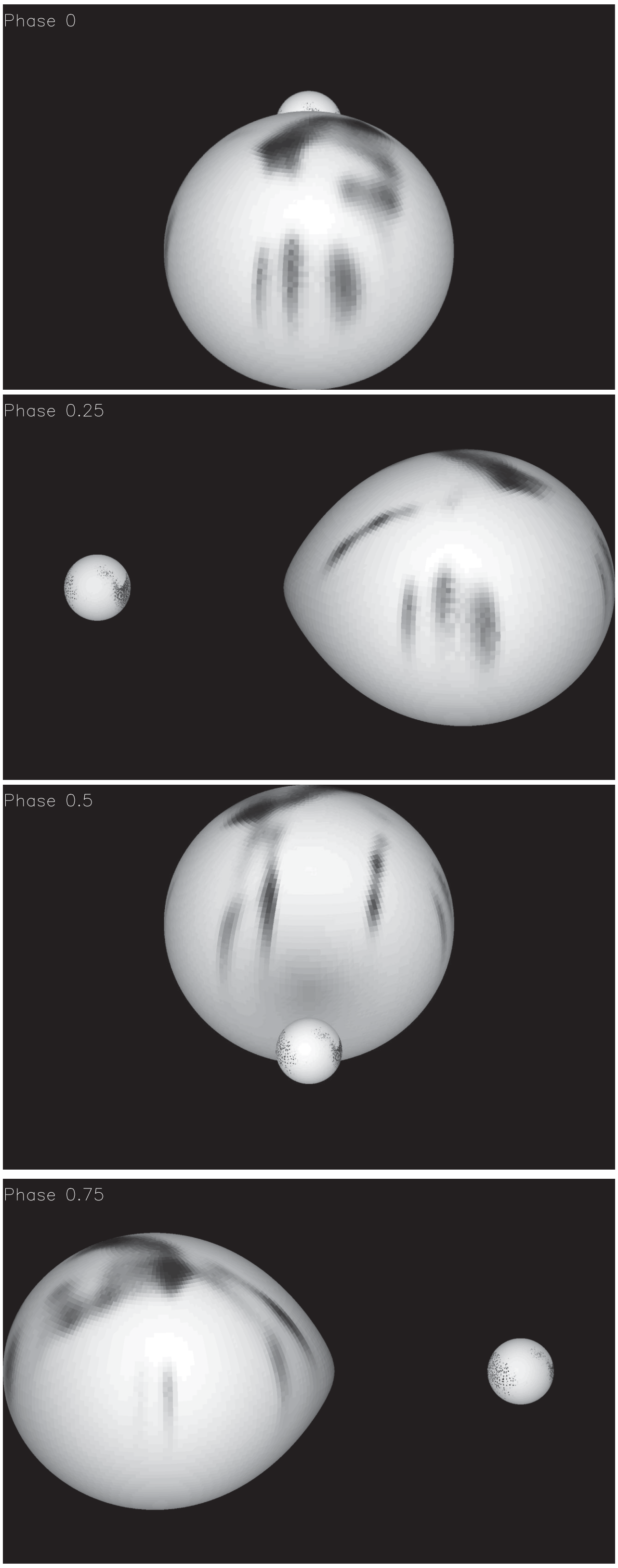

Figure 6. Images of SZ Psc at phases 0, 0.25, 0.5 and 0.75, of one orbital cycle (HJD2454067.04–2454071.00).

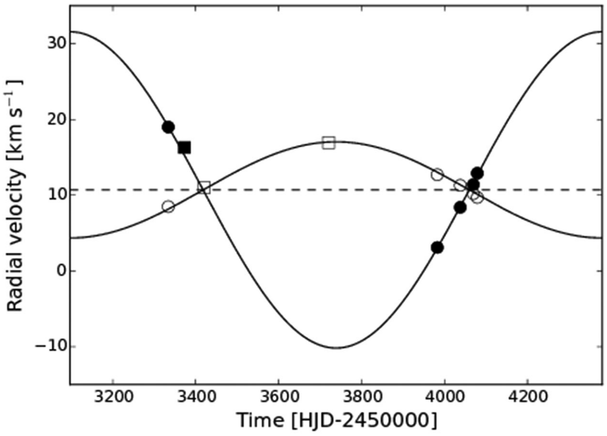

Figure 7. Radial velocities of the third body (filled circles) and the binary system (open circles), derived from each data set. The filled square represents the value derived by Glazunova et al. (2008) for the third component and the open squares represent the systemic velocities derived by Eaton & Henry (2007) for the binary. The lines show the sinusoidal fits.

Apart from deriving Doppler images, we also detected clear signatures of the third star in the LSD profiles of SZ Psc with high S/N, observed at various orbital phases. According to the strength of the absorption line of the third component during non-eclipse phase, we estimated that the contribution of it is about 5 per cent of the luminosity of the system, assuming that its line profile is the same as that of G dwarf star. However, the luminosity of the system is reduced by star-spots all the time, which leads to overestimate of the contribution of the third component. Our result is in good agreement with that of Eaton & Henry (2007), who estimate the contribution of the third component to be 3–4 per cent.

We present the radial velocity curve of the third body and the systemic velocity curve of the binary derived from each data set in Fig. 7. Combining a radial velocity value for the third body derived by Glazunova et al. (2008) in 2005 January and two for the binary system by Eaton & Henry (2007) in 2005 February and November, we try to find a solution to fit both radial velocity curves simultaneously, assuming a simple, circular orbit. As results, we find a period of 1283 ± 10 d and a radial velocity amplitude of 20.9 ± 0.9 km s^{-1} for the third component and 6.3 ± 0.3 km s^{-1} for the binary system (Fig. 7). Therefore, we may infer that the mass of the third star is about 0.9 M$_{\odot}$. Our results are consistent with those of Eaton & Henry (2007), who suggested that the radial velocity amplitude of the binary system is less than 8 km s^{-1} and the mass of the third component is about 0.9–1 M$_{\odot}$. If so, the existence of the third body alone is insufficient to account for the orbital period change of SZ Psc, according to Kalimeris et al. (1995). However, our period estimate is different from that of Eaton & Henry (2007), who found a period of 1143 or 1530 d from phasing their data and Popper (1988)'s, and excluded other periods. A possible reason is that the outer orbit of SZ Psc is eccentric. Because we assumed a circular orbit, we may have systematic errors in the estimate of the orbital period. It is obvious that our available data were too few to derive a precise orbital solution for the triple system, thus more spectroscopic observations are urgently needed in the future.

5 CONCLUSIONS

We derived the first Doppler images of the RS CVn-type binary SZ Psc from the spectral data sets obtained in 2004 and 2006 observing seasons. The new Doppler images reveal significant spot activities on the cooler component of SZ Psc, which is consistent with the results of photometric studies. But the distribution of star-spots is more complex than that revealed by light-curve modelling. The K subgiant exhibits star-spots at various latitudes and longitudes. The images do not indicate any large, stable polar cap, which is different from that of many other RS CVn-type binaries.

Another important result is the detection of clear absorption features contributed by a third component in the high S/N LSD profiles of SZ Psc observed at various orbital phases, which confirms that SZ Psc is a triple system. A preliminary solution of both radial velocity curves of the third star and the binary system indicates that the third component of SZ Psc has a mass of about 0.9 $M_\odot$ and an orbital period of 1283 ± 10 d.

Our results suggest that more high-resolution spectroscopic observations are required to further investigate the star-spot activity and the third body of SZ Psc.

ACKNOWLEDGEMENTS

This work has made use of the VALD data base, operated at Uppsala University, the Institute of Astronomy RAS in Moscow, and the University of Vienna. We would like to thank Prof. Jianyan Wei and Xiaojun Jiang for the allocation of observing time of the Xinglong 2.16-m telescope. We are also very grateful to the anonymous referee for helpful comments and suggestions that significantly improved the clarity and quality of this paper. This work is supported by National Natural Science Foundation of China through grant nos. 10373023, 10773027, 11333006 and U1431114, Chinese Academy of Sciences through project no. KJCX2-YW-T24.

REFERENCES

Barnes J. R., Collier Cameron A., Unruh Y. C., Donati J.-F., Hussain G. A. J., 1998, MNRAS, 299, 904
Barnes J. R., Lister T. A., Hilditch R. W., Collier Cameron A., 2004, MNRAS, 348, 1321
Barnes J. R., Collier Cameron A., Lister T. A., Pointer G. R., Still M. D., 2005, MNRAS, 356, 1501
Berdyugina S. V., Berdyugin A. V., Ilyin I., Tuominen I., 1998, A&A, 340, 437
Berdyugina S. V., Ilyin I., Tuominen I., 1999, A&A, 349, 863
Cao D.-T., Gu S.-H., 2012, A&A, 538, A130
Claret A., Bloemen S., 2011, A&A, 529, A75
Collier Cameron A., 1992, in Byrne P., Mullan D., eds, Lecture Notes in Physics, Vol. 397, Surface Inhomogeneities on Late-Type Stars. Springer-Verlag, Berlin, p. 33
Collier Cameron A., 1997, MNRAS, 287, 556
Collier Cameron A., 1999, in Hearnshaw J. B., Scarfe C. D., eds, ASP Conf. Ser. Vol. 185, Precise Stellar Radial Velocity. Astron. Soc. Pac., San Francisco, p. 233
Collier Cameron A., Unruh Y. C., 1994, MNRAS, 269, 814
Donati J.-F., Semel M., Carter B. D., Rees D. E., Collier Cameron A., 1997, MNRAS, 291, 658
Donati J.-F. et al., 2003, MNRAS, 345, 1145
Doyle J. G., Mitrou C. K., Mathioudakis M., Antonopoulou E., 1994, A&A, 283, 522
Eaton J. A., Hall D. S., 1979, ApJ, 227, 907
Eaton J. A., Henry G. W., 2007, PASP, 119, 259
Frasca A., Catalano S., 1994, A&A, 284, 883
Glazunova L. V., Yushchenko A. V., Tsymbal V. V., Mkrtichian D. E., Lee J. J., Kang Y. W., Valyavin G. G., Lee B.-C., 2008, AJ, 136, 1736
Granzer Th., Schüssler M., Caligari P., Strassmeier K. G., 2000, A&A, 355, 1087
Gu S.-H., Tan H.-S., Wang X.-B., Shan H.-G., 2003, A&A, 405, 763
Hall D. S., 1976, in Fitch W. S., ed., Proc. IAU Colloq. 29, Multiple Periodic Variable Stars. Reidel, Dordrecht, p. 287
Işık E., Schmitt D., Schüssler M., 2011, A&A, 528, A135
Jakate S., Bakos G. A., Fernie J. D., Heard J. F., 1976, AJ, 81, 250
Kalimeris A., Mitrou C. K., Doyle J. G., Antonopoulou E., Rovithis-livaniou H., 1995, A&A, 293, 371
Kang Y. W., Lee W-B., Kim H-I., Oh K-D., 2003, MNRAS, 344, 1227
Kochukhov O., Mantere M. J., Hackman T., Ilyin I., 2013, A&A, 550, A84
Kupka F., Piskunov N., Ryabchikova T. A., Stempels H. C., Weiss W. W., 1999, A&AS, 138, 119
Lanza A. F., Rodonò M., Mazzola L., Messina S., 2001, A&A, 376, 1011
Mackay D. H., Jardine M., Collier Cameron A., Donati J.-F., Hussain G. A. J., 2004, MNRAS, 354, 737
Popper D. M., 1988, AJ, 96, 1040
Ramsey L. W., Nations H. L., 1981, PASP, 93, 732
Strassmeier K. G., 2009, A&ARv, 17, 251
Strassmeier K. G., Bartus J., 2000, A&A, 354, 537
Strassmeier K. G., Hall D. S., Fekel F. C., Scheck M., 1993, A&AS, 100, 173
Tunca Z., 1984, Astrophys. Space Sci., 105, 23
Vincent A., Piskunov N. E., Tuominen I., 1993, A&A, 278, 523
Vogt S. S., Hatzes A. P., Misch A. A., Kürster M., 1999, ApJS, 121, 547
Xiang Y., Gu S.-H., Collier Cameron A., Barnes J. R., 2014, MNRAS, 438, 2307
Xiang Y., Gu S.-H., Collier Cameron A., Barnes J. R., 2015, MNRAS, 447, 567
Zhang L.-Y., Gu S.-H., 2008, A&A, 487, 709
Zhao G., Li H.-B., 2001, Chin. J. Astron. Astrophys., 1, 555

SUPPORTING INFORMATION

Additional Supporting Information may be found in the online version of this article:

Table 1. The observing log.
Appendix A. (http://www.mnras.oxfordjournals.org/lookup/suppl/doi:10.1093/mnras/stv2642/-/DC1)

This paper has been typeset from a TEX/LATEX file prepared by the author.

The Astronomical Journal, 151:104 (9pp), 2016 April doi:10.3847/0004-6256/151/4/104

LONG-TERM OPTICAL STUDIES OF THE BE/X-RAY BINARY RX J0440.9+4431/LS V+44 17

Jingzhi Yan[1], Peng Zhang[1,2], Wei Liu[1,2], and Qingzhong Liu[1]
[1] Key Laboratory of Dark Matter and Space Astronomy, Purple Mountain Observatory, Chinese Academy of Sciences, Nanjing, 210008, China; jzyan@pmo.ac.cn
[2] University of Chinese Academy of Sciences, Yuquan Road 19, Beijing, 100049, China

Received 2015 July 19; accepted 2016 February 24; published 2016 March 29

ABSTRACT

We present the spectroscopic and photometric observations on the Be/X-ray binary RX J0440.9+4431 from 2001 to 2014. The short-term and long-term variability of the Hα line profile indicates that one-armed global oscillations existed in the circumstellar disk. Several positive and negative correlations between the V-band brightness and the Hα intensity were found from the long-term photometric and spectroscopic observations. We suggest that the monotonic increase of the V-band brightness and the Hα brightness between our 2005 and 2007 observations might be the result of a continuous mass ejection from the central Be star, while the negative correlation in 2007–2010 should be caused by the cessation of mass loss from the Be star just before the decline in V-band brightness began (around our 2007 observations). With the extension of the ejection material, the largest circumstellar disk during the last two decades has been observed in our 2010 observations with an equivalent width of approximately -12.88 Å, which corresponds to a circumstellar disk with a size of 12.9 times the radius of the central Be star. Three consecutive X-ray outbursts peaking around MJD 55293, 55444, and 55591 might be connected with the largest circumstellar disk around the Be star. We also use the orbital motion of the neutron star as a probe to constrain the structure of the circumstellar disk and estimate the eccentricity of the binary system to be $\geqslant 0.4$. After three years of the Hα intensity decline after the X-ray outbursts, a new circumstellar disk was being formed around the Be star after our 2013 observations.

Key words: binaries: general – stars: emission-line, Be – stars: individual (RX J0440.9+4431) – X-rays: binaries

1. INTRODUCTION

Be/X-ray binaries are a major subclass of the high mass X-ray binaries in our Galaxy (Liu et al. 2006). The Be/X-ray binary system is composed of a Be star and a neutron star in an eccentric orbit (Reig 2011). The Be star, which is a non-supergiant rapid-rotating B-type star, showed the Balmer lines in emission at least once in its life (Porter & Rivinius 2003). Until the beginning of 2014, no Be-black hole system had been observed in the Be/X-ray binaries (Zhang et al. 2004; Belczynski & Ziolkowski 2009). The first Be-black hole system was first found in MWC 656 by Casares et al. (2014) in 2014 January. The optical emission in the Be/X-ray binary is mainly dominated by the Be star, while the X-ray emission reflects the physical condition in the vicinity of the neutron star. There are two different X-ray outbursts in the Be/X-ray binaries, namely Type I X-ray outbursts and Type II X-ray outbursts. Type I X-ray outbursts usually occurred around the periastron point of the neutron star, while Type II X-ray outbursts could happen at any orbital phase, which might be connected with the warping of the the outermost part of the circumstellar disk (Okazaki et al. 2013).

RX J0440.9+4431 was first discovered as a Be/X-ray binary from the *ROSAT* galactic plane survey data (Motch et al. 1997). Its optical counterpart is the variable star BSD 24–491 = LS V +44 17 = VES 826, with a spectral type of B0.2Ve (Reig et al. 2005). An X-ray pulsation of 202.5 ± 0.5 s was identified from the *RXTE*/PCA light curves of RX J0440.9+4431 in the energy band of 3–20 keV and its X-ray properties were similar to those of the other persistent Be X-ray binary pulsars, 4U 0352+309/X Per and RX J0146.9+6121/LS I+61 235 (Reig & Roche 1999). An X-ray outburst from RX J0440.9+4431 was observed between 2010 March 26 and 2010 April 15 by MAXI (Morii et al. 2010) and the following two small X-ray flares were also detected by *Swift*/BAT (Krivonos et al. 2010). An orbital period of 150.0 ± 0.2 days was estimated from three consecutive X-ray outbursts in the *Swift*/BAT light curve of RX J0440.9+4431 by Ferrigno et al. (2013). A ~32 keV cyclotron resonant scattering feature was discovered in the source spectrum and the magnetic field strength of the neutron star was estimated as $B \simeq 3.2 \times 10^{12}$ G (Tsygankov et al. 2012). The pulse profile has a sinusoidal-like single-peaked shape (Tsygankov et al. 2012) and a narrow dip structure was clearly seen in the pulse profile of the low energy bands (Usui et al. 2012).

The spectroscopic and photometric observations indicate that RX J0440.9+4431 showed a moderately reddened, $E(B-V) = 0.65 \pm 0.05$, which corresponds to a distance of $\sim 3.3 \pm 0.5$ kpc for a B0.2 V star (Reig et al. 2005). The Hα line had a double-peaked profile, varying from a symmetric structure to completely distorted on one side. The equivalent width (EW) of the Hα line and the near-infrared magnitudes showed a correlation and the variability of the Hα line was attributed to the physical changes in the Be star's circumstellar disk (Reig et al. 2005).

In this work, we present our optical spectroscopic observations from 2001 to 2014 and the synchronous photometric observations from 2007 to 2014 of RX J0440.9+4431.

2. OBSERVATIONS

2.1. Optical Spectroscopy

Most of our spectra of RX J0440.9+4431 were obtained with the 2.16 m telescope at Xinglong Station of National Astronomical Observatories. The optical spectroscopy with an intermediate resolution was made with a CCD grating spectrograph at the Cassegrain focus of the telescope. We took the red spectra covering from 5500 to 6700 Å. Sometimes low-

Table 1
Summary of the Spectroscopic Observations of LSV+44 17 between Our 2001 and 2014 Observations

Date (YYYY-MM-DD)	Exposure (s)	MJD	Dispersion (Å pixels^{-1})	EW(Hα) (–Å)	log(V/R)[a]	R_d/R_*
2001 Sep 25	1000	52177.828	1.20	0.85 ± 0.09	−0.16	2.3
2001 Sep 30	1000	52182.822	1.20	0.81 ± 0.05	0.04	2.2
2001 Oct 01	1000	52183.825	1.20	0.66 ± 0.07	−0.11	1.9
2002 Oct 23	1000	52570.776	1.20	1.83 ± 0.03	−0.04	3.7
2002 Oct 23	1200	52570.790	1.20	1.95 ± 0.12	0.00	3.8
2002 Oct 24	1000	52571.856	1.20	2.11 ± 0.15	−0.05	4.0
2002 Oct 24	1000	52571.879	1.20	2.18 ± 0.10	−0.06	4.1
2002 Oct 26	1000	52573.750	1.20	2.46 ± 0.15	−0.04	4.5
2002 Oct 26	1200	52573.763	1.20	2.69 ± 0.19	0.02	4.7
2002 Oct 26	1200	52573.845	1.20	2.16 ± 0.05	0.03	4.1
2002 Oct 27	1200	52574.821	1.20	2.31 ± 0.04	0.04	4.3
2002 Oct 28	1200	52575.785	1.20	2.62 ± 0.15	−0.01	4.6
2003 Oct 14	1200	52926.796	1.20	6.66 ± 0.30	−0.01	8.4
2003 Oct 15	800	52927.842	1.20	6.70 ± 0.49	−0.03	8.5
2003 Oct 16	100	52928.730	2.45	6.42 ± 0.17	…	…
2003 Oct 16	200	52928.732	2.45	6.38 ± 0.06	…	…
2004 Sep 22	900	53270.869	1.20	5.63 ± 0.12	−0.02	7.6
2004 Sep 26	600	53274.811	1.20	5.67 ± 0.08	−0.03	7.6
2005 Oct 21	900	53664.862	1.20	3.22 ± 0.13	0.04	5.3
2005 Oct 23	300	53666.740	2.45	3.01 ± 0.21	0.03	5.1
2005 Oct 24	900	53667.804	1.20	2.97 ± 0.19	−0.01	5.0
2006 Sep 27	1200	54005.829	1.02	6.68 ± 0.15	−0.02	8.5
2006 Sep 28	900	54006.786	1.02	6.09 ± 0.16	−0.05	8.0
2006 Sep 29	900	54007.786	1.02	6.94 ± 0.14	−0.04	8.7
2006 Oct 01	1200	54009.822	1.02	6.84 ± 0.19	0.02	8.6
2006 Oct 02	900	54010.816	1.02	7.47 ± 0.29	−0.01	9.1
2007 Oct 28	900	54401.879	1.02	6.43 ± 0.20	0.00	8.3
2007 Oct 31	900	54404.900	1.02	7.22 ± 0.21	0.05	8.9
2007 Nov 01	600	54405.825	1.02	7.07 ± 0.26	0.03	8.8
2007 Nov 16	600	54420.721	1.02	7.52 ± 0.24	0.02	9.1
2008 Oct 01	1200	54740.761	1.02	10.35 ± 0.51	0.02	11.2
2008 Oct 05	1200	54744.783	1.02	11.28 ± 0.36	0.01	11.8
2008 Oct 06	1200	54745.783	1.02	11.52 ± 0.13	0.01	12.0
2008 Oct 09	1200	54748.814	1.02	11.48 ± 0.13	0.01	12.0
2009 Oct 28	900	55132.841	1.02	11.50 ± 0.12	single	12.0
2009 Oct 29	900	55133.808	1.02	11.46 ± 0.23	0.11	12.0
2010 Oct 12	1200	55481.855	1.02	12.18 ± 0.36	single	12.4
2010 Oct 13	600	55482.861	1.02	12.88 ± 0.49	single	12.9
2010 Oct 14	1200	55483.767	1.02	12.72 ± 0.12	single	12.8
2010 Oct 15	1200	55484.809	1.02	12.59 ± 0.12	single	12.7
2011 Sep 17	300	55821.814	1.02	8.88 ± 0.31	single	10.2
2011 Sep 18	600	55822.790	1.02	9.01 ± 0.41	−0.04	10.2
2011 Sep 18	600	55822.830	1.02	9.05 ± 0.24	−0.10	10.3
2011 Sep 19	600	55823.805	1.02	8.65 ± 0.22	−0.07	10.0
2012 Mar 13[b]	600	55999.600	1.47	8.44 ± 0.12	…	9.8
2012 Mar 14[b]	500	56000.582	1.47	8.70 ± 0.11	…	10.0
2012 Mar 15[b]	300	56001.595	1.47	8.54 ± 0.16	−0.01	9.9
2012 Oct 16	600	56216.847	1.02	5.71 ± 0.16	0.08	7.7
2012 Oct 17	600	56217.773	1.02	5.35 ± 0.08	0.05	7.3
2012 Oct 17	600	56217.887	1.02	5.23 ± 0.11	0.06	7.2
2012 Oct 18	600	56218.779	1.02	5.17 ± 0.10	0.03	7.2
2012 Oct 19	600	56219.776	1.02	5.38 ± 0.04	0.06	7.4
2012 Oct 21	1200	56221.863	1.02	5.33 ± 0.11	0.04	7.3
2012 Oct 22	600	56222.858	1.02	4.96 ± 0.15	−0.01	7.0
2012 Oct 24	1200	56224.803	1.02	5.06 ± 0.12	0.02	7.1
2012 Oct 25	1200	56225.804	1.02	4.98 ± 0.09	−0.01	7.0
2013 Oct 25	300	56590.762	1.02	2.25 ± 0.22	0.06	4.2
2013 Oct 26	300	56591.806	1.02	2.40 ± 0.24	0.05	4.4
2013 Oct 27	600	56592.728	1.02	2.25 ± 0.18	0.10	4.2
2013 Oct 29	300	56594.803	1.02	2.53 ± 0.41	−0.12	4.5
2013 Oct 31	300	56596.705	1.02	2.67 ± 0.13	−0.03	4.7
2013 Nov 17[b]	900	56613.614	1.47	3.32 ± 0.13	−0.06	5.4
2013 Nov 23[b]	240	56619.633	1.47	3.02 ± 0.45	−0.03	5.1

Table 1
(Continued)

Date (YYYY-MM-DD)	Exposure (s)	MJD	Dispersion (Å pixels^{-1})	EW(Hα) (–Å)	log(V/R)[a]	R_d/R_*
2014 Sep 17	1200	56917.793	1.02	5.64 ± 0.16	0.05	7.6
2014 Sep 29	600	56929.836	1.02	5.40 ± 0.06	−0.03	7.4

Notes.
[a] $V/R = (I(V) - I_c)/(I(R) - I_c)$.
[b] The data are obtained with the Lijiang 2.4 m telescope.

resolution spectra (covering from 4300 to 6700 Å) were also obtained. In 2012 March and 2013 November, we also carried out the spectroscopic observations with the Yunnan Faint Object Spectrograph and Camera (YFOSC) instrument of the Lijiang 2.4 m telescope in the Yunnan Astronomical Observatory. The Grism #8 was used with a resolution of 1.47 Å pixel^{-1}, with a spectral range from 5050 to 9750 Å. The journal of our observations is summarized in Table 1, including observational date, exposure time, Modified Julian Date (MJD), and spectral resolution, respectively. All spectroscopic data were reduced with the IRAF[3] package. They were bias-subtracted, flat-field corrected, and had cosmic rays removed. Helium-argon spectra were taken in order to obtain the pixel-wavelength relations.

The EWs of the Hα line have been measured by selecting a continuum point on each side of the line and integrating the flux relative to the straight line between the two points using the procedures available in IRAF. The measurements were repeated five times for each spectrum and the error is estimated from the distribution of these values. The typical error for the measurements is within 1%, arising due to the subjective selection of the continuum. The results of Hα EWs are listed in Table 1 and plotted in Figure 1. The published data of Hα (adopted from Reig et al. 2005), are also plotted in Figure 1 with open symbols.

2.2. Optical Photometry

Since 2007, we performed systematic photometric observations on a sample of X-ray binaries with the 100 cm Education and Science Telescope (EST) and the 80 cm Tsinghua-NAOC Telescope (TNT) at Xinglong Station of NAOC. The EST, manufactured by EOS Technologies, is an altazimuth-mounted reflector with Nasmyth foci at a focal ratio of $f/8$. TNT is an equatorial-mounted Cassegrain system with a focal of $f/10$, made by AstroOptik, funded by Tsinghua University in 2002 and jointly operated with NAOC (Huang et al. 2012). Both telescopes are equipped with the same type of Princeton Instrument 1340 × 1300 thin back-illuminated CCD. The CCD cameras use standard Johnson-Cousins *UBVRI* filters made by Custom Scientific.

The photometric data reduction was performed using standard routines and aperture photometry packages in IRAF, including bias subtraction and flat-field correction. In order to study the variation of the optical brightness, we selected eight reference stars in the field of view (see Figure 2) to derive the differential magnitude of RX J0440.9+4431. We follow the algorithm of Broeg et al. (2009) to compute an artificial companion star using all the eight reference stars with different

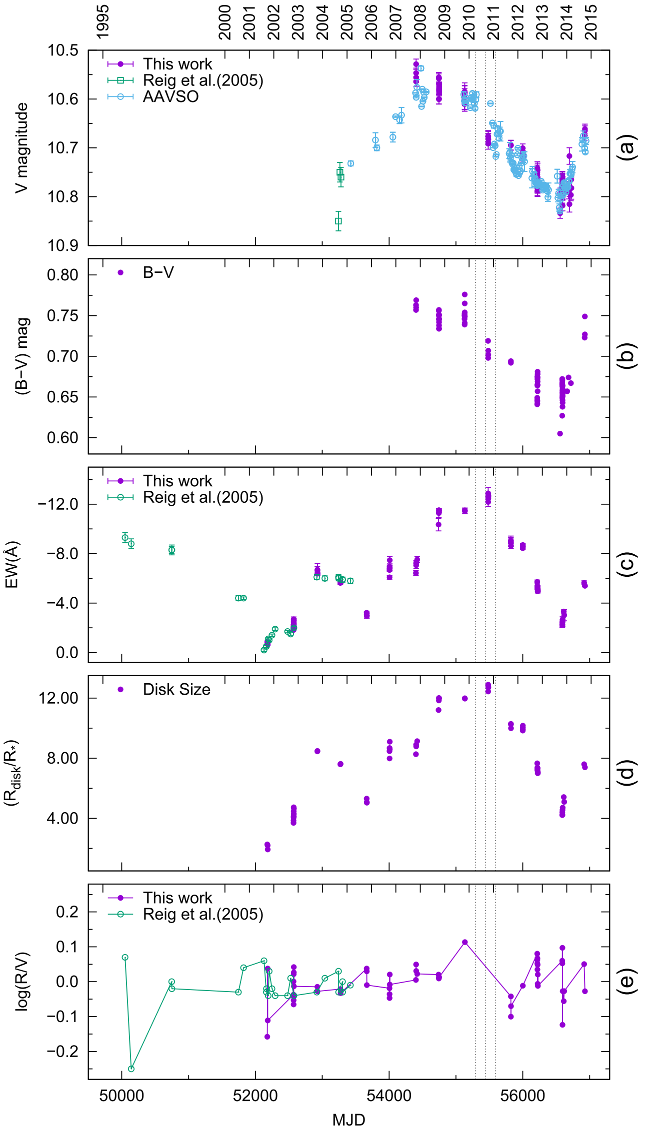

Figure 1. (a) *V*-band brightness between our 2007 and 2014 observations marked with filled circles. The public data adopted from Reig et al. (2005) and *AAVSO* are marked with open symbols; (b) ($B - V$) color index between our 2007 and 2014 observations; (c) the EWs of the Hα lines between our 2001 and 2014 observations marked with filled circles. The data adopted from Reig et al. (2005) are marked with open symbols; (d) the Hα emission region in the unit of the central star radius; (e) the logarithmic function of V/R between our 2001 and 2014 observations marked with filled circles and the public data adopted form Reig et al. (2005) marked with open symbols. Three dashed lines are marked as the time of three consecutive X-ray outbursts, peaked around MJD 55293, 55444, and 55591, respectively. The first day of each year is also marked at the top of each panel with a format of YYYY.

---

[3] IRAF is distributed by NOAO, which is operated by the Association of Universities for Research in Astronomy, Inc., under cooperation with the National Science Foundation.

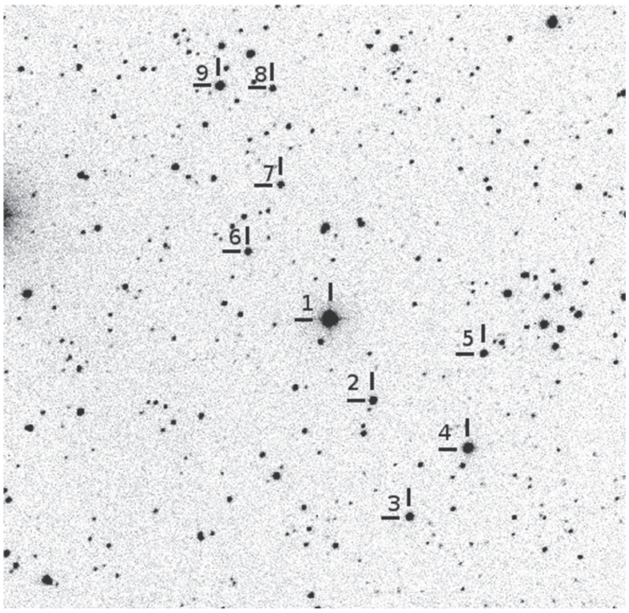

Figure 2. Field stars of RX J0440.9+4431 in *V*-band. RX J0440.9+4431 is marked with #1 and eight reference stars are marked with #2 to #8. North is at the bottom and east is to the left.

weights. The *BVRI* differential magnitudes and their errors are listed in Table 2 and plotted in Figure 3 together with the light curves of the reference star #8 in the right panel. In order to plot the same level with the target star, we add some offsets to the *BVRI* magnitudes of the reference star #8 in Figure 3.

In order to study the long-term optical brightness variability of the source, we also make use of the public optical photometric data from the international database of the American Association of Variable Star Observers (AAVSO).[4] Only the photometric observations made with the Johnson *V*-band filter are used and plotted in Figure 1 with 10 day bins. Using the secondary standard star C5 (our reference star #5 in Figure 2, with $\bar{V} = 14.625$ mag and $\bar{B} = 15.665$ mag) listed in Reig & Fabregat (2015), we also plot our *V*-band results with an offset of ~14.05 mag in Figure 1. In addition, we also adopt the photometric data in Reig et al. (2005) and plot them in Figure 1 with open symbols. The $(B - V)$ color of the source between our 2007 and 2014 observations is also plotted in Figure 1.

2.3. X-Ray Observations

The Burst Alert Telescope (BAT) on board *Swift* (Barthelmy 2000) has monitored RX J0440.9+4431 in the hard X-ray energy band (15–50 keV) since 2005 February. Three consecutive X-ray outbursts were detected between 2010 March and 2011 February (Ferrigno et al. 2013). The positions of the peak time for three X-ray outbursts are marked with three dashed lines in Figure 1.

3. RESULTS

3.1. Long-term and Short-term Variability of the Hα Line

The profile of Hα lines showed a subtle change during each observational run. We select one typical Hα line from each run during our 2001–2014 observations and plot them in Figure 4, which indicates that the Hα profile of RX J0440.9+4431 usually showed an obvious double-peaked profile, except for the observations in 2010, when the Hα line displayed a strong single-peaked structure. Symmetric double-peaked Hα lines were observed during 2001 and 2002 observations. The central depression of the double-peaked Hα line during our 2001 observations was below the stellar continuum, which was also reported in Reig et al. (2005). The intensity of Hα during the 2001 observations was in the lowest level during our 15 year observations. Its intensity showed an obvious increase in the following two years. The Hα intensity showed an abrupt decrease in 2005 and it had the same level as that in 2002. After that, the intensity of the Hα line kept increasing in the following five years and reached a peak value with an averaged EW of approximately −12.9 Å during our 2010 observations. It is interesting that asymmetric profiles with a strong red peak were observed during 2008 and 2009 observations, while only a nearly symmetric single-peaked Hα line was observed during 2010. After 2010, the intensity of the Hα line showed a rapid decline and had an EW of approximately −5 Å during our 2012 October observations. The typical Hα profile during 2011 was an asymmetric structure with a strong violet peak, while the profile during 2012 October with a stronger red peak. Figure 1 indicates that the intensity of the Hα line kept decreasing before our 2013 October observations and it had a faint nearly symmetric double-peaked profile in our 2013 October 26 spectrum. The Hα intensity during our 2013 October observation was at a low emission level, which is similar to the level during our 2012 observations. One moth later, we observed a stronger Hα line during our 2013 November observations. The Hα intensity kept increasing during the following year and its emission during our 2014 observations returned to the level during 2012 observations. The asymmetric Hα lines during our 2014 observations showed rapid changes, with a stronger violet peak in the 2014 September 17 spectrum, while a stronger red peak on 2014 September 29.

Following the method of Reig et al. (2005), we also define the V/R ratio of the Hα line as $V/R = (I(V) - I_c)/(I(R) - I_c)$, where $I(V)$, $I(R)$, and I_c are the intensities of the violet peak, red peak, and continuum, respectively. The V/R ratios of the Hα lines using logarithmic scales are listed in Table 1 and plotted in Figure 1, together with the data adopted from Reig et al. (2005) with open symbols. The V/R ratio could change rapidly within each observational run. In the long run we cannot see any periodic variation from the V/R ratio curves. In order to study the short-term variability of the Hα line, we plot the Hα lines observed in 2012 March and October at Lijiang Observatory and Xinglong Station, respectively, in Figure 5. On the right region of each spectrum, it is marked with the value of $\log(V/R)$. Due to the lower resolution of the spectra observed at Lijiang station, only an asymmetric profile with strong red peak was observed on 2012 March 13 and 14. A clearly double-peaked profile with a stronger red peak was observed on the spectrum of 2012 March 16. During the 2012 October observations, most of our spectra showed as an asymmetric profile with strong violet peak, except for the spectra observed on 2012 October 22 and 25 with a stronger red peak.

3.2. The Circumstellar Disk Size around the Be Star

The intensity of the Hα emission line can be used as an indicator of disk size around the Be star. Hanuschik (1989)

---

[4] http://www.aavso.org/

Table 2
Summary of the *BVRI* Photometric Observations of LSV+44 17 between our 2007 and 2014 Observations

MJD	*B* (mag)	*V* (mag)	*R* (mag)	*I* (mag)
54403.3002	−3.214 ± 0.010	−3.511 ± 0.010	…	…
54403.3895	−3.190 ± 0.010	−3.493 ± 0.010	…	…
54404.3290	−3.176 ± 0.010	−3.476 ± 0.010	…	…
54405.2250	−3.175 ± 0.010	−3.484 ± 0.010	…	…
54744.3119	−3.191 ± 0.010	−3.482 ± 0.010	…	…
54744.3177	−3.189 ± 0.010	−3.485 ± 0.010	…	…
54745.2810	−3.150 ± 0.010	−3.440 ± 0.010	…	…
54745.2863	−3.143 ± 0.011	−3.440 ± 0.010	…	…
54747.2616	−3.180 ± 0.010	−3.462 ± 0.011	…	…
54747.2666	−3.176 ± 0.011	−3.454 ± 0.012	…	…
54747.2703	−3.173 ± 0.011	−3.459 ± 0.012	…	…
54747.3697	−3.188 ± 0.011	−3.462 ± 0.012	…	…
54747.3746	−3.186 ± 0.011	−3.471 ± 0.012	…	…
54747.3794	−3.195 ± 0.011	−3.469 ± 0.013	…	…
54748.3333	−3.173 ± 0.010	−3.459 ± 0.010	…	…
54748.3394	−3.166 ± 0.010	−3.457 ± 0.010	…	…
55129.3571	−3.156 ± 0.012	−3.442 ± 0.012	…	…
55129.3580	−3.158 ± 0.012	−3.450 ± 0.012	…	…
55129.3589	−3.153 ± 0.012	−3.443 ± 0.012	…	…
55130.2832	−3.140 ± 0.012	−3.430 ± 0.012	…	…
55130.2841	−3.151 ± 0.012	−3.430 ± 0.012	…	…
55131.2841	−3.139 ± 0.019	−3.455 ± 0.018	…	…
55131.2850	−3.152 ± 0.019	−3.433 ± 0.018	…	…
55131.3613	−3.159 ± 0.015	−3.453 ± 0.015	…	…
55131.3622	−3.149 ± 0.015	−3.454 ± 0.014	…	…
55132.3163	−3.151 ± 0.015	−3.440 ± 0.014	…	…
55481.2514	−3.090 ± 0.011	−3.349 ± 0.011	−3.430 ± 0.014	−2.076 ± 0.012
55482.3408	−3.126 ± 0.011	−3.364 ± 0.011	−3.415 ± 0.014	−2.074 ± 0.011
55483.2688	−3.120 ± 0.011	−3.362 ± 0.011	−3.412 ± 0.014	−2.085 ± 0.011
55484.2269	−3.111 ± 0.012	−3.358 ± 0.012	−3.416 ± 0.017	−2.085 ± 0.011
55822.2986	−3.113 ± 0.011	−3.345 ± 0.010	−3.383 ± 0.013	−2.017 ± 0.011
55822.3428	−3.112 ± 0.011	−3.346 ± 0.010	−3.379 ± 0.012	−2.008 ± 0.011
55998.9640	…	−3.339 ± 0.009	…	…
56216.2009	−3.081 ± 0.012	−3.262 ± 0.014	−3.271 ± 0.015	−1.813 ± 0.010
56216.2775	−3.096 ± 0.012	−3.285 ± 0.014	−3.275 ± 0.014	−1.822 ± 0.010
56216.3818	−3.079 ± 0.014	−3.265 ± 0.015	−3.219 ± 0.014	−1.801 ± 0.011
56217.2308	−3.083 ± 0.011	−3.265 ± 0.013	−3.241 ± 0.013	−1.819 ± 0.010
56217.3613	−3.114 ± 0.011	−3.299 ± 0.013	−3.262 ± 0.013	−1.834 ± 0.010
56217.3988	…	−3.290 ± 0.015	−3.264 ± 0.014	−1.827 ± 0.010
56218.2771	−3.046 ± 0.012	−3.261 ± 0.013	−3.224 ± 0.013	−1.796 ± 0.010
56218.3386	−3.059 ± 0.012	−3.264 ± 0.013	−3.244 ± 0.013	−1.817 ± 0.010
56218.3571	−3.063 ± 0.012	…	−3.247 ± 0.013	−1.818 ± 0.010
56219.2072	…	−3.258 ± 0.017	−3.233 ± 0.015	−1.801 ± 0.011
56219.2783	−3.054 ± 0.013	−3.258 ± 0.015	−3.218 ± 0.015	−1.801 ± 0.011
56219.3524	−3.058 ± 0.013	−3.270 ± 0.015	−3.254 ± 0.015	−1.815 ± 0.011
56219.3939	…	−3.264 ± 0.015	−3.244 ± 0.015	−1.809 ± 0.011
56221.2912	−3.073 ± 0.012	−3.294 ± 0.014	−3.268 ± 0.014	−1.823 ± 0.011
56221.3704	−3.038 ± 0.012	−3.256 ± 0.015	−3.226 ± 0.018	−1.807 ± 0.011
56222.2445	−3.046 ± 0.012	−3.260 ± 0.013	−3.224 ± 0.013	−1.791 ± 0.010
56222.3022	−3.069 ± 0.012	−3.266 ± 0.013	−3.253 ± 0.013	−1.805 ± 0.010
56222.3430	−3.062 ± 0.012	−3.267 ± 0.014	−3.231 ± 0.013	−1.798 ± 0.010
56222.3824	−3.045 ± 0.012	−3.254 ± 0.014	−3.228 ± 0.013	−1.793 ± 0.010
56558.3092	−3.061 ± 0.013	−3.206 ± 0.011	−3.184 ± 0.011	−1.772 ± 0.009
56558.3107	…	−3.247 ± 0.010	−3.230 ± 0.011	−1.806 ± 0.009
56590.2584	−3.089 ± 0.011	−3.256 ± 0.013	−3.239 ± 0.015	−1.862 ± 0.012
56590.2057	−3.073 ± 0.011	−3.278 ± 0.013	−3.267 ± 0.015	−1.855 ± 0.012
56590.3155	−3.068 ± 0.011	−3.275 ± 0.013	−3.254 ± 0.015	−1.862 ± 0.012
56590.3705	−3.057 ± 0.011	−3.269 ± 0.013	−3.245 ± 0.015	−1.844 ± 0.012
56591.1350	−3.061 ± 0.012	−3.271 ± 0.014	−3.227 ± 0.017	−1.852 ± 0.013
56591.1910	−3.053 ± 0.012	−3.242 ± 0.015	−3.250 ± 0.017	−1.840 ± 0.013
56591.2440	−3.050 ± 0.012	−3.253 ± 0.015	−3.222 ± 0.018	−1.834 ± 0.013
56591.3051	−3.046 ± 0.013	−3.250 ± 0.015	−3.237 ± 0.017	−1.841 ± 0.013
56591.3678	−3.054 ± 0.012	−3.266 ± 0.015	−3.243 ± 0.018	−1.838 ± 0.013
56594.0885	−3.083 ± 0.011	−3.281 ± 0.011	−3.267 ± 0.012	−1.859 ± 0.010

Table 2
(Continued)

MJD	B (mag)	V (mag)	R (mag)	I (mag)
56594.1659	−3.086 ± 0.011	−3.277 ± 0.010	−3.255 ± 0.011	−1.854 ± 0.009
56594.2230	−3.083 ± 0.011	−3.261 ± 0.010	−3.247 ± 0.011	−1.847 ± 0.009
56594.2844	−3.067 ± 0.011	−3.253 ± 0.010	−3.240 ± 0.011	−1.837 ± 0.009
56594.3180	−3.062 ± 0.011	−3.258 ± 0.010	−3.245 ± 0.011	−1.833 ± 0.009
56594.3427	−3.060 ± 0.011	−3.255 ± 0.010	−3.241 ± 0.011	−1.833 ± 0.009
56594.3776	−3.061 ± 0.011	−3.254 ± 0.010	−3.238 ± 0.011	−1.832 ± 0.009
56595.1477	−3.060 ± 0.011	−3.255 ± 0.011	−3.241 ± 0.012	−1.835 ± 0.010
56595.2087	−3.087 ± 0.011	−3.270 ± 0.011	−3.249 ± 0.012	−1.855 ± 0.009
56595.3489	−3.050 ± 0.011	−3.248 ± 0.011	−3.218 ± 0.012	−1.817 ± 0.010
56595.3850	−3.018 ± 0.012	−3.222 ± 0.011	−3.187 ± 0.012	−1.778 ± 0.010
56596.1719	−3.058 ± 0.011	−3.249 ± 0.010	−3.230 ± 0.011	−1.837 ± 0.009
56596.2621	−3.045 ± 0.011	−3.245 ± 0.011	−3.229 ± 0.012	−1.828 ± 0.010
56664.1353	−3.062 ± 0.013	−3.259 ± 0.012	−3.246 ± 0.014	…
56685.0365	−3.035 ± 0.015	−3.249 ± 0.014	−3.238 ± 0.016	−1.868 ± 0.010
56697.0873	…	−3.323 ± 0.017	−3.332 ± 0.021	−1.901 ± 0.012
56697.9922	…	−3.225 ± 0.016	−3.256 ± 0.020	−1.873 ± 0.012
56719.9717	−3.037 ± 0.013	−3.244 ± 0.012	−3.261 ± 0.014	−1.894 ± 0.010
56724.9660	…	−3.275 ± 0.015	−3.290 ± 0.019	−1.914 ± 0.010
56725.9744	…	−3.258 ± 0.023	−3.257 ± 0.026	−1.904 ± 0.012
56926.3058	−3.102 ± 0.012	−3.365 ± 0.010	−3.403 ± 0.012	−2.079 ± 0.009
56928.3238	−3.007 ± 0.017	…	−3.376 ± 0.023	−2.050 ± 0.012
56929.2070	−3.090 ± 0.013	−3.379 ± 0.010	−3.417 ± 0.013	−2.093 ± 0.009
56929.2953	−3.108 ± 0.012	−3.375 ± 0.010	−3.410 ± 0.013	−2.087 ± 0.009

found a correlation between the ratio of the Hα double peak separation ($\Delta v_{\rm peak}$) and the Be star projected rotational velocity $v\sin i$, and the Hα EWs with a factor of two scatter given by

$$\log[\Delta v_{\rm peak}/2v\sin i] = -0.32\log(\mathrm{EW}_{\mathrm{H}\alpha}) - 0.20, \tag{1}$$

where, $\mathrm{EW}_{\mathrm{H}\alpha}$ is in a unit of −Å. Assuming a Keplerian circumstellar disk around the Be star, we can estimate the disk size using Huang's formula (Huang 1972),

$$R_d/R_* = (2v\sin i/\Delta v_{\rm peak})^2, \tag{2}$$

where R_d is the radius of the Hα emission region, and R_* is the radius of the central Be star. Following Equation (3) in Coe & Kirk (2015), we can estimate the disk size around the Be star using the Hα EWs with the following equation

$$\log\sqrt{R_*/R_d} = -0.32\log(\mathrm{EW}_{\mathrm{H}\alpha}) - 0.20. \tag{3}$$

The Hα emission regions are calculated by Equation (3) in the unit of the central star radius R_* and the results are listed in Table 1 and shown in Figure 1. The maximum circumstellar disk with a radius of $\sim 12.9R_*$ corresponds to the strongest Hα emission during our 2010 observations.

3.3. The Long-term Evolution of the BVRI-band Brightness

Our photometric observational results of RX J0440.9+4431 with *BVRI* filters are plotted in Figure 3. Only *BV*-band data are available between the 2007 and 2009 observations. After 2010, we monitored the source with the *BVRI* filters. Figure 3 indicates that the *V*-band brightness of RX J0440.9+4431 showed a continuous decrease between our 2007 and 2013 observations and it had a minimum brightness around MJD 56595. The source faded by about 0.3 mag during the six years. After our 2013 October observations, a rapid increase was observed in the *V*-band photometry and the system brightened by about 0.15 mag within nearly one year. The *B*-band observations showed the same evolutionary way as the *V*-band observations, but the *B*-band magnitudes decreased more slowly between our 2007 and 2013 observations with an amplitude of ~0.2 mag. The brightness of the source in *RI*-band observations has a more rapid variation. After the system reached a minimum brightness during our 2013 observations, the R and I brightness increased about 0.2 and 0.3 mag, respectively, within about one year.

The $(B-V)$ color index kept declining on average between our 2007 and 2013 observations, which indicates that the spectrum of the Be star became bluer and bluer. The bluer spectrum means that the contribution of the disk emission decreased by the depletion of the inner part of the disk once the mass supply from the Be star stopped around our 2007 observations (we will discuss this in the next section). With the diffusion of the circumstellar material around the Be star out into the outer space, its spectrum became bluer and bluer. When the brightness began to increase after the 2013 October observations, a reddening of $(B-V)$ was also observed simultaneously. This means that a new circumstellar disk was being formed around the Be star.

3.4. The Correlation between the Hα Intensity and the V-band Brightness

Due to the lack of *V*-band data before MJD ~ 53250, we can only study the correlation between the Hα emission and the *V*-band brightness after that time. Figure 1 indicates that the *V*-band brightness increased continuously between MJD ~ 53250 and ~54400 with an amplitude of 0.2 mag on average. During this period, the intensity of the Hα line showed a complicated variability. Subtle changes were observed between our 2003 and 2004 Hα intensity, changing from approximately –6.5 Å to approximately –5.8 Å. The Hα line had a low emission level with an averaged EW of −2.9 Å during our 2005 October observations. The optical brightness had an obvious increase after our 2005 observations. The intensity of the Hα line also became stronger during our 2006 September observations with

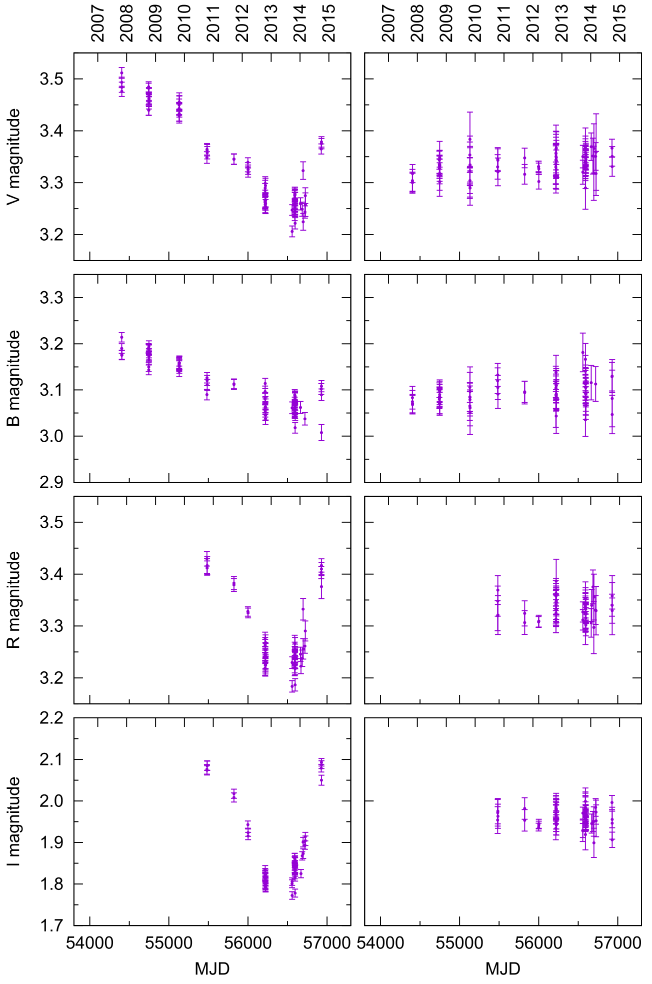

Figure 3. *BVRI* differential photometry of RX J0440.9+4431. The offsets of 4.2, 4.4, 4.1, and 3.8 mag, are added to the *V*, *B*, *R*, and *I* differential light curves of the reference star #8 and plotted them in the right panels. The first day of each year is also marked at the top of each panel with a format of YYYY.

an averaged EW of approximately −7.0 Å. The Hα emission during our 2007 November observations had the same level as that during 2006, while the synchronous photometric observations indicates that the *V*-band brightness of the system had the highest level in the last two decades. After that, the *V*-band brightness showed a continuous decline between our 2007 and 2013 September observations, with an amplitude of ~0.3 mag, which has been discussed above. Unlike the evolutionary behavior of the *V*-band brightness, the intensity of the Hα line showed an abrupt increase during our 2008 September observations. Its intensity kept increasing in the following two years and reached a maximum with an EW of approximately −12.9 Å during our 2010 October observations, which was the strongest Hα emission that has been reported in the literature. After 2010, the Hα intensity showed a continuously rapid decline and had a minimum EW of approximately −2.25 Å during our 2013 October observations, changing with an amplitude of ~10.35 Å within three years of observations. After they reached their minima around our 2013 October observations, both of the *V*-band brightness and the intensity of the Hα line showed a rapid increase. The *V*-band magnitude brightened about ~0.17 mag and the intensity of the Hα line was in a level of approximately −5.6 Å during our 2014 September observations.

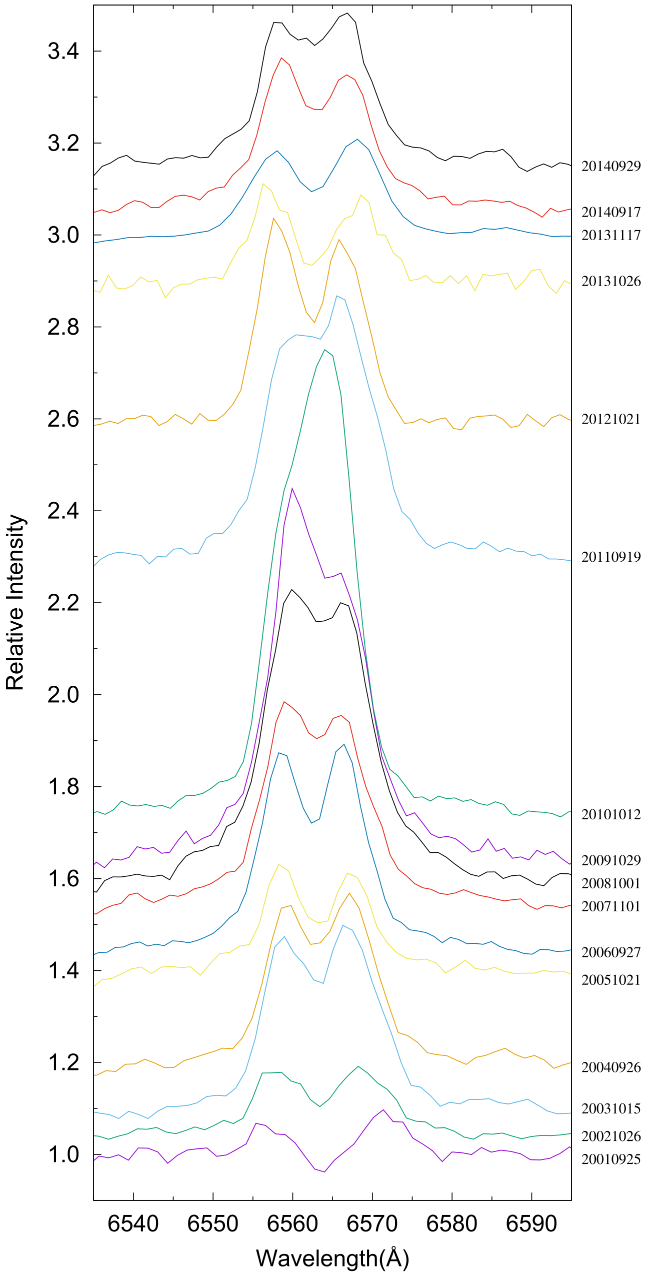

Figure 4. Hα profiles selected from our 2001–2014 observations (separated in rectified intensity for clarity). Observational date is marked on the right part of each spectrum with a format of YYYYMMDD.

4. DISCUSSIONS

We present the long-term optical spectroscopic observations (2001–2014) and the synchronous photometric observations (2007–2014) on the Be/X-ray binary RX J0440.9+4431. Combining with the public data, we studied the short-term and long-term activities of the system in optical.

The profile of the Hα line displays short-term and long-term V/R variability, which has been discussed by Reig et al. (2005). The cyclic V/R changes are observed in many single

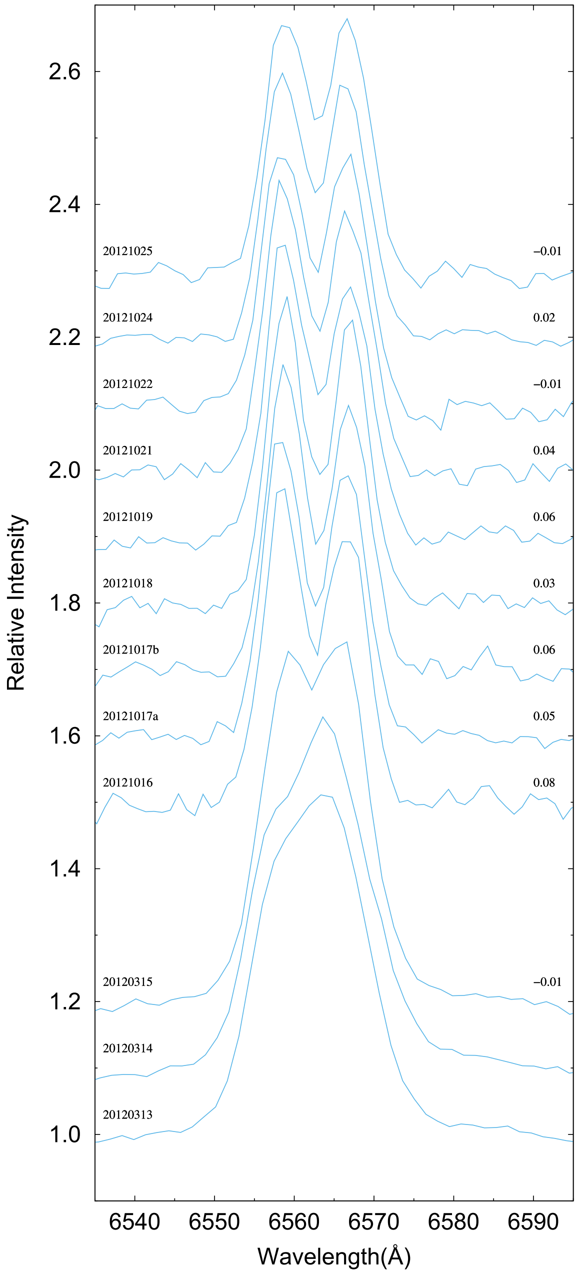

Figure 5. Evolution of the Hα profiles during our 2012 observations. The observational date and the V/R ratio are marked on the left and right wings of each spectrum, respectively.

Be stars (Porter & Rivinius 2003) and they might be connected with the density distributions of the material in the circumstellar disk. The popular theoretical explanations for the V/R variations is the one-armed oscillation model (Okazaki 1991). The V/R variability in Be/X-ray binaries might be also connected with the tidal interaction between the neutron star and the circumstellar disk around the Be star (Oktariani & Okazaki 2009).

As we discussed in the last section, the EW of the Hα line can be used to estimate the disk radii around the Be star. The disk loss event occurred in early 2001 had been discussed in Reig et al. (2005). A new disk was reforming during our 2001 and 2002 observations, and it reached a relative stable state during the following two years of observations. With the dissipation of the material, a relatively small disk was observed during our 2005 observations. After then both the optical brightness and the intensity of the Hα line showed rapid increase, implying that a larger disk had been formed during our 2006 observations. It is interesting that the emission of the Hα line during our 2007 observations had the same level as that during our 2006 observations, while the V-band brightness during 2007 was in the highest state for all the observations with ~10.5 mag. Even more interesting is that the intensity of the Hα line still kept increasing when the optical brightness declined after our 2007 observations. The circumstellar disk had the largest radii during our 2010 observations. For the next three years, the disk was in another rapid dissipation phase. The circumstellar disk was in another low state during our 2013 October observations, which is similar to our 2005 observations. A new circumstellar disk was being reformed after 2013 October.

The monotonic increase of the system brightness and the intensity of the Hα line observed between our 2005 and 2007 observations indicates that a larger and denser circumstellar disk was being formed during this period, which might be the result of a continuous mass ejection from the central Be star. The negative correlation between the V-band brightness and the Hα emission during our 2007–2010 observations (see Figure 1) should have a different physical mechanism with the positive one. The similar negative correlation between the optical brightness and the intensity of the Hα line has been observed in other Be/X-ray binaries, such as A 0535+26 (Yan et al. 2012b), 4U 0115+63 (Reig et al. 2007), MXB 0656–072 (Yan et al. 2012a), and SAX J2103.5+4545 (Camero et al. 2014). As discussed in our previous papers (Yan et al. 2012a, 2012b), only the inner parter of the circumstellar disk has a major contribution to the variability of the V-band brightness, while the Hα emission comes from the nearly entire disk (Slettebak et al. 1992; Stee et al. 1998; Carciofi 2011). The negative correlation between the V-band brightness and the Hα emission during our 2007–2010 observations might be explained as the result of the cessation mass supply from the Be star in the system. Rivinius et al. (2001) and Meilland et al. (2006) suggested that a low-density region would be developed after several months of the mass ejection from the surface of the Be star, basing on the observational results and the theoretical calculations, respectively. The mass ejection stopped just before the decline in the V-band brightness began (around our 2007 observations). This cessation of mass supply from the central Be star caused the depletion in the innermost part of the circumstellar disk and the fading in the V-band brightness. In another hand, the outer part of the disk was still growing. In other words, the viscous diffusion was still going on in the outer part. This could explain the increase of the Hα intensity when the V-band brightness showed a decrease after our 2007 observations.

When the outer part of the disk moved near the periastron passage of the neutron star, accretion rate onto the neutron star would increase and an Type I X-ray outburst could be triggered. Three consecutive X-ray outbursts, peaking around MJD 55293, 55444, and 55591, respectively, were observed in Be/X-ray binary RX J0440.9+4431. On the other hand, the circumstellar disk would be truncated by the orbital motion of the neutron star (Okazaki & Negueruela 2001). Figure 1 indicates that the intensity of the Hα line showed a rapid decline after our 2010 observations. Its EW changes from −12.9 to −2.3 Å within three years. After three years of the Hα intensity decline, the Be star in the system was in another active phase and a new circumstellar disk was being formed.

In Be/X-ray binaries, the neutron star can be used as a probe to constrain the physical structure of the circumstellar disk around the Be star. The three consecutive X-ray outbursts of RX J0440.9+4431 took place during the time when the system showed a strong Hα emission. During the X-ray outburst, the size of the circumstellar disk should be larger than the Roche lobe radius of the Be star at the periastron. The Roche lobe radius of a Be star R_L is given approximately by

$$R_L = D\frac{0.49q^{2/3}}{0.69q^{2/3} + ln(1 + q^{1/3})} \tag{4}$$

(Eggleton 1983). Here q is the mass ratio M_*/M_X, where M_* and M_X are the mass of the Be star and the neutron star, respectively, and D is the instantaneous distance between the binary. We can also estimate the semimajor axis of the binary system with Kepler's third law, $a^3 = P_{\rm orb} \times G(M_* + M_{\rm X})/4\pi^2$. For a B0.2Ve star (Reig et al. 2005), we take its mass and radius as $M_* = 18\ M_\odot$ and $R_* = 8\ R_\odot$, respectively (Negueruela & Okazaki 2001). The canonical mass of a neutron star is fixed to $M_{\rm X} = 1.4\ M_\odot$. With an orbital period of $P_{\rm orb} = 150$ days (Ferrigno et al. 2013), the semimajor axis is derived as $a \sim 319.4\ R_\odot \sim 40\ R_*$ and the Roche lobe size $R_L = 0.54D$. When the system showed the X-ray outburst, the largest circumstellar disk with a size of $R_d \sim 12.9\ R_*$ during our 2010 observations should larger than the Roche lobe radius of the Be star at the periastron. With these parameters, we can estimate the eccentricity of the binary orbit by $R_L(\text{periastron}) = 0.54a(1\text{–}e) \leqslant R_d(\max)$. Therefore, the Be/X-ray binary RX J0440.9+4431 should have an eccentric orbit with $e \geqslant 0.4$. Actually, the Be disk is not always circular. Sometimes, a Be disk becomes elongated. If the Be disk was elongated toward the periastron, the maximum disk size to be used in the above condition would be larger than the observed maximum Hα emission radius.

5. CONCLUSIONS

In this work, we report our optical spectroscopic and photometric observations on the Be/X-ray binary RX J0440.9+4431 between 2001 and 2014. The profile of the Hα line showed long-term and short-term V/R variabilities, which might be connected with the one-armed oscillation in the disk. The positive and negative correlations between the optical brightness and the intensity of the Hα line were observed in the system. The monotonic increase of the V-band brightness and the Hα brightness between our 2005 and 2007 observations might be the result of a continuous mass ejection from the central Be star. The negative correlation between the V-band optical brightness and the intensity of the Hα line between our 2007 and 2010 observations could be explained as the result of the cessation of mass supply from the central Be star around our 2007 observations. With the stop of the mass supply from the Be star, a low density region would be formed in the inner part of the disk and the fading in the V-band brightness was resulted in. But, the viscous diffusion was still going on in the outer part and the intensity of the Hα line kept increasing when the brightness showed a decline. With the outward motion of the ejected material, the largest circumstellar disk and the strongest Hα emission line during the last 20 years, with an EW of approximately −12.9 Å, was observed during our 2010 observations, which trigged three consecutive X-ray outbursts between 2010 March and 2011 February. After three years of the Hα decline, a new circumstellar disk was being formed after our 2013 observations. As a probe of the circumstellar disk structure, we use the orbital motion of the neutron star to estimate the eccentricity of the system as $e \geqslant 0.4$.

We thank the anonymous referee for his/her valuable comments to our manuscript. This work was supported in part by the 973 Program of China under grant 2013CB837000; the National Natural Science of China under grants 11273064, 11433009 and 11573071; and the Strategic Priority Research Program of CAS (under grant number XDB09000000). This work was partially Supported by the Open Project Program of the Key Laboratory of Optical Astronomy, National Astronomical Observatories, Chinese Academy of Sciences. We also acknowledge the support of the staff of the Lijiang 2.4 m telescope. Funding for the telescope has been provided by CAS and the People's Government of Yunnan Province.

REFERENCES

Barthelmy, S. D. 2000, Proc. SPIE, 4140, 50
Belczynski, K., & Ziolkowski, J. 2009, ApJ, 707, 870
Broeg, Ch., Fernández, M., & Neuhauser, R. 2009, AN, 326, 134
Camero, A., Zurita, C., Gutiérrez-Soto, J., et al. 2014, A&A, 568, 115
Carciofi, A. C. 2011, in IAU Symp. 272, Active OB Stars: Structure, Evolution, Mass Loss, and Critical Limits (Cambridge: Cambridge Univ. Press), 325
Casares, J., Negueruela, I., Ribo, M., et al. 2014, Natur, 505, 378
Coe, M. J., & Kirk, J. 2015, MNRAS, 452, 969
Eggleton, P. P. 1983, ApJ, 268, 368
Ferrigno, C., Farinelli, R., Bozzo, E., et al. 2013, A&A, 553, 103
Hanuschik, R. W. 1989, Ap&SS, 161, 61
Huang, F., Li, J. Z., Wang, X. F., et al. 2012, RAA, 12, 1585
Huang, S.-S. 1972, ApJ, 171, 549
Krivonos, R., Tsygankov, S., Lutovinov, A., Turler, M., & Bozzo, E. 2010, ATel, 2828, 1
Liu, Q. Z., van Paradijs, J., & van den Heuvel, E. P. J. 2006, A&A, 455, 1165
Meilland, A., Stee, P., Zorec, J., & Kanaan, S. 2006, A&A, 455, 953
Morii, M., Kawai, N., Sugimori, K., et al. 2010, ATel, 2527, 1
Motch, C., Haberl, F., Dennerl, K., et al. 1997, A&A, 323, 853
Negueruela, I., & Okazaki, A. T. 2001, A&A, 369, 108
Okazaki, A. T. 1991, PASJ, 43, 75
Okazaki, A. T., Hayasaki, K., & Moritani, Y. 2013, PASJ, 65, 41
Okazaki, A. T., & Negueruela, I. 2001, A&A, 377, 161
Oktariani, F., & Okazaki, A. T. 2009, PASJ, 61, 57
Porter, J. M., & Rivinius, T. 2003, PASP, 115, 1153
Reig, P. 2011, Ap&SS, 332, 1
Reig, P., & Fabregat, J. 2015, A&A, 574, A33
Reig, P., Larionov, V., Negueruela, I., et al. 2007, A&A, 462, 1081
Reig, P., Negueruela, I., Fabregat, J., et al. 2005, A&A, 440, 1079
Reig, P., & Roche, P. 1999, MNRAS, 306, 100
Rivinius, Th., Baade, D., Stefl, S., & Maintz, M. 2001, A&A, 379, 257
Slettebak, A., Collins, G. W., II, & Truax, R. 1992, ApJS, 81, 335
Stee, P., Vakili, D., Bonneau, D., & Mourard, D. 1998, A&A, 332, 268
Tsygankov, S. S., Krivonos, R. A., & Lutovinov, A. A. 2012, MNRAS, 421, 2407
Usui, R., Morii, M., Kawai, N., et al. 2012, PASJ, 64, 79
Yan, J. Z., Chaty, S., Zurita Heras, J. A., Li, H., & Liu, Q. Z. 2012a, ApJ, 753, 73
Yan, J. Z., Li, H., & Liu, Q. Z. 2012b, ApJ, 744, 37
Zhang, F., Li, X.-D., & Wang, Z.-R. 2004, ApJ, 603, 663

The Astronomical Journal, 151:125 (16pp), 2016 May doi:10.3847/0004-6256/151/5/125

UV–OPTICAL OBSERVATION OF TYPE Ia SUPERNOVA SN 2013dy IN NGC 7250

Qian Zhai[1,2,3], Ju-Jia Zhang[1,3], Xiao-Feng Wang[4], Tian-Meng Zhang[5], Zheng-Wei Liu[6], Peter J. Brown[7], Fan Huang[4],
Xu-Lin Zhao[4], Liang Chang[1,3], Wei-Min Yi[1,3], Chuan-Jun Wang[1,3], Yu-Xin Xin[1,3], Jian-Guo Wang[1,3], Bao-Li Lun[1,3],
Xi-Liang Zhang[1,3], Yu-Feng Fan[1,3], Xiang-Ming Zheng[1,3], and Jin-Ming Bai[1,3]
[1] Yunnan Observatories (YNAO), Chinese Academy of Sciences, Kunming 650011, China; jujia@ynao.ac.cn
[2] University of Chinese Academy of Sciences, Chinese Academy of Sciences, Beijing 100049, China
[3] Key Laboratory for the Structure and Evolution of Celestial Objects, Chinese Academy of Sciences, Kunming 650011, China
[4] Physics Department and Tsinghua Center for Astrophysics (THCA), Tsinghua University, Beijing 100084, China
[5] National Astronomical Observatories of China (NAOC), Chinese Academy of Sciences, Beijing 100012, China
[6] Argelander-Institut für Astronomie, Auf dem Hügel 71, D-53121, Bonn, Germany
[7] George P. and Cynthia Woods Mitchell Institute for Fundamental Physics & Astronomy, Texas A. & M. University, Department of Physics and Astronomy, 4242 TAMU, College Station, TX 77843, USA

Received 2015 August 8; accepted 2016 February 16; published 2016 April 26

ABSTRACT

Extensive and independent observations of Type Ia supernova (SN Ia) SN 2013dy are presented, including a larger set of *UBVRI* photometry and optical spectra from a few days before the peak brightness to ~200 days after explosion, and ultraviolet (UV) photometry spanning from $t \approx -10$ days to $t \approx +15$ days refers to the *B* band maximum. The peak brightness (i.e., $M_{\mathrm{B}} = -19.65 \pm 0.40$ mag; $L_{\max} = [1.95 \pm 0.55] \times 10^{43}$ erg s^{-1}) and the mass of synthesized ^{56}Ni (i.e., $M(^{56}\mathrm{Ni}) = 0.90 \pm 0.26\,M_{\odot}$) are calculated, and they conform to the expectation for an SN Ia with a slow decline rate (i.e., $\Delta m_{15}(B) = 0.90 \pm 0.03$ mag). However, the near infrared (NIR) brightness of this SN (i.e., $M_{\mathrm{H}} = -17.33 \pm 0.30$ mag) is at least 1.0 mag fainter than usual. Besides, spectroscopy classification reveals that SN 2013dy resides on the border of "core normal" and "shallow silicon" subclasses in the Branch et al. classification scheme, or on the border of the "normal velocity" SNe Ia and 91T/99aa-like events in the Wang et al. system. These suggest that SN 2013dy is a slow-declining SN Ia located on the transitional region of nominal spectroscopic subclasses and might not be a typical normal sample of SNe Ia.

Key words: galaxies: individual (NGC 7250) – supernovae: general – supernovae: individual (SN 2013dy)

1. INTRODUCTION

SN 2013dy, an SN Ia, was discovered at roughly a magnitude of ~17.2 mag on UT July 10.45 2013 (Universal Time is used throughout this paper) in an unfiltered image of the galaxy NGC 7250 by the Lick observatory supernova search (Casper et al. 2013). Its coordinates are R.A. = $22^{\mathrm{h}}18^{\mathrm{m}}17\overset{\mathrm{s}}{.}60$, decl. = $+40^{\circ}34'9''\!.54$ (J2000) and it is located at $2''\!.3$ west and $26''\!.4$ north of the center of the host galaxy (see Figure 1). It was well studied by Zheng et al. (2013, hereafter Z13) at early phase, based on the dense photometries ($t \approx -17$ to $+3$ days; the variable *t* denotes the time since *B* band maximum and is used throughout this paper) and spectra ($t \approx -16$ to -6 days). Pan et al. (2015, hereafter P15) also investigated this SN from the *BVrRiIZYJH* band photometry and UV–optical spectroscopy data set spanning from ~0.1 to ~500 days after explosion.

Based on the discovery and pre-discovery images, Z13 constrained the first-light time (i.e., JD 2456483.18) of SN 2013dy to be only 2.4 ± 1.2 hr before the first detection. This makes it the earliest known detection of an SN Ia. They inferred an upper limit on the radius of the progenitor star of $R_0 \leqslant 0.25\,R_{\odot}$ through the early-time observations, which is consistent with that of a white dwarf progenitor. The early rising light curve exhibits a broken power law with exponents of 0.88 and then 1.80, which suggests that the rising exponent of SNe Ia may vary with time. Besides, Z13 derived that SN 2013dy reached a *B* band maximum at ~17.7 days after first light with $m(B)_{\max} = 13.28 \pm 0.01$ mag. A spectrum taken at $t \approx -16$ days reveals a C II λ6580 absorption line comparable in strength to Si II λ6355. Such strong C II lines are not usually seen in normal SNe Ia, but similar features have been observed in a few superluminous SNe Ia (i.e., SN 2009dc; Taubenberger et al. 2010). This feature suggests that the progenitor star had significant unburned material.

In this paper, we present extensive and independent UV–optical photometry and optical spectroscopy of SN 2013dy. Additionally, the *BVRI* photometry of Z13 and the *BVRIYJH* photometry of P15 are also involved in the analysis. Note that the UV and *U* band photometry in this paper are unique and important for further investigation since these data are not involved in Z13 and P15. On the other hand, our dense *BVRI* photometry and low-resolution spectra can fill the observational gaps in Z13 and P15 in the first 200 days after explosion, which makes SN 2013dy a super well-sampled SN Ia. That could provide highly constraining information in investigating the properties of SNe Ia. Furthermore, the large data set presented in this paper can help us further understand the diversity of SNe Ia and their impact on cosmological applications.

The organization of this paper is as follows. Observations and data reductions are described in Section 2. Section 3 investigates the light and color curves, and estimates the extinction owing to the host galaxy. Section 4 presents the spectra evolution. In Section 5, we estimate the distance of this SN, construct the spectral energy distribution (SED) and bolometric light curve, estimate the mass of synthesized ^{56}Ni, and discuss the spectroscopic classification. A brief summary is given in Section 6.

2. OBSERVATIONS AND DATA REDUCTIONS

NGC 7250, the host galaxy of SN 2013dy, is an irregular galaxy characterized by the "dual cores" in the center; see

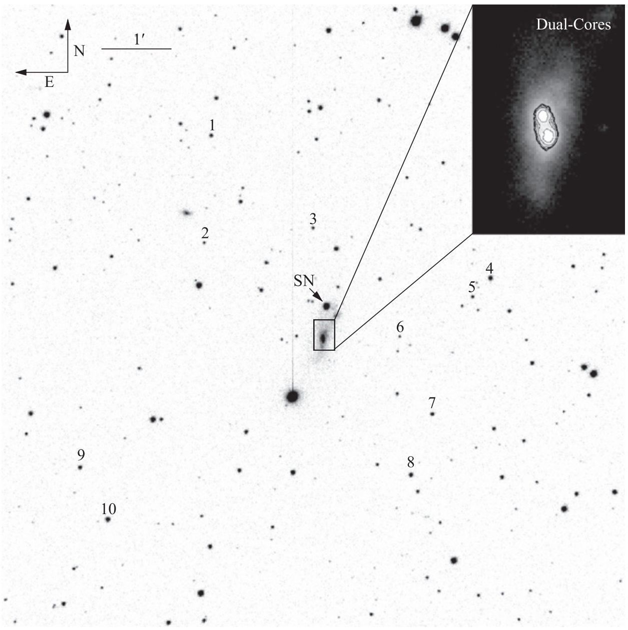

Figure 1. *R* band image of SN 2013dy and its reference stars, taken with the LJT and YFOSC on 2013 July 27.73. The mean FWHM of this image is $\sim 1\farcs10$ under the scale of $\sim 0\farcs283$/pix.

the top right panel of Figure 1. These two cores at a distance of $\sim 2\farcs38$ or ~230 pc refer to the distance of NGC 7250 derived in this paper (i.e., $D = 20.0 \pm 4.0$ Mpc). The dual-core feature might be interpreted by the interaction of two galaxies in the past. Z13also noted that there is a bright, blue region at $\sim 8\farcs7$ west and $\sim 6\farcs4$ south of this SN (projected distance $D = \sim 1.2$ kpc), which might relate to the merging history.

Our first observation of this supernova is in spectroscopy on 2013 July 14 (Zhang & Wang 2013; 4.76 days after the first light and published in Z13) with the Yunnan Faint Object Spectrograph and Camera (YFOSC; Zhang et al. 2014) mounted at the Li-Jiang 2.4 m telescope (hereafter LJT; Fan et al. 2015) of Yunnan Observatories (YNAO), China. About two weeks later, we started to monitor this transient intensively at LJT in both photometry and spectroscopy spanning from $t \approx +0$ to $t \approx +180$ days. Optical photometry data are also collected with the Tsinghua-NAOC 0.8 m telescope (hereafter TNT; Wang et al. 2008; Huang et al. 2012) at Xing-Long Observation of National Astronomical Observatories (NAOC), China, from $t \approx -2$ days to $t \approx +150$ days. Additionally, three spectra were obtained at the Xing-Long 2.16 m telescope (hereafter XLT) with the Bei-Jing Faint Object Spectrograph and Camera (BFOSC). Furthermore, this target was also observed by the UVOT (Roming et al. 2005) on board the *Swift* satellite (Gehrels et al. 2004), spanning from $t \approx -10$ days to $t \approx +15$ days in the UV and optical bands.

2.1. Photometry

2.1.1. Ground-based Observation

Table 1
Photometric Standards in the Field of SN 2013dy

Star	*U*(mag)	*B*(mag)	*V*(mag)	*R*(mag)	*I*(mag)
1	16.49(02)	16.32(02)	15.61(02)	15.29(01)	14.93(01)
2	17.61(04)	17.27(03)	16.57(01)	16.12(01)	15.78(01)
3	17.26(03)	17.09(03)	16.47(02)	16.05(01)	15.73(01)
4	16.52(02)	15.92(01)	15.09(01)	14.59(01)	14.22(01)
5	16.79(02)	16.72(01)	16.16(01)	15.78(01)	15.48(01)
6	18.18(02)	17.81(02)	17.05(03)	16.65(02)	16.26(01)
7	16.31(02)	16.27(03)	15.68(01)	15.34(01)	15.03(02)
8	15.77(02)	15.73(01)	15.18(01)	14.87(01)	14.56(01)
9	16.34(02)	16.20(01)	15.58(01)	15.22(01)	14.90(01)
10	16.36(03)	15.79(03)	14.97(01)	14.52(02)	14.18(01)

Note. Uncertainties, in units of 0.01 mag, are 1σ. See Figure 1 for the finding chart of SN 2013dy and the reference stars.

The ground-based optical photometry of SN 2013dy were obtained in the *UBVRI* bands with the LJT and TNT, covering the period from $t \approx -2$ days to $t \approx +180$ days. All of the CCD images are reduced using the IRAF[8] standard procedure, including the corrections for bias, overscan, flat field, and removal of cosmic rays. There were a few groups of templates obtained at LJT and TNT in the winter of 2014 when the SN vanished. These templates are applied to the host subtraction of the corresponding data. Based on the subtracted images, we measured the instrumental magnitude of this SN through the aperture photometry of the IRAF DAOPHOT package (Stetson 1987). Ten local standard stars in the field of SN 2013dy are labeled in Figure 1. These reference stars are converted to the standard Johnson *UBV* (Johnson et al. 1966) and Kron-Cousins *RI* (Cousins 1981) systems through transformations established by observing Landolt (1992) standard stars during several photometric nights. The magnitudes of these stars, as listed in Table 1, are then applied to transform the instrumental magnitudes of SN 2013dy to the standard *UBVRI* system, as listed in Table 2.

2.1.2. Space-based Observation

The *Swift* observatory (Gehrels et al. 2004) began observing SN 2013dy on 2013 July 17.09, about 10 days before the *B* band maximum, and continued for approximately 26 days. These photometric observations are performed in three UV filters (*uvw*2, *uvm*2, and *uvw*1) and three broadband optical filters (*uu*, *bb*, and *vv*). The photometry presented here are reduced using the *Swift* Optical/Ultraviolet Supernova Archive (SOUSA; Brown et al. 2014) reductions, including subtraction of the underlying host galaxy flux using *Swift*-UVOT observations from 2014 March and April. Table 3 lists the final UVOT UV/optical magnitudes of SN 2013dy. The results of *uvw*2 and *uvw*1 are also corrected for the "red tail" (Brown et al. 2010) of each filter. The color-term corrections (Poole et al. 2008) have been further applied to the magnitudes of the UVOT optical filters of the standard Johnson *UBV* bands when these data are plotted in the Figure 2.

2.2. Spectroscopy

A journal of the spectroscopic observation of SN 2013dy is given in Table 4, containing 21 low-resolution spectra spanning from $t \approx +0$ to +180 days; see also Figure 3. All spectra were

---

[8] IRAF, the Image Reduction and Analysis Facility, is distributed by the National Optical Astronomy Observatory, which is operated by the Association of Universities for Research in Astronomy (AURA), Inc. under cooperative agreement with the National Science Foundation (NSF).

Table 2
The *UBVRI* Photometry of SN 2013dy from the Ground-based Observations

MJD	Day[a]	*U*(mag)	*B*(mag)	*V*(mag)	*R*(mag)	*I*(mag)	Telescope
56498.11	−2.77	12.87(03)	13.38(01)	13.08(01)	12.96(01)	12.98(01)	TNT
56499.12	−1.76	12.88(02)	13.36(01)	13.04(01)	12.93(01)	13.00(01)	TNT
56500.72	−0.16	12.89(03)	13.28(01)	12.96(01)	12.85(01)	12.96(01)	LJT
56502.09	1.21	12.94(02)	13.28(01)	12.94(01)	12.82(01)	12.98(01)	TNT
56504.70	3.82	13.09(03)	13.36(01)	12.99(01)	12.87(01)	13.09(01)	LJT
56506.63	5.75	13.28(03)	13.44(01)	13.03(01)	12.93(01)	13.17(01)	LJT
56507.62	6.74	13.42(04)	13.52(01)	13.05(01)	12.97(01)	13.21(01)	LJT
56511.65	10.77	13.89(02)	13.82(02)	13.22(02)	13.15(02)	13.37(03)	LJT
56513.76	12.88	14.12(02)	14.01(02)	13.34(02)	13.26(03)	13.45(02)	LJT
56516.76	15.88	14.43(04)	14.29(03)	13.52(03)	13.38(02)	13.54(03)	LJT
56517.76	16.88	14.52(04)	14.38(01)	13.55(01)	13.42(01)	13.59(01)	LJT
56519.75	18.87	14.75(02)	14.52(01)	13.65(01)	13.51(01)	13.64(01)	LJT
56521.71	20.83	14.97(02)	14.73(01)	13.76(01)	13.59(01)	13.61(01)	LJT
56523.34	22.46	…	14.83(01)	13.85(01)	13.64(01)	13.57(01)	TNT
56526.04	25.16	15.44(06)	15.08(01)	13.94(01)	13.67(01)	13.51(01)	TNT
56526.78	25.90	15.38(02)	15.18(01)	13.97(01)	13.68(01)	13.49(01)	LJT
56527.74	26.86	15.47(02)	15.23(01)	14.03(01)	13.69(01)	13.46(01)	LJT
56528.03	27.15	15.53(04)	15.23(01)	14.05(01)	13.69(01)	13.48(01)	TNT
56529.05	28.17	15.60(03)	15.31(01)	14.10(01)	13.73(01)	13.45(01)	TNT
56530.03	29.15	15.71(05)	15.40(02)	14.14(01)	13.73(01)	13.44(01)	TNT
56532.49	31.61	15.84(04)	15.56(03)	14.28(02)	13.81(02)	13.43(03)	LJT
56535.21	34.33	16.01(03)	15.76(01)	14.42(01)	13.94(01)	13.49(01)	TNT
56537.50	36.62	16.05(02)	15.90(01)	14.55(01)	14.05(01)	13.58(01)	LJT
56540.51	39.63	16.23(04)	16.04(02)	14.68(03)	14.23(03)	13.74(02)	LJT
56545.50	44.62	16.45(03)	16.20(02)	14.89(02)	14.50(02)	14.09(03)	LJT
56546.34	45.46	…	16.14(02)	14.93(01)	14.55(01)	14.14(01)	TNT
56547.34	46.46	…	16.21(03)	14.97(01)	14.61(01)	14.23(01)	TNT
56550.32	49.44	…	16.24(02)	15.05(01)	14.68(01)	14.37(01)	TNT
56554.52	53.64	16.68(04)	16.35(03)	15.18(03)	14.88(02)	14.55(02)	LJT
56560.32	59.44	…	16.41(02)	15.33(01)	15.03(01)	14.81(01)	TNT
56561.31	60.43	…	16.43(02)	15.37(01)	15.06(01)	14.88(01)	TNT
56562.30	61.42	…	16.41(02)	15.38(01)	15.10(01)	14.93(01)	TNT
56563.30	62.42	…	16.51(04)	15.41(02)	15.19(01)	14.95(01)	TNT
56564.50	63.62	16.94(03)	16.44(01)	15.47(01)	15.18(01)	15.01(01)	LJT
56565.50	64.62	16.98(03)	16.54(01)	15.48(01)	15.21(01)	15.08(01)	LJT
56574.05	73.17	17.21(13)	16.56(03)	15.69(02)	15.49(02)	15.41(02)	TNT
56574.53	73.65	17.21(03)	16.62(01)	15.67(01)	15.46(01)	15.41(01)	LJT
56575.52	74.64	17.24(03)	16.65(01)	15.71(01)	15.49(01)	15.46(01)	LJT
56576.10	75.22	…	16.58(02)	15.73(01)	15.49(01)	15.46(01)	TNT
56576.52	75.64	17.27(03)	16.67(01)	15.74(01)	15.52(01)	15.50(01)	LJT
56576.96	76.08	…	16.66(02)	15.80(01)	15.56(01)	15.55(01)	TNT
56579.97	79.09	…	16.73(02)	15.83(01)	15.62(01)	15.67(01)	TNT
56583.52	82.64	17.43(03)	16.80(01)	15.93(01)	15.71(01)	15.77(01)	LJT
56584.96	84.08	…	16.68(03)	16.00(02)	15.76(02)	15.82(02)	TNT
56585.98	85.10	…	16.72(03)	15.96(02)	15.83(01)	15.86(02)	TNT
56586.97	86.09	17.48(13)	16.84(03)	16.01(02)	15.87(02)	15.90(02)	TNT
56588.95	88.07	…	16.82(02)	16.08(01)	15.90(01)	16.02(01)	TNT
56589.52	88.64	17.58(03)	16.86(01)	16.08(01)	15.91(01)	15.99(01)	LJT
56589.98	89.10	…	16.85(02)	16.11(01)	15.96(01)	16.06(01)	TNT
56594.52	93.64	17.73(03)	16.92(01)	16.21(01)	16.08(01)	16.17(01)	LJT
56595.18	94.30	17.76(03)	16.95(01)	16.25(01)	16.11(01)	16.20(01)	LJT
56596.18	95.30	17.82(03)	16.99(01)	16.28(01)	16.14(01)	16.23(01)	LJT
56601.96	101.08	…	17.03(02)	16.39(01)	16.33(01)	16.46(01)	TNT
56602.99	102.11	…	17.07(02)	16.41(01)	16.33(01)	16.50(01)	TNT
56603.98	103.10	…	17.07(02)	16.40(01)	16.34(01)	16.46(01)	TNT
56606.96	106.08	…	17.12(02)	16.38(01)	16.37(01)	16.51(01)	TNT
56608.00	107.12	…	17.16(02)	16.52(01)	16.47(01)	16.68(01)	TNT
56608.99	108.11	…	17.15(02)	16.52(01)	16.52(01)	16.72(02)	TNT
56610.49	109.61	18.01(03)	17.19(01)	16.52(01)	16.57(01)	16.65(01)	LJT
56610.99	110.11	…	17.18(02)	16.51(01)	16.49(01)	16.74(01)	TNT
56612.01	111.13	…	17.25(02)	16.69(02)	16.59(02)	16.80(02)	TNT
56612.48	111.60	18.23(03)	17.23(01)	16.61(01)	16.62(01)	16.72(01)	LJT
56612.96	112.08	…	17.22(02)	16.57(02)	16.60(02)	16.81(02)	TNT
56614.01	113.13	…	17.19(03)	16.53(02)	16.47(02)	16.83(02)	TNT

Table 2
(Continued)

MJD	Day[a]	U(mag)	B(mag)	V(mag)	R(mag)	I(mag)	Telescope
56615.12	114.24	…	17.21(03)	16.67(02)	16.54(02)	16.84(02)	TNT
56615.98	115.10	18.26(13)	17.28(02)	16.67(02)	16.69(02)	16.86(02)	TNT
56616.98	116.10	…	17.27(03)	16.56(05)	16.74(01)	16.94(02)	TNT
56617.97	117.09	…	17.33(02)	16.74(01)	16.79(01)	16.96(02)	TNT
56618.98	118.10	…	17.33(02)	16.78(02)	16.80(01)	17.03(02)	TNT
56619.97	119.09	…	17.35(03)	16.80(02)	16.86(02)	17.08(02)	TNT
56620.98	120.10	…	17.29(02)	16.77(01)	16.87(01)	17.08(02)	TNT
56621.98	121.10	…	17.31(02)	16.80(01)	16.88(01)	17.09(02)	TNT
56628.47	127.59	…	17.45(01)	16.92(01)	17.06(01)	17.17(01)	LJT
56629.96	129.08	…	17.46(03)	16.97(02)	17.09(02)	17.36(02)	TNT
56630.49	129.61	18.48(05)	17.48(01)	17.00(01)	17.11(01)	17.20(01)	LJT
56631.95	131.07	…	17.50(02)	17.00(01)	17.15(01)	17.32(02)	TNT
56632.98	132.10	…	17.56(02)	17.08(01)	17.22(02)	17.39(02)	TNT
56633.96	133.08	…	…	16.97(02)	17.20(02)	17.48(02)	TNT
56635.96	135.08	…	17.52(02)	17.10(02)	17.24(01)	17.44(02)	TNT
56636.92	136.04	…	…	16.94(02)	17.17(02)	17.57(02)	TNT
56639.93	139.05	…	17.64(03)	17.21(02)	17.34(02)	17.55(02)	TNT
56641.95	141.07	…	17.62(03)	17.18(02)	17.42(02)	17.51(02)	TNT
56645.96	145.08	…	17.72(02)	17.20(02)	17.40(02)	…	TNT
56646.96	146.08	…	17.69(02)	17.18(02)	17.49(02)	…	TNT
56647.54	146.66	…	17.69(02)	17.22(02)	17.54(01)	17.67(04)	LJT
56647.96	147.08	…	17.77(03)	17.28(02)	17.61(03)	…	TNT
56648.95	148.07	…	17.76(03)	17.28(02)	17.48(02)	…	TNT
56649.95	149.07	…	17.78(03)	17.34(02)	17.65(03)	…	TNT
56652.49	151.61	19.02(08)	17.87(02)	17.39(01)	17.63(03)	17.76(03)	LJT
56661.53	160.65	…	17.98(02)	17.52(02)	17.76(02)	17.96(03)	LJT
56664.55	163.67	…	18.04(02)	17.61(02)	17.80(02)	17.97(04)	LJT
56666.49	165.61	19.28(08)	18.07(03)	17.64(01)	17.89(02)	17.99(04)	LJT
56671.49	170.61	…	18.14(02)	17.76(02)	18.01(02)	18.14(06)	LJT
56674.50	173.62	19.47(09)	18.15(02)	17.71(01)	18.13(03)	18.21(05)	LJT
56681.49	180.61	…	18.24(03)	17.77(01)	18.17(02)	18.31(05)	LJT
56683.49	182.61	…	18.27(04)	17.79(02)	18.23(03)	18.35(06)	LJT

Note. Uncertainties (numbers in brackets), in units of 0.01 mag, are 1σ; MJD = JD−2400000.5.

[a] Relative to the B band maximum, JD = 2456501.38.

reduced using standard IRAF long-slit spectra routines. The flux calibration was done with the standard spectrophotometric flux stars observed at a similar airmass on the same night and were double-checked with the synthetic photometry computed using Bessell (1990) passbands. The spectra were further corrected for the atmospheric absorption and telluric lines at each observatory.

3. LIGHT CURVES OF SN 2013DY

Figure 2 shows the optical and UV light curves of SN 2013dy, overplotted with that of two well-sampled normal SNe Ia: SN 2011fe and SN 2003du. The *BVRI* photometry of Z13 and *BVRIYJH* photometry of P15 are also exhibited. Note that the solid lines in this figure are based on the photometry of SN 2011fe: the UV curves are derived from the *Swift* photometry presented in Brown et al. (2012) and fitted with a low order polynomial; the optical curves are derived from the photometry presented in Zhang et al. (2016b); the near infrared (NIR) curves are based on the photometry presented in Matheson et al. (2012). The light curves of SN 2011fe in the UV and optical are stretched by a factor of 1.20 on the horizontal axis. On the other hand, the *J* and *H* band curves of SN 2011fe are stretched by a factor of 1.10. The dashed lines are based on the photometry of SN 2003du (Stanishev et al. 2007) with a stretch factor of 1.05. The *Y* band photometry of SN 2013dy (P15) is also plotted in this figure and overplotted with a polynomial fit (dotted line). Detailed analyses are presented in the following sections.

3.1. Parameters of Photometry

Based on the photometry published in Z13, P15, and this paper, we derived the parameters of peak magnitudes, maximum dates, and light curve decline rates (i.e., Δm_{15}) through a low order polynomial fit, as listed in Table 5. It is found that SN 2013dy reaches a *B* band maximum brightness of 13.29 ± 0.01 mag on JD 2456501.38 ± 0.30 (2013 July 27.88), which is close to that in Z13 (i.e., $m_{\max}(B) = 13.28$ mag, JD = 2456500.88) and P15 (i.e., $m_{\max}(B) = 13.23$ mag, JD = 2456501.61). The observed *B* band decline rate is estimated as $\Delta m_{15}(B) = 0.90 \pm 0.03$ mag, which is close to the estimation in P15 (i.e., 0.92).

One can see that in Figure 2, the light curves of SN 2013dy resemble the stretched light curves of SN 2003du (i.e., $\Delta m_{15}(B) = 1.02$ mag; Stanishev et al. 2007) and SN 2011fe (i.e., $\Delta m_{15}(B) = 1.10$ mag; Munari et al. 2013), especially at $t < +20$ days. Note that the stretched curves of SN 2011fe decline with slower rates in the *VRI* bands but with a quicker rate in the *U* band than that of SN 2013dy and SN 2003du.

Table 3
Swift-UVOT Photometry of SN 2013dy

MJD	Day[a]	*uvw*2	*uvw*2$_{rc}$[b]	*uvm*2	*uvw*1	*uvw*1$_{rc}$[b]	*uu*	*bb*	*vv*
56490.12	−10.76	17.24(10)	19.31	18.89(23)	15.56(07)	15.83	13.80(04)	14.27(04)	14.04(05)
56492.61	−8.27	16.61(09)	18.39	18.10(14)	14.80(06)	14.96	13.13(03)	13.74(03)	13.58(04)
56492.61	−8.27	…	…	…	…	…	13.12(03)	13.72(03)	13.53(04)
56492.67	−8.21	…	…	…	…	…	13.09(03)	13.75(03)	13.41(04)
56492.67	−8.21	…	…	…	…	…	13.13(03)	13.66(03)	13.52(04)
56495.69	−5.19	…	…	…	14.46(06)	14.58	12.84(04)	…	…
56498.12	−2.76	16.17(08)	18.01	17.75(13)	14.42(05)	14.61	12.78(04)	13.28(04)	13.02(04)
56504.10	3.22	…	…	…	…	…	13.17(03)	13.28(03)	13.03(04)
56504.10	3.22	16.51(09)	19.60	17.74(10)	14.89(07)	15.50	13.07(03)	13.23(03)	12.95(03)
56504.16	3.28	…	…	…	…	…	13.12(03)	13.28(03)	13.04(04)
56504.16	3.28	…	…	…	…	…	13.05(03)	13.24(03)	13.00(03)
56507.50	6.62	…	…	…	…	…	13.44(04)	13.50(03)	13.09(04)
56507.50	6.62	…	…	…	…	…	13.50(03)	13.41(03)	13.08(03)
56507.77	6.89	16.81(10)	20.23	18.15(12)	15.32(07)	16.31	13.44(04)	13.44(03)	13.04(04)
56507.77	6.89	…	…	…	…	…	13.40(03)	13.38(03)	13.02(03)
56510.42	9.54	17.38(35)	22.51	…	15.47(07)	16.46	13.76(04)	13.59(03)	…
56510.42	9.54	…	…	…	…	…	13.72(04)	13.57(03)	…
56510.49	9.61	…	…	…	…	…	13.73(04)	13.44(03)	…
56510.49	9.61	…	…	…	…	…	13.74(04)	13.57(03)	…
56513.90	13.02	17.39(13)	21.47	18.78(18)	15.93(09)	17.47	14.18(05)	13.85(03)	13.43(04)
56513.90	13.02	…	…	…	…	…	14.16(04)	13.84(03)	13.31(04)
56516.10	15.22	…	…	…	…	…	14.54(06)	14.14(04)	13.54(04)
56516.10	15.22	17.56(14)	21.33	18.86(24)	16.27(09)	18.15	14.44(04)	14.10(03)	13.48(04)

Notes. Uncertainties (numbers in brackets), in units of 0.01 mag, are 1σ; MJD = JD−2400000.5.

[a] Relative to the date of the *B* band maximum, JD = 2456501.38.

[b] After "Red-tail" correction (Brown et al. 2010).

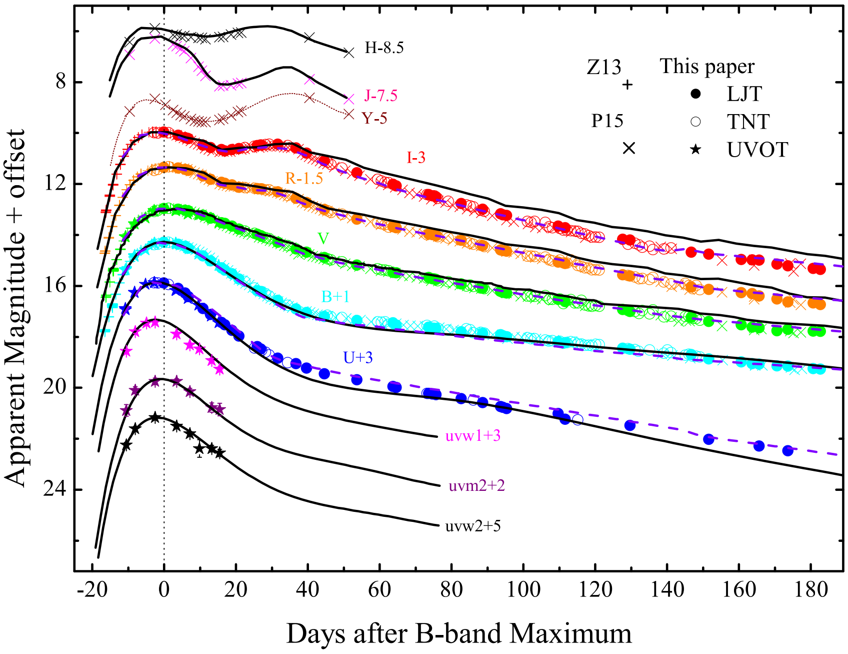

Figure 2. UV–optical–NIR light curves of SN 2013dy, which are shifted vertically for better display. The solid lines are derived from the photometry of SN 2011fe and the dashed lines from that of SN 2003du. The dotted line is for the interpolation of the *Y* band based on the photometry of SN 2013dy. See the text for detail.

3.2. Color Curves

Figure 4 shows the optical color curves of SN 2013dy, corrected for the Galactic reddening $E(B - V) = 0.15 \pm 0.02$ mag (Schlegel et al. 1998; Schlafly & Finkbeiner 2011) and the host galaxy reddening derived in Section 3.3. The Galactic reddening law (i.e., $R_V = 3.1$; Cardelli et al. 1989) is adopted for this correction. Overplotted are the color curves of SN 1999aa (Jha et al. 2006), SN 2003du (Stanishev et al. 2007), SN 2011fe (Zhang et al. 2016b), and SN 2012fr (Zhang et al. 2014). The overall color evolution of SN 2013dy is similar to that of SN 2003du, but distinctions are present in the colors of $U - B$ at the early phase. On the contrary, the

Table 4
Journal of Spectroscopic Observations of SN 2013dy

Date (UT)	MJD (−240000.5)	Epoch[a] (days)	Res. (Å)	Range (Å)	Exp. time (s)	Telescope (+Instrument)
2013 Jul 27.71	56500.71	−0.17	18	3500–9100	1200	LJT+YFOSC
2013 Jul 31.72	56504.72	+3.84	18	3430–8980	1200	LJT+YFOSC
2013 Aug 02.64	56506.64	+5.76	18	3430–8960	1200	LJT+YFOSC
2013 Aug 03.63	56507.63	+6.75	18	3410–9000	1200	LJT+YFOSC
2013 Aug 09.60	56513.63	+12.75	25	3470–8840	1800	XJT+BFOSC
2013 Aug 13.78	56517.78	+16.90	18	3430–9020	1200	LJT+YFOSC
2013 Aug 17.71	56521.71	+20.83	18	3450–9010	1200	LJT+YFOSC
2013 Aug 23.73	56527.73	+26.85	18	3620–8970	1200	LJT+YFOSC
2013 Sep 12.65	56547.65	+46.77	18	3380–9030	1200	LJT+YFOSC
2013 Sep 25.60	56560.65	+59.77	25	3500–8850	2400	XJT+BFOSC
2013 Sep 29.50	56564.50	+63.62	18	3420–9010	1800	LJT+YFOSC
2013 Oct 04.50	56569.50	+68.62	25	3770–8750	2400	XJT+BFOSC
2013 Nov 02.52	56598.52	+97.64	18	3400–9050	1800	LJT+YFOSC
2013 Nov 14.50	56610.50	+109.62	18	3400–9110	1800	LJT+YFOSC
2013 Nov 16.49	56612.49	+111.61	18	3390–9130	1800	LJT+YFOSC
2013 Nov 29.49	56625.49	+124.61	18	3480–9130	1350	LJT+YFOSC
2013 Dec 03.50	56630.50	+129.62	18	3530–9110	2700	LJT+YFOSC
2013 Dec 20.60	56646.60	+145.72	18	4070–9100	3000	LJT+YFOSC
2013 Dec 23.54	56649.54	+148.66	18	3950–9080	3600	LJT+YFOSC
2014 Jan 04.48	56661.48	+160.60	18	3610–9090	4200	LJT+YFOSC
2014 Jan 23.50	56680.50	+179.62	18	3520–9110	2700	LJT+YFOSC

Note. Journal of spectroscopic observations of SN 2013dy.

[a] Relative to the *B* band maximum on JD. 2456501.38.

$U-B$ color of SN 2013dy is similar to SN 1999aa; both are bluer than the others at $t < +5$ days. It might imply a similar temperature between SN 2013dy and SN 1999aa at this period. A larger scatter appears in the $V-I$ color of SN 2013dy and SN 2011fe at $t > +80$ days.

Figure 5 displays the $uvm2 - uu$ color of SN 2013dy based on the observations of *Swift*-UVOT and corrected for the extinction. Comparisons are made between the normal SN 2011fe (Brown et al. 2012), narrow-lined SN 2012fr (Zhang et al. 2014), 91T-like (Filippenko 1992a; Mazzali et al. 1995) event SN 2007cq (Brown et al. 2014), 99aa-like (Garavini et al. 2004) event iPTF 14bdn (Smitka et al. 2015), 02cx-like (Li et al. 2003) event SN 2005hk (Brown et al. 2014), and UV excess event SN 2011de (Brown 2014). These samples seem to be divided into two groups, where SN 2013dy, SN 2011fe, SN 2012fr, and iPTF 14bdn are located in the upper region with a redder color (i.e., $\geqslant$3 mag) than the remaining peculiar events (i.e., SN 2007cq, SN 2005hk, and SN 2011de). In general, the color of SN 2013dy is similar to that of iPTF 14bdn at $t > -5$ days. Before this period, iPTF 14bdn turns red monotonically, which is distinct from that of SN 2011fe and SN 2012fr. On the other hand, SN 2013dy presents a flatter curve and is located in the middle of this upper group. This might relate to the transitional position of SN 2013dy in the classification scheme (e.g., located on the border of normal and 91T/99aa-like events), as discussed in Section 5.4.

3.3. Extinction

The reddening due to the host galaxy can be estimated using several empirical methods. For example, the spectra published in Z13 exhibit significant Na I D absorption from both the host galaxy and the Milky Way. On the other hand, we can derive it according to the Lira–Phillips relation based on the intrinsic $B-V$ color at $+30 < t < +90$ days (Phillips et al. 1999). Additionally, the maximum-light color $B_{\rm max} - V_{\rm max}$ related to the decline rate can also be used to estimate the reddening of SNe Ia (e.g., Phillips et al. 1999; Wang et al. 2009a). All of these methods are introduced to calculate the host galaxy reddening of SN 2013dy, as listed in Table 6, and yield an average value $E(B-V)_{\rm host} = 0.20 \pm 0.10$ mag. Considering the Galactic reddening ($E(B-V) = 0.15 \pm 0.02$ mag), $E(B-V)_{\rm total} = 0.35 \pm 0.10$ mag is thus adopted in this paper.

4. SPECTRA

4.1. Temporal Evolution

4.1.1. Pre-maximum

Figure 6 displays the selected early spectra of SN 2013dy (Z13). Overplotted are the early spectra of SN 1999aa (Garavini et al. 2004), SN 2003du (Stanishev et al. 2007), SN 2009dc (Taubenberger et al. 2010), SN 2011fe (Nugent et al. 2011; Zhang et al. 2016b), SN 2012fr (Childress et al. 2013; Zhang et al. 2014), and iPTF 14bdn (Smitka et al. 2015) at similiar phases.

The early spectra of SN 2013dy consist of the absorption features from singly ionized intermediate-mass elements (IMEs, e.g., Si, S, Mg, and Ca) and Fe, which are usually seen in normal SNe Ia. Note that the absence of Fe III features in the early spectra of SN 2013dy would indicate a lower temperature than 91T/99aa events, which are characterized by the strong absorptions of double-ionized iron (Mazzali et al. 1995).

The first spectrum of SN 2013dy is characterized by the strong absorptions of unburnt carbon of C II λ6580. A weaker C II λ7234 feature is also visible. Though the absorption of C II λ6580 is not rarely seen in the normal SNe Ia (e.g., 25%; Parrent et al. 2011; Silverman & Filippenko 2012), it is usually not strong. Besides of SN 2013dy, such a strong absorption of

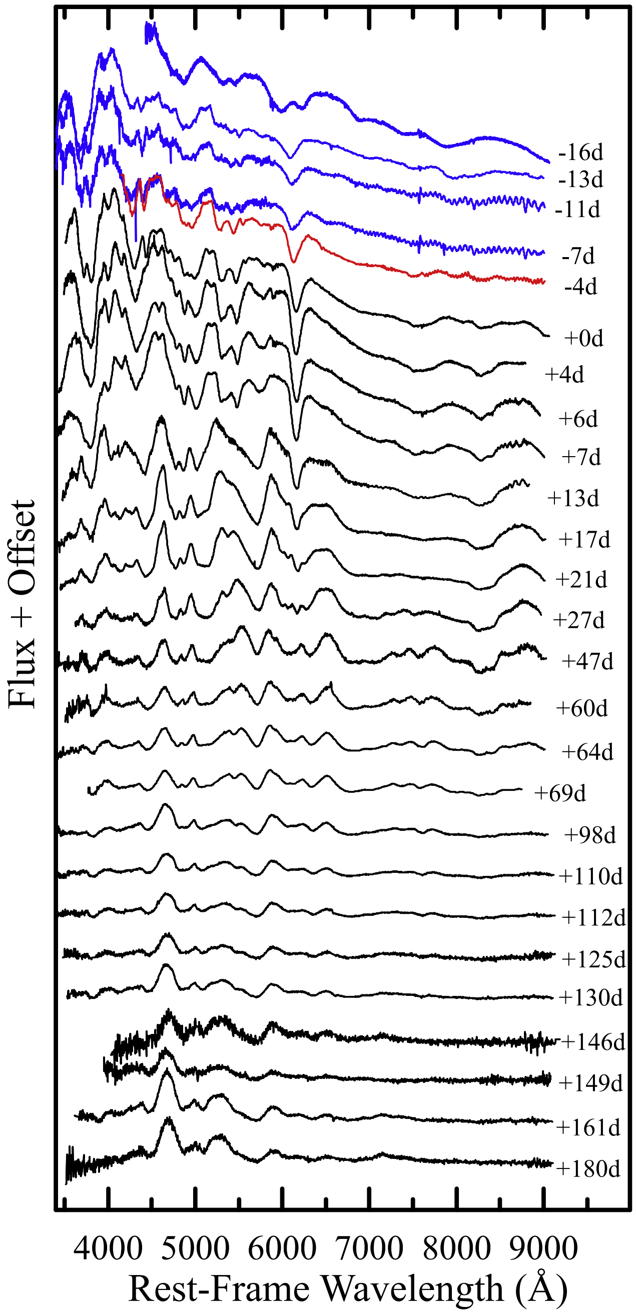

Figure 3. Optical spectra of SN 2013dy from $t \approx -16$ days to $t \approx +180$ days with arbitrary vertical offsets for clarity. The epochs are marked for better display. Note that the spectra at $t < +0$ days are published in Z13 (blue) and P15 (red).

Table 5
UV and Optical Light Curve Parameters of SN 2013dy

Band	λ_{eff} (Å)	t_{max}[a]	m_{peak} (mag[b])	Δm_{15} (mag[b])	M_{peak} (mag[b])
*uvw*2[c]	1928	498.07(40)	17.62(10)	2.49(20)	−16.90(60)
*uvm*2	2246	499.74(60)	17.65(08)	1.47(12)	−16.34(50)
*uvw*1[c]	2600	498.39(50)	14.47(10)	2.50(20)	−19.14(60)
U	3650	498.98(30)	12.88(05)	1.35(08)	−20.34(45)
B	4450	500.88(30)	13.29(01)	0.90(03)	−19.65(40)
V	5500	501.87(30)	12.94(01)	0.57(03)	−19.62(40)
R	6450	501.45(30)	12.83(02)	0.54(03)	−19.62(40)
I	7870	498.72(30)	12.95(02)	0.47(03)	−19.54(40)
Y[d]	9100	496.00(40)	13.58(04)	0.97(05)	−18.42(35)
J[d]	12500	499.37(30)	13.80(03)	1.69(05)	−18.02(35)
H[d]	16000	496.41(30)	14.37(03)	0.39(05)	−17.33(30)

Notes.
[a] Uncertainties of peak-light dates, in units of 0.01 days, are 1σ. The date is MJD−56000.
[b] Uncertainties of magnitudes, in units of 0.01 mag, are 1σ.
[c] The estimations of *uvw*2 and *uvw*1 are corrected for the "Red tail" of each filter (Brown et al. 2010).
[d] Based on the NIR photometry published in P15.

C II λ6580 was only found in the superluminous Ia SN 2009dc (Taubenberger et al. 2010). The spectrum of the very young SN 2011fe at $t \approx -16$ days exhibits rather weaker C II than that of SN 2013dy. On the other hand, the C II λ6580 line in SN 2013dy weakens rapidly, and most of the other SNe Ia are not obtained as early as this SN. In fact, three days later, the strength of the C II λ6580 line in SN 2013dy becomes as weak as that of SN 2003du at the same phase.

Note that the equivalent width (EW) ratio of C II λ6580 and Si II λ6355 in the spectrum of SN 2013dy at $t \approx -16$ days is R (C/Si) $= 0.48 \pm 0.04$, which is similar to that of SN 2009dc at $t \approx -10$ days (i.e., ∼0.50). It might imply a similar abundance of unburnt carbon in these two SNe Ia. However, the velocity distribution of C II λ6580 in SN 2013dy is 5700 ± 200 km s^{-1} and larger than that of SN 2009dc (i.e., ∼4000 km s^{-1}), which might indicate a wider distribution of unburnt carbon in the outer ejecta of the former.

At this phase, the blue-side absorption feature, the so-called high velocity features (HVFs; e.g., Mazzali et al. 2005a, 2005b), are gradually weakened in Ca II (i.e., H&K and IR triplet) with the emergence of the photometric component. The HVF of the Ca II IR triplet in the spectra of SN 2013dy begins at $v \approx 26{,}000$ km s^{-1}. Such an HVF is similarly seen in SN 2003du, SN 2011fe, and SN 2012fr. There is no evidence for the detached-HVF component of Si II λ6355 in the spectrum of SN 2013dy at $t \approx -16$ days. Two days later, the profile of Si II λ6355 becomes non-Gaussian, which might indicate two departing components in this absorption, and the bluer one should be the HVF of Si II.

At around $t \approx -7$ days, the spectrum of SN 2013dy resembles to that of the 99aa-like event iPTF 14bdn, especially for the profile of Ca II H&K and IR triplets, which are weaker than that in SN 2003du, SN 2011fe, and SN 2012fr. Additionally, the strength of Si II λ6355 in the spectrum of SN 2013dy is also weaker than in SN 2003du and SN 2011fe. It might indicate that the temperature of SN 2013dy is higher than that of SN 2003du and SN 2011fe, since a higher temperature might reduce the abundance of IMEs and reproduce the observed weakening of the IME lines in objects (Mazzali et al. 1995).

4.1.2. Around Maximum

Figure 7 displays the spectra of SN 2013dy in the first week after the *B* band maximum compared with that of SN 1999aa (Garavini et al. 2004), SN 2003du (Stanishev et al. 2007), SN 2011fe (Pereira et al. 2013), and SN 2012fr (Zhang et al. 2014).

In general, the spectra of SN 2013dy resemble that of SN 1999aa at $t \approx +0$ days. At this phase, the absorption feature of Si II λ6355 evolves to be the dominant feature in normal profile.

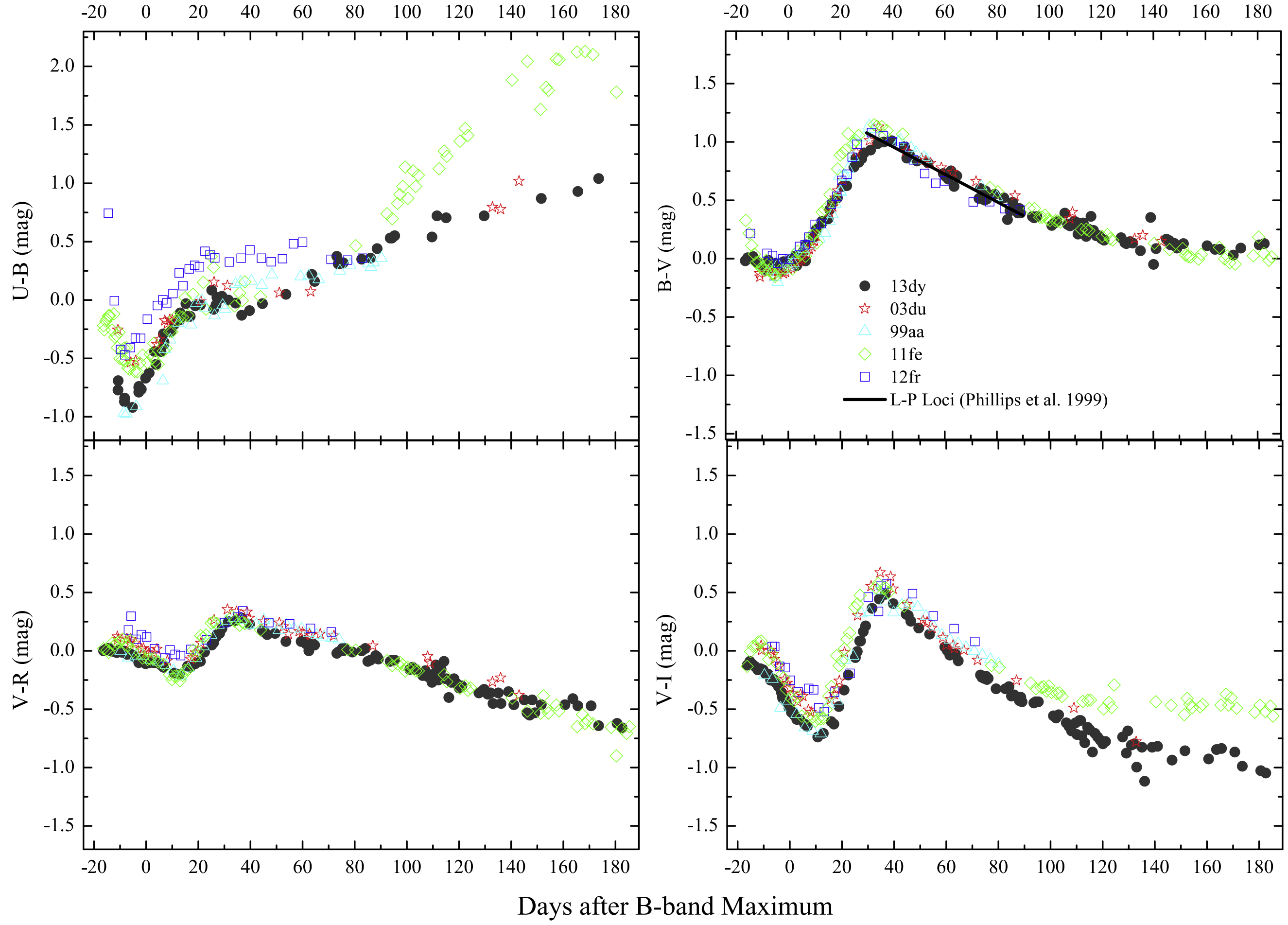

Figure 4. Optical color curves of SN 2013dy compared with those of SN 1999aa, SN 2003du, SN 2011fe, and SN 2012fr; see the text for details.

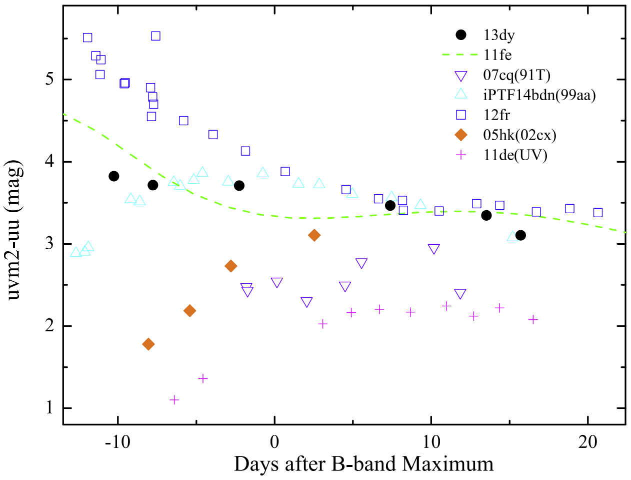

Figure 5. $uvm2 - uu$ color curve of SN 2013dy compared with that of SN 2011fe (normal), SN 2012fr (narrow-lined), SN 2007cq (91T-like), iPTF 14bdn (99aa-like), SN 2005hk (02cx-like), and SN 2011de (UV excess); see the text for details.

Table 6
The Host Extinction of SN 2013dy

Method	Details	Results (mag)
EW(Na I D)[a]	0.16EW-0.01[b]	0.07 ± 0.05
EW(Na I D)[a]	0.51EW-0.04[b]	0.23 ± 0.05
EW(Na I D)[a]	0.43EW-0.08[c]	0.15 ± 0.05
Color curve	$B_{\max} - V_{\max}$[d]	0.32 ± 0.05
Color curve	Lira–Phillips[e]	0.20 ± 0.05

Notes.
[a] EW(Na I D) = 0.53 Å, estimated by Z13.
[b] Turatto et al. (2003).
[c] Poznanski et al. (2011).
[d] Wang et al. (2009b).
[e] Phillips et al. (1999).

A minor absorption on the blue side of Na I D is likely due to Si II λ5972, which is absent in the early spectra. The line-strength ratio of Si II λ5972 to Si II λ6355, known as R(Si II) (Nugent et al. 1997), is an approximated indicator of the photospheric temperature, with a larger value corresponding to a lower temperature and smaller $\Delta m_{15}(B)$ (Hachinger et al. 2006).

The ratio between Si II λ5972 and Fe II near ~4800 Å (marked as R[Si/Fe]) shows a constant relation to the $\Delta m_{15}(B)$ (e.g., Hachinger et al. 2006). Hachinger et al. (2006) also suggested that the ratios of EW(Si II λ6355) and EW(S II, known as the "w" feature) to EW(Fe II), marked as R(Si/Fe) and R(S/Fe), respectively, might indicate the intrinsic temperature and brightness of SNe Ia. The behavior for the S II could be explained as the effect of increasing temperature, and

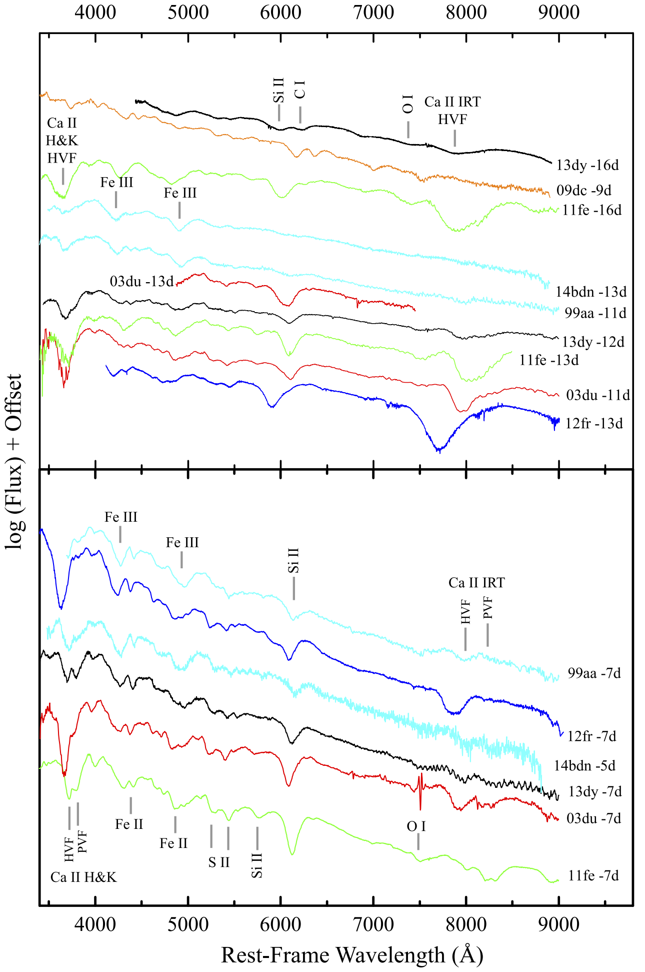

Figure 6. Early spectra of SN 2013dy overplotted with the spectra of SN 1999aa, SN 2003du, SN 2009dc, SN 2011fe, SN 2012fr, and iPTF 14bdn at the selected phases. All of these spectra were corrected with redshift and reddening.

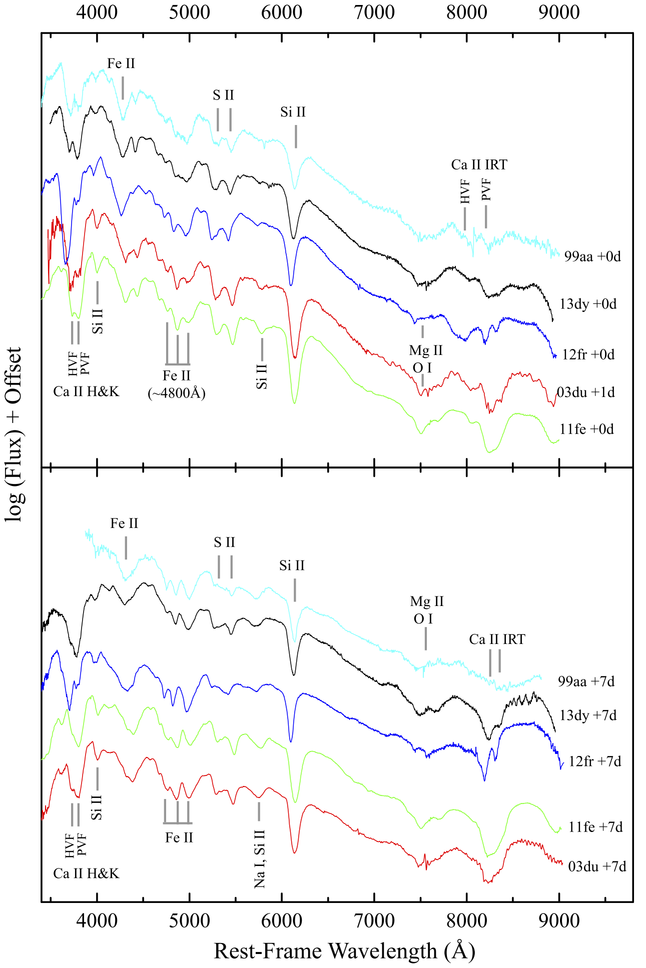

Figure 7. Spectra of SN 2013dy, SN 2012fr, SN 2011fe, SN 2003du, and SN 1999aa around maximum. All of these spectra were corrected with redshift and reddening.

the ratio between Si and Fe might reflect an abundance change. The SNe Ia with the smallest decline rates (e.g., $\Delta m_{15}(B) \leqslant 1.0$ mag) have more Fe near the maximum-light photosphere ($\sim$10,000 km s^{-1}) and the intermediate decliners have more IME and less Fe at a similar velocity (Mazzali et al. 2007). We note that the explosion velocity of SN 2013dy, SN 1999aa, SN 2003du, and SN 2011fe are similar and close to $\sim$10,000 km s^{-1} at around peak brightness. Thus, we can compare the temperature, brightness, and the mass of Fe in these SNe Ia through the R(S/Fe) and R(Si/Fe). The R(Si), R(S/Fe), R[Si/Fe], and R(Si/Fe) at $t \approx +0$ days for the selected sample are measured and listed in Table 7. We find that the relations of $\Delta m_{15}(B)$ and the EW ratios of our sample generally conform to the research of Hachinger et al. (2006). The smaller R(Si ii) and R(S/Fe) of SN 2013dy tend to indicate a higher temperature for this SN than that of the comparisons at $t \approx +0$ days. Moreover, this table might suggest a similar mass of Fe and brightness in SN 2013dy and SN 1999aa, which are larger than those in SN 2003du and SN 2011fe.

A notable distinction among SN 2013dy and the comparison SNe is the profile of the absorptions around 3800 Å, which can be attributed to the absorptions of Ca ii H&K. Such a difference might relate to the scatters in the $U - B$ color, and the behavior of Ca ii H&K at maximum light may be an indicator of intrinsic SN Ia color (Chotard et al. 2011; Foley et al. 2011; Blondin et al. 2012; Foley 2012). Based on these samples, we find that the SNe Ia with stronger HVFs of Ca ii H&K are usually redder in $U - B$ color around peak brightness.

Table 7
Parameters for the $\Delta m_{15}(B)$ – EW Ratio Relation

SN	Δm_{15}	R(Si ii)[a]	R(S/Fe)[b]	R[Si/Fe][c]	R(Si/Fe)[d]
2013dy	0.90	0.05	0.46	0.02	0.48
1999aa	0.83	0.07	0.55	0.04	0.58
2012fr	0.85	0.07	...	0.03	...
2003du	1.02	0.11	0.64	0.08	0.69
2011fe	1.10	0.14	0.68	0.11	0.74

Notes.
[a] EW(Si ii λ5972)/EW(Si ii λ6355).
[b] EW(S ii "w")/EW(Fe ii ~ 4800 Å).
[c] EW(S ii λ5972)/EW(Fe ii ~ 4800 Å).
[d] EW(S ii λ6355)/EW(Fe ii ~ 4800 Å).

4.1.3. A Few Months After Maximum

At $t \sim +3$ weeks (see the upper panel of Figure 8), the absorption of Si ii λ6355 of all the comparison SNe are

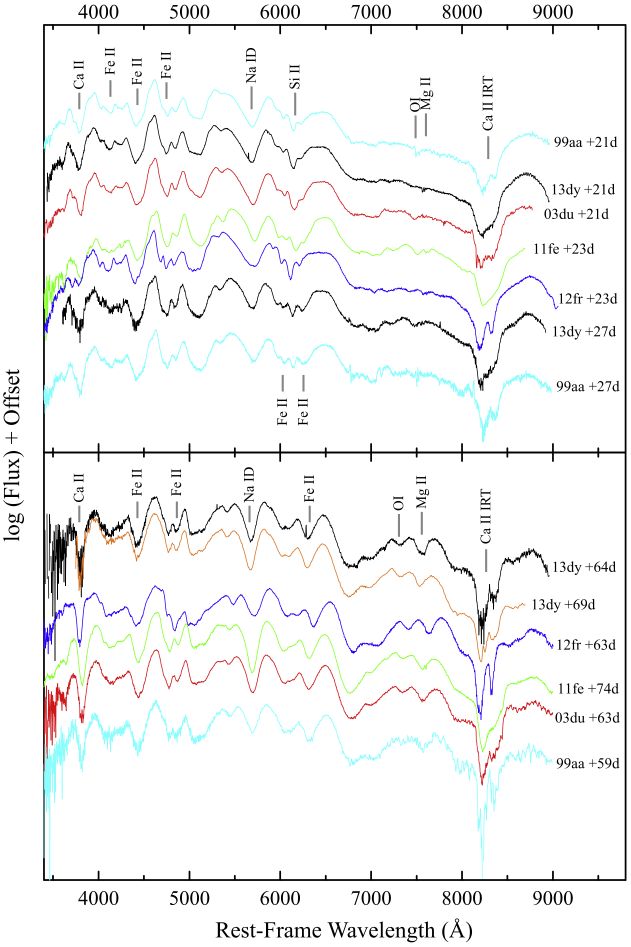

Figure 8. Spectra of SN 2013dy, SN 1999aa, SN 2003du, SN 2011fe, and SN 2012fr at a few months after maximum. All of these spectra were corrected with redshift and reddening.

contaminated by the surrounding absorption of iron-group elements. The spectra features decrease from the maximum and are dominated by the absorption of Na I D. Around ∼+2 to ∼+3 months after maximum, these spectra become stable without obvious evolution, while the iron-group elements become dominant. One interesting feature is the Ca II IR triplet feature at $t \approx +69$ days, where this triplet is clearly split into three components.

Note that the velocities of Ca II are similar to those of SN 2003du and SN 2011fe but slower than that of SN 2012fr. However, the absorptions of Na I D, O I, and Mg II appear to be faster in the former three SNe Ia than in the latter. This might suggest that the ejecta of SN 2013dy, SN 2003du, and SN 2011fe are well mixed, and a stratification structure might exist in the ejecta of SN 2012fr.

At $t > +4$ months, as presented in Figure 9, all of these samples become uniform and are dominated by the emission of iron-group elements. However, the difference can be found in the strength of some features, for example, the bump from 7000 to 7400 Å, which can contribute to the emission of [Fe II] λ7155 and [Ni II] λ7378 at $v \sim 2000\,\mathrm{km\,s^{-1}}$. Such a bump might indicate that SN 2013dy is approaching the nebular phase.

In summary, the above comparisons suggest that SN 2013dy shares major similarities with the normal SN Ia 2003du and SN 2011fe. On the other hand, the spectra of SN 2013dy are also very similar to those of SN 1999aa and iPTF 14bdn from one week before *B* band maximum.

4.2. Velocities of Ejecta

Figure 10 displays the ejecta velocities of SN 2013dy via the absorption features of some spectral lines, such as Ca II H&K, Si II λ4130, S II λ5633, Si II λ6355, C II λ 6580, C II λ7234, and the Ca II IR triplet. The location of the absorption minimum was measured using both the Gaussian fit routine and the direct measurement of the center of the absorption, and the results were averaged.

The HVF of the Ca II IR triplet at $t \approx -16$ days is $\sim$26,000 km s^{-1} which is close to that of SN 2011fe at the same phase and slower than that of SN 2012fr at $t \approx -14$ days (i.e., $\sim$31,000 km s^{-1}; Childress et al. 2013). At this phase, the velocity of Si II λ6355 is $\sim$17,200 km s^{-1} slower than that of the photospheric component of the Ca II IR triplet (i.e., $\sim$20,000 km s^{-1}) and faster than that of the C II features (i.e., $\sim$16,300 km s^{-1} and $\sim$15,000 km s^{-1} for λ 6580 and λ7234, respectively). Three days later, the velocity of C II λ6580 drops to about 13,000 km s^{-1}, which is close to the typical expansion velocity of this line in SNe Ia (Silverman & Filippenko 2012). It is notable for the velocity plateaus of the HVFs of Ca II from $t \approx -14$ to -6 days at $v \approx 20{,}000\,\mathrm{km\,s^{-1}}$, while the velocities of photospheric components (e.g., Ca II and Si II) are quickly declining.

After the maximum light, the velocity of Si II λ 6355 is $v \sim 10{,}450\,\mathrm{km\,s^{-1}}$ with a velocity gradient of $18 \pm 20\,\mathrm{km\,s^{-1}}$ day^{-1}. This gradient is derived from the velocity from $t \approx +0$ to $+13$ days and this line is not contaminated by the surrounding lines. Such a low velocity gradient is similarly seen for the velocity evolution of Ca II, which puts SN 2013dy into the LVG category of SNe Ia according to the classification scheme of Benetti et al. (2005). On the other hand, the velocity of S II λ5633 is slower but declines quicker. The IMEs of SN 2013dy generally have similar expansion velocities (e.g., $\sim$10,000 km s^{-1}), suggestive of a relatively uniform distribution of the burning products in the ejecta.

5. DISCUSSION

5.1. Distance

The observed velocity of NGC 7250 is 1166 km s^{-1}, which after correcting for the local group infall onto Virgo, Galaxy, and Shapley becomes 1410 km s^{-1} (Mould et al. 2000) or a distance $D = 19.58 \pm 2.0$ Mpc on the scale of $H_0 = 72\,\mathrm{km\,s^{-1}\,Mpc^{-1}}$. On the other hand, the distance derived from the Tully–Fisher relation of this galaxy is $D = 13.7 \pm 3.0$ Mpc (Tully et al. 2009; Nasonova et al. 2011), which was adopted in Z13 and P15 as the distance of SN 2013dy. Furthermore, we can calculate the distance from the WLR of SNe Ia (Phillips 1993; Blondin et al. 2012). The brightness of SNe Ia in the *H* band is relatively insensitive to the reddening and is more uniform around the peak compared to the corresponding values in the optical bands (Meikle 2000; Krisciunas et al. 2004; Barone-Nugent et al. 2012). Thus, we can estimate the distance to SN 2013dy based on its *H* band light curve published in P15.

Table 8 lists the distance derived from the above methods and an average value $D = 20.0 \pm 4.0$ Mpc is adopted. Note that the estimation from the *H* band brightness (i.e., $D = 31.3 \pm 3.0$ Mpc) is much larger than that inferred from

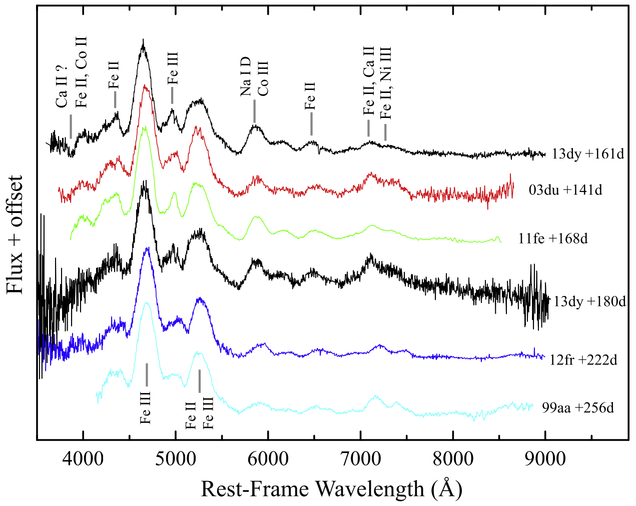

Figure 9. Spectra of SN 2013dy, SN 1999aa, SN 2003du, SN 2011fe, and SN 2012fr (Childress et al. 2015) near the nebular phase. These spectra are normalized accordingly based on the region of 4400–5000 Å. All of these spectra were corrected with redshift and reddening.

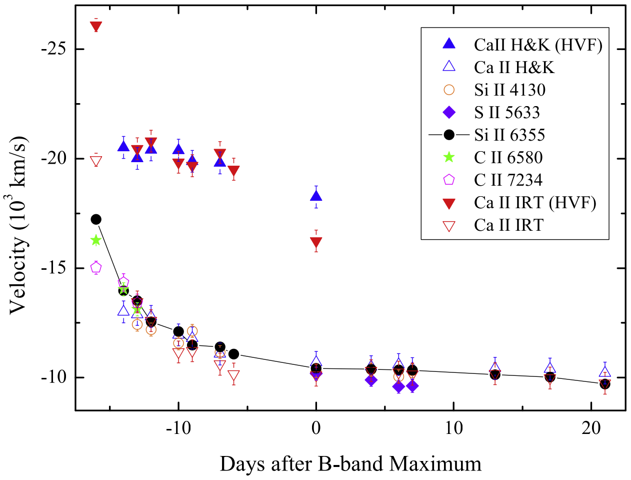

Figure 10. Velocity evolution of different elements inferred from the spectra of SN 2013dy.

Table 8
Estimations for the Distance of SN 2013dy

Method	Details	Results (Mpc)
Hubble Flow[a]	1410 km s^{-1}	19.6 ± 2.0
Tully–Fisher[b]	*JHK* bands	13.7 ± 3.0
Phillips Relation[c]	$\Delta m_{15}(B) = 0.90$	17.0 ± 3.0
Phillips Relation[d]	$\Delta m_{15}(B) = 0.90$	19.5 ± 3.0
NIR luminous[e]	*H* band	31.3 ± 3.0[f]

Notes.

[a] Corrected for Virgo infall, GA, and Shapley (Mould et al. 2000), on the scale of $H_0 = 72$ km s^{-1} Mpc^{-1}.

[b] Tully et al. (2009) and Nasonova et al. (2011).

[c] $\Delta m_{15}(B) = 0.90$; Phillips (1993).

[d] Modified Phillips (1993) relation from Figure 13 of Blondin et al. (2012) for the normal SNe Ia.

[e] From the *H* band light curve of SN 2013dy published by P15

[f] The error of extinction is involved.

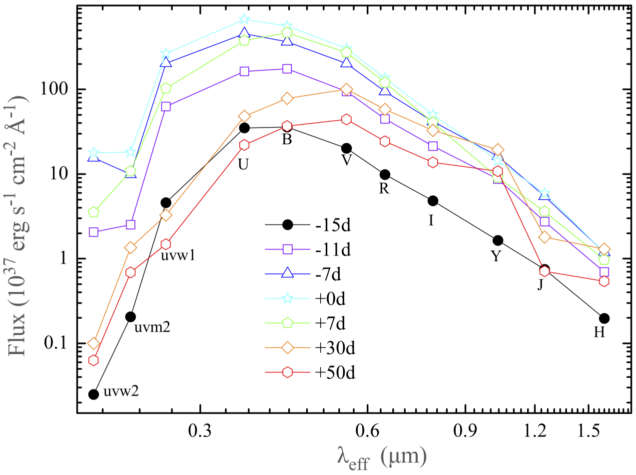

Figure 11. Spectral energy distribution of SN 2013dy at $t \approx -14, -11, -7, +0, +7, +30$, and +50 days. The positions of effective wavelength for each filter are marked.

other methods. It suggests that the intrinsic *H* band brightness of SN 2013dy (i.e., $M(H) = -17.33 \pm 0.24$ mag, if $D = 20.0$ Mpc or $M(H) = -16.51 \pm 0.24$ mag if $D = 13.7$ Mpc) is at least 1.0 mag lower than the normal (e.g., $M(H) = -18.432 \pm 0.017$ mag, Kattner et al. 2012; -18.40 ± 0.08 mag, Folatelli et al. 2010; -18.30 ± 0.04 mag, Barone-Nugent et al. 2012; -18.314 ± 0.024 mag, Weyant et al. 2014). Besides, Zhang et al. (2016a) pointed out that the peak *H* band brightness of SN 2011hr (an extreme 91T-like event, $\Delta m_{15}(B) = 0.93$ mag) is about 0.7 mag higher than the average. Therefore, the scatter of SNe Ia in the *H* band is about 2.0–2.5 mag for the SNe Ia with small decline rates (i.e., $\Delta m_{15}(B) \approx 0.90$). This larger scatter might be a challenge to the assumption that the NIR luminosities are more uniform in SNe Ia.

5.2. *Spectral Energy Distribution*

Based on the UV, optical, and NIR photometry (covering the wavelength from 1600 to 18000 Å) presented in Figure 2, we can construct the SED of SN 2013dy roughly through the observed fluxes in various passbands at the same epochs. The missing data can be obtained through interpolation of the adjacent data. Figure 11 displays the SED of SN 2013dy at $t \approx -15, -11, -7, +0, +7, +30$, and +50 days. Note that the *uvw*2 and *uvw*1 fluxes are corrected for the “red tail” effect (Brown et al. 2010). This figure shows a clear energy translation of SN 2013dy from blue to red in wavelength. A notable bump around the *Y* band at $t \geqslant +30$ days might relate to the deficit in the *J* and *H* bands.

To understand the energy transmission of SN 2013dy, we compare its SED with that of SN 2003du, SN 2011fe, SN 2012fr, and iPTF 14bdn at six selected phases; see Figure 12. It is notable that the NIR fluxes of SN 2013dy are much lower than those in SN 2003du and SN 2011fe. The lower flux of SN 2013dy in the *J* and *H* bands conforms to the bluer $V - J$ and $V - H$ color compared to those in SN 2011fe, as reported in Figure 5 of P15.

The SED could give a limit to the extinction of these SNe Ia. For example, the temperature of SN 2013dy should be lower

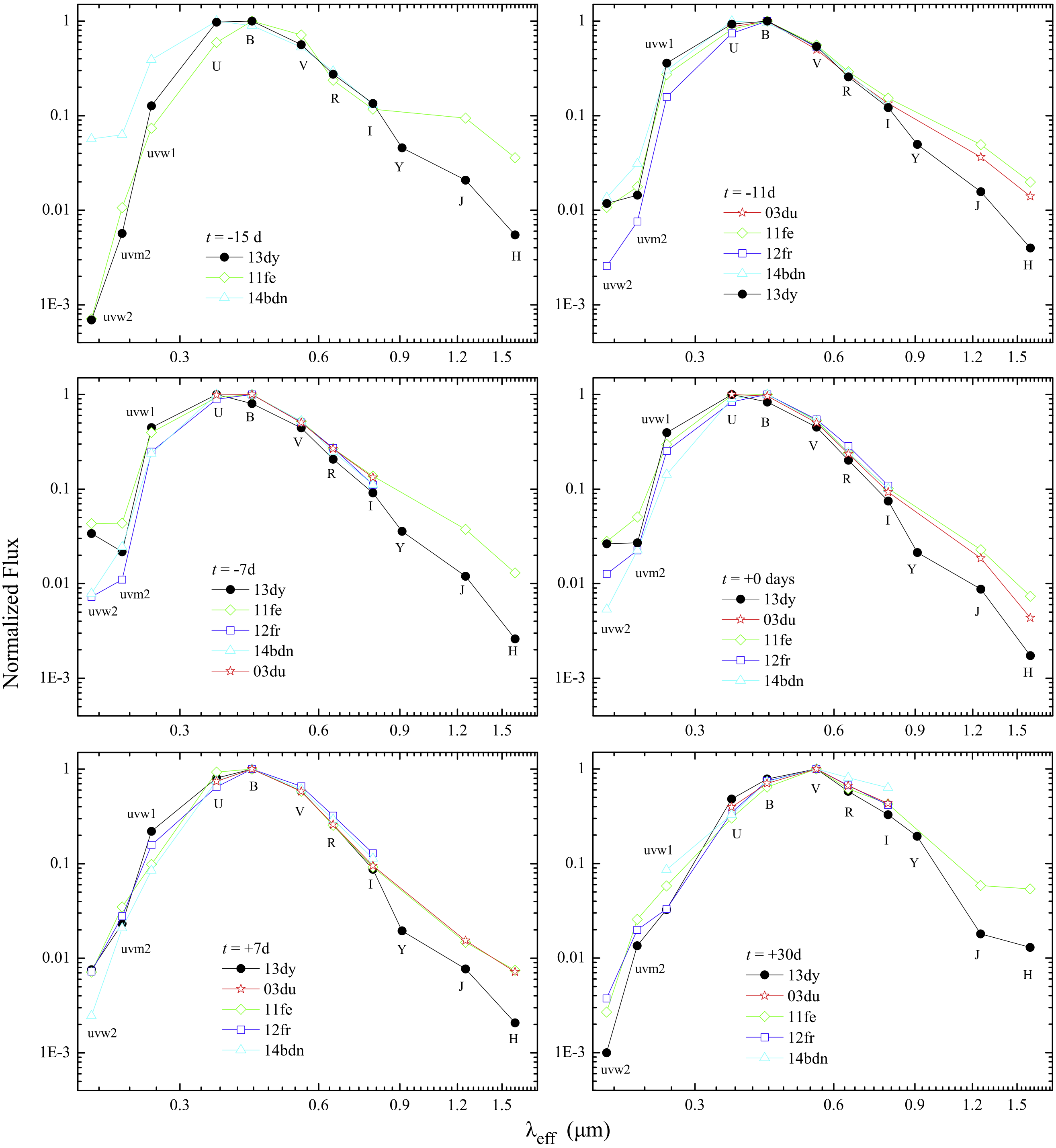

Figure 12. SED Comparison for SN 2003du, SN 2011fe, SN 2012fr, SN 2013dy, and iPTF 14bdn (99aa-like) at $t \approx -15$, -11, -7, $+0$, $+7$, and $+30$ days.

than that of iPTF 14bdn at $t < -7$ days owing to the absence of Fe III lines in the spectra of the former. On the other hand, SN 2013dy might have a higher temperature than that of SN 2003du and SN 2011fe in light of the comparison of spectral features. Furthermore, the reddenings of SN 2003du, SN 2011fe, and iPTF 14bdn are quite small (e.g., $E(B-V) < 0.03$). The sequence of temperature could give a region of extinction, i.e., $0.20 \leqslant E(B-V) \leqslant 0.30$, which conforms to the estimation in Section 3.3.

5.3. Bolometric Light Curve and the Mass of ^{56}Ni

Figure 13 displays the quasi-bolometric light curves of SN 2013dy derived from *UBVRI* photometry, compared with that of SN 1999aa, SN 2003du, SN 2011fe, and SN 2012fr. SN 2013dy is similar to SN 2012fr but with slightly higher luminosity.

We calculate the UV–optical–NIR ("uvoir," covering the wavelength from 1600 Å to 24000 Å) bolometric light curves of SN 2013dy at $-15 < t < +50$ days based on the

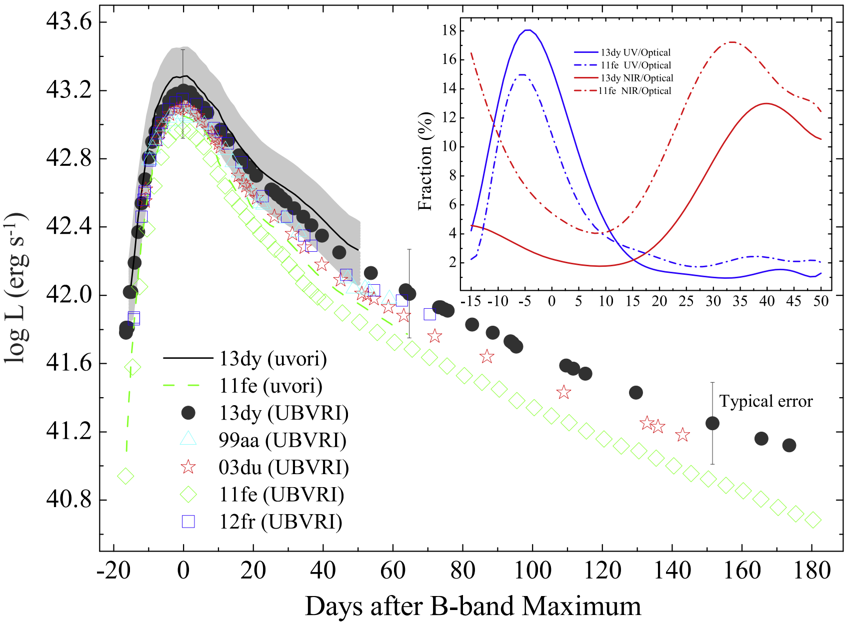

Figure 13. Quasi-bolometric *UBVRI* (3300–9000 Å) light curves of SN 2013dy compared with that of SN 1999aa, SN 2003du, SN 2011fe, and SN 2012fr. The "uvoir" (1600–24000 Å) of SN 2013dy and SN 2011fe are overplotted. The gray area shows the 1σ range of the "uvoir" bolometric luminosities of SN 2013dy considering the uncertainties from the distance (i.e., $D = 20.0 \pm 4.0$ Mpc). The fraction of UV (1600–3300 Å) and NIR (9000–24000 Å) flux to the optical flux for SN 2013dy and SN 2011fe are presented in the top right panel.

photometry presented in Figure 2. Note that the UV flux at $t < -10$ days is estimated through the stretched UV light curves of SN 2011fe, which might induce some errors because of the difference presented in Figure 5. The fluxes beyond the *H* band (i.e., 18000 to 24000 Å) are extrapolated through blackbody approximation. The missing fluxes at wavelengths shorter than the *Swift* UV filters (e.g., <1600 Å) or longer than 24000 Å are negligible. The "uvoir" bolometric light curve of SN 2011fe (Zhang et al. 2016b) is also overplotted in this figure. An obvious shoulder around $t \approx +40$ days of SN 2013dy implies a higher intrinsic luminosity than SN 2011fe.

The fraction of the UV (1600–3300 Å) and NIR (9000–24000 Å) to the optical flux of SN 2013dy and SN 2011fe is presented in the top right panel of Figure 13. Based on this panel, we find that the UV flux of SN 2013dy is relatively higher than that of SN 2011fe at the early phase while the NIR flux of the former is relatively lower. It also indicates that SN 2013dy has relatively stronger optical flux at $t > \sim +10$ days.

Based on the "uvoir" light curve, we estimate that SN 2013dy reaches its bolometric maximum (($L_{\max} = 1.95 \pm 0.55) \times 10^{43}$ erg s^{-1}) at about 0.9 days before the *B* band maximum. This could also be found in some bight SNe Ia (e.g., 91T/99aa-like events) and relates to the strong contribution at wavelengths shorter than the *B* band. The uncertainty of the peak flux includes the errors in the distance modulus, the observed magnitudes, the NIR corrections, and missing flux. Z13 found that the first-light time of SN 2013dy is JD 2456483.18, thus the rise time of the bolometric light curve (i.e., $t_{\rm rise} \approx 17.3$ days) is adopted in the following estimation. With the derived bolometric luminosity and the rise time of the bolometric light curve, the synthesized ^{56}Ni mass estimated using the Arnett law (Arnett 1982; Stritzinger & Leibundgut 2005) is $M(^{56}\mathrm{Ni}) = 0.90 \pm 0.26\,M_{\odot}$. This value is similar to that of SN 2012fr (0.88 $M_{\odot}$, Zhang et al. 2014) and larger than that of SN 1999aa (0.72 $M_{\odot}$, this paper), SN 2003du (i.e., $0.63 \pm 0.19\,M_{\odot}$, this paper; 0.68 $M_{\odot}$, Stanishev et al. 2007; 0.60 $M_{\odot}$, Stritzinger et al. 2006), and SN 2011fe (e.g., 0.53 $M_{\odot}$, Munari et al. 2013; 0.56 $M_{\odot}$, Mazzali et al. 2014).

On the other hand, we could estimate some explosion parameters of this SN by adopting the same method as in Taubenberger et al. (2010). The ejecta mass ($M_{\rm ej}$) and the total explosion energy ($E_{\rm ej}$) can be derived from the diffuse time $\tau_{\rm m}$ and ejecta velocity v, where $M_{\rm ej} \propto \tau_{\rm m}^2 v$ and $E_{\rm kin} \propto \tau_{\rm m}^2 v^3$. The diffuse time of SN 2013dy is 27.58 days, which is longer than that of SN 2011fe (i.e., 25.33 days). On the other hand, the velocity of Si II λ6355 of SN 2013dy at around maximum is 10,450 km s^{-1}, which is also slightly faster than that of SN 2011fe (i.e., 10,340 km s^{-1}). As a result, we find that $M_{\rm ej,13dy} \approx 1.20 M_{\rm ej,11fe}$ and $E_{\rm ej,13dy} \approx 1.22 E_{\rm ej,11fe}$. Note that these coefficients conform to the stretch factors adopted in Figure 2 for the light curve comparison. The mass of ^{56}Ni produced in SN 2013dy is 0.67 $M_{\odot}$ based on the estimation of SN 2011fe (e.g., 0.56 $M_{\odot}$, Mazzali et al. 2014) and the similar component assumption in Arnett's (1982) law. This result is independent of distance and extinction. It is smaller than the estimation of the bolometric curve. A smaller estimation for the ^{56}Ni mass of SN 2013dy might suggest a distinct energy and material distribution between SN 2013dy and SN 2011fe since only the opaque mass can be calculated from these simple analytic approaches.

5.4. Spectroscopy Classification

Spectroscopy classification schemes have recently been proposed to highlight the diversity of relatively normal SNe Ia. Benetti et al. (2005) classified the normal SNe Ia into LVG and HVG groups by the temporal velocity gradient of the Si II λ6355 line. Based on the EW of the absorption features of Si II λ5972 and Si II λ6355, Branch et al. (2006, 2009) suggested dividing the SN Ia sample into four groups: cool

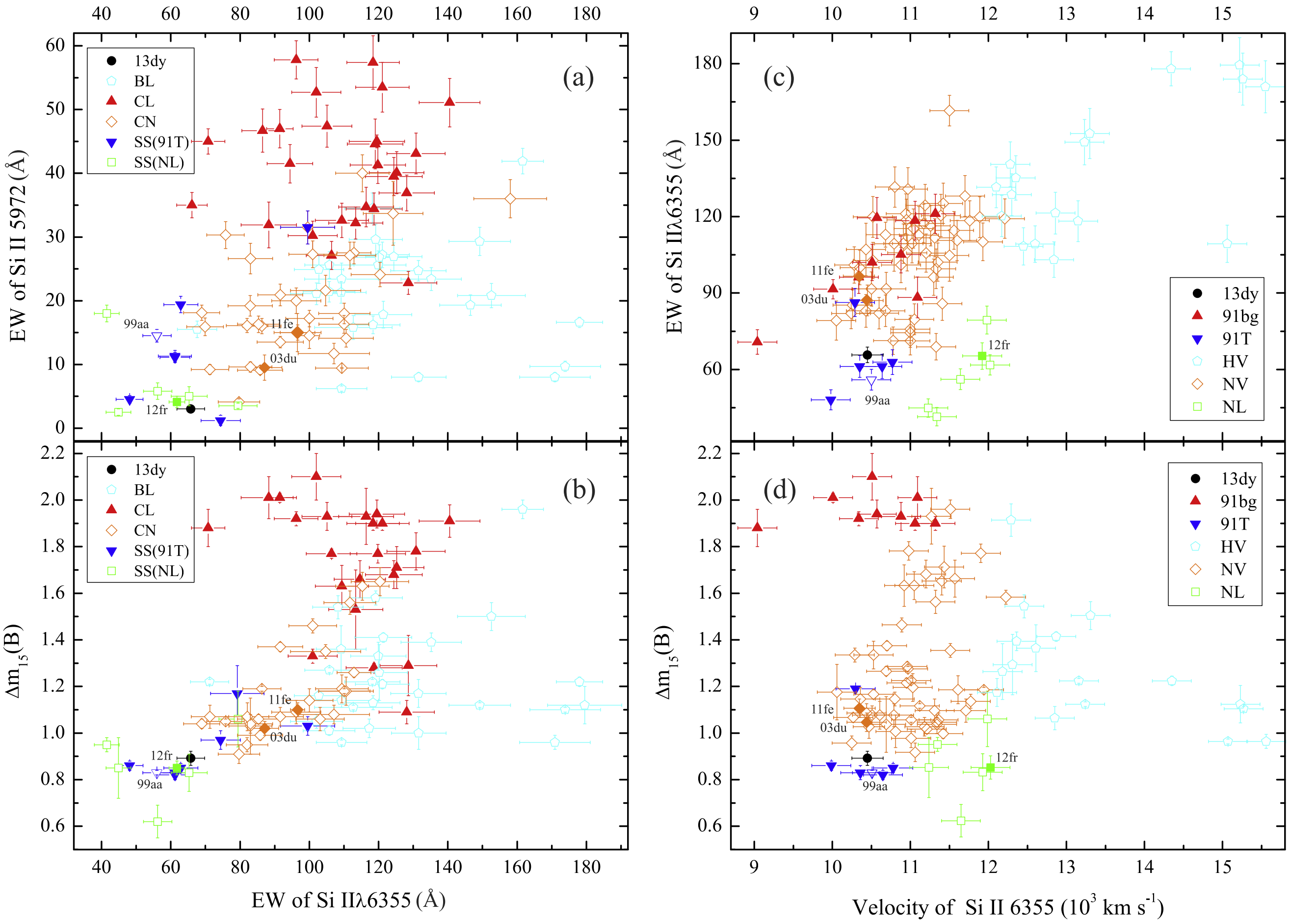

Figure 14. Comparison of various spectroscopic and photometric indicators from SN 2013dy with those from other SNe Ia as measured by Blondin et al. (2012), Silverman et al. (2012), Wang et al. (2009a), Zhang et al. (2014), and this paper. The selected sample have spectra within $t \pm 3$ days. Panel (a) and (b): the Si II λ5972 and $\Delta m_{15}(B)$ vs. Si II λ6355 at maximum light with subclasses defined by Branch et al. (2009); panel (c) and (d): the EW of Si II λ6355 and $\Delta m_{15}(B)$ vs. the velocity of Si II 6355 at maximum light with subclasses defined by Wang et al. (2009a).

(CL), shallow silicon (SS), core normal (CN), and broad line (BL). The CL group mainly consists of the faint objects like SN 1991bg (Filippenko 1992b). Besides the faint peculiar events like SN 2002cx (Li et al. 2003), the SS group mainly consists of the bright 91T/99aa-like events, the superluminous events (e.g., SN 2003fg, Howell et al. 2006; SN 2007if, Scalzo et al. 2010 and SN 2009dc, Taubenberger et al. 2010; Silverman et al. 2011), and the narrow-lined SNe Ia (NL; e.g., SN 2012fr; Zhang et al. 2014). We note that the small EW of Si II λ6355 could be derived from different profiles of this line, for example, absorption with smaller depth and larger width (e.g., 91T/99aa-like events) or with larger depth and small width (e.g., NL). Therefore, we divide the bright but generally normal members of SS into two subgroups, SS/91T-like and SS/NL, in the following discussion. On the other hand, Wang et al. (2009a) proposed using the expansion velocity of the Si II λ6355 line to distinguish the subclass with a higher Si II velocity (HV) from that with a normal velocity (NV). The HV SNe Ia are found to have redder $B - V$ colors (Wang et al. 2009a) and different locations within host galaxies in comparison to the NV ones (Wang et al. 2013), suggesting that the properties of their progenitors may be different.

The spectroscopy classification of SN 2013dy is compared with the large SNe Ia sample from the spectral spectral data sets of CfA (Blondin et al. 2012) and the Berkeley SuperNova Ia Program (Silverman et al. 2012) at $t \approx \pm 3$ days. However, SN 2013dy resembles the normal SN 2003du and SN 2011fe observationally. The weak Si II absorptions (i.e., ~70.7 Å and ~3.3 Å for Si II λ6355 and λ5972, respectively), however, put it into the transitional region of SS and CN at the near-side of the former in the Branch et al. (2006) diagram, as shown in Figures 14(a) and (c). It is difficult to distinguish the SS/91T-like from SS/NL in this scheme. SN 2013dy is also close to the NL SN 2012fr. However, the 91T/99aa-like events keep away from NL SNe Ia in the Wang et al. (2009a) diagram owing to the difference in velocity, as shown in Figures 14(b) and (d). In the Wang et al. (2009a) scheme, SN 2013dy and SN 2012fr are also separated and the former resides at the border between the NV and the 91T/99aa-like subclasses. The slow decline rate, the small EW of Si II absorptions, and the low velocity gradient resemble the properties of the 91T/99aa-like objects. Besides, the $U - B$ color of SN 2013dy is as blue as that of SN 1999aa at the early phase. However, the absence of Fe III lines in the early spectra of SN 2013dy is a clear distinction from 91T/99aa-like events.

6. CONCLUSION

We have presented extended observations of Type Ia SN 2013dy obtained at LJT, XLT, TNT, and *Swift*-UOVT.

Combined with the data published in Z13 and P15, this target is a well-sampled SN Ia with wide wavelength coverage (i.e., from ∼1600 Å to ∼18000 Å). In general, this SN resembles normal SNe Ia (e.g., SN 2003du and SN 2011fe) in both photometry and spectroscopy. Nevertheless, it also shares some similarities with the 99aa-like events, such as the $U-B$ and "$uvm2 - uu$" color before maximum, the small decline rate, the low velocity gradient, and the small ratios of R(Si II), R(S/Fe), and R(Si/Fe). However, the absence of Fe III lines in the early spectra of SN 2013dy might exclude it from 91T/99aa-like group.

A problem is the uncertainty of the distance. In general, the distance (i.e., $D \approx 20.0$ Mpc) derived from several methods seems to be more reasonable than the estimations from the Tully–Fisher relation of the host galaxy (i.e., $D \approx 13.7$ Mpc). Based on the larger one, we estimated the peak brightness (e.g., $M_{\max}(B) = -19.65 \pm 0.40$ mag), maximum bolometric luminosity ($[1.95 \pm 0.55] \times 10^{43}$ erg s^{-1}), and synthesized nickel mass ($0.90 \pm 0.26\,M_\odot$). The distance derived from the Tully–Fisher relation will yield fainter results (i.e., $M_B = -18.83 \pm 0.3$ mag; $L_{\max} = [9.05 \pm 2.50] \times 10^{42}$ erg s^{-1}; $M(^{56}\mathrm{Ni}) = 0.42 \pm 0.15\,M_\odot$) that are dimmer than the average SNe Ia and do not follow the WLR of SNe Ia well. Additionally, the H band luminosity of SN 2013dy is at least 1.0 mag fainter than the average SNe Ia. That might indicate inefficient emission translation from optical to NIR for SN 2013dy or imply that this SN is an intrinsically fainter SN Ia, although it shows a small $\Delta m_{15}(B)$. Moreover, the H band photometry of SN 2013dy and SN 2011hr suggests a larger scatter (i.e., ∼2.0–2.5 mag) among the SNe Ia with a slow decline rate (e.g., $\Delta m_{15}(B) \approx 0.90$ mag) and might challenge the assumption of the uniform NIR luminosity for SNe Ia.

On the other hand, it is difficult to put SN 2013dy into one subclass in the current classification system. The spectroscopy classification reveals that SN 2013dy might be a transitional event residing on the border of different subclasses, such as SS-CN in the Branch et al. (2006) classification scheme or NV-91T/99aa-like in the Wang et al. (2009a) classification system. Moreover, the diversity of the SNe Ia with small $\Delta m_{15}(B)$ and EWs of Si II (e.g., the superluminous SNe Ia, the 91T/99aa-like events, the SN 2012fr-like events, and SN 2013dy) might imply the only EW criterion is insufficient for the classification of this sample and indicate a complex construction of their ejecta.

All of these suggest that SN 2013dy might not be a typical SNe Ia, although it is normal in some respects. Further modeling work is essential to reveal the nature of this SN.

We thank the anonymous referee for constructive suggestions that helped to improve the paper. We acknowledge the support of the staff of the Li-Jiang 2.4 m telescope (LJT), Xin-Long 2.16 m telescope, and Tsinghua-NAOC 0.8 m telescope (TNT). Funding for the LJT has been provided by Chinese academe of science (CAS) and the People's Government of Yunnan Province. The TNT is owned by Tsinghua University and operated by the National Astronomical Observatory of the Chinese Academy of Sciences (NAOC). The data from UVOT comes from the *Swift* Data Center. We also thank Dr. Wei-Kang Zheng of UC Berkeley who provided the early *BVRI* photometry of SN 2013dy (Z13).

Financial support for this work has been provided by the National Science Foundation of China (NSFC, grants 11403096, 11178003, 11325313, 11133006, 11361140347, 11203034, 11203078, 11573069, 11303085, 11203070); the Major State Basic Research Development Program (2013CB834903); the Strategic Priority Research Program "The Emergence of Cosmological Structures" of the CAS (grant No. XDB09000000); the Key Research Program of the CAS (Grant NO. KJZD-EW-M06); the CAS "Light of West China" Program; the Youth Innovation Promotion Association of the CAS; the Open Project Program of the Key Laboratory of Optical Astronomy, NAOC, CAS; and the key Laboratory for Research in Galaxies and Cosmology of the CAS.

REFERENCES

Arnett, W. D. 1982, ApJ, 253, 785
Barone-Nugent, R. L., Lidman, C., Wyithe, J. S. B., et al. 2012, MNRAS, 425, 1007
Benetti, S., Cappellaro, E., Mazzali, P. A., et al. 2005, ApJ, 623, 1011
Bessell, M. S. 1990, PASP, 102, 1181
Blondin, S., Matheson, T., Kirshner, R. P., et al. 2012, AJ, 143, 126
Branch, D., Dang, L. C., & Baron, E. 2009, PASP, 121, 238
Branch, D., Dang, L. C., Hall, N., et al. 2006, PASP, 118, 560
Brown, P. J. 2014, arXiv:1408.1033v1
Brown, P. J., Breeveld, A. A., Holland, S., et al. 2014, AP&SS, 354, 89
Brown, P. J., Dawson, K. S., & Pasquale, M. 2012, ApJ, 753, 22
Brown, P. J., Roming, P. W., Milne, P., et al. 2010, ApJ, 721, 1608
Cardelli, J. A., Clayton, G. C., & Mathis, J. S. 1989, ApJ, 345, 245
Casper, C., Zheng, W., Li, W., Filippenko, A. V., & Cenko, S. B. 2013, CBET, 3588, 1
Childress, M. J., Hillier, D. J., Seitenzahl, I., et al. 2015, MNRAS, 454, 3815
Childress, M. J., Scalzo, R. A., Sim, S., et al. 2013, ApJ, 770, 29
Chotard, N., Gangler, E., Aldering, G., et al. 2011, A&A, 529L, 4C
Cousins, A. 1981, SAAOC, 6, 4
Fan, Y. F., Bai, J. M., Zhang, J. J., et al. 2015, RAA, 15, 918
Filippenko, A. V. 1992a, ApJL, 384, L15
Filippenko, A. V. 1992b, AJ, 104, 1543
Folatelli, G., Phillips, M. M., Burns, C. R., et al. 2010, AJ, 139, 120
Foley, R. J. 2012, ApJ, 748, 127
Foley, R. J., Sanders, N. E., & Kirshner, R. P. 2011, ApJ, 742, 89
Garavini, G., Folatelli, G., Goobar, A., et al. 2004, ApJ, 128, 387
Gehrels, N., Chincarini, G., Giommi, P., et al. 2004, ApJ, 611, 1005
Hachinger, S., Mazzali, P. A., & Benetti, S. 2006, MNRAS, 370, 299
Howell, D. A., Sullivan, M., Nugent, P. E., et al. 2006, Natur, 443, 308
Huang, F., Li, J. Z., Wang, X. F., et al. 2012, RAA, 11, 1585
Jha, S., Krishner, R. P., Challis, P., et al. 2006, AJ, 131, 527
Johnson, H., Iriarte, B., Mitchell, R., & Wisniewskj, W. 1966, CoLPL, 4, 99
Kattner, S., Leonard, D. C., Burns, C. R., et al. 2012, PASP, 124, 114
Krisciunas, K., Phillips, M. M., & Suntzeff, N. B. 2004, ApJL, 602, L81
Landolt, A. V. 1992, AJ, 104, 340
Li, W., Filippenko, A., Ryan, C., et al. 2003, PASP, 115, 453
Matheson, T., Joyce, R. R., Allen, L. E., et al. 2012, ApJ, 754, 19
Mazzali, P. A., Benetti, S., Altavilla, G., et al. 2005a, ApJ, 623L, 37
Mazzali, P. A., Benetti, S., Stehle, M., et al. 2005b, MNRAS, 357, 200
Mazzali, P. A., Danziger, I. J., & Turatto, M. 1995, A&A, 297, 509
Mazzali, P. A., Röpke, F. K., Benetti, S., & Hillebrandt, W. 2007, Sci, 315, 825
Mazzali, P. A., Sullivan, M., Hachinger, S., et al. 2014, MNRAS, 439, 1959
Meikle, W. P. S. 2000, MNRAS, 314, 782
Mould, J. R., Huchra, J. P., Freedman, W. L., et al. 2000, ApJ, 529, 786
Munari, U., Henden, A., Belligoli, R., et al. 2013, NewA, 20, 30
Nasonova, O. G., de Freitas Pacheco, J. A., & Karachentsev, I. D. 2011, A&A, 523, 104
Nugent, P. E., Baron, E., Branch, D., et al. 1997, ApJ, 485, 812
Nugent, P. E., Sullivan, M., Cenko, S. B., et al. 2011, Natur, 480, 344
Pan, Y.-C., Foley, R. J., Challis, P., et al. 2015, MNRAS, 452, 4307 (P15)
Parrent, J. T., Thomas, R. C., Fesen, R. A., et al. 2011, ApJ, 732, 30
Pereira, R., Thomas, R., Aldering, G., et al. 2013, A&A, 554, A27
Phillips, M. 1993, ApJL, 413, L105
Phillips, M., Lira, R., Suntzeff., N. B., et al. 1999, AJ, 118, 1766
Poole, T., Breeveld, A., Page, M., et al. 2008, MNRAS, 383, 627
Poznanski, D., Ganeshalingam, M., Silverman, J. M., & Filippenko, A. V. 2011, MNRAS, 415, L81

Roming, P., Kennedy, T., Mason, K., et al. 2005, SSRv, 120, 95

Scalzo, R., Aldering, G., Antilogus, P., et al. 2010, ApJ, 713, 1073

Schlafly, E. F., & Finkbeiner, D. P. 2011, ApJ, 737, 103

Schlegel, D., Finkbeiner, D., & Davis, M. 1998, ApJ, 500, 525

Silverman, J., Foley, R. J., Filippenko, A. V., et al. 2012, MNRAS, 425, 1789

Silverman, J., Ganeshalingam, M., Li, W., et al. 2011, MNRAS, 410, 585

Silverman, J. M., & Filippenko, A. V. 2012, MNRAS, 425, 1917

Smitka, M. T., Brown, P. J., Suntzeff, N. B., et al. 2015, ApJ, 813, 30

Stanishev, V., Goobar, A., Benetti, S., et al. 2007, A&A, 469, 645

Stetson, P. 1987, PASP, 99, 191

Stritzinger, M., & Leibundgut, B. 2005, A&A, 431, 423

Stritzinger, M., Mazzali, P. A., Sollerman, J., & Benetti, S. 2006, A&A, 460, 793

Taubenberger, S., Benetti, S., Childress, M., et al. 2010, MNRAS, 412, 2735

Tully, R. B., Rizzi, L., Shaya, E., et al. 2009, AJ, 138, 323

Turatto, M., Benetti, S., & Cappellaro, E. 2003, in From Twilight to Highlight: The Physics of Supernovae, ed. W. Hillebrandt, & B. Leibundgut (Berlin: Springer), 200

Wang, X., Filippenko, A. V., Ganeshalingam, M., et al. 2009a, ApJL, 699, L139

Wang, X., Li, W., Filippenko, A., et al. 2009b, ApJ, 697, 380

Wang, X., Li, W., Filippenko, A. V., et al. 2008, ApJ, 675, 626

Wang, X., Wang, L., Filippenko, A., et al. 2013, Sci, 340, 170

Weyant, A., Michael, W., Allen, L., et al. 2014, ApJ, 784, 105

Zhang, J. J., & Wang, X. F. 2013, CBET, 3558, 3

Zhang, J. J., Wang, X. F., Bai, J. M., et al. 2014, AJ, 148, 1

Zhang, J. J., Wang, X. F., Sasdelli, M., et al. 2016a, ApJ, 817, 1154

Zhang, K. C., Wang, X. F., Zhang, J. J., et al. 2016b, ApJ, in press (arXiv:1602.02951)

Zheng, W. K., Silverman, J. M., Filippenko, A. V., et al. 2013, ApJL, 778, L15 (Z13)

Publications of the Astronomical Society of the Pacific, 128:115005 (15pp), 2016 November
doi:10.1088/1538-3873/128/969/115005

The Xinglong 2.16-m Telescope: Current Instruments and Scientific Projects

Zhou Fan[1], Huijuan Wang[1], Xiaojun Jiang[1], Hong Wu[1], Hongbin Li[1], Yang Huang[2], Dawei Xu[3], Zhongwen Hu[4], Yinan Zhu[1], Jianfeng Wang[1], Stefanie Komossa[5], and Xiaoming Zhang[1]
[1] Key Laboratory of Optical Astronomy, National Astronomical Observatories, Chinese Academy of Sciences, 20A Datun Road, Chaoyang District, Beijing 100012, China; zfan@bao.ac.cn
[2] Department of Astronomy, Peking University, Beijing 100871, China
[3] Key Laboratory of Space Astronomy and Technology, National Astronomical Observatories, Chinese Academy of Sciences, 20A Datun Road, Chaoyang District, Beijing 100012, China
[4] Nanjing Institute of Astronomical Optics & Technology, National Astronomical Observatories, Chinese Academy of Sciences, 188 Bancang Street, Nanjing 210042, China
[5] Max-Planck-Institut fuer Radioastronomie, Auf dem Huegel 69, D-53121 Bonn, Germany
Received 2016 January 12; accepted 2016 May 16; published 2016 October 4

Abstract

The Xinglong 2.16-m reflector is the first 2-m class astronomical telescope in China. It was jointly designed and built by the Nanjing Astronomical Instruments Factory (NAIF), Beijing Astronomical Observatory (now National Astronomical Observatories, Chinese Academy of Sciences, NAOC), and Institute of Automation, Chinese Academy of Sciences in 1989. It is a Ritchey-Chrétien (R-C) reflector on an English equatorial mount and the effective aperture is 2.16 m. It had been the largest optical telescope in China for ~18 years until the Guoshoujing Telescope (also called Large Sky Area Multi-Object Fiber Spectroscopic Telescope, LAMOST) and the Lijiang 2.4-m telescope were built. At present, there are three main instruments on the Cassegrain focus available: the Beijing Faint Object Spectrograph and Camera (BFOSC) for direct imaging and low-resolution ($R \sim 500$–2000) spectroscopy, the spectrograph made by Optomechanics Research Inc. (OMR) for low-resolution spectroscopy (the spectral resolutions are similar to those of BFOSC) and the fiber-fed High Resolution Spectrograph (HRS; $R \sim 30{,}000$–65,000). The telescope is widely open to astronomers all over China as well as international astronomical observers. Each year there are more than 40 ongoing observing projects, including 6–8 key projects. Recently, some new techniques and instruments (e.g., astro-frequency comb calibration system, polarimeter, and adaptive optics) have been or will be tested on the telescope to extend its observing abilities.

Key words: instrumentation: miscellaneous – instrumentation: photometers – instrumentation: spectrographs – telescopes

Online material: color figures

1. Introduction

The 2.16-m reflector is an English equatorial mount telescope at Xinglong Observatory, and it obtained the first light in 1989, which was built/developed by the Chinese independently. The effective aperture of the telescope is 2.16 m, and the focal ratio of the primary mirror is f/3 (Su et al. 1989). The effective aperture of the secondary mirror is 0.717 m. Currently, there are two available foci for mounting astronomical observing instruments, the Cassegrain focus and the Coudé focus. For the Cassegrain focus, which is an R-C system, the focal ratio is f/9, and the scale on the focal plane is $10''\!.61\ \mathrm{mm}^{-1}$. While for the Coudé system, it is f/45, and the scale on the focal plane is $2''\!.12\ \mathrm{mm}^{-1}$. The most special character of the optical system is that the Cassegrain system and the Coudé system share the same secondary mirror and there is a relay mirror in the Coudé system, and both systems can sufficiently eliminate the spherical aberration and coma aberration (Su et al. 1989).

Since its first light in 1989, the 2.16-m telescope has been used in various scientific research fields in Galactic and extragalactic astrophysics, including the determination of stellar parameters (e.g., abundances, surface gravity, temperatures) of a large sample of stars, the discoveries of substellar and planetary companions of stars, studies of active galaxy nuclei (AGNs), including the identifications of high-redshift quasars, discoveries, and studies of supernovae, e.g., 1993J (Wang & Hu 1994), as well as time-domain science (e.g., supernovae, gamma-ray bursts, stellar tidal disruption events, and variable stars).

Although the 2.16-m telescope is the third largest optical telescope in China right now (smaller than LAMOST (Cui et al. 2012) and the Lijiang 2.4-m telescope (Fan et al. 2015), which were installed in 2008 and 2007, respectively), it plays an important role in Chinese astronomical observations. Every year there are hundreds of Chinese astronomers applying for observing time at the 2.16-m telescope, including significant numbers of new telescope users and graduate students. Therefore, it is of great importance and useful to describe the specific parameters and the observing ability of the telescope and its instruments to the telescope users, which could be very helpful for planning and carrying out observations and for the data reduction. This paper is organized as follows: the Xinglong Observatory is introduced in Section 2; the telescope and its instruments are described in Section 3; and the efficiencies of the telescope and its instruments also have been estimated in this section. The relevant science and projects based on observational data obtained by the 2.16-m telescope are described in Section 4; finally, a brief summary is given and some future facilities are discussed in Section 6.

2. The Xinglong Observatory

The Xinglong Observatory of National Astronomical Observatories, CAS (NAOC; IAU code 327, coordinates: 40° 23′39″ N, 117°34′30″ E) was founded in 1968. At present, it is one of most primary observing stations of NAOC. As the largest optical astronomical observatory site in the continent of Asia, it harbors nine telescopes with an effective aperture greater than 50 cm. These are LAMOST, the 2.16-m reflector, a 1.26-m optical, and near-infrared reflector, a 1-m Alt-Az reflector, an 85-cm reflector (NAOC-Beijing Normal University Telescope, NBT), an 80-cm reflector (Tsinghua University-NAOC, TNT), a 60/90-cm Schmidt telescope, a 60 cm reflector, and a 50-cm reflector. The average altitude of the Xinglong Observatory is ~960 m, and it is located at the south of the main peak of the Yanshan Mountains, in the Xinglong county, Hebei province, which is ~120 km northeast of Beijing. The mean and median seeing values of the Xinglong Observatory are 2.″0 and 1.″8, respectively, and on average, there are 117 photometric nights and 230 useful nights per year based on the data of 2007–2014 (Zhang et al. 2015). For most of the time, the wind speed is less than 4 m s^{-1} (the mean value is 2 m s^{-1}), and the sky brightness is ~21.1 mag arcsec^2 in the V band at the zenith (Zhang et al. 2015).

Each year, more than 100 astronomers use the telescopes of Xinglong Observatory to perform the observations for the studies on Galactic sciences (stellar parameters, extinction measurements, Galactic structures, exoplanets, etc.) and extragalactic sciences (including nearby galaxies, AGNs, high-redshift quasars), as well as time-domain astronomy (supernovae, gamma-ray bursts, stellar tidal disruption events, and different types of variable stars). In recent years, besides the basic daily maintenance of the telescopes, new techniques and methods have been explored by the engineers and technicians of Xinglong Observatory to improve the efficiency of observations. Meanwhile, the Xinglong Observatory is also a national popular-science and education base of China for training students from graduate schools, colleges, high schools, and other educational institutions throughout China, and it has hosted a number of international workshops and summer schools.

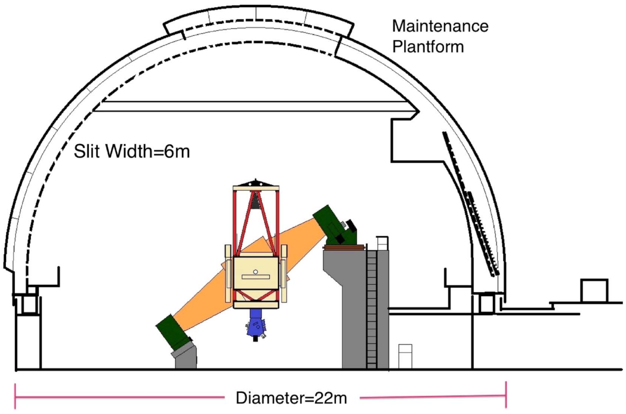

Figure 1. Illustration of the 2.16-m telescope at Xinglong Observatory, which is an English equatorial mount, in a large dome with a diameter of 22 m. (A color version of this figure is available in the online journal.)

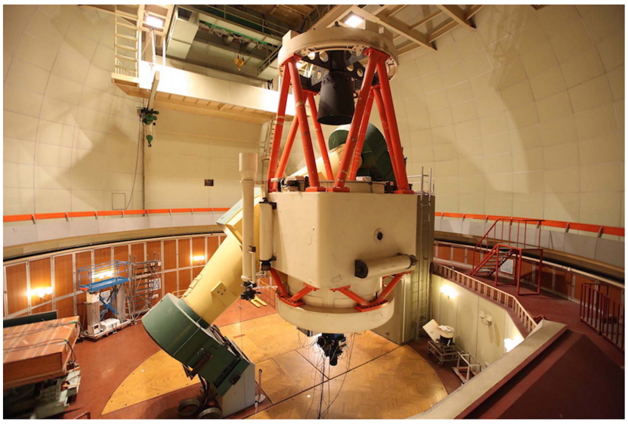

Figure 2. Xinglong 2.16-m telescope at Xinglong Observatory. (A color version of this figure is available in the online journal.)

3. The 2.16-m Reflector and Its Instruments

As shown in Figures 1 and 2, the telescope is an R-C system on an English equatorial mount. The effective aperture of the primary mirror is 2.16 m. Currently, there are three primary instruments available for the Cassegrain focus: BFOSC, OMR, and the fiber-fed HRS. Previously, a high-resolution spectrograph was mounted on the Coudé focus before the fiber-fed HRS was mounted in 2010. Since then, the Coudé focus has only been used for a few special experiments, such as adaptive optics tests. As shown in Figure 1, the diameter of the dome is 22 m, which is relative large for a 2-m-class telescope, due to its design. The rotation part of the telescope weighs 91 tons, and the pointing accuracy that is modified with the pointing model is rms = 10.″0. While the tracking precision of the telescope is rms = 20.″0 within 10 minutes, and rms = 50.″0 within 1 hour. The position precision of the telescope on the sky under guiding is rms < 0.″15 (Huang et al. 2015).

3.1. The BFOSC Instrument

The BFOSC is one of the primary instruments of the telescope, for which the design and processing of mechanism and electronics control; the design of grims and assembling and debugging of the whole system were done by the University of Copenhagen, and ESO provided consult and optical design of the focal reducer. It is available for the f/9 Cassegrain focus. The scale of the focal plane is 10.″61 mm^{-1}. As discussed in Section 1, it can be used for both imaging mode and spectroscopy mode, which is switchable. Figure 3 shows the optical layout of the BFOSC instrument, including the aperture wheel, filter wheel, grism/echelle wheel, calibration device, guiding device, collimator, shutter, camera, and the CCD detector.

There are eight positions on the aperture wheel: three of them for direct imaging, coronagraph mask, and focal adjusting plate, respectively, and the other five for long/short slit plates. For the long slits, the lengths are all 9.′4, and there are nine options for the slit widths (0.″6, 0.″7, 1.″1, 1.″4, 1.″8, 2.″3, 3.″6, 7.″0, and 14.″0). While for the short slits, the slit lengths are various for different slit widths: 3.″5 for slit width of 0.″6, 4.″0 for slit width of 1.″0, 3.″6 for slit width of 1.″6, and 3.″7 for both slit widths of 2.″3 and 3.″2. The coronagraph mask is used to block out the intense light from bright sources near the observing targets, with circular spots of which the diameters are 2.″0, 3.″0, 4.″0, 6.″0, 9.″0, and 12.″0.

For the filter wheel, there are several sets of filters available. The Johnson-Cousins *UBVRI* filters are for the broadband photometry. In addition, there are special filters used for the spectroscopic observing: the *Z* band for the transmitting spectral region $\lambda \geqslant 910$ nm, and the 385*LP* band for removing the second-order spectrum in the wavelength region $\lambda \leqslant 385$ nm. The transmission curves are shown in Figure 4.

Besides, a series of interference narrowband filters covering [O III] (rest-frame wavelength of λ5007A), Hα, and He II(rest-frame wavelength λ4686A) is also available for the BFSOC imaging mode. For series of [O III] band observations, there are eight filters of which the central wavelengths are between 500.9 and 536.0 nm with FWHM of 6 nm, corresponding to redshifts of 0–20000 km s^{-1}. While for the series of H_α bands, there are 11 filters of which the central wavelengths are between 656.2 and 706.0 nm with an FWHM of 7 nm, corresponding to redshifts of 0–22000 km s^{-1}. For the He bands, there are three filters of which the central wavelengths are between 447.1 and 468.6 nm with an FWHM of 6 nm. In addition, an [O III] filter with an FWHM of 13 nm and an H_α filter with FWHM of 14 nm are also provided for a redshift of $z = 0$. These filters can be used for the study of star-forming regions of nearby galaxies at different redshifts.

Table 1 presents the parameters of the grisms/prisms/echelle for the BFOSC instrument. From left to right in the columns are names, working spectral orders, reciprocal linear dispersions, dispersions, and wavelength coverages of the various grisms/prisms/echelle, respectively. The configurations can be chosen by the users depending on the different requirements of the projects. For grisms G3/G6/G10, the blue ends of wavelength coverages are limited by the cutoff of the atmospheric window, while for grisms G5/G8, the red ends are limited by the size of the CCD. The low dispersion grisms G10/G11/G12 are also used for the cross-disperser when mounted on the filter wheel. The echelle E13 is only used for measuring the velocity field of extended sources with the third-order spectrum, and the *V* band filter is recommended to be applied together with it to remove the other order of the spectrum.

Table 2 presents the spectral resolutions of some frequently using BFSOC grisms at a minimum slit width 0.″6 and a slit width of ~2.″3 used in typical seeing conditions, which are estimated with the emission lines of the planetary nebula (PN) IC4997. The observations were taken on 2014 November 24 and 2016 February 26, with gratings of G4, G6, G7, and G8 on BFOSC. Throughout the nights of the observations, the weather was clear, and the seeing was between ~2.″0 and 2.″4. The exposure time was 0.2–10 s depending on the dispersions of the different grisms. The shortest exposure of 0.2 s is considerably longer than the shutter speed of 1.5 ms.

For the calibration device, four lamps can be mounted at most. One is for the flat-fielding correction, and the other lamps can be used for wavelength calibration. The lights of the lamps illuminate the integrating sphere at first, then are modified to be f/9 light beam, and finally are reflected to the focal plane of the BFOSC instrument. The Fe lamp and Ne lamp are frequently used for the wavelength calibration.

On the guiding device, a mirror reflects the view outside of the observing field of view (FOV) to an ICCD, which is movable in 3D directions to find a proper guide star and also to adjust the focus. The FOV of the guiding device is 10′ × 20′, which is large enough to find a suitable guide star.

In 2010, an E2V 55–30–1–348 back-illuminated CCD, AIMO, was installed on the spectrograph, and the CCD controller was made by the Lick Observatory. The size of the CCD is 1242 × 1152 pixels with a pixel size of 22.5 μm. The pixel scale is 0.″457, and the FOV is 9.′46 × 8.′77 according to the size of the CCD. Figure 5 shows the quantum efficiency (QE) of the CCD. It can be seen that the maximum QE is higher than 90% around 5700 Å of the wavelength.

Table 3 lists the gains, readout noises, and readout speed of the BFOSC CCD at various readout times. Observers can

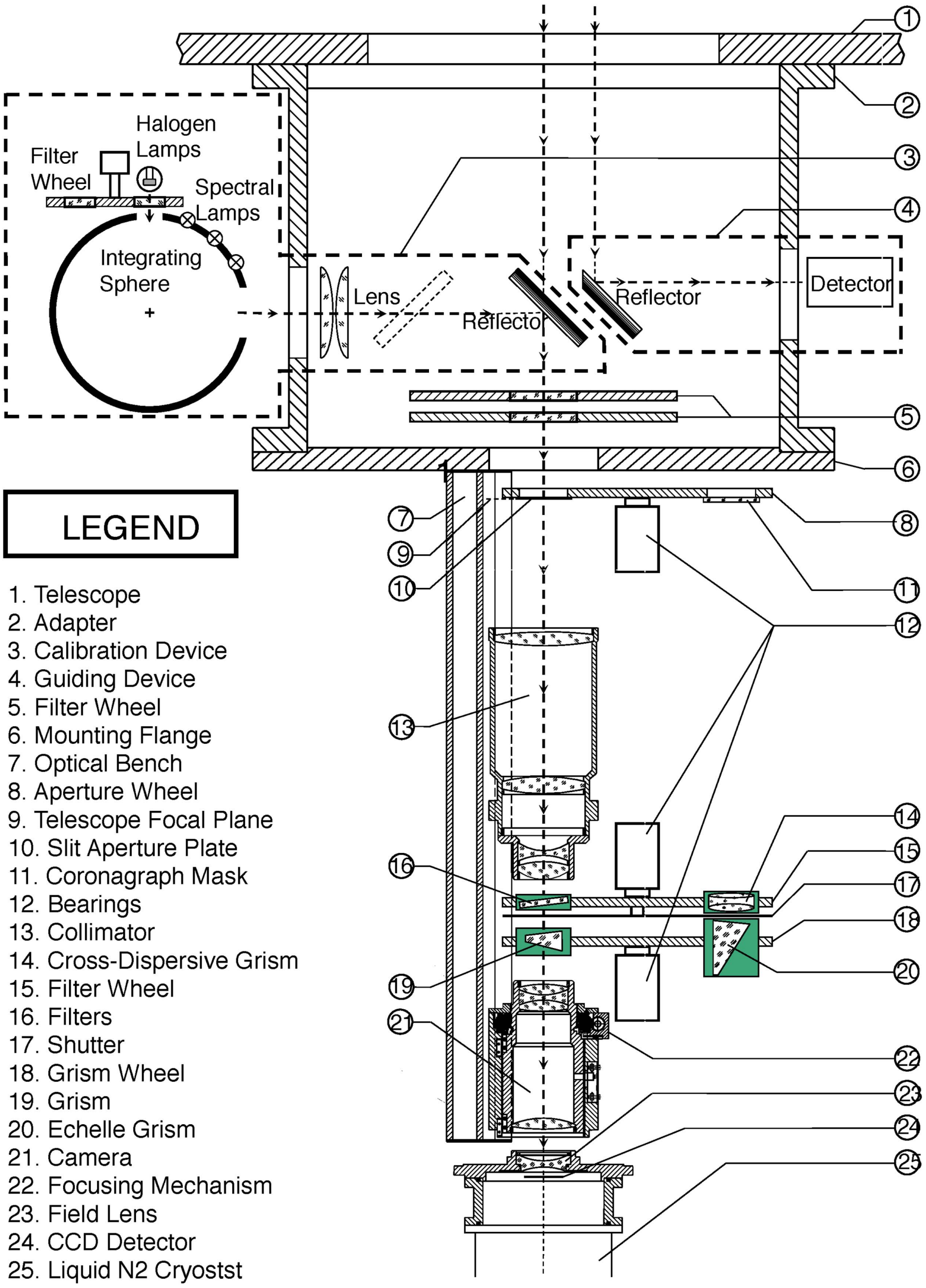

Figure 3. Optical and mechanical layout of the BFOSC instrument from Huang et al. (2012).
(A color version of this figure is available in the online journal.)

choose different options for the specific observations, and the slow readout speed is applied in most of the time.

There are six observing modes for the BFOSC instrument: (1) direct imaging, (2) long-slit spectroscopy, (3) slitless spectroscopy, (4) echelle grism spectroscopy, (5) coronograph mask, and (6) multiple-object spectroscopy. Figure 6 shows the optical layout of the lens and light path for the direct imaging mode and the spectroscopy observing mode, which could be switched in a few minutes.

Since 2012, a multi-object spectroscopy (MOS) observing mode of BFSOC is available for observers by placing a multiple-aperture mask on the aperture wheel (Zhou

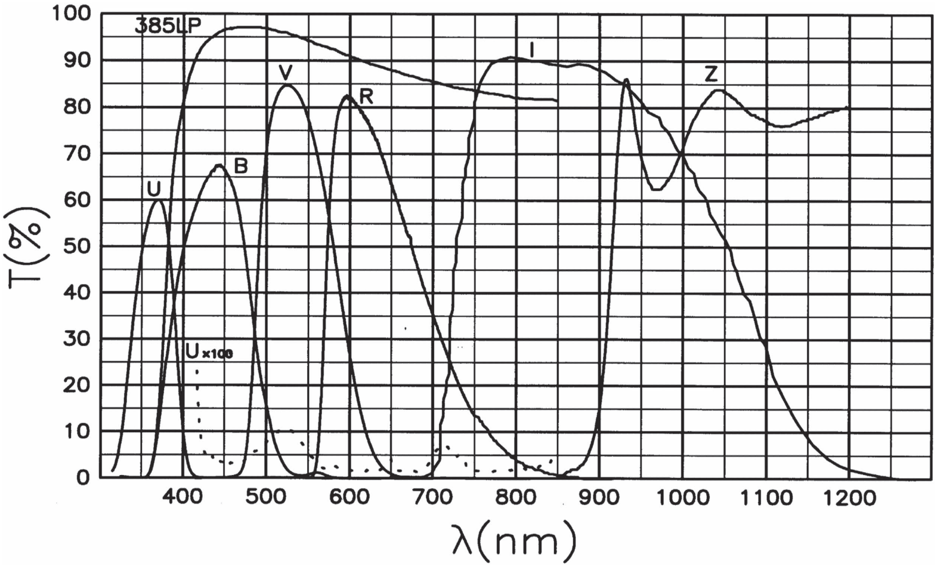

Figure 4. Transmission curves of the BFOSC filters, including the Johnson-Cousins *UBVRI* bands as well as the 385*LP* and *Z* bands for spectroscopic observations.

Table 1
The Parameters of Grisms/Prisms/Echelle for the BFOSC Instrument from Huang et al. (2012)

Name	Spec. Ord.	Rec. Lin. Disp. (Å mm^{-1})	Disp. (Å pix^{-1})	Wav. Range (Å)
P1		573–2547	8.6–38.2	4000–5600
G3	1	139	3.12	3300–6400
G4	1	198	4.45	3850–7000
G5	1	199	4.47	5200–10120
G6	1	88	1.98	3300–5450
G7	1	95	2.13	3870–6760
G8	1	80	1.79	5800–8280
G10	1	392	8.80	3300–6400
G11	1	295	6.63	3900–7300
G12	1	837	18.8	5200–10200
E9+G10	21–11	16.8–38.4	0.38–0.86	3300–6400
E9+G11	18–9	21.0–47.9	0.47–1.076	3900–7300
E9+G12	14–6	29.0–73.2	0.65–1.64	5200–10200
E13+V	3	33.1	0.75	4980–5990

et al. 2014). In this mode, 10–20 objects can be observed simultaneously, depending on the spatial distribution density of the targets. The MOS improves the observing efficiency of multiple-object observations, such as star-forming activities of H II regions of nearby galaxies, star clusters, or groups and clusters of galaxies.

Table 2
Spectral Resolutions of Several Frequently used Grisms of BFSOC at a Slit Width of 0.″6 and 2.″3, which is around the Typical Seeing

Wavelength	G4	G6	G7	G8	G4	G6	G7	G8
(Å)	0.″6				2.″3			
4341	531	1423	1204	⋯	246	463	478	⋯
4363	557	1503	1252	⋯	⋯	⋯	⋯	⋯
4861	⋯	⋯	⋯	⋯	262	538	521	⋯
4959					265	540	524	⋯
5007	620	1413	1328	⋯	265	555	532	⋯
6563	824	⋯	⋯	2245	321	⋯	⋯	820

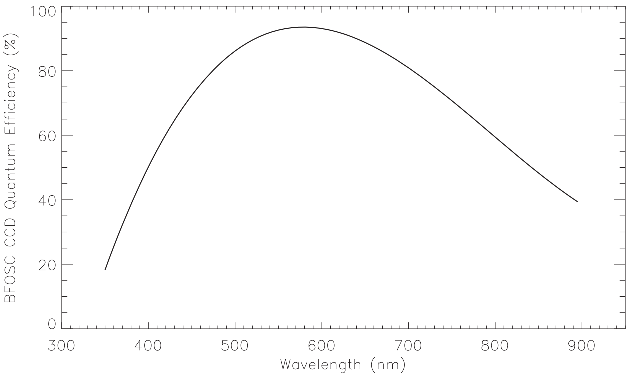

Figure 5. Quantum efficiency of the BFOSC CCD camera.

Table 3
Gains, Readout Noises, and Readout Speed of BFOSC CCD from Huang et al. (2012)

Readout Speed	Mode	Gain (e^{-} ADU^{-1})	Readout Noise (e^{-} pix^{-1})	Readout Time (second)
Fast	0	99.58	132.5	5
Fast	1	49.44	103.7	5
Fast	2	24.48	87.35	5
Median	0	2.33	6.80	8
Median	1	1.22	5.93	8
Median	2	0.50	6.06	8
Slow	0	2.43	3.25	28
Slow	1	1.13	2.58	28
Slow	2	0.50	2.46	28

The total efficiency of the observing system, including the atmosphere, telescope, and its instruments, is what the observers are mostly concerned about. In fact, there are a number of factors to be considered for calculating the total efficiency of the system, such as atmospheric extinction, reflectivity of primary and secondary mirror, transmissions of filters, and the quantum efficiency of the CCD. It can be estimated through observing standard stars in Equation (1):

$$\eta(\lambda) = \frac{F_{\mathrm{ADU}} \cdot G}{F_{\lambda} \cdot \delta\lambda \cdot S_{\mathrm{tel}}}. \quad (1)$$

In this formula, F_{ADU} is the observed number counts of a standard star per second (ADU s^{-1}), G is the gain of the CCD (e^{-1} ADU^{-1}), F_{λ} is theoretical photon flux of a standard star derived from its AB mag (photon s^{-1} cm^{-2} Å^{-1}), $\delta\lambda$ is the effective bandwidth of the filter in imaging observations or the dispersion of the grating for spectroscopic observations (Å), S_{tel} is the effective area of the primary mirror of the telescope (cm^{2}), and λ is the effective wavelength of the filter or the wavelength at which the efficiency is to be computed for the spectroscopy (Å).

In order to estimate the total efficiency of the 2.16-m telescope, a Landolt standard star PG2336+004B was observed on 2014 November 21 in the broadband *UBVRI* bands of the BFOSC photometric system by using Equation (1). The seeing was ~2.″0–3.″0 throughout the whole night of observations, and the airmass is ~1.3. Figure 7 is a plot of the total efficiency in different bands as a function of central wavelength. The atmospheric extinction, reflectivity of primary and secondary mirrors, transmissions of filters, QE of CCD, as well as other factors, were not corrected in the calculation. It can be seen that the total efficiency is relatively low in the *U* band (~2%) and *B* band (~7%), but it is relatively high in the *VRI* bands (~15%).

The limiting magnitude is also an important quantity to evaluate the observing ability of a telescope. Actually, at the same night on 2014 November 21, a Landolt standard star PG2336+004 was observed in the *UBVRI* bands. The airmass was ~1.3. The limiting magnitude (signal-to-noise ratio, S/N = 5) as a function of exposure time in the *UBVRI* bands are shown in Figure 8, and the same relations but for the limiting magnitudes of S/N = 10 are shown in Figure 9. It is noted that in the 640 s exposure the limiting magnitudes of the $B/V/R$ bands could reach ~22 mag in S/N = 5 and ~21 mag in S/N = 10. The limiting magnitude in the *U* band is the lowest because the sensitivity of the observing system in the blue band is relatively low, further affected by the effect of significant atmospheric extinction in the blue band. However, although the efficiency in the *I* band is similar to those of the *VR* bands, the night-sky background is much brighter (~2 times) than in the *VR* bands. In addition, the fringe of the CCD in the *I* band contributes significant noise. Although we have tried the de-fringing method introduced by Chen et al. (1987), it has not been improved significantly. Therefore, these factors together make the limiting magnitudes ~1 mag shallower than those in the *BVR* bands.

In order to estimate the efficiency of the spectroscopic system of BFOSC, the two ESO standard stars HR153 and HR9087 were observed on 2014 November 24, with several frequently used grisms (G4, G5, G6, G7, and G8) of the BFOSC instrument. The weather was clear, and the seeing was ~2.″4. The exposure time was 0.2–10 s according to the dispersions of the grisms. To make sure that most of the flux can be obtained and measured for estimating the efficiency, the slit was configured as 7.″0. The total efficiency, which is defined above, including atmospheric extinction and instruments, was calculated with Equation (1) and shown in Figure 10. For the grisms G4 and G5, the peak efficiencies are ~15% and ~10%, respectively, while for the other three grisms, the total efficiencies of the peak are ~5%. The filter 385*LP* was used for removing the second-order spectrum of wavelength $\lambda \geqslant 385$ nm.

For the limiting magnitude in the spectroscopic observations, the previous observations show that typically it could reach $V = 20$ mag of S/N = 5 in the grism G6, with an exposure of 1 hour, given by Huang et al. (2012).

3.2. The Spectrograph Made by Optomechanics Research Inc. (OMR)

The OMR is another low-resolution spectrograph available on the Cassegrain focus of the 2.16-m telescope. It was made by Optomechanics Research Inc. (Arizona, USA) at the end of 1994 and was tested on the 2.1-m telescope at Kitt Peak. Then, it was installed on the 2.16-m telescope of Xinglong Observatory in 1995 and was available to astronomers in 1996.

The optical layout of the OMR is shown in Figure 11. The system is composed of slit and decker assembly, filters, spectrograph, calibration system, collimator, gratings, CCD camera, guiding CCD camera, console, and data-collecting system.

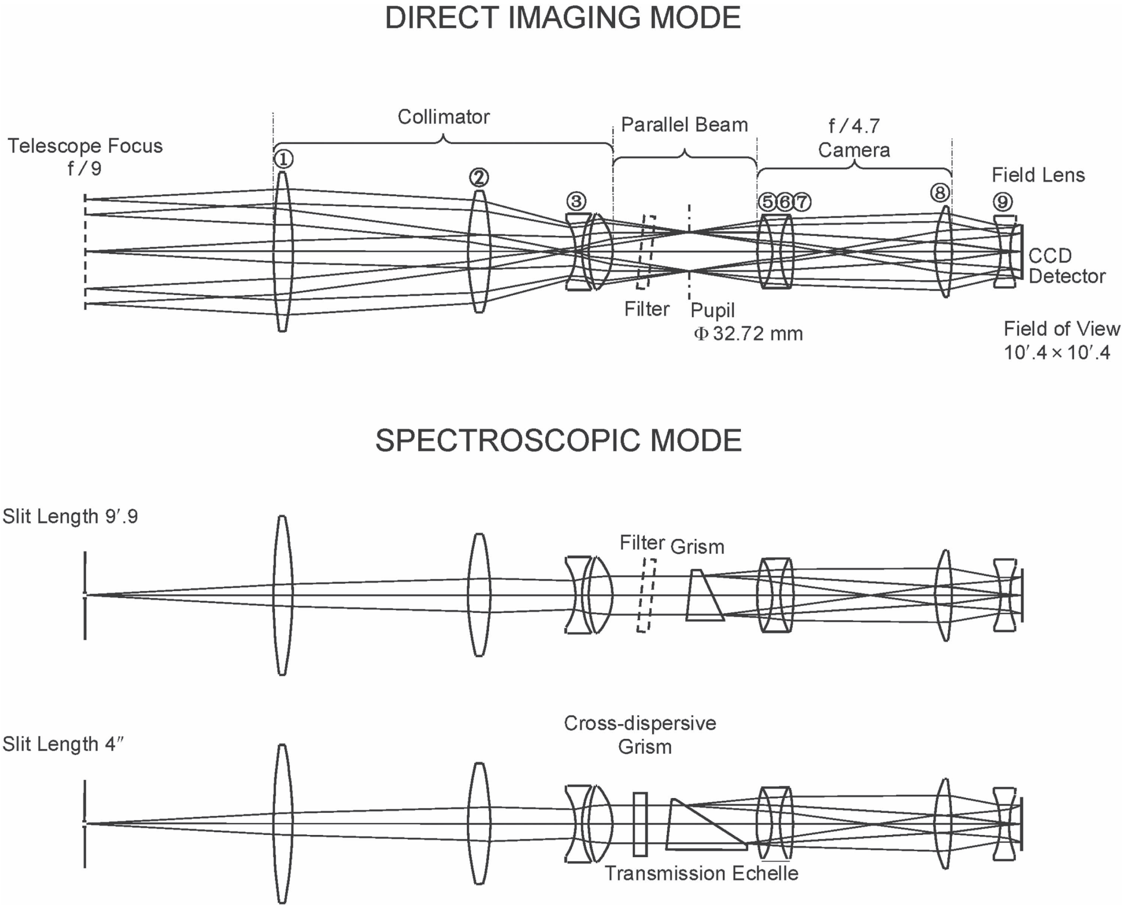

Figure 6. Layout of the lens of two different working modes of the BFOSC instrument from Huang et al. (2012).

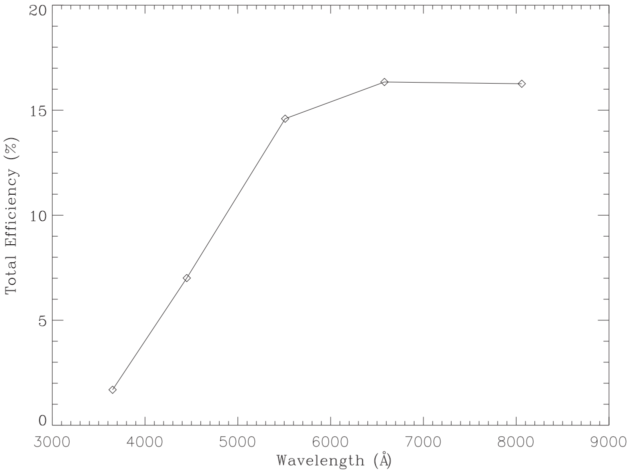

Figure 7. Total efficiency of the BFOSC photometric system including the atmosphere of the 2.16-m telescope in the *UBVRI* bands at an airmass of ~1.3.

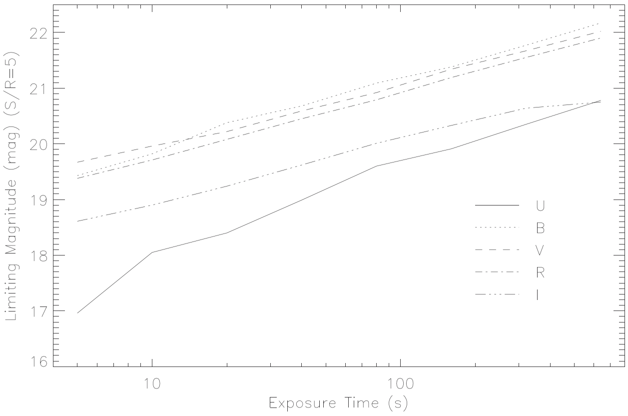

Figure 8. Limiting magnitudes in the *UBVRI* bands for the signal-to-noise ratio of S/N = 5 at an airmass of ~1.3.

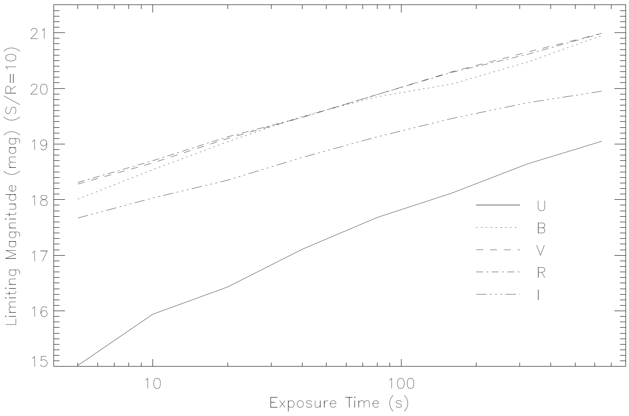

Figure 9. Same as in Figure 8, but for a signal-to-noise ratio of S/N = 10.

The slit and decker assembly is composed of decker, the slit width adjuster, calibration reflector, and driving device. The top surface of the slit is aluminized stainless steel with high reflecting power, while the slit edge was polished to be very sensitive and should not be touched. The slit is tilted by 20° with respect to telescope optical axis, and the projected slit width can be adjusted remotely through the main console in the range of 0.05–1.0 mm (corresponding to $0\farcs5$–$10\farcs6$), which is displayed on the main console via the voltage value. The size of the slit jaws is 32.8 mm × 38 mm, and the effective length of the slit is 28.8 mm (corresponding to $5\farcm1$). The slit jaw reflects the light to the guiding system.

There are six positions on the filter wheel for the filters of Clear, Corning 4–71, Schott *BNG*–37, *BG*–39, *GG*–475, and *RG*–695. All the filters have the same size of 25 mm × 25 mm. The central wavelengths of filters could be matched with the first- or second-order of the spectrum by the softwares automatically.

There are three wavelength calibration lamps (Fe-Ne, Fe-Ar, and He-Ar) and a flat-fielding lamp for the calibration device. All of lamps can be controlled remotely. For the Fe-Ne lamp, a standard 1.5-inch ISTC Model #WL-22810 is supplied, and other types of lamps actually can be used as well, such as Hamamatsu and Starna. The maximum working current is 20 mA, and the normal working current is 10–12 mA. The Fe-Ar lamp ISTC Model is #WL-22611. For the safety of He-Ar lamp, the DC power should be used for the supply. As for the flat-fielding lamp, the power is the standard 12 V DC, 1.5A halogen tungsten lamp (Sylvania #808-301550), and it usually can be used for 1000–2000 hours. Meanwhile, there are four condensers for the calibration lamps, which are made of quartz or pyrex glass. The diameters are 25 mm, and the focal lengths are $f = 38$ mm. The field lens is made of quartz, with a diameter of 38 mm and a focal length of 64 mm.

The mirror of the collimator is an off-axis parabolic aluminized reflector, made of pyrex glass. The aperture of the mirror is $D = 110$ mm, and the focal length is $f = 674$ mm. The off-axis angle is 8.1° and the focus can be adjusted remotely.

At present, there are six reflecting blazed gratings mounted on the OMR spectrograph. The gratings are made of aluminized pyrex glass and can be switched manually. The parameters of the blazed gratings are given in Table 4, including the number of the gratings, the grooves, groove areas, reciprocal linear dispersions, dispersions, blaze wavelengths of the first-order spectra, and the blaze angles. The overall working wavelength coverage of the gratings is ~3700–10000 Å. For the specific grating, the wavelength coverage is adjustable, and it can be estimated through parameters of Table 4 and the size of the CCD. For instance, the wavelength coverage of gratings of 1200 lines/mm is ~1380 Å, while for the grating of 300 line/mm, it is ~5420 Å. The SPEC software, which is the camera-controlling software designed and installed with the PI Spec-10 CCD camera, can recognize the gratings, and the wavelength coverage can be adjusted via SPEC according to the requirements of the observers.

The camera is a Schmidt-Cassegrain system. The useful aperture is $D = 100$ mm, and the focal length is $f = 150$ mm. The CCD mounted is a PI Spec-10 PIXIS 1340 × 400 scientific CCD detector, which delivers the highest sensitivity possible and >16–bit dynamic range for spectroscopy applications. The pixel size is 20 × 20 μm pixels, and the CCD size is 26.8 × 8.0 mm^2. The deepest cooling temperature is −75° C. The QE of the CCD is shown in Figure 12, which is midband.

The guiding system of the OMR is composed of a reflecting system and a CCD Camera. In the reflecting system, the slit reflecting mirror is aluminized and the rms of the surface flatness is $1/4\ \lambda$. For the transfer lens, the diameter is 50 mm, with a focal length of $f = 260$ mm. While for the focal lens, the diameter is 36 mm, with a focal length of $f = 85$ mm. Both of the lenses have been coated. The CCD camera is an Alta U42 CCD, made by Apogee Imaging Systems, Inc. The sensor is E2V CCD42–40, and the size is 2048 × 2048 pixels. The Gain is 1.3 $\mathrm{e}^-\ \mathrm{count}^{-1}$ and the maximum digitized well capacity is 82 k e^-. The dark current is 0.39 $\mathrm{e}^-\ \mathrm{pixel}^{-1}\ \mathrm{s}^{-1}$.

Similarly, the Landolt standard star Feige 66 was observed with two blazing gratings 1200B and 1200R of the OMR instrument and the total efficiencies (including the atmosphere extinction, the reflecting rate of mirrors, QE of CCD, etc.) have been computed through Equation (1). As described above, the central wavelength and coverage is adjustable; Figure 13 shows the total efficiencies of two gratings 1200B and 1200R, in two different central wavelength and wavelength coverages. It can be seen that the efficiency ranges from ~1% to ~2%, which is relatively lower than that of the BFOSC gratings.

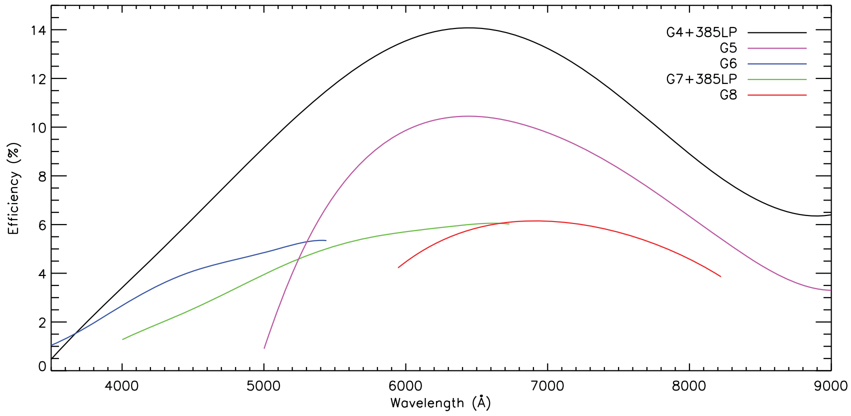

Figure 10. Total efficiencies estimated for grisms G4, G5, G6, G7, and G8 of the BFOSC instrument.
(A color version of this figure is available in the online journal.)

Typically, for a star of $V = 17.3$ mag in an exposure time of 1800s, the signal-to-noise ratio is S/N = 12 at wavelength of $\lambda = 5500$ Å; for a star of SDSS $g = 19.8$ mag in an exposure time of 3600 s, the signal-to-noise ratio is S/N = 5 on average for the whole band.

3.3. The Fiber-fed High Resolution Spectrograph (HRS)

Previously, an echelle spectrograph was mounted on the Coudé focus of the telescope for high-resolution spectroscopic observations. The special design of the optical system is to allow the Cassegrain system and the Coudé system to share the same secondary mirror and there is a relay mirror in the Coudé system. When switching between the two systems, the Coudé system can eliminate spherical aberration and coma aberration sufficiently just by slightly moving the secondary mirror (Su et al. 1989). The resolution power was between R = 16,000 and 170,000 (79 gr mm^{-1}) in the blue beam from 330 nm to 580 nm and R = 13,000 and 170,000 (31.6 gr mm^{-1}) in the red beam from 520 nm to 1100 nm. For an exposure time of 1 hour, the limiting magnitude could reach $V = 9.5$ in the red band and $V = 7.2$ mag in the blue band with a signal-to-noise ratio S/N = 100 (please see Zhao et al. 2000; Zhao & Li 2001).

Since 2010, a new fiber-fed High Resolution Spectrograph (HRS) has been developed by the Nanjing Institute of Astronomical Optics & Technology (NIAOT) to satisfy the scientific requirement of, for instance, exoplanet surveys, the study of stellar abundances, and stellar magnetic activities. The optical layout and light path are shown in Figure 14. The HRS system is available for the Cassegrain focus and composed of four parts: 1) the Cassegrain connector of the telescope; 2) the fiber connector and the micro-optical module for focal ratio changing; 3) the main body of the spectrograph; 4) the data-collecting part of the CCD camera.

The fiber-fed HRS observing mode could be switched to other instruments (such as BFOSC or OMR) conveniently through the Cassegrain focal interface of the telescope within only a few minutes. The calibration system of HRS, the I_2 cell and its heating system, as well as the tip/tilt system are mounted on the interface of the spectrograph. The whole main body is sealed in a protective box and the temperature variation is less than rms = 0.5°C for a week. At present, a $2''\!.4$ aperture fiber is configured and the tip/tilt system is working to improve the efficiency of the system when the seeing is ideal. The fiber of $1''\!.6$ is at the commissioning stage and it could be available very soon. An environmental controlling system can accurately keep the stability of both temperature and humidity for the HRS system. Furthermore, a sub-controlling system of pressure will be installed at this system in the future.

The basic parameters of HRS are listed in Table 5. The working wavelength coverage is 360–1000 nm, and the instrumental efficiency of the spectrograph is $\geqslant 34\%$ for the peak at a wavelength coverage of 640–790 nm (*RI* band), and $\geqslant 10\%$ for $\lambda > 4500$ Å (the whole working band), based on the tests of 2010 November 23. The spectral resolution is 32,000–106,000 for the spectrograph, and it is $R = 49{,}800$ at a fixed slit width of 0.19 mm (corresponding to $1''\!.8$) based on the test of 2011 April 12. The stability of the instrument for the velocity measurement is rms = ± 6 m s^{-1}, and the temperature is quite stable even for two weeks. The CCD camera is a back-illuminated first-order red-sensitive E2V CCD 203-82. The size is 4096 × 4096 pixels with a pixel size of 12 μm. The typical QE of the CCD is >90% under the temperature of −100°C in the wavelength coverage of ∼500–650 nm, which is shown as the solid line in Figure 15.

The liquid nitrogen (LN) holding time of the system is ∼20 hours, and the cooling temperature is −106°C. For *Gain* = 1.01 e$^-$/ADU, the readout noise (RON) is 2.84 e$^-$ at the readout speed of 50 k, 4.29 e$^-$ at readout speed of 100 k,

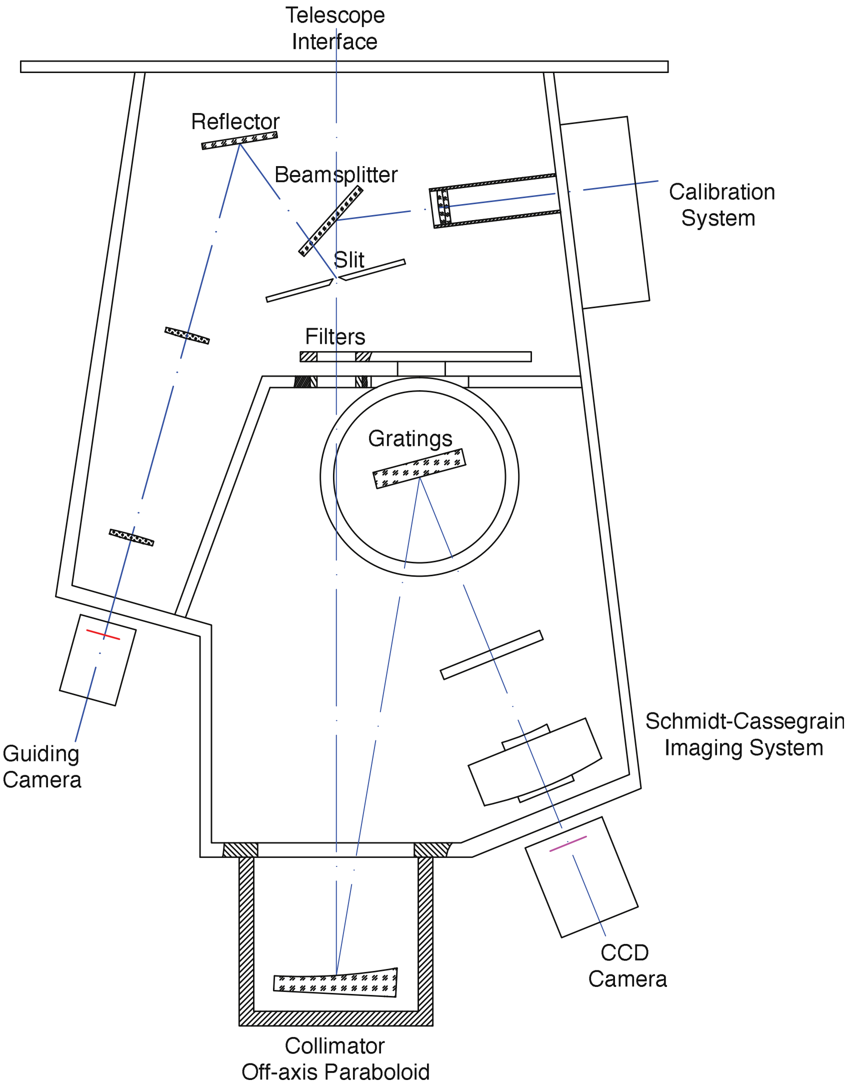

Figure 11. Optical layout of the OMR spectrograph.
(A color version of this figure is available in the online journal.)

and 7.88 e$^-$ at readout speed of 200 k. The distance between the nearby orders of the spectrum is ⩾20 pixels, and the two fibers (2.″4 aperture one and 1.″6 aperture one) can work at the same time. The aperture of the fiber is 100 μm (2.″4), and the fiber length is ~19 m. The FOV for the guiding camera is $3' \times 3'$, and in the guiding plate the aperture of pupil is 4.″0 in front of the fiber. The temperature variation of the system is rms = ±0.05°C for a whole night and rms = ±0.34°C for a week. The tip/tilt system is working normally on the Cassegrain focus. The system, including the astro-frequence comb instrument, is currently in its commissioning phase, and its radial velocity precision dose not yet reach its design goal of a few ~cm s^{-1}. It is expected that this goal will be achieved once commissioning is complete.

The guiding CCD camera is a GC1380, and the software *AVTUniCamViewer* is used for CCD controlling, exposure time configuration, and data collection. The telescope controlling software can monitor the guiding uncertainty of the guiding system.

An astro-frequency comb calibration system (Zhao et al. 2014, 2015), which is developed by Peking University (PKU), also was installed and is being tested on the 2.16-m telescope. The full spectral wavelength range of the astro-frequency comb is 160 nm and the central wavelength is 640 ± 20 nm. The observed spacing of the comb teeth is 29.01 GHz. Once working normally, it can greatly improve the measuring accuracy of the stellar radial velocity. The system has significant advantages over the I$_2$ cell (Wilken et al. 2010). It

Table 4
The Current Parameters of the OMR Gratings

No.	Grooves ($1\ mm^{-1}$)	Gro. Area (mm)	Rec. Lin. Disp. (Å mm^{-1})	Disp. (Å pix^{-1})	Blz. Wav. (1st order) (Å)	Blz. Ang. (°)
1	150	90 × 90	400	8.0	5000	2.2
2	300	90 × 90	200	4.0	8000	6.5
3	600	102 × 102	100	2.0	6500	11.3
4	1200	102 × 102	50	1.0	8000	28.7
5	300	102 × 102	200	4.0	4224	3.6
6	1200	102 × 102	50	1.0	4000	13.9

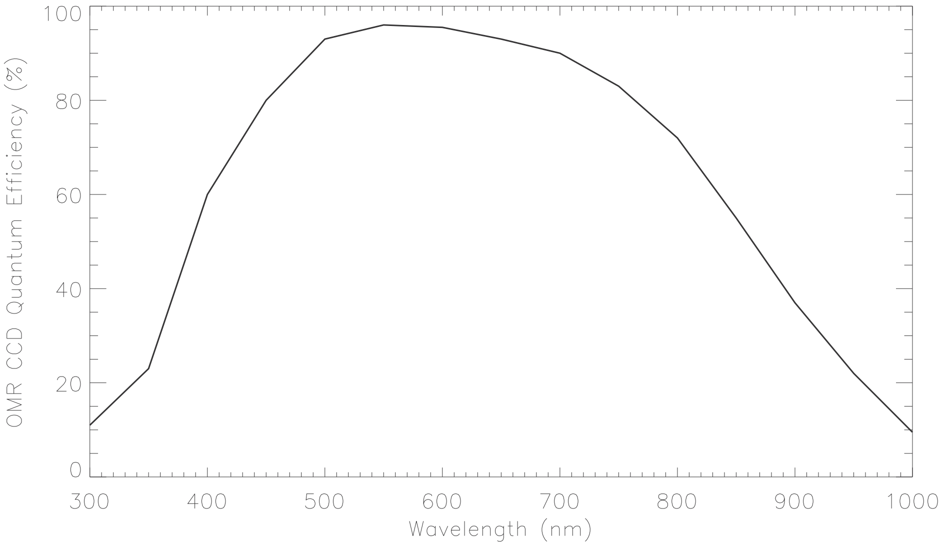

Figure 12. Quantum efficiency of the CCD camera of the OMR Spec-10, which is midband.

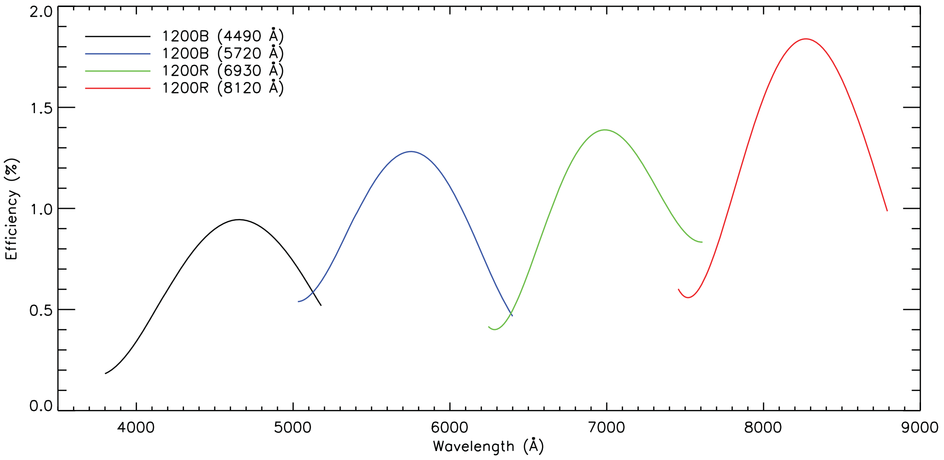

Figure 13. Total efficiency estimates with blazing gratings 1200B/1200R of the OMR, in two different central wavelengths and wavelength coverages. (A color version of this figure is available in the online journal.)

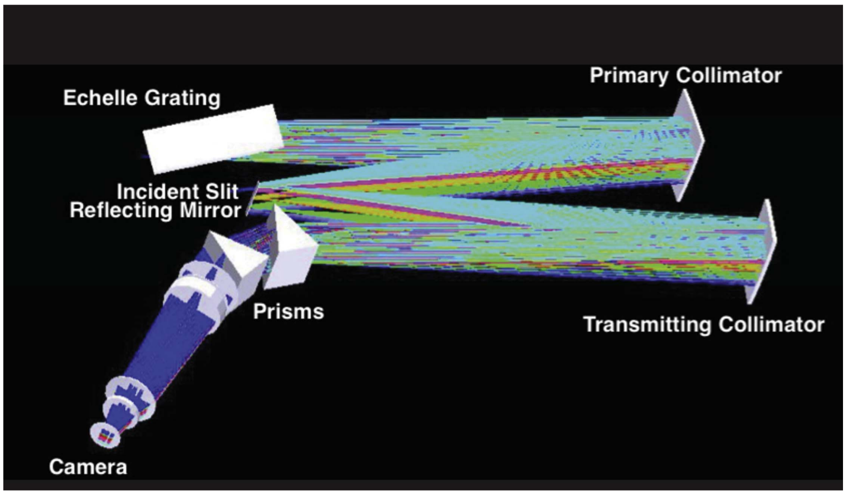

Figure 14. Optical layout and the light path of the fiber-fed HRS spectrograph.
(A color version of this figure is available in the online journal.)

Table 5
The Current Instrumental Parameters of the HRS

Tech. Index	Parameters	Notes
Wave. Cov.	3650–10,000 Å	ThAr lamp
Aper. of Fiber	2.″4/1.″6	
Spec. Res.	32,000–106,000	tested on 2011 Apr 12
Stab. of Inst.	± 6 m s^{-1}	Zhao et al. 2014
Effi.	34% at peak value $\geqslant$10% for $\lambda > 4500$ Å	tested on 2010 Nov 23
CCD Camera	E2V 4k × 4k 12 μm Scientific chip, class 1 On-chip Binning 50–200 KHz LN holding time: 20 hours (w/LN auto-filling) LN cooling	2 × 1 binning mode suggested
FOV of Guid. Cam.	3.′3 × 3.′3	
Temp. var./day	±0.°05	
Temp. var./week	±0.°34	

consists of a series of discrete, equally spaced spectral lines with equal intensity, and it is repeatable in a long timescale. Right now, the system has been set up, and the first spectrum simultaneously from the comb and the flat-fielding lamp has been obtained during the engineering run. Meanwhile, a 25 GHz AstroComb Optical Frequency calibration system manufactured by the MenloSystems company, also has been installed on the HRS instrument system recently. The spectral coverage is ~450–720 nm, with the central wavelength of 540 ± 30 nm. The flatness of the spectrum is rms < 5 dB, and the observed spacing of the comb teeth is 25 GHz. The luminous power of the system for the full spectral wavelength range is >10 μW. The two new calibration systems are at the commissioning stage. The two new systems are supposed to be applied in the end of this year.

In order to estimate the total efficiency (including the atmospheric extinctions and reflectivity of the primary/secondary mirrors, among others), a number of standard stars were observed with HRS on 2015 June 30. By using Equation (1), the final result shows that it is >2% at 5500 Å.

In addition, the limiting magnitudes are estimated. Figure 16 is a plot of the signal-to-noise ratio (S/N) at $\lambda = 5500$ Å as a function of exposure time for the stars from $V = 5$ mag to $V = 9$ mag for the HRS system, based on the observing data. For a $V = 9$ mag star, the typical signal-to-noise ratio S/N = 100 for an exposure time of 3000–3600 s. A few observing tests give the S/N in the typical observing conditions of 2012, for a star of $V = 8.85$ mag with an exposure time of 3600 s, the signal-to-noise ratio is S/N = 80 at wavelength of $\lambda = 6000$ Å, and for a star of $V = 7.83$ mag in 2400 s exposure, the signal-to-noise ratio is S/N = 150 at wavelength of $\lambda = 6000$ Å (provided by Xiaoling Yang and Yuqin Chen).

4. Scientific Projects

Since 1989, when the 2.16-m telescope saw its first light, a great many scientific research projects have been carried out in various fields, including: the study of nearby galaxies (star formation rates, gas, and dust content), AGNs and their supermassive black holes (SMBHs), quasars, stellar parameter determinations, exoplanets, supernovae (SNe), gamma-ray

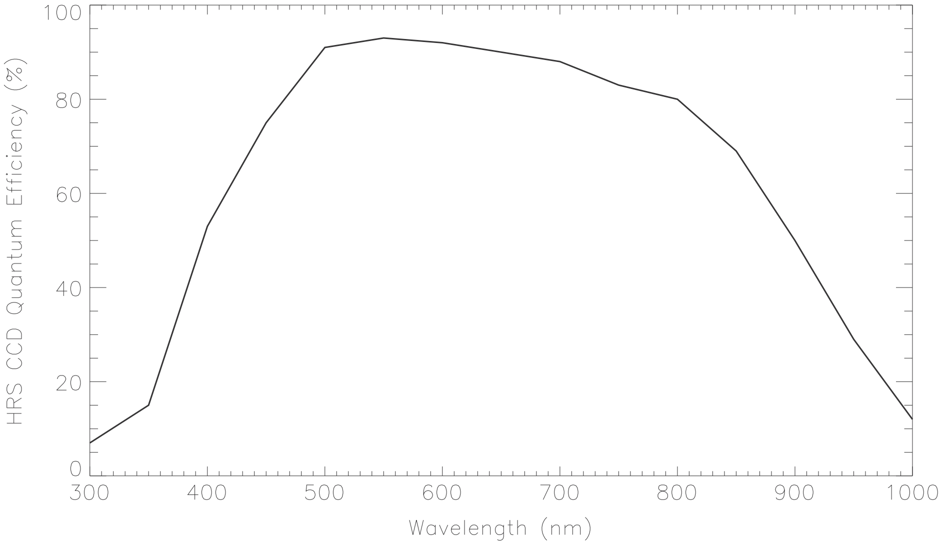

Figure 15. Quantum efficiency of the basic midband CCD camera used on the HRS at −100°C, which is shown by the solid line.

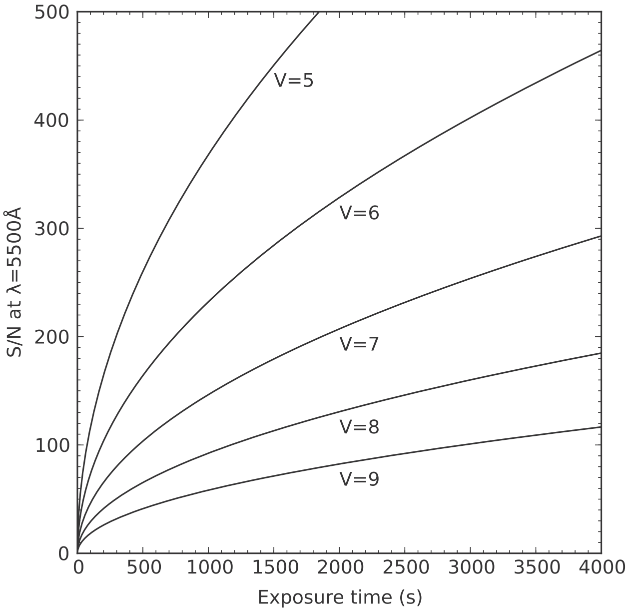

Figure 16. Signal-to-noise ratio at $\lambda = 5500$ Å as a function of exposure time for stars from $V = 5$ mag to $V = 9$ mag by using the fiber-fed HRS spectrograph.

bursts (GRBs), and follow-ups of tidal disruption events. When LAMOST was built, the 2.16-m telescope was also used for the LAMOST follow-up and stellar library observations.

Some of the scientific highlights obtained with the 2.16-m telescope are as follows. In 1993, Wang & Hu (1994) observed the spectra of supernova 1993J with the 2.16-m telescope and found the blueshifted oxygen lines only four months after the optical discovery of the supernova, which is different from the case of 1987A. Approximately 100 G-type giant stars of $V \sim 6$ mag have been monitored with the Coudé HRS system (Zhao & Li 2001). In a joint planet-search program between China and Japan, using the Xinglong 2.16-m telescope and Okayama Astrophysical Observatory (OAO), a number of substellar companions of intermediate-mass giant stars has been discovered by Liu et al. (2008, 2009). Later, a brown dwarf companion candidate was discovered by Wang et al. (2012) and a long-period giant planet has been discovered by Wang et al. (2014), which is actually the first exoplanet discovered jointly with the Subaru telescope, the OAO 1.88-m telescope, and the Xinglong 2.16-m telescope.

In recent years, in order to improve the efficiency of the telescope and to maximize the scientific output, 7–8 key projects with the telescope have been supported for 3–5 years. Each project usually owns ~20–40 nights per year, which allows us to carry out long-term observations and large-sample surveys. For instance, a number of quasars at intermediate redshift $2.2 < z < 3$ have been identified by Wu et al. (2011, 2013). An Hα imaging survey of ~1400 nearby ALFALFA galaxies is carried out to study the star formation rate and the stellar distributions. From 1997 to 2002, the spectra of ~100 blue compact galaxies (BCGs), which was the largest sample before SDSS, have been observed with the 2.16-m telescope, and the metallicity, extinction of dust, and star formation rate of the sample galaxies have been derived by Kong & Cheng (2002), Kong et al. (2002), Kong (2004), Shi et al. (2005), and Kong et al. (2002). A group from Peking University has discovered a high-redshift quasar ($z = 5.06$), J2202+1509, in 2014 November with the 2.16-m telescope, which is SDSS $i = 18.79$ mag (Wang et al. 2016). The redshift is derived from the emission lines, such as Lyα at a wavelength of 1216 Å and

Nv at a wavelength of 1240 Å. This demonstrates that the 2.16-m telescope is able to be used to discover and study high-redshift quasars.

5. Observing Time Application

Each year, the call for proposals begins around 20 October for the period of one month. Astronomers who are willing to use the telescope can submit proposals through the website http://astrocloud.china-vo.org before the deadline. After that, the proposals will be collected and reviewed by the Time Allocation Committee (TAC) of the 2.16-m telescope. The probability of observing nights obtained for observers highly depends on the mark ranking. The target-of-opportunity (ToO) follow-up observations, like transient SNe and GRBs, is supported, which are allowed to be applied and observed when the transient sources happen. The turnaround time (i.e., the time interval between a ToO alert and the start of the first observation) of the 2.16-m telescope depends on the system and configuration being used when it happens. It concludes with the following parts: the readout time of the last frame (~30–50 s); the time for changing the grisms and adjusting slit width and sometimes it takes even longer when the grism is not on the spectragraph (~5–10 minutes), the pointing time of the telescope (~1–5 minutes), the possible time for changing instrument and focusing (~5–10 minutes), etc. Therefore, it takes ~10–30 minutes in all for starting the ToO observations.

Since the first light of the 2.16-m telescope, there are astronomers from France, Japan, Taiwan, Hong Kong, etc., beyond China Mainland, applied and used the telescope and publish papers. Until now, there are more than 150 SCI papers published with the data obtained with the 2.16-m telescope since the first light. All these papers have been peer-reviewed, and most of them were published on the high-impact magazines in astrophysics, e.g., *ApJ*, *AJ*, *MNRAS*, and *A&A*, and the impact factors are around ~4–6, including the articles published in *Nature*. When the key projects are concluded, there will be numerous high-impact articles published in the future.

6. Summary and Discussion

As a 2-m-class optical astronomical telescope in China, the 2.16-m telescope of Xinglong Observatory of NAOC plays an important role in observational astronomy today. There are currently three primary instruments, the BFOSC, OMR, and the fiber-fed HRS, available for the telescope users. When the 2.16-m telescope saw the first light in 1989, various scientific projects were carried out, based on observations of the telescope in the research areas of nearby galaxies, AGNs, supernovae, GRBs, exoplanets, Galactic stars, time-domain astronomy, and many other sciences. Since the LAMOST spectroscopic survey started, the 2.16-m telescope has also been used for the LAMOST follow-ups, in order to identify interesting objects, and for stellar library observations. A great many remarkable studies have been done with the telescope, including the spectroscopic research of the supernova 1993J (Wang & Hu 1994). In recent years, in order to improve the utilizing efficiency of the telescope and the scientific output further, 7–8 key observing projects have been set up, in which the observers own 20–40 nights/year to carry our long-term observations and serial research.

In the future, a number of potential new instruments will be available to the 2.16-m telescope users to improve its observing abilities further, such as an imaging photopolarimeter *RoboPol* (see King et al. 2014), a prototype of which is currently in use at the 1.3-m telescope of the Skinakas Observatory in Crete, Greece, where it works well. A similar photopolarimeter will probably be installed at the 2.16-m telescope in the next one or two years, which will be the first astronomical photopolarimeter in China. It could be used for polarization measurements, for instance, of Seyfert galaxies, blazars, and GRBs. Further, an intermediate-resolution spectrograph (IRS) is being investigated. If it is installed and committed in the future, the projects of intermediate-resolution spectroscopic observations (e.g., X-ray binaries, bright stars, nearby galaxies, and a large number of fainter Galactic stars) could be carried out. In addition, the testing of the astro-frequency comb calibration system is at the commissioning stage. When it is finished, the precision of the radial velocity measurements of Galactic stars could be improved greatly, even to a few cm s^{-1}. Recently, a number of adaptive optics experiments were performed on the 2.16-m telescope by engineers from various Chinese institutes, which can improve the spatial resolution and signal-to-noise ratio of targets to a large extent. The exoplanet detection technology group from the Nanjing Institute of Astronomical Optics & Technology, NAOC, and the California State University, Northridge collaborated and built the High Performance Portable Adaptive Optics (HPAO), which is mounted on the Coudé focus of a 2.16-m telescope and succeeded after the testing observations. Although the limiting magnitude of the current HPAO system is faint to 3.8 mag in the *H* band, the system will be upgraded in the next step, and the results can be improved significantly.

This research was supported by the National Natural Science Foundation of China (NFSC) through grants 11003021, 11373003, 11273027, and 11303042 and National Key Basic Research Program of China (973 Program) 2015CB857002. Z. F. acknowledges a Young Researcher Grant of the National Astronomical Observatories, Chinese Academy of Sciences. We thank Yuqin Chen, Liang Wang, and Xiaoying Yang for providing the limiting magnitude measurements of the HRS instrument and thank Yingwei Chen for providing the picture of the 2.16-m telescope.

References

Chen, J. S., Fan, X. M., & Tan, X. Y. 1987, AcASn, 28, 303
Cui, X.-Q., Zhao, Y.-H., Chu, Y.-Q., et al. 2012, RAA, 12, 1197
Fan, Y.-F., Bai, J.-M., Zhang, J.-J., et al. 2015, RAA, 15, 918
Huang, L., Wei, J.-Y., Jiang, X.-J., et al. 2015, AR&T, 12, 44
Huang, L., Wu, H., & Li, H. B. 2012, BFOSC (Beijing Faint Object Spectrograph and Camera) Operating Manual, April
King, O. G., Blinov, D., Ramaprakash, A. N., et al. 2014, MNRAS, 442, 1706
Kong, X., & Cheng, F. Z. 2002, A&A, 389, 845
Kong, X., Cheng, F. Z., Weiss, A., et al. 2002, A&A, 396, 503
Kong, X. 2004, A&A, 425, 417
Li, D.-P. 2001, Opt. Instrum., 23, 2
Liu, Y.-J., Sato, B., Zhao, G., et al. 2008, ApJ, 672, 553
Liu, Y.-J., Sato, B., Zhao, G., & Ando, H. 2009, RAA, 9, 1
Shi, F., Kong, X., Li, C., & Cheng, F.-Z. 2005, A&A, 437, 849
Su, D.-Q., Zhou, B.-F., & Yu, X.-M. 1989, ScChA, 11, 1187
Wang, L., Sato, B., Omiya, M., et al. 2014, PASJ, 66, 118
Wang, L., Sato, B., Zhao, G., et al. 2012, RAA, 12, 84
Wang, L.-F., & Hu, J.-Y. 1994, Natur, 369, 380
Wang, F.-G., Wu, X.-B., Fan, X., et al. 2016, ApJ, 819, 24
Wilken, T., Lovis, C., Manescau, A., et al. 2010, MNRAS, 405, 16
Wu, X.-B., Wang, R., Schmidt, K. B., et al. 2011, AJ, 142, 78
Wu, X.-B., Zuo, W.-W., Yang, J.-Y., Yang, Q., & Wang, F.-G. 2013, AJ, 146, 100
Zhang, J.-C., Ge., L., Lu, X.-M., et al. 2015, PASP, 127, 1292
Zhao, G., & Li, H.-B. 2001, ChJAA, 1, 555
Zhao, G., Qiu, H.-M., Chen, Y.-Q., & Li, Z.-W. 2000, ApJS, 126, 461
Zhao, F., Wang, H., Zhao, G., et al. 2015, AR&T, 12, 1
Zhao, F., Zhao, G., Lo Curto, G., et al. 2014, RAA, 14, 1037
Zheng, W.-K., Qiu, Y.-L., Wang, J., et al. 2009, AR&T, 6, 2
Zhou, Z.-M., Wu, H., Huang, L., et al. 2014, RAA, 14, 1393

Publications of the Astronomical Society of the Pacific, 128:105004 (6pp), 2016 October
doi:10.1088/1538-3873/128/968/105004

The Night Sky Spectrum of Xinglong Observatory: Changes from 2004 to 2015

Ji-Cheng Zhang[1,2], Zhou Fan[2], Jing-Zhi Yan[3,4], Yerra Bharat Kumar[2], Hong-Bin Li[2], Dong-Yang Gao[1], and Xiao-Jun Jiang[2]
[1] Shandong Provincial Key Laboratory of Optical Astronomy and Solar-Terrestrial Environment, Institute of Space Sciences, School of Space Science and Physics, Shandong University, Weihai, 264209, China; jczhang@bao.ac.cn
[2] Key Laboratory of Optical Astronomy, National Astronomical Observatories, Chinese Academy of Sciences, Beijing 100012, China
[3] Purple Mountain Observatory, Chinese Academy of Sciences, Nanjing, China
[4] Key Laboratory of Dark Matter and Space Astronomy, Chinese Academy of Sciences, Nanjing, China

Received 2016 March 7; accepted 2016 March 21; published 2016 August 29

Abstract

We present spectroscopic measurements on the night sky of Xinglong Observatory for a period of 12 years from 2004 to 2015. The spectra were obtained on moonless clear nights using the OMR spectrograph mounted on a 2.16-m reflector with a wavelength coverage of 4000–7000 Å. The night sky spectrum shows the presence of emission lines from Hg I and Na I due to local artificial sources, along with the atmospheric emission lines, i.e., O I and OH molecules, indicating the existence of light pollution. We have monitored the night sky brightness during the whole night and found some decrement in the sky brightness with time, but the change is not significant. Also, we monitored the light pollution level in different azimuthal directions and found that the influence of light pollution from the direction of Beijing is stronger compared with that from the direction of Tangshan and other areas. An analysis of night sky spectra for the entire data set suggested that the zenith sky brightness of Xinglong Observatory has brightened by about 0.5 mag arcsec^{-2} in the V and B bands from 2004 to 2015. We recommend consecutive spectroscopic measurements of the night sky brightness at Xinglong Observatory in the future, not only for monitoring but also for scientific reference.

Key words: light pollution – instrumentation: spectrographs – methods: data analysis – site testing

Online material: color figures

1. Introduction

The Xinglong Observatory of the National Astronomical Observatories, Chinese Academy of Sciences (NAOC), is one of the major optical observatories in China, located at a distance of 120 km northeast from Beijing, China. The observatory hosts nine optical telescopes with apertures ranging from 0.5 to 4 m in diameter. There are about 63% spectroscopic nights per year to perform observations from this site (See Zhang et al. 2015).

Night sky brightness is one of the fundamental parameters of an optical observatory that restricts the limiting magnitude for any planned observations. The brightnesses of a moonless night sky are generated from natural sources, mainly contributed by airglow, zodiacal light, and integrated starlight (Leinert et al. 1998), and from artificial sources due to the lighting systems of neighboring towns (Della Prugna 1999). With the economic development and population growth of the surrounding cities, their attendant light pollution also grows. Jiang et al. (1999) presented an identification of the night sky emission lines of Xinglong Observatory with spectral coverage from 5300 to 8200 Å during 1996–1998 and found that Na I and Hg I lines from artificial sources are quite weak.

Previous studies on sky brightness have mainly measured sky brightness using broadband photometry. However, such measurements sometimes may be misleading, as they encompass both natural airglow and artificial sources (Massey & Foltz 2000). In order to better understand the contribution of atmospheric and artificial light sources, spectrophotometric measurements on sky brightness have been suggested, because they can clearly distinguish the artificial sources from the natural sources. Neugent & Massey (2010) presented a way to identify the contribution from the specific elements that influence overall sky brightness.

Spectrophotometric measurements have been widely used at various international optical observatories. Della Prugna (1999) presented a survey in Venezuela and Italy using a small spectrograph with spectral coverage from 4100 to 6400 Å. Night sky spectra of the Kitt Peak during 1988 were analyzed with wavelength coverage from 3800 to 6500 Å by Massey et al. (1990). Then Massey & Foltz (2000) presented an absolute spectrophotometry of the night sky from ~3700 to 6700 Å over two astronomical sites in southern Arizona, Kitt Peak, and Mount Hopkins, and measured for different azimuthal directions and different zenith distances, then

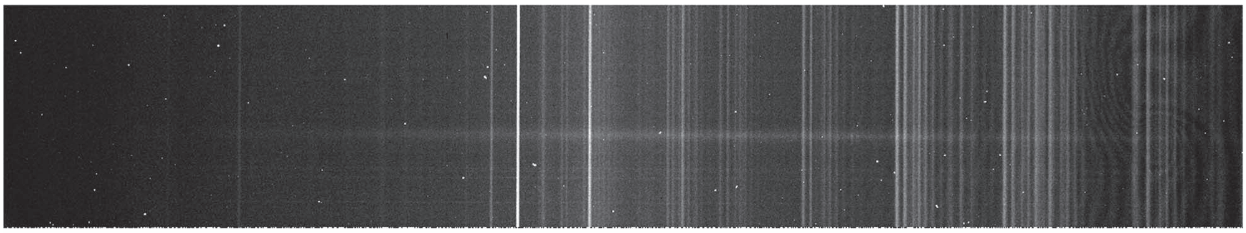

Original spectrum

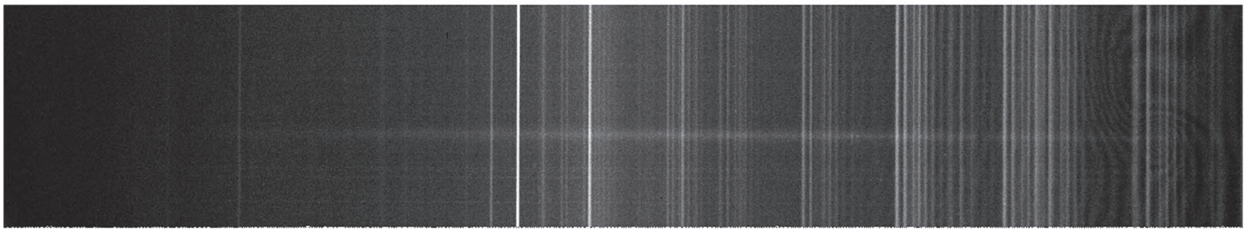

Corrected spectrum

Figure 1. Comparison of a sample 2D spectrum before (upper panel) and after (lower panel) cosmic-ray removal.

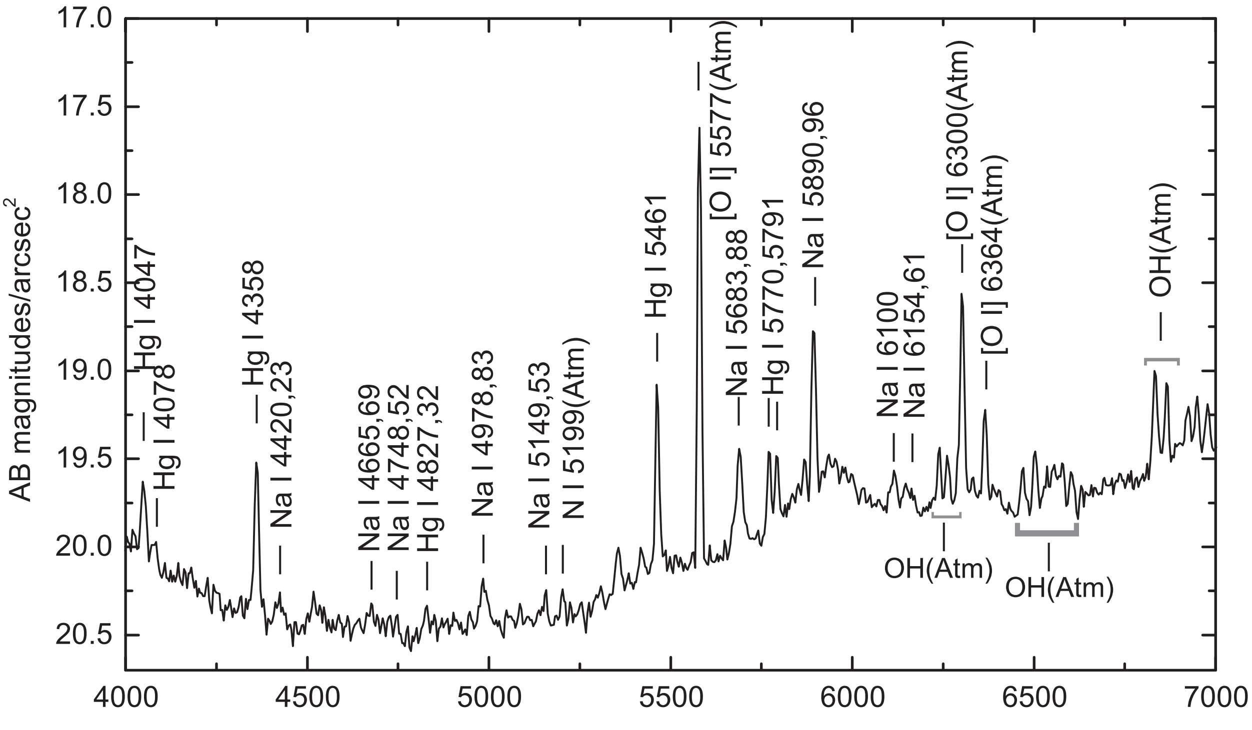

Figure 2. A typical spectrum in the range of 4000 to 7000 Å of the night sky at Xinglong Observatory. Emission lines from natural (atmosphere) and artificial (Hg and Na) sources are identified and marked.

converted to broadband magnitudes and gave a comparison with the night sky spectra in 1988. Neugent & Massey (2010) presented new absolute spectrophotometry of the Kitt Peak night sky during 2009–2010, and they strove to use the same observation and data reduction manner of Massey & Foltz (2000), and compared that with published data. Sheen & Byun (2004) presented the spectrophotometry of the night sky from the Bohyunsan Optical Astronomy Observatory (BOAO), which is located on top of Mount Bohyun, with nearly the entire visible wavelength from 3600 to 8600 Å, and the authors compared the night sky spectrum with that of Kitt Peak. Site testing for observatories also used the night sky spectra to analyze local light pollution (e.g., Sánchez et al. 2007; Moles et al. 2010). These night sky studies are mainly based on relative low-resolution spectra, but there may be different spectral coverage and blended lines. In order to identify as many lines as possible from the contribution of light pollution, Slanger et al. (2003) presented the night sky spectrum of light pollution at the Lick Observatory from 3800 to 9200 Å, with a high spectral resolution (R ~ 45000), and identified a large variety of lines from light pollution.

In this work, we study the night sky brightness for a period of 12 years using the spectroscopic measurements in visible wavelength. This paper consists of four sections. Section 1 gives a brief introduction of Xinglong Observatory and the research basis of night sky spectra around the world. Section 2 describes the details of our data acquisition and reduction. Analysis of the night sky spectrum at Xinglong Observatory and its results are presented in Section 3. We discuss our results and present our conclusions in Section 4.

2. Data Acquisition and Reduction

The spectral data used in our study were from observations of the 2.16-m reflector at Xinglong Observatory. The telescope is equipped with three instruments; (1) the Beijing Faint Object Spectrograph and Camera (BFOSC) available for imaging and low-resolution spectroscopy; (2) the spectrograph made by Optomechanics Research Inc.(OMR) for low-resolution spectroscopy; and (3) the Fiber-fed High Resolution Spectrograph (HRS). A detailed introduction and an up-to-date status report for these three instruments will be provided in Fan et al. (2016, in preparation). We searched the raw data from the OMR and BFOSC archives for our analysis. Because our study is by-product of the research interests of various observers who obtained data with different instruments, we need to select the appropriate data depending on our requirements, using the log files of the 2.16-m telescope recorded by astronomers on every observing night. This selection procedure is an essential yet complicated element of this study. The main criteria for selecting the low-resolution spectroscopic data are as follows: (1) moonless clear nights with good astronomical seeing; (2) exposure times should be at least 1800 seconds, and 3600 seconds is ideal; and (3) the preferable location for objects is at least 15° away from the galactic plane, as suggested by Massey & Foltz (2000). We ensure that all the selected data were observed with the same spectrograph set-up, leading to an accurate comparison. Finally, we decide to select the OMR data for our night sky spectrum analysis by considering the resolution, wide wavelength coverage, and long time span.

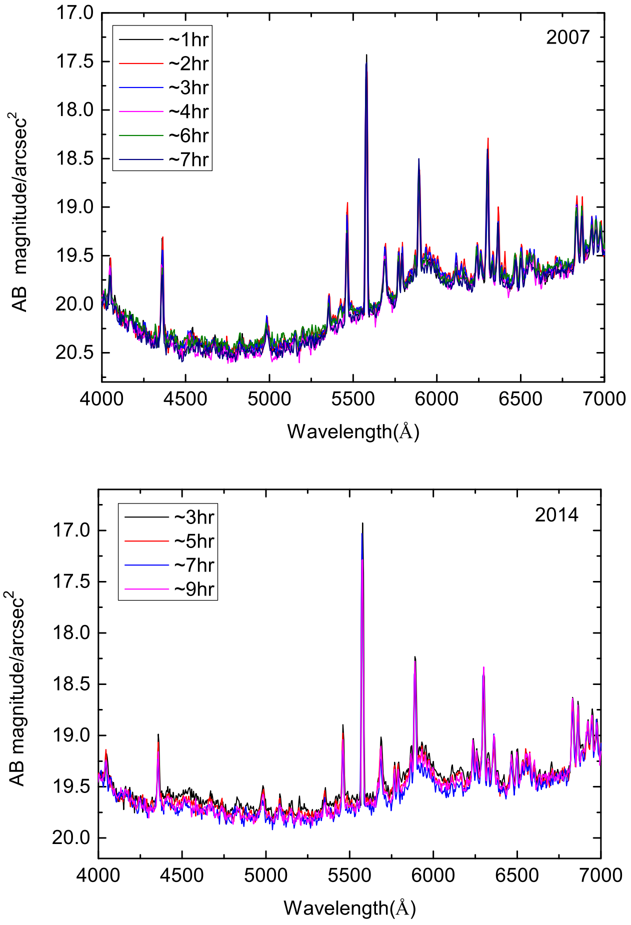

Figure 3. The variations in night sky brightness with time during 2007 and 2014 are shown.

(A color version of this figure is available in the online journal.)

OMR spectra are taken on a Princeton Instruments (PI) PIXIS 1340 × 400 CCD with a pixel size of 20 μm, and a pixel scale of $0\farcs96$. We selected the spectral data taken with the 300 l/mm grating, which provides a dispersion of 4.0 Å/pixel that covers the required wavelength coverage of 4000–7000 Å. As the mean and median seeing value of Xinglong Observatory over an year are $1\farcs9$ and $1\farcs7$, respectively (see Zhang et al. 2015), we selected a slit width around $2\farcs3$ in order to include more photons and improve the signal-to-noise ratio (S/N). There are different lamps for OMR wavelength calibration and flat-field correction; here we used the He-Ar lamp for our spectral wavelength calibration and the halogen tungsten lamp for flat-field correction. Every night more than two spectroscopic standard stars were observed for flux calibration.

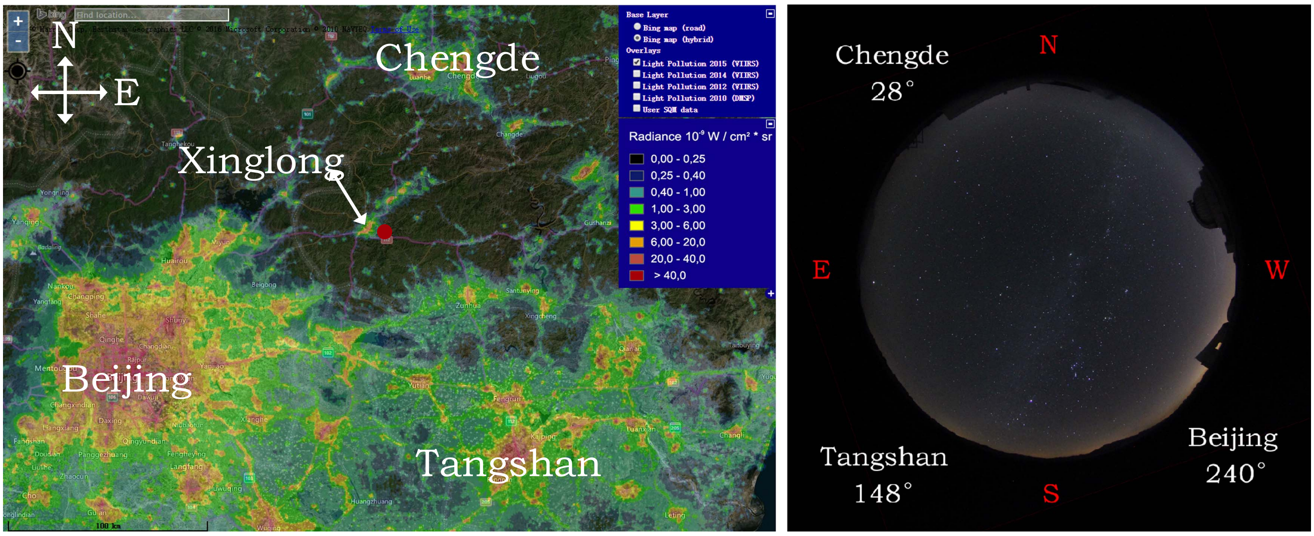

Figure 4. (left panel) Light pollution map showing the location of Xinglong Observatory (red dot) and main surrounding cities and towns. (right panel) Mirror-reflected All-sky Camera image.
(A color version of this figure is available in the online journal.)

Raw data were processed with the standard procedure, using various available tasks in Image Reduction and Analysis Facility (IRAF)[5] and Interactive Data Language (IDL). Since the dark current of CCD is negligible, we corrected for bias and flat-field in object images. The raw frames are contaminated with lots of cosmic rays due to long exposure times. To remove the influence of cosmic rays on the spectra of objects and the night sky, we used the cosmic-ray rejection provided by Laplacian edge detection. For details on the algorithms and introductions this involves, see van Dokkum (2001). Figure 1 shows the image before and after cosmic-ray removal. The upper panel is the original spectrum and the lower panel is the corrected spectrum with no cosmic rays, which suggests that Laplacian edge detection works well for removing the cosmic rays.

We extracted the portion of the night sky spectrum in the same frame and same dispersion direction as the stellar spectrum. We selected the "night sky" part as far as possible from the stellar contribution in order to avoid contamination from stellar lines. We also looked carefully at the contribution from faint stars in the frames and removed them using the standard tasks available in IRAF. Since spectra of the objects in CCD have a slight dispersion curvature, we have performed the curvature correction to avoid errors in the wavelength calibration. We have performed flux calibration of observed spectroscopic standard stars and used it as a reference to calibrate the night sky spectrum. The final spectra were corrected for extinction using a local atmospheric extinction file. We converted the flux units to erg $\mathrm{cm}^{-2}\,\mathrm{s}^{-1}\,\mathrm{\AA}^{-1}$ for further analysis. Because we are also interested in the broadband of sky brightness, we have measured the magnitudes in broadbands (Johnson system) B and V by convolving the night sky spectra with corresponding sensitivity curves.[6]

3. The Night Sky Spectrum and Its Results

The typical night sky spectrum of Xinglong Observatory is shown in Figure 2, and the emission lines from artificial and natural light sources are identified and marked. The artificial sources are known to be a mercury (Hg) vapor lamp, a low pressure sodium (Na) vapor lamp (LPS), and a high pressure sodium (Na) vapor lamp (HPS). Prominent Hg I lines are noticeable at 4047, 4358, 5461, 5770 and 5791 Å, and weak lines of Hg I are noticed at 4078, 4827, and 4832 Å. Na I emission lines at 4420, 4423, 4665, 4669, 4748, 4752, 4978, 4983, 5149, 5153, 6100, 6154, and 6161 Å are weaker compared to stronger lines at 5683, 5688, 5890, and 5896 Å. The strong Na emission lines in the region of 5500–5900 Å have contributions from both LPS and HPS, whereas other Na lines are from HPS. Oxygen emission lines in our spectra are mainly concentrated at 5577, 6300, and 6364 Å. OH molecule lines are mainly distributed in wavelengths redder than 6500 Å.

We chose the data one hour after the end of evening astronomical twilight (when the Sun is 18° below the horizon), when the sky becomes completely dark, to estimate the night sky brightness and monitored the sky for the whole night in one hour intervals to see whether there are any changes in the sky brightness in a single observing dark night. The sky brightness obtained during 2007 is shown in Figure 3. The altitudes of the telescope pointings for all spectra are over 60°. We noticed a little decrement

---

[5] IRAF is distributed by the National Optical Astronomy Observatory, which is operated by the Association of Universities for Research in Astronomy, Inc. (AURA) under cooperative agreement with the National Science Foundation.

[6] http://www.aip.de/en/research/facilities/stella/instruments/data/johnson-ubvri-filter-curves.

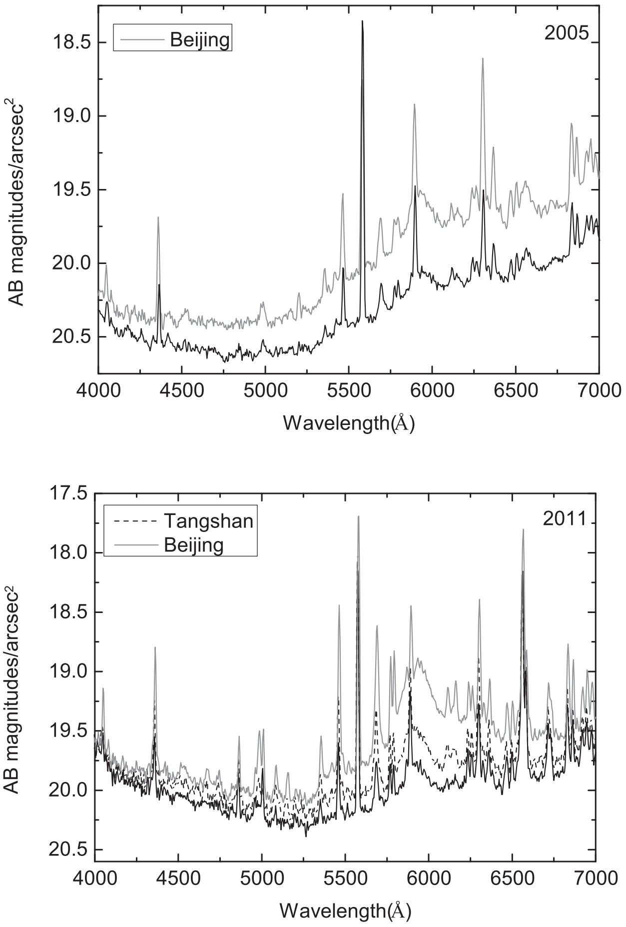

Figure 5. Comparison of night sky spectra at zenith with zenith distances around 50° toward the direction of Beijing in 2005. A similar comparison of Xinglong Observatory with zenith distances around 60° in the Beijing and Tangshan directions is shown for 2011.

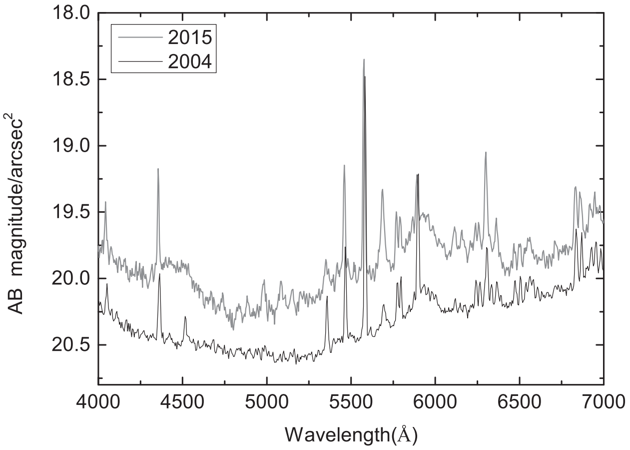

Figure 6. Comparison of the night sky spectra of Xinglong Observatory between 2004 and 2015.

in the sky brightness, but it was not significant. The same analysis for the data obtained during 2014 confirms a similar trend.

Figure 4 shows the locations of cities and towns around Xinglong Observatory in a light pollution map[7] and an All-sky Camera image of Xinglong Observatory. Note that the bright night sky at larger zenith distances is mainly influenced by the surrounding cities. We performed a quantitative analysis to check the change in night sky brightness at different zenith distances and azimuthal directions and found that the night sky is brighter toward the southwest, where Beijing is located. the relative sky brightness between the zenith and a zenith distance around 50° toward Beijing direction is shown in Figure 5. For comparison, we have selected data toward Tangshan and show it along with that corresponding to Beijing in Figure 5. This analysis suggests that the influence of light pollution from Tangshan is relatively insignificant compared to that from Beijing. Since the town of Xinglong is located west of Xinglong Observatory and very close compared with other cities, we also found that Xinglong contributes significant light pollution to the images of the All-sky Camera.

In order to check the changes in night sky brightness at Xinglong Observatory over the past years, representative night sky spectra from 2004 and 2015 are shown in Figure 6 for comparison. We notice a significant increase in the sky brightness in 2015 compared with 2004. Since we are concerned with whether the night sky brightness has changed during all these years from 2004 to 2015, we have analyzed the spectra for all the years and show the sample spectrum from each year in Figure 7. We found that the night sky brightness has tended to increase from 2004 to 2015. Table 1 shows the night sky brightness in broadbands B and V during these years; these broadband values were convolved by the corresponding night sky spectrum. We also found that the zenith sky brightness over Xinglong Observatory increased slightly between 2004 and 2015. The zenith sky has brightened by about 0.5 mag arcsec^{-2} in the B and V bands.

4. Conclusions

We have studied the night sky brightness at Xinglong Observatory using on spectroscopic measurements. Overnight monitoring of sky brightness suggests that the zenith night sky brightness decreases with time, but this decrease is not significant. We noticed strong emission lines from Hg I and Na I in the spectra, apart from natural light emission lines, indicating the influence of light pollution from the usage of mercury and sodium lamps in the cities surrounding Xinglong Observatory. The influence of light pollution from the direction of Beijing is stronger compared with that from the direction of Tangshan and other areas. We compared the night sky spectra for 12 years, from 2004 to 2015, and found a trend of increasing sky brightness

---

[7] The use of data from www.lightpollutionmap.info should be credited to "Jurij Stare, www.lightpollutionmap.info", but because the original data is sourced from the Earth Observation Group of the NOAA National Geophysical Data Center, it should also be credited as such.

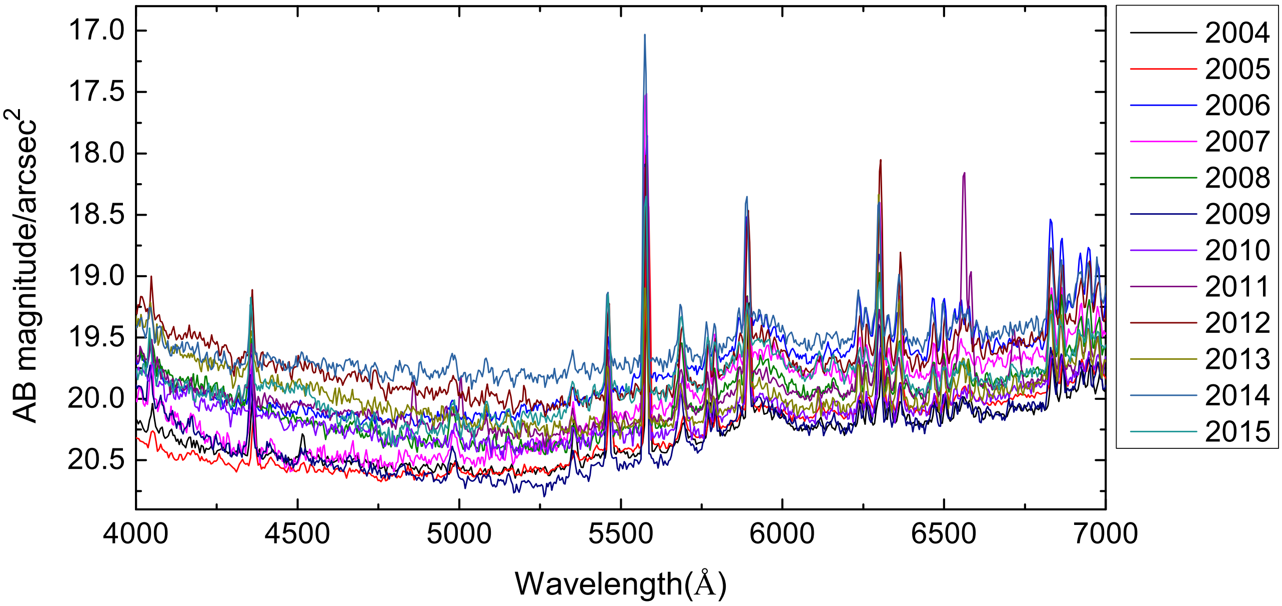

Figure 7. Sample night sky spectra of Xinglong Observatory over 12 years.
(A color version of this figure is available in the online journal.)

Table 1
Statistics of the Night Sky Brightness at Xinglong Observatory from 2004 to 2015

Year	Broadband	(mag arcsec^{-2})
	V	B
2004	20.35	20.37
2005	20.32	20.46
2006	19.80	19.91
2007	19.98	20.23
2008	20.11	19.91
2009	20.36	20.25
2010	20.17	20.02
2011	20.05	19.88
2012	19.90	19.68
2013	20.11	19.67
2014	19.56	19.59
2015	19.89	19.91

during the studied period. The convolution of broadband magnitudes suggests that the zenith sky has brightened by about 0.5 mag arcsec^{-2} in the V and B bands. Consecutive spectroscopic measurements in the night sky brightness at Xinglong Observatory in the future will be essential, not only for monitoring purposes, but also for scientific reference.

We thank the observers and night assistants of the 2.16-m telescope for their kind support with obtaining data. This work is partly supported by the National Natural Science Foundation of China under grant No.11373003 and the National Key Basic Research Program of China (973 Program) grant No. 2015CB857002. Y.B.K. thanks the Chinese Academy of Sciences Visiting Fellowship for Researchers from Developing Countries for support through grant 2013FFJB0008.

References

Della Prugna, F. 1999, A&AS, 140, 345
Jiang, X., Xu, D., & Hu, J. 1999, AcApS, 19, 220
Leinert, C., Bowyer, S., Haikala, L. K., et al. 1998, A&AS, 127, 1
Massey, P., Gronwall, C., & Pilachowski, C. A. 1990, PASP, 102, 1046
Massey, P., & Foltz, C. B. 2000, PASP, 112, 566
Moles, M., Sánchez, S. F., Lamadrid, J. L., et al. 2010, PASP, 122, 363
Neugent, K. F., & Massey, P. 2010, PASP, 122, 1246
Sánchez, S. F., Aceituno, J., Thiele, U., Pérez-Ramírez, D., & Alves, J. 2007, PASP, 119, 1186
Sheen, Y.-K., & Byun, Y.-I. 2004, JKAS, 37, 87
Slanger, T. G., Cosby, P. C., Osterbrock, D. E., Stone, R. P. S., & Misch, A. A. 2003, PASP, 115, 869
van Dokkum, P. G. 2001, PASP, 113, 1420
Zhang, J.-C., Ge, L., Lu, X.-M., et al. 2015, PASP, 127, 1292

RAA 2016 Vol. **16** No. **5**, 72 (8pp) doi: 10.1088/1674–4527/16/5/072
http://www.raa-journal.org *http://iopscience.iop.org/raa*

Research in
Astronomy and
Astrophysics

An isolated compact galaxy triplet

Shuai Feng[1,2], Zheng-Yi Shao[1†], Shi-Yin Shen[1,4], Maria Argudo-Fernández[1], Hong Wu[3], Man-I Lam[3], Ming Yang[3] and Fang-Ting Yuan[1]

[1] Key Laboratory for Research in Galaxies and Cosmology, Shanghai Astronomical Observatory, Chinese Academy of Sciences, Shanghai 200030, China; *zyshao@shao.ac.cn*†
[2] University of the Chinese Academy of Sciences, Beijing 100049, China
[3] Key Laboratory of Optical Astronomy, National Astronomical Observatories, Chinese Academy of Sciences, Beijing 100012, China
[4] Key Lab for Astrophysics, Shanghai 200234, China

Received 2015 June 23; accepted 2015 December 4

Abstract We report the discovery of an isolated compact galaxy triplet SDSS J084843.45+164417.3, which is first detected by the LAMOST spectral survey and then confirmed by a spectroscopic observation of the BFOSC mounted on the 2.16 meter telescope located at Xinglong Station, which is administered by National Astronomical Observatories, Chinese Academy of Sciences. It is found that this triplet is an isolated and extremely compact system, which has an aligned configuration and very small radial velocity dispersion. The member galaxies have similar colors and show marginal star formation activities. These results support the opinion that the compact triplets are well-evolved systems rather than hierarchically forming structures. This serendipitous discovery reveals the limitations of fiber spectral redshift surveys in studying such a compact system, and demonstrates the necessity of additional observations to complete the current redshift sample.

Key words: galaxies: group — galaxies: interaction — galaxies: star formation — galaxies: evolution

1 INTRODUCTION

A galaxy triplet constitutes the simplest galaxy group and the smallest N-body system that cannot be modeled analytically. In general, triplets have not received much attention in contrast to close pairs or rich groups of galaxies. So, the basic scenario describing their formation and evolution is still ambiguous. According to the popular hierarchical structure formation theory, it is naturally presumed that a triplet is formed through a close galaxy pair accreting a third remote galaxy. However, some recent evidence suggests that for lots of triplets, their member galaxies have similar properties and are supposed to be the remains of a long evolved dynamical system within a common dark matter halo (e.g. Duplancic et al. 2015 and Aceves 2001).

The first catalog of galaxy triplets was compiled by Karachentseva et al. (1979) and Karachentsev et al. (1988), which contains 84 isolated galaxy triplets from the northern hemisphere. These triplets were selected by visual inspection of Palomar Sky Survey plates, whose member galaxies have apparent magnitudes brighter than 15.7. About 64% of these targets were considered to be physical triplets with $\Delta v_{ij} < 500\ \mathrm{km\ s^{-1}}$ (Karachentsev & Karachentseva 1981, hereafter the K-sample). Based on this catalog, the basic properties of the galaxy triplets, e.g. integrated luminosity, diameter, velocity dispersion, as well as the spatial configuration, dynamics and dark matter content, have been estimated and discussed in detail (Karachentseva & Karachentsev 1982; Karachentseva & Karachentsev 1983; Karachentsev 1990; Chernin & Mikkola 1991; Anosova et al. 1992; Zheng et al. 1993 and Aceves 2001). For the southern sky ($\delta < 3°$), similar works have also been done on a sample of 76 isolated triplets, which are selected from the European Southern Observatory/Science and Engineering Research Council (ESO/SERC) and Palomar Observatory Sky Survey first release (POSS-I) (Karachentseva & Karachentsev 2000).

O'Mill et al. (2012) constructed a catalog of triplets with their primary galaxies ($Mr < -20.5$), hereafter called the O-sample, selected from a volume-limited sample in the Sloan Digital Sky Survey Data Release 7 (SDSS-DR7) (Abazajian et al. 2009). This catalog is comprised of 1092 triplets in a redshift range of $0.01 \leq z \leq 0.14$. However, due to the problem of fiber collision in SDSS (with a minimum separation of $55''$ between any two fibers), most of the companion galaxies in these systems were selected by only using their photometric redshifts ($z_{\rm phot}$). As a result of the relatively large uncertainty of $z_{\rm phot}$ (~ 0.0227), this catalog is inevitably contaminated by "projected triplets" and yet, in another respect, some of the real triplets could have been missed. In the O-sample, about one tenth of the triplets have spectroscopic redshifts for all their members. Duplancic et al. (2013, 2015) analyzed the configuration and dynamics of this sub-sample, and compared them with galaxy pairs and clusters. They found that the triplet galaxy members are more similar to the galaxies in compact groups and rich clusters than in galaxy pairs and concluded that the galaxy triplets may not be formed hierarchically. Very recently, Argudo-Fernández et al. (2015) published a sample of 315 isolated triplets in the local Universe ($z \leq 0.080$) using the spectroscopic redshifts ($z_{\rm spec}$) from SDSS DR 10 (hereafter the A-sample). In this sample, galaxies are considered to be physically bound to the primary galaxy at a projected separation up to $d \leq$450 kpc with a radial velocity difference of $\Delta v \leq 160\,{\rm km\,s^{-1}}$.

Given the limited data and studies summarized above, there are still not enough pieces to solve the puzzles of the formation and evolution scenario of the galaxy triplets. Any additional sample of physical triplets, especially compact cases, will be valuable for contributing to knowledge about this kind of system.

The galaxy system SDSS J084843.45+164417.3 (hereafter J0848+1644), which contains galaxies A, B and C (see Fig. 1 for details), is the spectroscopic triplet we report on and study in this paper. This triplet is not included in the A-sample because these three galaxies have very small angular distances and only galaxy B has a spectrum in SDSS, $z_{\rm spec} = 0.078829 \pm 0.000015$ (SpecObjID: 2565950139160094720) (Abazajian et al. 2009). Also, it is excluded from the O-sample since values for the $z_{\rm phot}$ of the other two galaxies ($z_{\rm phot} = (0.32, 0.08, 0.19)$ for galaxies A, B and C respectively) are all very different from $z_{\rm spec}$ of galaxy B. This galaxy triplet was reported as a galaxy pair in Shen et al. (2015), where they started a project that aims to compile the spectroscopic redshifts of all the main samples of galaxies ($r < 17.77$) that do not yet have redshifts measured in SDSS DR7 due to the problem of fiber collision. Their new redshift survey is being collected with the Guo Shou Jing Telescope (also known as the Large Sky Area Multi-Object Fiber Spectroscopic Telescope, hereafter LAMOST, Cui et al. 2012). Galaxy C is included in the complementary galaxy sample of the LAMOST spectral survey and its spectrum has been released in the LAMOST DR1 with $z_{\rm spec}$ = 0.07929 (Obsid: 78907168) (Luo et al. 2015)[1]. During the visual inspection of the galaxy pairs in Shen et al. (2015), we find that, including galaxy A, they very probably form a compact triplet system.

We have performed a follow-up spectroscopic confirmation of this triplet using the 2.16 meter optical telescope (hereafter 2.16 m) at Xinglong Station, administered by National Astronomical Observatories, Chinese Academy of Sciences (NAOC). In this paper, we first report the data from the spectroscopic observation on 2.16 m. After that, we combine all optical photometric and spectroscopic data and make a detailed study of this triplet. This paper is organized as follows. In Section 2, we describe the photometric and spectroscopic data of J0848+1644 and the measurements of the basic features of its members. In Section 3, we derive the global properties of this triplet, such as the compactness, configuration, environment, dynamical status, star formation rate (SFR), etc. Finally, we present discussions in Section 4 and list a summary in Section 5. Throughout this paper, we use cosmological parameters Ω_Λ = 0.7, Ω_M= 0.3 and $h = 0.7$.

2 OBSERVATIONS AND DATA REDUCTION

In this section, we describe the observation of triplet J0848+1644 from the 2.16 m telescope and our new photometric data reduction that is applied to the SDSS images. All measurements of individual member galaxies are summarized in Table 1.

2.1 Spectroscopy

2.1.1 Observations

Our follow-up spectroscopic observation was taken by the BAO Faint Object Spectrograph and Camera (hereafter BFOSC), that is mounted on the 2.16 m optical telescope, on 2013 Dec. 31. The long slit of BFOSC is 1.8″ wide and covered all three galaxies simultaneously (as shown in Fig. 1). The spectral wavelength coverage is from 3870 to 6760 Å, and the resolution is $R \sim 700$ at 5000 Å.

The spectroscopic data were reduced following the standard procedures using the NOAO Image Reduction and Analysis Facility (IRAF, version 2.16) software package, including the bias and flat-field correction of the CCD and cosmic-ray removal. Wavelength calibration was performed by comparing with the ferrum/argon lamp spectra, which was exposed at both the beginning and end of that observation. Flux calibration of all spectra was performed using the additional observation of the standard star, Feige 34. The atmospheric extinction was corrected with the mean extinction coefficients for Xinglong Station.

The resultant 1D spectra have typical S/N $\sim$ 14. For galaxy B, we plot the spectrum of SDSS (see Fig. 2) for comparison. These two spectra match very well in their overlapping wavelength range, which also demonstrates the reasonability of our flux calibration of BFOSC.

2.1.2 Radial velocities and emission line strengths

To get the redshift measurements from the BFOSC spectra, we first measure the radial velocities of each individual emission or absorption line (z_l) by using the IRAF package `splot`. The redshift of each galaxy is then calculated by averaging the results of all its adopted spectral lines, $z = \langle z_{\rm l} \rangle$, and the error is estimated from their dispersion, $z_{\rm err} = \sigma_{z_{\rm l}}/\sqrt{N_{\rm l}}$. Some of the identified lines are not strong enough or are blended with sky lines, and therefore

---

[1] Based on SDSS DR7 photometry, galaxy C (r=17.06) belongs to the main galaxy sample whereas galaxy A (r=18.45) does not.

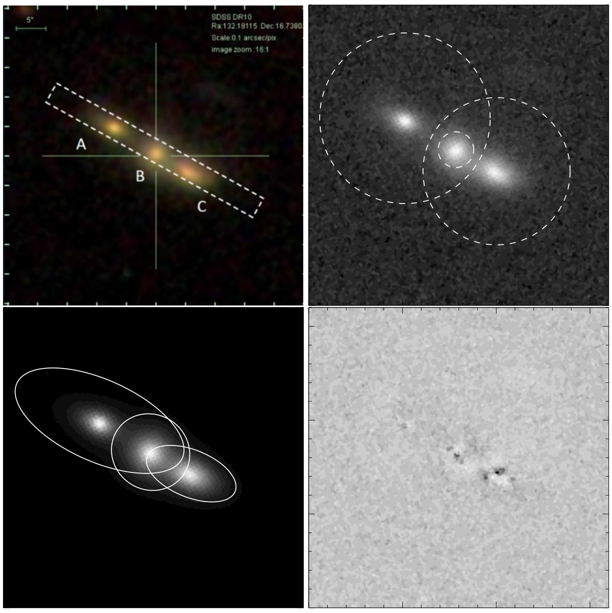

Fig. 1 Images of J0848+1644. *Top Left:* The optical image combined with SDSS g, r, i bands. The letters (A, B and C) labeled in the figure are used to denote the members of the triplet. The white dashed rectangle indicates the position of the long slit of the BFOSC that is mounted on the 2.16 m telescope. The $5''$ scale line at the top-left corner corresponds to 8.2 kpc at the redshift of this triplet. *Top Right:* The r-band SDSS frame image where the dashed circles indicate the Petrosian R_{90} from SDSS. *Bottom Left:* The best fitting model made by `GALFIT` where the solid lines indicate the isophotal ellipses enclosing 90% of the total model flux of individual galaxies. *Bottom Right:* Residual image of the best fitting; the grey scale from black to white indicates -5% to 8% of the maximum flux in the model image.

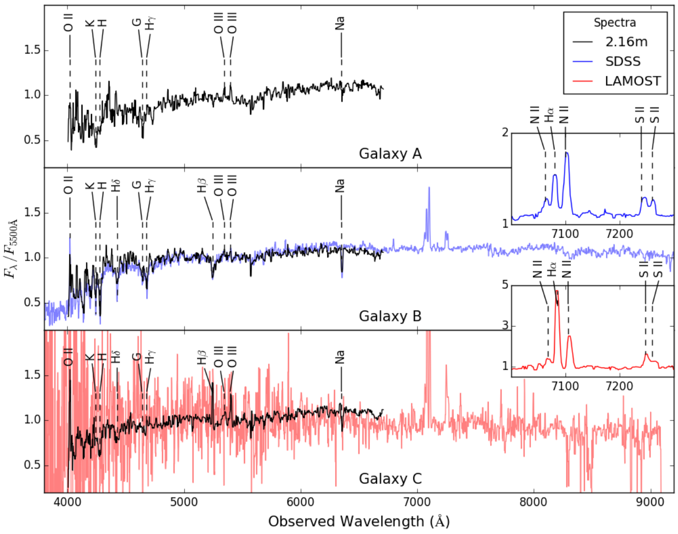

Fig. 2 The optical spectra of member galaxies of J0848+1644. The black lines are the spectra of the BFOSC that is mounted on the 2.16 m telescope. The blue and red lines are taken from SDSS for galaxy B and LAMOST for galaxy C respectively. All the spectra are normalized at 5500 Å and smoothed with a width of 11 Å. The redshifts of individual spectra are estimated by averaging the measurements of multiple spectral lines, whose species names are labeled with corresponding spectra in three main panels. Additionally, we show some spectral lines of SDSS and LAMOST spectra in small panels which are not covered by the 2.16 m telescope.

have not been used in the redshift calculation. The final adopted spectral lines for each spectrum are labeled in the main panels of Figure 2 and the redshift results are listed in Table 1. For galaxy B, the BOSFC redshift is in excellent agreement with the SDSS value ($z_{\mathrm{SDSS}} = 0.078829$). For galaxy C, the BOSFC redshift is also consistent with the LAMOST value ($z_{\mathrm{LAMOST}} = 0.0793$). Considering the internal consistency of the BOSFC spectra, we only take the BOSFC redshifts to study the kinematics and dynamics of J0848+1644 below.

Table 1 Observational and Derived Parameters of Individual Members of J0848+1644

Parameter	Unit	galaxy A	galaxy B	galaxy C
RA (J2000)	hh:mm:ss.ss	08:48:43.94	08:48:43.45	08:48:43.08
DEC (J2000)	dd:mm:ss.ss	$+$16:44:21.76	$+$16:44:17.36	$+$16:44:14.18
d_i [a]	kpc	13.97	–	10.44
$z_{\rm SDSS}$			0.078829±0.000015	
$z_{\rm LAMOST}$ [b]				0.07929
z		0.07852±0.00015	0.07848±0.00016	0.07883±0.00017
$v_{\rm r}$	km s^{-1}	23557±45	23544±48	23650±51
F(OII)	10^{-17} erg s^{-1} cm^{-2}	200.4	453.6	1396.1
$m_{\rm r}$ [c]		17.32	17.00	16.99
n_s [c]		6.0	2.1	1.6
$R_{\rm e}$ [c]	kpc	3.6	2.6	3.6
b/a [c]		0.45	0.94	0.50
θ [c]	degree	5.3	–5.2	7.6
$R_{a,90}$ [d]	kpc	21.0	9.0	11.0
$R_{c,90}$ [e]	kpc	14.9	8.9	8.3
$g-r$		0.75	0.77	0.78
$\log(M_*/M_\odot)$ [f]		10.51	10.66	10.67
SFR [g]	$M_\odot\cdot$ yr^{-1}	0.38	0.86	2.64
$\log({\rm SFR}/M_*)$		–10.9	–10.7	–10.3

[a] Projected distance from the central galaxy B.

[b] The redshift error of galaxy C is not provided in LAMOST DR1.

[c] Fitting parameters that were derived from `GALFIT` by modeling the r-band image with three Sersic profile components.

[d] Major axis of ellipse enclosing 90% of the model flux in the r-band.

[e] Radius of circle enclosing 90% of the model flux in the r-band.

[f] Stellar mass estimated according to Bell et al. (2003).

[g] Estimated from F (OII).

Besides the redshifts, the fluxes of OII emission lines of three BFOCS spectra have also been measured through a Gaussian fit and the correction of the long slit effect, which will be used as diagnostics of the current SFR of each galaxy.

2.2 Photometric measurements

The SDSS catalog has released a variety of photometric measurements for each galaxy, e.g. the Petrosian and model system (Stoughton et al. 2002; Abazajian et al. 2009). However, it is found that the SDSS photometric measurements have not been optimized for galaxies with close neighbors (Patton et al. 2011).

For J0848+1644, the galaxies A, B and C have sizes R_{90} (the circular aperture including 90% of the Petrosian flux) of 8.87, 1.84 and 7.65 arcsec respectively (the dashed circles in Fig. 3). The underestimation of the size of galaxy B is because the SDSS algorithm applies photometric measurements to each object after masking its neighbors. So, this small size further leads to an underestimation of the relevant Petrosian magnitude of galaxy B. To avoid such an over-subtraction, we reprocess the photometry of J0848+1644 using the frame image from the SDSS data archive. Rather than one by one, we analyze the photometry of their members simultaneously. We take the Sersic profile for each member galaxy and generate a combined fitting by using the 2D `GALFIT` routine (Peng et al. 2002).

The fitting results of the r-band image, including the total magnitude ($m_{\rm r}$), the Sérsic index ($n_{\rm s}$), the effective radius of the major axis ($R_{\rm e}$), the ellipticity (b/a) and the position angle of the major axis along the triplet alignment direction (θ), are listed in Table 1. The residual image of the model fitting is shown in the bottom right panel of Figure 1. For comparison, we plot the ellipse with $R_{a,90}$ that encloses 90% of the model flux with solid lines in the bottom left panel. It is clear that our fitting results do not suffer from the over-masking problem, so they should be more reliable for describing the photometric features of these member galaxies.

Similarly, we also fit the SDSS g-band image and further derive the $g-r$ color of each galaxy. The values listed in Table 1 are already corrected for Galactic extinction.

3 PHYSICAL PROPERTIES

In this section, we measure and discuss the global properties of J0848+1644 using the photometric and spectroscopic data described in the previous section, and summarize the results in Table 2.

3.1 Compactness and Configuration

The compactness of a galaxy triplet is defined as a measurement of the percentage of a system's total area that is filled by the light of member galaxies (Duplancic et al. 2013),

$$S = \frac{\sum_{i=1}^{3} R_{90}^2}{R_m^2}, \tag{1}$$

where R_{90} is the radius of a circle enclosing 90% of the model flux of a galaxy and R_m is the radius of the minimum enclosing circle that contains the geometric centers of all member galaxies in the triplet. The R_m of J0848+1644 is 12.2 kpc. Taking the R_{90} of galaxies in the $r-$band from our `GALFIT` fitting ($R_{c,90}$ in Table 1), the compactness is $S = 2.48$, which is far larger than those from the O-sample, whose median value is ~ 0.05.

It is worth mentioning that, for triplets, the apparent high compactness may be contaminated by the projection effect. Considering the projection, the apparent compactness actually represents its upper limit. At any rate, according to the S value, J0848+1644 has a very high probability of being a highly compact system.

Agekyan & Anosova (1968) suggested an elegant method (AA-map) to analyze the geometric configurations of triplet systems. They defined four types of configurations based on the shape of the triangle formed by their members.

Obviously, J0848+1644 has a chain-like (alignment) configuration (A-type) in the projected 2D AA-map. According to the simulation result of Duplancic et al. (2015), which counts the number of mock triplets in each area of the 3D and 2D AA-map, J0848+1644 has a 75% probability of having a real 3D alignment configuration and only a 5% probability of being located in the hierarchical region (H-type).

3.2 Environment

In environmental studies, a galaxy is typically defined as isolated if there is no neighboring galaxy with a difference in recessional velocity of $\Delta v \leq 500$ km s^{-1} at a particular projected distance, such as 1 Mpc. For J0848+1644, it is certainly an isolated galaxy system, since its nearest neighbor ($M_{\rm r} <$ –19.5) is 3.12 Mpc away.

To further quantify its isolation degree, following Argudo-Fernández et al. (2014), we also calculate another two parameters. One is the number density of neighboring galaxies $\eta_{k,\rm LSS}$, defined as follows

$$\eta_{k,\rm LSS} = \log\left(\frac{k-1}{V(r_k)}\right), \tag{2}$$

where $V(r_k) = \frac{4}{3}\pi r_k^3$ and r_k is the projected distance to the kth nearest neighbor of the large scale structure (LSS), with k equal to 5 or lower if there are not enough neighbors in the field. According to the data from SDSS, there are only four neighboring galaxies ($M_{\rm r} <$ –19.5) around with radial velocities $\Delta v \leq 500$ km s^{-1} in the volume of a 5 Mpc projected distance. For J0848+1644, the large scale number density of neighboring galaxies $\eta_{4,\rm LSS}$ is –2.10, which is much less than the median value of the A-sample ~ -1.4. This result even indicates that J0848+1644 is located in a lower density environment than other isolated triplets.

Another parameter is related to the tidal strength Q on the primary galaxy (here we use the central galaxy B instead) created by its neighbors i in the field

$$Q = \log\Big[\sum_i \frac{M_i}{M_P}\Big(\frac{D_P}{d_i}\Big)^3\Big], \tag{3}$$

where M_i is the stellar mass and d_i is the projected distance of the ith neighbor to the primary galaxy. $D_P = 2\alpha R_{90}$ is the diameter of the primary galaxy. It is scaled by a factor $\alpha = 1.43$ to recover D_{25} (Argudo-Fernández et al. 2014). Obviously, the larger the value of Q is, the less isolated the primary galaxy is.

For the triplet system, there are two measurements of the Q parameter. $Q_{\rm LSS}$ is generated by the neighbors of the triplet up to 5 Mpc, but excludes its own companion galaxies. This is an assessment of the isolation degree of the primary member galaxy in the LSS environment. On the other hand, $Q_{\rm Local}$ only considers two other members of the triplet (galaxies A and C for J0848+1644), which could represent the internal links within the system itself.

Stellar masses of galaxies are estimated by the relationship $\log_{10}(M/L_{\rm r}) = -0.306 + 1.097(g-r)$ from Bell et al. (2003). Thus, the Q parameters of J0848+1644 are $Q_{\rm LSS} = -5.70$ and $Q_{\rm Local} = 1.29$. It is worth mentioning that the $Q_{\rm triplet}$ may be overestimated because of the projection effect.

Compared with galaxy triplets in the A-sample as shown in Figure 3, $Q_{\rm LSS}$ (or $Q_{\rm Local}$) of J0848+1644 is much lower (or higher) than their median value of –5.0 (or –2.0). Additionally, the ratio of $Q_{\rm Local}/Q_{\rm total} = Q_{\rm Local}/(Q_{\rm LSS} + Q_{\rm Local}) \simeq 1.0$ shows uniform values. All these values clearly indicate that J0848+1644 is an extremely compact and isolated system.

3.3 Dynamics

To characterize the dynamics of J0848+1644, we calculate its projected harmonic radius $R_{\rm H}$, radial velocity dispersion $\sigma_{v_{\rm r}}$, dimensionless crossing time $H_0 t_c$ and virial mass $M_{\rm vir}$:

$$\begin{aligned} R_{\rm H} &= \Big(\frac{1}{N}\sum R_{ij}^{-1}\Big)^{-1}, & (4)\\ \sigma_{v_{\rm r}}^2 &= \frac{1}{N-1}\sum(v_{\rm r} - \langle v_{\rm r}\rangle)^2, & (5)\\ H_0 t_c &= H_0\pi R_{\rm H}/(\sqrt{3}\sigma_{v_{\rm r}}), & (6)\\ M_{\rm vir} &= 3\pi N R_{\rm H}\sigma_{v_{\rm r}}^2/(N-1)G, & (7) \end{aligned}$$

where values of R_{ij} are the projections of galaxy-galaxy separation and $N = 3$ for the triplet.

Based on the $v_{\rm r}$ results from the BFOSC spectra (see Table 1 for details), we have $R_{\rm H} = 14.5$ kpc and $\sigma_{v_{\rm r}} = 58.1$ km s^{-1}. Then, we can derive another two parameters, $H_0 t_c = 0.032$ and $\log(M_{\rm vir}/M_\odot) = 11.2$.

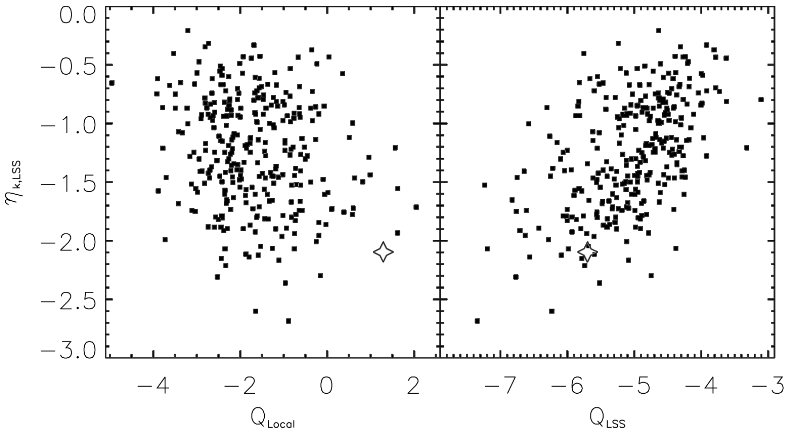

Fig. 3 The environment parameters of triplet J0848+1644 (*stars*) compared with other isolated triplets in the A-sample (*dots*).

It is very interesting that the $M_{\rm vir}$ of J0484+1644 is so small, even less than the total stellar mass of its member galaxies. We are not surprised by this result, because for a triplet system, the virial mass estimated by the radial velocity dispersion might be strongly related to the viewing angle. For example, if our line-of-sight happens to be perpendicular to the plane of three vectors representing the peculiar velocity of the triplet members, the $\sigma_{v_{\rm r}}$ could decrease to zero. So, this visual aspect reminds us that the $M_{\rm vir}$ estimation of a triplet system is only a combination of the velocity dispersion $\sigma_{v_{\rm r}}$ and scale length $R_{\rm H}$, which has the dimension of mass (Karachentseva & Karachentsev 2000). It cannot be considered as the true mass of individual triplets, but should be worthwhile in statistical analysis for a pretty large sample of triplets.

3.4 SFR

It is believed that galaxy interaction triggers star formation. The galaxies in compact groups are shown to have stronger star formation in comparison with those in fields (Gómez et al. 2003). For galaxy B or C of J0848+1644, we see a significant Hα emission line in their respective SDSS or LAMOST spectrum, which indicates their current star forming activities. Unfortunately, the LAMOST spectrum of galaxy C may be seriously affected by unreliable flux calibration and causes an unexpectedly stronger Hα emission which may lead to the wrong value of SFR.

Alternatively, we use the OII flux measured from the BFOSC spectra of all three galaxies to calibrate their SFR, following the relation of Kennicutt (1998),

$$\mathrm{SFR}(M_\odot\ \mathrm{yr}^{-1}) \sim 1.4 \times 10^{-41} L(\mathrm{OII})(\mathrm{erg\ s}^{-1}). \quad (8)$$

The SFR results, together with $\log(\mathrm{SFR}/M_*)$, are calculated and listed in Table 1. For galaxy B, these two values are all consistent with those derived from the Hα flux. Then, we can sum up the SFR parameters for the whole triplet system and list them in Table 2.

From the result, galaxies A and B have lower SFRs than C, which cause OIII to be too weak, and even Hβ to be too weak to override stellar absorption (see Fig. 2) (Kennicutt 1992).

4 DISCUSSION

4.1 Characteristics of J0848+1644

The most distinguished feature of J0848+1644 is its compactness. The parameter $S = 2.48$ is located in the most compact end for almost all current triplet samples. The lack of such compact triplets is partly because of the sampling bias of redshift sky surveys (see the next subsection for details), and the investigation of J0848+1644 provides a valuable example to reveal the nature of such a compact few body system. Combining with other properties, the apparent compactness seems to be real. All evidence points toward it coming from a sufficient dynamical evolution, while the interaction among member galaxies is still active.

From the projected 2D AA-map, J0848+1644 has a very high probability of having an aligned configuration rather than a hierarchical structure. It is believed that different configurations of the triplets may be reflecting different dynamical stages of the system. The A-type configuration therefore implies that it is a well formed system and its member galaxies may have co-evolved for a long time. Then, the diagnosis of isolation leads to more information about the relations between J0848+1644 and its environment. Generally speaking, the evolution of a galaxy may be affected by an external influence when the corresponding tidal force amounts to 1% of the internal binding force (Athanassoula 1984; Byrd & Howard 1992), which corresponds to a tidal strength of $Q = -2$. Obviously, J0848+1644 has $Q_{\rm LSS}$ (or $Q_{\rm Local}$) more than three orders of magnitude lower (or higher) than this level. That means this triplet has an extremely weak external influence from the LSS environment, but in contrast, has very strong internal connection among its members.

Additionally, the dimensionless crossing time $H_0 t_c$ is the ratio of the crossing time to the age of the Universe

Table 2 Global Physical Parameters of J0848+1644

Parameter	Unit	J0848+1644	Notes
S		2.48	Compactness parameter.
$\eta_{4,\mathrm{LSS}}$		–2.10	Projected number density.
Q_{LSS}		–5.70	Tidal force effect of LSS.
Q_{Local}		1.29	Tidal force effect in the triplet.
R_{H}	kpc	14.5	Projected harmonic radius.
$\sigma_{v_{\mathrm{r}}}$	km s^{-1}	58.1	Radial velocity dispersion.
$H_0 t_c$		0.032	Dimensionless crossing time.
$\log(M_{\mathrm{vir}}/M_{\odot})$		11.2	Virial mass. It may have a strong projection effect.
SFR	$M_{\odot}\cdot$ yr^{-1}	3.88	SFR
$\log(\mathrm{SFR}/M_{*})$		–10.51	sSFR

and is a convenient measurement of the dynamical stage of this system. For our triplet, $H_0 t_c = 0.035$ is similar to the median value of the O-sample (0.031) and not much longer than that of the K-sample (0.019). Obviously it is much less than 1, which indicates the sufficiency of dynamical evolution. The direct consequence of dynamical evolution is the member galaxies sinking into a deep gravitational well of the central region of the dark matter halo, which leads to a small velocity dispersion since it corresponds to a smaller amount of mass in the innermost part of the halo. The triplet J0848+1644 has a very small value of radial velocity dispersion. Although we have stated that it is probably due to the projection, it does not contradict the scenario of well evolution for this triplet.

The dynamical properties discussed above also reflect the physical features of three member galaxies. Overall, members of J0848+1644 are similar. They all have armless spherical shapes with similar luminosity and color. This similarity is regarded as more evidence of the long term co-evolution. All three members show significant but not strong activities indicative of current star formation, which means the interaction may continue to trigger star formation. It is worth mentioning that the colors and SFRs of these members are all near the boundary between two classifications of galaxies. They are a little bit bluer and a little bit more active than non-star-forming galaxies. We are not sure if this phenomenon is common for those very compact systems at their final stage, or it is just an individual case for J0848+1644. So, it is essential to find more examples of extremely compact triplets for future research.

4.2 Importance of Spectroscopic Redshifts

According to the spectroscopic observation taken with the BFOSC, which is mounted on the 2.16 m telescope, J0848+1644 is undoubtedly confirmed to be a bounded system, since the differences in z_{spec} of its members are much less than the typical radial velocity dispersions of triplet systems. The reasons why it was missed in previous samples, e.g. the O-sample and the A-sample that were all based on the SDSS, are the problem of fiber collision and the relatively large uncertainties in the z_{phot} measurements. These two factors are both related to the compactness of this triplet. Thus, there is a consequential question of whether these factors will seriously influence the study of few body systems.

The problem of fiber collision is common in many redshift surveys using fiber spectroscopy. Taking the minimum fiber separation of SDSS ($55''$) as a typical angular distance, even for low redshift galaxies ($z \sim 0.1$), the closet pairs of galaxies that can be observed in the same survey plate should have a distance larger than 100 kpc. So, usually we cannot find and identify a compact few body system by only using data from one scan of a fiber spectroscopic survey (see Shen et al. 2015). This is why O'Mill et al. (2012) use z_{phot} in their search for triplets. However, even taking the most accurate measurements of z_{phot} involves uncertainties of at least 5%, which lead to a difference of $1500\ \mathrm{km\ s^{-1}}$ in radial velocities at $z \sim 0.1$ and therefore is much larger than the typical velocity dispersion of poor galaxy groups. Furthermore, considering the neighboring effects in the photometric measurements (Section 2.2), like in J0848+1644, the uncertainties of radial velocity from z_{phot} are even larger.

For all of the above reasons, we believe that there is a significant fraction of compact triplets of galaxies that has not yet been identified in current samples. Such a compact system is still very rare, and we need to find more for further study.

The discovery and identification of the triplet J0848+1644 also demonstrates that it is really important to carry out a supplemental survey for current major galaxy redshift surveys, such as LAMOST, at least in the research field of compact few body systems (Shen et al. 2015). Fortunately, LAMOST has provided a good opportunity to undertake such a project. Although the LAMOST spectrum of galaxy C we used here is noisier than most ($\sim$92%) DR1 spectra, it still provides some vital information for our work, especially the obvious Hα emission line which provides a reliable redshift rather than z_{phot}.

It is not easy to estimate how many compact triplet systems could be found before we have a complete z_{spec} sample. However, as a comparison, we only used z_{phot} to search for triplets in the A-sample though they all have z_{spec} measurements, and found that more than 60% of the real triplets will be missed. This result strongly implies that a considerable amount of compact triplets will be found after some effective supplemental surveys.

5 SUMMARY

We summarize the main results of this work as follows.

(1) The LAMOST spectral survey, which supplies new spectroscopic measurements to the main sample galaxies without redshifts in SDSS due to the fiber collision, found indications of a possible triplet, J0848+1644. It is further confirmed to be a real triplet by the follow-up spectroscopic observation of the BFOSC mounted on the 2.16 m telescope at Xinglong Station of NAOC.

(2) We surmised that J0848+1644 is an extremely compact isolated triplet, with an aligned configuration and very small radial velocity dispersion. The member galaxies of this triplet have similar properties in terms of their shapes, colors and SFRs. It gives an additional example of compact triplets, which are supposed to be a co-evolved system rather than a hierarchically forming structure.

(3) Compact systems like J0848+1644, e.g. close pairs or poor groups, are difficult to compile by a redshift survey based on fiber spectroscopy or using the current photometric redshift techniques. The serendipitous discovery of J0848+1644 shows the importance of future projects aiming at conducting major redshift sky surveys like the LAMOST complementary galaxy survey (Shen et al. 2015).

Acknowledgements We sincerely thank the anonymous referee whose suggestions greatly helped us improve this paper. We are also grateful to the kind staff at the Xinglong 2.16 m telescope for their support during the observations. This work is supported by the 973 Program (Grant No. 2014CB845705), "Strategic Priority Research Program The Emergence of Cosmological Structures" of the Chinese Academy of Sciences (Grant No. XDB09030200) and the National Natural Science Foundation of China (Nos. 11390373, 11573050 and 11433003). This work is also supported by the Science Foundation of Shanghai (No. 16ZR1442100). Funding for the creation and distribution of the SDSS archive has been provided by the Alfred P. Sloan Foundation, the participating institutions, NASA, the National Science Foundation, the US Department of Energy, the Japanese Monbukagakusho and the Max Plank Society. The SDSS website is *http://www.sdss.org*. SDSS is managed by the Astrophysical Research Consortium for the participating institutions. The Large Sky Area Multi-Object Fiber Spectroscopic Telescope (LAMOST, now called the Guo Shou Jing Telescope) is a National Major Scientific Project built by the Chinese Academy of Sciences. Funding for the project has been provided by the National Development and Reform Commission. LAMOST is operated and managed by National Astronomical Observatories, Chinese Academy of Sciences.

References

Abazajian, K. N., Adelman-McCarthy, J. K., Agüeros, M. A., et al. 2009, ApJS, 182, 543

Aceves, H. 2001, MNRAS, 326, 1412

Agekyan, T. A., & Anosova, Z. P. 1968, Soviet Ast., 11, 1006

Anosova, Z. P., Kiseleva, L. G., Orlov, V. V., & Chernin, A. D. 1992, Soviet Ast., 36, 231

Argudo-Fernández, M., Verley, S., Bergond, G., et al. 2014, A&A, 564, A94

Argudo-Fernández, M., Verley, S., Bergond, G., et al. 2015, A&A, 578, A110

Athanassoula, E. 1984, Phys. Rep., 114, 321

Bell, E. F., McIntosh, D. H., Katz, N., & Weinberg, M. D. 2003, ApJS, 149, 289

Byrd, G. G., & Howard, S. 1992, AJ, 103, 1089

Chernin, A. D., & Mikkola, S. 1991, MNRAS, 253, 153

Cui, X.-Q., Zhao, Y.-H., Chu, Y.-Q., et al. 2012, RAA (Research in Astronomy and Astrophysics), 12, 1197

Duplancic, F., Alonso, S., Lambas, D. G., & O'Mill, A. L. 2015, MNRAS, 447, 1399

Duplancic, F., O'Mill, A. L., Lambas, D. G., Sodré, L., & Alonso, S. 2013, MNRAS, 433, 3547

Gómez, P. L., Nichol, R. C., Miller, C. J., et al. 2003, ApJ, 584, 210

Karachentsev, I. D. 1990, 3098, NASA Conference Publication, ed. J. W. Sulentic, W. C. Keel, & C. M. Telesco

Karachentsev, I. D., & Karachentseva, V. E. 1981, Astrofizika, 17, 5

Karachentsev, V. E., Karachentsev, I. D., & Lebedev, V. S. 1988, Astrofizicheskie Issledovaniia Izvestiya Spetsial'noj Astrofizicheskoj Observatorii, 26, 37

Karachentseva, V. E., & Karachentsev, I. D. 1982, Astrofizika, 18, 5

Karachentseva, V. E., & Karachentsev, I. D. 1983, Astrofizika, 19, 613

Karachentseva, V. E., & Karachentsev, I. D. 2000, Astronomy Reports, 44, 501

Karachentseva, V. E., Karachentsev, I. D., & Shcherbanovsky, A. L. 1979, Astrofizicheskie Issledovaniia Izvestiya Spetsial'noj Astrofizicheskoj Observatorii, 11, 3

Kennicutt, Jr., R. C. 1992, ApJ, 388, 310

Kennicutt, Jr., R. C. 1998, ARA&A, 36, 189

Luo, A.-L., Zhao, Y.-H., Zhao, G., et al. 2015, RAA (Research in Astronomy and Astrophysics), 15, 1095

O'Mill, A. L., Duplancic, F., García Lambas, D., Valotto, C., & Sodré, L. 2012, MNRAS, 421, 1897

Patton, D. R., Ellison, S. L., Simard, L., McConnachie, A. W., & Mendel, J. T. 2011, MNRAS, 412, 591

Peng, C. Y., Ho, L. C., Impey, C. D., & Rix, H.-W. 2002, AJ, 124, 266

Shen, S., Argudo-Fernández, M., Chen, L., et al. 2016, RAA (Research in Astronomy and Astrophysics), 16, 7

Stoughton, C., Lupton, R. H., Bernardi, M., et al. 2002, AJ, 123, 485

Zheng, J.-Q., Valtonen, M. J., & Chernin, A. D. 1993, AJ, 105, 2047

New Astronomy 46 (2016) 15–20

Contents lists available at ScienceDirect

New Astronomy

journal homepage: www.elsevier.com/locate/newast

Photometric study of the eclipsing binary GR Bootis

Z.L. Zhang[a], Y.P. Zhang[a], J.N. Fu[a,*], H.F. Xue[a]

Department of Astronomy, Beijing Normal University, Beijing 100875, China

HIGHLIGHTS

- We present time-series CCD photometry and low-resolution spectra for the eclipsing binary GR Boo.
- We analyze the variations of the orbital period and determine a new ephemeris formula.
- We firstly perform photometric analysis of GR Boo using the W-D program.
- The evolutionary status and physical nature of GR Boo are briefly discussed.

ARTICLE INFO

Article history:
Received 28 September 2015
Revised 8 November 2015
Accepted 12 November 2015
Available online 3 December 2015

Communicated by E.P.J van den Heuvel

Keywords:
Stars:binaries:close
Stars:binaries:eclipsing
Stars:individual (GR Boo)

ABSTRACT

We present CCD photometry and low-resolution spectra of the eclipsing binary GR Boo. A new ephemeris is determined based on all the available times of the minimum light. The period analysis reveals that the orbital period is decreasing with a rate of $dP/dt = -2.05 \times 10^{-10} d\ yr^{-1}$. A photometric analysis for the obtained light curves is performed with the Wilson–Devinney Differential Correction program for the first time. The photometric solutions confirm the W UMa-type nature of the binary system. The mass ratio turns out to be $q = 0.985 \pm 0.001$. The evolutionary status and physical nature of the binary system are briefly discussed.

1. Introduction

GR Boo was found in the ROTSE survey project by Akerlof et al. (2000) and identified as W UMa type eclipsing binary. Based on the survey data, Blattler and Diethelm (2001) provided light curves of GR Boo for the first time, and gave the linear epoch formula,

$$Min.I(HJD) = 2,451,996.5840 + 0^d.376670 \times E$$

Woźniak et al. (2004) compiled the NSVS catalog based on the ROTSE survey, in which GR Boo is number NSVS 7788990, and gave the light curve of GR Boo. Gettel et al. (2006) compiled 1022 contact binaries which were found in the ROTSE survey project into the catalog GGM2006, in which GR Boo is numbered as GGM2006 7788989. The parameters of GR Boo were given as : the period of 0.376675 days, the dimmest average magnitude in V band of 11.891 mag, the amplitude of variation of 0.439 mag, the absolute V magnitude of 4.462 mag ,the distance of 253 pc. Hoffman et al. (2009) derived the color index and a period of 0.37672 days based on the NSVS catalog. Pi et al. (2013) calculated an updated ephemeris and the change rate of the orbital period of GR Boo, and gave the new linear and quadratic ephemerides:

$$\begin{aligned} Min.I(HJD) &= 2,451,996.5849(\pm 0.0005) \\ &\quad + 0^d.37666986(\pm 0.00000008) \times E \\ Min.I(HJD) &= 2,451,996.5838(\pm 0.0003) \\ &\quad + 0^d.376671(\pm 0.000001) \times E \\ &\quad - 1^d.2(\pm 0.1) \times 10^{-10} \times E^2 \end{aligned}$$

However, no photoelectric study of the binary system has been available. The physical nature of the star system is not known. In order to get the photometric orbit solution, and further analyze the period change of this binary system, CCD photometric observations were carried out from 2011 to 2015. Light curves in V and R bands and new minimum times were obtained. In addition, we also obtained a low resolution spectrum of this eclipsing binary. In this paper, we present our study of GR Boo based on these observations.

2. Observations and data reduction

The CCD photometric observations were carried out using three telescopes from 2011 to 2015. Two nights of data in V and R bands were obtained with the 85 cm telescope located at the Xinglong station of the National Astronomical Observatories of China(NAOC), which was equipped with a *PI* 1024 × 1024 CCD camera at the main

---

[*] Corresponding author. Tel.: +8618910779526; fax: +8601058806319.
E-mail address: jnfu@bnu.edu.cn (J.N. Fu).

http://dx.doi.org/10.1016/j.newast.2015.11.002

Table 1
Coordinates and brightness in *V* of the variable, comparison and check stars.

Star	Name	R.A.(J2000)	DEC.(J2000)	m_V
Obj	GR Boo	14 59 54.54	+25 54 33.62	11.51
Comp	GSC 02020–00659	14 59 40.45	+25 51 44.90	10.96
Check	GSC 02020–00910	15 00 19.54	+25 49 48.90	12.32

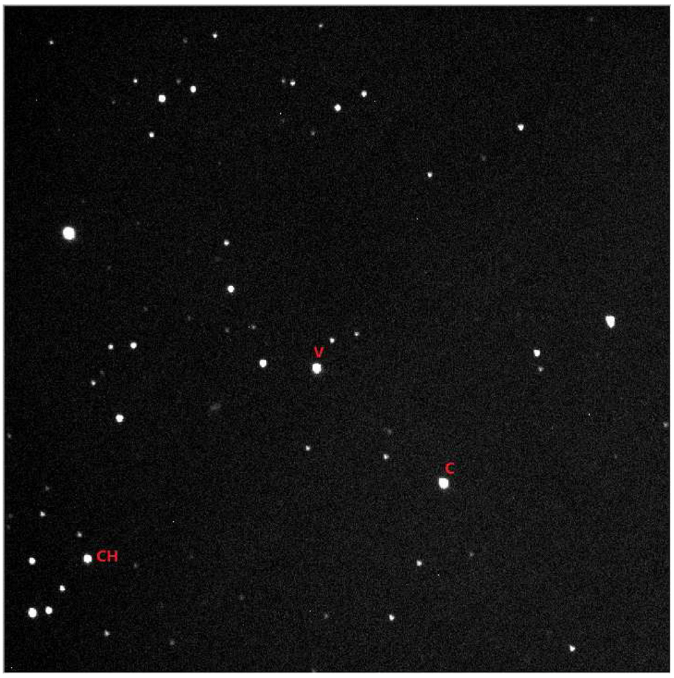

Fig. 1. A CCD image of GR Boo in V observed with the 85 cm telescope of Xinglong station. GR Boo, the comparison star and the check star are indicated.

focus, based on Zhou et al. (2009), corresponding to an image scale of 0.96 arcsec per pixel. The other three nights of data in *V* and *R* bands were obtained with the 60 cm telescope located at Xinglong station. The image scale is 1.056 arcsec per pixel. The last two nights of data in *V* and *R* bands and one night of data in *B*, *V*, *R* bands were collected with the 60 cm telescope located at the Yunnan Astronomical Obseratory (YNAO), equipped with a *DW*436 2048 × 2048 CCD camera, with an image scale of 0.37 arcsec per pixel. We selected GSC 02020–00659 and GSC 02020–00910 as the comparison star and check star, respectively. The coordinates and brightness in *V* of GR Boo, the comparison star and the check star are listed in Table 1. Fig. 1 shows a CCD image of GR Boo in *V* with the 85 cm telescope. Table 2 lists the information of the new photometric observations for GR Boo. The preliminary processing of the CCD frames (bias substraction and flatfield correction) was performed with the standard routines of CCDPROC in the IRAF software. Photometry was made using the DAOPHOT package. We applied a series of apertures to make the photometry. The best aperture was determined according to the least of the deviations of the magnitude differences between the comparison star and the check star.

Spectroscopic observations for GR Boo were made on May 14, 2012 using the 2.16m telescope located at Xinglong station. The BFOSC low-dispersion spectrometer was used during the observations. The used grating was *G*7 with a slit width of 1.8” and a line dispersion of 95 *x*00*C*5; /*mm*. The center wavelength was at 530 nm with the wavelength range of 380–680 nm. The data were reduced with IRAF and the obtained low-resolution spectrum is shown in Fig. 2. Comparing with the spectrum flow library from Pickles (1998), the spectral type of GR Boo was preliminarily identified as $G3V - G4V$.

Table 2
Photometric observations for GR Boo.YN60 = Yunnan Astronomical Observatory 60 cm telescope, XL60 = Xinglong Astronomical Observatory 60 cm telescope, XL85 = Xinglong Astronomical Observatory 85 cm telescope.

Date	Telescope	Filter	Frames	Hours
2011 May 07	YN60	V	80	4.4
2011 May 07	YN60	R	80	4.4
2011 May 15	XL60	V	155	4.9
2011 May 15	XL60	R	154	4.9
2012 Feb 13	YN60	V	65	4.9
2012 Feb 13	YN60	R	65	4.9
2013 May 03	XL60	V	218	7.6
2013 May 03	XL60	R	218	7.6
2013 May 06	XL60	V	122	4.9
2013 May 06	XL60	R	122	4.9
2013 Jun 12	XL85	V	147	3.3
2013 Jun 12	XL85	R	147	3.3
2013 Jun 13	XL85	V	263	5.8
2013 Jun 13	XL85	R	263	5.8
2015 Jan 27	YN60	V	133	2.0
2015 Jan 27	YN60	R	132	2.0
2015 Jan 27	YN60	B	132	2.0

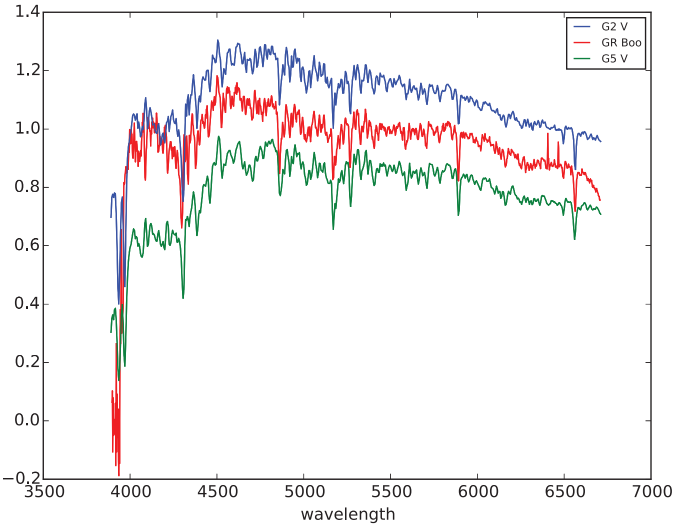

Fig. 2. The red: The spectrum of GR Boo, observed with the 2.16 m telescope of Xinglong station. The blue and green line are G2V and G5V from the Pickles (1998). (For interpretation of the references to color in this figure legend, the reader is referred to the web version of this article).

3. Period changes

8 new minimum times were obtained in total from the obtained light curves. We also collected minimum times from the literature since 1999. Table 3 lists all the minimum times we have obtained, with which one can perform period analysis of the system. Using the method of least square fitting, we determined the new linear and quadratic ephemerides, as:

$$Min.I(HJD) = 2,451,996.5462(\pm 0.0003) + 0^d.37666954(\pm 0.00000004) \times E \quad (1)$$

$$Min.I(HJD) = 2,451,996.5838(\pm 0.0002) + 0^d.37666954(\pm 0.00000006) \times E - 1^d.126(\pm 0.005) \times 10^{-10} \times E^2 \quad (2)$$

The $O - C$ residuals for all the times of minimum light according to the linear and quadratic ephemerides were calculated and listed in Table 3. According to the quadratic ephemeris, we plot the $O - C$

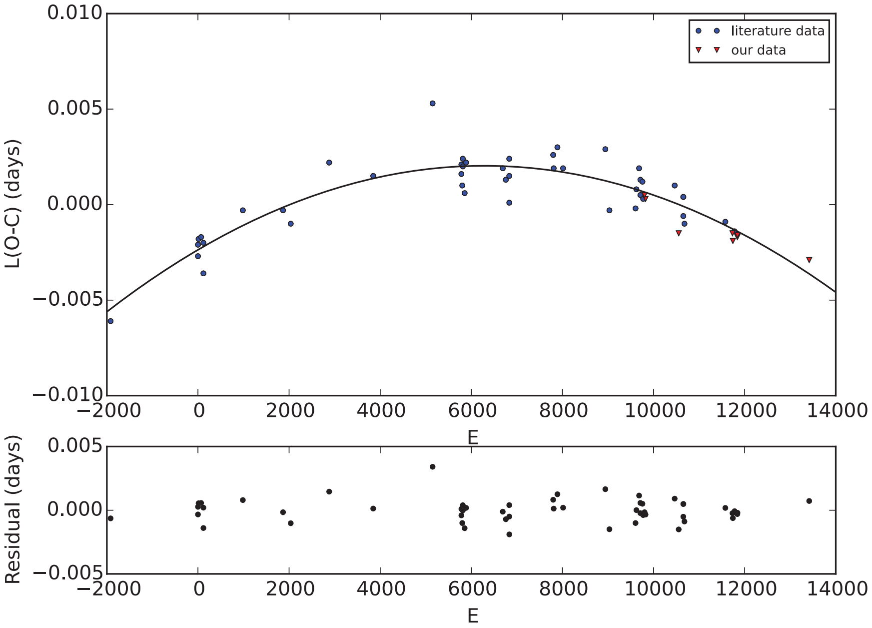

Fig. 3. The $O-C$ diagram of GR Boo. Filled circles represent the data collected from the literature, and the triangles represent the data from our observations. The quadratic fit is illustrated by the solid curve. The lower panel shows the residuals as the quadratic fit as Eq. (2).

diagram of GR Boo in Fig. 3, where the data from the literature are plotted as circles, our own data are plotted as triangles. The residuals of the fit are shown in the lower panel of Fig. 3. The scatter of the residuals is smaller than 0.0035 d. Hence, one finds that the orbital period of GR Boo appears to be decreases during last decade. We determined the rate of the period change of the binary system as $dP/dE = -1.12 \times 10^{-10} d\ cycle^{-1}$ or $dP/dt = -2.05 \times 10^{-10} d\ yr^{-1}$ from the quadratic ephemerides. The period decrease indicates mass transfer from the more massive component to the less massive component.

4. Photometric solution

In order to derive the photometric solution of GR Boo, we used the 2007 version of the WD code (Van Hamme and Wilson (2007);Wilson and Devinney (1971);Wilson (1979);Wilson (1990);Wilson (1994)) to analyze the data we observed in 2013. The photometric accuracy of the four nights data are 0.0033, 0.0071, 0.0060, 0.0103 in R band and 0.0028, 0.0050, 0.0063, 0.0113 in V band, respectively. With the derived linear ephemeris Eq. (1), we calculated the phases of all the measurements, and plotted the light curves in the form of differential magnitude versus phase in V and R band, respectively, in Fig. 4.

As can be seen in Fig. 4, the nearly equal minima reveal that GR Boo belongs to the W UMa type. The depths of the primary eclipse are 0.433 *mag* and 0.464 *mag*, in V and R band, respectively, which are slightly deeper than the depths of the secondary eclipses. With the complete light curves in V, R band, the photometric solution of the system was computed by means of the WD code. According to the spectral type determined from the spectrum, we take the effective temperature of the primary component(the star eclipsed at the primary minimum) of $T_1 = 5770$ K; the gravity-darkening coefficients of $g_1 = g_2 = 0.32$ for the two stars following Lucy (1967), and the bolometric albedos of $A_1 = A_2 = 0.5$ from Ruciński (1969). The initial bolometric (X_1, X_2, Y_1, Y_2) and monochromatic (x_1, x_2, y_1, y_1) limb-darkening coefficients of the components were adopted from van Hamme (1993). The adjustable parameters are listed as follows: the phase shift $x00F8;_0$, the orbital inclination i, the mean temperature of Star 2 T_2, the surface potentials Ω_1 and Ω_2 for both components, and the monochromatic luminosities of Star 1 L_{1V} and L_{1R} in V and R, respectively, and the mass ratio $q = m_2/m_1$.

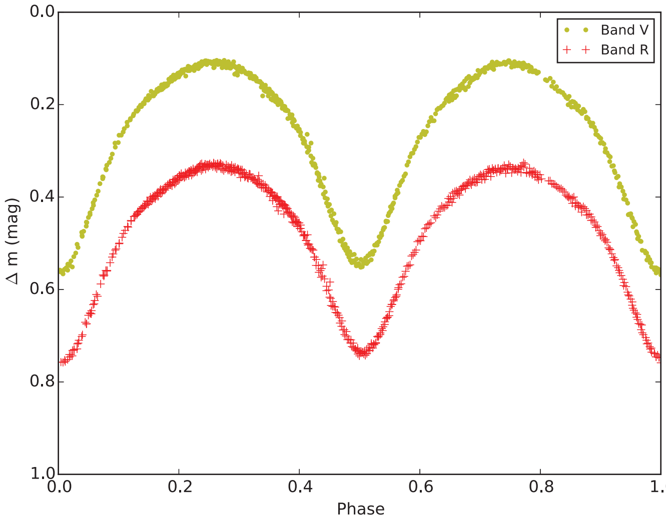

Fig. 4. Phase diagram of GR Boo in the V and R in 2013. The measurements are combined according to the linear ephemeris.

Although the mass ratio of the two component stars q is a sensitive parameter, we have no information of it neither from photometry nor spectroscopy. Hence, a set of test solutions has been made to approximate this value. Taking into account characteristics of the light curves, we assumed the q values ranging between 0.2 and 2 ,with an interval step of 0.1. As GR Boo is a contact system from the light curves, the dc program was run with the trial mass ratio in mode 3, and a converged solution was then reached. After an iteration process, we got a series of q values and the residuals, among which the smallest residual is discovered when the q value is around 0.9. Fig. 5 shows the sum of weighted residuals versus the value of the mass ratio q. Then the dc program was run with mass ratio q varying slightly around 0.9 with the smaller steps. Finally we obtained the best-fitting result at $q = 0.985 \pm 0.001$. The photometrical solution is given in Table 4. The theoretical light curves in V and R bands are plotted in

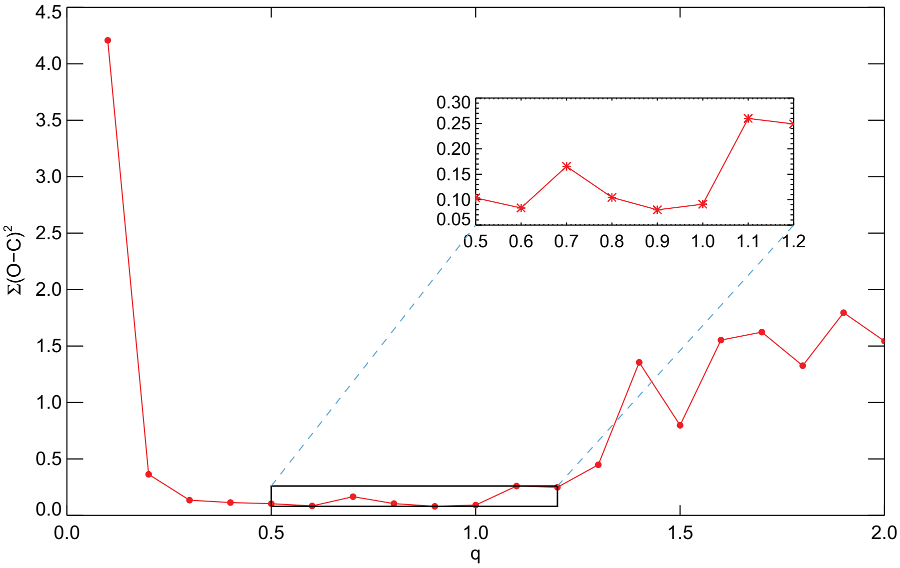

Fig. 5. The q values from 0 to 2.0, sum of weighted residuals $\sum(O-C)^2$ versus the mass ratio q, up right panel: Zoom-in of the inset rectangle domains.

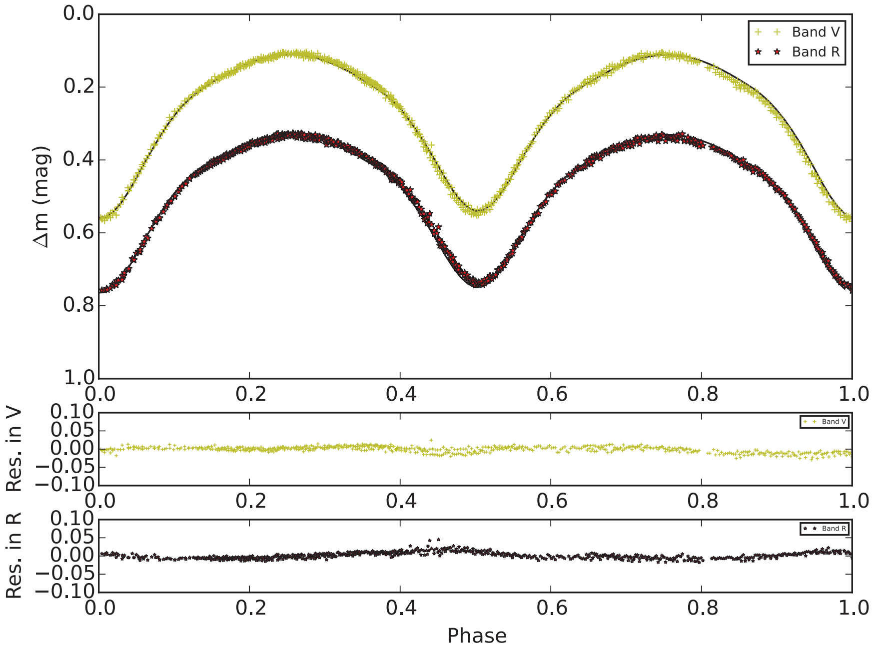

Fig. 6. Upper panel: The observed light curves in V, R bands (the circle dots) and theoretical light curves (the solid lines). Lower panel: the residual diagram.

the upper panel of Fig. 6, and the residuals are plotted in the lower panel.

5. Conclusions and discussion

According to the result of the period analysis and the photometric solutions, we arrived at following conclusions:

1. Based on Pi's research on the orbital period analysis of GR Boo, we added some new times of minimum light, and derived the new linear and quadratic ephemeris. It turns out that the orbital period of the binary system is decreasing at a rate of $dP/dE = -1.12 \times 10^{-10} d\ cycle^{-1}$ or $dP/dt = -2.05 \times 10^{-10} d\ yr^{-1}$ during last decades. One possible explanation for this phenomenon is that there is mass transfers from the more massive component to the less massive component. However, with all the available data we collected, it is not possible to identify whether there is any influence from the third body. More observations are needed to confirm this.
2. With the Wilson-Devinney code, a photometric solution of GR Boo was obtained for the first time. We thus confirm that GR Boo belongs to the W UMa-type. The temperature and the mass of the primary component are slightly higher than the values of the secondary, which indicates that GR Boo is an A-type contact system. The two components both fill in the Roche lobes.
3. A no-spot synthesis of the theoretical light curves of GR Boo fits the observed light curves which reveals that there was no spot on the system. This suggests that the system might be in a quiet phase of the magnetic activity as a Sun-like star. The decreasing period change does not look related with the conclusion of magnetic activity, which agrees with Yan-Ping et al. (2015), as well as Liao and Qian (2010). To examine this hypothesis, more observations are needed.

Table 3
Times of light minima of GR Boo and residuals calculated according to the new ephemerides. E = Cycle number.

HJD (2,400,000+)	E	$(O-C)_1$ (d)	$(O-C)_2$ (d)	Ref.
51,274.1280	−1918.0	−0.0061	−0.0005	1
51,996.3952	−0.5	−0.0027	−0.0003	2
51,996.5841	0.0	−0.0021	0.0003	2
52,001.4811	13.0	−0.0018	0.0006	2
52,022.5747	69.0	−0.0017	0.0006	2
52,041.4079	119.0	−0.0020	0.0002	2
52,041.5946	119.5	−0.0036	−0.0014	2
52,367.4171	984.5	−0.0003	0.0008	2
52,699.8280	1867.0	−0.0003	−0.0001	1
52,763.4844	2036.0	−0.0010	−0.0010	3
53,081.3967	2880.0	0.0022	0.0015	4
53,445.4471	3846.5	0.0015	0.0001	5
53,936.4397	5150.0	0.0053	0.0034	6
54,174.4911	5782.0	0.0016	−0.0004	7
54,174.4916	5882.0	0.0021	0.0001	6
54,181.8356	5801.5	0.0010	−0.0010	8
54,186.3570	5813.5	0.0024	0.0004	9
54,186.5450	5814.0	0.0020	0.0001	9
54,201.4220	5853.5	0.0006	−0.0014	9
54,213.4770	5885.5	0.0022	0.0002	9
54,516.5074	6690.0	0.0019	−0.0001	10
54,541.9320	6757.5	0.0013	−0.0007	11
54,570.3716	6833.0	0.0024	0.0004	12
54,570.5591	6833.5	0.0015	−0.0004	12
54,570.7460	6834.0	0.0001	−0.0019	23
54,933.4813	7797.0	0.0026	0.0009	10
54,937.8123	7808.5	0.0019	0.0002	13
54,968.5119	7890.0	0.0030	0.0013	10
55,015.4062	8014.5	0.0019	0.0002	14
55,364.7682	8942.0	0.0029	0.0017	15
55,398.4769	9031.5	−0.0003	−0.0015	16
55,614.4970	9605.0	−0.0002	−0.0010	17
55,621.6547	9624.0	0.0008	0	23
55,643.8793	9683.0	0.0019	0.0012	18
55,654.4247	9711.0	0.0005	−0.0001	19
55,654.6138	9711.5	0.0013	0.0006	19
55,671.5638	9756.5	0.0012	0.0005	23
55,677.4013	9772.0	0.0003	−0.0003	17
55,689.0783(9)	9803.0	0.0005	−0.0001	24
55,697.1765(1)	9824.5	0.0004	−0.0001	24
55,938.0573	10464.0	0.0010	0.0009	20
55,971.3898(4)	10552.5	−0.0016	−0.0016	24
56,009.4346	10653.5	−0.0006	−0.0005	21
56,009.6239	10654.0	0.0004	0.0005	21
56,009.6239	10654.0	0.0004	0.0005	23
56,018.8509	10678.5	−0.0010	−0.0009	22
56,356.9120	11576.0	−0.0009	0.0003	20
56,416.0485(1)	11733.0	−0.0015	−0.0001	24
56,419.0614(1)	11741.0	−0.0019	−0.0006	24
56,433.3754	11779.0	−0.0014	0	23
56,456.1636(1)	11839.5	−0.0017	−0.0002	24
56,457.1054(2)	11842.0	−0.0016	−0.0001	24
57,050.3586(3)	13417.0	−0.0029	0.0008	24

Notes. 1. Paschke and Brat (2006) 2. Blattler and Diethelm (2001) 3. Bulut et al. (2001) 4. Nomen-Torres and Escola-Sirisi (2001) 5. Simon et al. (2001) 6. Henden and Landolt (2001) 7. Hubscher et al. (2009a) 8. Nelson (2007) 9. Moschner et al. (2001) 10. Hubscher et al. (2010) 11. Nelson (2009) 12. Hubscher et al. (2009b) 13. Nelson (2010) 14. Diethelm (2010a) 15. Diethelm (2010b) 16. Diethelm (2011a) 17. Hubscher and Lehmann (2012) 18. Diethelm (2011b) 19. Hubscher et al. (2012) 23. Hoňková et al. (2013). 17. Hubscher and Lehmann (2012) 19. Hubscher et al. (2012) 20. Nelson (2013) 21. Hubscher et al. (2013) 22. Diethelm (2012) 23. Hoňková et al. (2013) 24. this study.

Table 4
Photometric solution of GR Boo.

Parameter	Best-fit value	Error
$q = m_2/m_1$	0.985	0.001
$T_1(K)$	5770^a	
$T_2(K)$	5696	±9
$g_1 = g_2$	0.32^a	
i	70.43	±0.07
$A_1 = A_2$	0.50^a	
$\Omega_1 = \Omega_2$	3.726	±0.004
$X_1 = X_2(bolo)$	0.370^a	
$Y_1 = Y_2(bolo)$	0.303^a	
$x_1 = x_2$(V)	0.249^a	
$x_1 = x_2$(R)	0.122^a	
$y_1 = y_2$(V)	0.590^a	
$y_1 = y_2$(R)	0.633^a	
$L_1/(L_1+L_2)(V)$	0.520	±0.001
$L_1/(L_1+L_2)(R)$	0.520	±0.001
r_1(pole)	0.3572	±0.0005
r_1(side)	0.3752	±0.0164
r_1(back)	0.4060	±0.0009
r_2(pole)	0.3547	±0.0005
r_2(side)	0.3724	±0.0006
r_2(back)	0.4033	±0.0009
$\sum(O-C)^2$	0.083	

Notes. ^{a}Assumed.

Acknowledgment

This work is supported by the Joint Fund of Astronomy of National Natural Science Foundation of China (NSFC) and Chinese Academy of Sciences through the Grant U1231202, and the National Basic Research Program of China (973 Program 2014CB845700 and 2013CB834900) and the Fundamental Research Funds for the Central Universities. We acknowledge the support of the staff of the Xinglong 2.16m telescope. This work was partially supported by the Open Project Program of the Key Laboratory of Optical Astronomy, NAOC, CAS. We are grateful to Dr. Nami Mowlavi and all the anonymous referee who has offered useful suggestions to improve the paper.

References

Akerlof, C., Amrose, S., Balsano, R., et al., 2000. AJ 119, 1901. doi:10.1086/301321. astro-ph/0001388.
Blattler, E., Diethelm, R., 2001. IBVS 5125, 1.
Bulut, I., Demircan, O., Erdem, A., et al., 2001. IBVS 5129, 1.
Diethelm, R., 2010. IBVS 5920, 1.
Diethelm, R., 2010. IBVS 5945, 1.
Diethelm, R., 2011. IBVS 5960, 1.
Diethelm, R., 2011. IBVS 5992, 1.
Diethelm, R., 2012. IBVS 6029, 1.
Gettel, S.J., Geske, M.T., McKay, T.A., 2006. AJ 131, 621. doi:10.1086/498016. astro-ph/0509819.
Henden, A.A., Landolt, A.U., 2001. IBVS 5166, 1.
Hoffman, D.I., Harrison, T.E., McNamara, B.J., 2009. AJ 138, 466. doi:10.1088/0004-6256/138/2/466.
Hoňková, K., Juryšek, J., Lehký, M., et al., 2013. OEJV 160, 1.
Hubscher, J., Braune, W., Lehmann, P.B., 2013. IBVS 6048, 1.
Hubscher, J., Lehmann, P.B., 2012. IBVS 6026, 1.
Hubscher, J., Lehmann, P.B., Monninger, G., et al., 2010. IBVS 5918, 1.
Hubscher, J., Lehmann, P.B., Walter, F., 2012. IBVS 6010, 1.
Hubscher, J., Steinbach, H.-M., Walter, F., 2009. IBVS 5889, 1.
Hubscher, J., Steinbach, H.-M., Walter, F., 2009. IBVS 5874, 1.
Liao, W.-P., Qian, S.-B., 2010. MNRAS 405, 1930. doi:10.1111/j.1365-2966.2010.16584.x. 1007.1125.
Lucy, L.B., 1967. ZA 65, 89.
Moschner, W., Bernhard, K., Frank, P., 2001. IBVS 5186, 1.
Nelson, R.H., 2007. IBVS 5760, 1.
Nelson, R.H., 2009. IBVS 5875, 1.
Nelson, R.H., 2010. IBVS 5929, 1.
Nelson, R.H., 2013. IBVS 6050, 1.
Nomen-Torres, J., Escola-Sirisi, E., 2001. IBVS 5130, 1.
Paschke, A., Brat, L., 2006. OEJV 23, 13.
Pi, Q.-F., Zhang, L.-Y., Chen, C.-Q., 2013. J. Guizhou Univ. (Nat. Sci.) 06, 35. doi:10.3969/j.issn.1000-5269.2013.06.009.
Pickles, A.J., 1998. PSAP 110, 863. doi:10.1086/316197.
Ruciński, S.M., 1969. AcA 19, 245.
Simon, V., Sobotka, P., Marek, P., et al., 2001. IBVS 5131, 1.
van Hamme, W., 1993. AJ 106, 2096. doi:10.1086/116788.
Van Hamme, W., Wilson, R.E., 2007. ApJ 661, 1129. doi:10.1086/517870.
Wilson, R.E., 1979. ApJ 234, 1054. doi:10.1086/157588.
Wilson, R.E., 1990. ApJ 356, 613. doi:10.1086/168867.
Wilson, R.E., 1994. PASP 106, 921. doi:10.1086/133464.
Wilson, R.E., Devinney, E.J., 1971. ApJ 166, 605. doi:10.1086/150986.

Woźniak, P.R., Vestrand, W.T., Akerlof, C.W., Balsano, R., Bloch, J., Casperson, D., Fletcher, S., Gisler, G., Kehoe, R., Kinemuchi, K., Lee, B.C., Marshall, S., McGowan, K.E., McKay, T.A., Rykoff, E.S., Smith, D.A., Szymanski, J., Wren, J., 2004. AJ 127, 2436. doi:10.1086/382719. astro-ph/0401217.

Yan-Ping, Z., Ming-Dong, J., Xiao-Bin, Z., et al., 2015. ChA&A 39, 28. doi:10.1016/j.chinastron.2015.01.009.

Zhou, A.-Y., Jiang, X.-J., Zhang, Y.-P., et al., 2009. RAA 9, 349. doi:10.1088/1674-4527/9/3/010.

Star clusters and black holes in galaxies across cosmic time
Proceedings IAU Symposium No. 312, 2014
Y. Meiron, S. Li, F.-K. Liu & R. Spurzem, eds.

doi:10.1017/S1743921315007814

Spectroscopic study of formation, evolution and interaction of M31 and M33 with star clusters

Zhou Fan[1] **and Yanbin Yang**[2]

[1]Key Laboratory of Optical Astronomy, National Astronomical Observatories, Chinese Academy of Sciences, 20A Datun Road, Chaoyang Dist., Beijing, China
email: `zfan@bao.ac.cn`

[2]GEPI, Observatoire de Paris, CNRS, 5 Place Jules Janssen, Meudon F92195, France

Abstract. The recent studies show that the formation and evolution process of the nearby galaxies are still unclear. By using the Canada France Hawaii Telescope (CFHT) 3.6m telescope, the PanDAS shows complicated substructures (dwarf satellite galaxies, halo globular clusters, extended clusters, star streams, etc.) in the halo of M31 to ~ 150 kpc from the center of galaxy and M31-M33 interaction has been studied. In our work, we would like to investigate formation, evolution and interaction of M31 and M33, which are the nearest two spiral galaxies in Local Group. The star cluster systems of the two galaxies are good tracers to study the dynamics of the substructures and the interaction. Since 2010, the Xinglong 2.16m, Lijiang 2.4m and MMT 6.5m telescopes have been used for our spectroscopic observations. The radial velocities and Lick absorption-line indices can thus be measured with the spectroscopy and then ages, metallicities and masses of the star clusters can be fitted with the simple stellar population models. These parameters could be used as the input physical parameters for numerical simulations of M31-M33 interaction.

Keywords. galaxies: individual (M31) – galaxies: individual (M33) – galaxies: star clusters – globular clusters: general – star clusters: general

1. Introduction

From 2008 to 2011, the Pan-Andromeda Archaeological Survey (PanDAS), which covers > 300 deg^2 M31-M33 field with CFHT 3.6m Telescope, was conducted by McConnachie *et al.* (2009). The survey discovered several new stellar stream features surrounding M31 and M33, respectively. It was found that dozens of dwarf galaxies and halo star clusters are distributed to the outer halo ~ 150 kpc from the center of M31. Observational evidences indicated that the structures may be due to M33 orbits around M31. The M31-M33 interaction was suggested by HI observations previously. Since the star clusters are much brighter than stars, the halo star clusters are good tracers to study the dynamics of the interactions.

2. Observations and analysis

Since 2010, we have started to observe the spectroscopy of the star clusters in the halo of M31 with the red channel spectrograph of 6.5m MMT and BFOSC/OMR spectrograph of Xinglong 2.16m telescope. The star clusters of M31 were selected from RBC v.4 (http://www.bo.astro.it/M31; Galleti *et al.* 2004). The Lick absorption-line indices (see Worthey *et al.* 1994) of the spectroscopy were measured and fit with the stellar population model of Thomas *et al.* (2011), and then the ages, [Fe/H] and [α/Fe] can be derived, which provides the clues of the formation and evolution of the two galaxies. Meanwhile,

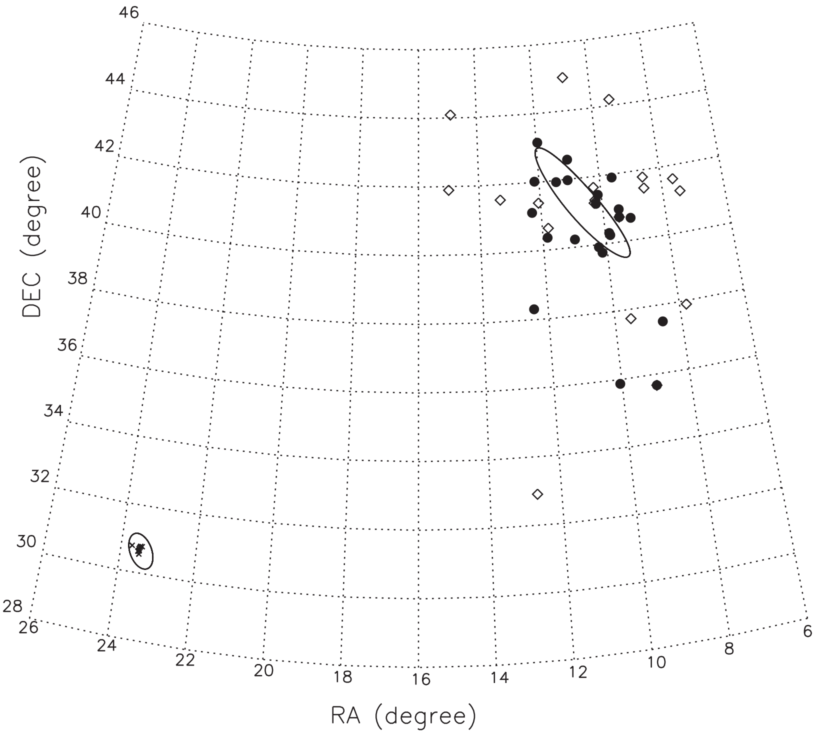

Figure 1. The distribution of star clusters that we have observed in M31 (larger ellipse) and M33 (smaller ellipse) field. The filled circles represent M31 star clusters observed with MMT; the open squares and crosses are star clusters of M31 and M33 observed with Xinglong 2.16m telescope, respectively.

the radial velocity V_r can be estimated by fitting the absorption lines, which can be used to study the dynamics of the star cluster system as well as for tracing the dynamics of M31-M33 interaction.

Figure 1 shows the distribution of star clusters that we have observed so far with MMT and Xinglong 2.16m telescope. The open squares represent the M31 clusters observed with Xinglong 2.16m telescope and analyzed in Fan *et al.* (2011) and Fan *et al.* (2012). The filled circles are M31 clusters observed with MMT and the crosses show M33 star clusters observed with BFOSC spectrograph of Xinglong 2.16m telescope in Nov. 2014.

In the future, more spectroscopic observations are planed to be conducted with Lijiang 2.4m, and Guoshoujing (LAMOST) telescopes. The sample will be enlarged and more informations will be derived for the numerical simulations of the interaction of M31 and M33 galaxies.

Acknowledgements

This research is supported by the National Natural Science Foundation of China Grant No. 11373003 and National Key Basic Research Program of China (973 Program) No. 2015CB857002.

References

Fan, Z., Huang, Y. F., Li, J. Z., Zhou, X., Ma, J., *et al.* 2011, *RAA*, 11, 1298
Fan, Z., Huang, Y. F., Li, J. Z., Zhou, X., Ma, J., & Zhao, Y. H. 2012, *RAA*, 12, 829
Galleti, S., Federici, L., Bellazzini, M., Fusi Pecci, F., & Macrina, S. 2004, *A&A*, 416, 917
McConnachie, A. W., *et al.* 2009, *Nature*, 461, 66
Perina, S., Cohen, J. G., Barmby, P., *et al.* 2010, *A&A*, 511, A23
Thomas, D., Maraston, C., & Johansson, J. 2011, *MNRAS*, 412, 2183
Worthey, G., Faber, S. M., Gonzalez, J. J., & Burstein, D. 1994, *ApJS*, 94, 687

From Interstellar Clouds to Star-Forming Galaxies:
Universal Processes?, E42, 1 of 2
Proceedings IAU Symposium No. 315, 2016
P. Jablonka, Ph. André, & F. van der Tak, eds.

doi:10.1017/S1743921316008036

Spectroscopic Observations of Hundreds of Star Formation Regions in M33

Xu Kong, Ning Hu and Fuzhen Cheng

CAS Key Laboratory for Research in Galaxies and Cosmology, Department of Astronomy,
University of Science and Technology of China, Hefei, Anhui 230026, China
email: `xkong@ustc.edu.cn`

Abstract. Star-formation regions in nearby galaxies provide an excellent laboratory to study star formation processes, evolution of massive stars and the properties of the surrounding interstellar medium. A wealth of information can be obtained from their spectral analysis of the emission lines and the stellar continuum. Considering these, we proposed a long-term project "Spectroscopic Observations of the Star Formation Regions in Nearby Galaxies". The primary goal of this project is to observe spectroscopy of star formation regions in 20 nearby galaxies, with the NAOC 2.16 m telescope and the Hectospec/MMT multifiber spectrograph. With the spectra of a large sample of star formation regions, combining multi-wavelength data from UV to IR, we can investigate, understand and quantify the dust extinction, star formation rate, metal abundance, and the two-dimensional distributions of stellar population properties of nearby galaxies. It will be important for a better understanding of galaxy formation. Here we report on the observations, data reduction, and analysis of the spectra of ~ 400 star formation regions in M33, via multifiber spectroscopy with Hectospec at the MMT.

Keywords. H II regions, galaxies: abundances, galaxies: individual (M33).

---

1. Introduction and Observation

The spatial-resolved spectroscopic data are very important for understanding the internal composition and kinematic characteristics of a galaxy, and therefore its formation, structure, and evolution. The IFU (Integral Field Unit) spectrograph is the most important tool for this kind of observations. Some systematic two-dimensional spectroscopic observations on galaxies were successively made recently, but most of these observations are limited on the central region of large galaxies or small galaxies, because the fields of view of most IFUs are relative small (Kong et al. 2014).

M33 (NGC 598) is one of the closest spiral galaxies of the Local Group. The proximity of M33, together with its large angular size (optical size $53' \times 83'$), and its intermediate inclination ($i = 53\,\mathrm{deg}$), allows detailed studies of its stellar populations and ionized nebulae. M33 is a galaxy rich in star formation regions (H II regions). Several catalogs of the M33 H II regions have been published. Their spectroscopy was obtained since the 1970s, however, most of them are small and inhomogeneous.

To obtain a large, homogeneous set of spectra for H II regions in M33, we have used the MMT/Hectospec, its has a wide field of view (1 degree diameter field) and large number of fibers (300 in total) for multi-object spectroscopy. The targets for the multi-object spectroscopy were selected from narrow-band Hα image. M33 has more than 400 H II regions, the spectroscopic data were acquired in Oct. 9 (M33–A, red), Oct. 12 (M33–B, green), and Oct. 15 (M33–C, blue), 2013, as shown in Figure 1. The exposure time of each is 5400 s. The MMT/Hectospecs 270 line mm^{-1} grating was used, which provides a dispersion of 1.2 Å/pixel. Our spectra cover the wavelength range of 3650–9150 Å at ~ 5 Å resolution.

2. Data Reduction and Implications

The spectra were reduced using the publicly available HSRED software (written by R. Cool). All observations were bias subtracted, overscan corrected, and trimmed. The science exposures were

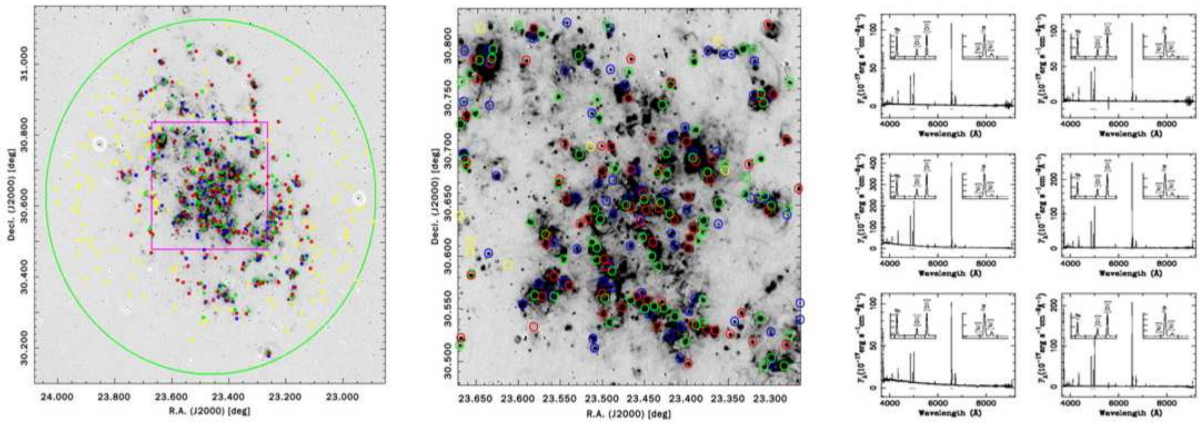

Figure 1. Left: Location of M33 H II regions and the sky background (yellow) observed with Hectospec, overlaid on the M33 Ha image. The green circle shows the Hectospec field. Middle: The M33 center region is expanded, most of bright H II regions were observed by MMT/Hectospec. Right: The example spectra of six star formation regions in M33.

flat fielded and combined together to eliminate cosmic rays, and the one-dimensional spectra were extracted and wavelength calibrated. In the right panel of Figure 1, as an example, we show the spectra of some H II regions. The emission-line fluxes were measured with the package SPLOT of IRAF.

With the spectra of a large sample of star formation regions, combining multi-wavelength image data from UV to IR, we can investigate, understand and quantify the dispersion of the IRX (the total-IR to UV flux ratio) $-\beta$ relation and gradients and physical properties of galaxies.

Based on multi-wavelength photometry data, many work have found that individual H II regions of nearby galaxies have a large dispersion in the IRX$-\beta$ diagram (Mao *et al.*2012). Considering there have simple star formation histories and have strong emissiom lines, H II regions in nearby galaxies are ideal targets to quantify the nature of the dispersion for galaxies in the IRX$-\beta$ diagram. Combining multi-wavelength data from UV to IR, we will investigate, understand and quantify the nature of the deviation from the starbursts IRX$-\beta$ correlation (Kong *et al.*2004). It will be important for a better understanding of the interaction of dust and radiation in dusty star-forming galaxies.

The spectra of those H II can also be used to study the radial metallicity gradients of galaxies (with much larger radius), calibrate metallicity estimation with different method (such as strong line method and T_e method), investigate the radial distribution of dust properties, stellar populations and star formation.

This study has used the observational time of the 2.16 m telescope at the Xinglong station of the National Astronomical Observatories of China, and the observational time of the MMT telescope obtained via the TAP program.

References

Kong, X., Charlot, S., Brinchmann, J., & Fall, S. M. 2004, *MNRAS*, 349, 769
Kong, X., Lin, L., Li, J.-r., *et al.* 2014, *ChA&A*, 38, 427
Mao, Y.-W., Kennicutt, R. C., Jr., Hao, C.-N., Kong, X., & Zhou, X. 2012, *ApJ*, 757, 52

中国科学院国家天文台
NATIONAL ASTRONOMICAL OBSERVATORIES
CHINESE ACADEMY OF SCIENCES

中国科学院光学天文重点实验室
Key Laboratory of Optical Astronomy, National Astronomical Observatories
Chinese Academy of Sciences

兴隆观测基地网站二维码　兴隆观测基地微信平台

编辑：任娟娟　翟　萌
赵　勇　范　舟
排版：任娟娟
封面摄影：陈颖为

中国科学院国家天文台兴隆观测基地
Xinglong Observatory
National Astronomical Observatories
Chinese Academy of Sciences
http://www.xinglong-naoc.org